Cranfield UNIVERSITY

CRANFIELD UNIVERSITY

STUART P. ANDREWS

MODELLING AND SIMULATION OF FLEXIBLE AIRCRAFT: HANDLING QUALITIES WITH ACTIVE LOAD CONTROL

SCHOOL OF ENGINEERING

PhD THESIS

This page is intentionally left blank.

CRANFIELD UNIVERSITY

SCHOOL OF ENGINEERING

PhD THESIS

Academic Year 2010-11

Stuart P. Andrews

Modelling and Simulation of Flexible Aircraft: Handling Qualities with Active Load Control

Supervisor: Dr Alastair K. Cooke

March 2011

This page is intentionally left blank.

Abstract

The study of the motion of manoeuvring aircraft has traditionally considered the aircraft to be rigid. This simplifying assumption has been shown to give quite accurate results for the flight dynamics of many aircraft types. As modern transport aircraft have developed however, there has been a marked increase in the size and weight of these aircraft. This trend is likely to continue with the development of future blended-wing-body and supersonic transport aircraft. This increase in size and weight has brought about a unique set of aeroelastic and handling quality issues.

The aerodynamic forces and moments acting on an aeroplane have traditionally been represented using the aerodynamic derivative approach. It has been shown that this quasi-steady aerodynamic model inadequately predicts the aircraft's stability characteristics, and that the inclusion of unsteady aerodynamics "greatly improves the fidelity" of aircraft models.

This thesis thus presents a novel numerical simulation of an aeroelastic aeroplane for real-time analysis. The model is built around the standard six degree-of-freedom equations of motion for a rigid aeroplane using the mean-axes system, and includes unsteady aerodynamics and structural dynamics. This is suitable for pilot-in-the-loop simulation, handling qualities and flight loads analysis, and control law development. The dynamics of the structure are modelled as a set of normal modes, and the equations of motion are realised in state-space form. The unsteady aerodynamic forces acting on the aeroplane are described by an indicial state-space model, including unsteady tailplane downwash and compressibility effects. An implementation of the model is presented in the MATLAB/Simulink environment.

The interaction between the flight control system, the aeroelastic system and the rigid-body motion of the aeroplane can result in degraded handling qualities, excessive actuator control, and fatigue problems. The introduction of load alleviation systems for the management of loads due to manoeuvres and gusts is also likely to result in the handling qualities of the aeroplane being degraded.

This thesis presents a number of studies into the impact of structural dynamics, unsteady aerodynamics, and load alleviation on the handling qualities of a flexible civil transport aeroplane. The handling qualities of the aeroplane are assessed against a number of different handling qualities criteria and flying specifications, including the Neal-Smith, Bandwidth, and CAP criterion. It is shown that aeroelastic effects alter the longitudinal and lateral-directional characteristics of the aeroplane, resulting in degraded handling qualities. Manoeuvre and gust load alleviation are similarly found to degrade handling qualities, while active mode control is shown to offer the possibility of improved handling qualities.

Keywords: Flexible, Elastic, Civil Transport, Aeroplane, Flight Dynamics, Handling Qualities, Aeroelasticity, Aeroservoelasticity, Structural Dynamics, Unsteady Aerodynamics, Load Alleviation

This page is intentionally left blank.

Acknowledgements

I would like to express my sincerest gratitude to my supervisor, Dr. Alastair Cooke, for his continual advice, guidance, and support throughout the past four years. My thanks also go to Dr. James Whidbourne and Mike Cook, and to the other past and present members of the Dynamics, Simulation and Control group, especially Mudassir Lone, Pierre-Daniel Jameson, Peter Thomas, and Sunan Chumalee.

I would also like to acknowledge Airbus for their financial support. In particular, I would like to thank Nicky Aversa, Tom Wilson, Paul Kealy, Amalia Anastasia and Isabelle Bloy, and all those in Filton and Toulouse who have provided assistance and technical support during my studies.

I would like to save my deepest gratitude for my family, without whose love and support I would not have achieved so much: to my parents Peter and Yvonne, my brother Mark, and to my girlfriend Hanyi and all our family. I also wish to express my thanks to my friends Longxian, Liyun, Daqing, and Gautam for their assistance and encouragement. A special mention also goes to Shaun Watson for his continued friendship and support.

This page is intentionally left blank.

Contents

List of Tables

List of Figures

Nomenclature

Base Symbols

Of the large number of symbols required in this thesis, several have more than one meaning. All instances of these symbols are listed here, however the meaning should be clear from the context in which the symbol is used.

Latin Alphabet

a	Lift-curve slope	
$\mathbf{a}$	Acceleration vector	ms^{-2}
$\mathfrak{A}$	Aerodynamic matrix	
$A_{()}$	Unsteady aerodynamic coefficient	
a_n	Nacelle lift-curve slope	
a_s	Speed of sound	ms^{-1}
a_0	Aerofoil viscous lift-curve slope	
a_{0_T}	Aerofoil inviscid lift-curve slope	
a_{1_w}	Wing viscous lift-curve slope	
AR	Wing aspect ratio	
b	Semi-chord length	m
b	Wing span	m
b	Fuselage fore-body bluffness parameter	
$\mathfrak{b}$	Aerodynamic mathematical series coefficient	
$b_{()}$	Unsteady aerodynamic coefficient	
B	Fuselage forebody profile drag parameter	
BM	Bending moment	Nm
c	Chord length	m
$\bar{c}$	Standard mean chord length	m
c_f	Trailing-edge flap chord length	m
c_r	Root chord length	m
c_t	Tip chord length	m
c_0	Centre-line chord length	m
$\mathbf{C}$	Structural global damping matrix	
C^*	C^* control variable	
$C(k)$	Theodorsen's Function	
C_{CL}	Fuselage geometric coefficient	
C_D	Aerodynamic drag coefficient	
C_D^*	Aerodynamic drag coefficient based on $(volume)^{2/3}$	
C_{DG}^*	Datum aerodynamic drag coefficient based on $(volume)^{2/3}$	
$C_{\mathfrak{D}}$	Drag coefficient	
$C_{\mathfrak{D}_o}$	Profile drag coefficient	

$C_{\mathfrak{D}_{\text{in}}}$	Induced drag coefficient	
$C_{\mathfrak{D}_{\text{in}_{\text{tv}}}}$	Induced trailing vortex drag coefficient	
$C_{\mathfrak{D}_{\text{in}_{\text{tv}}}}$	Induced lift-dependent viscous drag coefficient	
C_F	Flat plate skin friction coefficient	
C_{F0}	Flat plate boundary layer transition correction factor	
$C_{\mathfrak{L}}$	Lift coefficient	
$C_{\mathfrak{L}_a}$	Lift coefficient due to aerofoil	
$C_{\mathfrak{L}_f}$	Lift coefficient due to flap	
$C_{\mathfrak{L}_q}$	Lift coefficient due to aerofoil pitch rate	
$C_{\mathfrak{L}_\alpha}$	Lift coefficient due to aerofoil angle of attack	
$C_{\mathfrak{L}_\zeta}$	Lift coefficient due to flap angle	
$C_{\mathfrak{L}_{\dot{\zeta}}}$	Lift coefficient due to flap rate	
C_M	Aerodynamic pitching-moment coefficient	
$C_{\mathfrak{M}}$	Pitching-moment coefficient	
$C_{\mathfrak{M}_a}$	Pitching-moment coefficient due to aerofoil	
$C_{\mathfrak{M}_f}$	Pitching-moment coefficient due to flap	
$C_{\mathfrak{M}_q}$	Pitching-moment coefficient due to aerofoil pitch rate	
$C_{\mathfrak{M}_\alpha}$	Pitching-moment coefficient due to aerofoil angle of attack	
$C_{\mathfrak{M}_\zeta}$	Pitching-moment coefficient due to flap angle	
$C_{\mathfrak{M}_{\dot{\zeta}}}$	Pitching-moment coefficient due to flap rate	
C_N	Normal force coefficient	
C_{N_α}	Normal force coefficient at zero angle of attack	
C_{N_c}	Cross flow normal force coefficient	
C_{PL}	Fuselage geometric coefficient	
C_V	Fuselage geometric coefficient	
C_S	Fuselage geometric coefficient	
d	Perpendicular distance between a point and a vortex line	m
D	Linear direction cosine matrix	
D	Fuselage body diameter	m
$\mathfrak{D}$	Drag force	N
D_b	Fuselage body base diameter	m
e	Exponential function	
E	Angular direction cosine matrix	
E	Young's modulus	Pa
Ei	Exponential integral function	
$\mathbf{f}$	Force vector	m
$\mathfrak{f}$	Aerodynamic mathematical series coefficient	
$F_{(\,)}$	Aerofoil flap geometry parameters	
$F_{(\,)}$	Structural generalised force	
F_b	Fuselage forebody profile drag parameter	
F_M	Fuselage forebody profile drag parameter	
F_{M1}	Fuselage forebody profile drag parameter	
F_{M2}	Fuselage forebody profile drag parameter	
g	Acceleration due to gravity	ms^{-2}

$\mathfrak{g}$	Aerodynamic downwash coefficient	
G	Structural shear modulus	Pa
$\mathfrak{G}$	Aerodynamic downwash coefficient	
$g_{(\,)}$	Unsteady aerodynamic coefficient	
$G_{(\,)}$	Unsteady aerodynamic coefficient	
h	Vertical heave displacement	m
$\mathbf{h}$	Angular momentum vector	kgm^2s^{-1}
$H(z)$	Z-domain transfer function	
H_{d_w}	Vertical turbulence velocity transfer function	
H_{ϕ_W}	Indicial transfer function	
i	Aerodynamic span-wise station index	
I	Structural second moment of inertia	m^4
I_0	Rigid body inertia tensor	kgm^2
I'	Relative elastic body inertia tensor	kgm^2
j	Aerodynamic span-wise station index	
J	Structural torsion constant	m^4
k	Total number of aerodynamic span-wise stations	
K	Structural nodal stiffness matrix	Nm
$\mathbf{K}$	Structural global stiffness matrix	Nm
$k_{(\,)}$	Unsteady aerodynamic coefficient	
k_c	Profile drag camber factor	
k_M	Profile drag compressibility factor	
k_1	Profile drag parametric factor	
k_2	Profile drag parametric factor	
k_3	Profile drag parametric factor	
k_4	Profile drag parametric factor	
K_a	Lift-curve slope correction factor	
K_{ARI}	FCS control gain (Aileron-rudder interlink loop)	
K_c	FCS control gain (C* loop)	
$K_{\mathfrak{D}_{ivc}}$	Lift-dependent viscous drag factor	
$K_{f(w)}$	Body-wing interaction correction factor	
K_i	FCS control gain (Integral loop)	
K_m	FCS control gain (Feed-forward loop)	
K_M	Normalised drag correction factor	
K_p	FCS control gain (Roll loop)	
K_p	Neal-Smith pilot model variable	
K_q	FCS control gain (Pitch rate loop)	
K_{qc}	FCS control gain (C* loop)	
K_r	FCS control gain (Yaw loop)	
K_{tr}	Normalised drag correction factor	
$K_{w(f)}$	Wing-body interaction correction factor	
l	Wing trailing-edge to tail leading-edge horizontal distance	m
L	x-axis moment	Nm
L	Structural beam length	m

L	Atmospheric lapse rate	Km^{-1}
$\mathfrak{L}$	Lift force	N
$\mathfrak{L}_{()}$	Aerodynamic downwash integrand coefficient	
l_a	Fuselage aft-body boat-tail length	m
l_c	Fuselage cylinder length	m
l_d	Gust length	m
l_{d_w}	Vertical turbulence length scale	
l_f	Fuselage fore-body length	m
l_m	Fuselage mid-body length	m
l_n	Nacelle length	m
l_n	Equivalent root chord leading-edge position to nose distance	m
l_1	Wing mid-chord to tail leading-edge horizontal distance	m
l_t	Tip chord leading-edge position to nose distance	m
m	Mass	kg
$\mathbf{m}$	Moment vector	Nm
M	y-axis moment	Nm
M	Structural nodal mass matrix	kg
M	Low-order Equivalent System (LOES) mismatch	
$\mathbf{M}$	Structural global mass matrix	kg
$\mathfrak{M}$	Pitching moment	Nm
$M_{()}$	Structural generalised mass	
Ma	Mach number	
n	Aerodynamic span-wise station index	
N	z-axis moment	Nm
n_z	Normal acceleration	g
p	x-axis rate of rotation (roll)	$rads^{-1}$
$\mathbf{p}$	Linear momentum vector	$kgms^{-1}$
P	Atmospheric pressure	Pa
$P_{()}$	Structural modal internal stress pattern	
q	y-axis rate of rotation (pitch)	$rads^{-1}$
q	Generalised coordinate	
Q	Generalised force	
q_d	Dynamic pressure	Pa
r	z-axis rate of rotation (yaw)	$rads^{-1}$
r	Maximum body radius	m
r	Absolute distance between a point and a vortex line	m
$\mathbf{r}$	Rigid body distance vector	m
R	Gas constant	$JKg^{-1}K^{-1}$
R	Aerofoil quarter-chord to nacelle inlet (vertical)	m
Re	Reynolds number	
Re_c	Reynolds number based on aerofoil chord	
Re_L	Reynolds number based on fuselage length	
r'	Aerofoil quarter-chord to nacelle lip (diagonal)	m
$\mathbf{r}'$	Relative elastic distance vector	m

s	Laplace variable	
s	Wing semi-span	m
s_0	Fuselage radius	m
S	Wing area	m^2
S	Sutherland's constant	
S_b	Fuselage reference area	m^2
S_e	Exposed wing area	m^2
St	Strouhal number	
SF	Shear force	N
t	Time	s
t	Aerofoil thickness	m
T	Atmospheric temperature	K
T	Structural nodal to global transformation matrix	
T	Kinetic energy	J
t_m	Maximum aerofoil thickness	m
$t_{0.75}$	Aerofoil thickness at $x = 0.75c$	m
T_P	Engine thrust	N
$T_{P_{max}}$	Maximum engine thrust	N
$T_{q_{\mathfrak{L}}}$	Aerofoil pitch rate time lift constant	
$T_{q_{\mathfrak{M}}}$	Aerofoil pitch rate pitching-moment time constant	
T_R	Roll mode time constant	
$T_{\alpha_{\mathfrak{L}}}$	Aerofoil angle of attack lift time constant	
$T_{\alpha_{\mathfrak{M}}}$	Aerofoil angle of attack pitching-moment time constant	
$T_{\xi_{\mathfrak{L}}}$	Flap angle lift time constant	
$T_{\dot{\xi}_{\mathfrak{L}}}$	Flap rate lift time constant	
$T_{\xi_{\mathfrak{M}}}$	Flap angle pitching-moment time constant	
$T_{\dot{\xi}_{\mathfrak{M}}}$	Flap rate pitching-moment time constant	
$\mathbf{u}$	State-space input vector	
$\mathbf{u}$	Structural geometric coordinate vector	
U	x-axis total velocity	ms^{-1}
U	Potential energy	J
$u_{(\,)}$	State-space input variable	
v	Aerodynamic span-wise station index	
$\mathbf{v}$	Velocity vector	ms^{-1}
V	Volume	m^3
V	y-axis total velocity	ms^{-1}
V_{co}	Cross-over velocity	ms^{-1}
V_T	Total velocity	ms^{-1}
w	Downwash velocity	ms^{-1}
W	z-axis total velocity	ms^{-1}
w_t	Downwash velocity due to trailing vortex	ms^{-1}
w_b	Downwash velocity due to bound vortex	ms^{-1}
w_d	Gust velocity	ms^{-1}
w_{dw}	Vortex induced velocity	ms^{-1}

$\bar{w}_{dw}$	Vortex induced downwash velocity	ms^{-1}
w_n	Nacelle width	m
x	x-axis distance	m
$\mathbf{x}$	State-space state vector	
X	x-axis force	N
$x_{(\,)}$	State-space state variable	
x_{ac}	Aerofoil aerodynamic centre measured from aerofoil mid-chord	
x_b	Root chord leading-edge position to nose distance	m
x_{cp}	Fuselage centre of pressure	m
x'_{cp}	Fuselage centre of pressure change due to aft-body	m
x_d	Gust penetration length	m
x_e	Centre of flap rotation measured from aerofoil mid-chord	
x_t	Aerofoil leading-edge to maximum thickness length	m
x_{tr}	Boundary layer transition location	
x_α	Centre of aerofoil rotation measured from aerofoil mid-chord	
x_0	Fuselage axis origin	m
y	y-axis distance	m
$\mathbf{y}$	State-space output vector	
Y	y-axis force	N
$y_{(\,)}$	State-space output variable	
z	z-axis distance	m
z	Wing trailing-edge to tail leading-edge vertical distance	m
z_n	Aerofoil quarter-chord to nacelle inlet (vertical)	m
z_{t1}	Aerofoil thickness at position 1	m
z_{t2}	Aerofoil thickness at position 2	m
Z	z-axis force	N
Z_r	Neal-Smith pilot model variable	

Greek Alphabet

α	Angle of attack	rad
α_{f_a}	Elastic deflection angle of attack of the fuselage aftbody	rad
α_{f_b}	Total angle of attack of the fuselage aft-/fore-body	rad
α_{f_f}	Elastic deflection angle of attack of the fuselage forebody	rad
α_g	Angle of attack due to gust	rad
$\alpha_{\mathfrak{L}}$	Unsteady circulatory lift angle of attack	rad
$\alpha_{\mathfrak{M}}$	Unsteady circulatory pitching moment angle of attack	rad
α_n	Nacelle angle of attack	rad
α_T	Tailplane angle of attack	rad
α_ϕ	Effective unsteady angle of attack	rad
β	Angle of side-slip	rad
β	Prandtl-Glauert compressibility factor	
χ	Non-dimensional span-wise position	
ϵ	Tailplane downwash angle	rad
η	Elevator deflection angle	rad
η	Non-dimensional span-wise position	
$\boldsymbol{\eta}$	Generalised coordinate vector	

η_T	Tailplane setting angle	rad
γ	Adiabatic index	
γ	Aerofoil trailing-edge camber angle	rad
Γ	Dihedral angle	rad
Γ	Vortex strength	m^2s^{-1}
λ	Taper ratio	
λ^*	Normalised drag parameter	
λ^*_G	Datum normalised drag parameter	
Λ	Sweep angle	rad
Λ_0	Leading-edge sweep angle	rad
$\Lambda_{\frac{1}{2}}$	Half-chord sweep angle	rad
$\Lambda_{\frac{1}{4}}$	Quarter-chord sweep angle	rad
μ	Dynamic viscosity	Pas
μ	Aerodynamic span-wise station index	
ν	Kinematic viscosity	m^2s^{-1}
ν	Aerodynamic span-wise station index	
ω	Aerofoil oscillatory frequency	$rads^{-1}$
$\boldsymbol{\omega}$	Rate of rotation vector	$rads^{-1}$
$\omega_{(\,)}$	Structural modal natural frequency	$rads^{-1}$
ω_{BW}	Pitch-attitude bandwidth	$rads^{-1}$
$\omega_{BW_{gain}}$	Pitch-attitude gain bandwidth	$rads^{-1}$
$\omega_{BW_{phase}}$	Pitch-attitude phase bandwidth	$rads^{-1}$
ω_{dr}	Dutch-roll mode natural frequency	$rads^{-1}$
ω_p	Phugoid mode natural frequency	$rads^{-1}$
ω_s	Short period mode natural frequency	$rads^{-1}$
ω_{180}	Pitch-attitude 180° phase lag bandwidth	$rads^{-1}$
ϕ	Bank attitude	rad
$\boldsymbol{\phi}$	Structural mode shape vector	
$\phi_{(\,)}$	Structural mode shape	
ϕ_p	Neal-Smith pilot model variable	
ϕ_W	Wagner function	
ϕ_1	Wing height angle	rad
ψ	Yaw attitude	rad
ψ_K	Kussner function	
ρ	Density	Kgm^{-3}
σ_{d_w}	Vertical turbulence intensity	
τ	Throttle position	
τ	Aerofoil trailing-edge angle	rad
τ	Non-dimensional time	
τ_a	Aerofoil trailing-edge parameter	
τ_{au}	Cambered aerofoil trailing-edge parameter	
τ_e	Pitch-attitude phase delay (LOES)	s
τ_i	Neal-Smith pilot model variable	
τ_l	Neal-Smith pilot model variable	

τ_n	Normal-acceleration phase delay (LOES)	s
τ_p	Pitch-attitude phase delay (Bandwidth criterion)	s
τ_P	Engine time constant	
θ	Pitch attitude	rad
θ_f	Fuselage elastic pitch attitude	rad
θ_r	Fuselage cockpit pitch attitude	rad
θ_{rf}	Cockpit elastic pitch attitude	rad
Θ	Twist angle	rad
$\mathbf{\Theta}$	attitude vector	$rads^{-1}$
ξ	Aileron deflection angle	rad
ξ	Flap deflection angle	rad
$\xi_{(}$	Structural modal generalised coordinate	
ζ	Rudder deflection angle	rad
$\zeta_{(}$	Structural modal damping coefficient	
ζ_{dr}	Dutch-roll mode damping coefficient	
ζ_p	Phugoid mode damping coefficient	
ζ_s	Short period mode damping coefficient	

Note that here a subscript ( ) indicates a positive integer value, and a superscript T indicates the matrix transpose.

Subscripts

a	Aerodynamic component
c	Control component
cm	Centre of mass
c_ξ	Aileron control component
c_ζ	Elevator control component
c_η	Rudder control component
B	Body axis system
d	Gust component
d	Demanded control deflection
dw	Downwash component
f	Fuselage component
$f(w)$	Body-wing interaction coefficient
f_{co}	Carry-over fuselage component
f_a	Aft-fuselage component
f_f	Fore-fuselage component
f	Fuselage component
g	Gravitational component
G	Global axis system
h	Tailplane component
i	Aerodynamic span-wise station index
i	Structural modal index
j	Aerodynamic span-wise station index
I	Earth axis system
$\mathfrak{L}$	Aerodynamic coefficient lift component

$\mathfrak{M}$	Aerodynamic coefficient pitching moment component
N	Nodal axis system
n	Nacelle component
n	Aerodynamic span-wise station index
p	Propulsive component
P	Engine axis system
qs	Aerodynamic coefficient quasi-steady component
th	Basic thickness component
v	Aerodynamic span-wise station index
v	Fin component
w	Wing component
W	Wind axis system
$w(f)$	Wing-body interaction coefficient
XX	Component about x-axis for x-axis rotation
XY	Component about y-axis for x-axis rotation
XZ	Component about z-axis for x-axis rotation
YX	Component about x-axis for y-axis rotation
YY	Component about y-axis for y-axis rotation
YZ	Component about z-axis for y-axis rotation
ZX	Component about x-axis for z-axis rotation
ZY	Component about y-axis for z-axis rotation
ZZ	Component about z-axis for z-axis rotation
0	Datum condition
0	Reference axis system
μ	Aerodynamic span-wise station index
ν	Aerodynamic span-wise station index
ξ	Aerodynamic coefficient flap component

Superscripts

B	Body axis system
c	Circulatory component
g	Gust component
G	Global axis system
I	Earth axis system
N	Nodal axis system
nc	Non-circulatory component
W	Wind axis system
0	Reference axis system

This page is intentionally left blank.

CHAPTER 1

Introduction

1.1 Background

The first flight of the Wright Flyer on December 17th, 1903 lasted 12 seconds and covered just 120 ft [Figure 1.1]. Today, the wingspan of the Airbus A380, which entered service in 2007, is over twice this distance (261.6 ft, 79.75 m). As the aeroplane has evolved it has increased in size, weight, and range. This is especially true for modern civil transport aircraft [Figure 1.2]. In 1952, the first jet-powered civil transport airliner, the de Havilland Comet, entered into service. The Comet had a wingspan of 35 m, an empty weight of 34,200 kg, and a range of 2,800 nautical miles. The latest Boeing 747-8I, which is due to enter service in 2011, is expected to have a wingspan of 68.45 m, empty weight of over 210,000 kg, and a range of 8,000 nautical miles. This increase in size and weight has brought about a unique set of aeroelastic and handling quality issues.

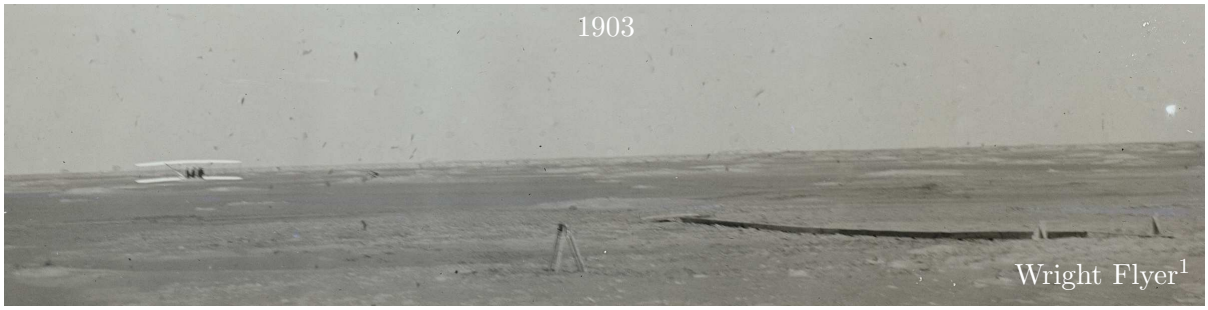

Figure 1.1: First flight of the Wright Flyer

The study of the motion of manoeuvring aircraft has typically considered the aircraft to be rigid. This simplifying assumption has been shown to give quite accurate results for the flight dynamics of many aircraft types. It has also been shown that rigid body motions can be ignored when considering the airframe flexibility of an aircraft in steady level flight, for example as required for aeroelastic flutter analysis. However, it was identified

[1] Wright and Wright [1903]

even in the first days of flight that the airframe structure was not rigid. For those early aeroplanes, including the Wright Flyer, this flexibility was employed with varying degrees of success for lateral roll control of the aeroplane. While "wing-warping" was replaced by ailerons for lateral control as the standard by 1915, the airframe remained flexible. This flexibility prompted much research into the new field of aeroelasticity; the study of the interaction of the inertial, aerodynamic, and elastic forces. However, while the study of aeroelasticity continued in earnest, very little consideration was given to the rigid-body motion of the flexible aeroplane. In fact, it was not until the 1960s that a complete definition of the equations of motion for a flexible aeroplane was derived [Milne, 1962].

As modern transport aircraft have developed, there has been a marked increase in the size and weight of these aircraft. This trend is likely to continue with the development of future blended-wing-body and supersonic transport aircraft. This is in addition to the many other requirements on the aircraft designer, such as improving fuel efficiency and increasing payload and range. This has often been achieved by reducing structural weight, and this can result in an increase in structural flexibility. The effect of this increase in structural flexibility and aircraft mass is a reduction in the natural frequencies of the elastic airframe. As the flexible-body natural frequencies are reduced, and move closer to the frequencies of the rigid-body aircraft dynamics, interaction between the rigid-body and flexible-body dynamics of the aeroplane is increased. The aeroplane can no longer be considered rigid.

Figure 1.2: Evolution of the modern civil transport aircraft

The aerodynamic forces and moments acting on an aeroplane have traditionally been represented using the stability and control derivative approach [Bryan, 1911]. These steady aerodynamic derivatives are expressed as a function of the aeroplane's instantaneous translational and rotational velocities. It was recognised in the 1920s however that this aerodynamic derivative approach was inadequate due to time-dependent aerodynamic effects, such as the convective time delay due to tailplane downwash [Cowley and Glauert, 1921]. However, while incorporating time-dependent downwash effects, this remains only a quasi-steady model; a function of the instantaneous acceleration of the aeroplane. A number of recent studies into aircraft flight dynamics have found that this quasi-steady aerodynamic model inadequately predicted the aircraft's stability characteristics [Shearer and Cesnik, 2005; Abramov et al., 2005]. Greenwell [2004] identified the importance of including unsteady aerodynamics, noting that it "greatly improves the fidelity" of aircraft models.

[2] © Pingstone [1964]
[3] CC BY SA Marmet [1976]
[4] CC BY SA Douchet [2010]

The handling qualities of an aeroplane describe the ease and effectiveness by which a pilot may control the aeroplane while completing some defined task or mission. At the time of the Wright brother's first flight in 1903, there was little understanding of the handling qualities of aircraft. Wright [1901] said in 1901 that the challenges of construction and powered flight were understood, but the problems of "balance and steering" remained unsolved and were of the utmost importance. The handling qualities of aircraft were then largely dependent on the basic aerodynamic stability and control of the airframe [Gibson, 1999]. In the next 30 years, aircraft designers largely left the design of aircraft stability and control to empirical estimates and a "cut-and-try" approach [McRuer et al., 1973]. It was not until the 1940s that efforts began in earnest to study the behaviour of the motion of an aeroplane. There now exist many handling qualities criteria which aid the designer in the design of the aircraft and the specification of its dynamic characteristics [Cook, 1997]. The Cooper-Harper rating scale provides a formal assessment of the pilot's opinion and comments on the handling qualities of the aircraft [Cooper and Harper, 1969].

As the interaction between the rigid- and flexible-body dynamics of the aeroplane is increased, the handling qualities of the aeroplane have been shown to become degraded [Yen, 1977]. This degradation in handling qualities is exhibited as an increase in the required compensation by the pilot to achieve the same task, or alternatively, a reduction in the task completion performance. This was found to occur even where the lowest structural natural frequency was three times greater than the rigid-body short period frequency [Waszak and Schmidt, 1985a].

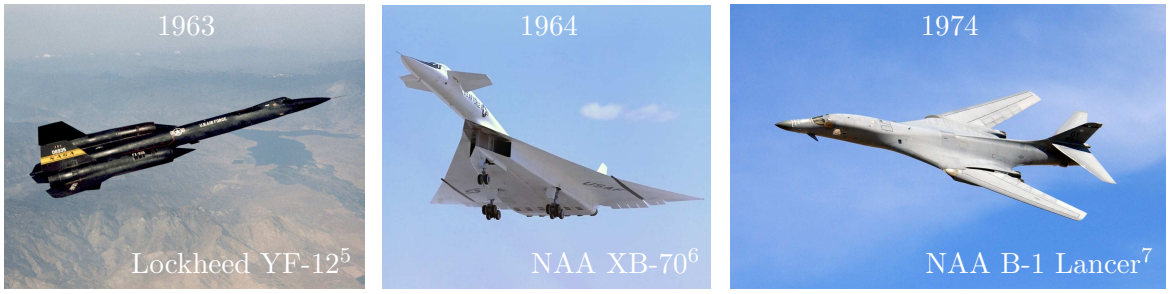

Figure 1.3: Focus of flexible aircraft handling qualities research

The handling qualities of the Rockwell B-1B Lancer bomber [Figure 1.3] have been investigated by a number of authors. Yen [1977] found that as the natural frequencies are reduced, the handling qualities were degraded as the aeroelastic dynamics interact with the rigid-body dynamics. This resulted in lower Cooper-Harper ratings by the pilots in the study. This degradation in handling qualities was attributed to rigid-flexible mode interaction. This lowered the frequency of the rigid-body short-period mode, and caused the phugoid mode to split into positive and negative real roots, degrading the pilot's tracking ability.

The aeroelastic deformation of the airframe can also contribute towards the occurrence of Aircraft-Pilot Coupling (APC). An APC, or Pilot-Induced Oscillation (PIO), is an inadvertent and undesirable zero-damped or unstable oscillation which is the result of

[5] © NASA Dryden Flight Research Centre Photo Collection [1972]
[6] © NASA Dryden Flight Research Centre Photo Collection [1965]
[7] © Valenca [2004]

the closed-loop pilot-aircraft coupling. These events can occur during common high gain tasks, such as aerial refuelling and formation flying [McRuer, 1995]. APCs can occur as a result of changes in pilot behaviour or be triggered by external events such as a system failure or stores release, and can involve rigid-body, aeroelastic and control dynamics. Excessive time delays in the response of an aircraft can also result in reduced handling qualities and an increased susceptibility to APCs [Hoh et al., 1982]. These delays can arise from existing sources, such as actuator lags and FCS delays, or from the delays incurred by the dynamic response of the aircraft structure and the unsteady nature of the aerodynamic forces.

Examples of aeroelastic APCs include the Lockheed YF-12, Boeing C-17A Globemaster III, Boeing 777, as well as rotorcraft such as the Sikorsky CH-53E Super Stallion and Bell-Boeing V-22 Osprey [Norton, 1996; McRuer, 1995]. The mechanisms driving these aeroelastic APCs can be classified into three categories [Norton, 1995]. Type 1 PIOs are the result of the perceived aeroelastic deformation of the airframe by the pilot at the cockpit. Type 2 PIOs are due to the modification of the rigid-body motion due to aeroelastic deformation. Finally, Type 3 PIOs are aeroelastic Pilot Augmented Oscillations (PAO), which occur when cockpit accelerations produce unintentional pilot control inputs. The latter was identified by Schmidt and Raney [2001] as "biodynamic-feedthrough" in a study of the B-1B Lancer. This in some circumstances resulted in "biodynamic-coupling", a resonant coupling of the pilot's muscular response and the structural vibrations of the airframe.

Figure 1.4: Development of aircraft load alleviation systems

There exist many handling qualities criteria and flying qualities specifications to aid in the specification and design of an aeroplane's dynamic characteristics. For example, both civil and military flying qualities specifications exist which define the minimum performance requirements for a given aircraft type and flight phase. It is quite common that an aeroplane's dynamic characteristics do not meet these flying and handling qualities requirements, and it is often therefore necessary to modify, or augment, the dynamic characteristics of the aircraft. This Stability Augmentation System (SAS) is an integral part of the modern aeroplane's Flight Control System (FCS). It is also common to modify the control and stability characteristics of the aircraft to improve performance in pilot manoeuvre and target tracking tasks. This system is known as a Control Augmentation System (CAS), and together these two systems are known as Control and Stability Augmentation Systems (CSAS). In addition to the CSAS, it is increasingly common to find a

[8] © NASA Dryden Flight Research Centre Photo Collection [2001]
[9] © NASA Dryden Flight Research Centre Photo Collection [1997]
[10] © Pingstone [2009]

Load Alleviation Function (LAF) in many large civil and military aircraft. The purpose of this LAF system is commonly to manage and reduce loads due to manoeuvres and gusts or to improve passenger ride comfort. This has been included on aircraft such as the Boeing B-52, Lockheed L-1011, and Airbus A340 [Figure 1.4].

Aeroservoelasticity is the interaction between the Flight Control System (FCS), aerodynamics and the inertia and elasticity of the aeroplane structure. The FCS includes any number of motion sensors, including accelerometers and rate gyros, which measure the aircraft rigid-body motion. These signals are typically fed back through several flight control laws to the aeroplane control surfaces. Aeroservoelastic problems typically occur when these signals are contaminated with the measured motion of the flexible aircraft modes. This "structural coupling" can result in excessive actuator control, fatigue problems, and in the event of flutter dramatic and often catastrophic failure of the structure [Wright and Cooper, 2007].

Structural dynamics can then, in certain circumstances, have a noticeable and measurable effect on the flight dynamics and handling qualities of an aeroplane. This has been found to be significant for long, slender-fuselaged aircraft, such as the B-1B Lancer bomber. This "structural coupling" can result in degraded handling qualities, an increase in the susceptibility to APCs, and aeroservoelastic problems. These effects are of particular significance for modern transport aircraft, which continue to increase in size [Mitchell et al., 2003].

1.2 Aim and Objectives

The aim of this research is to investigate and explain the influence of aeroelastic effects on the handling and flying qualities of a modern, large civil transport aircraft. This will focus on the assessment of the individual and coupled impact of unsteady aerodynamics and structural flexibility on the handling and flying qualities of the aircraft. The results shall be compared to those of the classical rigid aircraft. The study shall include identifying the effect of the flight control system, and in particular the different components of the load alleviation function, on the handling qualities of the flexible aircraft.

The objectives of this research are as follows:

- Develop a numerical model in the MATLAB/Simulink environment for simulation of a flexible aeroplane
  - Develop a generic model framework for the simulation of a flexible aeroplane.
  - Capture the effects of unsteady aerodynamics and structural dynamics.
  - Enable real-time simulation of a flexible aeroplane in order to facilitate pilot-in-the-loop simulation.
  - Apply the model to the simulation of an aeroplane representative of a modern, large civil transport aircraft.
- Investigate flexible aircraft flying and handling qualities

  - Influence of aeroelastic effects
    * Assess the impact of unsteady aerodynamics and structural flexibility on the open-loop stability characteristics of the aeroplane.
    * Review the influence of aeroelasticity on the longitudinal and lateral-directional handling qualities of the aeroplane.
  - Influence of load alleviation and active control
    * Identify influence of manoeuvre, gust and active load alleviation on aeroplane dynamic characteristics.
    * Establish effect of load alleviation on flexible aeroplane handling qualities.

1.3 Contributions to Knowledge

This thesis presents the following contributions to knowledge:

- A complete, modular numerical simulation of a flexible aeroplane, including both unsteady aerodynamics and structural dynamics and a representative flight control system, capable of real-time, pilot-in-the-loop simulation, and suitable for modern control law development.
- A study into the impact of aeroelastic effects and airframe component stiffness on the open- and closed-loop longitudinal and lateral-directional stability characteristics and handling qualities of a modern, flexible civil transport aircraft.
- A study into the closed-loop handling qualities of a flexible civil transport aircraft with manoeuvre, gust, and active mode control.

1.4 Summary

In summary, this thesis describes the development of an aeroelastic, flexible aeroplane model and its application in the MATLAB/Simulink environment. The impact of aeroelastic effects and load alleviation on the open- and closed-loop dynamic characteristics and handling qualities of the aeroplane are assessed and reviewed.

Chapter 2 presents a review of the history, development, and state-of-the-art of flexible aircraft simulations. This focuses on aeroelastic, flexible structure and unsteady aerodynamic models, Flight Control Systems (FCS), aeroservoelasticity, and flexible aircraft handling qualities.

Chapter 3 presents the definition of the equations of motion for a flexible aeroplane using the mean-axes system.

Chapter 4 derives the mathematical model of the aerodynamic, gravitational, control, and propulsive forces acting on the flexible aeroplane. This includes the definition of a state-space unsteady aerodynamic model suitable for real-time simulation, as well as estimates of the aerodynamic properties of the airframe from empirical estimates.

Chapter 5 describes the example numerical simulation, validation and verification of a flexible large civil transport aircraft, the Aeroplane AX-1, in the MATLAB/Simulink environment.

Chapter 6 discusses the impact of structural dynamics and unsteady aerodynamics on the open-loop dynamic and stability characteristics of the aeroplane. A Control and Stability Augmentation (CSAS) and Load Alleviation Function (LAF) are designed as part of the flexible aircraft FCS. The impact of unsteady aerodynamics on the closed-loop aircraft is then discussed.

Chapter 7 assesses the influence on airframe component stiffness on the longitudinal and lateral-directional handling qualities of the flexible aircraft using existing handling qualities criteria and specifications. The impact of LAF systems, including Manoeuvre Load Alleviation (MLA), Gust Load Alleviation (GLA) and Active Mode Control (AMC), on the aeroplane handling qualities is reviewed.

Chapter 8 contains a summary of findings, concluding remarks and recommendations for further work.

Appendices A through D provide the aerodynamic, structural and geometric data that describe the implementation in MATLAB/Simulink of a flexible aeroplane simulation of the Aeroplane AX-1.

This page is intentionally left blank.

CHAPTER 2

Literature Review

This section presents a review of the history, development and state-of-the-art of flexible aircraft simulation and handling qualities analysis. This focuses on aeroelastic, flexible structure and unsteady aerodynamic models, Flight Control Systems (FCS), aeroservoelasticity, and flexible aircraft handling qualities.

2.1 Flexible Aircraft Modelling and Simulation

The recent interest in flexible aircraft is not new. The phenomenon now known as divergence was identified by Brewer [1913] in 1913, and the first documented occurrence of flutter was in 1916 with the Handley Page O/400 bomber [Lanchester, 1916]. It was clear then that the aeroplane was not rigid, and the interaction of inertial, aerodynamic and elastic forces, a field which would become known as aeroelasticity, was already a topic of great interest in the 1910s. Those aeroelastic phenomena, including divergence and flutter, are conveniently summarised in Collar's Triangle of Forces [Figure 2.1].

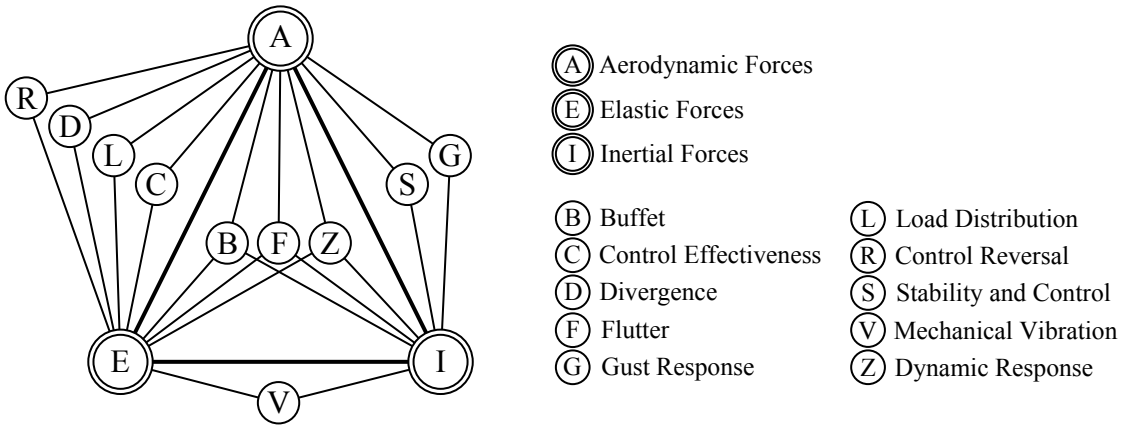

Figure 2.1: Collar's Triangle of Forces [Collar, 1978]

The equations of motion for a flexible aeroplane were considered as early as the 1920s [Lamb, 1920]. During the 1920s and 1930s, research continued into aeroelasticity and saw the development of both time- and frequency-domain unsteady aerodynamic models [Wagner, 1925; Kussner, 1936; Garrick, 1938], and a formal definition and solution to the flutter problem [Frazer and Duncan, 1928a]. Research continued into static aeroelasticity [Diederich, 1950; Skoog and Brown, 1951] and flutter [Theodorsen and Garrick, 1942; Theodorsen, 1949; Barmby et al., 1951] during the 1940s and 1950s.

While the study of static and dynamic aeroelasticity continued, very little consideration was given to the rigid-body dynamics of the flexible aeroplane. One of the first examples to consider the rigid-body motion however was Frazer and Duncan [1928b], which showed that the flutter speed increased when the rigid-body degrees of freedom were included. Even up until the early 1960s though, the study of aeroplane stability and control had still typically assumed the aircraft to be rigid and limited to small perturbations. This allowed the use of existing aerodynamic stability and control derivatives [Bryan, 1911]. The effects of aeroelasticity were later included by modifying the aerodynamic derivatives for quasi-steady aeroelastic effects, such as the influence of fuselage stiffness on tailplane lift [Bisplinghoff et al., 1955; Etkin, 1959]. This approach assumed that the frequencies of the rigid-body modes of interest were sufficiently separated from the frequency of the elastic and aerodynamic modes, such that these effects could be assumed to be quasi-steady and no extra degrees of freedom were added to the system. It was not until the early 1960s that a more complete definition of the equations of motion for a flexible aeroplane was derived by Milne [1962].

Milne [1962] introduces the concept of the mean-axes system [Lamb, 1920; Hemp, 1947]. The aeroplane equations of motion are defined about a *mean-axes* coincident with the aeroplane centre of mass. This effectively decouples the rigid-body and flexible-body equations of motion where the flexible-body modes are described by orthogonal *normal modes*. This method is then applied to a case only where longitudinal flexibility is considered, and no spanwise flexibility is included in the calculation of the aerodynamic forces. While the application is limited to only a simple case, the equations of motion presented by Milne [1962] form the fundamental basis for several important later works [Dusto et al., 1974; Yen, 1977; Waszak et al., 1987a,b].

The mean-axes system is applied by Dusto et al. [1974] in the digital computer program FLEXSTAB. The flexible-body dynamics are expressed in terms of normal modes, and these are coupled using the mean-axes system with the rigid-body equations of motion. The unsteady aerodynamic forces are expressed as a function of frequency, and are calculated using a panel method. The equations of motion are only given as a function of a linear, small perturbation about a reference condition however, and FLEXSTAB itself was notably "time consuming" and required "significant manual effort" to set up the simulation [Samareh and Bhatia, 2000].

Waszak and Schmidt [1988], and earlier Yen [1977]; Waszak et al. [1987a,b]; and Waszak and Schmidt [1985a,b], together present one of the first complete studies into the handling qualities of a flexible aeroplane. The equations of motion are derived using the mean-axes system [Milne, 1962], and the rigid-body equations are identical to those of the rigid aircraft. The airframe structure is assumed to be a collection of lumped masses, though each point mass is assumed to have no rotational inertia, and is approximated using two [Yen, 1977] or four [Waszak and Schmidt, 1985a,b] normal modes. Similarly [Milne,

1962], it is assumed that any structural deflections are small, and the rigid-body inertia tensor remains constant.

Common to studies using normal modes to approximate the structure is the simplification of the equations of motion by truncation of the flexible aeroplane structural normal modes [Reschke, 2005; Baluch et al., 2007; Lee et al., 2007]. This is in fact the most common method of simplification, though other methods exist, including residualisation and balanced reduction [Waszak et al., 1992]. Waszak et al. [1992] noted that all simplification methods have both advantages and disadvantages, and for the case of truncation, modes should be removed when that degree of freedom is much faster than the dynamics of interest, remembering in addition that higher frequency modes are less likely to be excited.

Notable in these studies is the decoupling of the rigid- and flexible-body equations of motion. In the derivation of the equations of motion using the mean-axes system [Milne, 1962], it is assumed that any structural deformation is small. Though it is not then required that the inertia tensor remain constant, decoupling completely the rigid- and flexible-body equations of motion with the exception of aerodynamic terms, this is commonly assumed [Yen, 1977; Waszak and Schmidt, 1988]. However, for high aeroplane rotational rates and low aerodynamic loads, inertial coupling can be significant [Waszak et al., 1992]. Olsen [1999] shows that rigid-body rotation can influence the flexible-body motion, reducing the natural frequency for the case of a simple pendulum. This was reiterated by Nguyen [2008], who also notes that for high rigid-body rotation rates, the rigid-body rotation contributes to the effective stiffness of the wing, modifying the apparent natural frequency. Olsen [1999] identifies that this inertial coupling effect is significant where the flexible-body frequency is less than 1.3–1.5 times the rigid-body frequency.

Buttrill et al. [1987] is one of the first examples of attempts to take account of these effects. The translational equations of motion derived by Buttrill et al. [1987] are identical to those of Waszak and Schmidt [1988], however the rotational equations include additional terms accounting for the variation in the aeroplane inertia tensor and flexible-body rates. The flexible structure equations of motion are also modified to include the effects of rigid-body angular acceleration, Coriolis acceleration, and centrifugal acceleration. Tuzcu [2001], and later Meirovitch and Tuzcu [2002a,b] and Meirovitch and Tuzcu [2003a], also addressed this issue, publishing a new "unified" approach to the modelling and simulation of a flexible aeroplane. The calculation of the equations of motion by Tuzcu [2001] differs markedly from the approach taken previously by the likes of Waszak and Schmidt [1988]. Tuzcu [2001] argues that as the rigid- and flexible-body equations of motion remain coupled through the aerodynamic forces when using the mean-axes system, the advantages of this system are "questionable", while the transformation of the aerodynamic forces into the mean-axes system is "tedious". Unlike previous studies which have used normal modes, Tuzcu [2001] models the wing, fuselage, and empennage as cantilever beams, cantilevered at the fuselage origin and free to undergo torsion and bending in one or two degrees of freedom. The flexible- and rigid-body coupled "hybrid" equations of motion are then derived for the flexible aeroplane as a whole, including both the rigid-body and flexible-body degrees of freedom. The model is also separated into a non-linear "quasi-rigid flight dynamic" model, used for trim only, and a linear, small perturbation "extended perturbation" model, which includes the flexible degrees of freedom. An extension of this model is presented by Meirovitch and Tuzcu [2003b], which replaces the structural model with normal modes in order reduce the order of the

model. These are here termed "shape functions" so as to avoid confusion with the, albeit incorrect, assumption, perpetuated by Meirovitch and Tuzcu [2003b] themselves, that use of normal modes decouples the rigid- and flexible-body motions. In fact, it is the use of the mean-axes system which allows this decoupling [Milne, 1962]. The same problem of inertial coupling is addressed by Nguyen [2008]. Nguyen [2008] considers the inertial forces due to high rigid-body rotational rates acting on the wing structure, however any inertial coupling of the structural deflections with the rigid-body motion is neglected.

As part of NASA's High Speed Research program (HSR) in the 1990s, a number of studies investigated the modelling and simulation of a flexible High Speed Civil Transport aircraft (HSCT). McCarty et al. [1992] investigated and analysed the critical issues for the design and development of a HSCT aircraft. Based on previous experience in the development of supersonic aircraft, such at the XB-70 and B-1, aeroelasticity was identified as a major challenge in the HSCT design process. It was identified by McCarty et al. [1992] that, at that time, while the current state-of-the-art in unsteady aerodynamics and structural dynamics was adequate for aeroelastic analysis, it was unsuitable for predicting the rigid-body behaviour of the flexible aircraft. It was explained that this situation was the result of the separation of rigid-body and flexible-body analysis, with responsibility for the aircraft's rigid body behaviour traditionally residing with the stability and control group, while the dynamics group had responsibility for flexible-body behaviour [McCarty et al., 1992]. The HSCT program resulted in the development of the Boeing "Reference H" design, which was published in 1994 through 1996 as a series of increasingly detailed mathematical models [Dawdy et al., 1994; Stephens et al., 1995a,b; Churchill, 1996]. Sotack et al. [1999] describes the mathematical modelling and simulation of the Cycle 1 "Reference H" aircraft in MATLAB/Simulink [Jackson et al., 1999]. This assumed a rigid-structure aircraft model, though the influence of quasi-static structural deformation on the aerodynamic forces and moments was included through an added-mass term in the standard rigid-body equations of motion. A similar model of the Cycle 3 "Reference H" aircraft was developed by Raney et al. [2001, 2002] in NASA Langley Research Centre's Visual-Motion Simulator (VMS). In this model, structural dynamics were included in a similar approach to the earlier B-1 model developed by Waszak and Schmidt [1985a,b] in NASA Langley's VMS. Again, quasi-static aeroelastic effects were modelled, though Raney et al. [2001] includes these effects by estimating the influence of structural deflections on the steady aerodynamic derivatives.

However, even though aeroelasticity had been identified as a major challenge in the development of the HSCT by McCarty et al. [1992], and a number of studies had since investigated this issue, it was found by Mitchell et al. [2003] that even ten years later the problem of modelling flexible aircraft was as difficult as ever. This was found to be particularly important for modern transport aircraft, especially given the increasing size of this aircraft type [Mitchell et al., 2003].

While many of these studies have considered conventional aircraft configurations, recent interest has focused on the development of High-Altitude Long-Endurance (HALE) aircraft. The characteristics of HALE aircraft, namely high aspect ratio, very flexible wings, where the "separation between the elastic and rigid body motions no longer exists" [Tuzcu et al., 2006], requires an integrated, non-linear formulation in order to accurately model the rigid- and flexible-body dynamics [Shearer and Cesnik, 2005]. Shearer and Cesnik [2005], and previously Patil and Hodges [1998]; Patil et al. [1999]; and Cesnik and Brown [2002], develops a non-linear, large deformation aeroelastic flexible aircraft model. This

shares many similarities with the approach taken for a purely aeroelastic analysis where rigid-body motion is not considered [Librescu et al., 2006; G.Romeo et al., 2006].

Common to many of these HALE aircraft models is the calculation of the aerodynamic forces using finite-state theory [Peters et al., 1995], a two-dimensional, inviscid, incompressible unsteady aerodynamic model. A number of other aerodynamic models also exist, including the steady Vortex Lattice Method (VLM), unsteady indicial transfer function and state-space models, and the unsteady Doublet Lattice Method (DLM), often expressed in the time domain using a Rational Function Approximation (RFA) [Greenwell, 2004; Kier, 2005]. Due to the high calculation costs for some of these models however, notably the DLM [Kier, 2005], the calculation cost for an aerodynamic model is an important factor when deciding on which model to use. For example, Yen [1977] extended the earlier steady aerodynamic stability and control derivative approach to the flexible aeroplane, and these "quasi-steady" derivatives for deflection of the airframe normal modes are calculated using strip theory. This is in agreement with [Milne, 1962], where the rigid- and flexible-body modes are only coupled through the aerodynamics, however no attempt is made to account for unsteady aerodynamic effects. The aerodynamic forces calculated by Tuzcu [2001] also use steady aerodynamic strip theory, though it was acknowledged that this was only a demonstration and an improved aerodynamic model should be developed in the future. Similarly, Siepenkotter and Alles [2005] applies a steady strip theory approach to the calculation of the aerodynamic forces, while also employing the familiar mean-axes system in the decoupling of the flexible- and rigid-body motions. Greenwell [2004] notes that while the validity of a model is often measured by how closely it matches experimental data, the inclusion of unsteady aerodynamics "greatly improves the fidelity" of the model and that it can be expected that unsteady aerodynamics will be significant at some flight condition. Tuzcu [2007] addressed the problem of including unsteady aerodynamic effects, describing the calculation of the aerodynamic forces using a modified strip theory [Yates, 1958], where the local spanwise lift coefficient is modified for magnitude and phase by the local reduced frequency, analogous to Theodorsen's function [Theodorsen, 1949]. Tuzcu [2007] only considers the circulatory component of the lift however, and neglects the non-circulatory component. Both circulatory and non-circulatory aerodynamic forces are considered by Nguyen [2008], in contrast to Tuzcu [2007], though only for a two-dimensional section. It is noted by Baker et al. [1999] however that while a frequency-domain aerodynamic model, such as [Theodorsen, 1949], is suitable for aeroelastic analysis, modern control theory is based on the time-domain state-space approach and a frequency-domain aerodynamic model may not be suitable given "the challenges of transforming between the two domains consistently".

It can be seen then that there are several different approaches to both the derivation of the equations of motion and the calculation of the aerodynamic forces acting on the aeroplane. While it is acknowledged that inertial coupling effects can be significant [Waszak et al., 1992], and many authors have addressed this issue [Tuzcu, 2001; Cesnik and Brown, 2002], these effects are most significant where the frequencies of flexible-body modes are close to those of the rigid-body modes [Olsen, 1999], and the decoupled equations of motion are still commonly used [Schmidt and Raney, 2001; Siepenkotter and Alles, 2005]. Several different methods for the calculation of the aerodynamic forces have also been developed, both steady [Waszak and Schmidt, 1985a,b; Tuzcu, 2001] and unsteady [Cesnik and Brown, 2002; Tuzcu, 2007]. While some of these aerodynamic models may be suitable for aeroelastic analysis, these models may be unsuitable for real-time analysis

[Samareh and Bhatia, 2000] or control law development [Baker et al., 1999]. Let us then consider an aerodynamic model suitable for real-time aircraft flight dynamics analysis and control law development.

2.2 Unsteady Aerodynamics

The aerodynamic forces and moments acting on an aeroplane have traditionally been represented using the stability and control derivative approach [Bryan, 1911]. These steady aerodynamic derivatives are expressed as a function of the aeroplane's instantaneous translational and rotational velocities. It was recognised even by the 1920s however that the aerodynamic derivative approach was inadequate due to time-dependent aerodynamic effects. Cowley and Glauert [1921] identified the effect of tailplane downwash, a convective time delay in the downwash field induced by the wing, on the pitch damping derivative. This effect was approximated by a simple time lag by Cowley and Glauert [1921], and incorporated into the aerodynamic derivative approach as an acceleration derivative. This method assumes that the aerodynamic forces can be expressed as a Taylor series expansion [Etkin, 1959], treating the acceleration derivatives as additional terms in the series. While incorporating time-dependent aerodynamic effects, this remains only a quasi-steady model. There have been a number of studies more recently into aircraft flight dynamics which have included fully unsteady aerodynamic effects [Shearer and Cesnik, 2005; Abramov et al., 2005]. Abramov et al. [2004, 2005] have also considered the effects of unsteady aerodynamics on the dynamics and stability of fighter aircraft at high incidence. It was found that at low incidence for both longitudinal and lateral-directional manoeuvres the quasi-steady and unsteady aerodynamic models predict similar aircraft stability characteristics for this aircraft type. However, at high incidence angles the coupling between the rigid-body and unsteady aerodynamic modes was found to be much stronger, and the quasi-steady aerodynamic model inadequately predicted the aircraft's stability characteristics. There have otherwise been relatively few studies to suggest whether the inclusion of unsteady aerodynamic effects is necessary or what effect this has on aircraft flight dynamics [Greenwell, 2004]. Greenwell [2004] does note that the inclusion of unsteady aerodynamics "greatly improves the fidelity" of aircraft models, and that as "unsteady effects are significant then they will be of importance at some flight condition". A number of unsteady aerodynamic models exist, so then let us then consider several of the most widely used models for analysis.

Wagner [1925] first developed an indicial model of the unsteady aerodynamics of a two dimensional aerofoil in the 1920s. This described the unsteady response of the linear aerodynamic system to a unit step change in pitch. This is equivalent to the later Kussner function for entry of an aerofoil into a gust [Kussner, 1936]. The Wagner function represents the circulatory lift generated by the wing in incompressible flow, and accounts for the effect of the vortices shed in the wake. This indicial admittance model is most commonly approximated by a second-order exponential function [Jones, 1945]. The Wagner function is however only applicable to incompressible flow, and it has been shown that the effects of compressibility on the aerodynamic response are significant [Leishman, 1994]. The exact solution in compressible flow is only known for a short period of time [Lomax et al., 1952], however a number of studies have calculated the indicial response from experimental data in the frequency domain for compressible flow [Lomax et al.,

1952; Mazelsky and Drischler, 1952; Drischler, 1956]. These models include the compressible, non-circulatory lift component, which which was shown to be time-dependent in compressible flow [Mazelsky, 1951]. It can be argued that there is no advantage in analysing the circulatory and non-circulatory components separately in compressible flow [Bisplinghoff et al., 1955], and recently Marzocca et al. [2000] suggested an alternative combined third-order indicial function for an aerofoil in compressible flow. The response of the indicial aerodynamic system to arbitrary motion can then be calculated using the superposition, or Duhamel, integral [Bisplinghoff et al., 1955]. Alternatively, the Wagner function can be expressed in transfer function [Dowell, 1980] or state-space [Leishman and Nguyen, 1990] form. The unsteady aerodynamic forces for a three-dimensional wing can then be calculated using strip theory [Barmby et al., 1951; Lomax et al., 1952; Tobak, 1954]. This three-dimensional indicial model has been used in a number of recent aeroelastic studies [Qin et al., 2002; Na et al., 2005; Librescu et al., 2006]. The advantage of the indicial aerodynamic model is both ease of modelling and fast simulation times [Kier, 2005], and good correlation with higher fidelity CFD results [Sitaraman and Baeder, 2004].

A similar indicial methodology has been used to calculate the aerodynamic forces of wing-tail combinations [Jones and Fehlner, 1940; Klein, 1999]. This is an extension of the quasi-steady downwash lag effect proposed by Cowley and Glauert [1921]. Klein [1999] found that for aircraft with long tail arms, such as a large transport aircraft, the quasi-steady model of Cowley and Glauert [1921] was insufficient, and an unsteady formulation should be considered. A number of previous studies [Hofstee et al., 2003; Kier, 2005] into aircraft loads and flight dynamics, where unsteady aerodynamic effects are considered, have not considered this effect, either in its steady or unsteady form.

Analogous to the Wagner function in the time-domain is the Theodorsen function in the frequency-domain. The complex Theodorsen function describes the change in amplitude and phase of the aerodynamic forces for an harmonically oscillating aerofoil [Theodorsen, 1935; Theodorsen and Garrick, 1942]. Given as a function of the reduced frequency, it is often expressed is terms of modified Bessel functions or Hankel functions [Bisplinghoff et al., 1955; Fung, 1969]. Again, the unsteady aerodynamic forces for a three-dimensional wing can be expressed using the Theodorsen function in combination with strip theory [Yates, 1958]. Edwards [1979] showed that the Theodorsen function and the Wagner function could be equated using the Fourier transform. Although quite different in form, Theodorsen's function and the Wagner function are equivalent, and can be considered different representations of the "same" dynamic system [Leishman and Nguyen, 1990].

Goman and Khrabrov [1994] also proposed a state-space unsteady aerodynamic model, similar in form to that of Leishman and Nguyen [1990]. Unlike Leishman and Nguyen [1990], the state variables represent a physical feature of the flow, and are not formally assigned. Goman and Khrabrov [1994] proposes two different state variables, the instantaneous position of the flow separation point and the position of the vortex breakdown. The unsteady effects are divided into two groups, quasi-steady and transient effects. The quasi-steady effects, which include circulation and boundary-layer lags, which tend to delay flow separation and reattachment, are approximately proportional to pitch rate, and are given by an argument shift. The second group describes the dynamic properties of the separated flow, and is modelled using a first-order differential equation. This is linked as a non-linear function to the steady aerodynamic characteristics. The result is a first-order aerodynamic model which shows good agreement with experimental data. This

has been used in a number of studies into the flight dynamics aircraft at high incidence [Abramov et al., 2004, 2005].

The state-space aerodynamic model suggested by Peters et al. [1995] is also commonly used in aeroelastic aircraft analysis [Patil and Hodges, 1998; Shearer and Cesnik, 2005]. In common with Goman and Khrabrov [1994], the choice of state variables describes the physical flow itself, in this case the Glauert induced flow coefficients. While this has a number of advantages, in its present form it is less efficient than earlier second-order approximations for the Wagner function, requiring four to nine states compared to just two [Jones, 1940]. Peters et al. [1995] notes that this finite state model can be applied in the frequency- and time-domains as desired, and easily coupled with structural and control equations. This is a characteristic shared with all state-space models [Leishman and Nguyen, 1990; Goman and Khrabrov, 1994].

Another common unsteady aerodynamic model is the Doublet Lattice Method (DLM) [Blair, 1994]. This is an extension of the the Vortex Lattice Method (VLM) to a harmonically oscillating surface with the addition of an oscillating doublet [Albano and Rodden, 1969]. The result is a complex aerodynamic matrix in the frequency-domain. In order to express the result in the time-domain, a number of approaches have been applied, including using rational functions and Padé approximants [Vepa, 1977; Baker et al., 1999]. This method has been used for the simulation of HALE aircraft [Wang et al., 2006]. As a derivative of the VLM, this method shares the VLM's high aerodynamic prediction accuracy, however the disadvantage of this method is the slow calculation time, an order of magnitude slower than the indicial method [Kier, 2005].

We can see therefore that there have been a number of different unsteady aerodynamic models developed, both in the time- and frequency-domains. The importance of including unsteady aerodynamic effects in the modelling of aircraft flight dynamics has also been identified [Greenwell, 2004]. An indicial state-space method appears to lend itself to real-time aircraft simulation and control-law development [Peters et al., 1995], providing both suitably accurate estimates of aerodynamic forces [Sitaraman and Baeder, 2004], and quick calculation times [Kier, 2005]. It has also been found important to include compressibility [Leishman, 1994] and unsteady downwash effects [Klein, 1999] to ensure the accuracy of the aerodynamic estimation; this is particularly significant for a large civil transport aircraft.

2.3 Handling Qualities

The flying and handling qualities of an aircraft describe the ease with which the pilot can control and manoeuvre the aeroplane in the completion of some task or mission [Cook, 1997]. Flying qualities are defined here as the pilot's opinion and perception of the short-term dynamics of the aeroplane. The pilot's opinion is formed from the short-term characteristics of the aeroplane in response to pilot control, which may be influenced by a number of complex parameters, such as rigid-body natural frequency and damping ratio. Handling qualities on the other hand can be seen as the pilot's opinion on the ease and effectiveness of completing some defined mission or operational task. This can be influenced by the flying qualities of the aeroplane, but also by other parameters such as cockpit configuration and flight display information.

Adequacy for selected task	Aircraft characteristics	Demands on pilot in selected task	Pilot rating	Flying level
Satisfactory	Excellent	Pilot compensation not a factor	1	1
Satisfactory	Good	Pilot compensation not a factor	2	1
Satisfactory	Fair	Minimal pilot compensation required	3	1
Unsatisfactory - warrants improvement	Minor deficiencies	Moderate pilot compensation required	4	2
Unsatisfactory - warrants improvement	Moderate deficiencies	Considerable pilot compensation required	5	2
Unsatisfactory - warrants improvement	Tolerable deficiencies	Extensive pilot compensation required	6	2
Unacceptable - requires improvement	Major deficiencies	Adequate performance not attainable	7	3
Unacceptable - requires improvement	Major deficiencies	Considerable pilot compensation required	8	3
Unacceptable - requires improvement	Major deficiencies	Intense pilot compensation required for control	9	3
Catastrophic - improvement mandatory	Major deficiencies	Control will be lost during operation	10	–

Table 2.1: Cooper-Harper pilot opinion rating scale [Harper and Cooper, 1986]

The level of flying qualities is commonly defined in one of two ways, using level of flying qualities or pilot-rating. Flying quality levels, of which there are three, describe the ability of the aircraft to complete a task or mission for which it was designed. Each level describes the adequacy of the aircraft to complete the task, as well as the pilot workload required in order to complete that task. These increment from Level 1, which indicates the aircraft is completely adequate for the particular flight task considered, to Level 3, which indicates extremely poor flying qualities such that very high pilot workload is required and mission performance is highly degraded. The most common pilot-rating scheme used is the Cooper-Harper rating scale [Cooper and Harper, 1969]. This provides a formal assessment of the pilot's opinion and comments on the handling qualities of the aircraft. The Cooper-Harper rating scale varies from 1 to 10, where a pilot-rating of 1 indicates excellent aircraft characteristics and no pilot compensation requirement, and a rating of 10 indicates major deficiencies in the aircraft characteristics and that the pilot lost control of the aircraft for some period of the operation. A relationship between pilot-rating and flying quality level is defined, and for each pilot-rating there is an equivalent flying level [Table 2.1].

There exist many handling qualities criteria which aid the designer in the definition of the aircraft and the specification of its dynamic characteristics [Cook, 1997]. Both civil and military flying qualities specifications also exist which define the minimum performance requirements for a given aircraft. These aircraft flying specifications and handling qualities criteria can be specified in several ways. Military and civil flying specifications for example, such as MIL-STD-1797A and FAR 25 respectively, are commonly defined in terms of pole-zero specifications [MIL-STD-1797A, 1990; FAR:25(B), 1994]. This can

be in terms of minimum damping and natural frequency, or pole-position, for example, or zero-position, such as the incidence lag variable T_{θ_2} [Gibson, 1999]. Criteria can also be defined in terms of frequency response, such as minimum gain and phase margins, for example the Bandwidth Criterion [Hoh et al., 1982], or time response, such as the C* Criterion [Tobie et al., 1966]. Criteria can also be defined based on pilot models, such as the Neal-Smith Criteria which estimates aircraft flying qualities based on pilot model compensation requirements [Neal and Smith, 1971].

Many of these handling qualities criteria and flying specifications assume the aircraft exhibits classical, low-order characteristics. In order to estimate the handling qualities of an highly augmented aeroplane, an approach known as Low-order Equivalent System (LOES) modelling has been developed [Hodgkinson et al., 1976]. The LOES model describes a linearised, reduced-order transfer function model of the high-order aeroplane. Existing established low-order criteria may then be used to estimate the handling qualities of the aeroplane using this LOES model. However, while LOES modelling has been shown to provide accurate estimates for the handling qualities of highly augmented aircraft, its applicability to aeroelastic, flexible aircraft should be treated with caution [Hodgkinson et al., 1976]. It has been the case that very few existing criteria make direct reference to aeroelastic effects and their influence on handling qualities.

In general, flying specification requirements vary for different phases of a flight or mission. Certain pilot tasks associated with different flight phases require more stringent requirements in order to achieve that task successfully. Those tasks requiring similar flying qualities are commonly grouped together into three flight phase categories: Categories A, B, and C [MIL-STD-1797A, 1990]. The first category, Category A, describes non-terminal flight phases which require rapid manoeuvring, precision tracking or flight-path control. This might include tasks such as air-to-air combat, in-flight refuelling and formation flying. Category B describes non-terminal flight phases which would typically involve gradual manoeuvres without precision tracking, including climb, cruise, loiter, and descent. Finally, Category C describes terminal flight phases achieved using gradual manoeuvres requiring accurate flight-path control, for example take-off, approach and landing.

Aircraft are categorised broadly into four classes based on size, weight and manoeuvrability [MIL-STD-1797A, 1990]. Class I includes light, small aircraft such as light utility and trainer aircraft. Class II covers medium weight, low to medium manoeuvrability aircraft, which includes light or medium transport aircraft, tactical bombers and antisubmarine aircraft. The third class, Class III, includes large, heavy, low manoeuvrability aircraft such as heavy transport and bomber aircraft. Finally, Class IV covers high-manoeuvrability aircraft such as attack, fighter and air superiority aircraft. Civil transport aircraft are considered to be Class III aircraft, i.e. they can be described as being large, heavy aircraft, with low to medium manoeuvrability.

2.3.1 Longitudinal Flying Specifications

The relevant military flying specifications define minimum and maximum values for the natural frequency and damping for the longitudinal and lateral-directional rigid-body modes of the aeroplane [MIL-STD-1797A, 1990]. These flying specifications define maximum and minimum values for SPPO frequency and damping for each flight phase [Table

2.2]. The phugoid mode natural frequency should be well apart from the SPPO frequency, generally of the order $\omega_p/\omega_s \leq 0.1$, and minimum values of damping ratio are given [Table 2.3].

	Minimum SPPO Damping Ratio					
	Phase A		Phase B		Phase C	
Level	Min	Max	Min	Max	Min	Max
1	0.350	1.30	0.300	2.00	0.500	1.30
2	0.250	2.00	0.200	2.00	0.350	1.30
3	0.100	-	0.100	-	0.250	-

Table 2.2: Longitudinal SPPO mode flying specifications [MIL-STD-1797A, 1990]

Level	Phugoid Damping Ratio
1	0.0400
2	0.000
3	$\leq$ 0.000 with period $>$ 55.0s

Table 2.3: Longitudinal phugoid mode flying specifications [MIL-STD-1797A, 1990]

2.3.2 Lateral-Directional Flying Specifications

The maximum value of the roll mode time constant is defined in Table 2.4. No minimum value is defined, but is believed to be in the range of 6-10 seconds. MIL-STD-1797A [1990] specifies the minimum time to double amplitude for each flying quality level. It is however more convenient here to express this criteria in terms of the spiral mode time constant given in Table 2.5 [Cook, 1997]. Acceptable values for dutch-roll mode damping and frequency are similarly given in Table 2.6.

	Maximum Time Constant, s		
Level	Phase A	Phase B	Phase C
1	1.40	1.40	1.40
2	3.00	3.00	3.00
3	-	-	-

Table 2.4: Lateral-directional roll mode flying specifications [MIL-STD-1797A, 1990]

	Minimum Time Constant, s		
Level	Phase A	Phase B	Phase C
1	17.3	28.9	17.3
2	11.5	11.5	11.5
3	7.20	7.20	7.20

Table 2.5: Lateral-directional spiral mode flying specifications [MIL-STD-1797A, 1990]

	Dutch Roll Frequency and Damping								
	Phase A			Phase B			Phase C		
Level	ζ	$\zeta\omega$	ω	ζ	$\zeta\omega$	ω	ζ	$\zeta\omega$	ω
1	0.190	0.350	0.500	0.080	0.150	0.500	0.080	0.100	0.500
2	0.020	0.050	0.500	0.020	0.050	0.500	0.020	0.050	0.500
3	0.000	-	0.400	0.000	-	0.400	0.000	-	0.400

Table 2.6: Lateral-directional dutch-roll flying specifications [MIL-STD-1797A, 1990]

2.4 Flight Control

It is often the case with many modern aircraft to employ some form of Flight Control System (FCS). An FCS is commonly comprised of air data sensors, accelerometers, and rate gyros measuring the aircraft states, such as velocity and attitude, together with actuators which control the aerodynamic control surface deflections and throttle. The aircraft response is then fed back, typically using negative rate feedback, to the control surface actuators. A control law may be implemented by including one, or several, control functions in the control, forward or feedback paths, each of which can influence the aircraft dynamics differently. The purpose of the FCS may include control and stability augmentation to improve an aircraft's flying and handling qualities or manoeuvre and tracking ability, ride comfort improvement, or manoeuvre and gust load alleviation.

2.4.1 Control and Stability Augmentation

It is quite common that an aircraft's dynamic characteristics do not meet flying and handling qualities requirements. It is often therefore necessary to modify, or augment, the dynamic characteristics of the aircraft. This is known as a Stability Augmentation System (SAS), and is an integral component of the FCS in many modern aircraft. In addition to a SAS, it is common to modify the control and stability characteristics of the aircraft to improve performance in pilot manoeuvre and target tracking tasks; this is known as a Control Augmentation System (CAS). Together, these two systems are known as a Control and Stability Augmentation Systems (CSAS). The CSAS control law may be implemented by including one, or several, control functions in the control, forward or feedback paths, each of which can influence the aircraft dynamics differently [Cook, 1997].

The closed-loop control and stability characteristics of the aircraft are primarily designed using the feedback path, while the control path may be used to modify the control signal-response properties of the aircraft without altering its closed-loop characteristics. The forward path can be used to both influence the closed-loop characteristics of the aircraft, as well as providing some control signal response shaping.

SAS have typically used negative rate feedback in order to improve the control and stability characteristics of the aircraft; this is often simply achieved by improving the damping properties of rigid-body aircraft modes through rate feedback. For example, the damping of the Short Period Pitching Oscillation (SPPO) mode can be improved by using pitch-rate feedback to artificially increase damping. Where it is necessary to perform precision pilot tracking tasks, a CSAS using a Rate Command-Attitude Hold (RCAH) system has been found to be effective in improving the dynamic characteristics of the aircraft. For example, in pitch-response, it has been found that a normal acceleration demand system provides good manoeuvrability, while pitch-rate demand is able to offer good tracking characteristics. As a result of the decoupling of the longitudinal and lateral-directional dynamics of the aircraft, it is common to design the longitudinal and lateral-directional CSAS control laws separately from each other.

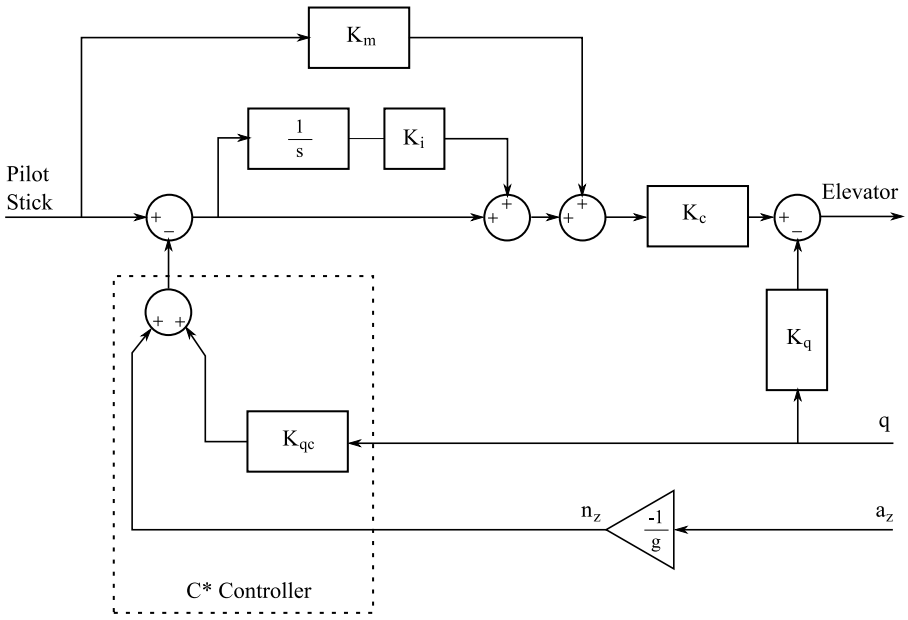

Figure 2.2: Longitudinal CSAS controller block diagram [Favre, 1996]

Favre [1996] describes typical transport aircraft longitudinal and lateral-directional control laws, shown in Figures 2.2 and 2.3 respectively. The longitudinal pitch control law is described by Favre [1996] as being a C* control law type. A RCAH-type controller is used to achieve good tracking accuracy, referred to as a "Pilot command auto-trim", which holds a stick command after the pilot releases the stick and a steady state has been achieved. The load factor demand is also limited to within the structural design capability for full stick deflection [Chatrenet, 1990]. The lateral-directional control law is described as being a roll rate demand, proportional to stick deflection, and limited to $15°\text{sec}^{-1}$ [Favre, 1996]. The roll damping coefficient is kept above 0.6 for all flight cases using roll rate feedback. Bank angle protection, together with several other features,

are also incorporated for safety reasons. Above 33°, positive spiral stability is introduced with stick deflection proportional to bank angle. The yaw controller is described as a classical yaw damper [Favre, 1996]. The objective of the control law is to minimise side-slip, as calculated mainly using the lateral acceleration, and to improve dutch-roll damping. Dutch roll dynamics are improved using yaw rate feedback, and the roll-yaw coordination in turn entry is improved using an aileron-rudder interlink.

2.4.2 Load Alleviation

In addition to the CSAS control law, it is increasingly common to find a Load Alleviation Function (LAF) in many large civil and military aircraft. The purpose of this is commonly to reduce manoeuvre loads, known as Manoeuvre Load Alleviation (MLA); and gust loads, known as Gust Load Alleviation (GLA); improving passenger ride comfort, for example a Comfort In Turbulence (CIT) function [Favre, 1996]; and reduce structural dynamic deformations, termed here Active Mode Control (AMC). The LAF system may be comprised of one, or all, of these components, but the general principle behind all of the components is the management and reduction of aerodynamic and inertial loads on the structure, for example reducing wing root bending moment and shear.

The MLA function is designed to reduce manoeuvre loads by deploying some combination of wing primary and secondary control surfaces, i.e. ailerons, spoilers and, optionally, flaps, in response to measured aircraft fuselage normal acceleration. Deployment rates are generally slow, and elevator is commonly used in conjunction with wing control surfaces to compensate for the modified pitching moment. Through deployment of control surfaces, the intention is to modify the lift distribution acting on the wing, moving the centre of lift inboard. This reduces the lift moment arm and thereby reducing wing root bending moment [Figure 2.4].

The turbulent motion of the air through which the aircraft flies results in altering the aerodynamic forces and moments applied to the aircraft, in turn exciting aircraft rigid-body motion. The purpose of a GLA system is the reduction or cancellation of these gust effects. This is achieved through rapid deployment of wing control surfaces in response to aircraft normal acceleration. By deploying wing control surfaces, it is possible to reduce the excitation energy of the gust, reducing the magnitude of the aerodynamic and inertial forces applied to the structure. In this way, for example, both gust-induced wing root bending moment and shear force may be reduced.

The MLA and GLA systems are designed to alleviate manoeuvre and gust loads by managing the aerodynamic loads acting on the wing. The reduction of structural deflections and inertial loading is achieved indirectly through this method. An AMC system however is designed to artificially augment, or increase, damping for particular aircraft structural modes. Through measurement and active response to structural accelerations, structural deflections are reduced directly. This is similarly achieved through deflection of aircraft control surfaces, e.g. aileron, rudder and elevator. In this way, the energy absorbed by the structure from a gust or manoeuvre may be dissipated more quickly. This can have the effect of reducing loads or improving passenger ride comfort, e.g. by reducing fuselage accelerations.

Early systems separated the development of CSAS and LAF systems. This was often

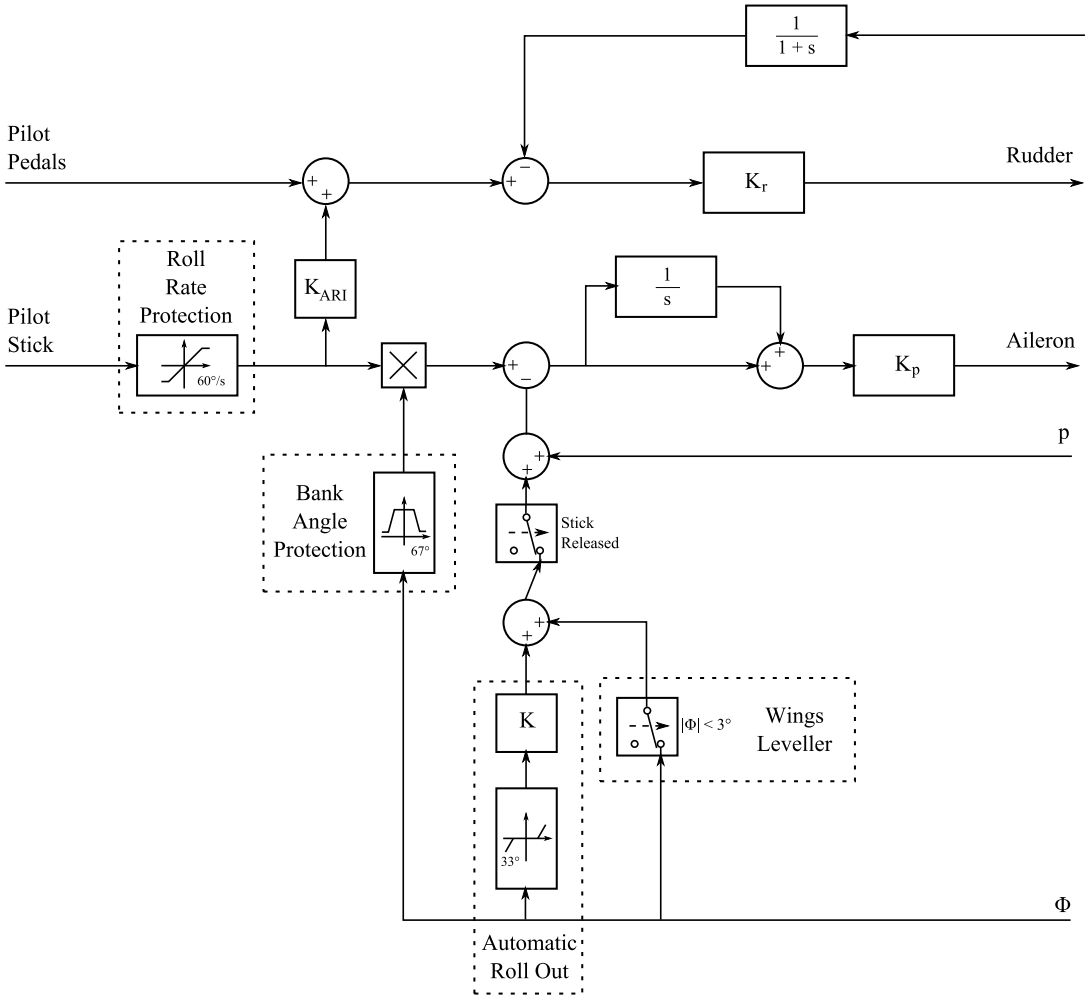

Figure 2.3: Lateral-directional CSAS controller diagram [Favre, 1996]

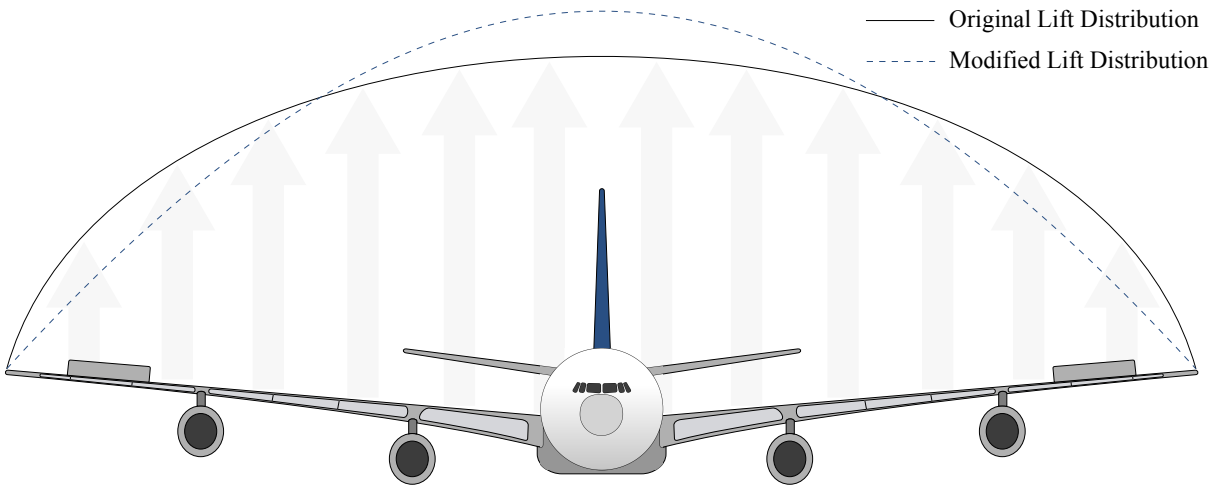

Figure 2.4: Initial and resultant aircraft lift distribution for MLA control deployment

because the LAF system was designed after the initial development of the aircraft, for example with the Boeing B-52 Stratofortress [Burris and Bender, 1969]. However, this decision was also influenced by the "natural reluctance" of the pilot and flight crew to relinquish control of the aircraft to the FCS [Disney and Eckholdt, 1976]. A brief review of these early systems provides a valuable insight into the design and workings of LAF systems in general.

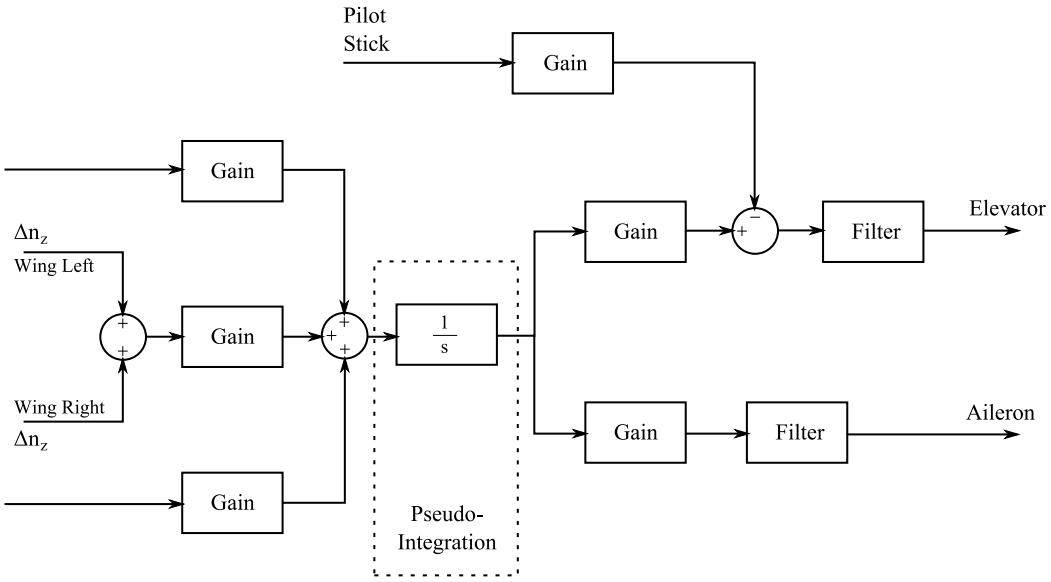

Figure 2.5: Boeing B-52 longitudinal LAMS block diagram [Burris and Bender, 1969]

Typical of an early AMC function is the system found on the North American Rockwell XB-70 [Wykes et al., 1970]. This system is designed as an active structural mode control system, the purpose of which is to reduce the energy absorbed by the structure due to a gust as well as dissipating that energy quicker by augmenting structural damping. The XB-70 control system separates rigid-body motion from structural motion by subtracting the normal acceleration sensed at the nominal aircraft centre of gravity from the acceleration sensed by accelerometers mounted on the wings. The isolation of the structural, or rigid-body, acceleration is a recurring problem in the design of the FCS, both for CSAS and LAF functions. This was traditionally achieved by filtering the control signal, and for example, the Boeing 747 LAF system uses bandpass filtered wing acceleration to isolate structural acceleration from rigid-body acceleration [Anon., 1980]. Alternatively, the structural deflections can be estimated using a blend of sensors signals. For example, the LAF system developed by Burris and Bender [1969] for the Boeing B-52 bomber, referred to as a Load Alleviation and Mode Stabilisation (LAMS) system, uses a blend of rate gyro and accelerometer signals. The longitudinal LAMS system uses four rate-gyros, located in the fore- and aft- fuselage and one in each wing, with the signals blended to produce pitch rate, and two structural modal rates. The lateral-directional system similarly uses six rate gyros in the fuselage to estimate yaw rate, roll rate and one structural mode, driving the rudder and ailerons asymmetrically. The structural rates are integrated to approximate structural deflections, and the feedback signals are gain and phase adjusted.

The B-52's LAMS system is described as being designed to alleviate structural loads while flying through gusts and turbulence. The system drives the elevators, ailerons

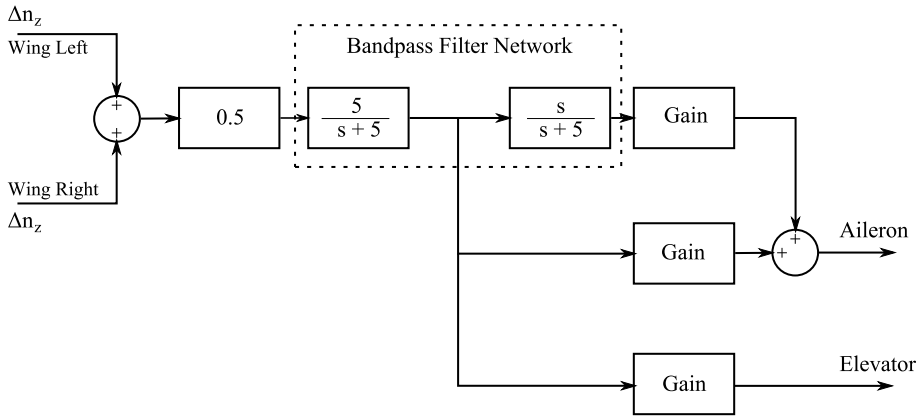

Figure 2.6: Boeing 747 WLA block diagram [Anon., 1980]

and spoilers. Control of the ailerons and spoilers provides direct control of wing loading through modification of the lift distribution, while the elevator provides indirect load alleviation by increasing pitch damping in response to gusts, as well as compensating for the pitching moment due to aileron and spoiler deployment [Burris and Bender, 1969]. A simplified block diagram shows the longitudinal LAMS system [Figure 2.5].

Wykes et al. [1970] also notes the importance of careful placement of wing accelerometers in order to best estimate the correct structural accelerations. This was also considered by Anon. [1980] in the development of the Boeing 747 system. The Boeing 747 wing accelerometers are placed where the deflection of the structural mode of interest, namely the first wing bending mode, is largest, but deflections of other modes are much less.

The purpose of the 747 system was the reduction of aerodynamic loads due to manoeuvre, primarily, and gust. Anon. [1980] describes the Manoeuvre Load Control (MLC) function which uses outboard aileron deflections to modify the lift distribution, reducing manoeuvre loads. Gust load alleviation is achieved indirectly for lower-frequency gusts through the quasi-steady MLC function, and directly through active control, or Elastic Mode Suppression (EMS), of the first wing bending mode. The control law uses an averaged wing accelerometer feedback loop to estimate aircraft vertical acceleration, which controls ailerons, plus elevator to counteract the aileron-induced pitching moment [Figure 2.6]. The 747 LAF system does not control the elevator, and therefore pitch-response to gust, directly. This is in contrast to a number of other LAF systems, including the system found on the B-52 [Burris and Bender, 1969]. The result of direct elevator control is that these systems act to damp the pitch the response of the aircraft, including the pilot-demanded response. It is necessary then to add a stick-control surface forward path signal parallel to the existing SAS path in order to maintain the desired handling qualities.

The B-52 LAMS concept was demonstrated on a second aircraft, the Lockheed C-5 Galaxy. The results of this study prompted the development of a similar load alleviation system, but for the purpose of reducing wing loads rather than fatigue loads. This was known as the Active Lift Distribution Control System (ALDCS) [Disney and Eckholdt, 1976]. The ALDCS uses two control law channels, controlling the ailerons and elevators [Hargrove, 1976]. The first channel controls the ailerons symmetrically using a feedback

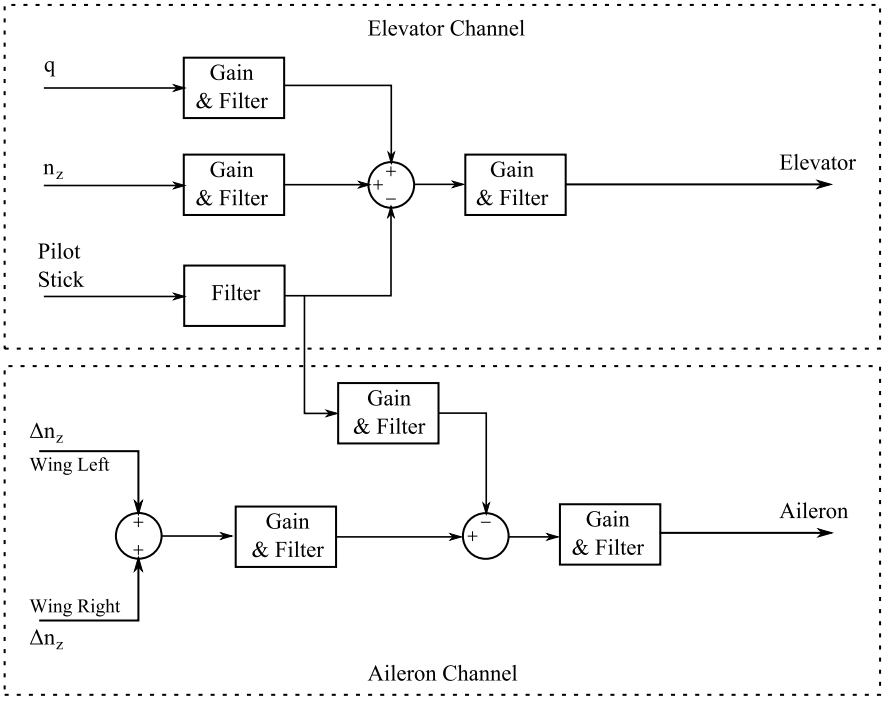

Figure 2.7: Lockheed C-5 ALDCS block diagram [Disney and Eckholdt, 1976]

signal from two accelerometers mounted in each wing at an outboard wing station. The feedback signal from each wing is averaged, and the signal filtered to remove higher frequencies above the bandwidth of the ALDCS system. A pilot stick feed-forward path signal to aileron is used to provide abrupt manoeuvre load control. The second channel controls the elevator, providing manoeuvre and gust load alleviation [Hargrove, 1976]. This channel uses two feedback signals, measured from a fuselage-mounted accelerometer and a fuselage pitch-rate gyro, plus a feed-forward path signal from the stick. The accelerometer and rate gyro signals are used to augment pitch damping, reducing the excitation of SPPO-induced gust loads and compensating for pitch-response due to aileron deployment. Similar to the B-52 system [Burris and Bender, 1969], a pilot stick feed-forward signal is used to restore handling qualities which are degraded by the ALDCS system. A block diagram shows the two control channels [Figure 2.7].

As can be seen from these simple examples, load alleviation fundamentally regards the modification of lift distribution through control of the aerodynamic control surfaces for the reduction of gust and manoeuvre induced loads. This can be for the reduction of loads, improving ride comfort, or reducing fatigue. This may take the form of load control, such as the Boeing 747 WLA [Anon., 1980] and the Lockheed C-5 ALDCS systems [Disney and Eckholdt, 1976], or active control of structural modes, such as the Boeing 747 EMS or North American Rockwell XB-70 systems [Wykes et al., 1970]. Feedback loops can utilise filtered acceleration data from wing and fuselage mounted accelerometers, or similarly mounted rate gyros. Pilot stick feed-forward path control is also necessary where the aircraft pitch response is actively controlled through the LAF system [Burris and Bender, 1969].

2.4.3 Aeroservoelasticity and Integrated Control

Aeroservoelasticity is the interaction between the Flight Control System (FCS), the aerodynamics and the elastic structure. This is easily summarised in the extension of Collar's Triangle of Forces proposed by Wright and Cooper [2007] to include control forces [Figure 2.8]. The FCS includes any number of motion sensors, including accelerometers and rate gyros, which measure the aircraft rigid-body motion. These signals are then fed back through a control law, which may include a combination of CSAS and LAF functions, to the control surface actuators. Aeroservoelastic problems typically occur when these signals are contaminated with the measured motion of the flexible aircraft modes. This "structural coupling" can result in excessive actuator control and fatigue problems. It can also cause dramatic and catastrophic failure of the structure in the event of flutter.

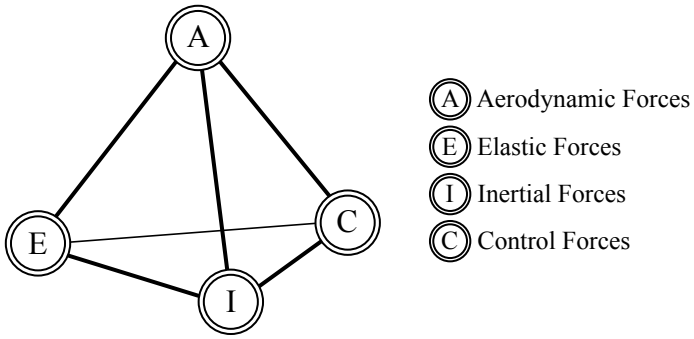

Figure 2.8: Aeroservoelastic Pyramid of Forces [Wright and Cooper, 2007]

Traditionally passive methods have been used to limit the interaction of the FCS with the structural dynamics. Low-pass and notch filters have commonly been used in the forward and feedback paths of the control law to ensure stability and reduce pilot excitation of structural modes [Livet et al., 1994b]. This ensures that any errant signals containing flexible-body motion are sufficiently attenuated at the critical frequencies. The careful selection of sensor placement locations has also been utilised in order to minimise the contamination of rigid-body signals [Al-Shehabi and Newman, 2002]. In its most simple application, this has traditionally involved the manual placement of sensors near to a structural node by inspection of the characteristic modes of the structure. This process is complicated however by the conflicting signal requirements for CSAS and LAF systems. Mass balancing and increased structural stiffness have been used to limit and reduce the interaction [Kubica and Livet, 1994b]. However, as the frequencies of the flexible modes are reduced, the interaction between the structure and the aircraft flight control system dynamics becomes significant.

Tuzcu and Meirovitch [2005] studied the effect of the inclusion of structural flexibility on the stability of a flexible aeroplane with feedback control. Comparing the linearised eigenvalues for a business jet aircraft model, Tuzcu and Meirovitch [2005] shows that the rigid aircraft is stable with feedback control, as is the constrained aeroelastic aircraft model. However, when the feedback control for the rigid aircraft is used with the flexible aircraft, which Tuzcu [2007] shows has similar dynamics to the separate rigid and constrained aeroelastic model and is stable, the system is found to be unstable. Tuzcu et al. [2006] also considers this problem for the case of a HALE aircraft. The controller in this case is designed using optimal state feedback to ensure some degree of robustness,

however when the rigid aircraft controller is used with the flexible aircraft, it is again found that several flexible modes are driven unstable. A similar result was found by Kubica and Livet [1994b], who showed when a classical eigen-structure assignment method is used to design the feedback control, the result for a flexible aircraft is that the system may result in being unstable.

The result of this undesirable interaction between the FCS and the aeroelastic aircraft is the development of integrated flight control laws, combining the functions of both CSAS and LAF systems, developed around the complete aeroelastic aircraft. As aircraft have increased in size however, the frequencies of the flexible modes have reduced, and the interaction between the rigid-body and flexible-body modes has increased. It therefore becomes difficult to reduce structural coupling without reducing the bandwidth of the flight control law [Kubica, 1998]. As such it is increasingly common today to design an integrated flight control system for an aircraft, combining the functions of both CSAS and LAF systems [Kubica, 1998].

Kubica and Livet [1994b] proposed such an integrated control law for a flexible aircraft for longitudinal control. Kubica and Livet [1994b] showed that eigen-structure assignment was unsuitable for control of the flexible aircraft, as the strong interaction of the flexible and rigid modes drove some flexible modes to be unstable. It was therefore proposed that the Linear Quadratic Gaussian (LQG) method was proposed to design the controller. This gave good results, with a good compromise between robustness and performance. Kubica and Livet [1994b] concluded that LQR with weighted output feedback was unsuitable however due to the limited degrees of freedom. In a second paper, Kubica and Livet [1994b] proposed an improvement to this methodology, using state weighting, which was found to give good results and improved the flexible mode damping. A different approach to the LQR method was suggested by Ward and Ly [1994], who proposed using parameter optimisation to synthesise the control law. A C* control-law was developed using this method, and the results were close to the optimum robustness and performance of the LQR model. Livet et al. [1994b] also considered robust flight control of a flexible aircraft in lateral flight using iterative quadratic optimisation under linear inequality constraints. This methodology had been proposed earlier by Livet et al. [1994a], and was now applied to a flexible aircraft. The rigid body poles were migrated into a "performance trapezium", while the flexible modes were considered simply with the aim to improve damping only.

One issue that Kubica and Livet [1994b] did not address was the location of sensors in the aircraft. There have been a number of studies into the suitable placement of aircraft sensors, including manual [Newman and Buttrill, 1995] and optimal [Al-Shehabi and Newman, 2002] location selection. In the control of longitudinal fuselage modes, fuselage accelerometer sensors would typically be located at the nose and tail, structural anti-nodes, but several other locations, including mounting sensors on the engines [Kubica and Garrec, 2004], have been considered. The issue of sensor location was addressed in a second paper on the topic of integrated control by Kubica and Livet [1994a]. By using observability gramians, it was shown that the aft accelerometer gave the best information about each of the elastic modes. Controllability gramians were also used by Kubica and Livet [1994a] to observe the influence of inputs on the states of the system, i.e. the effect of different control surface deflections on the elastic modes. It was also suggested by Livet et al. [1994b] that the number of sensors could be increased, effectively "creating" new degrees of freedom, to improve the performance of the control law.

It can be seen then that there are a number of approaches which can be used in the development of an integrated control law for a flexible aeroplane. There are also a number of advantages to an integrated approach to the design of the FCS. The aeroservoelastic advantages include increased effective structural damping, reducing fatigue loading; and the avoidance of aeroservoelastic phenomenon including flutter and control surface limit-cycle oscillations. With regards to the rigid-body motion of the aircraft, the advantages are an increased controller bandwidth, which gives the possibility of improving structural damping and handling qualities, as well reducing the aircraft susceptibility to PIOs [Kubica, 1998].

2.5 Flexible Aircraft Handling Qualities

2.5.1 Stability, Dynamics and Handling Qualities

While there have been numerous studies into the flight dynamics and handling qualities of aircraft, in general they have been concerned only with the motion of rigid aircraft [Cook, 1997]. Up until the 1970s, while there had been much interest in aeroelasticity, which generally ignored rigid body motions, there remained very little interest in considering the flight dynamics and handling qualities of flexible aircraft. This is in part because prior to World War II, the study of aircraft dynamics was largely of little interest to aeroplane designers, who often left the design of aircraft stability and control to empirical estimates and a "cut-and-try" approach [McRuer et al., 1973]. It is also in part because aircraft until the 1950s and 1960s, with the notable exception of the Hughes H-4 Hercules, had been relatively small. For these smaller aircraft, the natural frequencies of the structural modes were often much higher than the rigid-body frequencies, and the rigid- and flexible-body dynamics may be considered decoupled. The aircraft response was then sufficiently accurately estimated using a rigid aircraft model [Wright and Cooper, 2007]. With the introduction of larger, modern aircraft, the natural frequencies of the structure became much closer to the rigid-body frequencies [Schmidt and Raney, 2001]. It is then necessary to consider the rigid- and flexible-body dynamics simultaneously. Since the development of the equations of motion for a flexible aeroplane in the 1960s [Milne, 1962], there have been several studies into the flight dynamics and handling qualities of these aircraft, though the number remains relatively few.

The most complete study into the handling qualities of flexible aircraft was conducted by a number of authors in the late 1970s and 1980s. In a number of different studies, the handling qualities of the flexible Rockwell B-1B Lancer bomber [Figure 2.9] were investigated. Yen [1977] undertook a parametric analysis of the effect of aeroelastic natural frequency on handling qualities and pilot rating, varying the frequencies of the two included structural modes. Yen [1977] showed that as the natural frequencies are reduced, the handling qualities are degraded as the aeroelastic dynamics interact with the rigid-body dynamics. This was attributed to rigid-flexible mode interaction, lowering the natural frequency of the rigid-body short-period mode, and causing the phugoid mode to split into positive and negative real roots, degrading the pilot's tracking ability. This was confirmed in a study by Waszak and Schmidt [1985a,b], who analysed the open-loop and closed-loop characteristics of the aircraft, extending the the Neal-Smith Criteria [Neal and Smith, 1971] for high-order dynamic systems to an aeroelastic aircraft for the closed-loop

analysis. Waszak and Schmidt [1985a,b] found that as the frequencies of the elastic modes were decreased, the handling qualities of the aircraft were reduced and that this also correlated with a reduction in the bandwidth of the aircraft. It was found that the effect on handling qualities could occur even where the flexible mode frequencies were several times higher than the rigid-body frequencies. These results were confirmed in a study by Schmidt [1985], who showed that aeroelastic effects were noticeable in the handling qualities even where the lowest structural frequency was three times the rigid-body short-period mode frequency. Yen [1977] also attributed the reduction in handling qualities to the effect of flexibility on the perceived angle of attack. It was shown that the angle of attack perceived by the pilot is a function not only of the rigid-body angle of attack, but also of the flexibility of the fuselage and the position of the cockpit station. This contribution due to fuselage flexibility was found to increase as the natural frequencies of the structure were reduced. This resulted in reduced pilot ratings as the pilot found it difficult to distinguish between rigid- and flexible-body modes. These results were validated in NASA Langley Research Centre's Visual-Motion Simulator [Waszak et al., 1987a,b; Schmidt and Raney, 2001]. While the earlier models of Yen [1977] and Waszak and Schmidt [1985a,b] did not include the flight control system, Waszak et al. [1987a,b] also included a conventional control and stability augmentation system.

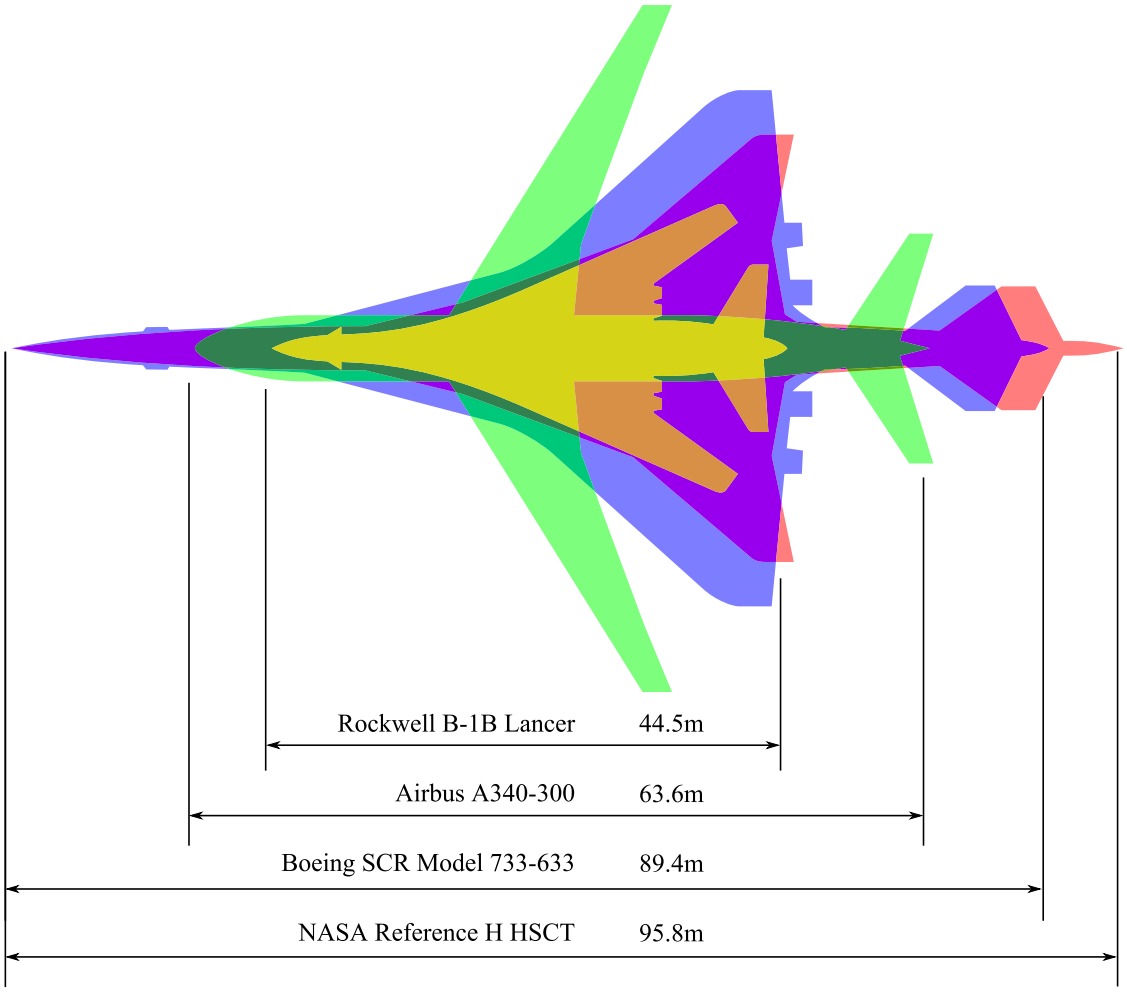

Figure 2.9: Size comparison of flexible aircraft[1]

[1] Derivative work of Tillier [2006]

The configuration of the B-1B Lancer shares a number of similarities with many Supersonic Transport aircraft (SST) designs. In response to the development of the Concorde SST by the Bristol Aeroplane Company and Sud Aviation in the early 1960s, the US Government commissioned the development of a commercial airliner to compete with the European SST. Boeing's entry, the Model 733-197, more commonly known publicly as the Boeing 2707, closely resembled the future B-1B Lancer bomber, featuring a similar swing-wing design. Numerous technical, environmental and political issues resulted in the US Government cutting funding for the SST program in 1971, and the development of the Boeing Model 733 was cancelled. There have since been several research programs conducted by NASA, notably the Supersonic Cruise Research Program (SCR) between 1972 and 1982; and the High Speed Research program (HSR) between 1986 and 1999.

Boeing had considered a variety of alternative SST design configurations in the late 1950s, all under the name Model 733. As part of the SCR program, Ashkenas et al. [1983b] investigated the flying and ride qualities of another 733 variant, the Model 733-633, a delta-wing design more similar in size and configuration to Concorde [Figure 2.9]. A total of 10 longitudinal fuselage bending modes are considered in "Model C" by Ashkenas et al. [1983b], increasing in frequency and complexity from 7.16 to 40.46 rad s^{-1}. Unsteady aerodynamics are included as a discrete function of reduced-frequency. Ashkenas et al. [1983b] applies a number of frequency- and time-domain flying qualities criteria in order to assess the flying and ride qualities of the aircraft, including equivalent system phase-delay estimation, bandwidth, and time-domain response envelopes. In agreement with many of the finding for the B-1B Lancer, high frequency vertical acceleration and an increase in the effective time delay in pitch-attitude response was witnessed at the pilot's station. The latter was attributed to the low-frequency bending modes seen at the pilot's station. It was also found that high-frequency pilot station acceleration feed-through could lead to a pilot-induced oscillation involving a "high" frequency flexible mode where the pilot regresses to a pure proportional gain control in response to an upset or other "stressful occurrence". Joshi and Kelkar [1996] also used the model developed by Ashkenas et al. [1983b] to investigate the robustness of LQG-type controllers to un-modelled flexible modes.

As part of the HSR program, NASA awarded a contract to Boeing and Douglas Aircraft Company to develop the High Speed Civil Transport aircraft (HSCT). The HSCT would fly 300 passengers at Mach 2.4, and the design process culminated in the development of the Boeing "Reference H" design in 1996. The "Reference H" design shared many similarities with the delta-wing Model 733, and in turn the B-1 Lancer bomber [Figure 2.9]. A number of studies have investigated the simulation and flying qualities of the HSCT.

Raney et al. [2001, 2002] conducted a study in NASA Langley Research Centre's Visual-Motion Simulator (VMS) using the Cycle 3 "Reference H" HSCT aircraft. Six flexible modes were considered, both symmetric and asymmetric, though again only including fuselage bending modes. Raney et al. [2001] studied the effectiveness of several measures in order to reduce the impact of aircraft flexibility on piloting tasks, which included structural stiffening (by increasing the natural frequency of the flexible modes), increased modal damping, active mode control, and the cancellation of vibration-induced visual cues. Stiffness ratios of 1.0 through 1.6 were considered, resulting in an increase in the first fuselage bending mode from 7.85 to 12.56 rad s^{-1}. Modal damping ratios of 0.07, 0.15, and 0.3 were also considered. These values are all much greater than the 0.02 that

was used Waszak and Schmidt [1985a,b]. It was found that structural stiffening and the elimination of visual cues provided little improvement in alleviating the influence of aircraft flexibility on piloting tasks. The latter suggests the importance of non-visual cues, namely acceleration, in piloting tasks, in agreement with Ashkenas et al. [1983b], though the magnitude of visual perturbations at the pilot's station was found to be small, in the order of +/-1 degrees. It was found by Raney et al. [2001] however that increased modal damping and active mode control offered significant improvements in pilot rating. The latter might be expected given the former, assuming that active mode control essentially provides an artificial increase in the damping of certain structural modes. Schmidt and Raney [2001] identified the effect of "biodynamic-feedthrough" in a study of the B-1B Lancer and the HSCT aircraft. This interaction of structural vibrations with the pilot's bio-mechanical dynamics was found to result in the closed-loop system being lightly damped or unstable. This in some circumstances resulted in "biodynamic-coupling", a resonant coupling of the pilot's muscular response and the structural vibrations which resulted in the direct feed through of the vibration of elastic modes through the pilot's arm and into the control stick. Several occur

In a review of the history and state-of-the-art of handling qualities research, Mitchell et al. [2003] reiterates the importance of structural interactions in the analysis of handling qualities, primarily quoting the findings of Schmidt and Raney [2001] and earlier authors [Waszak and Schmidt, 1985a,b]. These early studies focused on two aircraft, the Rockwell B-1 Lancer bomber [Yen, 1977; Waszak and Schmidt, 1985a,b], and a supersonic transport aircraft [Schmidt and Raney, 2001], both of which share a similar slender fuselage and highly swept wing configurations, quite different from the modern transport aircraft.

A number of authors have since then considered the flight dynamics and stability of flexible aircraft, though the focus of attention has primarily been guided by the development of very flexible HALE aircraft. Shearer and Cesnik [2005] analyse the longitudinal and lateral flight dynamics of a HALE aircraft, comparing the response of rigid-, linear- and non-linear-structure aircraft models. It was found that the rigid aircraft simulation was insufficient to accurately capture the dynamics of the aircraft. Moreover, it was also found that a non-linear simulation was required to capture the aircraft response in lateral manoeuvres due to the high flexibility of this aircraft type, however in longitudinal manoeuvres it was found that a linear simulation was sufficient to properly capture the aircraft dynamics of even this highly flexible aircraft. Su and Cesnik [2006] also consider the flight dynamics of a similar aircraft type. Comparing the eigenvalues for the linearised rigid and flexible aircraft models, Su and Cesnik [2006] show the influence of the inclusion of structural flexibility on the short-period and phugoid modes, lowering the short-period frequency and driving the phugoid mode unstable in the high weight configuration. This is a similar finding to that of Yen [1977] for the more conventional Rockwell B-1 Lancer aircraft type. However, that is not to say that the inclusion of flexibility effects is always destabilising. Tuzcu et al. [2006] compared the linearised eigenvalues for a rigid and flexible HALE aircraft model. The rigid aircraft had unstable phugoid and spiral modes, while the flexible aircraft's phugoid mode was stable, and the time constant of the spiral mode was increased in comparison to the rigid aircraft. It can be concluded that flexibility had a stabilising effect in this case.

Tuzcu [2007] also recently analysed the effects of rigid-body motion on aeroelastic stability. Linearising the aeroelastic model at a number of flight points, Tuzcu [2007] used a "trial and error" iterative approach to identify the divergence and flutter speed of a

simulated business jet from the linearised eigenvalues. It was found that inclusion of the rigid-body degrees of freedom altered the aeroelastic stability of the aircraft, in this case increasing the flutter speed. This is in agreement with the earlier results of Frazer and Duncan [1928b].

It can be seen then that the effects of the flexible structure have a noticeable and measurable effect on the flight dynamics and handling qualities of many aircraft types [Yen, 1977; Schmidt and Raney, 2001; Shearer and Cesnik, 2005]. These effects are of particular significance for modern transport aircraft, which continue to increase in size [Mitchell et al., 2003]. However, research has until now has focused only on other aircraft types [Yen, 1977; Schmidt and Raney, 2001; Shearer and Cesnik, 2005], and has not included the influence of the flight control system [Yen, 1977; Waszak and Schmidt, 1985a,b], or modern load alleviation or active mode control systems [Waszak et al., 1987a,b].

2.5.2 Aircraft-Pilot Coupling

The aeroelastic deformation of the airframe can also contribute towards the occurrence of Aircraft-Pilot Coupling (APC). An APC, or Pilot-Induced Oscillation (PIO), is an inadvertent and undesirable oscillation which is the result of the closed-loop pilot-aircraft coupling. Although APCs can vary widely, they can generally be regarded as a zero-damped or unstable oscillation of the aircraft motion which is caused by poorly phased pilot control. That is not to say that the pilot is responsible for APC, however the pilot is certainly a contributing factor in such events. These events can occur during common high gain tasks, such as aerial refuelling, precision tracking, and formation flying [McRuer, 1995], however APCs themselves are generally very rare. APCs can occur as a result of excessive time delays, changes in pilot behaviour or be triggered by external events such as a system failure or stores release, and can involve rigid body and control dynamics. APCs can also involve the aeroelastic airframe dynamics.

Norton [1995] categorises aeroelastic APCs as one of three types. Type 1 PIOs are described as being the result of aeroelastic deformation of the fuselage such that the cockpit and pilot experience changes in attitude and acceleration, prompting the pilot to intentionally counteract this perceived rigid-body motion. This can occur in the frequency range of 1-2Hz as the pilot interacts with these higher frequency flexible modes [McRuer, 1995]. The pilot's reaction may be the result of vestibular cues, such as cockpit acceleration and attitude changes due to fuselage deformations. It may also be the result of visual cues, such as the change in perceived attitude due to aeroelastic deformation, or the influence of aeroelastic deformation on FCS feedback sensory data and visual displays. The latter is often minimised through careful placement of sensory accelerometers and rate gyros at structural nodes as well as filtering of the feedback signal. Type 2 PIOs are described as being the result of aeroelastic deformation such that the rigid-body aircraft response is modified, and the pilot responds to these dynamics, attempting to counteract this motion. This can be the result of the modification of the aerodynamic forces due to aeroelastic deformation, such as changes in wing incidence due to aeroelastic torsion or tailplane incidence due to fuselage deflections. It may also be due to feedback of structural deformations to control surfaces through the FCS, a problem known as aeroservoelasticity. Finally, the third category is aeroelastic Pilot Augmented Oscillations (PAO). This occurs when accelerations at the cockpit station produce unintentional control inputs by

the pilot. This bio-dynamic feedback can occur in the range 0.3-0.8Hz, as the aeroelastic accelerations interact with the neuromuscular dynamics of the pilot, as well as in the range 2-3Hz, the natural frequency of the pilot limb/controller [McRuer, 1995]. An example of an aeroelastic or rigid-body PAO is roll-ratcheting.

There exist in the literature several examples of APC that have been caused by aeroelastic coupling. These include the Lockheed YF-12, Boeing C-17A Globemaster III, Boeing 777, Rutan Model 76 Voyager, and General Dynamics F-111, as well as rotorcraft such as the Sikorsky CH-53E Super Stallion and Bell-Boeing V-22 Osprey [Norton, 1996; McRuer, 1995].

The configuration of the YF-12 is typical of supersonic military aircraft of the time, with a long, slender fuselage similar to both the XB-70 and B-1. In the case of the YF-12 however, the resultant low frequency first fuselage bending mode resulted in two recorded cases of APC [Smith and Berry, 1975]. The first case was relatively benign, described as "bothersome" [Smith and Berry, 1975], and was caused by small amplitude bobbling motion at the cockpit due to the excitation of the fuselage bending mode at 2.5Hz by frequent pilot elevon inputs. The aircraft motion was the result of the coupled aeroelastic and rigid-body motion, however the pilot found it difficult to distinguish between these two modes, and instinctively tried to control this motion manually. The second case was much more extreme, experiencing normal accelerations of -1 to 3g, and was initiated by a faulty trim switch failure. Both cases occurred during air-to-air refuelling, a task known to require high pilot gains and concentration [Smith and Berry, 1975]. A similar longitudinal APC was experienced in the development of the Boeing 777 [Norton, 1996]. Again, frequent pilot elevator input excited a fuselage bending mode, resulting in a coupled aircraft response. The occurrence of this phenomenon was shown to increase in frequency with proximity to the ground, again a task known to require high pilot gains/urgency [McRuer, 1995]. These three cases may be considered Type 1 PIOs. For the Voyager aircraft, a symmetrical wing bending mode was the cause of a Type II PIO [Norton, 1995]. Following a vertical gust or sudden pilot elevator input, a symmetrical wing bending mode was excited. This coupled with a fuselage bending mode, resulting in pitch accelerations at the cockpit, which could result in a PIO unless the pilot was "especially attentive". Wing flexibility has also resulted in several cases of APCs. In the case of the C-17A, an antisymmetric wing bending mode excited an outboard engine pitching motion, causing lateral accelerations at the cockpit which produced an inadvertent pilot control input through shaking of pilot-stick system [Norton, 1995]. This resulted in a roll-ratcheting oscillation. This is an example of a Type III aeroelastic PAO.

These examples show the effect that aeroelasticity can directly have on the occurrence of APCs. It is known that aeroelastic effects can also increase time delays. Several APCs, such as the Space Shuttle ALT-5 APC [Ashkenas et al., 1983a], and the Dryden Digital Fly-by-Wire F-8 studies [Berry et al., 1982], have shown that excessive time delays can be an important contributing factor in APCs, and McRuer [1995] attributes the most common cause of Category I APCs to excessive high frequency lags. It can therefore be expected that aeroelastic effects can also indirectly contribute towards APCs.

2.6 Summary

A number of different approaches to the derivation of the equations of motion for a flexible aeroplane have been developed. This research has focused on slender, flexible aircraft, such as the Rockwell B1-B Lancer bomber [Schmidt, 1985], and very flexible aircraft, for example HALE aircraft [Shearer and Cesnik, 2005]. Inertial coupling effects, for example, are often neglected [Schmidt and Raney, 2001; Siepenkotter and Alles, 2005], though these effects have been found to be significant where the separation of rigid- and flexible-body modal frequencies is small [Olsen, 1999]. Structural flexibility has been included as a quasi-steady [Etkin, 1959] or dynamic effect [Waszak and Schmidt, 1985a,b], while simplification of the structural model is commonly achieved by using a truncated normal mode set [Baluch et al., 2007; Lee et al., 2007]. Several different approaches to the calculation of the aerodynamic forces have also evolved, both steady [Tuzcu, 2001] and unsteady [Cesnik and Brown, 2002; Tuzcu, 2007]. Many of these aerodynamic models have been suitable for aeroelastic analysis, though they have generally been unsuitable for real-time simulation [Samareh and Bhatia, 2000] or control law development [Baker et al., 1999].

The importance of including unsteady aerodynamic effects in the modelling of aircraft flight dynamics has been identified [Greenwell, 2004]. The influence of compressibility [Leishman, 1994] and unsteady downwash effects [Klein, 1999] have also been found to be significant. However, in general the effects of unsteady aerodynamics have been neglected when modelling the rigid-body dynamics of the aeroplane [Etkin, 1959; Hancock, 1995]. Unsteady aerodynamic models, both in the time- and frequency-domains, have been developed previously, including two-dimensional indicial models, such as the Wagner and Kussner functions [Wagner, 1925; Kussner, 1936]; the analogous frequency-domain Theodorsen function [Theodorsen, 1949]; and the three-dimensional DLM [Blair, 1994]. Some of these models, such as the indicial method, lend themselves to a modern, real-time state-space representation of the aerodynamics of the aeroplane.

The flying and handling qualities of an aircraft describe the ease with which the pilot can control and manoeuvre the aeroplane in the completion of some task or mission [Cook, 1997]. It has been shown that the effects of the elastic structure of the flexible aeroplane have a noticeable and measurable effect on the flight dynamics and handling qualities of many aircraft types [Yen, 1977; Schmidt and Raney, 2001; Shearer and Cesnik, 2005]. These effects are of particular significance for modern transport aircraft, which continue to increase in size [Mitchell et al., 2003].

It is quite common that an aircraft's dynamic characteristics do not meet flying and handling qualities or loads requirements, and the dynamics of the aeroplane are often augmented, or modified, by FCS systems, such as the CSAS and LAF control laws. Aeroservoelasticity is the interaction between the FCS, the aerodynamics and the elastic structure. It has been found that structural flexibility can result in both rigid-body [Tuzcu and Meirovitch, 2005] and flexible-body [Kubica and Livet, 1994b] aeroservoelastic instabilities, as well as an increased susceptibility to APCs [Norton, 1995]. However, the influence of the flight control system [Waszak and Schmidt, 1985a,b] or modern load alleviation systems [Waszak et al., 1987a,b] have often not been included in the analysis of aeroplane handling qualities.

In summary then, while a number of different methods have been developed in order to

model a flexible aircraft, these have not, in one model, included unsteady aerodynamics, been suitable for real-time, pilot-in-the-loop simulation or control-law development, included FCS CSAS and LAF systems, or focused on the modern, flexible civil transport aircraft.

CHAPTER 3

Definition of Equations of Motion

In this section, the derivation of the equations of motion for a flexible aeroplane using the mean-axes system is presented, together with description of the beam-element model of the structure.

3.1 Elastic-body Equations of Motion

Let us first define the equations of motion for a flexible, elastic body. To that we may then apply the mean-axes assumption, decoupling the rigid-body motion of the continuous flexible body system from the local relative elastic deformation of the flexible body.

Consider a discrete point mass, of density ρ and volume dV. The point mass, moving through space with velocity $\mathbf{v}$ and position $\mathbf{r}$, has the translational linear momentum:

$$\begin{aligned} d\mathbf{p} =& \rho \mathbf{v} dV \\ =& \rho \frac{d\mathbf{r}}{dt} dV \end{aligned} \tag{3.1.1}$$

Let the position of the point, $\mathbf{r}$, be expressed in an inertial reference frame, $\mathbf{r}_0$, such that the position of the point in this frame is given by:

$$\mathbf{r}' = \mathbf{r} - \mathbf{r}_0 \tag{3.1.2}$$

The linear momentum of the discrete point mass is then given by:

$$\begin{aligned} d\mathbf{p} =& \rho \left(\frac{d\mathbf{r}_0}{dt} + \frac{d\mathbf{r}'}{dt} \right) dV \\ =& \rho \left(\mathbf{v}_0 + \frac{d\mathbf{r}'}{dt} \right) dV \end{aligned} \tag{3.1.3}$$

For a body comprised of an assembly of masses, the discrete mass may be replaced by a continuous system of masses. The mass of the entire body is given by integrating over the volume of the body:

$$m = \int_V \rho dV \tag{3.1.4}$$

and the body's centre of mass is located at:

$$\mathbf{r}_{cm} = \frac{1}{m} \int_V \rho \mathbf{r}_0 dV \tag{3.1.5}$$

The total linear momentum of the body is then given by:

$$\mathbf{p} = \int_V \rho \left(\mathbf{v}_0 + \frac{d\mathbf{r}'}{dt} \right) dV \tag{3.1.6}$$

Let the angular velocity of the body-axes reference frame be $\boldsymbol{\omega}$, such that the operators d/dt and $\{d/dt + \boldsymbol{\omega}\times\}$ be equivalent [Milne, 1962]. The total linear momentum is then given by:

$$\mathbf{p} = \mathbf{v}_0 \int_V \rho dV + \boldsymbol{\omega} \times \int_V \rho \mathbf{r}_0 dV + \int_V \rho \frac{d\mathbf{r}'}{dt} dV + \boldsymbol{\omega} \times \int_V \rho \mathbf{r}' dV \tag{3.1.7}$$

Substituting Equations 3.1.4 and 3.1.5 into Equation 3.1.8 yields:

$$\mathbf{p} = m\mathbf{v}_0 + m\boldsymbol{\omega} \times \mathbf{r}_{cm} + \int_V \rho \mathbf{v}' dV + \boldsymbol{\omega} \times \int_V \rho \mathbf{r}' dV \tag{3.1.8}$$

The angular momentum of a point mass may be similarly described. The angular momentum of the point mass is given by:

$$\begin{aligned} d\mathbf{h} =& \mathbf{r} \times \mathbf{p} \\ =& \mathbf{r} \times \mathbf{v} \rho dV \end{aligned} \tag{3.1.9}$$

Substituting Equation 3.1.2:

$$\begin{aligned} d\mathbf{h} &= (\mathbf{r}_0 + \mathbf{r}') \times (\mathbf{v}_0 + \mathbf{v}') \, \rho dV \\ &= \left[(\mathbf{r}_0 \times \mathbf{v}_0) + (\mathbf{r}_0 \times \mathbf{v}') + (\mathbf{r}' \times \mathbf{v}_0) + (\mathbf{r}' \times \mathbf{v}') \right] \rho dV \end{aligned} \tag{3.1.10}$$

The angular momentum of the body is given by the integral over the volume of the body, and hence is given by:

$$\mathbf{h} = \int_V \mathbf{r}_0 \rho dV \times \mathbf{v}_0 + \int_V (\mathbf{r}_0 \times \mathbf{v}') \, \rho dV + \int_V \mathbf{r}' \rho dV \times \mathbf{v}_0 + \int_V (\mathbf{r}' \times \mathbf{v}') \, \rho dV \tag{3.1.11}$$

Letting the angular velocity of the body-axes reference frame be $\boldsymbol{\omega}$ [Milne, 1962], the total angular momentum of the body is thus given by:

$$\begin{aligned}
\mathbf{h} = & \int_V \mathbf{r}_0 \rho dV \times (\mathbf{v}_0 + \boldsymbol{\omega} \times \mathbf{r}_0) + \int_V (\mathbf{r}_0 \times (\mathbf{v}' + \boldsymbol{\omega} \times \mathbf{r}')) \, \rho dV \\
& + \int_V \mathbf{r}' \rho dV \times (\mathbf{v}_0 + \boldsymbol{\omega} \times \mathbf{r}_0) + \int_V (\mathbf{r}' \times (\mathbf{v}' + \boldsymbol{\omega} \times \mathbf{r}')) \, \rho dV
\end{aligned} \tag{3.1.12}$$

$$\begin{aligned}
\mathbf{h} = & \int_V \mathbf{r}_0 \rho dV \times \mathbf{v}_0 + \int_V \left(\mathbf{r}_0^2 \boldsymbol{\omega} - \mathbf{r}_0 \left(\mathbf{r}_0 \cdot \boldsymbol{\omega} \right) \right) dV \\
& + \int_V (\mathbf{r}_0 \times \mathbf{v}') dV + \int_V \left(\left(\mathbf{r}_0 \cdot \mathbf{r}' \right) \boldsymbol{\omega} - \mathbf{r}' \left(\mathbf{r}_0 \cdot \boldsymbol{\omega} \right) \right) dV \\
& + \int_V \mathbf{r}' \rho dV \times \mathbf{v}_0 + \int_V \left(\left(\mathbf{r}' \cdot \mathbf{r}_0 \right) \boldsymbol{\omega} - \mathbf{r}_0 \left(\mathbf{r}' \cdot \boldsymbol{\omega} \right) \right) dV \\
& + \int_V (\mathbf{r}' \times \mathbf{v}') dV + \int_V \left(\mathbf{r}'^2 \boldsymbol{\omega} - \mathbf{r}' \left(\mathbf{r}' \cdot \boldsymbol{\omega} \right) \right) dV
\end{aligned} \tag{3.1.13}$$

Or, substituting for I_0 and I' [Milne, 1962]:

$$\begin{aligned}
\mathbf{h} = & \int_V \mathbf{r}_0 \rho dV \times \mathbf{v}_0 + (I_0 + I') \cdot \boldsymbol{\omega} \\
& + \int_V (\mathbf{r}_0 \times \mathbf{v}') dV + \int_V \mathbf{r}' \rho dV \times \mathbf{v}_0 + \int_V (\mathbf{r}' \times \mathbf{v}') dV
\end{aligned} \tag{3.1.14}$$

where I_0 and I', the inertia tensor of the rigid body and the inertia tensor due to relative elastic deformation respectively, are given by:

$$I_0 = \int_V \left(\mathbf{r}_0^2 - \mathbf{r}_0 \mathbf{r}_0 \right) dV \tag{3.1.15}$$

$$I' = \int_V \left(\mathbf{r}'^2 + 2 \left(\mathbf{r}_0 \cdot \mathbf{r}' \right) - \left(\mathbf{r}' \mathbf{r}_0 + \mathbf{r}_0 \mathbf{r}' \right) - \mathbf{r}' \mathbf{r}' \right) dV \tag{3.1.16}$$

Finally, substituting Equations 3.1.4 and 3.1.5, and assuming that any elastic deformation is small and so second and higher-order displacements are neglected [Milne, 1962]:

$$\begin{aligned}
\mathbf{h} = & m \mathbf{r}_{cm} \times \mathbf{v}_0 + (I_0 + I') \cdot \boldsymbol{\omega} \\
& + \int_V (\mathbf{r}_0 \times \mathbf{v}') dV + \int_V \mathbf{r}' \rho dV \times \mathbf{v}_0
\end{aligned} \tag{3.1.17}$$

in which:

$$I_0 = \int_V \left(\mathbf{r}_0^2 - \mathbf{r}_0\mathbf{r}_0\right) dV \tag{3.1.18}$$

$$I' = \int_V \left(2\left(\mathbf{r}_0 \cdot \mathbf{r}'\right) - \left(\mathbf{r}'\mathbf{r}_0 + \mathbf{r}_0\mathbf{r}'\right)\right) dV \tag{3.1.19}$$

3.2 Mean-axes System

The mean-axes system is defined such that it does not remain fixed at some material point within the body, but is free to float relative to the body. The mean-axes is chosen such that the relative angular and linear momenta with respect to the body axes is zero at every instant in time [Milne, 1962]. This may be defined as:

$$\int_V \rho \frac{d\mathbf{r}'}{dt} dV = \int_V \rho \mathbf{r}_0 \frac{d\mathbf{r}'}{dt} dV = 0 \tag{3.2.1}$$

As a result, the inertial coupling between the overall body reference frame and the elastic deformation of the body is reduced, and effectively the rigid-body motion of the body can be decoupled from its elastic deformation.

In practice [Milne, 1962], this is equivalent to specifying:

$$\int_V \rho \mathbf{r}' dV = \int_V \rho \mathbf{r}_0 \mathbf{r}' dV = 0 \tag{3.2.2}$$

If the origin of the mean-axes is chosen to be the centre of mass of the reference body, i.e. located at $\mathbf{r}_{cm}$, then Equation 3.2.2 states that the origin of the mean-axes shall always located at the instantaneous centre of mass of the body [Milne, 1962].

Applying the mean-axes definition (Equations 3.2.1 and 3.2.2) to the linear and angular momentum equations (Equations 3.1.8 and 3.1.17) and defining the axes origin to be the centre of mass of the reference body, then the linear and angular momentum is given by:

$$\mathbf{p} = m\mathbf{v}_0 \tag{3.2.3}$$

$$\mathbf{h} = \left(I_0 + I'\right)\boldsymbol{\omega} \tag{3.2.4}$$

Equations 3.2.3 and 3.2.4 are identical to those of the standard rigid-body equations of motion, where the inertia of the body, $(I_0 + I')$, corresponds to that of the deformed elastic structure. It is assumed however that the elastic deformation is small, and so changes in the inertia of the body due to elastic deformation may be neglected [Waszak and Schmidt, 1988]. In this way, the inertia of the body is given only by the inertia of the undeformed structure, I_0. Thus the rigid-body motion of the aircraft and the flexible deformation of its elastic structure are only coupled through the aerodynamic forces and moments [Figure 3.1].

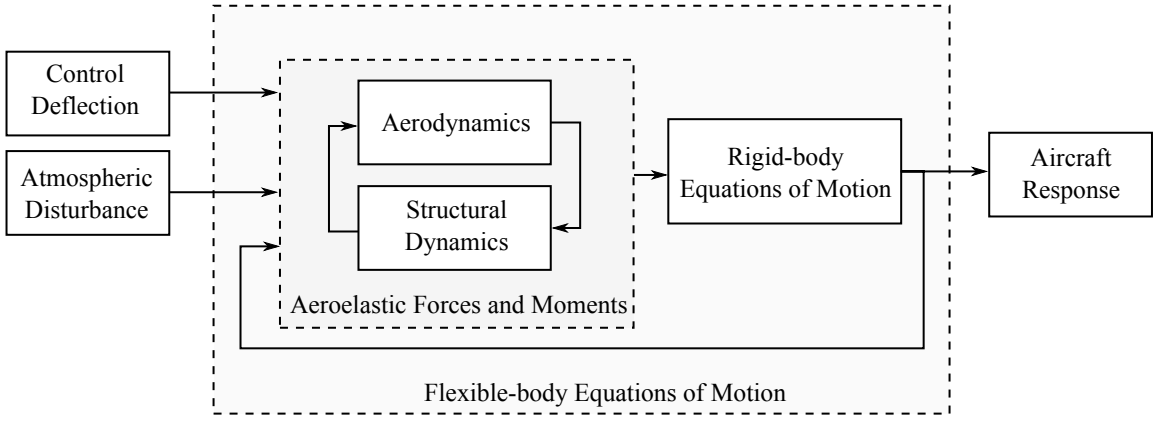

Figure 3.1: Mean-axes flexible aircraft equations of motion

3.3 Rigid-body Equations of Motion

Given the mean-axes assumption, the rigid-body linear and angular momentum of the continuous elastic body is identical to the momentum given by the standard rigid-body equations of motion. Newton's second law states that the rate of change of momentum of a body is equal to the force acting on that body. The translational and rotational kinematic equations of motion for the rigid-body aircraft are then expressed in the inertial frame of reference [Figure 3.2] by:

$$\frac{d\mathbf{p}}{dt} = \frac{dm\mathbf{v}}{dt} = \mathbf{f} \tag{3.3.1}$$

$$\frac{d\mathbf{h}}{dt} = \frac{dI\boldsymbol{\omega}}{dt} = \mathbf{m} \tag{3.3.2}$$

where $\mathbf{p}$ and $\mathbf{h}$ are the linear and angular momentum of the rigid-body given by Equations 3.2.3 and 3.2.4 respectively. It is convenient however to express the equations of motion in a non-inertial body-axes reference frame [Stengel, 2004]. The body-axes angular rate is related to the inertial angular rate by:

$$\boldsymbol{\omega}_B = D_I^B \boldsymbol{\omega}_I \tag{3.3.3}$$

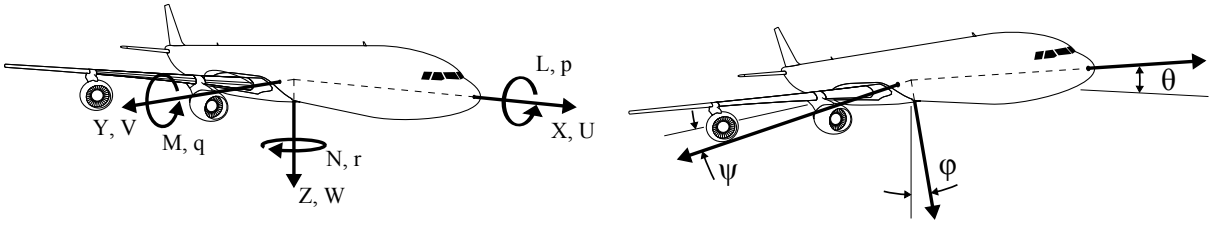

Figure 3.2: Translational and rotational moving axis system

In order to transform motion variables from one axes system to another, a sequence of rotations about each axis is performed in turn to bring the two axes systems into alignment [Figure 3.2]. The three right-handed rotations defining the attitude of the aircraft

are called Euler angles. The direction cosine matrix, D_I^B, that defines this transformation relationship between inertial and body-axes is given by:

$$D_I^B = \begin{bmatrix} \cos\theta\cos\psi & \cos\theta\sin\psi & -\sin\theta \\ \sin\phi\sin\theta\cos\psi - \cos\phi\sin\psi & \sin\phi\sin\theta\sin\psi + \cos\phi\cos\psi & \sin\phi\cos\theta \\ \cos\phi\sin\theta\cos\psi + \sin\phi\sin\psi & \cos\phi\sin\theta\sin\psi - \sin\phi\cos\psi & \cos\phi\cos\theta \end{bmatrix} \tag{3.3.4}$$

The body's angular momentum, expressed in the body-axes reference frame, is given by:

$$\mathbf{h}_B = I_B \boldsymbol{\omega}_B \tag{3.3.5}$$

where $\boldsymbol{\omega}_B$ is the body-axes inertia tensor. Hence:

$$\frac{d\mathbf{h_B}}{dt} = I_B \frac{d\boldsymbol{\omega}_B}{dt} = \mathbf{m}_B \tag{3.3.6}$$

The body-axes and inertial-axes inertia tensors are related by a "similarity transformation" [Stengel, 2004]. The similarity transform and its inverse is given by:

$$I_B = D_I^B I_I D_B^I \tag{3.3.7}$$
$$I_I = D_B^I I_B D_I^B \tag{3.3.8}$$

Given a body in the body-axis reference frame that is rotating with respect to the inertial reference frame, the angular momentum of the body in the inertial frame is given by:

$$\frac{d\mathbf{h}_I}{dt} = \left[\frac{d\mathbf{h}_B}{dt}\right]_I + \boldsymbol{\omega}_I \times \mathbf{h}_I \tag{3.3.9}$$
$$= D_B^I \frac{d\mathbf{h}_B}{dt} + \boldsymbol{\omega}_I \times \mathbf{h}_I \tag{3.3.10}$$

Applying the similarity transform to $\boldsymbol{\omega}_I$ and substituting into Equation 3.3.10:

$$\frac{d\mathbf{h}_I}{dt} = D_B^I \frac{d\mathbf{h}_B}{dt} + D_B^I \boldsymbol{\omega}_B D_I^B \times \mathbf{h}_I \tag{3.3.11}$$
$$= D_B^I \frac{d\mathbf{h}_B}{dt} + D_B^I \boldsymbol{\omega}_B \times \mathbf{h}_B \tag{3.3.12}$$

Rearranging for $d\mathbf{h}_B/dt$:

$$\frac{d\mathbf{h}_B}{dt} = D_I^B \frac{d\mathbf{h}_I}{dt} + \boldsymbol{\omega}_B \times \mathbf{h}_B \tag{3.3.13}$$

Substituting $\mathbf{m}_I$ for $d\mathbf{h}_I/dt$:

$$\frac{d\mathbf{h}_B}{dt} = D_I^B \mathbf{m}_I + \boldsymbol{\omega}_B \times \mathbf{h}_B \tag{3.3.14}$$

$$= \mathbf{m}_B + \boldsymbol{\omega}_B \times \mathbf{h}_B \tag{3.3.15}$$

Rearranging for $\boldsymbol{\omega}_B$, the rotational acceleration of the body is given by [Stengel, 2004]:

$$\frac{d\boldsymbol{\omega}_B}{dt} = I_B^{-1} \left(\mathbf{m} - \boldsymbol{\omega}_B \times I_B \boldsymbol{\omega}_B \right) \tag{3.3.16}$$

It is similarly convenient to express the translational equations of motion in the body-axes reference frame [Stengel, 2004]. Applying the similarity transformation:

$$\frac{d\mathbf{p}_B}{dt} = D_I^B \frac{d\mathbf{p}_I}{dt} - \boldsymbol{\omega}_B \times \mathbf{p}_B \tag{3.3.17}$$

Rearranging and dividing through by mass, the linear translational acceleration of the body is given by [Stengel, 2004]:

$$\frac{d\mathbf{v}_B}{dt} = \frac{\mathbf{f}_B}{M} - \boldsymbol{\omega}_B \times \mathbf{v}_B \tag{3.3.18}$$

A further six kinematic equations of motion are required to define the position and attitude of the aircraft. These are given by:

$$\frac{d\mathbf{r}_I}{dt} = D_B^I \mathbf{v}_B \tag{3.3.19}$$

$$\frac{d\boldsymbol{\Theta}_I}{dt} = E_B^I \boldsymbol{\omega}_B \tag{3.3.20}$$

where the axes transformation from body- to inertial-axes of the angular rotation rates, $\boldsymbol{\omega}_B$, is achieved using the axis transformation, E_B^I, given by:

$$E_B^I = \begin{bmatrix} 1 & \sin\phi\tan\theta & \cos\phi\tan\theta \\ 0 & \cos\phi & -\sin\phi \\ 0 & \sin\phi\sec\theta & \cos\phi\sec\theta \end{bmatrix} \tag{3.3.21}$$

3.4 Elastic-structure Equations of Motion

3.4.1 Structural Model

The airframe of the flexible aircraft is modelled as a beam element structure [Berry, 1989]. A beam element is defined between two nodes, where each node is free to move

in six degrees of freedom. A stiffness matrix is defined for each beam element, and the complete global stiffness matrix defined by summing the contributions to each degree of freedom from each beam element stiffness matrix. A mass matrix is similarly defined for each node, and the complete global mass matrix defined by summing the contributions from each node.

The stiffness matrix for a three-dimensional beam element is the summation of the stiffness matrices for a beam element in bending, and a bar element in axial extension and torsion. If we first consider a two-dimensional beam element [Figure 3.3], this element has four degrees of freedom; two rotational and two translational, namely $\left[\begin{array}{cccc} z_1 & \Phi_1 & z_2 & \Phi_2 \end{array}\right]$. The element stiffness matrix is given by Equation 3.4.1, where E is Young's modulus, I the second moment of inertia, and L the length of the beam.

$$K = \begin{bmatrix} \frac{12EI}{L^3} & \frac{6EI}{L^2} & \frac{-12EI}{L^3} & \frac{6EI}{L^2} \\ \frac{6EI}{L^2} & \frac{4EI}{L} & \frac{-6EI}{L^2} & \frac{2EI}{L} \\ \frac{-12EI}{L^3} & \frac{-6EI}{L^2} & \frac{12EI}{L^3} & \frac{-6EI}{L^2} \\ \frac{6EI}{L^2} & \frac{2EI}{L} & \frac{-6EI}{L^2} & \frac{4EI}{L} \end{bmatrix} \tag{3.4.1}$$

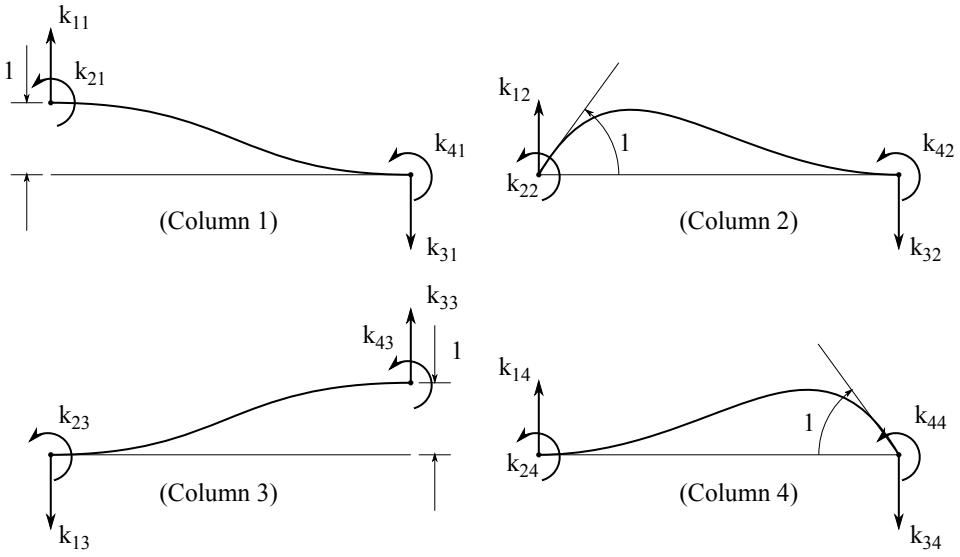

Figure 3.3: Degrees of freedom for a two-dimensional beam element

If we then consider the bar element in axial extension, the stiffness matrix is then given for the degrees of freedom $\left[\begin{array}{cc} x_1 & x_2 \end{array}\right]$ by:

$$K = \begin{bmatrix} \frac{AE}{L} & \frac{-AE}{L} \\ \frac{-AE}{L} & \frac{AE}{L} \end{bmatrix} \tag{3.4.2}$$

where A is the area of the beam. Finally, for a bar element in torsion, where the degrees of freedom are $\left[\begin{array}{cc} \Theta_1 & \Theta_2 \end{array}\right]$, the stiffness matrix is given Equation 3.4.3, where G is the shear modulus of the beam and J the torsion constant.

$$K = \begin{bmatrix} \frac{GJ}{L} & \frac{-GJ}{L} \\ \frac{-GJ}{L} & \frac{GJ}{L} \end{bmatrix} \tag{3.4.3}$$

For a three-dimensional beam element, which has a total of twelve degrees of freedom, i.e. $\begin{bmatrix} x_1 & y_1 & z_1 & \Phi_1 & \Theta_1 & \Psi_1 & x_2 & y_2 & z_2 & \Phi_2 & \Theta_2 & \Psi_2 \end{bmatrix}$. The total stiffness matrix is found by summing the bending, axial and torsional stiffness matrix contributions for each of the three planes; X-Y, X-Z, and Y-Z. The total stiffness matrix is then given for a beam element of degrees of freedom by [Cook et al., 1989]:

$$K = \begin{bmatrix} \frac{AE}{L} & 0 & 0 & 0 & 0 & 0 & \frac{-AE}{L} & 0 & 0 & 0 & 0 & 0 \\ 0 & \frac{12EI_Z}{L^3} & 0 & 0 & 0 & \frac{6EI_Z}{L^2} & 0 & \frac{-12EI_Z}{L^3} & 0 & 0 & 0 & \frac{6EI_Z}{L^2} \\ 0 & 0 & \frac{12EI_Y}{L^3} & 0 & \frac{-6EI_Y}{L^2} & 0 & 0 & 0 & \frac{-12EI_Y}{L^3} & 0 & \frac{-6EI_Y}{L^2} & 0 \\ 0 & 0 & 0 & \frac{GJ}{L} & 0 & 0 & 0 & 0 & 0 & \frac{-GJ}{L} & 0 & 0 \\ 0 & 0 & \frac{-6EI_Y}{L^2} & 0 & \frac{4EI_Y}{L} & 0 & 0 & 0 & \frac{6EI_Y}{L^2} & 0 & \frac{2EI_Y}{L} & 0 \\ 0 & \frac{6EI_Z}{L^2} & 0 & 0 & 0 & \frac{4EI_Z}{L} & 0 & \frac{-6EI_Z}{L^2} & 0 & 0 & 0 & \frac{2EI_Z}{L} \\ \frac{-AE}{L} & 0 & 0 & 0 & 0 & 0 & \frac{AE}{L} & 0 & 0 & 0 & 0 & 0 \\ 0 & \frac{-12EI_Z}{L^3} & 0 & 0 & 0 & \frac{-6EI_Z}{L^2} & 0 & \frac{12EI_Z}{L^3} & 0 & 0 & 0 & \frac{-6EI_Z}{L^2} \\ 0 & 0 & \frac{-12EI_Y}{L^3} & 0 & \frac{6EI_Y}{L^2} & 0 & 0 & 0 & \frac{12EI_Y}{L^3} & 0 & \frac{6EI_Y}{L^2} & 0 \\ 0 & 0 & 0 & \frac{-GJ}{L} & 0 & 0 & 0 & 0 & 0 & \frac{GJ}{L} & 0 & 0 \\ 0 & 0 & \frac{-6EI_Y}{L^2} & 0 & \frac{2EI_Y}{L} & 0 & 0 & 0 & \frac{6EI_Y}{L^2} & 0 & \frac{4EI_Y}{L} & 0 \\ 0 & \frac{6EI_Z}{L^2} & 0 & 0 & 0 & \frac{2EI_Z}{L} & 0 & \frac{-6EI_Z}{L^2} & 0 & 0 & 0 & \frac{4EI_Z}{L} \end{bmatrix} \tag{3.4.4}$$

For a beam element orientated arbitrarily with respect to the global axis system, the stiffness matrix for the element is given in the global axis system by [Cook et al., 1989]:

$$K_G = T^T K_N T \tag{3.4.5}$$

The global stiffness matrix is then assembled by summing the contributions for each degree of freedom from each individual stiffness matrix. For example, for a two-dimensional two element beam [Figure 3.4] with degrees of freedom $\begin{bmatrix} z_1 & \Phi_1 & z_2 & \Phi_2 & z_3 & \Phi_3 \end{bmatrix}$, the individual beam element stiffness matrices are given by:

$$K_A = \begin{bmatrix} a_{1,1} & a_{1,2} & a_{1,3} & a_{1,4} \\ a_{2,1} & a_{2,2} & a_{2,3} & a_{2,4} \\ a_{3,1} & a_{3,2} & a_{3,3} & a_{3,4} \\ a_{4,1} & a_{4,2} & a_{4,3} & a_{4,4} \end{bmatrix} \begin{matrix} -z_1 \\ -\Phi_1 \\ -z_2 \\ -\Phi_2 \end{matrix} \qquad K_B = \begin{bmatrix} b_{1,1} & b_{1,2} & b_{1,3} & b_{1,4} \\ b_{2,1} & b_{2,2} & b_{2,3} & b_{2,4} \\ b_{3,1} & b_{3,2} & b_{3,3} & b_{3,4} \\ b_{4,1} & b_{4,2} & b_{4,3} & b_{4,4} \end{bmatrix} \begin{matrix} -z_2 \\ -\Phi_2 \\ -z_3 \\ -\Phi_3 \end{matrix} \tag{3.4.6, 3.4.7}$$

The global stiffness matrix for this structure is then given by:

$$\mathbf{K} = \begin{bmatrix} a_{1,1} & a_{1,2} & a_{1,3} & a_{1,4} & 0 & 0 \\ a_{2,1} & a_{2,2} & a_{2,3} & a_{2,4} & 0 & 0 \\ a_{3,1} & a_{3,2} & a_{3,3}+b_{1,1} & a_{3,4}+b_{1,2} & b_{1,3} & b_{1,4} \\ a_{4,1} & a_{4,2} & a_{4,3}+b_{2,1} & a_{4,4}+b_{2,2} & b_{2,3} & b_{2,4} \\ 0 & 0 & b_{3,1} & b_{3,2} & b_{3,3} & b_{3,4} \\ 0 & 0 & b_{4,1} & b_{4,2} & b_{4,3} & b_{4,4} \end{bmatrix} \begin{matrix} -z_1 \\ -\Phi_1 \\ -z_2 \\ -\Phi_2 \\ -z_3 \\ -\Phi_3 \end{matrix} \tag{3.4.8}$$

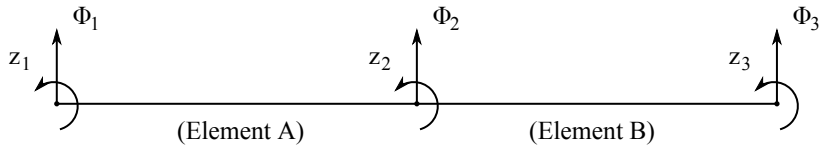

Figure 3.4: Two element beam degrees of freedom

A lumped mass matrix, M_i, for each node is found from the mass and inertia properties of that node, and is given by:

$$M_i = \begin{bmatrix} M & 0 & 0 & 0 & M_Z & -M_Y \\ 0 & M & 0 & M_Z & 0 & -M_X \\ 0 & 0 & M & M_Y & -M_X & 0 \\ 0 & M_Z & M_Y & I_{XX} & -I_{XY} & -I_{XZ} \\ M_Z & 0 & -M_X & -I_{XY} & I_{YY} & -I_{YZ} \\ -M_Y & -M_X & 0 & -I_{XZ} & -I_{YZ} & I_{ZZ} \end{bmatrix} \tag{3.4.9}$$

where M is the mass, $M_{(.)}$ the mass moment, and $I_{(..)}$ the moment of inertia of the node.

The mass matrix for the global system is then found from:

$$\mathbf{M} = \begin{bmatrix} M_1 & 0 & \cdots & 0 \\ 0 & M_2 & \cdots & 0 \\ \vdots & \vdots & \ddots & \vdots \\ 0 & 0 & \cdots & M_n \end{bmatrix} \tag{3.4.10}$$

3.4.2 Equations of Motion

The beam element structure can be assumed to be a system of connected rigid bodies, $m_1, m_2, ..., m_n$, where the displacements of those bodies are given by the coordinates $u_1, u_2, ..., u_n$. The kinetic energy of the total beam element system is then given by:

$$T = \frac{1}{2}\sum_{j=1}^{n} m_j \dot{u}_j^2 \tag{3.4.11}$$

It is useful to express the equations of motion in the generalised coordinate system q. The coordinate transformation is given by:

$$u_j = \sum_{k=1}^{n} \frac{\partial u_j}{\partial q_k} q_k \tag{3.4.12}$$

The kinetic energy of the system, after some manipulation, can then be rewritten:

$$T = \sum_{j=1}^{n} \left(\frac{\partial T}{\partial q_j}\dot{q}_j + \frac{\partial T}{\partial q_j} q_j \right) \tag{3.4.13}$$

Let us then write the jth Lagrange equation in generalised coordinates [Hurty and Rubinstein, 1964]:

$$\frac{d}{dt}\left(\frac{\partial T}{\partial \dot{q}_j}\right) - \frac{\partial T}{\partial q_j} = Q_j \tag{3.4.14}$$

If we consider the generalised force, Q_j, to be composed of the applied force Q_{A_j}, the inertial force Q_{E_j}, and the damping force Q_{D_j}, Equation 3.4.14 can be rewritten:

$$\frac{d}{dt}\left(\frac{\partial T}{\partial \dot{q}_j}\right) - \frac{\partial T}{\partial q_j} + \frac{\partial U}{\partial q_j} - Q_{D_j} = Q_{A_j} \tag{3.4.15}$$

where the elastic force Q_{E_j} for a linear, elastic structure is conservative, and the work done by the applied force is stored as the potential, or *strain*, energy U, given by Castigliano's first theorem $Q_{E_j} = -\partial U/\partial q_j$ [Hurty and Rubinstein, 1964].

It is convenient to replace the structural damping forces of the system with an equivalent viscous damping force. The energy associated with the viscous damping force is given by the Rayleigh dissipation function R, where $\partial R/\partial \dot{q}_j = Q_{D_j}$. Rewriting the jth Lagrange equation in terms of R yields:

$$\frac{d}{dt}\left(\frac{\partial T}{\partial \dot{q}_j}\right) - \frac{\partial T}{\partial q_j} + \frac{\partial U}{\partial q_j} + \frac{\partial R}{\partial \dot{q}_j} = Q_{A_j} \tag{3.4.16}$$

In practice the real structure is likely to have a low value of internal damping. Let us assume then that the structure is *ideal*, and that there is no internal damping. In free vibration, the only forces acting on the structure are then those due to the inertial and elastic forces. The elastic force, Q_E, is equal and opposite to the inertial force, and in the generalised coordinates η is given by:

$$\begin{aligned} \mathbf{M}\ddot{\eta} &= -Q_E \\ &= -\mathbf{K}\eta \end{aligned} \tag{3.4.17}$$

If we assume harmonic motion, i.e. $\eta = \eta e^{i\omega t}$, then Equation 3.4.17 yields:

$$-\mathbf{M}\omega^2\eta + \mathbf{K}\eta = 0 \tag{3.4.18}$$

Rearranging, and dividing through by k and ω^2:

$$\left(\mathbf{K}^{-1}\mathbf{M} - \frac{1}{\omega^2}\right)\eta = 0 \tag{3.4.19}$$

The structure can be said to have a number of *normal modes*. In each mode, every point in the structure oscillates harmonically at the same frequency and in the same phase. This mode can be described as characteristic of the structure, and the frequency at which it oscillates the *natural frequency* of the structure. These natural frequencies, $\boldsymbol{\omega}$, and normal mode shapes, $\boldsymbol{\phi}$, of the structure are given by the eigenvalues and eigenvectors respectively of the solution to the characteristic equation:

$$\det\left[\left(\mathbf{K}^{-1}\mathbf{M} - \frac{1}{\omega^2}\right)\eta\right] = 0 \tag{3.4.20}$$

It can be shown that these normal modes are orthogonal and decoupled [Hurty and Rubinstein, 1964], and the use of these free-free modes satisfy the criteria for the mean-axis system [Milne, 1962].

Let us then rewrite the rth Lagrange equation in terms of the generalised coordinate η:

$$\frac{d}{dt}\left(\frac{\partial T}{\partial \dot{\eta}_j}\right) - \frac{\partial T}{\partial \eta_j} + \frac{\partial U}{\partial \eta_j} + \frac{\partial R}{\partial \dot{\eta}_j} = Q_{A_j} \tag{3.4.21}$$

After some manipulation [Hurty and Rubinstein, 1964], Equation 3.4.21 can be shown to yield the familiar decoupled equation of motion for the rth mode:

$$\ddot{\eta}_r + 2\zeta_r\omega_r\dot{\eta}_r + \omega_r^2\eta_r = \frac{Q_r}{N_r} \tag{3.4.22}$$

where the generalised force, Q_r, and generalised mass, N_r are given by:

$$Q_r = {\phi_r}^T\mathbf{F}\phi_r \tag{3.4.23}$$

$$N_r = {\phi_r}^T\mathbf{M}\phi_r \tag{3.4.24}$$

$$\tag{3.4.25}$$

For n modes, the n equations of motion can then be expressed in state space form as:

$$\dot{\mathbf{x}} = \begin{bmatrix} \mathbf{0} & \mathbf{I} \\ \boldsymbol{\omega}^2 & 2\boldsymbol{\zeta}\boldsymbol{\omega} \end{bmatrix} \mathbf{x} + \begin{bmatrix} \mathbf{0} \\ \mathbf{N}^{-1} \end{bmatrix} \mathbf{F} \tag{3.4.26a}$$

$$\boldsymbol{\eta} = \begin{bmatrix} \mathbf{I} & \mathbf{0} \end{bmatrix} \mathbf{x} \tag{3.4.26b}$$

The response in geometric coordinates is then given by the coordinate transformation:

$$\mathbf{u} = \boldsymbol{\phi}\boldsymbol{\eta} \tag{3.4.27}$$

This page is intentionally left blank.

CHAPTER 4

Calculation of Forces and Moments

This section derives the mathematical model of the aerodynamic, gravitational, control, and propulsive forces acting on the flexible aeroplane. This includes the definition of a state-space unsteady aerodynamic model suitable for real-time simulation, as well as estimates of the aerodynamic properties of the airframe from empirical estimates.

4.1 Force and Moment Contributions

The total resultant external forces, $\mathbf{f}$, and moments, $\mathbf{m}$, acting on the origin of the body axes can be expressed as the sum of their contributions. These disturbing force and moment contributions are [Bryan, 1911]: *a*erodynamic; *c*ontrol; *p*ropulsive; *g*ravitational; and atmospheric *d*isturbant. The force and moment equations can then be expressed as:

$$\mathbf{f} = \mathbf{f}_a + \mathbf{f}_c + \mathbf{f}_p + \mathbf{f}_g + \mathbf{f}_d \tag{4.1.1a}$$

$$\mathbf{m} = \mathbf{m}_a + \mathbf{m}_c + \mathbf{m}_p + \mathbf{m}_g + \mathbf{m}_d \tag{4.1.1b}$$

The external force and moment vectors, $\mathbf{f}$ and $\mathbf{m}$ respectively, are alternatively given by:

$$\mathbf{f} = \begin{bmatrix} X \\ Y \\ Z \end{bmatrix} \qquad \mathbf{m} = \begin{bmatrix} L \\ M \\ N \end{bmatrix} \tag{4.1.2, 4.1.3}$$

4.2 Aerodynamic and Control

The aerodynamic force and moment contributions can then defined as those due to the wing, tailplane and fin; the fore- and aft-fuselage; and the nacelles [Figure 4.1]. The aerodynamic force and moment equations can then be expressed as:

$$\mathbf{f}_a = \mathbf{f}_{a_w} + \mathbf{f}_{a_h} + \mathbf{f}_{a_v} + \left(\mathbf{f}_{a_{fco}} + \mathbf{f}_{a_{ff}} + \mathbf{f}_{a_{fa}}\right) + \mathbf{f}_{a_n} \tag{4.2.1a}$$

$$\mathbf{m}_a = \mathbf{m}_{a_w} + \mathbf{m}_{a_h} + \mathbf{m}_{a_v} + \left(\mathbf{m}_{a_{fco}} + \mathbf{m}_{a_{ff}} + \mathbf{m}_{a_{fa}}\right) + \mathbf{m}_{a_n} \tag{4.2.1b}$$

Similarly, the control force and moment contributions can then defined as those due to aileron, elevator and rudder deflections [Figure 4.1]. The control force and moment equations can then be expressed as:

$$\mathbf{f}_c = \mathbf{f}_{c_\xi} + \mathbf{f}_{c_\zeta} + \mathbf{f}_{c_\eta} \tag{4.2.2a}$$

$$\mathbf{m}_c = \mathbf{m}_{c_\xi} + \mathbf{m}_{c_\zeta} + \mathbf{m}_{c_\eta} \tag{4.2.2b}$$

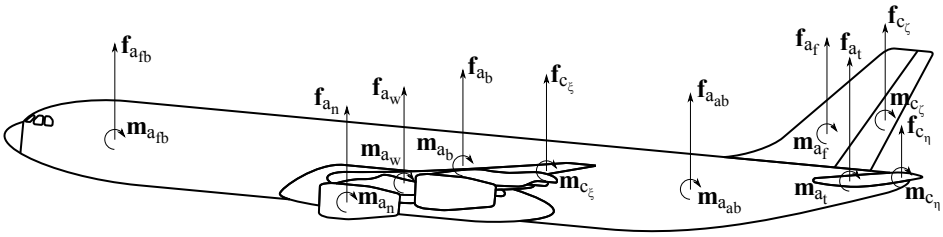

Figure 4.1: Aircraft aerodynamic and control forces and moments [ESDU 94009]

4.2.1 Wing, Tailplane, and Fin

This section describes the unsteady aerodynamic model which estimates the unsteady aerodynamic and control forces and moments. The forces and moments due to the wing, tailplane, and fin; aileron; elevator; and rudder are then calculated as follows [Figure 4.2]:

- The aerodynamic loads that act on the aircraft wing and tailplane are a function of the angle of attack at each aerodynamic station, or in the case of the fin, the side-slip angle [Section 4.2.1.1].
- The angle of attack of the tailplane is also function of the unsteady downwash field due to the influence of the wing [Section 4.2.1.2].
- The local unsteady lift coefficient is then calculated as a function of the non-circulatory and circulatory unsteady indicial aerodynamics [Section 4.2.1.3].
- The three dimensional lift coefficient for each station is calculated in combination with modified strip theory [Section 4.2.1.4].
- The total drag coefficient can then be calculated by adding the induced drag coefficient, calculated from the three-dimensional lift distribution given by modified strip theory, to the profile drag coefficient [Section 4.2.1.6].
- Finally, the forces and moments acting about the aircraft centre of gravity are calculated [Section 4.2.1.8].

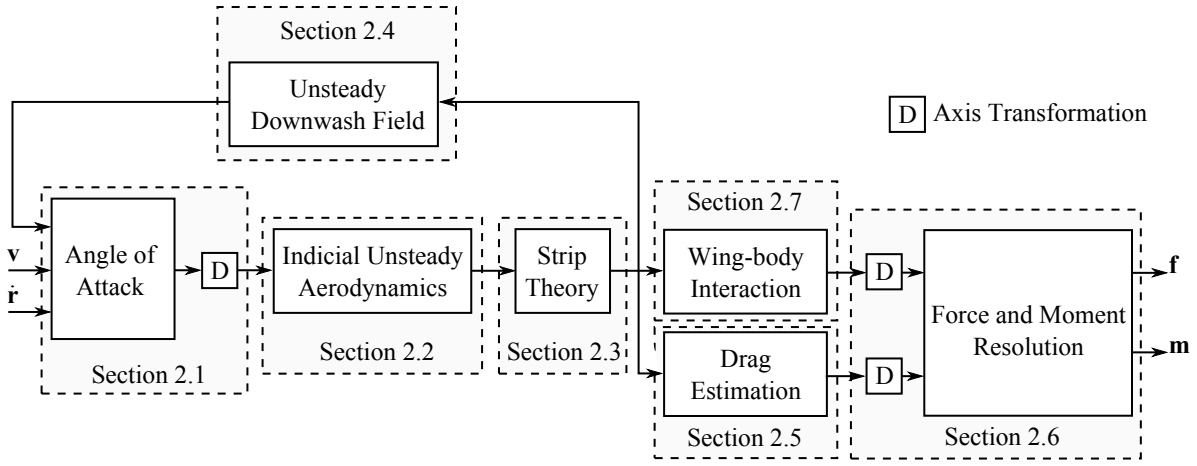

Figure 4.2: Calculation of unsteady aerodynamic forces and moments acting on aircraft

4.2.1.1 Angle of Attack

The local air velocities at each aerodynamic station are found first in body axis in terms of the component along the x-, y- and z-axes given by the terms U,V, and W respectively. The velocity at any point P, offset from the centre of gravity O, is the sum of the linear velocity at O, plus additional terms due to the rotation about O [Figure 4.3]. The total induced velocity at P due to the roll, pitch, and yaw rates, $p, q,$ and r respectively, of the aircraft is then given, in body axis, by:

$$U_P = U_O + \dot{x} - ry + qz \tag{4.2.3a}$$
$$V_P = V_O + \dot{y} - pz + rx \tag{4.2.3b}$$
$$W_P = W_O + \dot{z} - qx + py \tag{4.2.3c}$$

or alternatively:

$$\mathbf{v}_P = \mathbf{v}_O + \dot{\mathbf{r}} + \boldsymbol{\omega} \times \mathbf{r} \tag{4.2.4}$$

where x, y, and z are the position of P in the flexible aircraft, and $\dot{x}$, $\dot{y}$, and $\dot{z}$ are the velocity of the structure at P. The velocity of the aircraft centre of gravity, in body axis, is given by U_O, V_O and W_O.

It is necessary then to resolve the body axis velocity of the aerodynamic control point, $\mathbf{v}_P$, into the local nodal-axes system. The three rotations that define the nodal-axes are the rigid and elastic twist angle, Θ, the elastic yaw angle, Λ, and the rigid and elastic dihedral angle, Γ. These rigid and elastic properties of the wing at each node station are obtained from the dynamic model of the structure. The relationship between the two axis systems is defined by the direction cosine matrix, D_B^N:

$$D_B^N = \begin{bmatrix} \cos\Theta\cos\Lambda & \cos\Theta\sin\Lambda & -\sin\Theta \\ \sin\Gamma\sin\Theta\cos\Lambda - \cos\Gamma\sin\Lambda & \sin\Gamma\sin\Theta\sin\Lambda + \cos\Gamma\cos\Lambda & \sin\Gamma\cos\Theta \\ \cos\Gamma\sin\Theta\cos\Lambda + \sin\Gamma\sin\Lambda & \cos\Gamma\sin\Theta\sin\Lambda - \sin\Gamma\cos\Lambda & \cos\Gamma\cos\Theta \end{bmatrix} \tag{4.2.5}$$

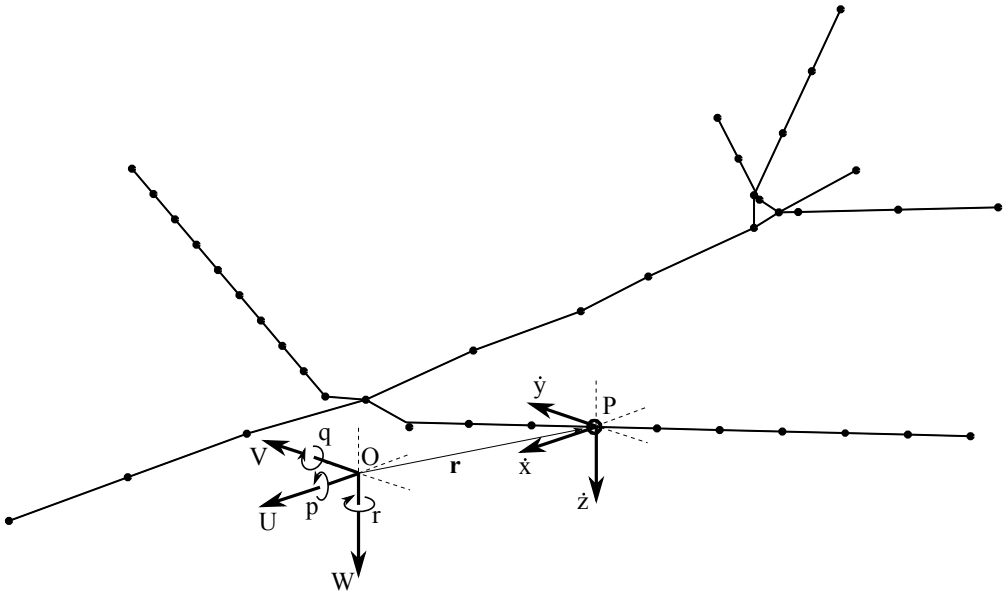

Figure 4.3: Local air velocity at a point P relative to the origin O

The axis transformation of the velocities from body to node axis is then given by:

$$\mathbf{v}_N = D_B^N \mathbf{v}_P \tag{4.2.6}$$

Finally, the angle of attack at each node is then given by:

$$\alpha = \tan^{-1}\left(\frac{W_N}{U_N}\right) \tag{4.2.7}$$

4.2.1.2 Indicial Tailplane Downwash

The tailplane is positioned in the wake of the wing, and as a result experiences a downwash which reduces the angle of attack of the tailplane [Figure 4.4]. This transient, unsteady change in the downwash field behind the wing is known as the downwash lag effect.

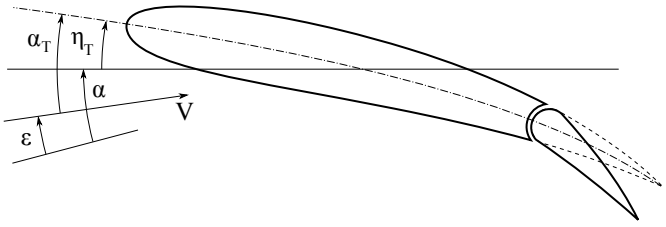

Figure 4.4: Angle of attack at the tailplane

This effect can be explained by considering the wing as it moves forward in flight. The wing leaves in its wake a vortex sheet. Initially there is no disturbance at the tailplane, and as the tailplane enters the wake of the wing downstream of this vorticity, there is an induced upwash at the tailplane. As the vortices move downstream of the tailplane, this is reversed, and the tailplane then experiences a downwash [Figure 4.9].

Jones and Fehlner [1940] first developed a model of the unsteady downwash at the tailplane using an indicial methodology. Jones and Fehlner [1940] showed that following a sudden change in the circulation about the wing, a vortex is generated at the trailing-edge of the wing. As the tail moves towards this vortex, the induced velocity at the tail leading-edge due to the vortex was given by the expression:

$$w_{dt} = \frac{1}{2\pi}\left(\frac{1}{l - Vt} - \frac{1}{l_1}\right) \tag{4.2.8}$$

where the wing-tail dimensions, l and l_1, are given in Figure 4.5. It was assumed by Jones and Fehlner [1940] that the tail was positioned directly in the wake of the wing, which results in a singularity in the solution where l equals Vt. This approximation was also made by Klein [1999], who applied a similar indicial methodology to Jones and Fehlner [1940] in modelling the tailplane downwash.

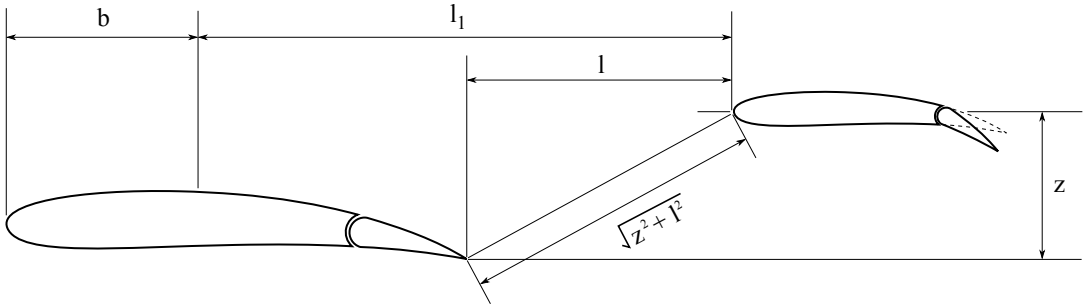

Figure 4.5: Tailplane downwash geometry

Here however the induced velocity is calculated for a tailplane offset vertically from directly downstream of the wing [Figure 4.5]. It has been assumed that the starting and bound vortices can be replaced by a single vortex located at the centre-chord of the wing. This is agreement with the assumptions made by Jones and Fehlner [1940].

The induced velocity at a point due to a vortex of strength Γ is given by the Biot-Savart law:

$$\bar{w}_{dw} = \frac{\Gamma}{2\pi d} \tag{4.2.9}$$

where d is the perpendicular distance of the vortex from the point. With reference to Figure 4.5, the distance d is equal to $\sqrt{z^2 + l^2}$, whereby the induced velocity is then given by:

$$\bar{w}_{dw} = \frac{\Gamma}{2\pi}\frac{1}{\sqrt{z^2 + l^2}} \tag{4.2.10}$$

Where the induced downwash, w_{dw}, is expressed as a function of the induced velocity, $\bar{w}_{dw}$:

$$w_{dw} = \bar{w}_{dw}\frac{l}{\sqrt{z^2 + l^2}} \tag{4.2.11}$$

The induced downwash is therefore equal to:

$$w_{dw} = \frac{\Gamma}{2\pi} \frac{l}{z^2 + l^2} \tag{4.2.12}$$

If the convecting vortex moves downstream at a velocity V, the distance d varies at a rate Vt. The induced downwash is then given as:

$$w_{dw} = \frac{\Gamma}{2\pi} \frac{l - Vt}{z^2 + (l - Vt)^2} \tag{4.2.13}$$

The induced downwash is then given by:

$$w_{dw} = \frac{\Gamma}{2\pi} \left(\frac{l - Vt}{z^2 + (l - Vt)^2} - \frac{l_1}{z^2 + l_1^2} \right) \tag{4.2.14}$$

The variation of induced downwash at the tail following a unit increase in circulation, Γ, of a wake vortex is shown in Figure 4.6.

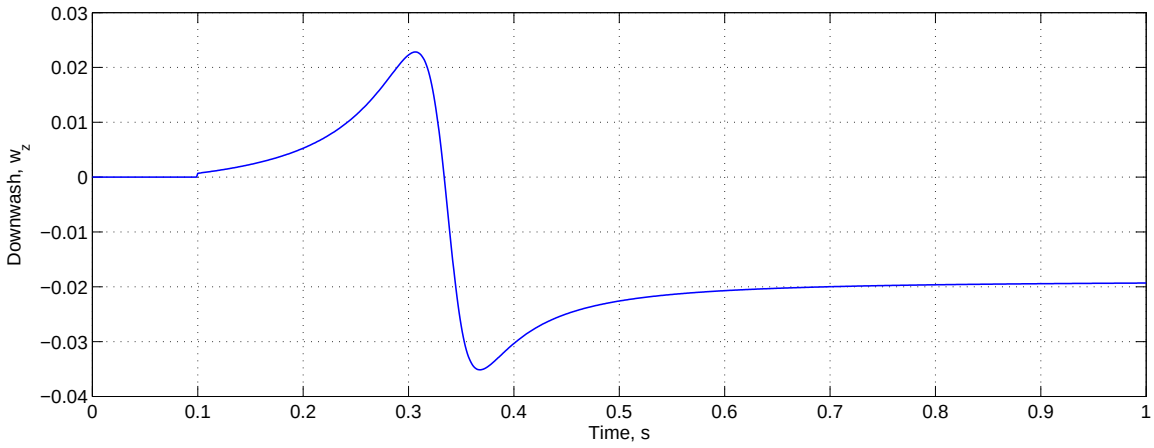

Figure 4.6: Downwash at the tailplane following unit step increase in circulation

A convenient approach to analysing this linear system might be the Laplace transform. This can be understood to be a transformation from the time domain, as a function of t, into the frequency, or s, domain. We might then generate a transfer function for the relationship between input and output, knowing the Laplace transform of the step input is $1/s$, in order to simulate the system. However, the Laplace transform of Equation 4.2.14 is non-trivial, and yields an expression in terms of the exponential function $e^{-\tau s}$ and $Ei\,(x)$, an exponential integral [Abramowitz and Stegun, 1972]. While the time delay $e^{-\tau s}$ might be approximated by a Padé approximant, there is no convenient polynomial approximation for $Ei\,(x)$. The Laplace transform of 4.2.14 does therefore not yield a transfer function in a convenient rational function form, and so an alternative method of modelling this system was developed.

A Finite Impulse Response (FIR) filter is a discrete-time filter. It describes the response of a system to an impulse, or Kronecker delta, input. It is finite because the response settles to zero in a finite number of discrete-time samples. The output of a discrete filter,

y, is given in the time-domain as a function of the weighted sum of the input u at the current time n plus a finite number of previous inputs, N:

$$y(n) = \sum_{i=0}^{N} b_i u[n-i] \tag{4.2.15}$$

The impulse response can be calculated if we substitute for the input u the Kronecker delta impulse δ, which has a value of 1 at t is equal to zero and 0 at all other time steps. The impulse response at time n can then be seen to be given by the coefficient b_i at time n:

$$h(n) = \sum_{i=0}^{N} b_i \delta[n-i] \tag{4.2.16}$$

$$= b_n \tag{4.2.17}$$

The Z-transform of the impulse response, remembering that the Z-transform of the impulse input is 1, yields the transfer function of the FIR filter:

$$H(z) = \frac{b_0 + b_1 z^{-1} \ldots + b_{N-1} z^{N-1} + b_N z^N}{1} \tag{4.2.18}$$

If we remember that the derivative of our system response input, a step, is an impulse, then the impulse response of the system is given by the derivative of Equation 4.2.14. If we consider the time-dependent component of this equation, i.e. the first term within the parentheses, the derivative yields:

$$\frac{w_{dw}(t)}{dt} = \frac{2V(l - V t)^2}{\left((l - V t)^2 + z^2\right)^2} - \frac{V}{(l - V t)^2 + z^2} \tag{4.2.19}$$

In order to approximate this response using an FIR filter, a sample rate of 500Hz, i.e. a discrete time step of 0.002 seconds, and a total sample time of 5 seconds was necessary. The impulse response of the time-dependent component of the system, i.e. Equation 4.2.19, is shown in Figure 4.7. The non-time-dependent component of the system, i.e. the second term within the parentheses of Equation 4.2.14, is merely a scalar transform that shifts the step response down on the y-axes. The step response of the FIR filter, including the non-time-dependent component, is compared to the analytical algebraic response in Figure 4.8. It can be seen that the FIR filter provides a good match to the analytical response. However, the FIR filter introduces 2,500 additional discrete states into the aeroelastic aircraft model system for each two-dimensional spanwise position, as well as forcing the selection of the time step in any time-marching solution.

A more convenient approximation would be a low-order, continuous model. A balanced realisation of the FIR filter transfer function, given by Equation 4.2.18, was performed. The order of the system was reduced by eliminating those states having little contribution

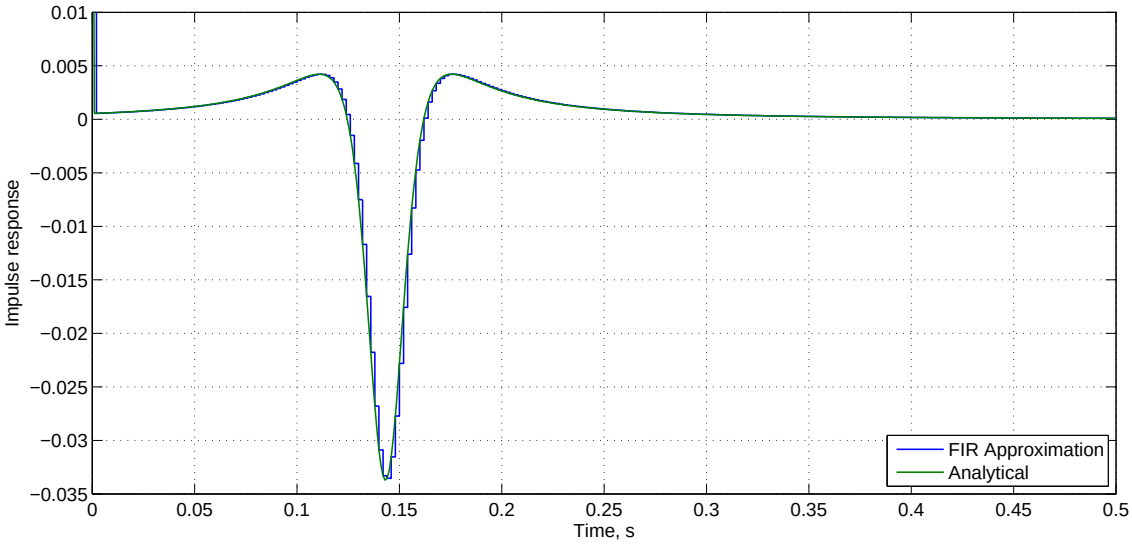

Figure 4.7: Impulse response of time-dependent downwash transfer function approximation

to the input/output of the system by analysis of the Hankel singular values of the states. A Hankel singular value threshold of 1×10^{-3} was chosen, which yielded a reduced-order model with on average 30 discrete states. The discrete-time system was then converted into a continuous, state-space system. The impulse response of the continuous, reduced-order model is compared with the analytical response in Figure 4.8. Finally, the response of the system to an arbitrary input is given by the sum of the time-dependent component, represented by the reduced-order, continuous state-space model, and the non-time-dependent component given by the second term within the parentheses of Equation 4.2.14.

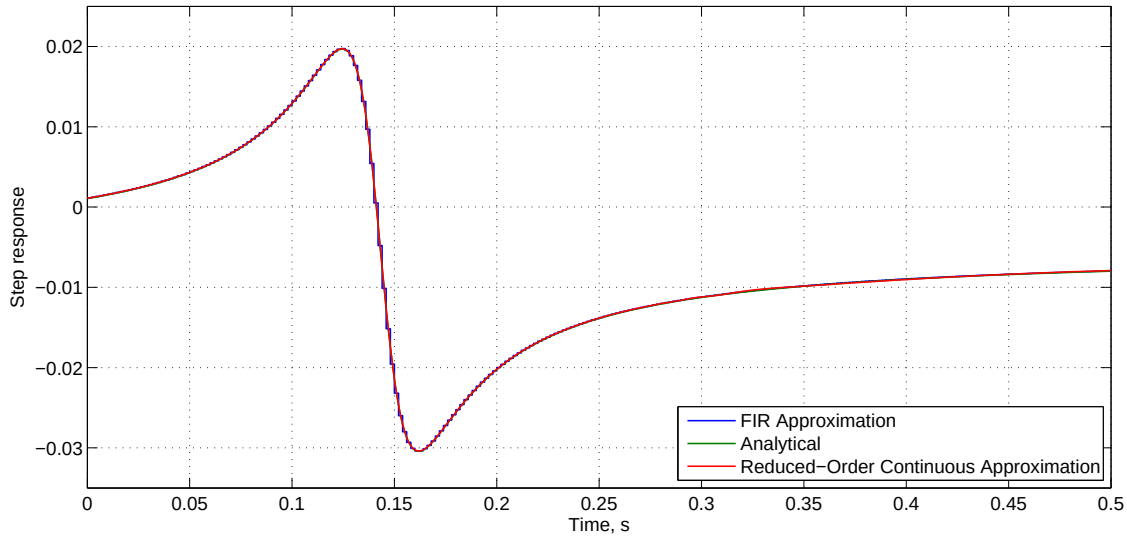

Figure 4.8: Step response of downwash transfer function approximation

The angle of attack at the tailplane, shown in Figure 4.4, is then given by the following

equation, assuming a tailplane setting angle, η_T:

$$\begin{aligned}\alpha_T =& \alpha - \epsilon + \eta_T \\ =& \tan^{-1}\left(\frac{W}{U}\right) - \tan^{-1}\left(\frac{W_b - W_{b_{dw}}}{U_b}\right) + \eta_T \end{aligned} \tag{4.2.20}$$

4.2.1.3 Indicial Unsteady Aerodynamics

The unsteady lift of a harmonically oscillating wing-flap-tab combination was first considered by Theodorsen [1949] and Theodorsen and Garrick [1942], who showed that the lift produced by a thin rigid aerofoil in non-stationary flow was equal to:

$$C_{\mathfrak{L}_a} = \frac{\pi b}{V^2}\left(\ddot{h} + V\dot{\alpha} + bx_\alpha\ddot{\alpha}\right) + 2\pi C(k)\left(\frac{\dot{h}}{V} + \alpha + b\left(\frac{1}{2} - x_\alpha\right)\frac{\dot{\alpha}}{V}\right) \tag{4.2.21}$$

where $C(k)$ is Theodorsen's Function, a complex number dependant on the reduced frequency k. This gives the change in magnitude and phase of the resultant lift force due to the unsteadiness of the flow.

The reduced frequency k, or Strouhal number St, is the non-dimensional oscillatory frequency of the aerofoil and is equal to $\omega c/2V$, where ω is the oscillatory frequency of the aerofoil. This characterises the dynamical variation of the flow with time and is used as a measure of the flow "unsteadiness". The Strouhal number, or reduced frequency, describes the relative importance of temporal inertial forces to convective inertial forces. Figure 4.10 shows the variation in magnitude and phase of the aerodynamic lift force as a function of Mach number and the oscillatory frequency of the aerofoil. This is derived from the indicial model presented by Leishman [1994], and is shown for a range of Mach numbers and oscillatory frequencies typical for a large aircraft. At low reduced frequencies, the aerodynamic lift force is dominated by the circulatory loads. At higher reduced frequencies however, above 0.25, the non-circulatory loads become more significant and the change in the sign of the phase angle is due to these non-circulatory effects. It can be seen that the effects of compressibility on the unsteady lift response are also significant.

The first group of terms in Equation 4.2.21, the "non-circulatory" or "apparent-mass" terms, represent the effect generated by the acceleration of the aerofoil. This creates a pressure difference across the aerofoil surface, causing the aerofoil to effectively carry the surrounding air with it. This response is primarily governed by the inertia of the fluid, and the pressure wave reflections generated. Mazelsky [1952] showed that this lift died away very quickly in subsonic flow. This is in contrast to the incompressible flow case where the lift dies away instantaneously and is therefore not considered.

The second group of terms represent the "circulatory" response, which is generally much more important for aircraft wings and provides the main lifting force. This describes the effect on the lift of vortices shed in the wake, and may be modelled using the Wagner function or any of its exponential approximations.

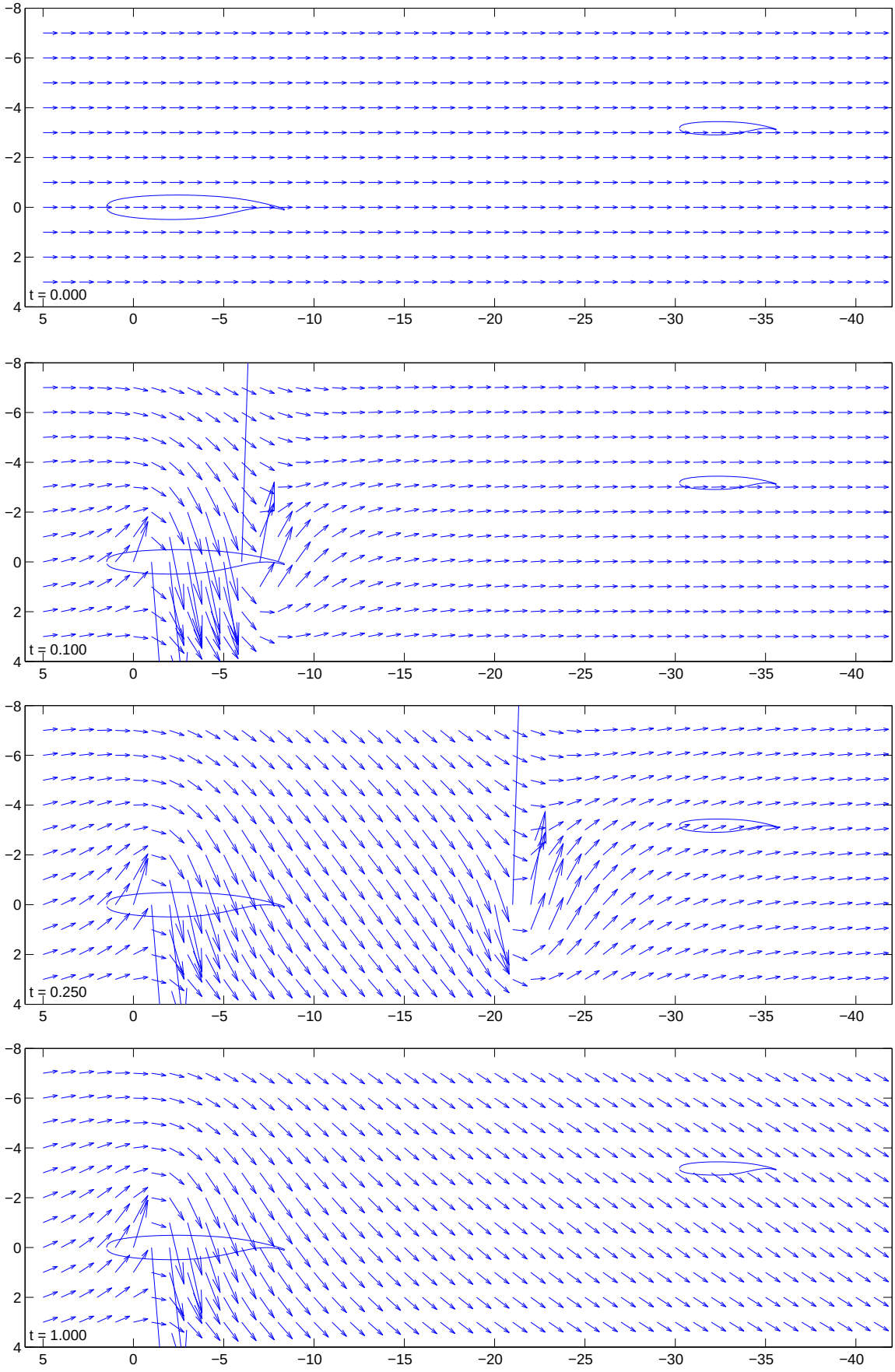

Figure 4.9: Downwash field aft of the wing following step change in circulation

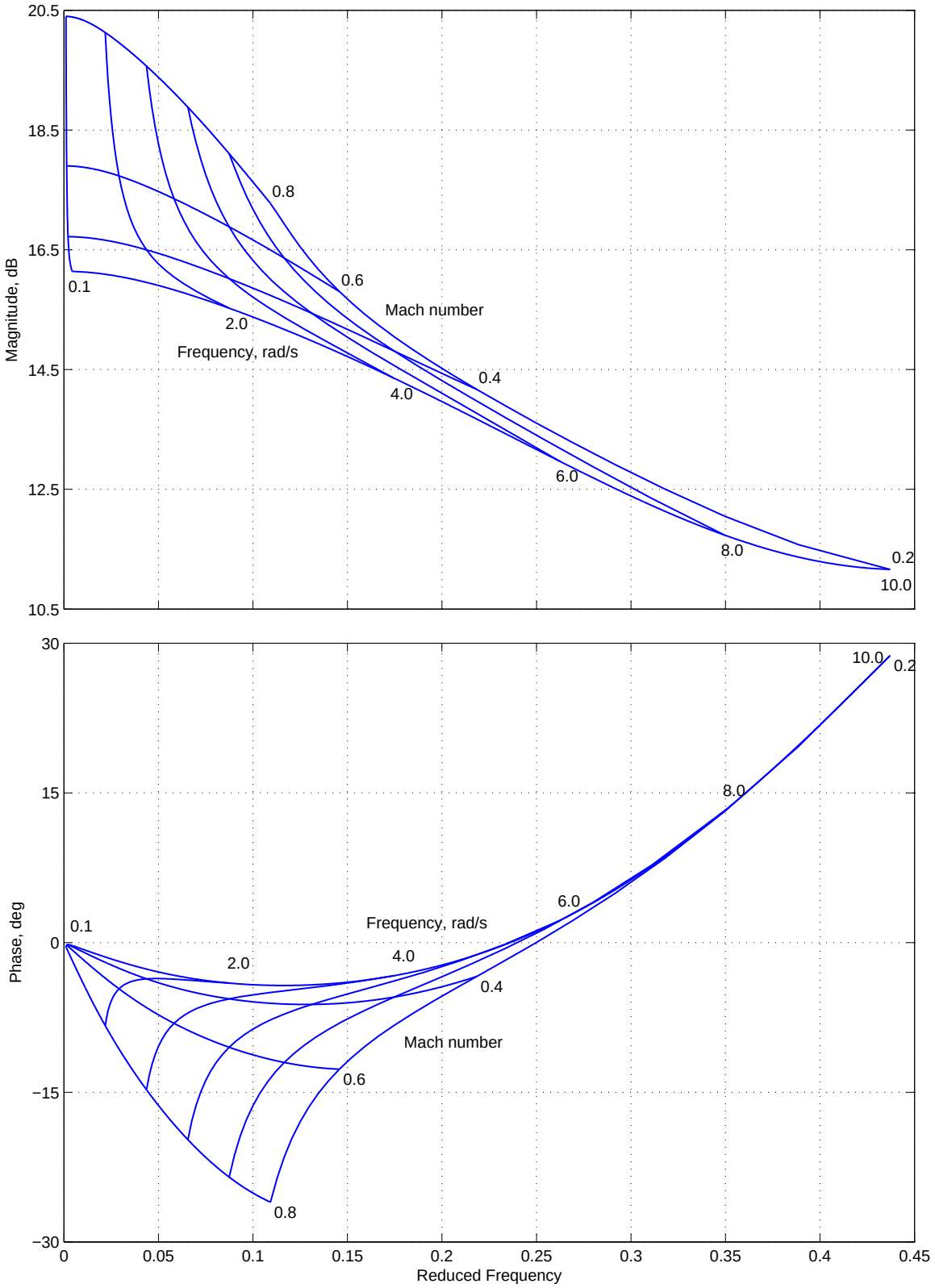

Figure 4.10: Bode plot showing variation of aerodynamic phase and gain with Mach number and aerofoil oscillatory frequency

Theodorsen and Garrick [1942] also showed that the additional lift due to a trailing edge flap was equal to:

$$C_{\mathfrak{L}_f} = \frac{b}{V^2}\left(-VF_4\dot{\xi} - bF_1\ddot{\xi}\right) + 2\pi C(k)\left(\frac{F_{10}\xi}{\pi} + \frac{bF_{11}\dot{\xi}}{2\pi V}\right) \tag{4.2.22}$$

where the first group of terms in Equation 4.2.22 again represent the non-circulatory response, and the second group the circulatory response.

Alternatively, the unsteady aerodynamics of a two-dimensional aerofoil can be simulated through an indicial admittance model [Wagner, 1925]. Wagner described the response of the linear aerodynamic system to a unit step input using the indicial Wagner function, ϕ_W. It represented the build up of circulatory lift generated by the aerofoil, and accounted for the effect of the vortices shed in the wake [Figure 4.11]. It is commonly approximated by a second order exponential function, such as that derived by Jones [1945]:

$$\phi_W(\tau) \simeq 1 - 0.165e^{-0.0455\tau} - 0.335e^{-0.3\tau} \tag{4.2.23}$$

where τ is the non-dimensional time $2Vt/c$. The effective unsteady angle of attack of the aerofoil is then given by:

$$\alpha_\phi = \phi_W \alpha \tag{4.2.24}$$

Equation 4.2.23 can be expressed in the more general form:

$$\phi_W(t) = 1 - A_1 e^{-b_1 \frac{2V}{c} t} - A_2 e^{-b_2 \frac{2V}{c} t} \tag{4.2.25}$$

Taking the Laplace transform of the step response [Equation 4.2.25] yields:

$$\phi_W(s) = \frac{1}{s} - \frac{A_1}{s + \frac{2V}{c}b_1} + \frac{A_2}{s + \frac{2V}{c}b_2} \tag{4.2.26}$$

The transfer function describing the response of the aerodynamic system to a step input, given that the Laplace transform of a step input is $1/s$, is then expressed as:

$$H_{\phi_W} = 1 - \frac{A_1 s}{s + \frac{2V}{c}b_1} + \frac{A_2 s}{s + \frac{2V}{c}b_2} \tag{4.2.27}$$

The proper transfer function $A_1 s/\left(s + \frac{2V}{c}b_1\right)$ can be rewritten as the sum of a strictly proper transfer function and a constant:

$$\frac{A_1 s}{s + \frac{2V}{c}b_1} = -\frac{A_1 \frac{2V}{c} b_1}{s + \frac{2V}{c}b_1} + A_1 \tag{4.2.28}$$

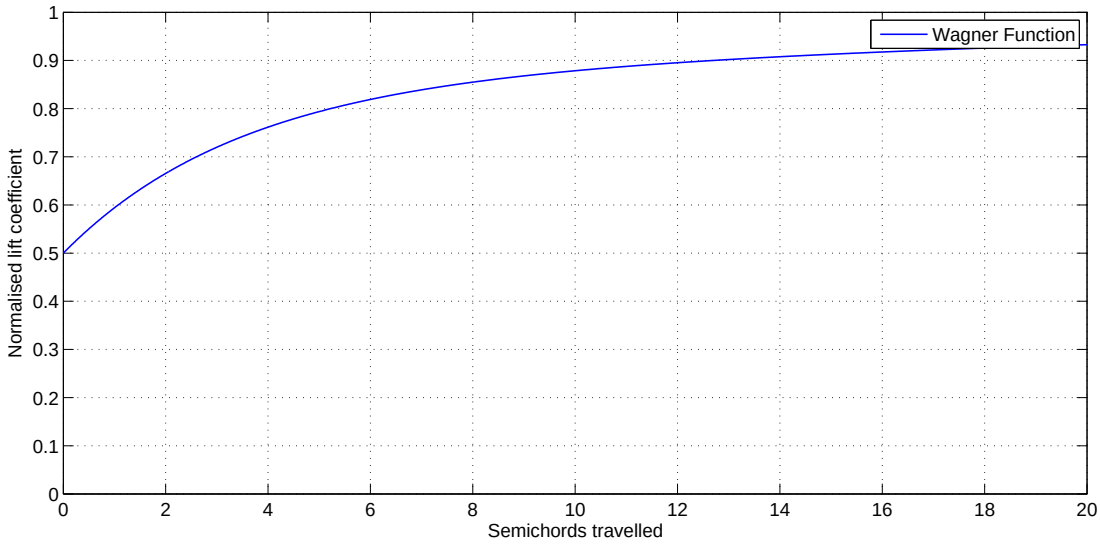

Figure 4.11: Wagner function for the indicial lift response of a heaving aerofoil

The strictly proper transfer function can then easily be expressed in state-space controllable canonical form, while the constant A_1 is given by the trivial solution $y = \left[\ A_1\ \right] u$:

$$x = \frac{2V}{c}\left[\ -b_1\ \right] x + \left[\ 1\ \right] u \tag{4.2.29a}$$

$$y = -\frac{2V}{c}\left[\ A_1 b_1\ \right] x + \left[\ A_1\ \right] u \tag{4.2.29b}$$

The complete transfer function H_{ϕ_W} can then be expressed in state-space form, as given by Equations 4.2.30a and 4.2.30b. This state-space form is particularly convenient for integration and solution with an existing aircraft simulation model.

$$\dot{\mathbf{x}} = \frac{2V}{c}\begin{bmatrix} -b_1 & 0 \\ 0 & -b_2 \end{bmatrix}\mathbf{x} + \begin{bmatrix} 1 \\ 1 \end{bmatrix} u \tag{4.2.30a}$$

$$y = \frac{2V}{c}\left[\ A_1 b_1 \quad A_2 b_2\ \right]\mathbf{x} + \left[1 - A_1 - A_2\right] u \tag{4.2.30b}$$

The Wagner function is only applicable to incompressible flow however. More recently, Leishman [1994] has attempted to correct for the effects of compressibility using the Prandtl-Glauert correction factor β, where $\beta = 1/\sqrt{1 - Ma^2}$:

$$\phi_W(\tau) \simeq 1 - 0.918e^{-0.366\beta^2\tau} - 0.082e^{-0.102\beta^2\tau} \tag{4.2.31}$$

in which the coefficients of Equation 4.2.31 were obtained from experimental flutter data.

This two-dimensional indicial method can be applied to the calculation of the the lift of a three-dimensional wing by introducing strip theory. Using this approach, the unsteady

spanwise loading distribution on the wing can be calculated. In the following section, an indicial model of the two dimensional unsteady aerodynamics of an aerofoil-flap are presented. The unsteady aerodynamic loads of the three-dimensional wing are then given by the sum of three-dimensional circulatory forces and the two-dimensional non-circulatory forces [Figure 4.12].

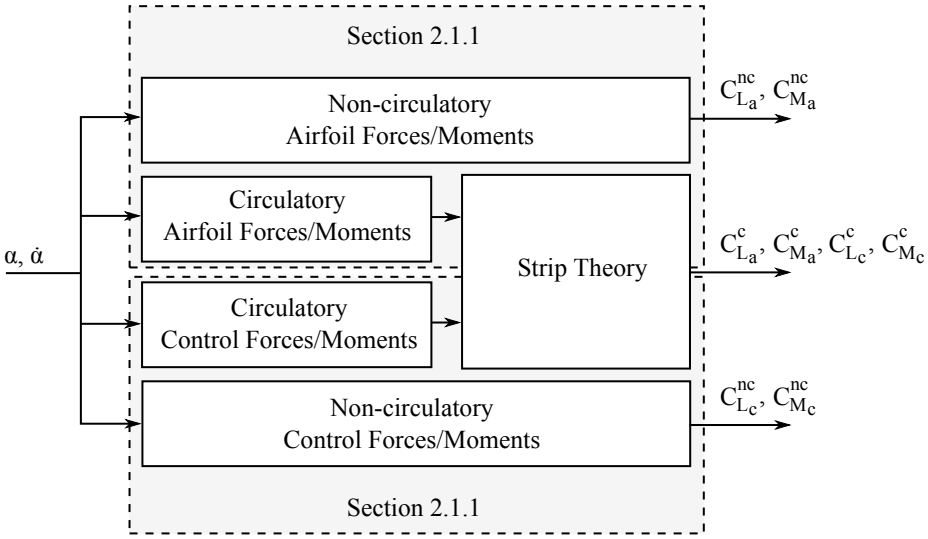

Figure 4.12: Calculation of three-dimensional lift forces and moments on wing

Aerofoil Indicial Forces and Moments

Leishman [1988] presented a state-space model of the unsteady aerodynamic loads acting on a two-dimensional aerofoil in subsonic flow. This took a similar form to the second-order exponential approximation for the Wagner function developed by Jones [1945]. This methodology has been implemented here, with the exponential coefficients corrected to those suggested by Leishman [1993].

The local lift coefficient at each spanwise station of the three-dimensional wing is estimated from the sum of the two-dimensional non-circulatory lift, $C^{nc}_{\mathfrak{L}}$, and the three-dimensional circulatory lift, $C^{c}_{\mathfrak{L}}$. The circulatory lift component is calculated from the local unsteady angle of attack distribution, α_i, for the wing using a modified strip theory [Weissinger, 1947]. This is presented in Section 4.2.1.4.

The unsteady lift acting on each spanwise station can be seen to be the sum of the circulatory lift at each spanwise station, $C^{c}_{\mathfrak{L}_i}$, the non-circulatory lift due to angle of attack, $C^{nc}_{\mathfrak{L}_\alpha}$, and the non-circulatory lift due to pitch rate, $C^{nc}_{\mathfrak{L}_q}$:

$$C_{\mathfrak{L}_i} = C^{c}_{\mathfrak{L}_i} + C^{nc}_{\mathfrak{L}_{\alpha_i}} + C^{nc}_{\mathfrak{L}_{q_i}} \tag{4.2.32}$$

where the local circulatory lift coefficient at station i, $C^{c}_{\mathfrak{L}_i}$, is given by Equation 4.2.67 of Section 4.2.1.4 for m spanwise stations:

$$C^{c}_{\mathfrak{L}_i} = \frac{1}{c_i} \sum_{j=1}^{k} \mathfrak{A}_{ij} \mathfrak{G}_j \alpha_{j_{\mathfrak{L}}} \tag{4.2.33}$$

The local unsteady angle of attack, which represents the circulatory lift response for each spanwise station, may be modelled as an exponential approximation of the Wagner function. This is expressed in state-space form by [Leishman, 1988]:

$$\alpha_{j_{\mathfrak{L}}} = \frac{1}{\beta}\left(\frac{2V_T}{c}\right)\beta^2 \begin{bmatrix} A_1 b_1 & A_2 b_2 \end{bmatrix} \begin{bmatrix} x_1 \\ x_2 \end{bmatrix} \tag{4.2.34a}$$

$$\begin{bmatrix} \dot{x}_1 \\ \dot{x}_2 \end{bmatrix} = \left(\frac{2V_T}{c}\right)\beta^2 \begin{bmatrix} -b_1 & 0 \\ 0 & -b_2 \end{bmatrix} \begin{bmatrix} x_1 \\ x_2 \end{bmatrix} + \begin{bmatrix} 1 \\ 1 \end{bmatrix} \alpha_{j_{3/4}} \tag{4.2.34b}$$

where:

$$\alpha_{j_{3/4}} = \alpha_j + \frac{q_j}{2} \tag{4.2.35}$$

$$q_j = \dot{\alpha_j} c / V_T \tag{4.2.36}$$

The two-dimensional non-circulatory lift at spanwise station i due to angle of attack, $C^{nc}_{\mathfrak{L}_{\alpha_i}}$, and the non-circulatory lift due to pitch rate, $C^{nc}_{\mathfrak{L}_{q_i}}$ are then given by Leishman [1988] in state-space form as:

$$C^{nc}_{\mathfrak{L}_{\alpha_i}} = \frac{4}{Ma}\dot{x}_3 \tag{4.2.37a}$$

$$\dot{x}_3 = -\frac{1}{T_\alpha}x_3 + \alpha_i \tag{4.2.37b}$$

$$C^{nc}_{\mathfrak{L}_{q_i}} = \frac{1}{Ma}\dot{x}_4 \tag{4.2.38a}$$

$$\dot{x}_4 = -\frac{1}{T_q}x_4 + q_i \tag{4.2.38b}$$

The non-circulatory lift was assumed by Mazelsky [1952] to die away exponentially from its initial value given by piston theory. Based on this approach, Leishman [1988] approximates the non-circulatory time constants, T_α and T_q, to be equal to:

$$T_\alpha = k_1 \left((1 - Ma) + \pi\beta Ma^2 (A_1 b_1 + A_2 b_2)\right)^{-1} \frac{c}{a_s} \tag{4.2.39}$$

$$T_q = 2k_2(1 - 2x_\alpha)\left((1 - Ma)(1 - 2x_\alpha) + 2\pi\beta Ma^2 (A_1 b_1 + A_2 b_2)\right)^{-1} \frac{c}{a_s} \tag{4.2.40}$$

Leishman [1993] obtained the coefficients $A_1, A_2, \ldots$ after deriving suitable indicial lift approximations from experimental oscillatory measurements. The coefficients were shown to correlate well with the experimental measurements, as well as providing a good match to CFD results.

$$\begin{array}{lll} A_1 = 0.918 & b1 = 0.366 & k_1 = 0.85 \\ A_2 = 0.082 & b2 = 0.102 & k_2 = 0.73 \end{array}$$

Following the same methodology for the calculation of the unsteady aerodynamic lift force, the pitching moment is also comprised of circulatory and non-circulatory components:

$$C_{\mathfrak{M}_i} = C^c_{\mathfrak{M}_{\alpha_i}} + C^c_{\mathfrak{M}_{q_i}} + C^{nc}_{\mathfrak{M}_{\alpha_i}} + C^{nc}_{\mathfrak{M}_{q_i}} \tag{4.2.41}$$

The local spanwise circulatory pitching moment due to angle of attack, $C^c_{\mathfrak{M}_{\alpha_i}}$, may be calculated from the local circulatory lift force and the distance between the aerodynamic centre and elastic axis, that is:

$$C^c_{\mathfrak{M}_{\alpha_i}} = C^c_{\mathfrak{L}_i}(x_\alpha - x_{ac}) \tag{4.2.42}$$

The local circulatory pitching moment due to pitch rate, $C^c_{\mathfrak{M}_{q_i}}$, is similarly calculated. This is given by:

$$C^c_{\mathfrak{M}_{q_i}} = \frac{1}{c_i}\sum_{j=1}^{k} \mathfrak{A}_{ij}\mathfrak{G}_j \alpha_{i_{\mathfrak{M}_q}} \tag{4.2.43}$$

where the local unsteady effective angle of attack, $\alpha_{j_{\mathfrak{M}_q}}$, is given by [Leishman, 1988]:

$$\alpha_{j_{\mathfrak{M}_q}} = -\frac{1}{16\beta} b_5 \beta^2 \left(\frac{2V_T}{c}\right) x_7 \tag{4.2.44a}$$

$$\dot{x}_7 = -b_5\beta^2\left(\frac{2V_T}{c}\right)x_7 + q \tag{4.2.44b}$$

The non-circulatory components of the pitching moment at station i, $C^{nc}_{\mathfrak{M}_{\alpha_i}}$ and $C^{nc}_{\mathfrak{M}_{q_i}}$, the pitching moment due to angle of attack and pitch rate respectively, were then given by Leishman [1988]:

$$C^{nc}_{\mathfrak{M}_{\alpha_i}} = -\frac{1}{Ma}\begin{bmatrix} -\frac{A_3}{b_3 T_{\alpha_{\mathfrak{M}}}} & -\frac{A_4}{b_4 T_{\alpha_{\mathfrak{M}}}} \end{bmatrix}\begin{bmatrix} x_5 \\ x_6 \end{bmatrix} - \frac{1}{Ma}\alpha_i \tag{4.2.45a}$$

$$\begin{bmatrix} \dot{x}_5 \\ \dot{x}_6 \end{bmatrix} = \begin{bmatrix} -\frac{1}{b_3 T_{\alpha_{\mathfrak{M}}}} & 0 \\ 0 & -\frac{1}{b_4 T_{\alpha_{\mathfrak{M}}}} \end{bmatrix}\begin{bmatrix} x_5 \\ x_6 \end{bmatrix} + \begin{bmatrix} 1 \\ 1 \end{bmatrix}\alpha_i \tag{4.2.45b}$$

$$C^{nc}_{\mathfrak{M}_{q_i}} = -\frac{7}{12Ma}\dot{x}_8 \tag{4.2.46a}$$

$$\dot{x}_8 = -\frac{1}{T_{q_{\mathfrak{M}}}} x_8 + q_i \tag{4.2.46b}$$

where:

$$T_{\alpha_{\mathfrak{M}}} = \left[\frac{A_3 b_4 + A_4 b_3}{b_3 b_4 (1 - Ma)}\right] \frac{c}{a_s} \tag{4.2.47}$$

$$T_{q_{\mathfrak{M}}} = \left[\frac{7}{15(1 - Ma) + 3\pi\beta Ma^2 b_5}\right] \frac{c}{a_s} \tag{4.2.48}$$

The coefficients $A_3, A_4, \ldots$ are given by Leishman [1988]:

$$\begin{array}{ll} A_3 = 1.50 & b3 = 0.25 \\ A_4 = -0.5 & b4 = 0.10 \\ & b5 = 0.50 \end{array}$$

Control Indicial Forces and Moments

As with the aerodynamic forces on an aerofoil section, the forces due to the arbitrary motion of a trailing-edge control surface are the sum of both a circulatory and non-circulatory component. The lift force due to trailing-edge control surface deflection at span-wise station i is then given by:

$$C_{\mathfrak{L}_{\xi_i}} = C^c_{\mathfrak{L}_{\xi_{qs_i}}} + C^{nc}_{\mathfrak{L}_{\xi_i}} + C^{nc}_{\mathfrak{L}_{\dot{\xi}_i}} \tag{4.2.49}$$

The local circulatory lift coefficient due to trailing-edge control surface deflection, $C^c_{\mathfrak{L}_{\xi_{qs_i}}}$, at station i of m is then given by:

$$C^c_{\mathfrak{L}_{\xi_{qs_i}}} = \frac{1}{c_i} \sum_{j=1}^{k} \mathfrak{A}_{ij} \mathfrak{G}_j \alpha_{\mathfrak{L}_{j_{\xi_{qs}}}} \tag{4.2.50}$$

The local effective unsteady angle of attack due to trailing-edge control surface deflection, $\alpha_{\mathfrak{L}_{j_{\xi_{qs}}}}$, is then given in state space form by [Leishman, 1994]:

$$\alpha_{\mathfrak{L}_{j_{\xi_{qs}}}} = \frac{1}{\beta} \begin{bmatrix} (b_1 b_2)(2V_T/c)^2\beta^4 & (A_1 b_1 + A_2 b_2)(2V_T/c)\beta^2 \end{bmatrix} \begin{bmatrix} x_9 \\ x_{10} \end{bmatrix} \tag{4.2.51a}$$

$$\begin{bmatrix} \dot{x}_9 \\ \dot{x}_{10} \end{bmatrix} = \begin{bmatrix} 0 & 1 \\ -b_1 b_2 (2V_T/c)^2\beta^4 & -(b_1 + b_2)(2V_T/c)\beta^2 \end{bmatrix} \begin{bmatrix} x_9 \\ x_{10} \end{bmatrix} + \begin{bmatrix} 0 \\ 1 \end{bmatrix} \xi_{j_{qs}} \tag{4.2.51b}$$

where the quasi-steady trailing-edge control surface angle, $\xi_{j_{qs}}$ is:

$$\xi_{j_{qs}} = \left[\frac{F_{10}\xi_j}{\pi} + \frac{F_{11}\dot{\xi}_j c}{4\pi V_T}\right] \tag{4.2.52}$$

The non-circulatory component of the indicial response at station i, $C^{nc}_{\mathfrak{L}_{\xi_i}}$ and $C^{nc}_{\mathfrak{L}_{\dot{\xi}_i}}$, to trailing-edge control surface deflection and trailing-edge control surface rate respectively are given by [Leishman, 1994]:

$$C^{nc}_{\mathfrak{L}_{\xi_i}} = \frac{2(1-x_e)}{Ma}\dot{x}_{11} \tag{4.2.53a}$$

$$\dot{x}_{11} = -\frac{1}{T_\xi}x_{12} + \xi_i \tag{4.2.53b}$$

$$C^{nc}_{\mathfrak{L}_{\dot{\xi}_i}} = \frac{(1-x_e)^2}{4Ma}\frac{c}{V_T}\dot{x}_{12} \tag{4.2.54a}$$

$$\dot{x}_{12} = -\frac{1}{T_{\dot{\xi}}}x_{12} + \frac{(1-x_e)^2}{2}\frac{\dot{\xi}_i c}{V_T} \tag{4.2.54b}$$

The non-circulatory time constants, T_ξ and $T_{\dot{\xi}}$, assuming the same exponential decay as for the aerofoil section, were presented by Leishman [1994] as:

$$T_\xi = (1-x_e)\left[(1-Ma) + F_{10}\beta^{-1}Ma^2\sum_{i=1}^{2}A_i b_i\right]^{-1}\frac{c}{a_s} \tag{4.2.55}$$

$$T_{\dot{\xi}} = \frac{(1-x_e)^2}{2}\left[(1-Ma)(1-x_e) + F_{11}\pi^{-1}\beta^2 Ma^2\sum_{i=1}^{2}A_i b_i\right]^{-1}\frac{c}{a_s} \tag{4.2.56}$$

Leishman [1994] showed that the unsteady pitching moment due to trailing-edge control surface deflected was, like the lift force before, the sum of the non-circulatory and circulatory components:

$$C_{\mathfrak{M}_{\xi_i}} = C^c_{\mathfrak{M}_{\xi_{qs_{\mathfrak{M}_i}}}} + C^{nc}_{\mathfrak{M}_{\xi_i}} + C^{nc}_{\mathfrak{M}_{\dot{\xi}_i}} \tag{4.2.57}$$

The local circulatory pitching moment due to trailing-edge control surface deflection, $C^c_{\mathfrak{M}_{\xi_{qs_{\mathfrak{M}_i}}}}$, at station i of m is then given by:

$$C^c_{\mathfrak{M}_{\xi_{qs_{\mathfrak{M}_i}}}} = \frac{1}{c_i}\sum_{j=1}^{m}\mathfrak{A}_{ij}\mathfrak{G}_j\alpha_{\mathfrak{M}_{j_{\xi_{qs_{\mathfrak{M}}}}}} \tag{4.2.58}$$

The circulatory component due to the quasi-steady trailing-edge control surface angle, $C^c_{\mathfrak{M}_{\xi_{qs_{\mathfrak{M}}}}}$, is then given by [Leishman, 1994]:

$$\alpha_{\mathfrak{M}_{j_{\xi_{qs_{\mathfrak{M}}}}}} = \frac{1}{2\beta}b_3\beta^2\frac{2V_T}{c}x_{13} \tag{4.2.59a}$$

$$\dot{x}_{13} = -\frac{2V_T}{c}b_3\beta^2 x_{13} + \xi_{j_{qs_{\mathfrak{M}}}} \tag{4.2.59b}$$

in which:

$$\xi_{j_{qs_{\mathfrak{M}}}} = -\left(\frac{F_4 + F_{10}}{2\pi\beta}\right)\xi - \left[\frac{2F_1 - 2F_8 - (2x_e + 1)F_4 + F_{11}}{8\pi\beta}\right]\frac{\dot{\xi}_j c}{V_T} \tag{4.2.60}$$

The non-circulatory components at station i, $C^{nc}_{\mathfrak{M}_{\xi_i}}$ and $C^{nc}_{\mathfrak{M}_{\dot{\xi}_i}}$, can then be expressed as the following state-space models:

$$C^{nc}_{\mathfrak{M}_{\xi_i}} = -\frac{(1 - x_e)(2 + x_e)}{2Ma}\dot{x}_{14} \tag{4.2.61a}$$

$$\dot{x}_{14} = -\frac{1}{T_{\xi_{\mathfrak{M}}}}x_{14} + \xi_i \tag{4.2.61b}$$

$$C^{nc}_{\mathfrak{M}_{\dot{\xi}_i}} = -\frac{(1 + x_e)^3 - (12x_e - 4) - 3/2(1 - x_e)^2}{12Ma}\dot{x}_{15} \tag{4.2.62a}$$

$$\dot{x}_{15} = -\frac{1}{T_{\dot{\xi}_{\mathfrak{M}}}}x_{15} + \dot{\xi}_i \tag{4.2.62b}$$

where the non-circulatory time constants, $T_{\xi_{\mathfrak{M}}}$ and $T_{\dot{\xi}_{\mathfrak{M}}}$, are given by:

$$T_{\xi_{\mathfrak{M}}} = (1 - x_e)(2 + x_e)[3(1 - Ma) + 2(F_4 + F_{10})\beta Ma^2 b_3]^{-1}\frac{c}{a_s} \tag{4.2.63}$$

$$\begin{aligned} T_{\dot{\xi}_{\mathfrak{M}}} =& ((1 + x_e)^3 - (12x_e - 4) - (3(1 - x_e)^2/2))(9(1 - Ma)(1 - x_e) \\ &+ 6(F_1 - F_8 - (x_e + 0.5)F_4 + (F_{11}/2))\beta Ma^2 b_3)^{-1}\frac{c}{a_s} \end{aligned} \tag{4.2.64}$$

The terms F_1, F_4, F_{10} and F_{11} are defined only by the geometry and dimensions of the aerofoil and trailing-edge control surface [Theodorsen, 1949]. Given the geometric properties shown in Figure 4.13, F_1 through F_{11} are calculated using the following expressions:

$$F_1 = x_e \cos^{-1} x_e - 1/3(2 + x_e^2)\sqrt{1 - x_e} \tag{4.2.65a}$$

$$F_4 = x_e\sqrt{1 - x_e} - \cos^{-1} x_e \tag{4.2.65b}$$

$$F_8 = x_e \cos^{-1} x_e - 1/3(2x_e^2 + 1)\sqrt{1 - x_e} \tag{4.2.65c}$$

$$F_{10} = \sqrt{1 - x_e^2} + \cos^{-1} x_e \tag{4.2.65d}$$

$$F_{11} = (1 - 2x_e)\cos^{-1} x_e + (2 - x_e)\sqrt{1 - x_e^2} \tag{4.2.65e}$$

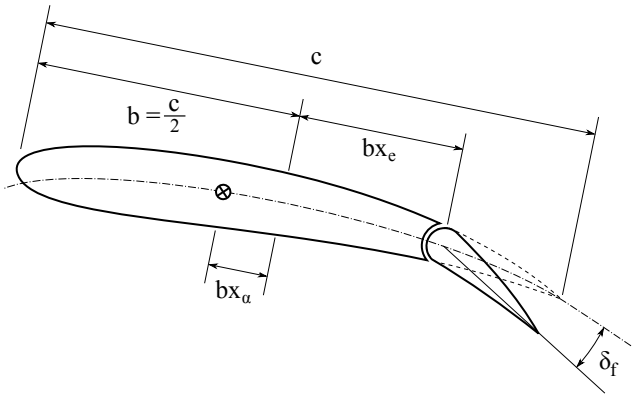

Figure 4.13: Aerofoil and control surface geometry

4.2.1.4 Modified Strip Theory

The modified strip theory presented by Weissinger [1947], and later developed by DeYoung and Harper [1948], enables the calculation of the spanwise aerodynamic loading on a swept, arbitrary planform wing. Given the local lift coefficient at a series of spanwise stations, and assuming the wing has no discontinuities in twist, the lift, induced drag and pitching moment may be calculated. Using this simplified lifting-surface theory, the effects of compressibility may also be taken into account.

Weissinger [1947] showed that the finite wing could be represented by a series of horseshoe vortices [Figure 4.14]. By finding the solution to the integral equation, which gives the downwash at any point due to the integrated effect of a number of trailing vortex sheets and bound vortices, the loading distribution may be found. The downwash at some point, (x, y), due an arbitrary horseshoe vortex is equal to the sum of the effect on the downwash due to its trailing vortex sheet and the bound vortex, given by:

$$\begin{aligned} w =& w_t + w_b \\ =& \frac{d\Gamma}{4\pi d}(\cos\theta_1 + \cos\theta_2) + \frac{\Gamma dds}{4\pi r^3} \end{aligned} \tag{4.2.66}$$

where d is the perpendicular distance from the point (x, y) to the vortex line, $d\Gamma$ is the trailing vortex strength at a given spanwise station, and Γ is the strength of the bound vortex for some small element, ds.

Applying the boundary conditions that the flow must be tangential to the plate at the three-quarter chord line, Weissinger [1947] showed that the loading at k spanwise wing stations can then be found from the solution of k simultaneous linear equations. DeYoung and Harper [1948] summarised the calculations, and showed that the solution was equal to:

$$c_i C_{\mathfrak{L}i} = \sum_{j=1}^{k} \mathfrak{A}_{ij} \mathfrak{G}_j \alpha_j \tag{4.2.67}$$

where $\mathfrak{G}_j$ is defined by:

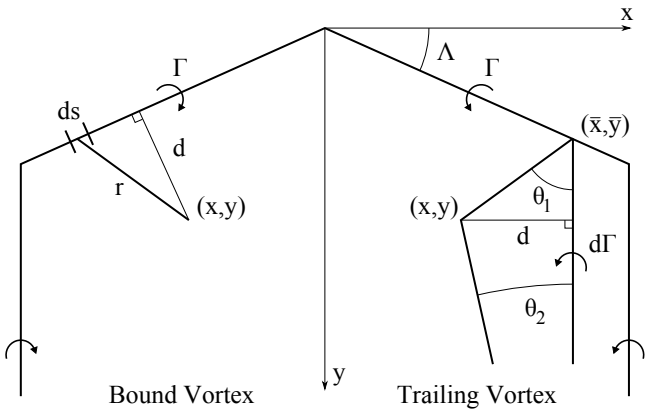

Figure 4.14: Downwash induced by the trailing vortex sheet and bound vortex

$$\mathfrak{G}_j = \frac{1}{2b} \tag{4.2.68}$$

and where, $\mathfrak{A}_{ij}$ is equal to, for $j = i$:

$$\mathfrak{A}_{ij} = 2\mathfrak{b}_{ii} + \frac{b}{c_i}\mathfrak{g}_{ii} \tag{4.2.69a}$$

else, where $j \neq j$:

$$\mathfrak{A}_{ij} = -2\mathfrak{b}_{ij} + \frac{b}{c_i}\mathfrak{g}_{ij} \tag{4.2.69b}$$

where $\mathfrak{b}_{ij}$ is defined by, for $j = i$:

$$\mathfrak{b}_{ii} = \frac{k+1}{4\sin\chi_i} \tag{4.2.70a}$$

else, where $j \neq i$:

$$\mathfrak{b}_{ij} = \frac{sin\chi_j}{(\cos\chi_j - \cos\chi_i)^2}\frac{1-(-1)^{j-i}}{2(k+1)} \tag{4.2.70b}$$

and where, for $\mathfrak{g}_{ii} = \mathfrak{g}_{ij}$ when $i = j$:

$$\mathfrak{g}_{ij} = -\frac{1}{2(\mathfrak{K}+1)}\left(\frac{\mathfrak{T}_{i,0}\mathfrak{f}_{j,0} + \mathfrak{T}_{i,\mathfrak{K}+1}\mathfrak{f}_{j,\mathfrak{K}+1}}{2} + \sum_{\mu=1}^{\mathfrak{K}}\mathfrak{T}_{i\mu}\mathfrak{f}_{j\mu}\right) \tag{4.2.71}$$

where $\mathfrak{T}_{v,\mu}$ is found from, for $\bar{\eta} \leq 0$:

$$\mathfrak{T}_{i,\mu} = \frac{1}{((b/c_i)(\eta - \bar{\eta})} \left(\frac{\sqrt{[1 + b/c_i(|\eta| + \bar{\eta}) \tan \Lambda]^2 + (b/c_i)^2(\eta - \bar{\eta})^2}}{1 + (b/c_i)(|\eta| + \eta) \tan \Lambda} - 1 \right) + \frac{2 \tan \Lambda \sqrt{[1 + (b/c_i)|\eta| \tan \Lambda]^2 + (b/c_i)^2 \eta^2}}{[1 + (b/c_i)(|\eta| - \eta) \tan \Lambda][1 + (b/c_i)(|\eta| + \eta) \tan \Lambda]} \tag{4.2.72a}$$

and, for $\bar{\eta} \geq 0$:

$$\mathfrak{T}_{i,\mu} = \frac{1}{((b/c_i)(\eta - \bar{\eta})} \left(\frac{\sqrt{[1 + b/c_i(|\eta| - \bar{\eta}) \tan \Lambda]^2 + (b/c_i)^2(\eta - \bar{\eta})^2}}{1 + (b/c_i)(|\eta| - \eta) \tan \Lambda} - 1 \right) \tag{4.2.72b}$$

where:

$$\eta = \cos \frac{v\pi}{k+1} \tag{4.2.73}$$

$$\bar{\eta} = \cos \frac{\mu\pi}{k+1} \tag{4.2.74}$$

and where $\mathfrak{f}_{j,\mu}$ is equal to:

$$\mathfrak{f}_{j,\mu} = \frac{2}{k+1} \sum_{\nu=1}^{k} \nu \sin \nu\chi_j \cos \nu\chi_\mu \tag{4.2.75}$$

where:

$$\chi_n = \frac{n\pi}{k+1} \tag{4.2.76}$$

$$\chi_\mu = \frac{\mu\pi}{\mathfrak{K}+1} \tag{4.2.77}$$

The effects of compressibility may be accounted for using the Prandtl-Glauert correction factor, β. If the sweep angle of the wing is corrected for compressibility, $\Lambda_\beta = \tan^{-1} \tan \Lambda/\beta$, and the ratio b/c_i also corrected by the factor β, then the effects of compressibility may be fully taken into account.

The variation of local lift-curve slope with spanwise position may be also be taken into account. DeYoung and Harper [1948] showed that, given the local lift-curve slope, which may be derived from experimental data, and the theoretical lift-curve slope for a two dimensional aerofoil, 2π, the correction factor, K_{a_i} maybe calculated as such:

$$K_{a_i} = \frac{a_i}{2\pi/\beta} \tag{4.2.78}$$

The local ratio b/c_i may then be corrected for the variation of local lift coefficient, a_i, by multiplying by the correction factor $1/K_{a_i}$.

The lift distribution for a typical rigid swept wing is shown in Figure 4.15. The lift distribution for the elastic wing presented here is also function of the local dynamic twist angle due to elastic deformation, which in turn is dependent on the unsteady wing loading.

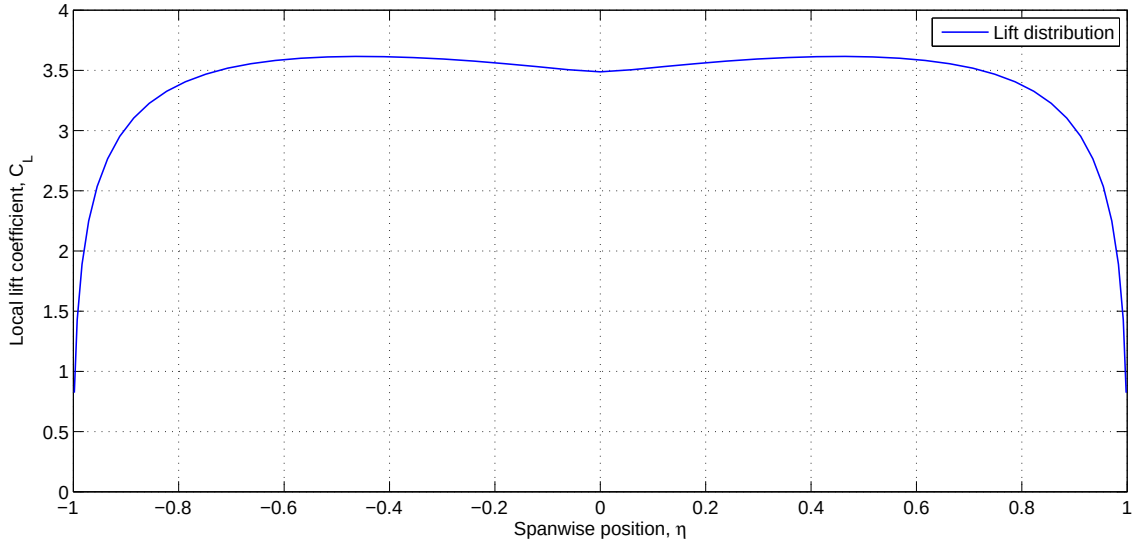

Figure 4.15: Local lift distribution for typical large aircraft wing

4.2.1.5 Actuator Dynamics

The aeroplane control forces and moments are generated by the deployment of aerodynamic control surfaces. The deployment of these control surfaces is achieved by the controlled activation of an actuator or actuation system. The actuation system often employs complex hydraulic, mechanical and electrical components. However, for flight control system design and analysis, the actuation system is commonly approximated as a first- or second-order time-invariant system [Stringer, 1976].

Kubica and Livet [1994b] presents a second-order transfer function representation of the aileron actuator:

$$\frac{\xi}{\xi_d} = \frac{-1.77s + 399}{s^2 + 48.2s + 399} \tag{4.2.79}$$

while a second- and third-order representation of the elevator and rudder actuators is given respectively by [Livet et al., 1994b]:

$$\frac{\eta}{\eta_d} = \frac{-8.42s + 2046}{s^2 + 102.87s + 2046} \tag{4.2.80}$$

$$\frac{\zeta}{\zeta_d} = \frac{-12.6s^2 - 1185s + 27350}{s^3 + 77.7s^2 + 3331s + 27350} \tag{4.2.81}$$

In addition to the actuator dynamics defined above, saturation limits are defined for each control surface in Table 4.1 [Jackson, 2006].

	Limit, deg	
Control Surface	Max	Min
Aileron	−25	+25
Elevator	−30	+15
Rudder	−32	+32

Table 4.1: Control surface actuator saturation limits [Jackson, 2006]

4.2.1.6 Drag Estimation

The drag force at each spanwise station i can be expressed as the sum of the the profile drag, $C_{\mathfrak{D}_0}$, and the induced drag, $C_{\mathfrak{D}_{in}}$. The induced drag can be further expressed as the sum of the contributions due to the induced drag due to the trailing vortices, $C_{\mathfrak{D}_{in_{tv}}}$, and lift-dependent viscous drag, $C_{\mathfrak{D}_{in_{vc}}}$. This may be expressed in coefficient form as such:

$$\begin{aligned} C_{\mathfrak{D}} =& C_{\mathfrak{D}_0} + C_{\mathfrak{D}_{in}} \\ =& C_{\mathfrak{D}_0} + \left(C_{\mathfrak{D}_{in_{tv}}} + C_{\mathfrak{D}_{in_{vc}}}\right) \end{aligned} \tag{4.2.82}$$

The value of the induced drag due to the trailing vortices $C_{\mathfrak{D}_{in_{tv}}}$ is derived from the lift distribution obtained through strip theory. DeYoung and Harper [1948] showed that the induced drag could be calculated by considering the induced angle as equal to half the downwash at some infinite point downstream of the wing. The induced drag, $C_{\mathfrak{D}_{i_{tv}}}$, for the spanwise station i is then given by:

$$C_{\mathfrak{D}_{i_{tv}}} = \frac{1}{c_i}\mathfrak{G}_i \left(\mathfrak{b}_{ii}\mathfrak{G}_i - \sum_{j=1}^{k}{}' \mathfrak{b}_{ij}\mathfrak{G}_j \right) \tag{4.2.83}$$

where $\mathfrak{b}_{ii}$ is defined by Equations 4.2.70a and 4.2.70b and $\mathfrak{G}_i$ is defined by Equation 4.2.68. The prime on the summation, $\sum'$, indicates that the value for $j = i$ is not summed. The total trailing vortex induced drag component can be found by integrating the value of the local spanwise drag coefficient across the span.

The lift-dependent viscous drag component, $C_{\mathfrak{D}_{in_{vc}}}$, can be estimated from empirical data [ESDU 07003]. It is necessary to calculate the local section inviscid and viscous lift-curve slopes, as well as the viscous lift-curve slope of the wing [ESDU 07002]. This is possible from empirical estimates using ESDU 72024, ESDU 70011, and ESDU 97020. The local wing section lift-dependent viscous drag factor, $K_{\mathfrak{D}_{ivc}}$, is then given by ESDU 07003 as being equal to:

$$K_{\mathfrak{D}_{ivc}} = \frac{1.15}{a_{1_w}} \left(1 - \left(\frac{a_0}{a_{0_T}} \right)_\eta \right) \tag{4.2.84}$$

where a_{1_w} is the viscous lift-curve slope of the wing, a_0 is the viscous lift-curve slope of the aerofoil section, and a_{0_T} is inviscid lift-curve slope of the aerofoil section. The correction factor 1.15 is found from comparison to empirical data.

The lift-dependent viscous drag coefficient is then given by:

$$C_{\mathfrak{D}_{ivc}} = K_{\mathfrak{D}_{ivc}} C^2_{\mathfrak{L}_i} \tag{4.2.85}$$

The full calculation of the profile drag coefficient, $C_{\mathfrak{D}_0}$, and viscous drag factor, $K_{\mathfrak{D}_{ivc}}$, are given in Appendices A.3.1 and A.3.2 respectively.

4.2.1.7 Wing-body Interaction

The lift of the wing and tailplane is modified by the addition of the fuselage. The lift produced by the inboard section of the wing and tailplane, the "carry-over lift", is reduced, while the lift produced by the outboard exposed section is increased slightly [ESDU 94009].

The lift of the outboard stations is given by:

$$(C_{\mathcal{L}_i})_{w(f)} = K_{w(f)} (C_{\mathcal{L}_i}) \tag{4.2.86}$$

while for the inboard stations:

$$(C_{\mathcal{L}_i})_{f(w)} = K_{f(w)} (C_{\mathcal{L}_i}) \tag{4.2.87}$$

The calculation of the coefficients $K_{w(f)}$ and $K_{f(w)}$ is described in detail in Appendix A.1.

4.2.1.8 Force and Moment Resolution

The total aerodynamic forces and moments acting at a spanwise station i are then given by:

$$\mathfrak{L} = q_d S C_{\mathfrak{L}_i} \tag{4.2.88}$$
$$\mathfrak{D} = q_d S C_{\mathfrak{D}_i} \tag{4.2.89}$$
$$\mathfrak{M} = q_d S c_i C_{\mathfrak{M}_i} \tag{4.2.90}$$

where q_d is the dynamic pressure, $\frac{1}{2}\rho V_T^2$, and S is wing, tailplane or fin area, and c_i the local chord length.

It is necessary to resolve the aerodynamic forces given in wind-axes, see Figure 4.16, into the nodal-axes system. The aerodynamic and control forces and moments expressed in nodal-axes are then given by:

$$\begin{aligned}\mathbf{f}_N &= (\mathbf{f_a} + \mathbf{f}_c)_N \\ &= -\begin{bmatrix} +\cos(\alpha_i) & 0 & +\sin(\alpha_i) \\ 0 & +1 & 0 \\ -\sin(\alpha_i) & 0 & +\cos(\alpha_i) \end{bmatrix} \begin{bmatrix} \mathfrak{D} \\ 0 \\ \mathfrak{L} \end{bmatrix} \end{aligned} \tag{4.2.91}$$

$$\mathbf{m}_N = \begin{bmatrix} 0 \\ \mathfrak{M} \\ 0 \end{bmatrix} \tag{4.2.92}$$

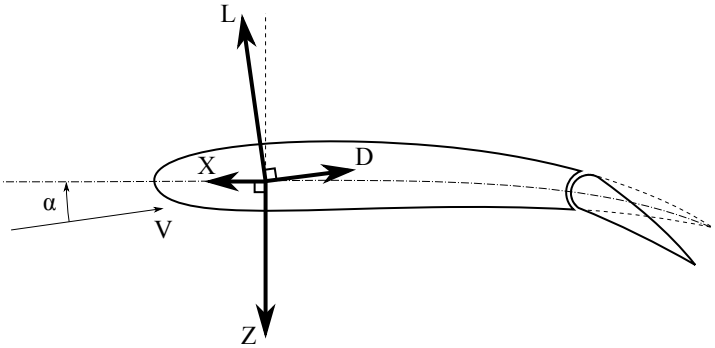

Figure 4.16: Forces and moments in wind- and body-axes

The aerodynamic forces acting on the origin of the axes system, O, in body-axes, are then given by:

$$\mathbf{f}_B = D_B^{N^{-1}} \mathbf{f}_N \tag{4.2.93}$$

where D_B^N is the direction cosine matrix defined in Section 4.2.1.1.

The aerodynamic moments acting on the origin of the axes system, with reference to Figure 4.17, are then given by:

$$\mathbf{m}_B = D_B^{N^{-1}} \mathbf{m}_N + \mathbf{r} \times \mathbf{f}_B \tag{4.2.94}$$

The forces and moments acting on each structural node in body-axes are calculated using a similar method. The aerodynamic moments are then calculated not about the axis origin but the coordinates of local structural node.

4.2.1.9 Structural Internal Forces

It is necessary to calculate the shear forces, bending moments and torques acting on the airframe structure, hereby referred to as the internal forces. As with the dynamic response of the airframe, a set of generalised coordinates may also be used to approximate the internal forces. Bisplinghoff et al. [1955] proposed two methods to approximate these internal forces; the first is referred to as the Mode Displacement (MD) method.

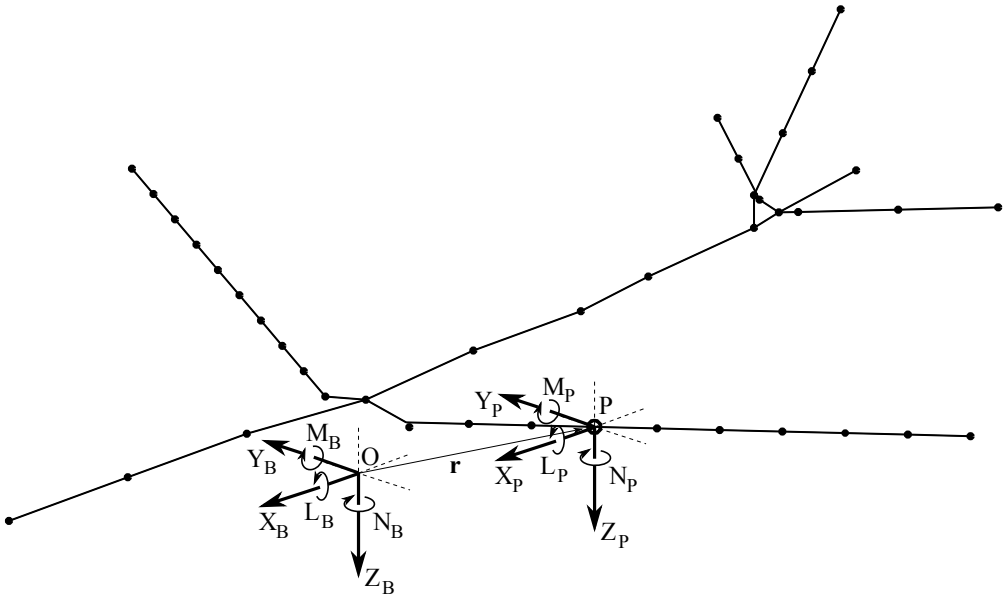

Figure 4.17: Forces and moments about the origin O due to a point P

Application of the normal mode method yields the total dynamic response of the aircraft as the superposition of n normal modes:

$$x = \sum_{i=1}^{n} \phi_i \xi_i \tag{4.2.95}$$

For each normal mode there is an associated internal stress pattern P_i. In the MD method, the principle of superposition similarly applies to this stress pattern set, and the total internal stress pattern is given by:

$$P = \sum_{i=1}^{n} P_i \xi_i \tag{4.2.96}$$

The stress pattern corresponding to each normal mode is equal to the external loading necessary to deform that mode with unit amplitude. For a lumped mass system, the external loading at station j is equal to:

$$P(j)_i = m_j \omega_i^2 \phi(j)_i \tag{4.2.97}$$

The shear and bending moment distribution for the wing, for example, can then be found at each spanwise station η:

$$SF(\eta) = \sum_{j=\eta}^{1} \sum_{i=1}^{n} P(j)_i \xi_i \tag{4.2.98}$$

$$BM(\eta) = l \sum_{j=\eta}^{1} SF(j) \tag{4.2.99}$$

The difficulty with the MD method is that the known static internal forces are approximated as a function of the number of modes chosen [Hurty and Rubinstein, 1964]. This method poorly approximates any point loads, such as applied by the engines, as there is a tendency to "smooth" these loads due to the modal generalised force approximation. Bisplinghoff et al. [1955] also noted that this method shows poor convergence, particularly in the estimation of the shear force. Bisplinghoff et al. [1955] suggested a second method, the Mode Acceleration (MA) method. Using this method the internal forces due to the static loading are first calculated separately, assuming the structure is static. The modal approximation is then used to separately calculate the internal forces due to the dynamic response, i.e. the velocity and acceleration. Referring to the ith mode equation of motion:

$$\ddot{\xi}_i + 2\zeta_i\omega_i\dot{\xi}_i + \omega_i^2\xi_i = \frac{F_i}{M_i} \tag{4.2.100}$$

If we assume that the external loading is applied to the structure statically, and the acceleration, $\ddot{\xi}_i$, and velocity, $\dot{\xi}_i$, are zero, the static modal amplitude is given by:

$$\xi_{i_{static}} = \frac{F_i}{M_i\omega_i^2} \tag{4.2.101}$$

The total modal displacement is then given by:

$$\xi_i = \frac{F_i}{M_i\omega_i^2} - \frac{2\zeta_i\omega_i\dot{\xi}_i}{\omega_i^2} - \frac{\ddot{\xi}_i}{\omega_i^2} \tag{4.2.102}$$

or, substituting Equation 4.2.101:

$$\xi_i = \xi_{i_{static}} - \xi_{i_{dynamic}} \tag{4.2.103}$$

where:

$$\xi_{i_{dynamic}} = \frac{2\zeta_i\omega_i\dot{\xi}_i}{\omega_i^2} + \frac{\ddot{\xi}_i}{\omega_i^2} \tag{4.2.104}$$

The static shear force and bending moment, $SF(\eta)_{static}$ and $BM(\eta)_{static}$ respectively, can then be calculated using standard methods assuming the structure is rigid. The internal force terms which account for the flexible response of the structure are then given by:

$$SF(\eta)_{dynamic} = \sum_{j=\eta}^{1}\sum_{i=1}^{n} P(j)_i\xi_{i_{dynamic}} \tag{4.2.105}$$

$$BM(\eta)_{dynamic} = l\sum_{j=\eta}^{1} SF(j)_{dynamic} \tag{4.2.106}$$

A third method is the Force Summation (FS) method. This method splits the force contributions into internal, i.e. due to structural velocity and acceleration, and external, i.e. aerodynamic, loading. This is similar to the MA method. However, the FS method does not use a modal approximation in the calculation of the internal forces. The internal loading is given by:

$$P = \mathbf{M}\ddot{x} + \mathbf{C}\dot{x} \tag{4.2.107}$$
$$= \mathbf{M}\phi\ddot{\xi} + \mathbf{C}\phi\dot{\xi} \tag{4.2.108}$$

where $\mathbf{M}\phi$ and $\mathbf{C}\phi$ are the half generalised mass and damping matrices respectively. The disadvantage with the FS method is that $\mathbf{M}$ and $\mathbf{C}$ can be large and the process to calculate the internal loading is computationally expensive, and unsuitable for real-time simulation. In the simulation presented here the calculation of the internal forces is only completed as a post-processing step and so the FS method is used.

4.2.2 Fuselage

The steady aerodynamic model defines the aerodynamic forces and moments due to the fuselage, given by the component forces due to the fore- and aft-fuselage, and the nacelles using empirical estimates as a function of angle of attack and side-slip [Figure 4.18].

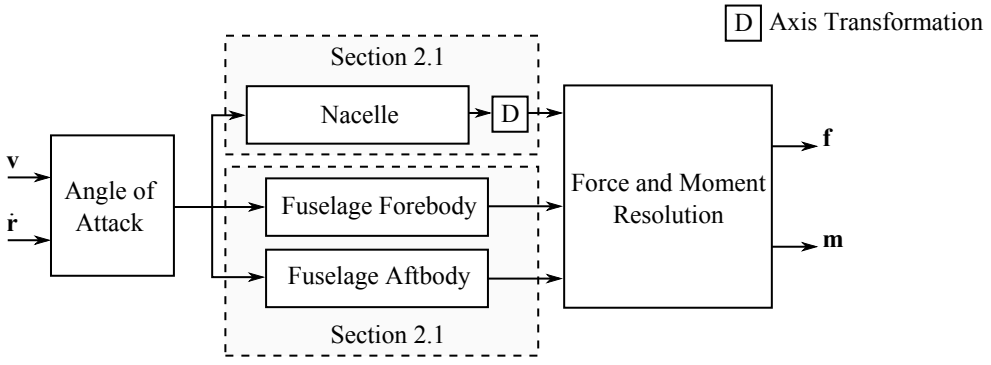

Figure 4.18: Calculation of steady aerodynamic forces acting on aircraft

The aerodynamic forces and moments due to the fuselage, $\mathbf{f}_b$ and $\mathbf{m}_b$ respectively, are estimated as the sum of the aerodynamic forces and moments due to the lift of the forebody, aftbody, and carry-over lift of the fuselage in the presence of the wing. This can be expressed as:

$$\mathbf{f}_b = \mathbf{f}_{fb} + \mathbf{f}_{ab} + \mathbf{f}_{bco} \tag{4.2.109}$$
$$\mathbf{m}_b = \mathbf{m}_{fb} + \mathbf{m}_{ab} + \mathbf{m}_{bco} \tag{4.2.110}$$

Considering the fuselage forebody firstly, the aerodynamic properties of the forebody may be estimated from empirical data and slender-body theory [ESDU 89008; ESDU 89014].

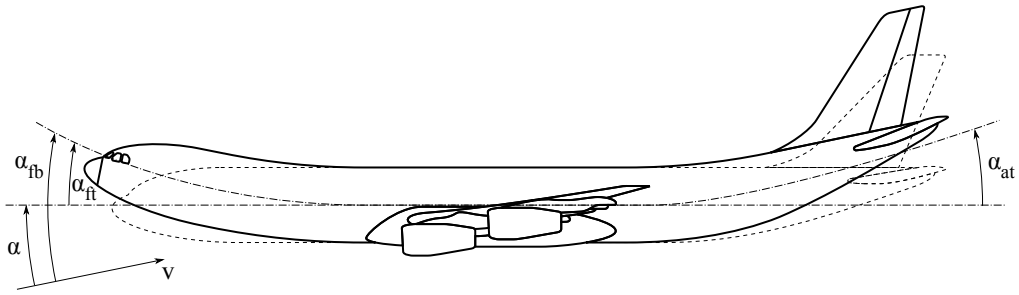

Figure 4.19: Angle of attack of the fuselage forebody and aftbody

The fuselage is approximated as an axi-symmetric body of revolution. The normal force coefficient, in body-axes, for the fuselage forebody is then given by [ESDU 89014]:

$$C_N = C_{N\alpha} \sin\alpha \cos\alpha + \frac{4}{\pi}\frac{L}{D} C_{PL} C_{Nc} \tag{4.2.111}$$

where $C_{N\alpha}$ is the normal force slope at zero angle of attack calculated using ESDU 89008. The second term represents cross-flow effects, which result as the flow breaks away from the body on the leeward side, causing symmetric vortex formation. The geometric coefficient C_{PL} is calculated in ESDU 77028, while the cross flow normal force coefficient, C_{Nc}, is given in Figure 1 of ESDU 89014 as a function of Mach number and angle of attack.

The centre of pressure is given forward of the axes origin by:

$$x_{cp} = x_0 - \frac{(C_m)_0}{C_N} D \tag{4.2.112}$$

where x_0 is the longitudinal location of the axes origin, D is the maximum diameter of the fuselage, and the pitching moment coefficient, $(C_m)_0$, is given by:

$$(C_m)_0 = (C_m)_{0\alpha} \sin\alpha \cos\alpha - \frac{2}{\pi}\left(\frac{L}{D}\right)^2 C_{PL} C_{CL} C_{Nc} \tag{4.2.113}$$

The second term again represents the result of cross-flow effects on the pitching moment. The geometric coefficient C_{CL} is again given in ESDU 77028. The full calculation of the normal force coefficient C_N and centre of pressure x_{cp} is given in Appendix A.2.1.

The angle of attack of the fuselage forebody, α_{fb}, is a function of the elastic deformation of the fuselage and the angle of attack of the rigid-body aircraft [Figure 4.19]. This is given by:

$$\alpha_{fb} = \alpha + \alpha_{ft} \tag{4.2.114}$$

The forces and moments due to the forebody in body-axes are then given by [4.20]:

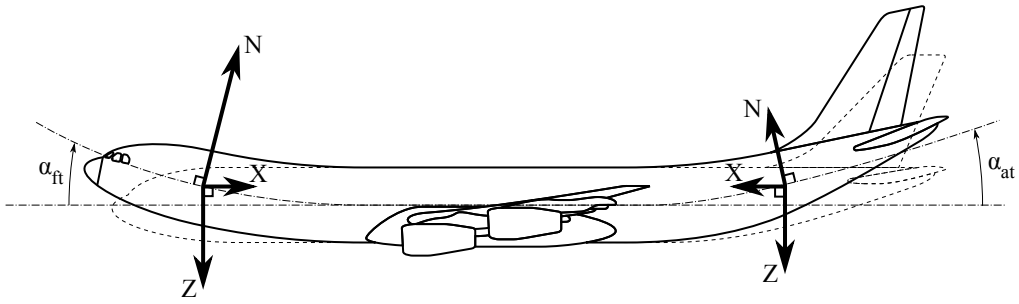

Figure 4.20: Normal force resolution for fuselage forebody and aftbody

$$\mathbf{f}_{fb} = qS_b \begin{bmatrix} 0 \\ 0 \\ -C_N \end{bmatrix} \tag{4.2.115}$$

$$\mathbf{m}_{fb} = qS_b \begin{bmatrix} 0 \\ -C_N x_{cp} \\ 0 \end{bmatrix} \tag{4.2.116}$$

$$\tag{4.2.117}$$

where S_b is the reference area for the fuselage, given by the maximum cross sectional area $\pi D^2/4$.

The aerodynamic properties of the aftbody of the fuselage may also be estimated from empirical data and slender-body theory [ESDU 87033]. The fuselage is again approximated as an axi-symmetric body of revolution, and the change in normal force due to the aftbody shape is given by [ESDU 87033]:

$$\Delta C_N = \Delta C_{N\alpha} \sin\alpha \cos\alpha \left(1 - \sin^{0.6}\alpha\right) + \Delta C_{Dc} \sin^2\alpha \tag{4.2.118}$$

in which the first term, $\Delta C_{N\alpha}$, the inviscid contribution, is calculated using slender-body theory. The second term, ΔC_{Dc}, is the viscous cross-flow contribution. The angle of attack for the fuselage aftbody is similarly given by:

$$\alpha_{fb} = \alpha - \alpha_{at} \tag{4.2.119}$$

The centre of pressure for the change in normal force due to the aftbody is approximated by:

$$x'_{cp} = x_0 - 0.5 l_a \tag{4.2.120}$$

where l_a is the length of the aftbody boat-tail. The full calculation of the normal force coefficient ΔC_N and centre of pressure x'_{cp} is given in Appendix A.2.2.

The forces and moments due to the fuselage aftbody about the axes origin are then given by:

$$\mathbf{f}_{fb} = qS_b \begin{bmatrix} 0 \\ 0 \\ -\Delta C_N \end{bmatrix} \tag{4.2.121}$$

$$\mathbf{m}_{fb} = qS_b \begin{bmatrix} 0 \\ -\Delta C_N x'_{cp} \\ 0 \end{bmatrix} \tag{4.2.122}$$

$$\tag{4.2.123}$$

The profile drag of the fuselage may also be estimated, assuming the fuselage is again modelled as an axi-symmetric body of revolution [ESDU 78019]. The profile drag coefficient for the fuselage is given by [ESDU 78019]:

$$C_D = \left\{ \frac{C_V^{2/3}}{2\left(2\pi L/D\right)^{1/3} C_S} \right\} C_D^* \tag{4.2.124}$$

where C_D^* is the body profile drag coefficient based on $(volume)^{2/3}$. The geometric coefficients C_V and C_S are given by the following equations respectively, and can be calculated using ESDU 77028:

$$C_V = \frac{4V}{\pi D^2 L} \tag{4.2.125}$$

$$C_S = \frac{S}{\pi D L} \tag{4.2.126}$$

The full calculation of the profile drag coefficient C_D is given in Appendix A.2.3. The forces acting on the aircraft, assuming the profile drag acts axially about the axis origin, are then given by:

$$\mathbf{f}_b = qS_b \begin{bmatrix} C_D \\ 0 \\ 0 \end{bmatrix} \tag{4.2.127}$$

Finally, the carry-over lift of the body, which is a function of the lift on the wing and tailplane, is described in Section 4.2.1.7.

4.2.3 Nacelle

The lift-curve slope of the engine nacelle, and thereby the aerodynamic forces and moments generated, may also be estimated. The nacelle is essentially modelled as an annular aerofoil with a correction made for the upwash due to the wing [ESDU 77012]. The lift is assumed to act at the nacelle lip [ESDU 77012].

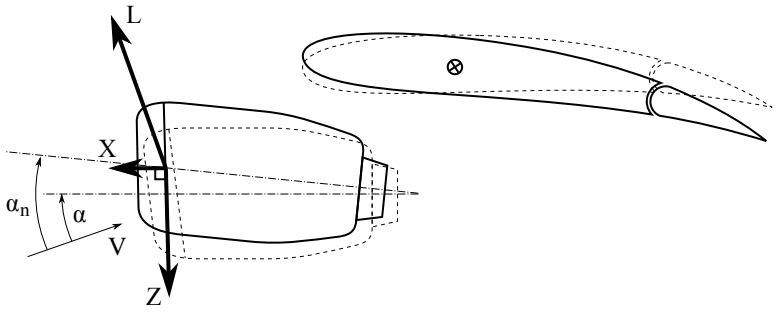

Figure 4.21: Normal force resolution for fuselage forebody and aftbody

The lift curve slope of the nacelle, a_n, is given in Figure 1 of ESDU 77012 as a function of the ratio of the width to the length of the nacelle, w/l. The lift-curve slope of the nacelle, $(a_n)_w$, in the influence of the upwash of the wing is then given by:

$$(a_n)_w = a_n \left(1 + \frac{r' (a_1)_w c}{4\pi R^2}\right) \tag{4.2.128}$$

The lift curve slope of the wing, $(a_1)_w$, can be estimated using ESDU 70011, with the equivalent straight-tapered wing again approximated using ESDU 76003, and the geometric dimensions r', R^2 are given in Figure A.20 of Appendix A.4. The full calculation of the nacelle lift-curve slope is given in Appendix A.4.

The lift of the nacelle is then given by:

$$L_n = qwl\,(a_n)_w\,\alpha_n \tag{4.2.129}$$

where α_n is the angle of attack of the nacelle, including the elastic deformation of the structure [Figure 4.21]. The side-force generated by the nacelle due to side-slip angle β_n is similarly calculated for the lift-curve slope a_n.

The forces and moments due to the nacelle, in body axes, about the axes origin can then be expressed as:

$$\mathbf{f}_n = -\,qlw \begin{bmatrix} +\cos(\alpha_n) & 0 & +\sin(\alpha_n) \\ 0 & +1 & 0 \\ -\sin(\alpha_n) & 0 & +\cos(\alpha_n) \end{bmatrix} \begin{bmatrix} 0 \\ a_n\beta_n \\ (a_n)_w\,\alpha_n \end{bmatrix} \tag{4.2.130}$$

$$\mathbf{m}_n = \mathbf{r} \times -qlw \begin{bmatrix} +\cos(\alpha_n) & 0 & +\sin(\alpha_n) \\ 0 & +1 & 0 \\ -\sin(\alpha_n) & 0 & +\cos(\alpha_n) \end{bmatrix} \begin{bmatrix} 0 \\ a_n\beta_n \\ (a_n)_w\,\alpha_n \end{bmatrix} \tag{4.2.131}$$

4.3 Propulsive

The dynamics of each engine are represented by a first-order system:

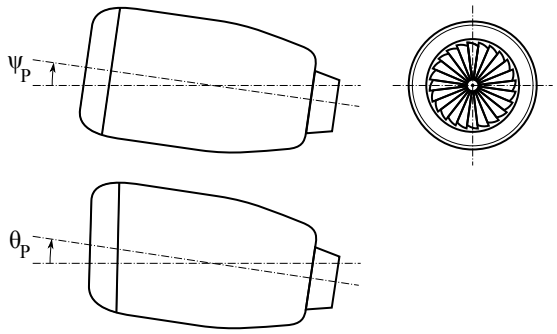

Figure 4.22: Engine installation setting geometry

$$\frac{T_P}{T_{P_\tau}} = \frac{T_{P_{max}}}{1 + \tau_P s} \tag{4.3.1}$$

where $T_{P_{max}}$ and τ_P are the maximum thrust and engine time constant respectively, and in which T_{P_τ} is the throttle setting position. The maximum thrust and engine time constant are assumed to vary with altitude, airspeed, and temperature. This is implemented in the "Turbofan Engine System" model in the MATLAB/Simulink Aerospace Blockset [MathWorks Inc., 2009].

Assuming the thrust of the engine, T_p, acts along the x-axis of the engine-axes system, the total engine forces in body-axes are then given by:

$$\mathbf{f}_P = D_P^B \begin{bmatrix} T_P \\ 0 \\ 0 \end{bmatrix} \tag{4.3.2}$$

where the direction cosine matrix, D_P^B, which defines the transformation from engine- to body-axes is given by:

$$D_P^B = \begin{bmatrix} \cos\theta_P \cos\psi_P & -\sin\phi_P & \cos\phi_P \sin\theta_P \\ \cos\theta_P \sin\phi_P & \cos\phi_P & \sin\phi_P \sin\theta_P \\ -\sin\theta_P & 0 & \cos\theta_P \end{bmatrix} \tag{4.3.3}$$

in which the engine setting angles θ_P and ψ_P are shown in Figure 4.22.

The total engine moment about the axes origin for an engine at point $\mathbf{r}$ is then given by:

$$\mathbf{m}_P = \mathbf{r} \times \mathbf{f}_P \tag{4.3.4}$$

4.4 Gravitational

The gravitational force acting on the body due to the mass of the aircraft, m, and gravitational acceleration, g, is assumed to act vertically downwards in earth-axes. Expressed in body-axes, the forces acting on the aircraft are then given by:

$$\mathbf{f}_g = D_I^B \begin{bmatrix} 0 \\ 0 \\ mg \end{bmatrix} \tag{4.4.1}$$

where D_I^B is the direction cosine matrix defined in Equation 3.3.4.

The gravitational forces and moments acting on structural node i are calculated by multiplying the nodal structural mass matrix $\mathbf{M_i}$, by the acceleration vector $\mathbf{a}$:

$$\mathbf{f}_{g_i} = \mathbf{M_i} D_I^B \mathbf{a} \tag{4.4.2}$$

where $\mathbf{a}$ is given by:

$$\mathbf{a} = \begin{bmatrix} 0 & 0 & g & 0 & 0 & 0 \end{bmatrix}^T \tag{4.4.3}$$

4.5 Atmospheric

4.5.1 Atmospheric Model

The principle aerodynamic properties of the earth's atmosphere, i.e. pressure, temperature and density, vary with altitude. Anon. [1955] provides an atmospheric model for the estimation of these parameters at any altitude. The Anon. [1955] model divides the atmosphere into several layers, each with a linear temperature distribution.

Let us assume that the aircraft operates only in the first layer, the troposphere, which extends to an altitude of 36,080ft. The temperature at an altitude h is then given by [Anon., 1955]:

$$T = T_0 - Lh \tag{4.5.1}$$

where the lapse rate L is given in Table 4.2.

Assuming the air obeys the perfect gas law, the speed of sound at altitude h is then given by:

$$a = \sqrt{\gamma RT} \tag{4.5.2}$$

Anon. [1955] then expresses the pressure and density respectively by:

$$P = P_0 \left(\frac{T}{T_0} \right)^{5.2561} \tag{4.5.3}$$

$$\rho = \rho_0 \left(\frac{T}{T_0} \right)^{4.2561} \tag{4.5.4}$$

Finally, the dynamic viscosity is given by [Anon., 1955]:

$$\mu = \mu_0 \left(\frac{T}{T_0}\right)^{3/2} \left(\frac{T_0 + S}{T + S}\right) \tag{4.5.5}$$

Parameter	Notation	Value
Temperature (sea-level)	T_0	288.16 K
Density (sea-level)	ρ_0	1.225 kgm^{-3}
Pressure (sea-level)	P_0	101,325 Pa
Viscosity (sea-level)	μ_0	1.793 $\times 10^{-5}$ Pas
Lapse rate (troposphere)	L	0.006500
Sutherland's constant	S	120
Gas constant	R	287.1 $Jkg^{-1}K^{-1}$
Adiabatic index	γ	1.400

Table 4.2: Standard atmospheric parameters [Anon., 1955]

4.5.2 Turbulence

The air through which the aircraft flies is however not at rest; this can be attributed to a phenomenon known as turbulence. Turbulence can result when large bodies of air collide at high altitudes, known as *clear air turbulence*, or be the result of weather storms, and can cause abrupt and dramatic changes in velocity. As the velocity of the air, the gust velocity, changes, it alters the effective angle of attack of the aircraft, generating large aerodynamic loads on the airframe which excite the rigid- and flexible-body dynamics of the aircraft.

The gust velocity, $\mathbf{v}_{d_E} = \begin{bmatrix} u_d & v_d & w_d \end{bmatrix}'$, is defined in earth-axes. Expressed in body-axes, the gust velocity is given by:

$$\mathbf{v}_{d_B} = D_I^B \mathbf{v}_{d_E} \tag{4.5.6}$$

where D_I^B is the direction cosine matrix defined in Section 4.2.1.1.

4.5.2.1 Discrete Tuned Gust and Continuous Turbulence

Two common techniques for simulating the gust velocity are the discrete tuned gust and continuous turbulence methods.

A discrete gust is represented by a 1 - Cosine function, defined by the gust length, l_d and the maximum gust velocity w_{d_0} [Figure 4.23]. It is given by the expression:

$$w_d = \frac{w_{d_0}}{2} \left(1 - \cos \frac{2\pi x_d}{l_d}\right) \tag{4.5.7}$$

where x_d is the penetration of the aircraft into the gust field, and for which $0 \leq x_d \geq l_d$. It is clear that the nose and tail of the aircraft will encounter the gust field at different times, and the gust penetration distance x_d should be calculated separately for each position of interest on the aircraft.

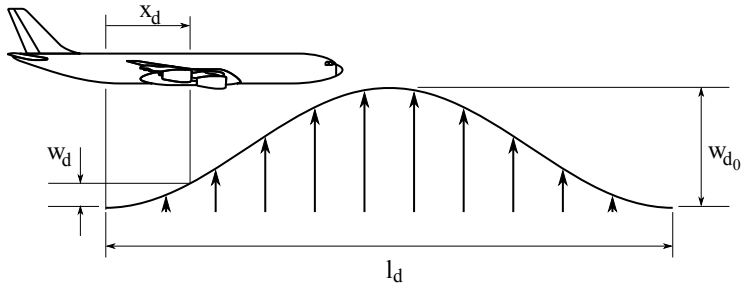

Figure 4.23: Aircraft penetration into a discrete tuned gust field

While the gust velocity of the discrete tuned gust is deterministically known, continuous turbulence is a stochastic process. The gust velocity of the continuous turbulence is assumed to be represented by a power spectral density function which matches experimental atmospheric data. One commonly used velocity spectrum is the Von Karman representation [Anon., 1990]. A time-domain velocity signal with the correct gust characteristics can be generated by passing a random signal through a suitable filter. For example, the transfer function for the vertical gust velocity is given by [Anon., 1990]:

$$H_{d_w} = \frac{\sigma_{d_w}\sqrt{\frac{1}{\pi}\frac{2l_{d_w}}{|\mathbf{v}|}}\left(0.3398\left(\frac{2l_{d_w}}{|\mathbf{v}|}\right)^2 s^2 + 2.7478\frac{2l_{d_w}}{|\mathbf{v}|}s + 1\right)}{0.1539\left(\frac{2l_{d_w}}{|\mathbf{v}|}\right)^3 s^3 + 1.9754\left(\frac{2l_{d_w}}{|\mathbf{v}|}\right)^2 s^2 + 2.9958\frac{2l_{d_w}}{|\mathbf{v}|}s + 1} \tag{4.5.8}$$

where σ_{d_w} is the turbulence intensity and l_{d_w} the turbulence length scale. Similar expressions are defined for lateral, H_{d_v}, and longitudinal, H_{d_u}, continuous turbulence velocities [Anon., 1990].

4.5.2.2 Indicial Unsteady Aerodynamics

The aerodynamic response of a two-dimensional aerofoil entering a gust can be approximated by an indicial function. This takes a similar form to the indicial approximation for an aerofoil experiencing changes in angle of attack and heave obtained by Wagner [Wagner, 1925]. The Kussner function, $\psi(s)$, developed by Kussner [1936], represents the non-dimensional lift development due to a sharp-edged gust. It may be plotted as a function of semi-chords travelled [Figure 4.24], increasing from 0 at $t = 0$ to 1 at $t = \infty$. It is often approximated as an exponential function, such as:

$$\psi s = 1 - 0.5e^{-0.130s} - 0.5e^{-s} \tag{4.5.9}$$

Like the Wagner function however, the Kussner function is only applicable to incompressible flow. Leishman [1996] more recently proposed an exponential approximation as a function of Mach number in compressible flow:

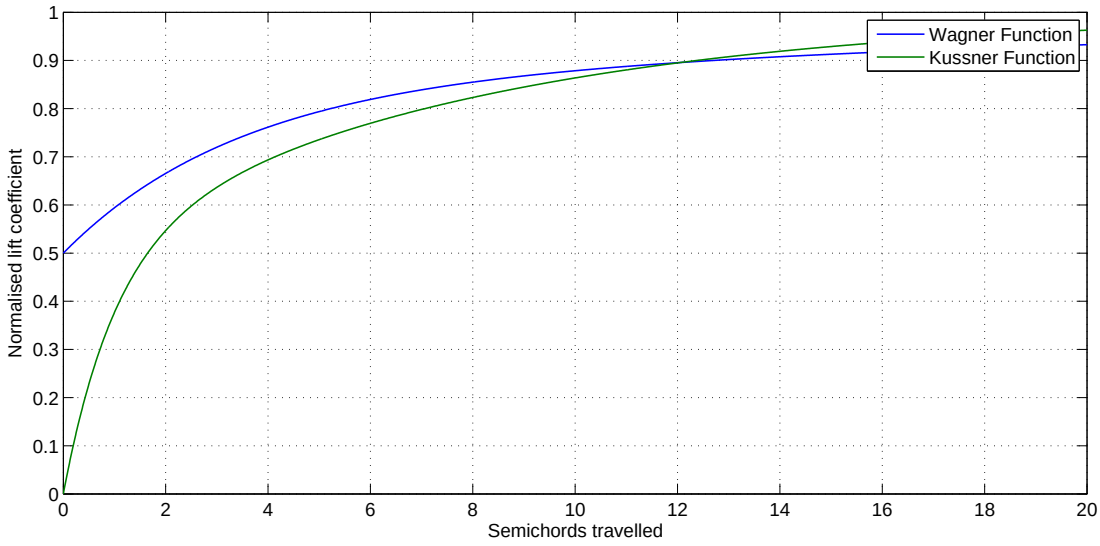

Figure 4.24: Wagner and Kussner function for aerofoil indicial lift response

$$\psi s = 1 - G_1 e^{-\beta^2 g_1 s} - G_2 e^{-\beta^2 g_2 s} \tag{4.5.10}$$

where the coefficients G_1, G_2, g_1, and g_2 were calculated to be equal to 0.527, 0.473, 0.100, and 1.367 respectively.

In order to facilitate integration into a simulation model, Leishman [1996] developed this indicial approximation in state-space form:

$$C_N^g = \frac{a}{\beta} \left[\begin{array}{cc} g_1 g_2 \beta^4 (2V/c)^2 & (G_1 g_1 + G_2 g_2)\beta^2 (2V/c)^2 \end{array} \right] \tag{4.5.11}$$

$$\left[\begin{array}{c} \dot{z}_1 \\ \dot{z}_2 \end{array} \right] = \left[\begin{array}{cc} 0 & 1 \\ -g_1 g_2 \beta^4 (2V/c)^2 & -(g_1 + g_2)\beta^2 (2V/c)^2 \end{array} \right] + \left[\begin{array}{c} 0 \\ 1 \end{array} \right] \alpha_g \tag{4.5.12}$$

The angle of attack due to gust, α_g, is then given in body-axis by:

$$\alpha_g = \tan^{-1}\left(\frac{W + w_d}{U + u_d}\right) - \tan^{-1}\left(\frac{W}{U}\right) \tag{4.5.13}$$

CHAPTER 5

Numerical Simulation of a Flexible Aeroplane

This chapter describes the example numerical simulation, validation and verification of a flexible large civil transport aircraft, the Aeroplane AX-1, in the MATLAB/Simulink [MathWorks Inc., 2009] environment.

5.1 Introduction

A numerical example, based around a fictional, generic large aeroplane, is detailed in order to simulate and analyse the effects of structural flexibility and unsteady aerodynamics on the handling qualities of aircraft. The generic aeroplane type model, referred to as the Aeroplane AX-1[1] for convenience, is closely representative of the large, four-engined, long-range, wide-body civil transport aircraft in operation today with many airlines around the world [Figure 5.1].

Figure 5.1: Drawing of Aeroplane AX-1

The Aeroplane AX-1 seats up to 316 passengers in a two-class configuration, or 295 passengers in a three-class configuration [Table 5.1]. The AX-1 has a range of 13,700km,

[1]The identity of the aircraft modelled, its specification and airframe mass and structural stiffness properties remain confidential, and are withheld here from publication.

and cruises at Mach 0.82 at 36,000 ft. The AX-1 is powered by four high-bypass turbofan engines, with each engines producing 151.2 kN of thrust at sea-level [Jackson, 2006]. The Flight Control System (FCS) of the AX-1 is representative of the digital fly-by-wire flight control system found on any modern, civil transport aircraft. The FCS controls two independent outboard ailerons, a trimmable tailplane and independent port and starboard elevators in the pitch-axis, and a single rudder in yaw-axis. Pilot control is achieved using a central yoke controller and rudder pedals, and the FCS includes a number of protections, including stall, over-speed and manoeuvre protection [Jackson, 2006].

Performance specification	
Seating capacity	295 (3-class)
Cargo capacity	19.7m^3
Maximum range	13,700km
Cruising speed	Mach 0.820
Operational empty weight	130,200kg
Maximum take-off weight	276,500kg
Service ceiling	41,100ft

Table 5.1: Aeroplane AX-1 performance parameters [Jackson, 2006]

5.2 Aerodynamic Model

5.2.1 Aerodynamic Data

The aerodynamic forces and moments generated by the aircraft are estimated as the sum of the forces and moments generated by each individual airframe component. The major airframe components are: wing, tailplane, and fin; fuselage; and nacelles. The geometry of the Aeroplane AX-1 is shown in Appendix D. The aerodynamic data for the aircraft model has been estimated across a limited flight envelope [Table 5.2]. This data is presented in tabular and graphical form as a function of Mach number, Reynolds number and angle of attack in Appendix A.

	Range	
Envelope	Minimum	Maximum
Altitude, ft	0.000	30,000
Mach number	0.050	0.800
Angle of Attack, deg	-10.0°	$+15.0^\circ$

Table 5.2: Aerodynamic model data flight envelope

The wing, tailplane, and fin are modelled using the same indicial unsteady aerodynamic strip theory model described in Section 4.2. The geometric properties of these components are detailed in Table 5.3. The two-dimensional aerodynamic characteristics for each aerodynamic station, including the lift- and pitching-moment curve slopes and profile drag coefficient, are calculated in Appendix A.3.

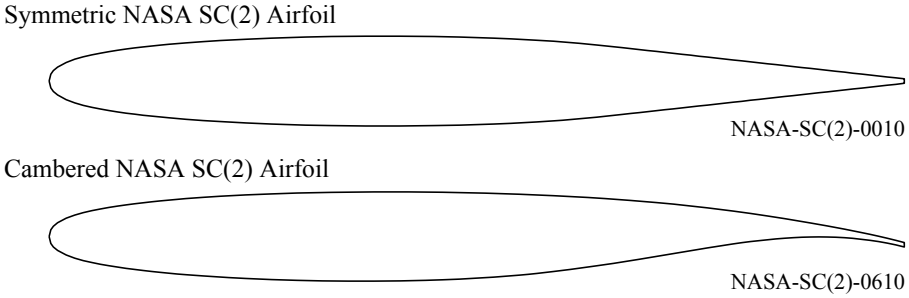

Figure 5.2: NASA SC(2) symmetric and cambered aerofoil series [Harris, 1990]

The two-dimensional aerofoil section is assumed to be a supercritical aerofoil profile typical of those designed for use in the transonic flow conditions experienced during cruise. The aerofoil section profile of the wing was derived for several thickness-to-chord ratios from the NASA SC(2) series cambered aerofoil profiles [Harris, 1990]. The aerofoil section of the tailplane and fin is assumed to have a symmetric profile and is derived from the same NASA SC(2) series [Figure 5.2]. The thickness-to-chord distribution for the wing is given in Table A.14 of Appendix A. The tailplane and fin are assumed to have a uniform spanwise thickness-to-chord ratio of 8%.

Component	Dimension	Value
Wing	Area, m^2	363.1
	Aspect ratio	9.260
	Taper ratio	0.2900
	Quarter-chord sweep, deg	30.00
	Mean aerodynamic chord, m	7.279
Tail	Area, m^2	71.45
	Aspect ratio	5.270
	Taper ratio	0.3780
	Quarter-chord sweep, deg	30.00
	Mean aerodynamic chord, m	3.932
Fin	Area, m^2	45.20
	Aspect ratio	1.524
	Taper ratio	0.3970
	Quarter-chord sweep, deg	40.00
	Mean aerodynamic chord, m	5.788

Table 5.3: Wing, tailplane and fin geometric properties

The three-dimensional lift distribution of the wing, tailplane, and fin is estimated using a modified strip theory [Section 4.2.1.4]. The number of aerodynamic stations in the modified strip theory model influences the accuracy of the resulting lift distribution estimate. Increasing the number of stations increases the accuracy of the estimate of the lift distribution, but also increases the order of the complete unsteady aerodynamic state-space model. To assess the influence of the number of stations on the estimated lift distribution, the number of stations was increased from 7, the value suggested by DeYoung and Harper [1948], to 301, a value nominally equal to the result given for an

infinitely large number of stations [Figure 5.3]. It was found that a value between 21 and 35 stations provided an estimate for the lift distribution within 0.8468% and 0.2877% respectively of the distribution given by 301 stations, while remaining small enough that the order of unsteady aerodynamic state-space model remains relatively low. The wing was thus modelled using 35 stations, while the tailplane and fin are modelled using 21 stations.

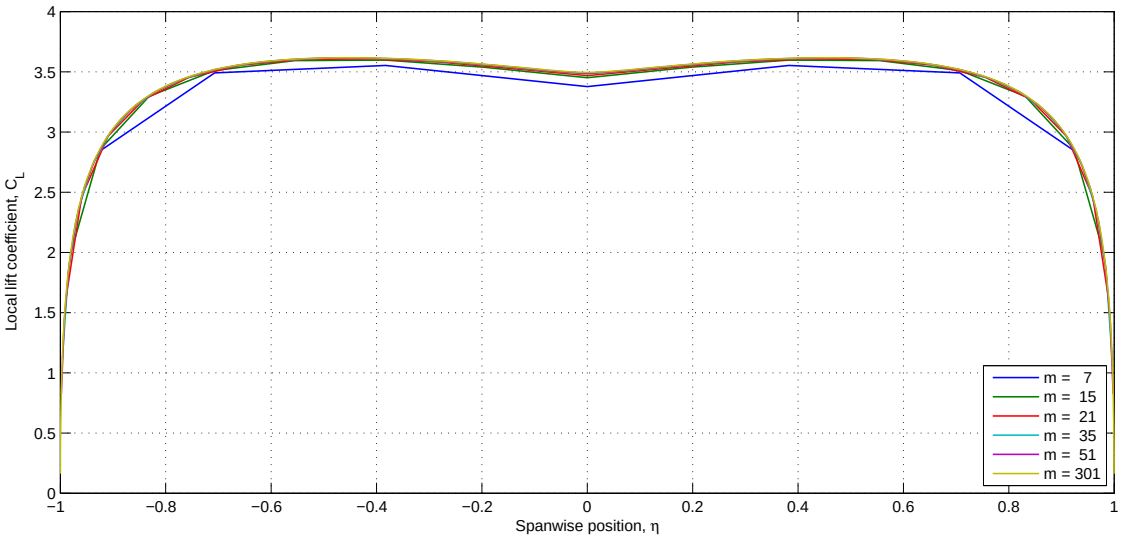

Figure 5.3: Variation of local lift distribution estimate with strip theory stations

The aerodynamic forces and moments generated by the fuselage and nacelles due to lift and drag are estimated from empirical data using a number of ESDU data items [Appendices A.2 and A.4]. The geometric properties of the Aeroplane AX-1 fuselage and nacelle are given in Tables A.3 and A.20 of Appendix A respectively. The fuselage of the AX-1 may be modelled as an axi-symmetric body of revolution, while the four engine nacelles of the AX-1 are modelled as an annular aerofoil.

5.2.2 Validation and Verification

The aerodynamic model of the wing, tailplane and fin is derived in large part from the work of Leishman and Nguyen [1990], Leishman [1994], Hariharan and Leishman [1996], Weissinger [1947], and DeYoung and Harper [1948]. The implementation of these indicial aerodynamic and modified strip theory models respectively is described in detail in Section 4. The MATLAB/Simulink implementation of this model [Appendix C] has been verified against results given by Leishman [1994] and DeYoung and Harper [1948]. It can be assumed therefore that the model here is a true and accurate representation of the original model, and may be assumed to be valid within those bounds defined by each author respectively. The aerodynamic model of the fuselage and nacelles is similarly derived from a number of separate ESDU data items [Section 4]. This model again has been verified against the data given in those data items, and may be assumed to valid within the bounds defined in each item respectively.

In order assess the validity, both qualitatively and quantitatively, of the complete aerodynamic model of the aircraft, the aerodynamic derivatives were extracted from the non-

linear rigid-aircraft model at a number of flight points. This was achieved by trimming the aircraft model at each flight point in turn, and perturbing the aerodynamic model by a small perturbation in each of the linear and angular velocity inputs (1 m s^{-1} and 1 deg s^{-1} respectively). Each of the 36 longitudinal and lateral-directional aerodynamic derivatives, referred to body-axis, was then calculated by dividing the resulting change in force or moment in each of the degrees of freedom by the initial perturbation. The derivatives were then expressed in the standard aero-normalised form [Cook, 1997], and converted into wind-axis for comparison with empirical estimates. The complete set of normalised aerodynamic derivatives for a single flight point (120 m s^{-1} and 3,000 ft) are shown in Table 5.4. There are additionally several linear acceleration derivatives which are a function of the vertical acceleration $\dot{W}$. These terms primarily estimate the influence of the tailplane downwash lag of the pitch response. It is not possible to extract these derivatives from the non-linear model using the method described above, and therefore these derivatives are not considered here. That is not to underestimate the importance of these derivatives, however the effects of the time-dependent downwash field are modelled here as a wholly unsteady aerodynamic effect.

	Perturbation					
Derivative	U	V	W	p	q	r
X	**−0.04330**	+0.001104	**+0.1310**	+0.001256	**+0.07829**	−0.0008658
Y	+0.000	**−0.2827**	+0.000	**−0.1041**	−0.0009958	**+0.1131**
Z	**−0.8695**	−0.003604	**−5.089**	+0.0002766	**−2.891**	−0.02189
L	+0.000	**−0.1097**	+0.000	**−0.2538**	−0.003090	**+0.08146**
M	**−0.2261**	+0.0002671	**−2.468**	+0.0003770	**−12.36**	−0.005705
N	−0.001129	**+0.03821**	+0.000	**+0.009450**	+0.0003178	**−0.07496**

Table 5.4: Aircraft longitudinal and lateral-directional aerodynamic derivatives at 120 m s^{-1} and 3,000 ft

It can firstly be seen that the aircraft exhibits the expected classical decoupling of the longitudinal and lateral-directional aerodynamics. The cross-coupling derivatives, for example Z_p and L_W, are all either zero or negligibly small. The remaining decoupled longitudinal and lateral-directional derivatives are shown in bold in Table 5.4. The total derivatives were compared with empirical estimates for the entire aircraft estimated using the following ESDU data items: ESDU 86021, ESDU 85010, ESDU 84002, ESDU 82011, and ESDU 81032. The aerodynamic derivatives, in wind-axis, estimated using these ESDU data items are given in Table 5.5. All of the derivatives extracted from the non-linear model match the ESDU estimates in both sign and magnitude, and many of the derivatives, for example L_p, M_q and Z_U, are within 15% of the ESDU estimates.

While the total value of each of the aerodynamic derivatives closely matches the value estimated using the ESDU data items, it is also important to validate the individual contribution towards the total derivative from each of the aircraft components. Figure 5.4 shows the contribution of the fin, fuselage, wing, tail, fin and nacelles to the total aerodynamic derivative value for the 18 decoupled longitudinal and lateral-directional derivatives. A second flight point, at 180 m s^{-1} and 9,000 ft, is also shown. A number of empirical and analytical methods may be used to estimate the value of each of the aerodynamic derivatives [Etkin, 1959; Hancock, 1995; Cook, 1997]. While the accuracy

	Perturbation					
Derivative	U	V	W	p	q	r
X	−0.02746	—	+0.2840	—	+0.000	—
Y	—	−0.7416	—	−0.01780	—	+0.1560
Z	−0.9853	—	−6.051	—	−4.275	—
L	—	−0.1374	—	−0.2231	—	+0.06718
M	+0.000	—	−3.468	—	−13.24	—
N	—	+0.1035	—	−0.002125	—	−0.1010

Table 5.5: ESDU-approximated longitudinal and lateral-directional aerodynamic derivatives at 120 m s^{-1} and 3,000 ft

of these methods is typically low, it provides a useful method to assess the contribution of each airframe component to the total derivative value. The derivative components shown in Figure 5.4 match both quantitatively and qualitatively the results from these simple empirical estimates. For example, the derivative L_p is dominated by the rolling moment generated by the wing due to the antisymmetric velocity distribution over the wing surface. This results in an antisymmetric variation in lift and drag generated by the port and starboard wings, and this generates a restoring rolling moment [Cook, 1997]. The fuselage, fin and tail also make small contributions to the value of this derivative. The correct breakdown of this aerodynamic derivative is reflected in Figure 5.4.

The aerodynamic properties of the aeroplane are a function of airspeed, or Mach number, and as such the aerodynamic derivatives will change with airspeed. The derivatives are to a lesser extent also a function of Reynolds number, which varies with airspeed and altitude. Figure 5.4 shows the aerodynamic derivatives for two flight points, at 120 m s^{-1} and 3,000 ft, and 180 m s^{-1} and 9,000 ft. In subsonic flight, the effects of compressibility are conveniently approximated by the Prandtl-Glauert correction factor β. Let us consider the derivative Z_W, which may be approximated as the sum of the drag coefficient and the lift-curve slope of the aircraft [ESDU 86021, 2003]. If we scale the total Z_W derivative for the first flight point, −5.090, by the corresponding value of β, the result, −5.670, is a close match for the value extracted from the non-linear model, −5.570. This trend is repeated for the remaining aerodynamic derivatives, and the results similarly show a close match at this, and other, flight points with the ESDU data item approximations.

A number of different approximations were made by the ESDU data items and by the model presented here for the calculation of the aerodynamic derivatives, however the results from both models predict the same sign and magnitude for all of the derivatives, and the majority of the derivatives are within 30% for the two methods. The breakdown of the individual airframe contributions for each derivative also matches empirical and analytical methods. The value of the aerodynamic derivatives extracted from the model also vary as a function of Mach number as predicted by the Prandtl-Glauert correction factor. The aerodynamic model is therefore judged to be qualitatively and quantitatively valid.

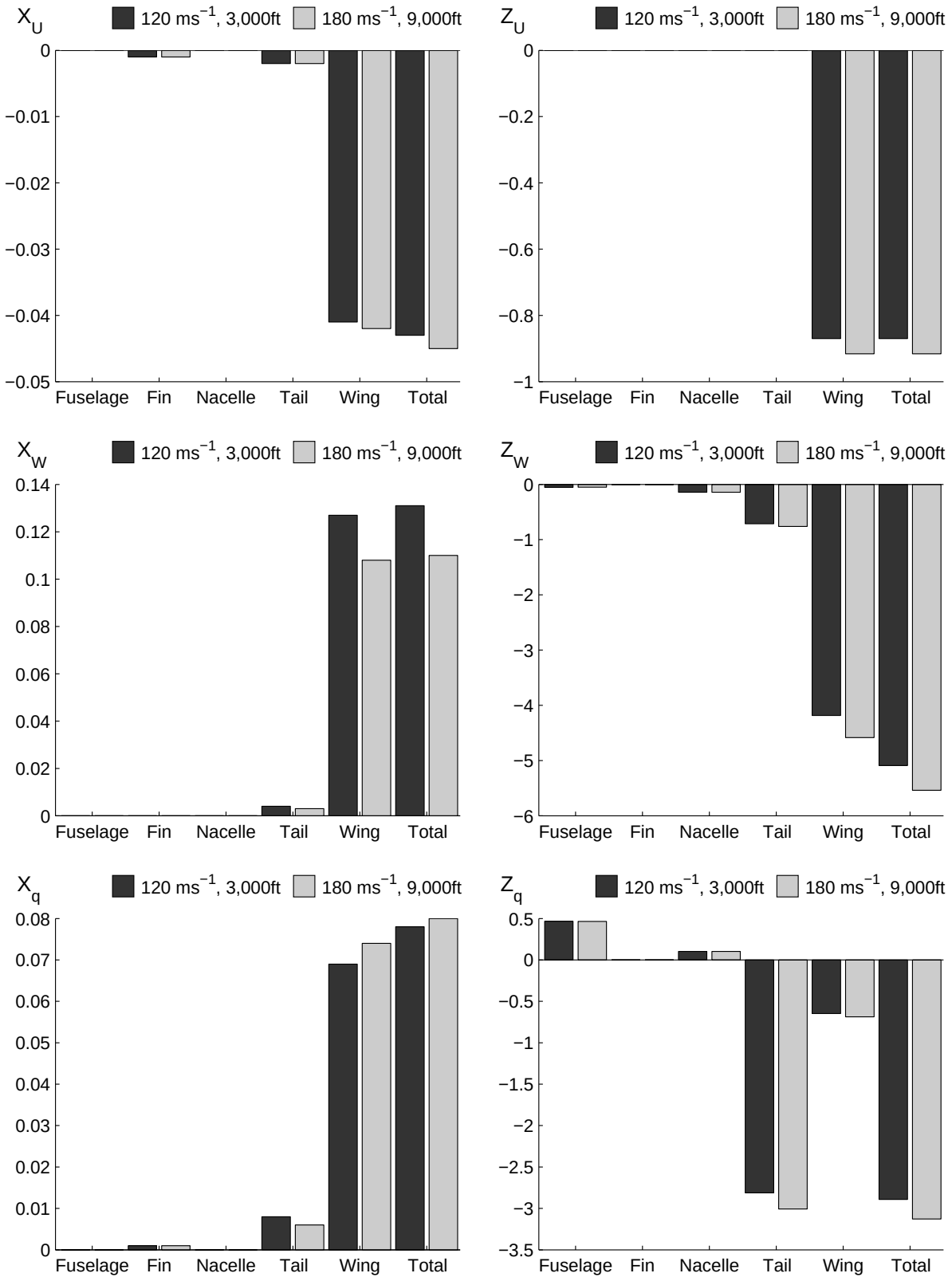

Figure 5.4: Aircraft longitudinal and lateral-directional aerodynamic derivatives

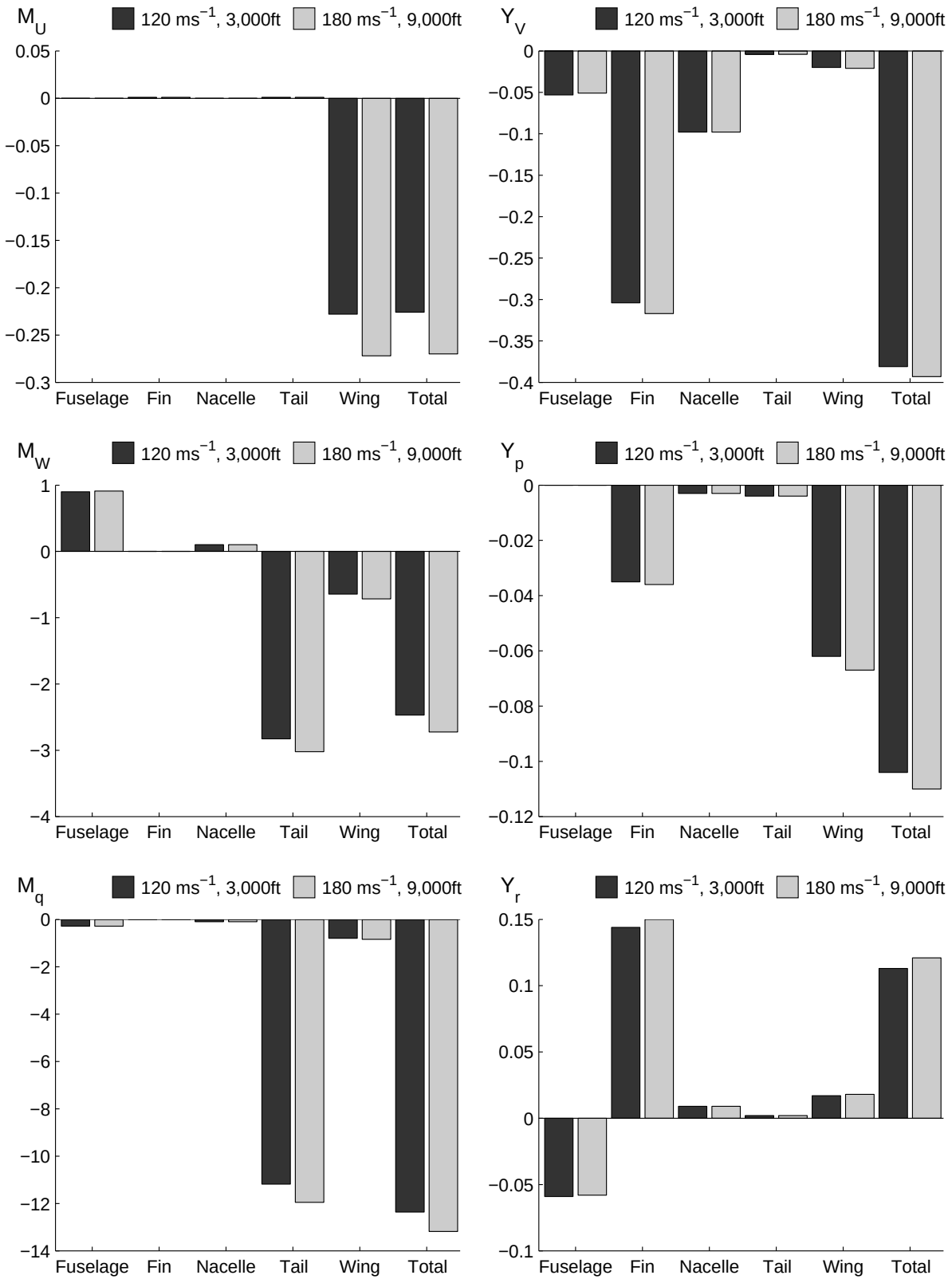

Figure 5.4: Aircraft longitudinal and lateral-directional aerodynamic derivatives (continued)

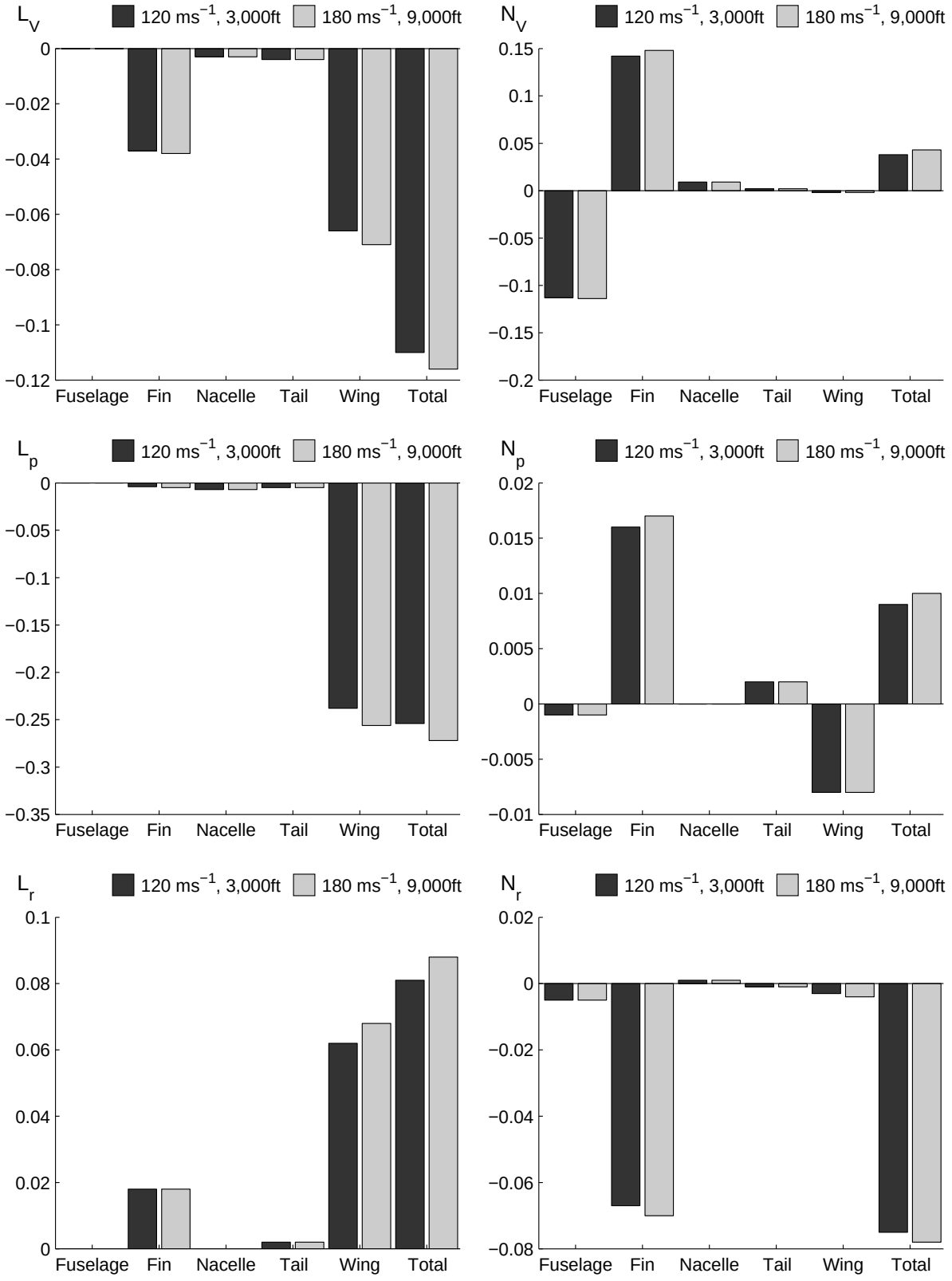

Figure 5.4: Aircraft longitudinal and lateral-directional aerodynamic derivatives (continued)

5.3 Structural Model

5.3.1 Mass and Stiffness

The airframe structure is approximated as a beam element model [Section 3.4.1]. The structural model is composed of 39 beam-elements connecting 40 nodes [Figure 5.5]. Each node is free to move in all six degrees of freedom. Each beam-element is defined in terms of its bending stiffness in two degrees of freedom, $EI_{(.)}$, torsional stiffness, GJ, and axial extension stiffness, EA. The bending and torsional stiffness of the beam is assumed to vary linearly along the length of the beam [Berry, 1989]. It is assumed that any deformation of the elastic structure is small in comparison with the overall size of the body, and thus the deformation can be described by a set of linear equations. Shear deformation of each beam-element is assumed to be small and is neglected. In order to isolate the rigid-body motion, and produce a set of free-free normal modes, the structural model is "grounded" using three low-stiffness "spring" beams [Figure 5.5]. The complete description of the structural model is provided in Appendix B.

The mass properties of each node are defined in terms of its total mass, M, mass moment, $M_{(.)}$, and inertia, $I_{(..)}$. Figure 5.6 shows the Operational Weight Empty (OWE) mass distribution of the airframe. The complete mass model, described in Appendix B, defines the additional mass of the passengers, cargo and fuel and its distribution. It is assumed that the elastic deformation of the airframe is small, and thus the rigid-body inertia tensor is constant and calculated only from the mass distribution of the undeformed structure. Figures 5.7 and 5.8 show the mass model for light and heavy fuel-load configurations respectively.

The construction of the mass and stiffness matrices was performed using BEMMODES [Berry, 1989].

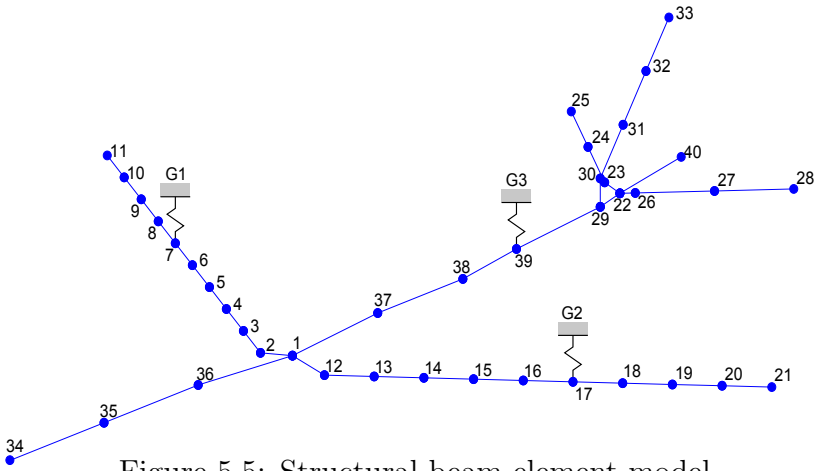

Figure 5.5: Structural beam-element model

5.3.2 Modal Analysis

Eigen-analysis of the the mass and stiffness matrices yields a set of normal modes characteristic of the structure [Section 3.4.2]. The stiffness of the three "spring" beams was set at 1×10^6, and the eigen-analysis results give the first six rigid-body modes at a frequency of 0.001 rad s^{-1}. Two models were considered in addition to the OWE mass cases,

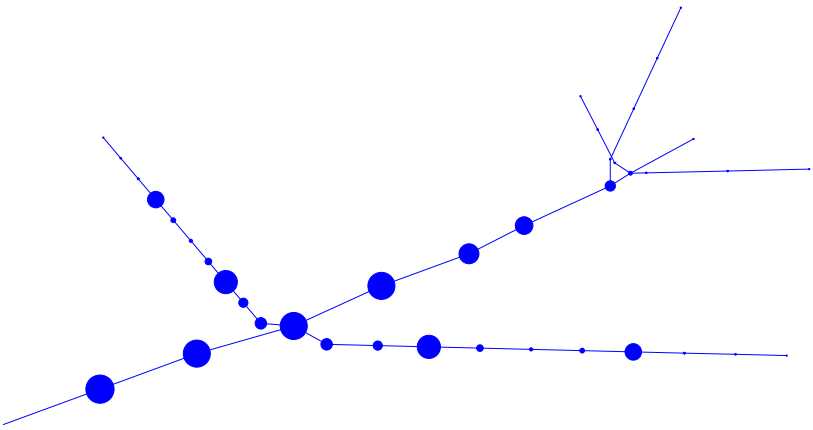

Component	Mass, kg
Airframe (OWE)	131,000
Fuel	0.000
Passengers	0.000
Cargo	0.000
Total	131,000

Centre of Gravity: -5.16m

Figure 5.6: Structural mass model - Operational Weight Empty configuration

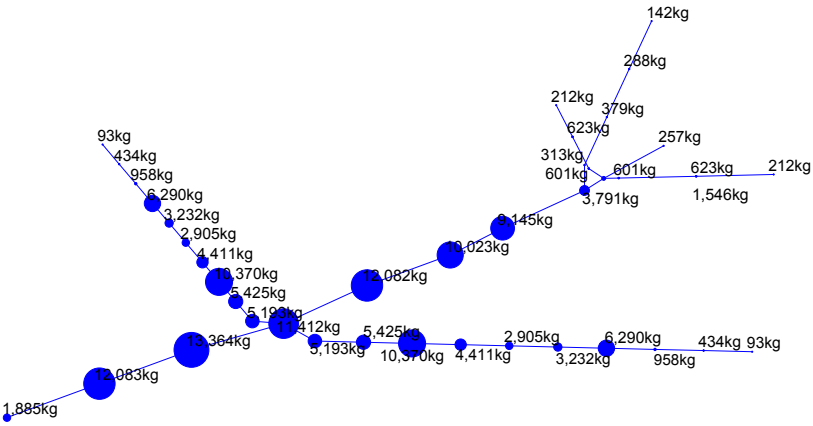

Component	Mass, kg
Airframe (OWE)	131,000
Fuel	22,000
Passengers	4,930
Cargo	9,480
Total	168,000

Centre of Gravity: -5.43m

Figure 5.7: Structural mass model - light, low fuel load configuration

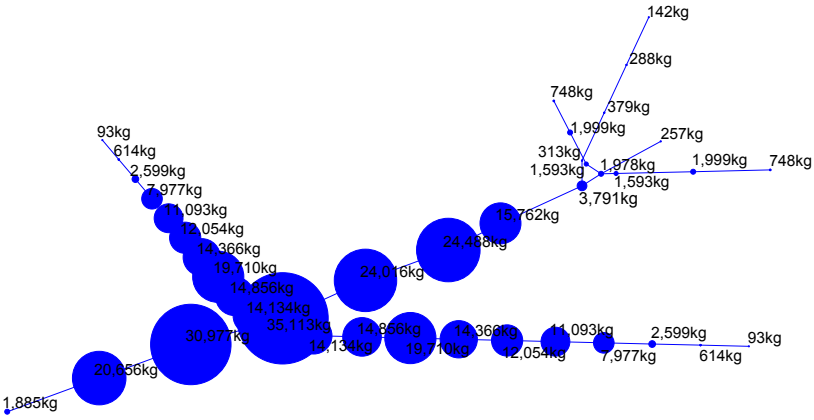

Component	Mass, kg
Airframe (OWE)	131,000
Fuel	79,200
Passengers	19,600
Cargo	22,200
Total	252,000

Centre of Gravity: -5.44m

Figure 5.8: Structural mass model - heavy, full fuel load configuration

a heavy, full fuel-load configuration typical of Maximum Take-Off Weight (MTOW), as well as light, low fuel-load configuration typical of Maximum Landing Weight (MLW). Table 5.6 shows the comparable natural frequencies of the structural modes for the three configurations considered, and it can be seen that the natural frequencies are reduced with increasing mass. The total mode set was truncated at 12 modes. This provides a realistic compromise between calculation cost and model fidelity. This mode set includes the first and second wing-bending and -torsion modes, fuselage and fin bending modes. Figure 5.9 shows the first four normal mode shapes for the OWE case, while the remaining mode shapes for this and the other mass cases can be found in Appendix B.

	Frequency, rad s^{-1}		
Mode	OWE	Light	Heavy
1	7.958	7.296	6.135
2	7.958	7.296	6.135
3	8.698	8.024	6.803
4	14.89	13.69	11.46
5	16.82	16.45	15.45
6	16.82	16.45	15.45
7	16.92	15.81	13.34
8	17.25	16.53	14.51
9	20.44	18.72	14.87
10	21.43	19.52	15.46
11	21.43	19.52	15.46
12	21.51	19.14	15.84

Table 5.6: Structure normal mode frequencies for OWE, light and heavy mass cases

5.3.3 Validation

The modes for the OWE mass case were compared to Ground Vibration Test (GVT) data and modes estimated from a higher-fidelity model[2]. The OWE model modes show a close correlation to the GVT data, with the natural frequency of the first wing bending mode matching the GVT data to within 2.0%. Higher modes, including wing fore/aft bending and fuselage lateral bending, match the GVT data within 15.0% [Table 5.7].

Mode	Frequency, Hz	Error, %
Wing bending	1.268	2.052
Rear fuselage bending	2.370	11.79
Wing fore/aft bending	3.412	4.784
Fuselage bending	3.424	5.493
Fuselage lateral bending	3.795	9.678

Table 5.7: Percentage error between OWE modal frequencies and GVT data

[2]The structural stiffness properties of the aircraft modelled remain confidential, and are withheld here from publication.

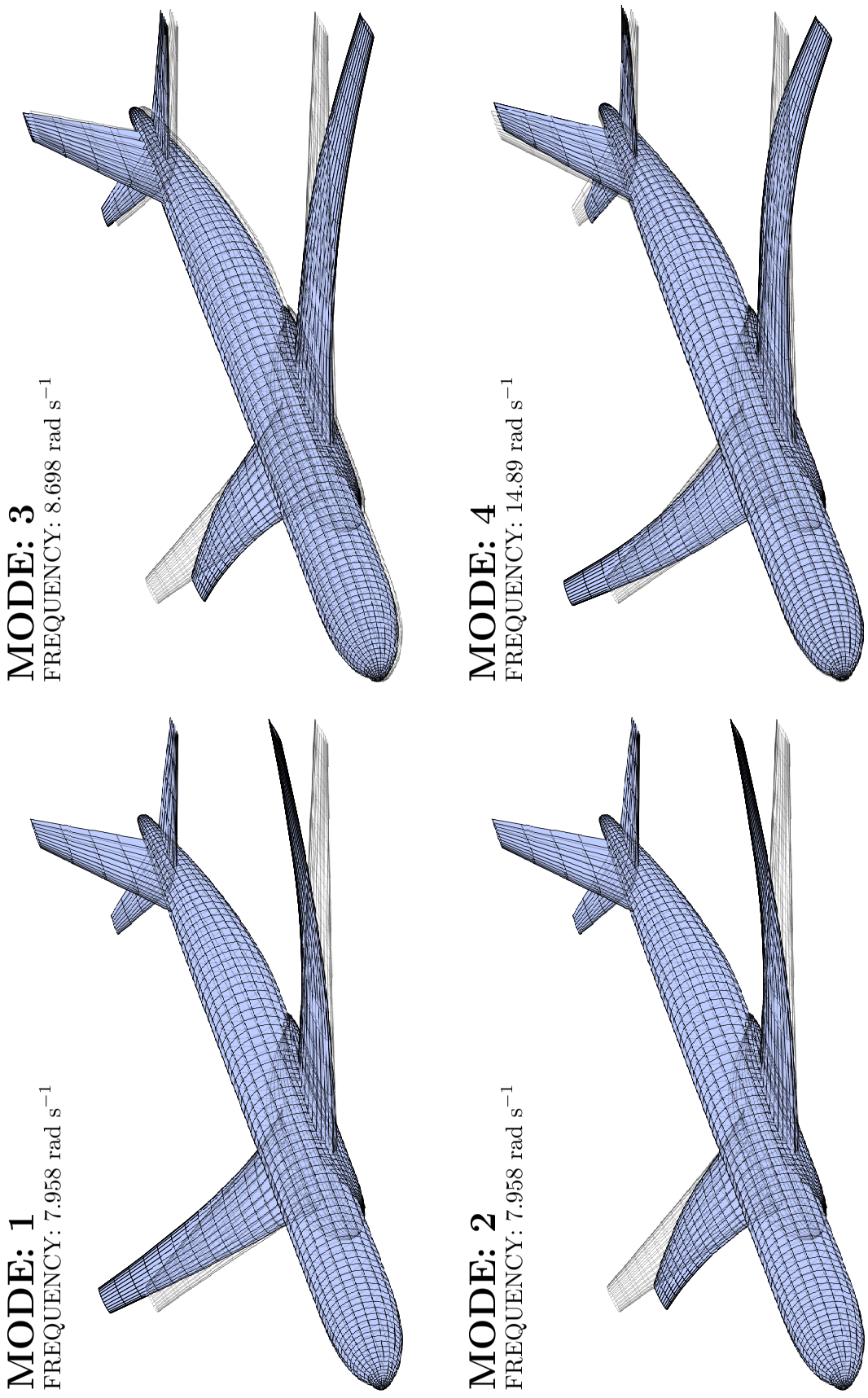

Figure 5.9: Airframe structure normal modes 1 through 4 for OWE mass case

5.4 MATLAB/Simulink

An implementation of the aeroelastic flexible aircraft model has been developed in MATLAB/Simulink [Figure 5.10][3]. The aircraft model itself is implemented in Simulink, incorporating a number of user-defined functions, as well as existing blocks from the standard Simulink and Aerospace Blockset libraries. This is capable of real-time simulation, and therefore suitable for pilot-in-the-loop simulation. A number of real-time visualisation tools are provided within the program, including a real-time beam element flexible aircraft animation. Initialisation and post-processing MATLAB scripts and functions are included for trim and linearisation of the model, as well the calculation of the structural internal forces. The model is described in detail in Appendix C.

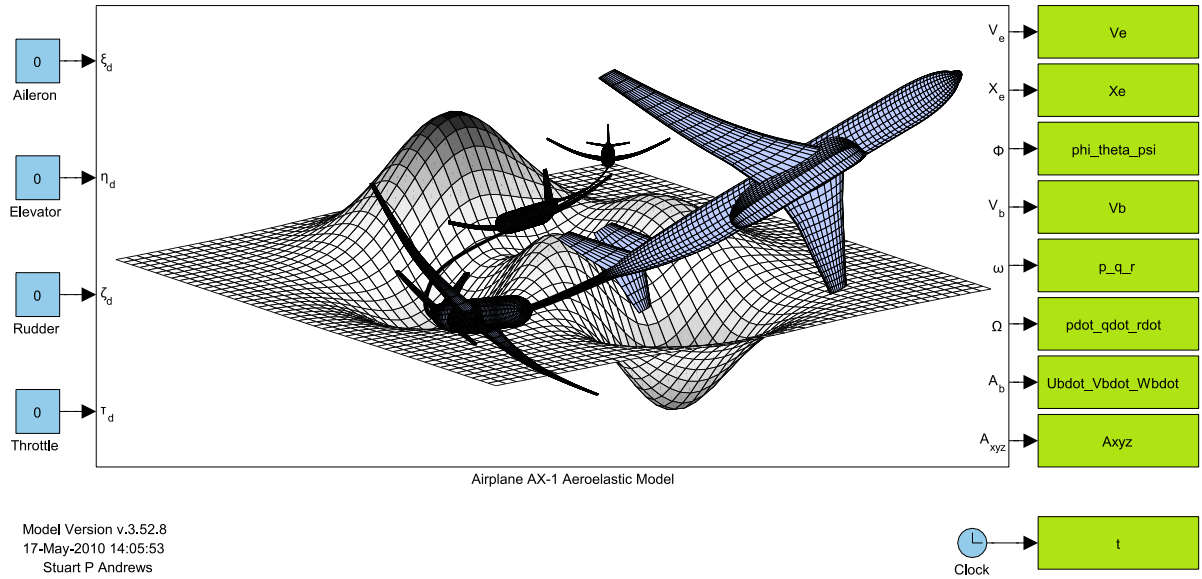

Figure 5.10: MATLAB/Simulink Aeroelastic Aircraft Model

[3]A copy of the MATLAB/Simulink model is available on request from Dr. A.K. Cooke, Senior Lecturer, Cranfield University, MK43 0AL, UK. Telephone: +44 (0)1234 750111 x5307, Email: a.cooke@cranfield.ac.uk

CHAPTER 6

Dynamic and Stability Characteristics

This chapter discusses the impact of structural dynamics and unsteady aerodynamics on the open-loop dynamic and stability characteristics of the aeroplane. A Control and Stability Augmentation (CSAS) and Load Alleviation Function (LAF) are designed as part of the flexible aircraft FCS. The impact of unsteady aerodynamics on the closed-loop aircraft is then discussed.

6.1 Assessment of Aeroplane Characteristics

In order to illustrate and assess both the dynamics and stability of the rigid-body aircraft, and the impact of structural dynamics and unsteady aerodynamics on these characteristics, three model variants were trimmed and linearised at a number of flight points. The three model variants considered were:

- **Model A: Rigid Aeroplane**
  The model dynamics are defined by the standard rigid-body equations of motion, including actuator dynamics. The downwash at the tailplane is assumed to be defined by the steady aerodynamic model. The quasi-steady aerodynamic forces are then calculated as a function of angle of attack, α, and rate of change of angle of attack, $\dot{\alpha}$, only. Structural flexibility, either elastic or quasi-rigid, is not considered [Table 6.1].

States	Count
Rigid-body dynamics	12
Actuator dynamics	14
Total	26

Table 6.1: Model A rigid aeroplane model states

- **Model B: Aeroelastic Aeroplane, including Structural Flexibility**
  The standard rigid-body equations of motion, applying the mean-axis system approximations, describe the aeroplane rigid body dynamics. The elastic structural dynamics are described by 12 modes using the normal mode method. The downwash at the tailplane is still assumed to be defined by the steady aerodynamic model. The local angle of attack now includes structural deflections and velocities. The quasi-steady aerodynamic forces are then calculated as a function of angle of attack, α, and rate of change of angle of attack, $\dot{\alpha}$, only [Table 6.2].

States	Count
Rigid-body dynamics	12
Structural dynamics	24
Actuator dynamics	14
Total	50

Table 6.2: Model B aeroelastic aeroplane model states

- **Model C: Aeroelastic Aeroplane, including Structural Flexibility and Unsteady Aerodynamics**
  The standard rigid-body equations of motion, applying the mean-axis system approximations, describe the aeroplane rigid body dynamics. The elastic structural dynamics are described by 12 modes using the normal mode method. The unsteady downwash field at the tailplane is now described by the indicial downwash model. The local angle of attack again includes structural deflections and velocities. However, the fully unsteady aerodynamic forces are now described by the indicial aerodynamic model, again as a function of angle of attack, α, and rate of change of angle of attack, $\dot{\alpha}$ [Table 6.3].

States	Count
Rigid-body dynamics	12
Structural dynamics	24
Unsteady aerodynamics	870
Actuator dynamics	14
Total	920

Table 6.3: Model C aeroelastic aeroplane model states

The aeroplane mass case considered in this analysis is characteristic of a heavy, full fuel load configuration. The total mass of the aeroplane is 252,000kg, and the centre of gravity is located 5.435m aft of the axis origin. The "wind-off" natural frequencies of the structure are given in Table 5.6 in Section 5.3.

Each of the models was trimmed and linearised at the flight points shown in Figure 6.1. All airspeeds are given in True Airspeed (TAS). The characteristic roots of each linearised model are shown in Figures 6.2, 6.3, and 6.4 for the three models respectively. For the

sake of brevity, only the rigid-body and flexible structure poles are shown in the positive imaginary axis, and the unsteady aerodynamic poles, of which there are over 800, are not shown. The results are limited to those flight points where it was possible to calculate a level-flight trim condition.

In order to simplify trim of the model, a reduced-order version of the model was produced. This included only the rigid-body and structural states; a total of 36 states. A trim, or equilibrium point, was found for each flight point where the steady-state value for each of the state derivatives, with the exception of the aircraft position, was equal to zero. In order to calculate the trimmed states values for the full-order model, the steady-state state equation yields the solution:

$$x = -A^{-1}Bu \tag{6.1.1}$$

where x is the state vector for the full-order model assuming $\dot{x}$ is equal to zero.

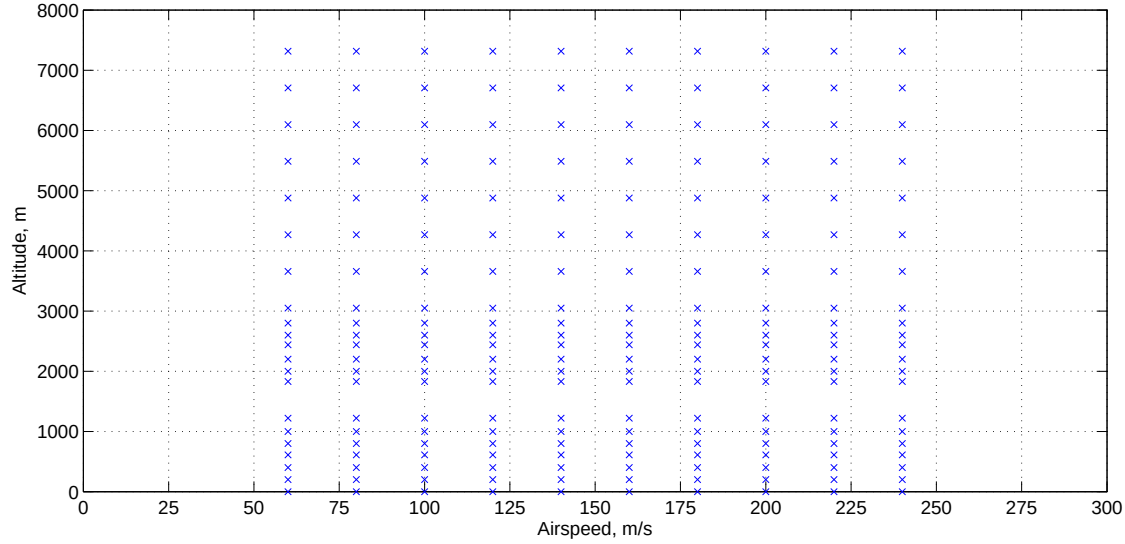

Figure 6.1: Trim and linearisation flight points

Let us consider the dynamics of Model A, the first, rigid aeroplane model [Figure 6.2]. Firstly, we can see that the aeroplane exhibits classical, second-order, longitudinal and lateral-directional dynamics, and is stable at all flight points considered. The longitudinal dynamics are characterised by the Short-Period Pitching Oscillation (SPPO) and phugoid modes. The SPPO mode varies between a frequency of 1.151 and 4.720 rad s^{-1}, with an average damping ratio of 45.02%. The slower phugoid mode varies between a frequency of 0.04520 rad s^{-1}, with damping 0.2431%, to 0.1108 rad s^{-1} and damping 8.031%. The lateral-directional dynamics are characterised by the dutch-roll, roll and spiral modes. The dutch-roll mode varies between a frequency 1.1591 rad s^{-1}, with damping ratio 21.32%, to a frequency of 0.5076 rad s^{-1} and damping 26.42%. The time constant of the non-oscillatory roll and spiral modes meanwhile vary between 0.2021 and 0.7304 seconds, and 32.72 and 98.23 seconds, respectively.

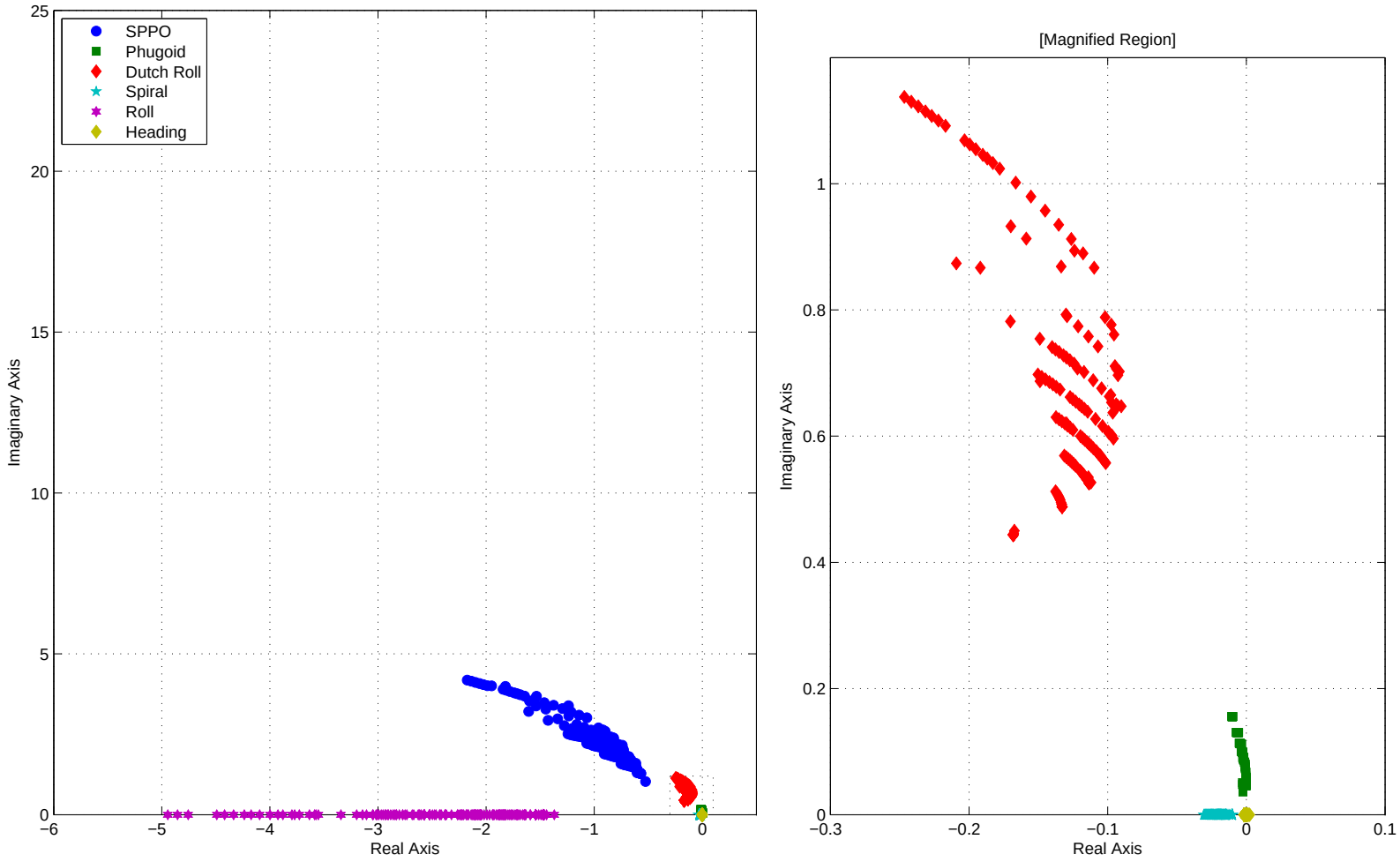

Figure 6.2: Model A aeroplane pole map, rigid aeroplane

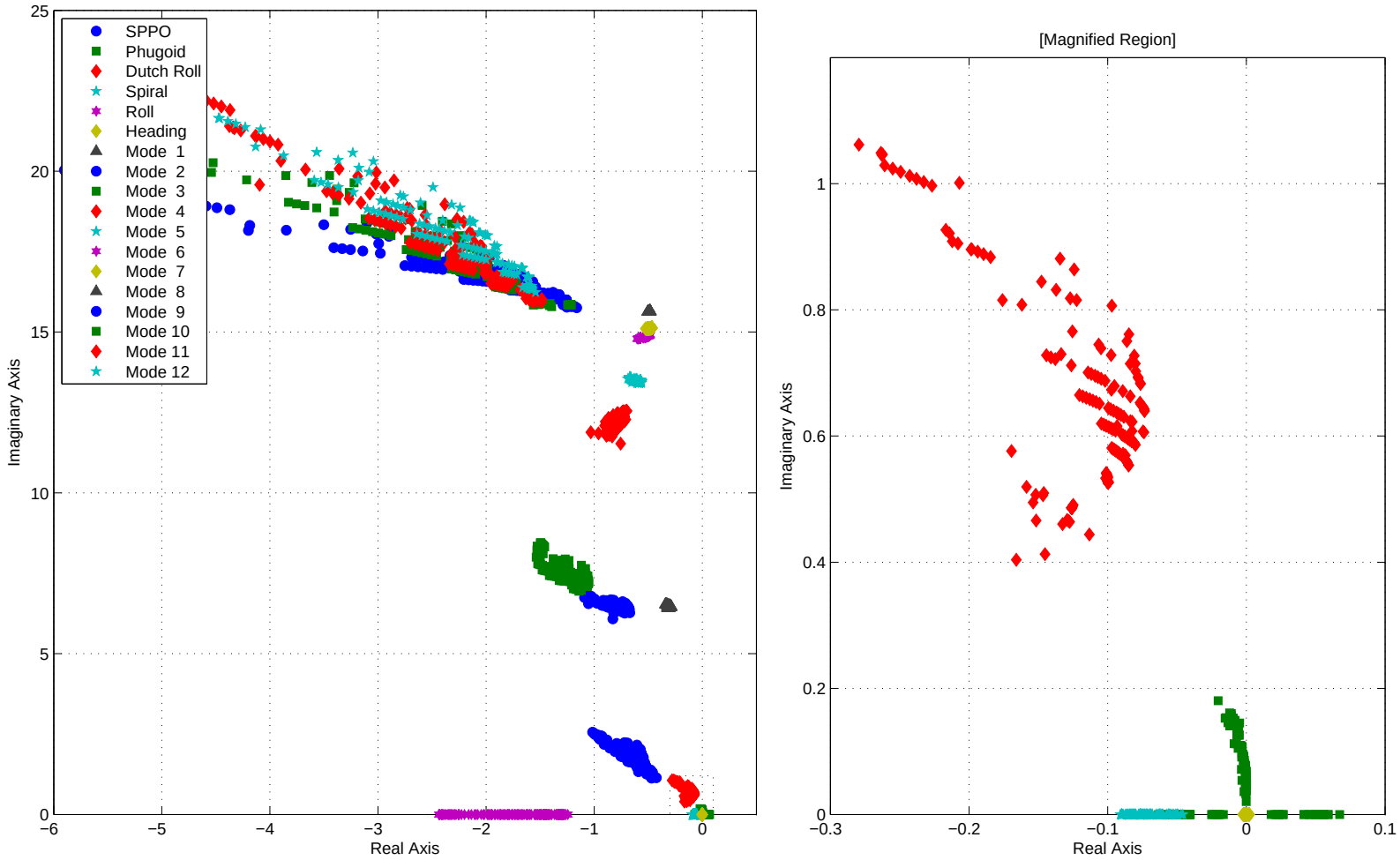

Figure 6.3: Model B aeroplane pole map, including structural flexibility

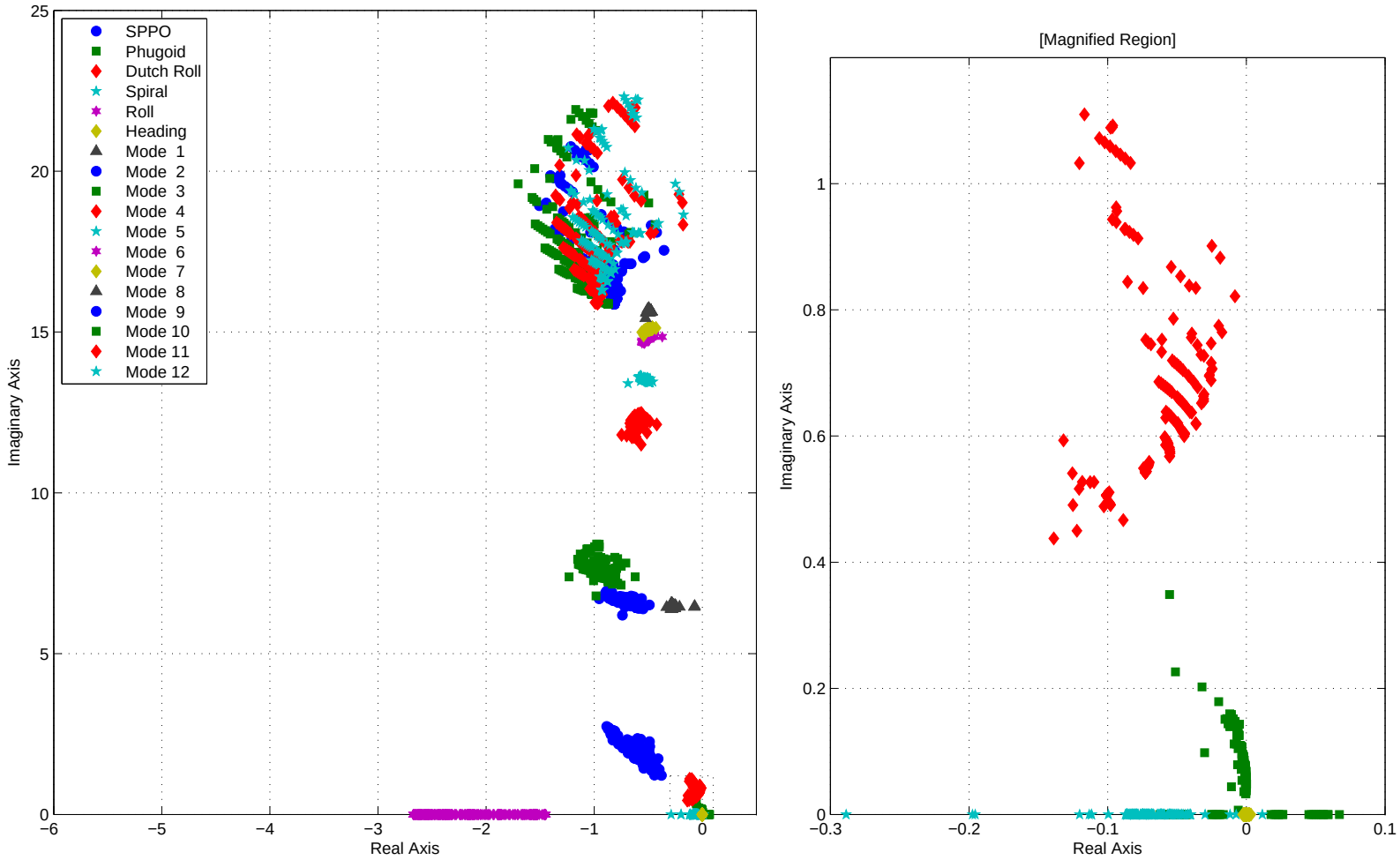

Figure 6.4: Model C aeroplane pole map, including structural flexibility and unsteady aerodynamics

The second model, Model B, includes the dynamics of the flexible structure [Figure 6.3]. We can clearly see in Figure 6.3 the addition of the 12 characteristic roots of the structural dynamics. With reference to Model A, we can see that the inclusion of structural dynamics has a large effect on the 'longitudinal and lateral stability and dynamics of the aeroplane. Table 6.4 shows the variation of the phugoid mode roots with airspeed for the flexible and rigid aircraft models at sea-level. We can see that at low speeds the effect of structural dynamics on the phugoid mode is small, however at higher speeds the frequency of the phugoid mode is reduced and ultimately splits into a pair of unstable, non-oscillatory real roots. This trend can be seen at all altitudes in Figure 6.3. The SPPO mode is also affected by inclusion of structural flexibility. The frequency of the SPPO mode is reduced considerably, together with a smaller reduction in the damping ratio [Table 6.5]. Again, it was found that this effect is more significant at higher airspeeds.

At low airspeeds, and consequently low dynamic pressures and hence aerodynamic loads, the incremental structural deformation of the aeroplane is small. As a result, the influence of structural flexibility on the rigid-body dynamics of the aeroplane is small or negligible. Conversely, at higher airspeeds structural deformation of the airframe is greater and the influence of structural flexibility is found to be significant. The effect of dynamic pressure is exhibited in the modification of the longitudinal and lateral-directional rigid-body modes due to dynamics of the flexible structure.

	Phugoid mode root	
Airspeed, m s^{-1}	Rigid	Flexible
80	-0.01020 ± 0.1556i	-0.009580 ± 0.1519i
100	-0.005920 ± 0.1302i	-0.005176 ± 0.1259i
120	-0.003692 ± 0.1119i	-0.003110 ± 0.1066i
140	-0.002566 ± 0.09820i	-0.002046 ± 0.09100i
160	-0.001914 ± 0.08699i	-0.001449 ± 0.07670i
180	-0.001138 ± 0.07942i	-0.001751 ± 0.03617i
200	-0.0008472 ± 0.06869i	± 0.02630
220	-0.0004103 ± 0.06091i	± 0.04942
240	-0.0001256 ± 0.04667i	± 0.05414

Table 6.4: Phugoid mode characteristic roots for rigid and flexible structure models at sea-level

The effect of structural flexibility can be seen to be equally significant for the lateral-directional dynamics of the aeroplane. The maximum roll-mode time constant is increased from 0.2021 to 0.4109 seconds, though unlike the longitudinal dynamics the effect is apparent at all airspeeds [Table 6.6]. While the effect of structural flexibility is to "slow" the roll mode, the opposite is the case for the spiral mode. The spiral mode time constant is decreased for all flight points by the inclusion of structural flexibility to a range between 11.23 and 20.14 seconds. Structural flexibility can be seen to have less influence on the frequency of the dutch-roll mode, however the damping ratio is reduced considerably [Table 6.7]. It can be seen for the range of altitudes given in Table 6.7 that there is an uniform average reduction in the damping ratio of 0.04801, equivalent to a 30.0% reduction in damping. The influence on the frequency of the dutch-roll mode is much

less, and it can be seen that the frequency change varies between +2.50 % at sea-level to -4.50% at 24,000ft between the rigid and flexible aircraft models.

	SPPO mode roots	
Airspeed, m s^{-1}	Rigid	Flexible
80	-0.4981 ± 1.278i	-0.4981 ± 1.278i
100	-0.6109 ± 1.453i	-0.5117 ± 1.373i
120	-0.6843 ± 1.671i	-0.5651 ± 1.549i
140	-0.7492 ± 1.883i	-0.5739 ± 1.644i
160	-0.8726 ± 2.163i	-0.6253 ± 1.802i
180	-1.008 ± 2.454i	-0.6730 ± 1.923i
200	-1.162 ± 2.805i	-0.7184 ± 2.041i
220	-1.348 ± 3.082i	-0.7631 ± 2.170i

Table 6.5: SPPO mode characteristic roots for rigid and flexible structure models at 10,000 ft

Model C, the third and final model, includes unsteady aerodynamic effects [Figure 6.4]. This includes the indicial aerodynamic model which describes the forces and moments acting on the wing, tailplane, and fin, as well as the unsteady downwash model. The effect of unsteady aerodynamics on the longitudinal and lateral-directional characteristics of the aeroplane are much less significant than the inclusion of structural dynamics. The SPPO, phugoid, spiral modes remain largely unaffected by the inclusion of unsteady aerodynamics. The roll mode is affected by the inclusion of unsteady aerodynamics, however the the effect is relatively small when compared to the influence of structural dynamics. The roll mode time constant is decreased, with a range of 0.3371 to 0.6862 seconds across the flight points considered. The dutch-roll mode however can be seen to be significantly affected by the unsteady aerodynamic effects [Table 6.7]. The average damping ratio is reduced by 0.06691, equivalent to a 45.0% reduction in damping. It can be seen in Figure 6.4 that at airspeeds above 240 m s^{-1} this mode is likely to become unstable, as the real component of the oscillatory root crosses the real axis. The change in frequency of the dutch-roll mode is again less significant, and it can be seen in Table 6.7 that the frequency change varies between 0.00% at sea-level to +6.30% at 24,000ft between the flexible aircraft and unsteady aerodynamic models.

It is not the purpose of this model to study flutter, as for piloted simulation it can quite reasonably be assumed that the aircraft will operate in normal conditions below the flutter speed at all points in the flight envelope. However, it is important to accurately predict the variation of aerodynamic damping on the structural modes. This does also provide a method for the prediction of the flutter speed with the inclusion of rigid-body motion however, and the model itself provides a convenient method for the time-domain simulation of flutter. It can be seen in Figures 6.3 and 6.4 that Models B and C, the quasi-steady and unsteady aerodynamic models respectively, differ greatly in the prediction of the structural mode aerodynamic damping terms. This difference is most significant for modes 9 through 12. Figures 6.5 and 6.6 show the predicted structural mode damping and frequency for the quasi-steady and unsteady aerodynamic models at an altitude of 200ft. It can be seen that both aerodynamic models predict an increase in structural mode frequency with airspeed. The quasi-steady aerodynamic model however also predicts a

	Roll mode roots	
Airspeed, m s^{-1}	Rigid	Flexible
80	-0.6795	-0.7774
100	-0.6493	-0.7693
120	-0.5566	-0.6895
140	-0.4728	-0.6132
160	-0.4059	-0.5607
180	-0.3513	-0.5224
200	-0.3060	-0.4439
220	-0.2634	-0.4140

Table 6.6: Roll mode characteristic roots for rigid and flexible structure models at 8,000ft

	Dutch roll mode roots		
Altitude, m	Rigid	Flexible	Unsteady Aerodynamic
0.000	-0.1373 ± 0.6301i	-0.1047 ± 0.6200i	-0.0580 ± 0.6385i
609.6	-0.1309 ± 0.6200i	-0.0993 ± 0.6142i	-0.0547 ± 0.6318i
1219	-0.1250 ± 0.6099i	-0.0944 ± 0.6085i	-0.0519 ± 0.6251i
1829	-0.1196 ± 0.6001i	-0.0900 ± 0.6029i	-0.0495 ± 0.6186i
2438	-0.1147 ± 0.5903i	-0.0861 ± 0.5972i	-0.0475 ± 0.6122i
3048	-0.1104 ± 0.5808i	-0.0828 ± 0.5916i	-0.0460 ± 0.6060i
3657	-0.1065 ± 0.5715i	-0.0799 ± 0.5861i	-0.0449 ± 0.5999i
4267	-0.1032 ± 0.5623i	-0.0824 ± 0.6079i	-0.0494 ± 0.6205i
5486	-0.1297 ± 0.6202i	-0.0807 ± 0.5882i	-0.0447 ± 0.6023i
6096	-0.1014 ± 0.5573i	-0.0809 ± 0.5890i	-0.0447 ± 0.6031i
6706	-0.1053 ± 0.5692i	-0.0809 ± -0.5891i	-0.0445 ± 0.6033i
7315	-0.1018 ± 0.5587i	-0.0814 ± -0.5903i	-0.0445 ± 0.6046i

Table 6.7: Dutch roll mode characteristic roots for rigid structure, flexible structure and unsteady aerodynamic models at 140 m s^{-1}

large increase in damping, while the unsteady aerodynamic model predicts a reduction in damping. It may be extrapolated then that the unsteady aerodynamic model predicts flutter to occur at some speed above 240 m s^{-1}.

It is the aim that the complete aeroplane model, including flexible structure and unsteady aerodynamic effects, be capable of real-time simulation. This will enable real-time pilot-in-the-loop analysis using the complete aeroelastic aircraft model. Table 6.8 shows the calculation times for the three models for a 10-second level-flight simulation in MATLAB/Simulink.[1] This simulation was performed using the complete non-linear model. It can be seen that the calculation of the structural dynamics has a low computational cost, increasing the total calculation time compared to the standard rigid aircraft model by 1.857 seconds, or 25.92%. The computational cost of the unsteady aerodynamics is higher, increasing the calculation time by 6.179 seconds, or 86.25% compared to the standard rigid aircraft model. Despite this however, the total calculation time for the full aeroelastic aircraft model is the same order of magnitude required for real-time simulation. It can be expected therefore that with optimisation that this model is quite suitable for real-time simulation.

Model	Calculation time, s
A: Rigid	7.164
B: Flexible Structure	9.021
C: Flexible Structure, Unsteady Aerodynamics	15.20

Table 6.8: Calculation time for 10-second level-flight simulation in MATLAB/Simulink

[1]Performed in 64-bit MATLAB/Simulink R2009a on a dual 3.0GHz Intel Xeon X5450 machine with 4Gb RAM running Windows Vista SP1. Simulink solver was the variable time-step `ODE23` Bogacki-Shampine solver with relative tolerance 1×10^{-3} and maximum time step of 0.01 seconds.

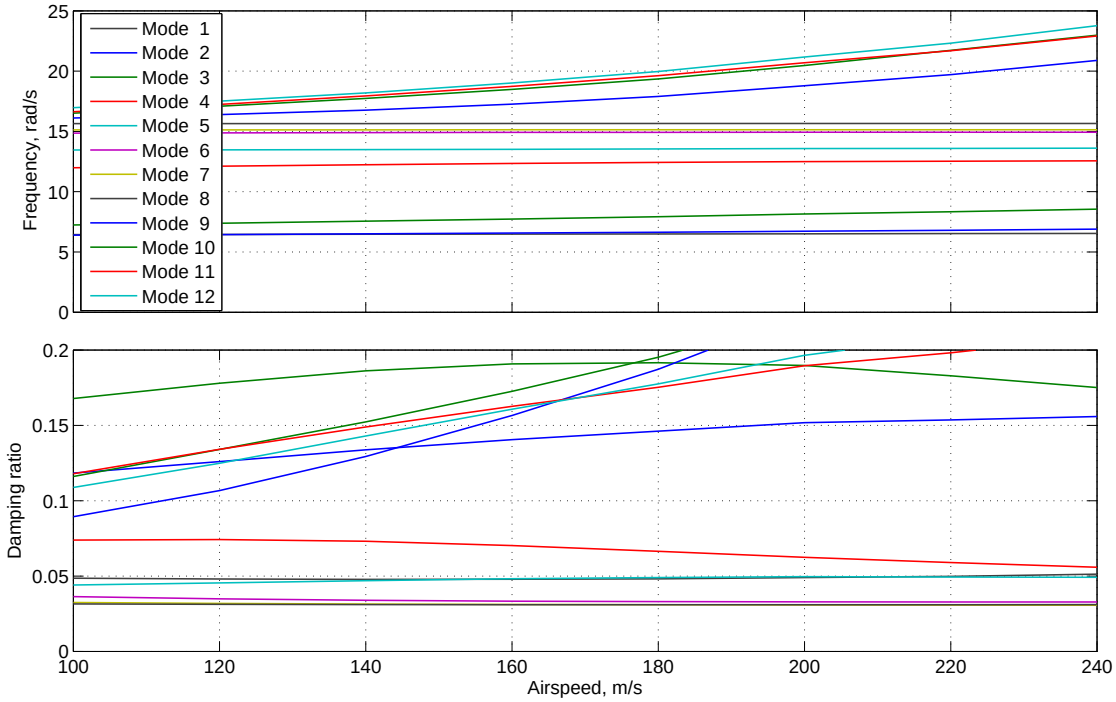

Figure 6.5: Quasi-steady aerodynamic aeroplane model structural mode damping and frequency at 200 ft

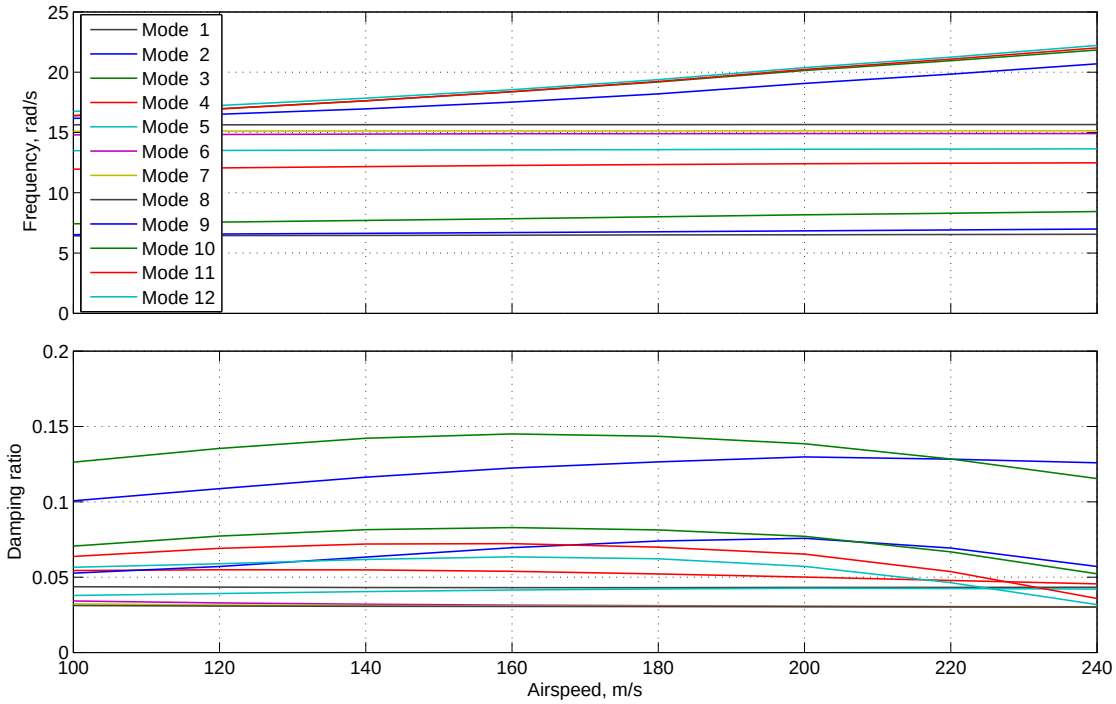

Figure 6.6: Unsteady aerodynamic aeroplane model structural mode damping and frequency at 200 ft

6.2 Flight Control System Design

6.2.1 Control and Stability Augmentation

6.2.1.1 Longitudinal

The open-loop longitudinal dynamic and stability characteristics of the Aeroplane AX-1 aeroplane model are shown in Table 6.9. Three model variants are again considered: Model A, including a rigid structure and with steady aerodynamics; Model B, including a flexible structure, and with steady aerodynamics; and finally Model C, with a flexible structure and unsteady aerodynamics. The open-loop longitudinal characteristics were calculated from the linearised system described in Section 6.1. Figure 6.7 shows a pole-zero map for the three model variants, including the unsteady aerodynamic poles which lie along the negative real-axis. Four flight points are considered, at 140 and 180 m s^{-1} and 2000 and 10,000 ft. The controller gains are calculated for the second model variant, Model B, including a flexible structure, and with steady aerodynamics, in order to meet MIL-STD-1797A [1990]. Model A and C variants are included in order to assess the robustness of the flight control system to the fidelity of the aeroplane model.

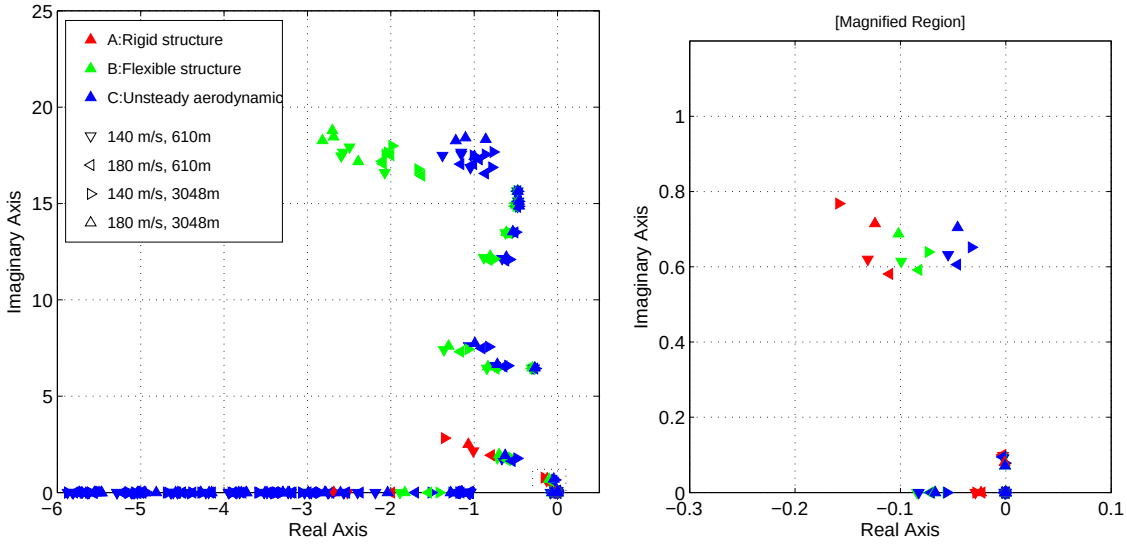

Figure 6.7: Pole-zero map for open-loop system variants

The "measured" acceleration of the aeroplane, notionally given for an Inertial Measurement Unit (IMU) located at the rigid aircraft's centre of gravity, includes both rigid-body and flexible-body accelerations. In order to isolate the rigid-body acceleration from this measured value it is necessary to filter the acceleration output of the system model. A number of different filters were considered, including both first- and second-order Butterworth, Chebyshev Type I and Elliptic filters [Figure 6.8]. The filter should provide a reduction in magnitude above the SPPO frequency with minimal phase lag. A first-order Butterworth filter, with a cut-off frequency of 5.000 rad s^{-1}, was implemented for all three axes as this provided the smallest phase lag of the filters considered and avoids any complications of resonance with the Chebyshev and Elliptic filters.

		Flight Point							
		2000 ft				10000 ft			
		140 m s^{-1}		180 m s^{-1}		140 m s^{-1}		180 m s^{-1}	
Mode	Model Variant	Frequency, rad s^{-1}	Damping	Frequency, rad s^{-1}	Damping	Frequency, rad s^{-1}	Damping	Frequency, rad s^{-1}	Damping
SPPO	A: Rigid Structure	2.380	0.4249	3.130	0.4321	2.090	0.3810	2.730	0.3932
	B: Flexible Structure	1.940	0.3732	1.890	0.2922	1.780	0.3391	2.090	0.3361
	C: Unsteady Aerodynamics	1.880	0.3551	1.840	0.2639	1.730	0.3168	2.030	0.3100
Phugoid	A: Rigid Structure	0.09821	0.02622	0.07860	0.01346	0.09981	0.03143	0.08051	0.01342
	B: Flexible Structure	0.09179	0.02309	0.07781	0.01172	0.09480	0.02839	0.07113	0.008608
	C: Unsteady Aerodynamics	0.09179	0.02518	0.07781	0.01310	0.09480	0.03032	0.07113	0.01023

Table 6.9: Open-loop aeroplane longitudinal characteristics

		Flight Point							
		2000 ft				10000 ft			
		140 m s^{-1}		180 m s^{-1}		140 m s^{-1}		180 m s^{-1}	
Mode	Model Variant	Frequency, rad s^{-1}	Damping	Frequency, rad s^{-1}	Damping	Frequency, rad s^{-1}	Damping	Frequency, rad s^{-1}	Damping
SPPO	A: Rigid Structure	3.750	0.7351	4.290	0.7582	3.190	0.7249	4.230	0.7468
	B: Flexible Structure	3.270	0.6462	3.100	0.6466	2.760	0.6590	3.920	0.6352
	C: Unsteady Aerodynamics	3.040	0.6276	2.960	0.6210	2.650	0.6413	3.540	0.6067
Phugoid	A: Rigid Structure	$\tau = 100.0$s/Inf		$\tau = 357.0$s/Inf		$\tau = 55.01$s/Inf		0.0022	0.727
	B: Flexible Structure	$\tau = 86.02$s/Inf		0.004702	0.9459	$\tau = 49.18$s/Inf		0.002812	0.7791
	C: Unsteady Aerodynamics	$\tau = 86.02$s/Inf		0.004702	0.9431	$\tau = 49.18$s/Inf		0.002812	0.7679

Table 6.10: Closed-loop aeroplane longitudinal characteristics

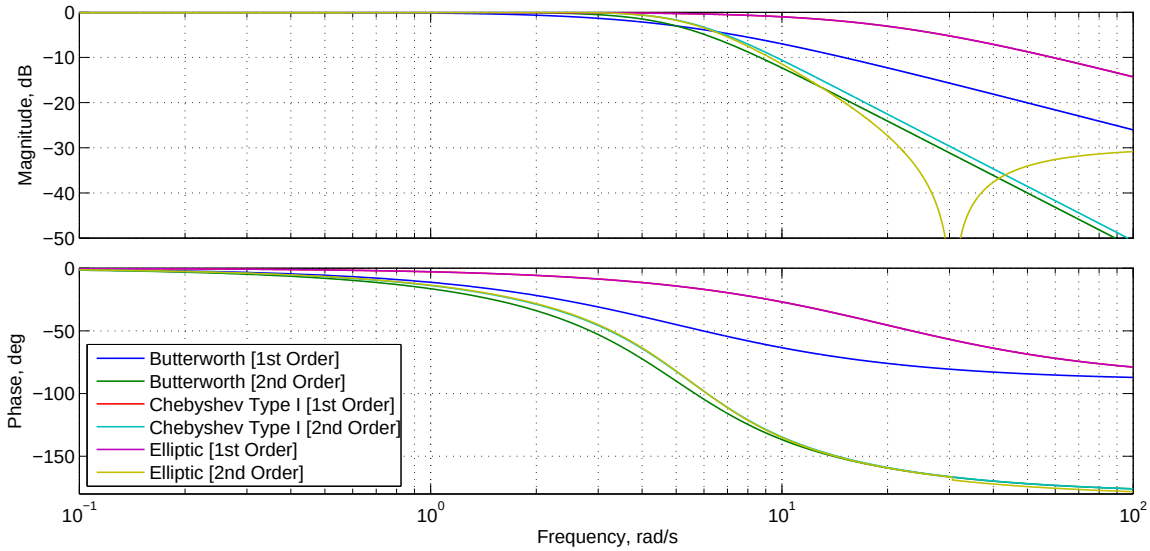

Figure 6.8: Bode plot for system acceleration output filter

In order to improve SPPO damping, a pitch-rate feedback SAS will be used. This is shown as the inner-loop feedback in Figure 6.9. This FCS design is representative of those used in a typical modern transport aircraft, and is described as being a Rate Command-Attitude Hold (RCAH) system [Cook, 2007]. In order to initially achieve a closed-loop SPPO damping ratio of 0.50, an inner-loop pitch-rate feedback gain, K_q, was selected [Table 6.11]. A root-locus plot [Figure 6.10] shows the significant influence of pitch-rate feedback on the SPPO and phugoid modes, as well as several of the high-frequency structural modes. Of these structural modes, one mode is driven unstable by pitch-rate feedback, but only at extremely high gain values.

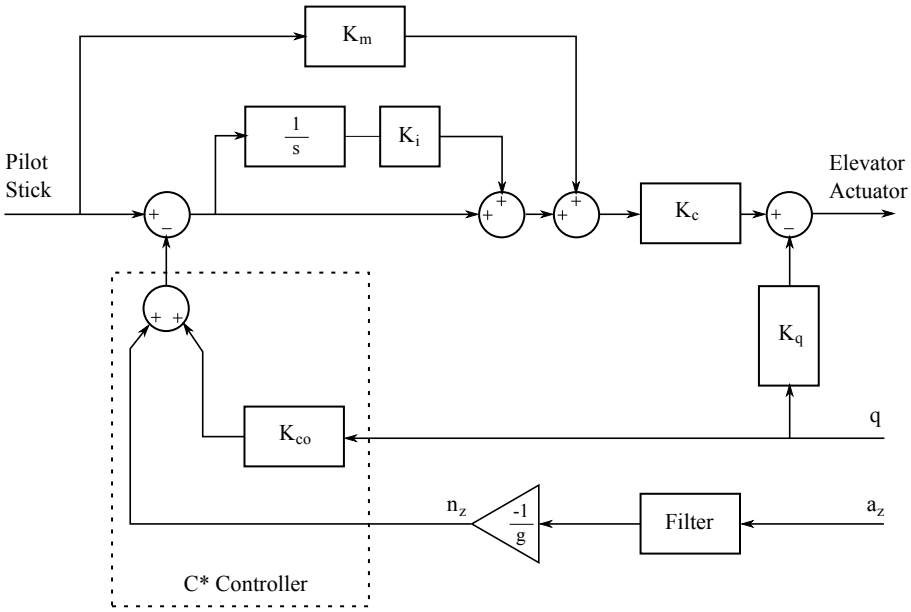

Figure 6.9: Longitudinal CSAS controller structure

	Flight Point			
	2000 ft		10000 ft	
Gain	140 m s^{-1}	180 m s^{-1}	140 m s^{-1}	180 m s^{-1}
K_q	0.1980	0.3140	0.2740	0.2200
K_{co}	6.000	6.000	6.000	6.000
K_c	0.1800	0.1630	0.1580	0.2050
K_m	0.9880	1.150	1.410	0.6560
K_i	0.8500	0.8500	0.7000	1.020

Table 6.11: Closed-loop system longitudinal controller gains

A C*-type controller is used to provide a normal acceleration demand control system. The C* criteria [Tobie et al., 1966], is defined as a blend of normal acceleration and pitch rate, given by the following equation, where n_z is the normal load factor at the cockpit, q is pitch-rate, and V_{co} is the cross-over velocity, defined by Tobie et al. [1966] as 122 m s^{-1}:

$$C^* = n_z + \frac{V_{co}}{g} q \tag{6.2.1}$$

Any longitudinal CSAS combining pitch-rate and normal acceleration is often termed a C* controller [Cook, 1997], and for this system a normal load factor/pitch-rate gain ratio, K_{co}, of 6.00 was found to give good results. This is shown as the outer-loop feedback in Figure 6.9. A gain, K_c, was then selected to give the required performance [Table 6.11]. The SPPO mode damping was selected to be 0.75, such that the damping ratio of the closed-loop aeroplane with the inclusion of an integral controller remains sufficiently high. A root-locus plot [Figure 6.11] shows the significant influence of C* feedback on the SPPO and phugoid modes. Again, several of the high-frequency structural modes are affected, and one mode is driven unstable, though again only at extremely high gain values.

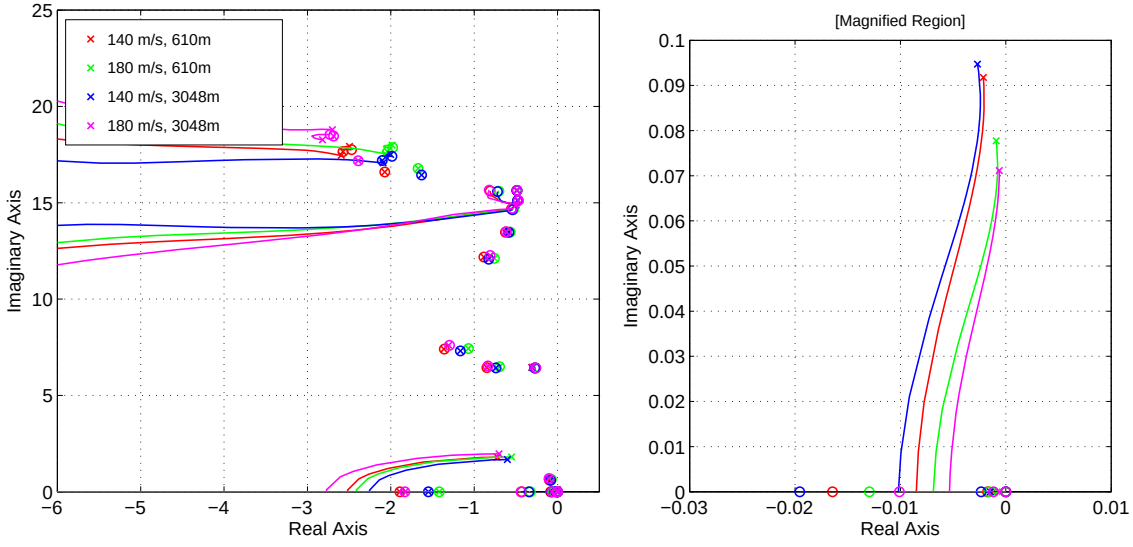

Figure 6.10: Root-locus plot for longitudinal inner-loop pitch-rate feedback

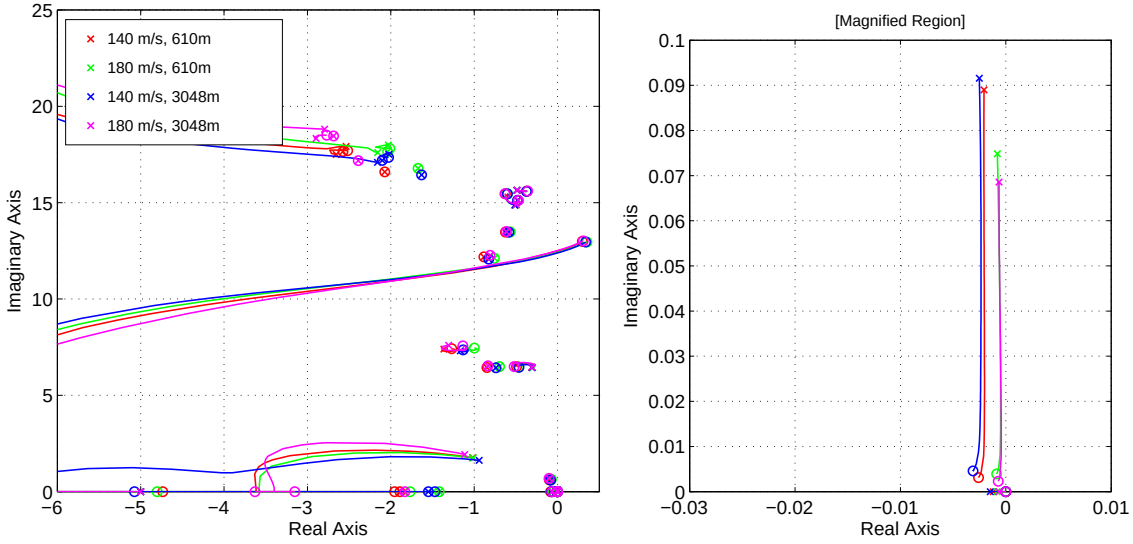

Figure 6.11: Root-locus plot for longitudinal outer-loop C* feedback

In order to achieve an attitude-hold characteristic, and also improve the dynamic tracking behaviour of the aircraft, an integral term was added to the controller. To minimise the phase lag effect of the integrator at the short-period frequency, an integrator gain, K_i, was chosen from analysis of the phase bode plot [Figure 6.12]. Gain values for K_i of 0.1, 0.2, 0.5, 1.0, and 2.0 were investigated and compared to the system characteristics without the integral term, represented by K_i value of 0.0. It was decided that a phase lag of 15° at the short-period frequency was acceptable, and as such the gain values for K_i were selected [Table 6.11]. The damping ratio of the SPPO mode is reduced by the inclusion of integral control, however this is acceptable due to the selection of a relatively high damping ratio in the design of the C* feedback loop [Table 6.12]. A forward path gain, K_m, was then selected to correctly assign unit steady-state gain to the system response [Table 6.11].

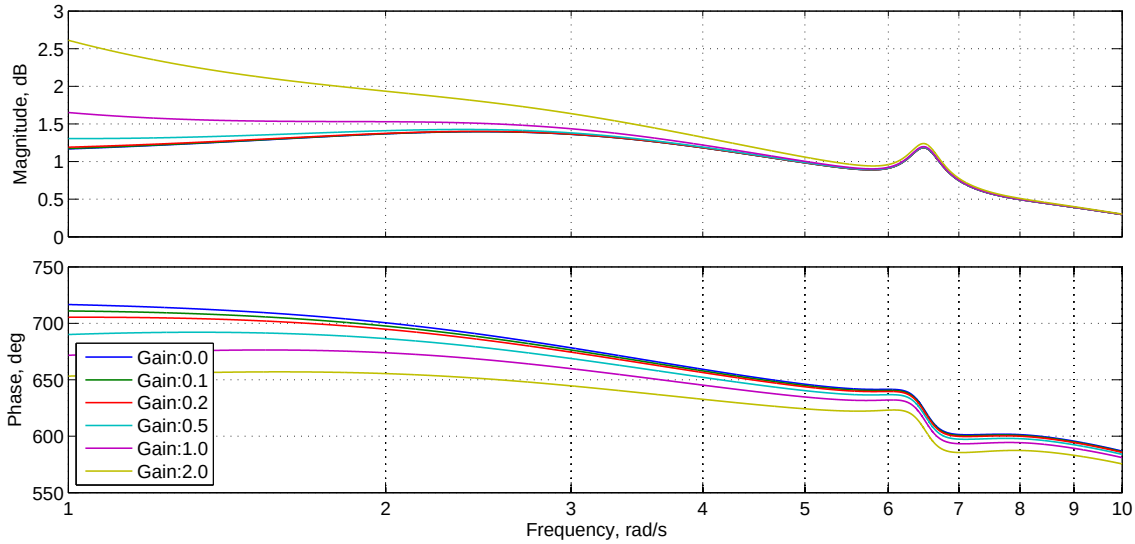

Figure 6.12: Bode plot for outer-loop integral controller gains

	Open-loop		Inner-loop		Outer-loop		Closed-loop	
Mode	Frequency, rad s^{-1}	Damping	Frequency, rad s^{-1}	Damping	Frequency, rad s^{-1}	Damping	Frequency, rad s^{-1}	Damping
SPPO	1.890	0.2921	2.021	0.5000	3.062	0.7511	3.095	0.6470
Phugoid	0.07781	0.01180	0.07473	0.01121	0.05431	0.01231	0.005012	0.9451
Dutch Roll	0.6431	0.1142	0.6431	0.1142	0.6431	0.1142	0.6431	0.1142
Roll	$\tau = 0.7042$s		$\tau = 0.7042$s		$\tau = 0.7042$s		$\tau = 0.7042$s	
Spiral	$\tau = 17.70$s		$\tau = 17.70$s		$\tau = 17.70$s		$\tau = 17.70$s	
Flexible Mode 1	6.450	0.04612	6.446	0.04589	6.500	0.04231	6.499	0.04120
Flexible Mode 2	6.530	0.1072	6.526	0.1072	6.526	0.1072	6.526	0.04081
Flexible Mode 3	7.510	0.1429	7.507	0.1430	7.487	0.1441	7.489	0.1446
Flexible Mode 4	12.14	0.06211	12.14	0.06211	12.14	0.06211	12.14	0.06211
Flexible Mode 5	13.49	0.04235	13.49	0.04235	13.49	0.04235	13.49	0.04235
Flexible Mode 6	14.88	0.03282	14.89	0.03312	14.94	0.03601	14.94	0.03614
Flexible Mode 7	15.12	0.03103	15.12	0.03103	15.12	0.03102	15.12	0.03102
Flexible Mode 8	15.65	0.03102	15.65	0.03102	15.64	0.03102	15.64	0.03102
Flexible Mode 9	16.87	0.1002	16.87	0.09988	16.87	0.09987	16.87	0.09987
Flexible Mode 10	17.67	0.1167	17.74	0.1208	17.77	0.1149	17.79	0.1149
Flexible Mode 11	17.77	0.1151	17.77	0.1151	17.93	0.1151	17.93	0.1151
Flexible Mode 12	18.10	0.1102	18.11	0.1118	18.41	0.1629	18.46	0.1610

Table 6.12: Open- and closed-loop aeroplane longitudinal, lateral-directional and flexible dynamics at 180 m s^{-1} and 2,000 ft

The final closed-loop longitudinal characteristics of the aircraft are shown in Table 6.10 and Figure 6.13. For all of the flight points considered, the damping of the SPPO mode has been increased to an acceptable average value of 0.65. However, the phugoid mode has for two of the cases been reduced to a stable, non-oscillatory pair of real roots. The time constant of the phugoid mode for these two cases, 86 and 49 seconds respectively, is sufficiently long that their influence on the short-term dynamics of the aeroplane is small, and it can be expected that this is easily controllable by the pilot.

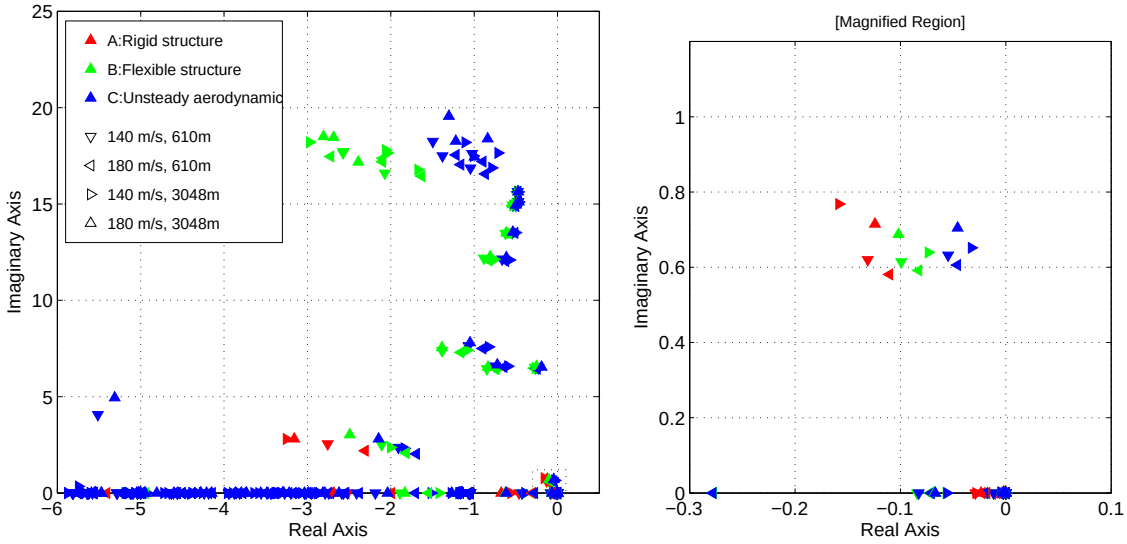

Figure 6.13: Pole-zero map for closed-loop system variants

Figure 6.13 additionally shows the closed-loop characteristics of the Model A and C variants: rigid structure, with steady aerodynamics; and flexible structure, with unsteady aerodynamics respectively. These are calculated using the gains selected for the second model variant given in Table 6.11. Section 6.1 showed that the influence of the inclusion of structural flexibility was a significant reduction in the natural frequency, and a smaller reduction in the damping ratio, of the SPPO mode. The damping and natural frequency of the phugoid mode were also shown to be reduced. This effect was found to be less significant at lower airspeeds. This is evident in the characteristics of the open-loop SPPO and phugoid modes given in Table 6.9 for the three model variants. Using the controller gains calculated for the Model B variant, it can be seen that the higher SPPO natural frequency for the rigid aeroplane is reflected in the closed-loop characteristics of the Model A variant aeroplane [Table 6.10]. The higher SPPO damping ratio for rigid Model A also results in slightly higher than acceptable closed-loop damping. The Model A closed-loop phugoid mode is reduced to a stable, non-oscillatory pair of real roots at one of the flight points considered (180 m s^{-1} and 2,000 ft), and the phugoid mode time constant is increased at the other flight points considered.

The influence of unsteady aerodynamics on the longitudinal aeroplane characteristics was seen in Section 6.1 to be relatively small. As such the open-loop characteristics of the second and third model variants, i.e Models B and C respectively, are very similar [Table 6.9]. It can be seen then that the longitudinal controller is robust with regards to the inclusion of unsteady aerodynamic effects, with the closed-loop characteristics of the third Model C variant very similar to those of the second variant [Table 6.10]. The influence of

the controller on the flexible aircraft modes is relatively small [Table 6.12], and as such the closed-loop structural modes for the third Model C variant are also broadly similar to the open-loop characteristics [Figure 6.13].

Figure 6.14 shows the open- and closed-loop aeroplane response to a unit pulse C* command for the three model variants. It can be seen the closed-loop aeroplane responds with much improved settling time and reduced overshoot for the second and third model variants. The first variant, which was noted to have higher SPPO frequency and damping, shows a small increase in the response overshoot and an increased settling time. It can be seen that the unit C* demand results in a unit response after a short initial transient for the closed-loop aeroplane (the open-loop aeroplane response is scaled here for comparison purposes). The aeroplane pitch attitude behaves as expected, with the rate of change of attitude equal to the pitch rate. After the demand returns to zero, the transient is again excited before the C* response quickly returns to zero. The pitch attitude is held nominally constant at 0.4231 radians, though it takes several seconds to reach its steady state value. This is expected given the heavily damped, or long time-constant non-oscillatory, closed-loop phugoid mode.

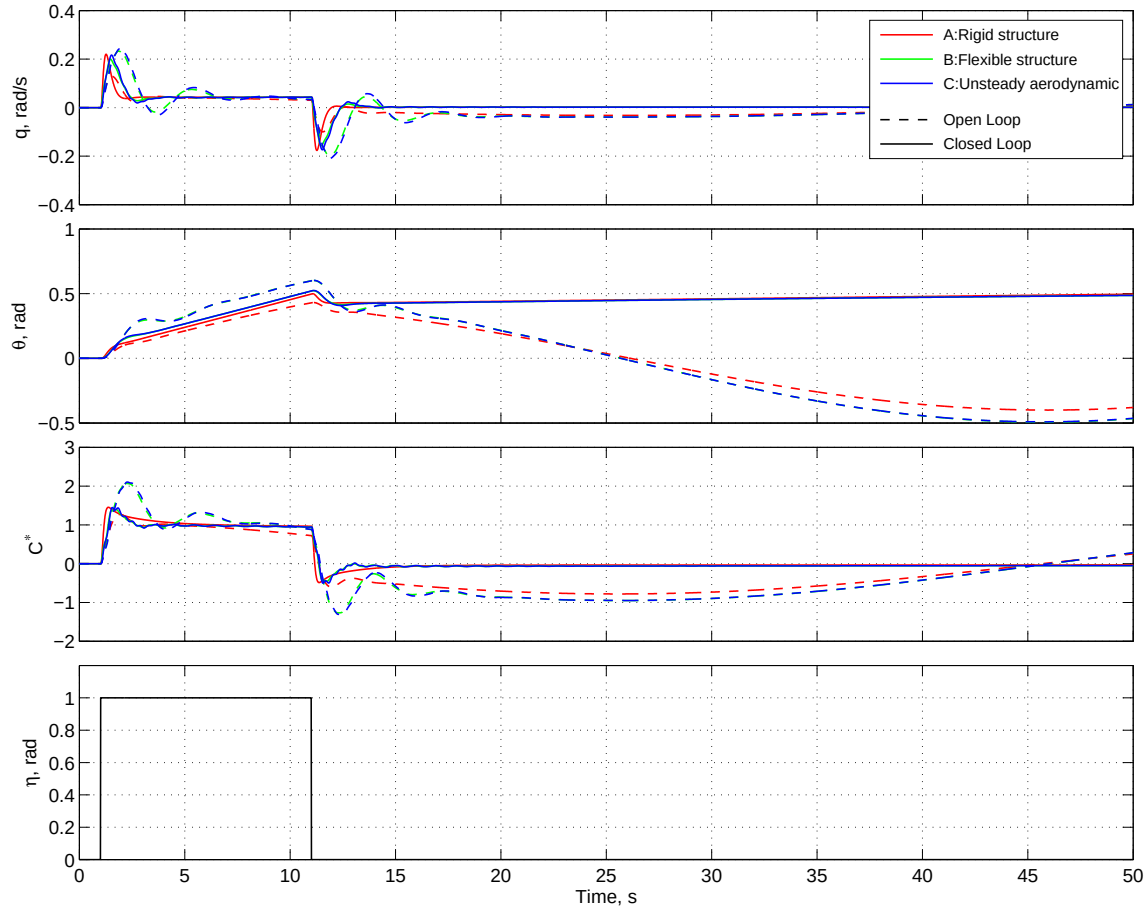

Figure 6.14: Open- and closed-loop aeroplane response to elevator pulse input at 180 m s^{-1} and 2,000 ft

6.2.1.2 Lateral-Directional

A lateral-directional CSAS control law has also been developed for the flexible Aeroplane AX-1 model. Similarly with the longitudinal law, the typical lateral-directional law is described as a RCAH-type controller [Cook, 2007], and is shown in Figure 6.15. The open-loop lateral-directional dynamic and stability characteristics of the Aeroplane AX-1 aeroplane model are shown in Table 6.13. Figure 6.7 shows the pole-zero map for the three model variants, Models A, B and C. The same four flight points are again considered, at 140 and 180 m s^{-1} and 2000 and 10,000 ft. The controller gains are again selected for the second model variant, Model B, in order to meet MIL-STD-1797A [1990]. The Model A and C variants are provided again for comparison and robustness analysis.

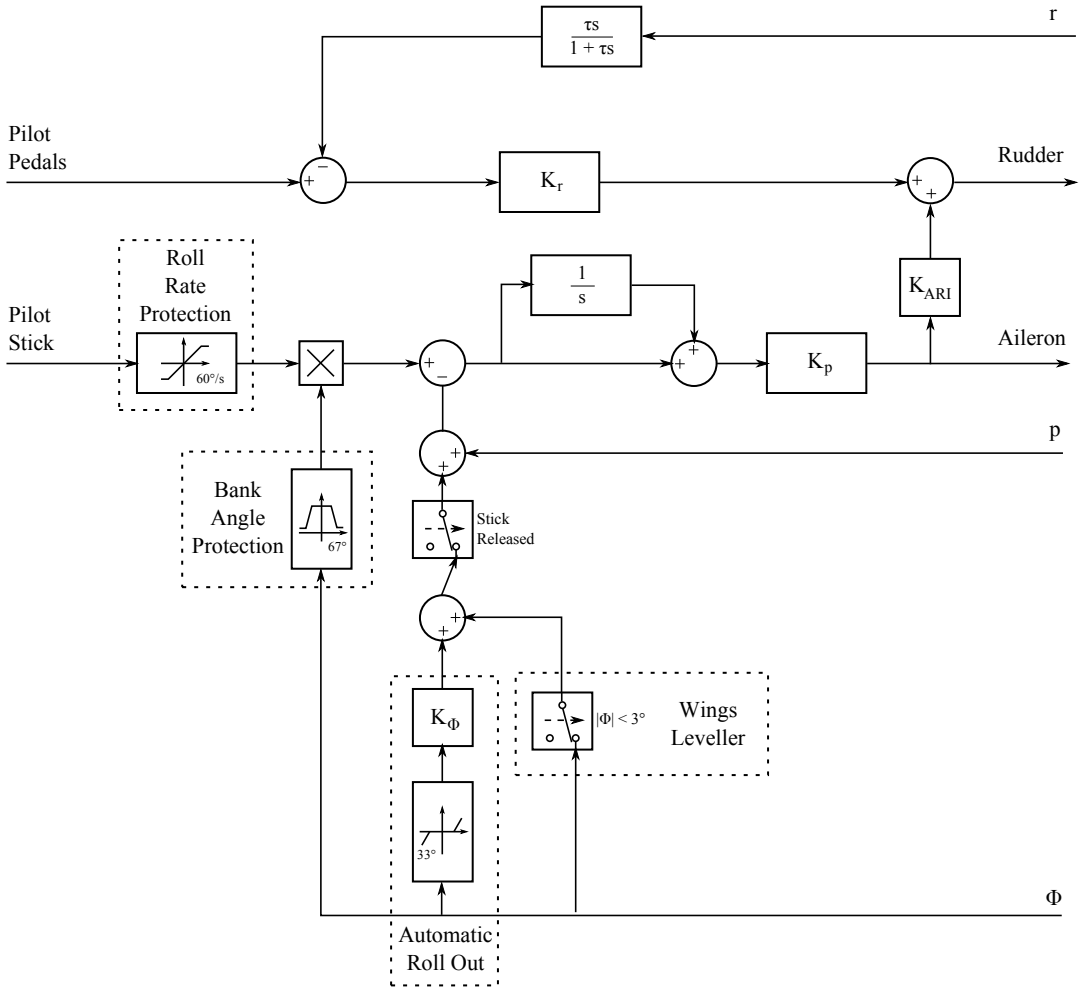

Figure 6.15: Lateral-directional CSAS controller structure

An Aileron-Rudder Interconnect (ARI) control loop was first specified for each of the model variants. This open-loop path is designed in order to improve roll performance by maintaining zero side-slip in roll, providing the component of yaw-rate necessary to achieve roll about the aircraft stability-axis [McLean, 1990]. A gain, K_{ARI}, was selected from visual analysis of the roll response to aileron to minimise dutch-roll coupling [Table 6.14].

		Flight Point							
		2000 ft				10000 ft			
		140 m s^{-1}		180 m s^{-1}		140 m s^{-1}		180 m s^{-1}	
Mode	Model Variant	Frequency, rad s^{-1}	Damping	Frequency, rad s^{-1}	Damping	Frequency, rad s^{-1}	Damping	Frequency, rad s^{-1}	Damping
Dutch Roll	A: Rigid Structure	0.6326	0.2070	0.7841	0.2019	0.5910	0.1868	0.7255	0.1712
	B: Flexible Structure	0.6217	0.1603	0.6437	0.1141	0.5970	0.1382	0.6951	0.1473
	C: Unsteady Aerodynamics	0.6338	0.08624	0.6519	0.05029	0.6083	0.07632	0.7061	0.06501
Roll	A: Rigid Structure	$\tau = 0.3966$s		$\tau = 0.2950$s		$\tau = 0.5021$s		$\tau = 0.3725$s	
	B: Flexible Structure	$\tau = 0.5286$s		$\tau = 0.7042$s		$\tau = 0.6451$s		$\tau = 0.5458$s	
	C: Unsteady Aerodynamics	$\tau = 0.4573$s		$\tau = 0.6621$s		$\tau = 0.5839$s		$\tau = 0.4903$s	
Spiral	A: Rigid Structure	$\tau = 34.72$s		$\tau = 35.59$s		$\tau = 44.05$s		$\tau = 42.55$s	
	B: Flexible Structure	$\tau = 11.89$s		$\tau = 17.70$s		$\tau = 13.91$s		$\tau = 14.75$s	
	C: Unsteady Aerodynamics	$\tau = 12.12$s		$\tau = 17.89$s		$\tau = 14.12$s		$\tau = 16.45$s	

Table 6.13: Open-loop aeroplane lateral-directional characteristics

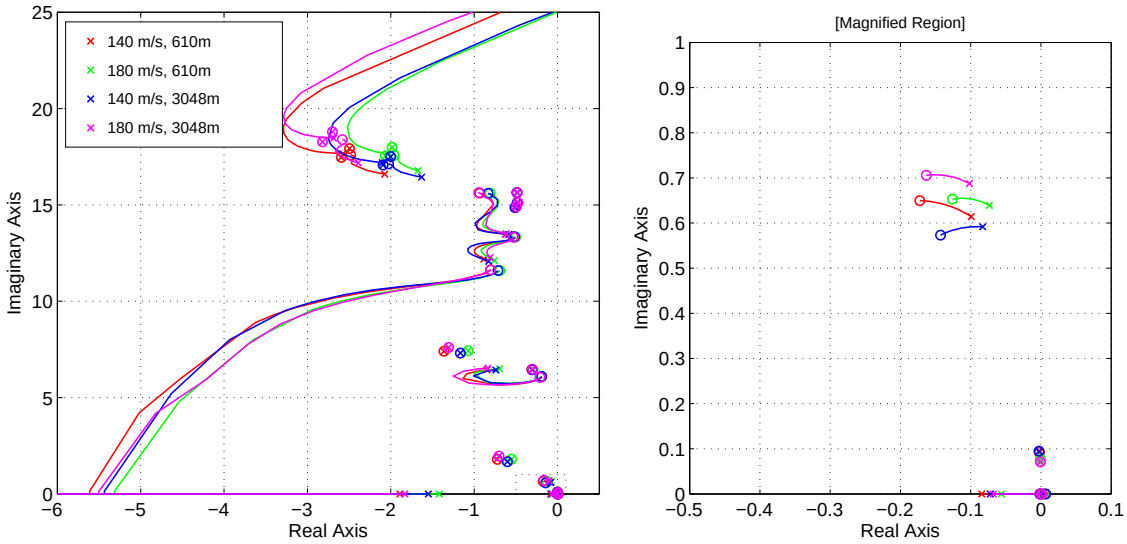

Figure 6.16: Root-locus plot for lateral-directional roll-rate feedback

In order to speed up the roll-subsidence mode, a roll-rate SAS will be developed. From analysis of the root-locus plot [Figure 6.16], a roll-rate feedback gain, K_p, was selected [Table 6.14]. The non-oscillatory roll mode was designed to have a time constant of 0.4 seconds, well within civil and military flying specifications for Category A, Level 1 flight [MIL-STD-1797A, 1990]. This is considered the less critical loop [Stevens and Lewis, 1992], and is closed first. An integrator loop, with unit gain K_i, was incorporated into the control law to improve the roll response and provide an attitude-hold characteristic. A forward path gain, K_m, was then chosen to achieve the correct unit steady-state gain response. The roll-rate Proportional (P) and Proportional plus Integral (P+I) feedback closed-loop aircraft characteristics are shown in Table 6.15.

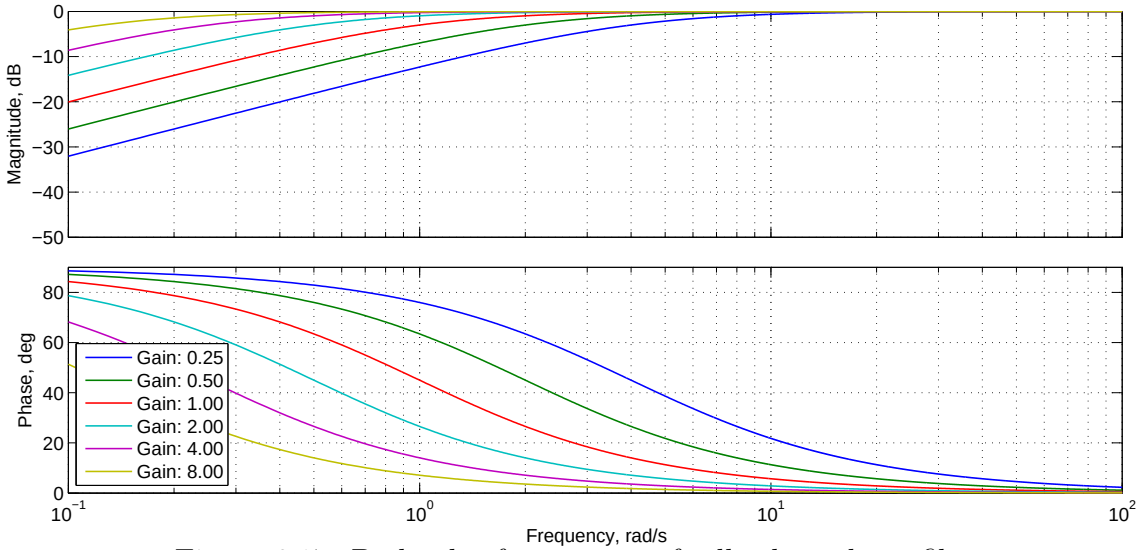

Figure 6.17: Bode plot for yaw-rate feedback washout filter

As yaw-rate has a steady non-zero value in a coordinated turn, a washout filter was used in the feedback loop. The high-pass filter characteristic of the washout filter removes the low frequency steady-state component of yaw rate. Selection of the filter time constant is a

compromise between providing adequate dutch-roll damping and minimising interference in turn entry. Analysis of several time constant values [Figure 6.17] shows the influence of the time constant on the gain and phase characteristics of the filter. A time constant value, τ_w for the washout filter of 2.000s was selected in order to provide an adequate yaw-rate gain at the dutch-roll frequency.

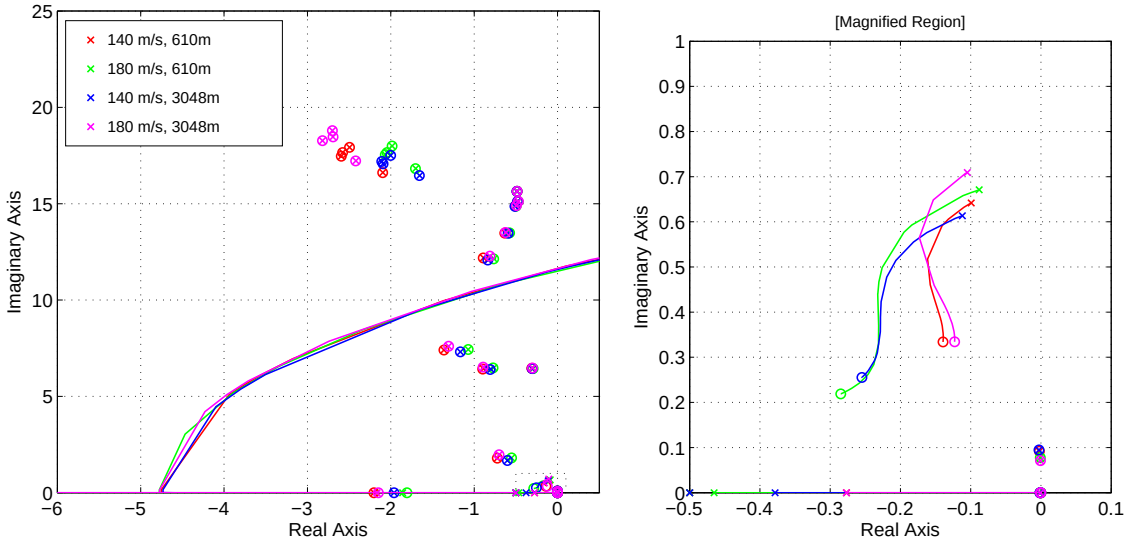

Figure 6.18: Root-locus plot for lateral-directional yaw-rate feedback

In order to increase dutch-roll damping, yaw-rate feedback was then implemented. Again from analysis of the root-locus plot [Figure 6.18], a yaw-rate feedback gain, K_r, was selected [Table 6.14] such that the dutch-roll frequency and damping satisfies the criteria for Category A, Level 1 flight [MIL-STD-1797A, 1990]. The characteristic modes of the open- and closed-loop aeroplane are shown in Table 6.15 for a single flight point at 180 m s^{-1} and 2000 ft.

	Flight Point			
	2000 ft		10000 ft	
Gain	140 m s^{-1}	180 m s^{-1}	140 m s^{-1}	180 m s^{-1}
K_p	0.2930	0.5520	0.5640	0.2600
K_m	0.1820	0.3390	0.2780	0.1940
K_i	1.000	1.000	1.000	1.000
K_r	1.140	0.6740	0.5590	0.9180
K_{ARI}	0.2000	0.2000	0.2500	0.1000
K_ϕ	0.07500	0.07500	0.07500	0.07500

Table 6.14: Closed-loop system lateral-directional controller gains

The final closed-loop lateral-directional characteristics of the aircraft are shown in Table 6.16 and Figure 6.20. It can be seen that for one of the flight points considered (180 m s^{-1}, 2000 ft), the closed-loop rigid aircraft model, Model A, roll mode root is transformed into a pair of heavily damped oscillatory roots. This is due to the interaction with the faster aileron actuator root and the relatively high roll-rate feedback gain required for

the Model B flexible aircraft at this flight point. While a completely rigid aircraft is perhaps unrealistic, this is evidence that should structural flexibility be overestimated, and the structure be in fact much stiffer than is modelled, then roll-rate feedback may have unintended results. It was noted for the open-loop model in Section 6.1 that unsteady aerodynamics reduces dutch-roll mode damping. This reduction in damping is also evident in the closed-loop aircraft, and in this case a yaw-rate feedback gain was selected to provide an adequate damping margin to meet flying specifications with the inclusion of unsteady aerodynamic effects. If this were not the case, then unsteady aerodynamics may have a significant detrimental effect on the aircraft's handling qualities.

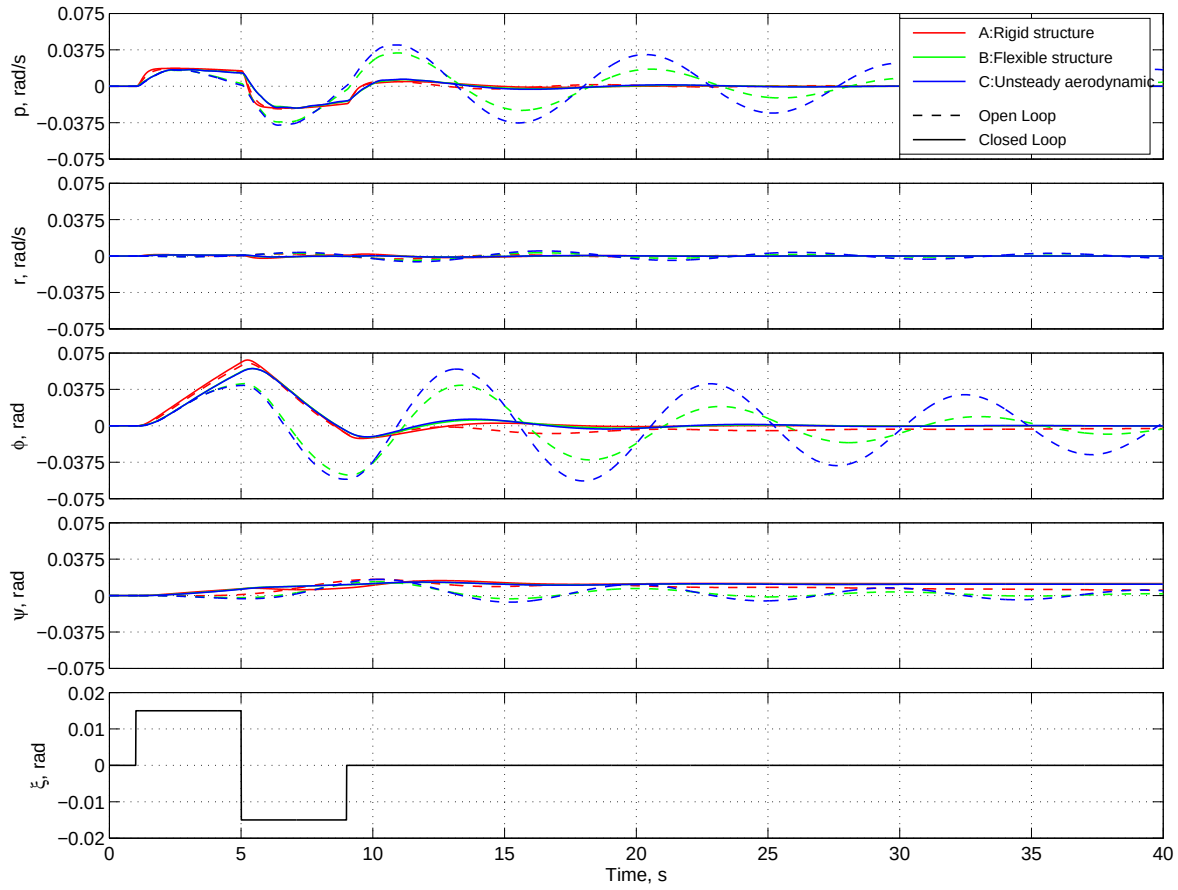

Figure 6.19: Open- and closed-loop aeroplane response to aileron doublet input at 180 m s^{-1} and 2,000 ft

Figure 6.19 shows the open- and closed-loop aeroplane response to aileron doublet for each of the three model variants. The open-loop Model B and C variants show significant roll and dutch-roll coupling in response to aileron. This in part can be explained by the increased incidence angle required at trim for the flexible structure variants due to deformation of the wing structure in flight. Also evident in the open-loop response is the reduced dutch-roll mode damping for the third Model C unsteady aerodynamic variant. The roll and dutch-roll mode coupling is considerably reduced for these two variants for the closed-loop aeroplane, and the roll response matches more closely the rigid aircraft model. The roll response is still slowed by the inclusion of structural flexibility however.

	Open-loop		p-feedback (P)		p-feedback (P+I)		r-feedback	
Mode	Frequency, rad s^{-1}	Damping	Frequency, rad s^{-1}	Damping	Frequency, rad s^{-1}	Damping	Frequency, rad s^{-1}	Damping
SPPO	1.890	0.2921	1.888	0.2921	1.888	0.2921	1.888	0.2921
Phugoid	0.07790	0.01183	0.07790	0.01183	0.07790	0.01183	0.07790	0.01183
Dutch Roll	0.6428	0.1143	0.6554	0.1348	0.6765	0.1302	0.6180	0.3001
Roll	$\tau = 0.7043$s		$\tau = 0.4000$s		$\tau = 0.5371$s		$\tau = 0.5286$s	
Spiral	$\tau = 17.70$s		$\tau = 28.33$s		$\tau = 2.137$s		$\tau = 2.739$s	
Flexible Mode 1	6.450	0.04687	6.450	0.04687	6.450	0.04687	6.450	0.04687
Flexible Mode 2	6.530	0.1071	6.516	0.1172	6.527	0.1172	6.528	0.1172
Flexible Mode 3	7.510	0.1435	7.507	0.1435	7.507	0.1435	7.507	0.1435
Flexible Mode 4	12.14	0.06184	12.16	0.06289	12.16	0.06321	12.16	0.06334
Flexible Mode 5	13.49	0.04287	13.50	0.04287	13.59	0.04287	13.50	0.04287
Flexible Mode 6	14.88	0.03264	14.88	0.03264	14.88	0.03264	14.88	0.03264
Flexible Mode 7	15.12	0.03128	15.12	0.03128	15.12	0.03128	15.12	0.03128
Flexible Mode 8	15.65	0.03134	15.65	0.03134	15.65	0.03134	15.65	0.03134
Flexible Mode 9	16.87	0.1004	16.91	0.1008	16.91	0.1011	16.91	0.1013
Flexible Mode 10	17.67	0.1167	17.67	0.1167	17.67	0.1167	17.67	0.1167
Flexible Mode 11	17.77	0.1154	17.78	0.1154	17.78	0.1154	17.78	0.1154
Flexible Mode 12	18.10	0.1103	18.10	0.1103	18.10	0.1103	18.10	0.1103

Table 6.15: Open- and closed-loop aeroplane longitudinal, lateral-directional and flexible dynamics at 180 m s^{-1} and 2,000 ft

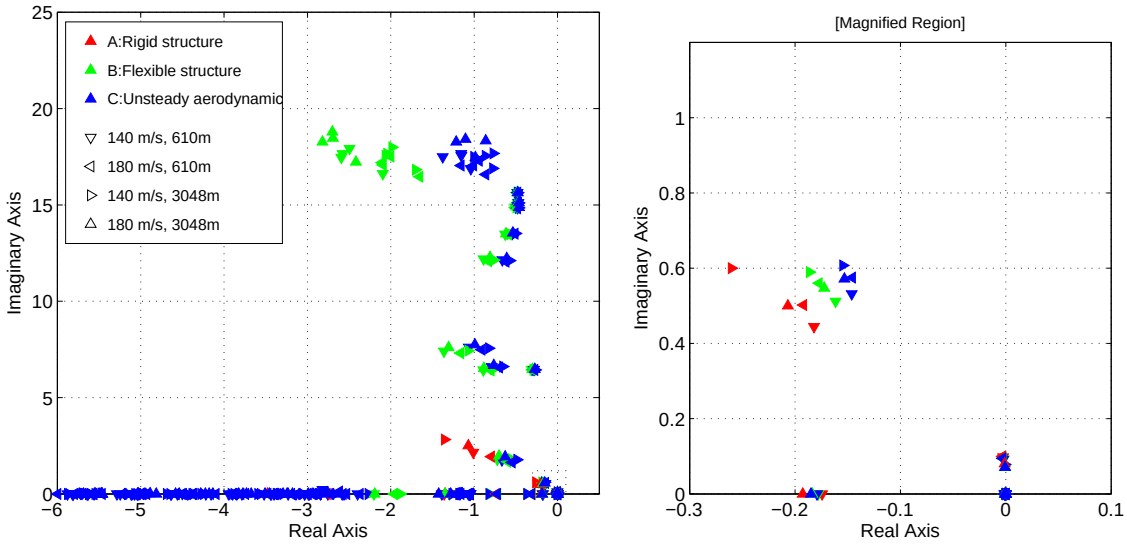

Figure 6.20: Pole-zero map for closed-loop system variants

The lateral-directional FCS incorporates several safety features designed to limit the achievable roll-rate and bank-angle of the aircraft [Cook, 2007], as shown in Figure 6.15. A rate-limiter in the control path is designed to limit the maximum roll rate to 60 deg s^{-1}. The command signal is then scaled by the bank-angle protection feedback gain [Table 6.14]. This has a value of unity at low bank angles, progressively reducing to zero as the aircraft bank-angle reaches the maximum allowed value, in this case 67°. The FCS is described as an attitude-hold controller below 33°, however above this bank-angle on release of the stick, the aeroplane automatically rolls back and holds at 33° [Figure 6.15]. The gain, K_ϕ, is selected in order to achieve a desired roll back rate of 0.20 rad s^{-1} [Table 6.14]. The roll response of the closed-loop aeroplane, with and without the inclusion of these protection features, is shown in Figure 6.21 for a single flight point (180 m s^{-1}, 2,000 ft).

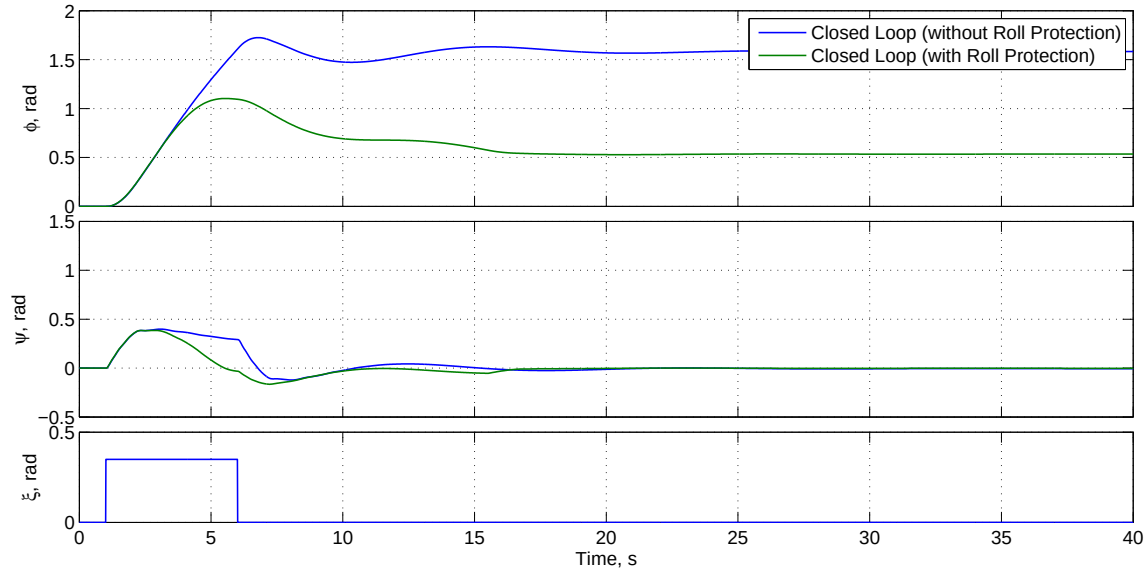

Figure 6.21: Closed-loop aeroplane response, with and without roll protection features, to aileron pulse input at 180 m s^{-1} and 2,000 ft

		Flight Point							
		2000 ft				10000 ft			
		140 m s^{-1}		180 m s^{-1}		140 m s^{-1}		180 m s^{-1}	
Mode	Variant	Frequency, rad s^{-1}	Damping	Frequency, rad s^{-1}	Damping	Frequency, rad s^{-1}	Damping	Frequency, rad s^{-1}	Damping
Dutch Roll	A: Rigid Structure	0.4802	0.3786	0.6537	0.3982	0.5365	0.3571	0.5410	0.3820
	B: Flexible Structure	0.5368	0.3002	0.6194	0.3004	0.5884	0.3005	0.5736	0.3006
	C: Unsteady Aerodynamics	0.5514	0.2651	0.6253	0.2463	0.5932	0.2449	0.5921	0.2590
Roll	A: Rigid Structure	$\tau = 0.3288$s		7.014	0.9182	$\tau = 0.3617$s		$\tau = 0.2870$s	
	B: Flexible Structure	$\tau = 0.4525$s		$\tau = 0.5286$s		$\tau = 0.5083$s		$\tau = 0.4568$s	
	C: Unsteady Aerodynamics	$\tau = 0.4172$s		$\tau = 0.4413$s		$\tau = 0.4218$s		$\tau = 0.3854$s	
Spiral	A: Rigid Structure	$\tau = 5.747$s		$\tau = 2.747$s		$\tau = 3.257$s		$\tau = 5.181$s	
	B: Flexible Structure	$\tau = 5.525$s		$\tau = 2.739$s		$\tau = 3.195$s		$\tau = 5.405$s	
	C: Unsteady Aerodynamics	$\tau = 5.587$s		$\tau = 2.725$s		$\tau = 3.185$s		$\tau = 3.405$s	

Table 6.16: Closed-loop aeroplane lateral-directional characteristics

6.2.2 Load Alleviation Systems

6.2.2.1 Manoeuvre Load Alleviation

In order to reduce the wing loading during accelerated manoeuvres, a Manoeuvre Load Alleviation (MLA) function has been designed. The controller is designed using fuselage load factor, i.e. vertical normal acceleration, feedback to control aileron deflection [Figure 6.22]. A number of flight points are again considered: 4,000, 8,000 and 12,000 ft at 180 m s^{-1}. The complete Model C flexible structure, unsteady aerodynamic model variant is considered alone here. A longitudinal and lateral-directional CSAS controller was designed for these flight points, and the gains are shown in Table 6.17. The closed-loop dynamic and stability characteristics of the aeroplane model are shown in Table 6.18 and Figure 6.23.

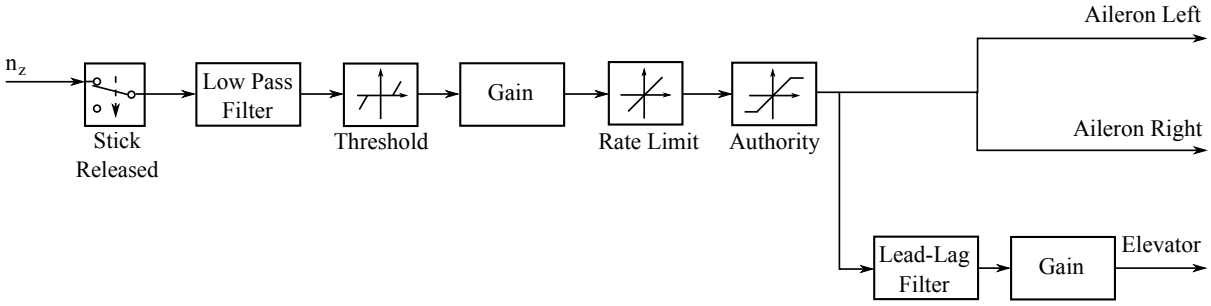

Figure 6.22: Manoeuvre Load Alleviation (MLA) controller structure

The MLA system uses normal acceleration feedback to deploy symmetric ailerons, reducing the wing loading by altering the lift distribution on the wing and moving the centre of pressure inwards. In order to isolate the rigid-body acceleration from the measured acceleration feedback, a first-order Butterworth filter, with a cut-off frequency of 5 rad s^{-1}, is again employed.

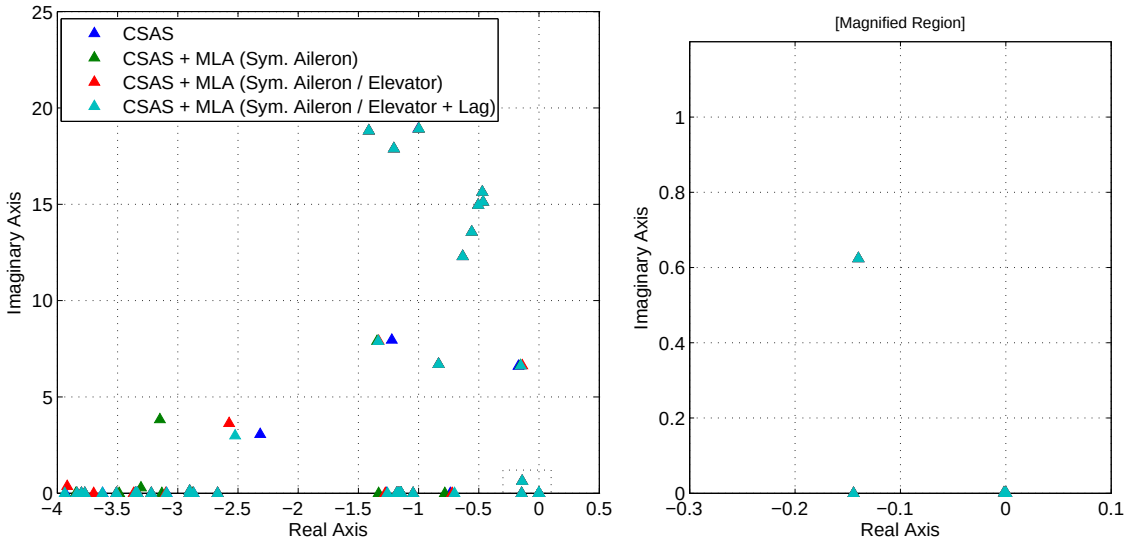

Figure 6.23: Pole-zero map for CSAS and MLA with elevator pitch compensation at 4,000 ft

	Flight Point		
Gain	4000 ft	8000 ft	12000 ft
K_q	0.1840	0.2010	0.2310
K_{co}	6.000	6.000	6.000
K_c	0.2320	0.2160	0.1980
K_{m_c}	0.6640	0.6400	0.5920
K_{i_c}	1.100	1.100	1.000
K_p	0.1420	0.2180	0.3060
K_{m_p}	0.1120	0.1630	0.1610
K_{i_p}	1.000	1.000	1.000
K_r	0.5170	0.7020	0.6890
K_{ARI}	0.0500	0.0750	0.1000
K_ϕ	0.07500	0.07500	0.07500
K_e	0.1360	0.1370	0.1350
K_g	0.2000	0.2000	0.2000

Table 6.17: Closed-loop system CSAS and MLA controller gains at 180 m s^{-1}

A feedback gain, K_g, was initially chosen to provide adequate load alleviation within the flight envelope while minimising the influence of the MLA system on the rigid-body and elastic modes [Table 6.17]. It can be seen from Figure 6.23 however that acceleration feedback to aileron alone has a considerable effect on the SPPO mode in particular, increasing both frequency and damping, while also reducing the damping of the first wing bending mode. This is a result of the pitching moment due to symmetric aileron deployment [Figure 6.24]. The MLA system should be designed not to influence the rigid-body modes, and a second feedback loop to elevator was added to reduce the influence of the MLA system on the aircraft rigid-body response [Figure 6.22]. A gain, K_e, was selected to cancel the pitching response of symmetric aileron deployment [Table 6.17]. This has the desired effect, reducing the pitching response to aileron [Figure 6.24].

However due to an approximate 25° phase lag between aileron and elevator pitch response at the SPPO frequency [Figure 6.25], the second feedback loop is only partially successful in cancelling the influence of the MLA system on the SPPO mode. A lead-lag filter, $(s + 20)/(s + 10)$, was then added to correct for the phase difference in elevator and aileron pitch response. This can be seen to be much more effective at cancelling the pitch response due to aileron deployment [Figure 6.24], and the closed-loop MLA SPPO damping and frequency are very similar to the CSAS system [Figure 6.23].

This process was repeated for each of the flight points considered, and the closed-loop characteristics for each of the three flight points is given in Table 6.19. The influence on the rigid- and flexible-body modes can be seen to be small, with only a small increase in SPPO frequency for the 4,000 ft case, and a small reduction in SPPO damping for all the three cases considered. The reduction in damping for the first wing bending mode (Flexible Mode 1) is also limited to 0.03 for each of the three cases.

A number of secondary functions were then added to the MLA system to improve its performance [Figure 6.22]. A rate-limiter was added to limit control surface retraction rates to 10 deg s^{-1}, simulating a reduction in the transient response and fatigue wear on the actuator system. A threshold of 0.2 was added to minimise unnecessary deployment of

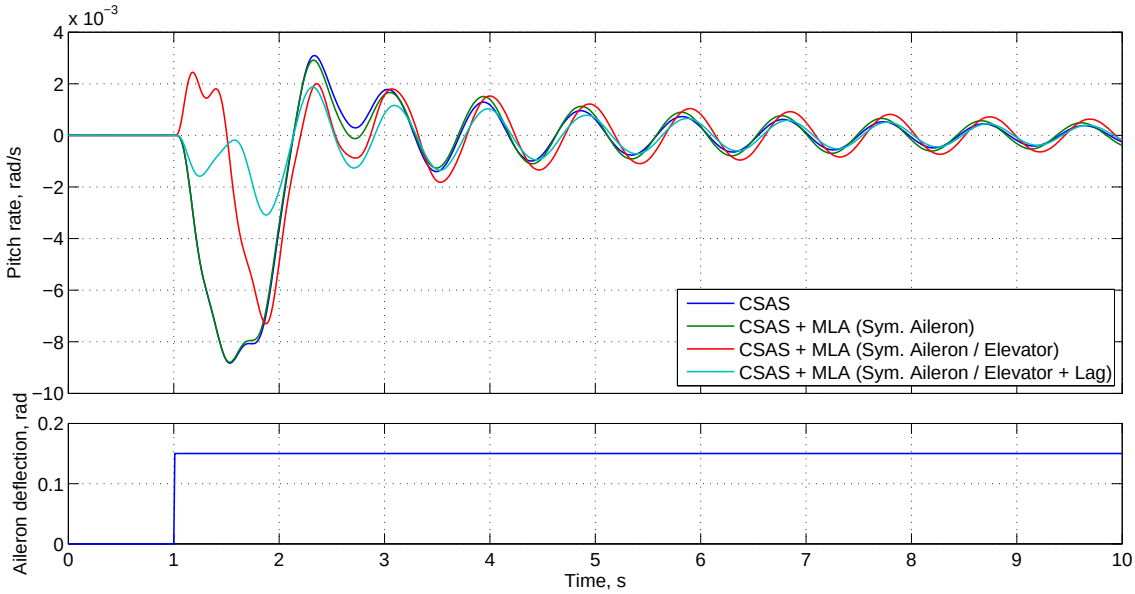

Figure 6.24: Aeroplane pitch response to symmetric aileron for CSAS and MLA with elevator pitch compensation at 4,000 ft

	4000 ft		8000 ft		12000 ft	
Mode	Frequency, rad s^{-1}	Damping	Frequency, rad s^{-1}	Damping	Frequency, rad s^{-1}	Damping
SPPO	3.840	0.6032	3.651	0.5989	3.430	0.6062
Phugoid	0.002134	0.780	0.003165	0.735	0.003230	0.770
Dutch Roll	0.6392	0.2189	0.6154	0.2342	0.6243	0.2470
Roll	$\tau = 0.3751$s		$\tau = 0.3792$s		$\tau = 0.3840$s	
Spiral	$\tau = 6.944$s		$\tau = 5.794$s		$\tau = 4.625$s	
Flexible Mode 1	6.600	0.02641	6.600	0.02833	6.526	0.03048
Flexible Mode 2	6.754	0.1243	6.730	0.1171	6.704	0.1109
Flexible Mode 3	8.046	0.1522	7.927	0.1386	7.821	0.1283
Flexible Mode 4	12.31	0.05248	12.27	0.05030	12.22	0.04866
Flexible Mode 5	13.57	0.04132	13.56	0.04041	13.55	0.03946
Flexible Mode 6	14.97	0.03466	14.97	0.03312	14.96	0.03303
Flexible Mode 7	15.13	0.03102	15.13	0.03102	15.12	0.03102
Flexible Mode 8	15.64	0.03048	15.64	0.03048	15.64	0.03048
Flexible Mode 9	17.92	0.06712	17.63	0.06043	17.36	0.05280
Flexible Mode 10	18.87	0.07546	18.49	0.06960	18.14	0.06412
Flexible Mode 11	18.94	0.05301	18.58	0.04811	18.23	0.04339
Flexible Mode 12	20.65	0.06876	19.94	0.06812	19.30	0.06503

Table 6.18: Closed-loop CSAS aeroplane longitudinal, lateral-directional and flexible dynamics at 180 m s^{-1}

the MLA system, as well as a switch to activate the MLA system only during commanded manoeuvres.

Figure 6.26 shows the response of the closed-loop aeroplane at 4,000 ft to a C* pulse demand, with and without the MLA system enabled. The response of the aeroplane in pitch with the MLA system enabled closely matches the response with the system disabled. This confirms the findings from analysis of the pole-zero characteristics that the MLA system should not interfere with the rigid-body response of the aeroplane. The symmetric aileron deflection can be seen in the response with the MLA system enabled, in addition to the compensatory elevator deflection in the elevator response.

It can be seen in Figure 6.27 that the effect of enabling MLA is a significant reduction in wing-root bending moment. The small difference in wing root shear force is a result of the increased tailplane loading due to positive compensatory elevator deflection [Figure 6.26]. Table 6.20 shows the peak wing root loading for the same manoeuvre at the three flight points considered. There is an average 6.1% reduction in wing root bending moments for the flight cases considered, while wing-root shear force is reduced by an average 2.9%.

The purpose of the MLA system is to reduce wing loading by altering the lift distribution on the wing during accelerated manoeuvres. It can be seen then that this MLA system, using normal acceleration feedback to deploy symmetric ailerons, satisfies this design criteria, providing a significant reduction in wing loading, with only a small influence on the rigid-body modes of the aeroplane.

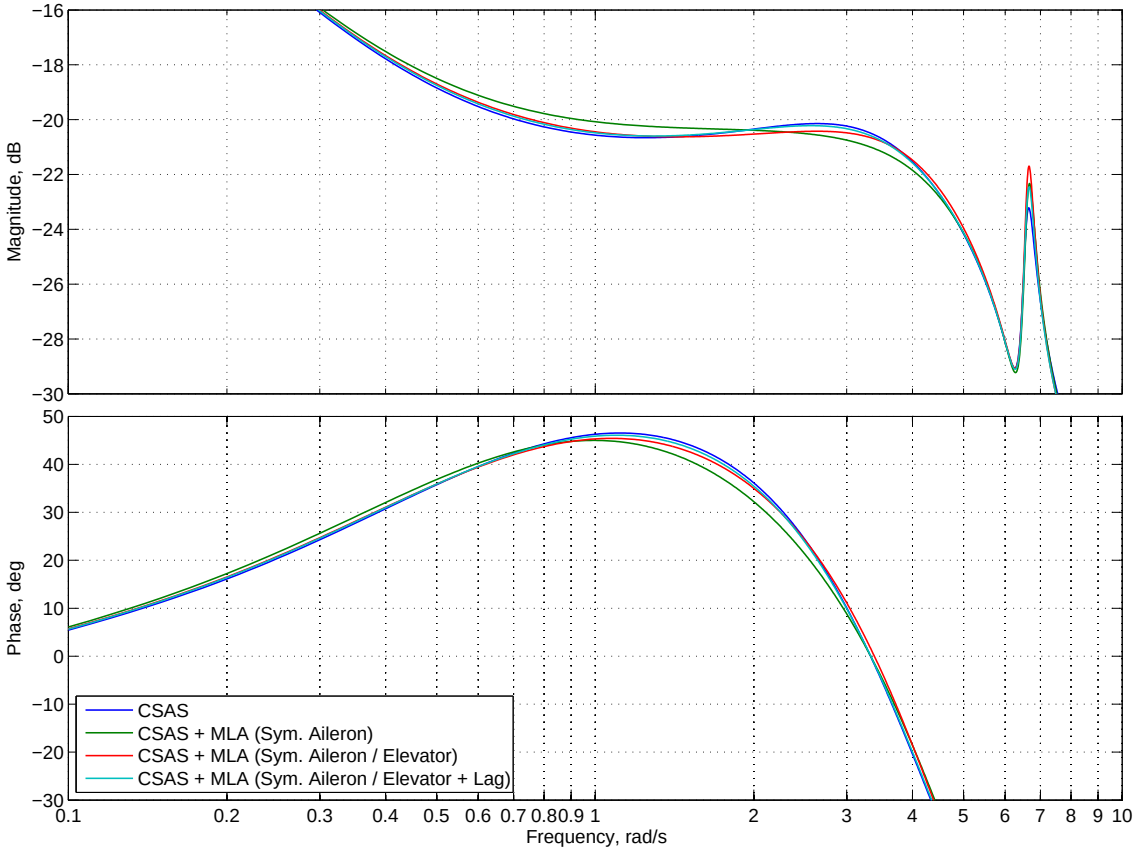

Figure 6.25: Bode plot for elevator-pitch rate response for CSAS and MLA with elevator pitch compensation at 4,000 ft

	4000 ft		8000 ft		12000 ft	
Mode	Frequency, rad s^{-1}	Damping	Frequency, rad s^{-1}	Damping	Frequency, rad s^{-1}	Damping
SPPO	3.911	0.6449	3.672	0.6231	3.414	0.6304
Phugoid	0.002048	0.7801	0.003124	0.7347	0.003227	0.7698
Dutch Roll	0.6392	0.2189	0.6154	0.2343	0.6243	0.2470
Roll	$\tau = 0.3751$s		$\tau = 0.3792$s		$\tau = 0.3840$s	
Spiral	$\tau = 6.925$s		$\tau = 5.794$s		$\tau = 4.625$s	
Flexible Mode 1	6.622	0.02340	6.581	0.02489	6.547	0.02887
Flexible Mode 2	6.754	0.1243	6.729	0.1171	6.704	0.1109
Flexible Mode 3	8.000	0.1674	7.865	0.1512	7.749	0.1370
Flexible Mode 4	12.31	0.05248	12.27	0.05030	12.22	0.04866
Flexible Mode 5	13.57	0.04132	13.56	0.04041	13.55	0.03947
Flexible Mode 6	14.97	0.03466	14.97	0.03312	14.96	0.03301
Flexible Mode 7	15.13	0.03102	15.13	0.03102	15.12	0.03102
Flexible Mode 8	15.64	0.03048	15.64	0.03048	15.64	0.03048
Flexible Mode 9	17.92	0.06712	17.63	0.05988	17.36	0.05321
Flexible Mode 10	18.87	0.07546	18.49	0.06960	18.14	0.06412
Flexible Mode 11	18.94	0.05301	18.57	0.04811	18.24	0.04339
Flexible Mode 12	20.65	0.06876	19.94	0.06812	19.30	0.06503

Table 6.19: Closed-loop MLA aeroplane longitudinal, lateral-directional and flexible dynamics at 180 m s^{-1}

	F_z, N		M_x, Nm	
Altitude, ft	CSAS	CSAS-MLA	CSAS	CSAS-MLA
4,000	-1.023×10^6	-9.942×10^5	$+1.003 \times 10^7$	$+9.379 \times 10^6$
8,000	-1.021×10^6	-9.909×10^5	$+1.033 \times 10^7$	$+9.703 \times 10^6$
12,000	-1.025×10^6	-9.951×10^5	$+1.067 \times 10^7$	$+1.007 \times 10^7$

Table 6.20: Wing-root peak loading response to C* demand with and without MLA

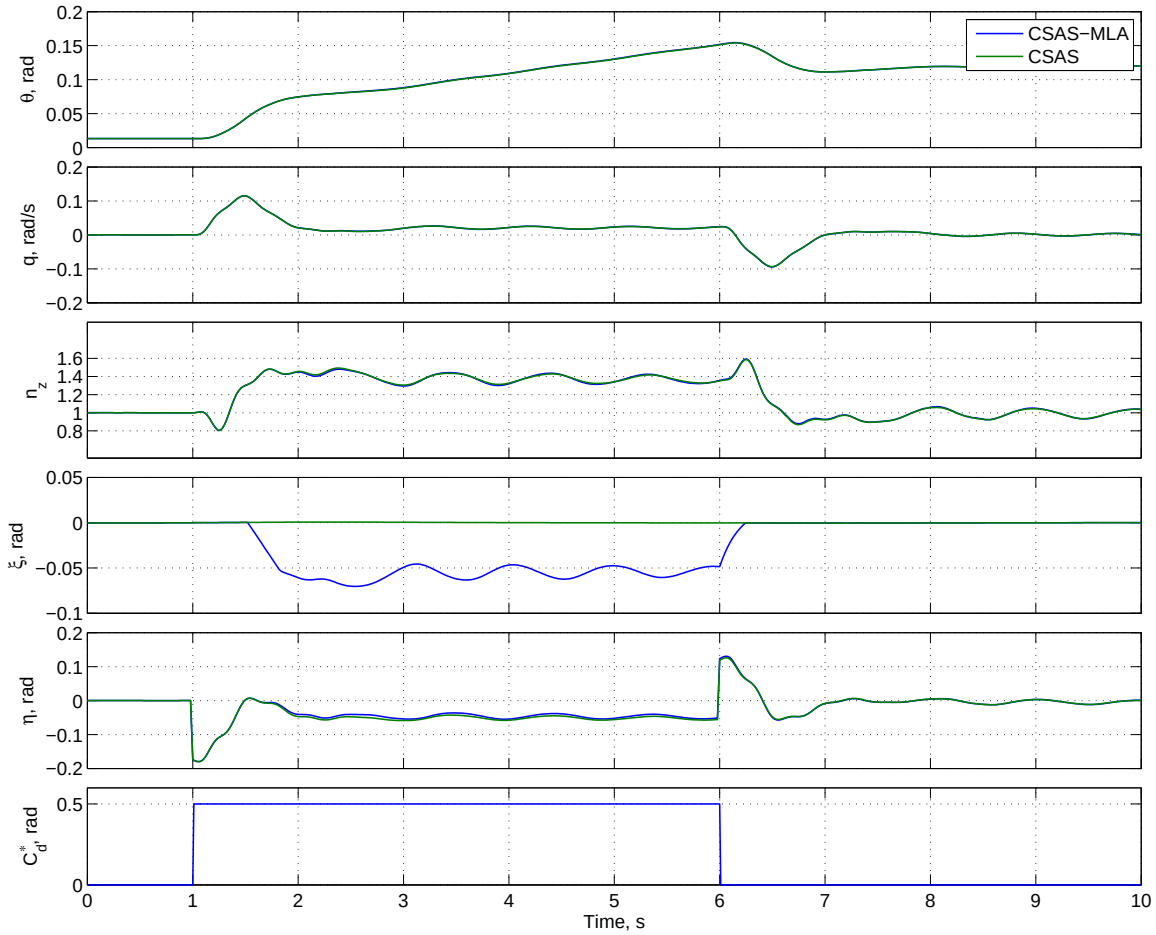

Figure 6.26: Aeroplane response to C* demand with and without MLA at 4,000 ft

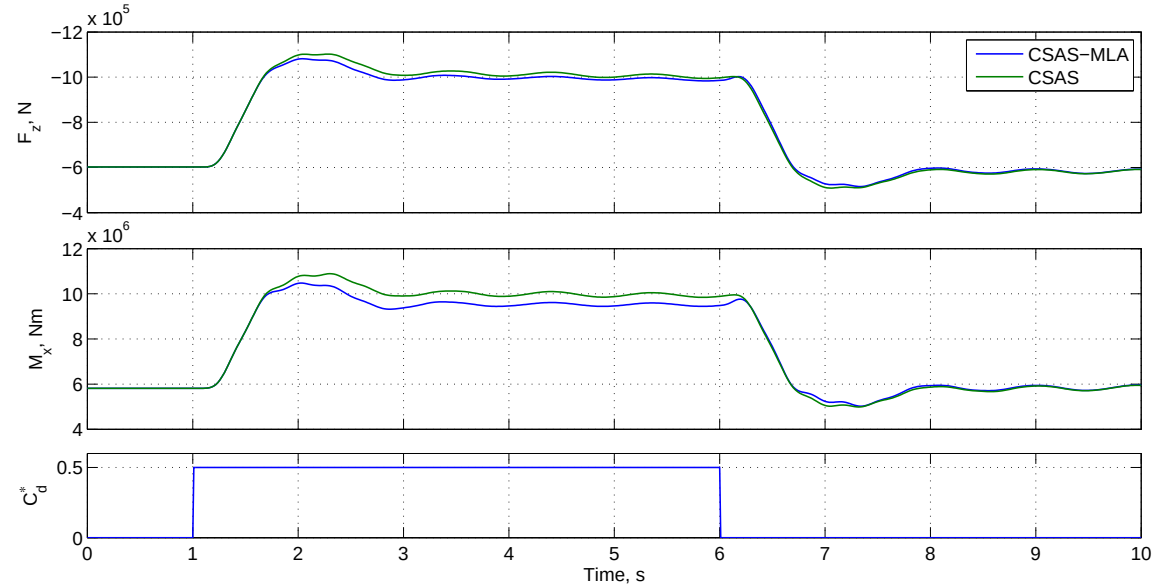

Figure 6.27: Wing root loading response to C* demand with and without MLA at 4,000 ft

6.2.2.2 Gust Load Alleviation

A Gust Load Alleviation (GLA) function has been designed in order to reduce the transient loads on the wing due to Discrete Tuned Gusts (DTG) and Continuous Turbulence (CT). A block diagram showing the structure of the control law is shown in Figure 6.28. As with the Manoeuvre Load Alleviation system, the GLA system again uses a fuselage load factor feedback loop to control aileron and elevator. The same aileron and elevator gains as the MLA system, K_g and K_e respectively, are used here. A number of flight points are again considered: 4,000, 8,000 and 12,000 ft at 180 m s^{-1}.

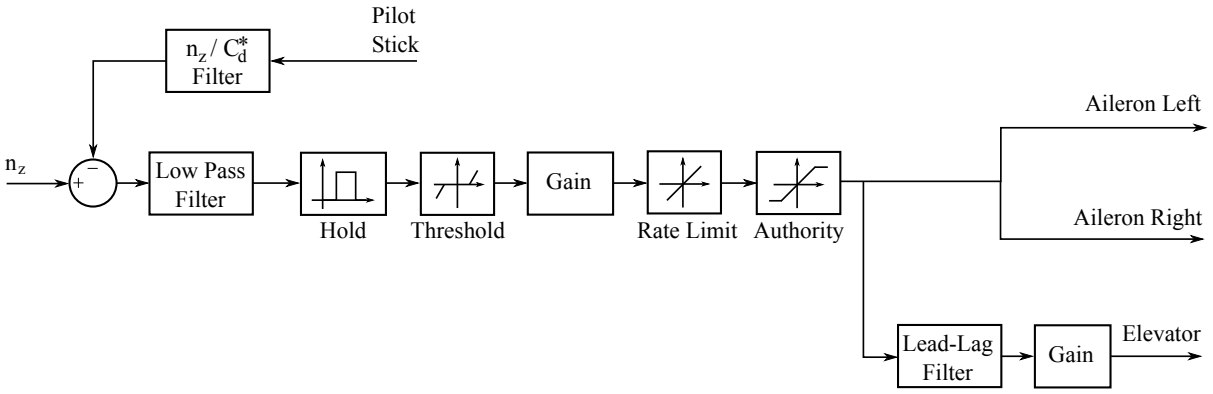

Figure 6.28: Gust Load Alleviation (GLA) controller structure

In order to reduce the interaction of the GLA system with the rigid-body dynamics, the commanded normal acceleration is subtracted from the measured acceleration [Figure 6.28]. The GLA system then acts on this acceleration value in order to reduce the wing loading. This is in order to prevent GLA activation during accelerated manoeuvres. However, in order to correctly subtract the commanded normal acceleration, it is necessary to estimate the normal acceleration response to control demand. This is made more difficult as the response changes with flight condition. For the flight points considered here, a sixth-order filter approximation of the normal acceleration response to C* demand was derived from the full-order response at an altitude of 8,000 ft [Equation 6.2.2]. This was calculated by truncating the order of the system based on the Hankel Singular Values (HSV), or "energy", of the system states. The normal acceleration response to a unit step C* demand for the transfer function approximation and the three flight points considered is shown in Figure 6.29. It can be seen that the transfer function approximation provides a close match to the full-order model at the three flight points considered, though it is unlikely this would be the case at other flight points where the longitudinal rigid-body dynamics of the aeroplane differ greatly. In reality, the choice of an appropriate filter would consider all cases within the flight envelope, however this study is limited to only the three flight points and so no other cases are considered here.

$$\frac{n_z}{C_d^*} = \frac{27.80s^6 - 1370s^5 + 7521s^4 - 49140s^3 + 24620s^2 - 343.1s + 1.054}{468.0s^6 + 2018s^5 + 26200s^4 + 70980s^3 + 31790s^2 + 1165s + 2.785} \tag{6.2.2}$$

Figure 6.30 shows the response of the aeroplane to a unit C* pulse demand with and without the GLA system. The response of the aeroplane with GLA overlays the response of the CSAS-only aeroplane exactly and the results are identical. This is because the GLA

is not activated at any point during the manoeuvre, as can be seen from the zero aileron deflection response [Figure 6.30 / 4]. This is due to the measured normal acceleration not exceeding the minimum threshold value of 0.2. While the measured normal acceleration is not cancelled completely by the filter approximation [Figure 6.30 / 3], it is sufficiently masked to cancel any commanded GLA aileron deflection.

In addition to the rate limit and authority features described for the MLA system, the GLA system includes a short hold function. The purpose of this is to minimise the transient response of the system, and prevent the controller actively tracking normal acceleration to ensure a "passive" load alleviation system. A hold of 0.5 seconds was chosen to provide good load alleviation characteristics in continuous turbulence with the rapid deployment necessary for discrete tuned gusts.

The effectiveness of the load alleviation system was considered for both Discrete Tuned Gusts (DTG) and Continuous Turbulence (CT), and is shown in Figures 6.31 and Figure 6.32 respectively for a single flight point at 4,000 ft. Table 6.21 shows the peak loading for both gusts types and all three flight points. The GLA system produces an average 4.4% and 3.0% reduction in wing root bending moment and shear force respectively for the 350ft DTG. This is reduced to 0.21% and 0.16% respectively for the 100ft gust as the effectiveness of the GLA system is limited by the maximum response rate of the system to the shorter, quicker gust length. This has the effect of shortening the critical gust length, as the gust loading for longer gust lengths is reduced below that of the shorter gust lengths by the GLA system. While the CT wind model is a stochastic function, and therefore after any period of time a gust of greater velocity magnitude is probable, the short time period analysed [Figure 6.32] is sufficient to estimate the effectiveness of the GLA system. It can be seen then in Table 6.21 that the GLA system achieves a 8.2% and 5.0% reduction in peak wing root bending moment and shear force respectively.

		F_z, N		M_x, Nm	
Altitude	Gust	CSAS	CSAS-GLA	CSAS	CSAS-GLA
4,000ft	DTG, 350ft	-1.408×10^6	-1.358×10^6	$+1.383 \times 10^7$	$+1.314 \times 10^7$
	DTG, 175ft	-1.404×10^6	-1.391×10^6	$+1.430 \times 10^7$	$+1.410 \times 10^7$
	DTG, 100ft	-1.295×10^6	-1.292×10^6	$+1.333 \times 10^7$	$+1.329 \times 10^7$
	CT	-1.156×10^6	-1.095×10^6	$+1.093 \times 10^7$	$+0.996 \times 10^7$
8,000ft	DTG, 350ft	-1.324×10^6	-1.287×10^6	$+1.336 \times 10^7$	$+1.280 \times 10^7$
	DTG, 175ft	-1.313×10^6	-1.304×10^6	$+1.367 \times 10^7$	$+1.353 \times 10^7$
	DTG, 100ft	-1.212×10^6	-1.210×10^6	$+1.273 \times 10^7$	$+1.271 \times 10^7$
	CT	-1.086×10^6	-1.034×10^6	$+1.085 \times 10^7$	$+0.989 \times 10^7$
12,000ft	DTG, 350ft	-1.247×10^6	-1.218×10^6	$+1.291 \times 10^7$	$+1.245 \times 10^7$
	DTG, 175ft	-1.229×10^6	-1.224×10^6	$+1.308 \times 10^7$	$+1.299 \times 10^7$
	DTG, 100ft	-1.136×10^6	-1.135×10^6	$+1.220 \times 10^7$	$+1.218 \times 10^7$
	CT	-1.027×10^6	-0.984×10^6	$+1.032 \times 10^7$	$+0.982 \times 10^7$

Table 6.21: Wing-root peak loading response to Discrete Tuned Gust (DTG) and Continuous Turbulence (CT) with and without GLA

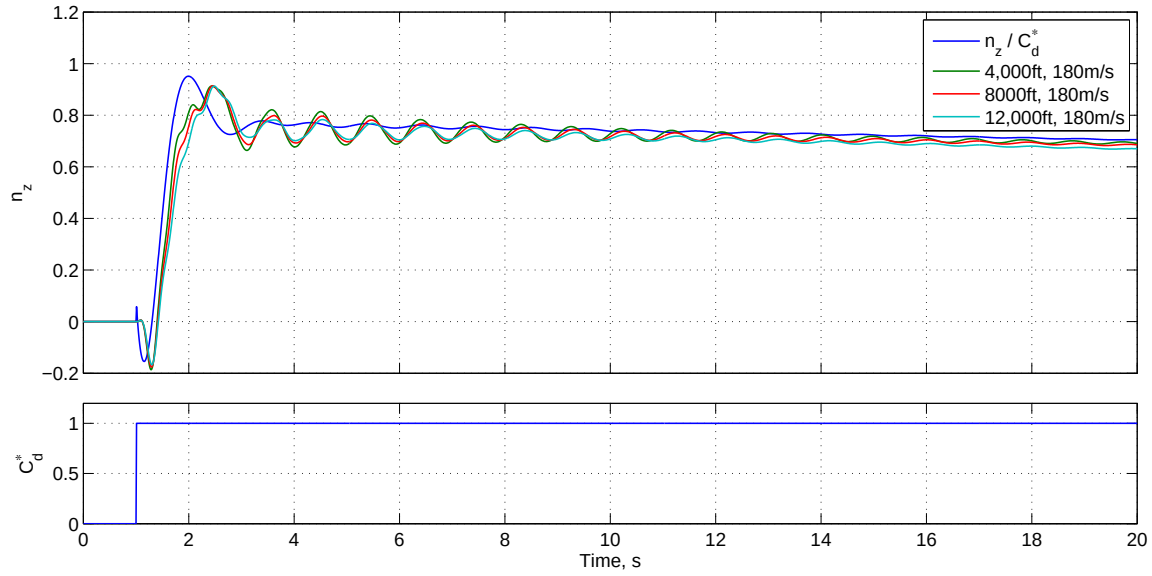

Figure 6.29: Aeroplane normal acceleration and longitudinal approximation response to unit step C* demand

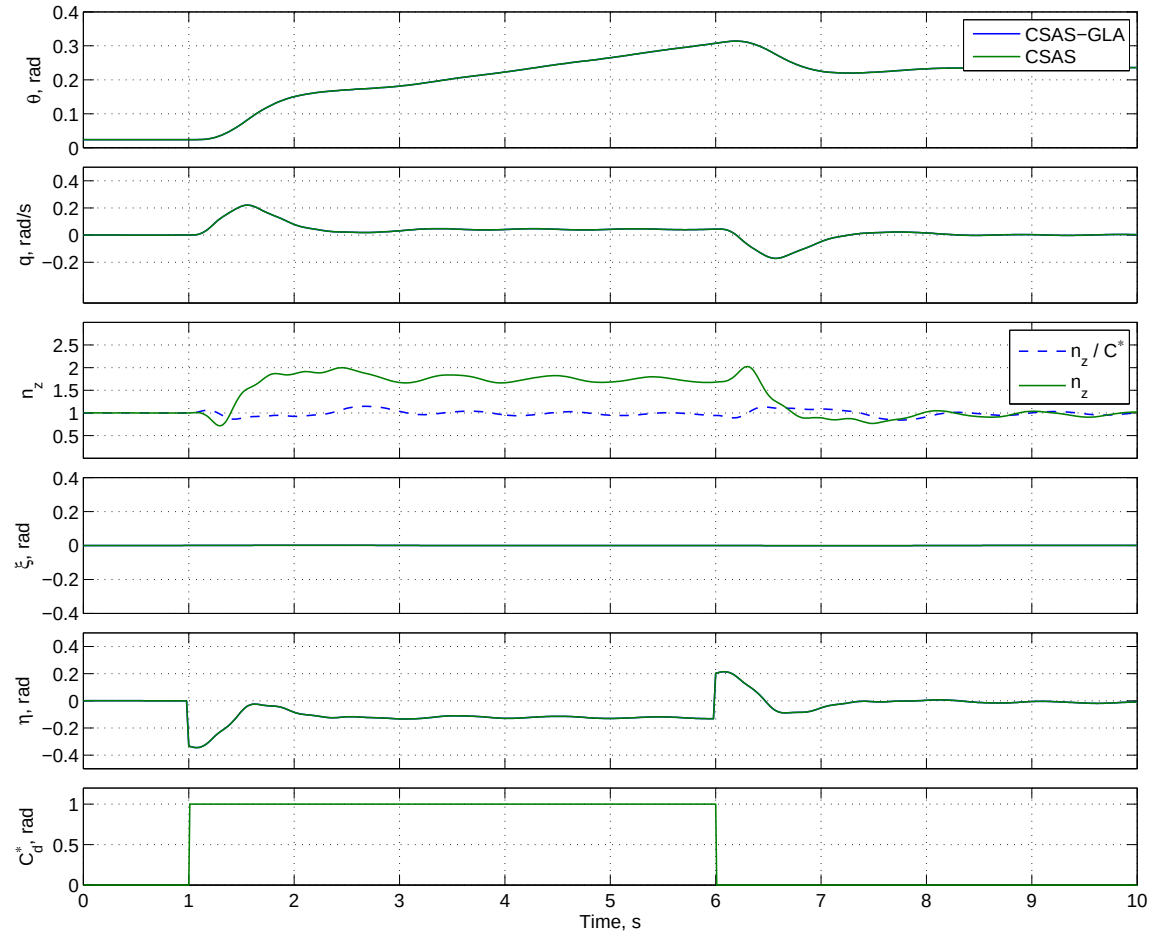

Figure 6.30: Aeroplane response to C* demand with and without GLA at 8,000 ft

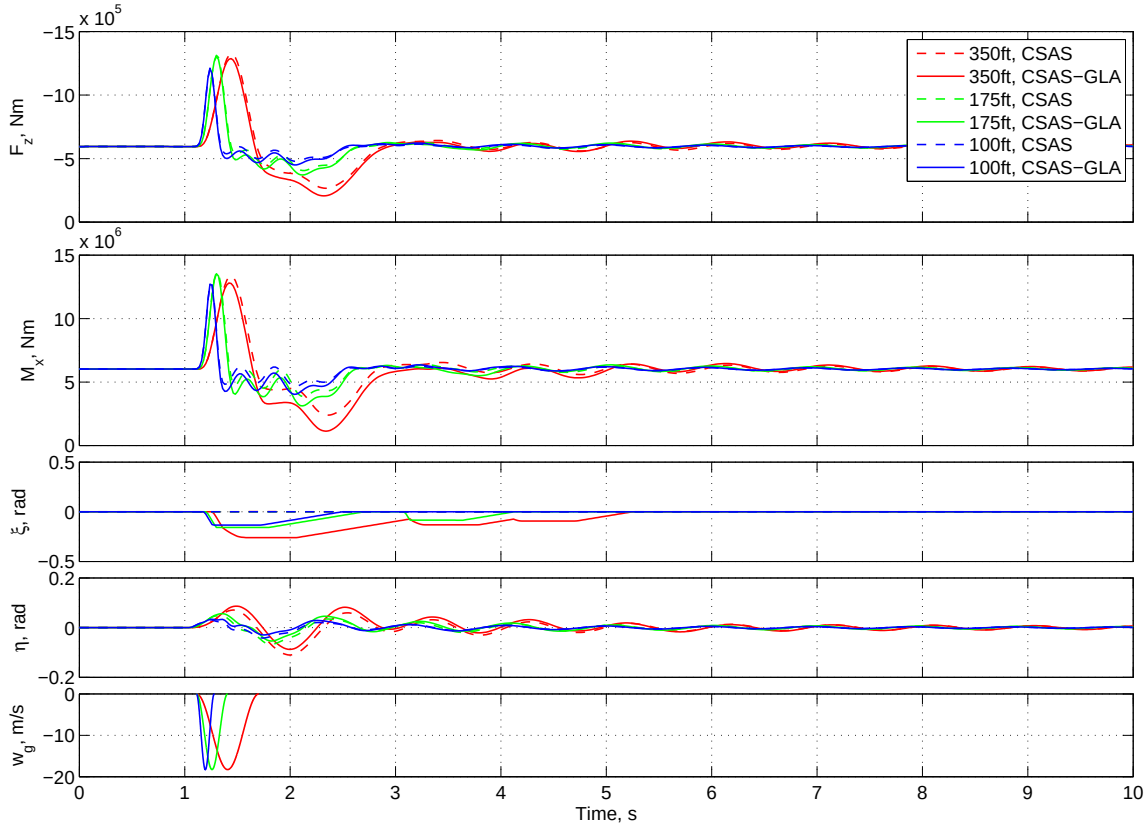

Figure 6.31: Wing root loading response to Discrete Tuned Gust (DTG) with and without GLA at 4,000 ft

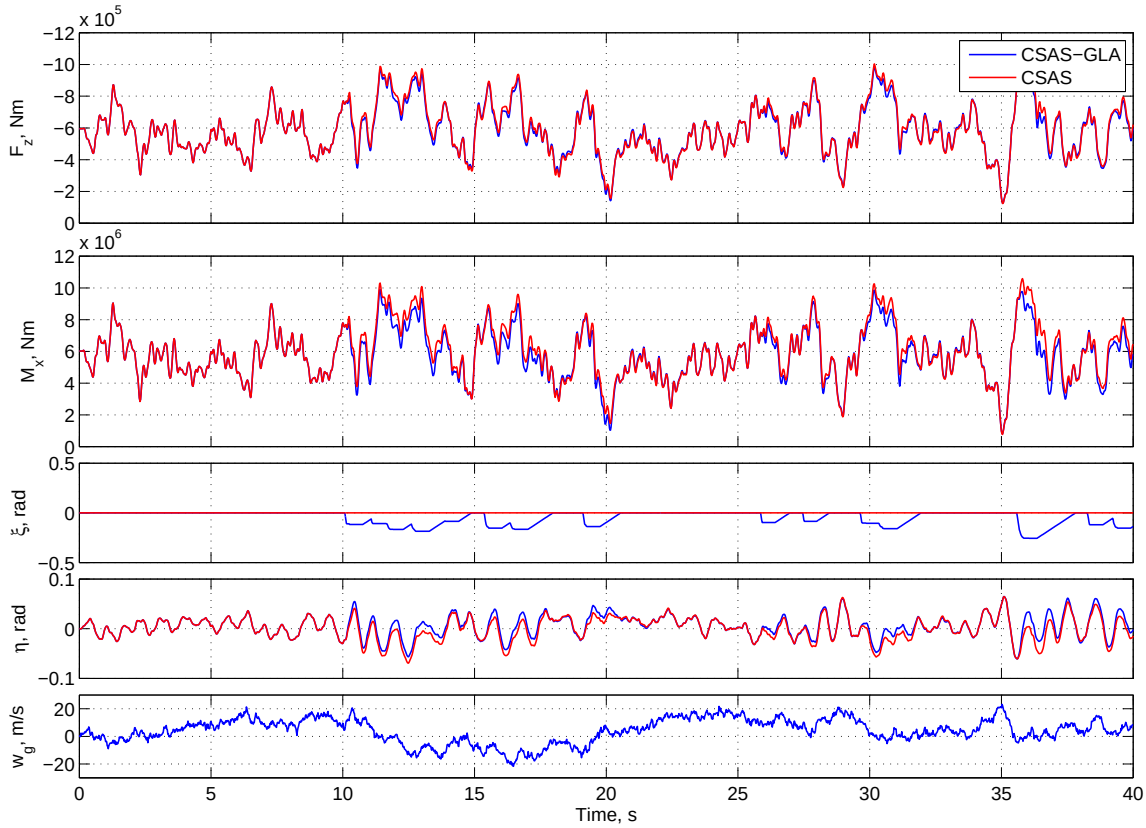

Figure 6.32: Wing root loading response to Continuous Turbulence (CT) with and without GLA at 4,000 ft

6.2.2.3 Active Mode Control

In order to improve the damping of one, or a number of, flexible modes, structural mode acceleration feedback can be used. Here, additional accelerometers are specified, and acceleration feedback is used to improve structural damping of the first wing bending mode. Gain selection is achieved using the second Model B model variant, not including the effects of unsteady aerodynamics, and the results again compared with the full Model C aeroelastic variant. A number of flight points are again considered: 4,000, 8,000 and 12,000 ft at 180 m s^{-1}. The closed-loop CSAS dynamic and stability characteristics of the aeroplane model are given previously in Table 6.18.

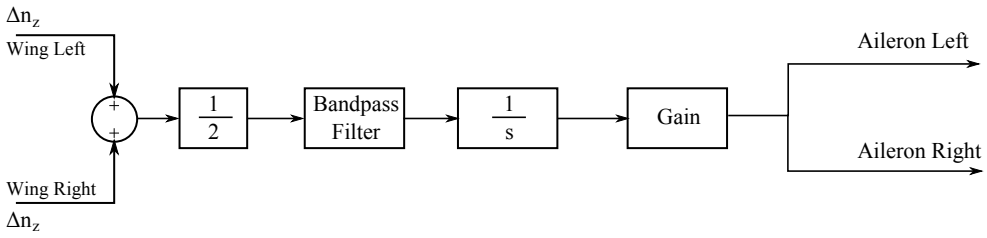

Figure 6.33: Active Mode Control (AMC) controller structure

The structure of the Active Mode Control (AMC) law is given in Figure 6.33. In order to measure the acceleration component of the first wing bending mode, accelerometers must be selected and located on the wing. The value from these accelerometers is averaged to isolate the symmetric component of the acceleration. A band-pass filter, which must be designed, is used to isolate the mode of interest, and the signal is integrated in order to provide the correct control phasing for damping improvement. In order to select the correct structure for the control law however, it is important to understand the influence of the control inputs, i.e. the aircraft control surfaces, on the modal response of the structure.

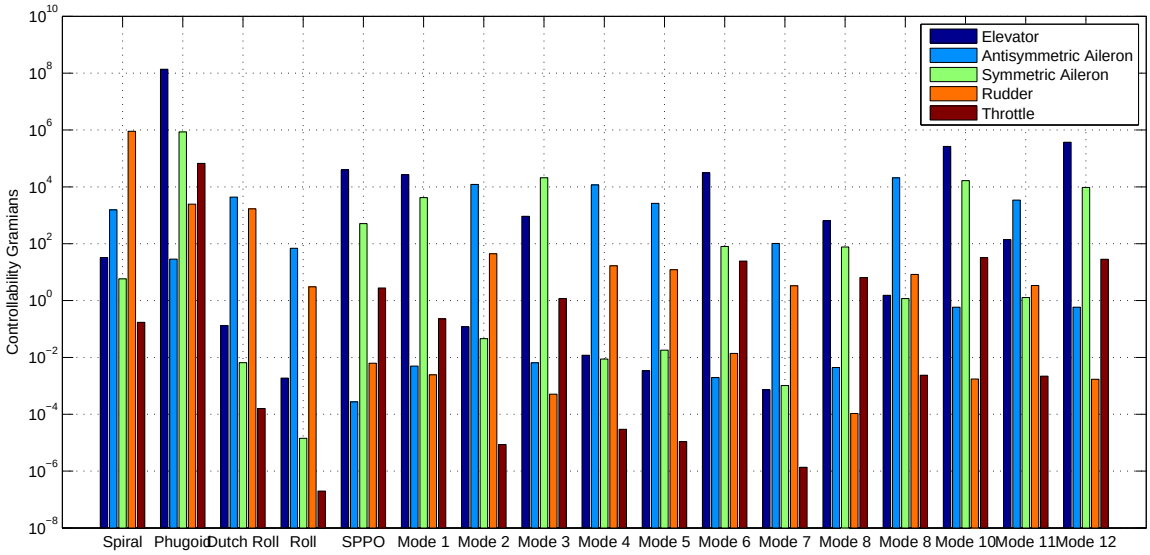

Figure 6.34: Aeroplane system controllability gramians at 180 m s^{-1} and 4,000 ft

Controllability and observability gramians are a valuable tool to determine the influence of the control inputs and outputs on a system's response. Controllability and observability are important properties of any system. A system may be considered controllable, or more formally completely state controllable, if for any given system of n-th order there exists a state variable feedback control law that makes it possible to move all of its open-loop poles to any arbitrary position so that it is possible to completely define the n-th order closed-loop characteristic polynomial of the system. The observability of a system is the dual of its controllability. A system may be described as being completely observable if the internal states of a system may be completely and uniquely inferred at any time from the system's output [Dorf and Bishop, 2001; Franklin et al., 2002].

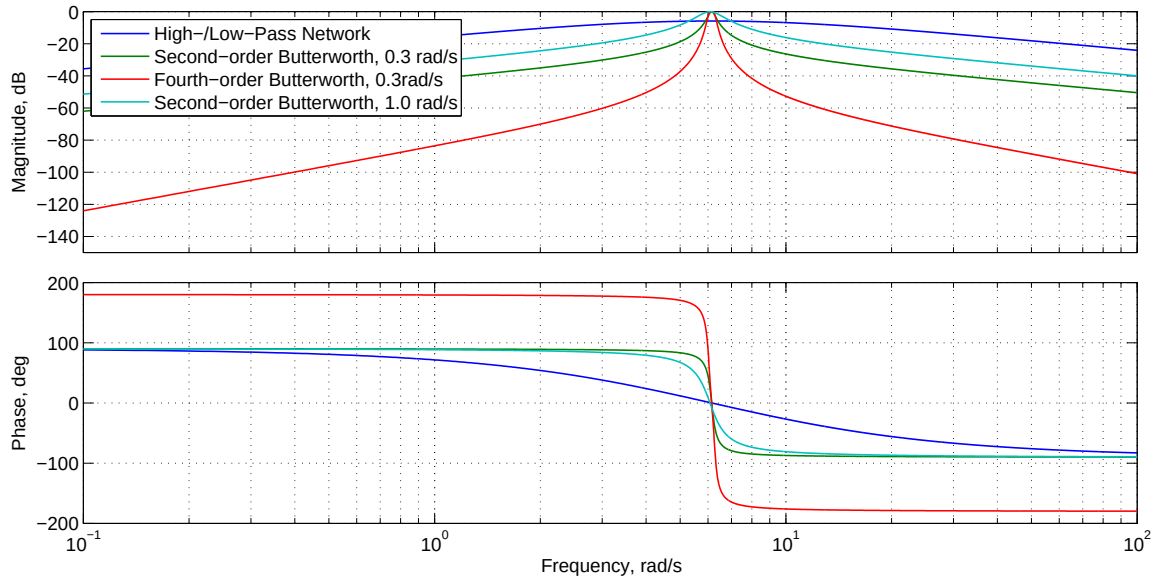

Figure 6.35: Bode plot for first- and second-order accelerometer filters

For a time-invariant system, the controllability and observability gramians are given by the solution to the Lyapunov equations. Figure 6.34 shows the controllability gramians for the linearised aeroplane model at 180 m s^{-1} and 4,000 ft. Controllability gramians can be used to determine the influence of multiple inputs on the system's states in a multiple input system, such as the aeroplane model considered here. It is clear that different inputs, in this case control surface deflections, influence the rigid-body and flexible modes of the aircraft differently; this is reflected by the controllability gramians of the system. For example, the rigid-body longitudinal phugoid mode is seen to be controllable using elevator, symmetric aileron and throttle, while anti-symmetric aileron and rudder can be seen to have little effect. It can also be seen that the first two flexible modes, symmetric and anti-symmetric first wing bending respectively, are controllable using symmetric, i.e. elevator, throttle, and symmetric aileron, and asymmetric, i.e. anti-symmetric aileron and rudder, control deflections respectively. In order to improve the first wing bending mode damping ratio, while minimising the influence on the longitudinal rigid-body aircraft characteristics, symmetric aileron control was selected for use in the AMC law.

In order to isolate the acceleration of the first wing bending mode, a band-pass filter was used to filter the feedback signal. A number of band-pass filters were considered, including a high- and low-pass filter network [Anon., 1980], first- and second-order Butterworth filters with a frequency range of 0.3 and 1.0 rad s^{-1}:

$$F_1 = \frac{6.30s}{(s+6.00)(s+6.30)} \tag{6.2.3a}$$

$$F_2 = \frac{0.300s}{s^2+0.300s+37.8} \tag{6.2.3b}$$

$$F_3 = \frac{0.0947s^2}{(s^2+0.209s+36.5)(s^2+0.216s+39.1)} \tag{6.2.3c}$$

$$F_4 = \frac{s}{s^2+s+37.8} \tag{6.2.3d}$$

Figure 6.35 shows the phase and gain characteristics of the four filters. The high- and low-pass filter network provides a gentle phase roll-off, however this accompanies an equally gentle drop-off in gain, dropping only 2.1dB at the SPPO rigid-body frequency. As a result, use of this filter in the feedback control law has a significant influence on the rigid-body modes, reducing the damping of the SPPO mode significantly. Second- and fourth-order Butterworth filters, with a frequency range of 0.3 rad s^{-1} can be seen to have good gain characteristics, with a drop-off of 30.1 and 60.2 dB at the SPPO frequency respectively. The phase roll-off gradient for the fourth-order filter is high however, and has significant phase lead and lag above and below the filter band-pass frequency respectively. A fourth filter, a second-order Butterworth filter with frequency range 1.0 rad s^{-1}, was also considered. This filter has similar characteristics to the first second-order Butterworth filter considered, as would be expected, but has a less steep drop-off in phase and gain, particularly at the second wing bending mode frequency, dropping 7.2dB compared to 16.3dB for the first Butterworth filter considered.

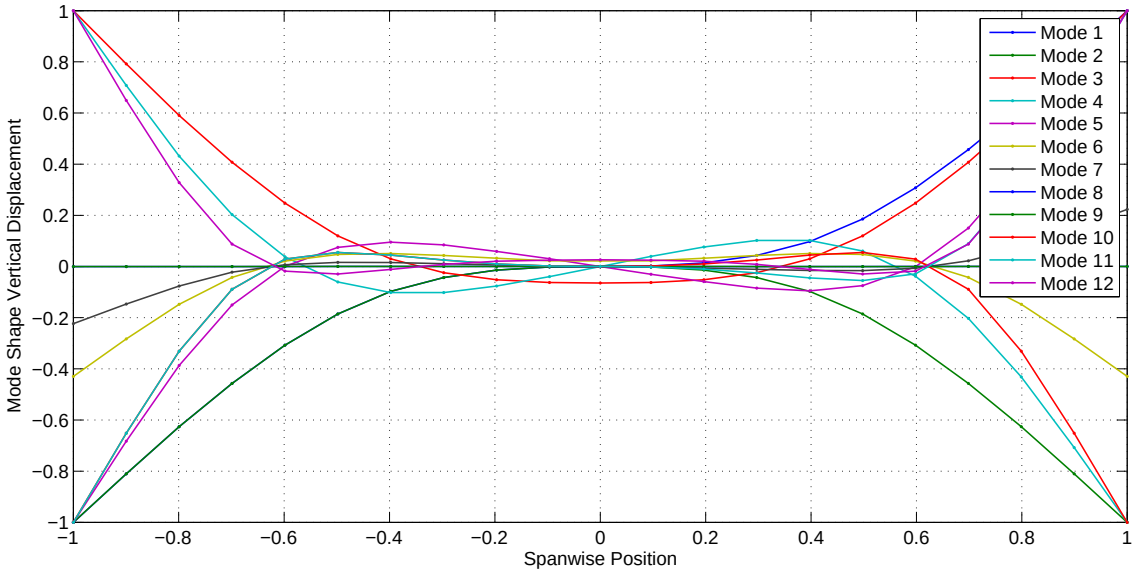

Figure 6.36: Aeroplane wing spanwise mode shapes

Figure 6.37 / 1 shows the response of the four filters to wing acceleration following a unit step load input. The accelerometer is located in this case at the wing tip. The absolute response of the first wing bending mode is shown for comparison. The gentle gain drop-off of the high- and low-pass filter network is reflected in the response of the

filter including much of the response of the higher frequency modes. The second- and fourth-order Butterworth filters successfully filter much more of the higher frequency modes, though the fourth-order filter is much slower to track the input signal. The second-order Butterworth filter was chosen for use in the AMC law, with a frequency range of 1.0 rad s^{-1} to allow for small changes in the first wing bending mode frequency with flight point.

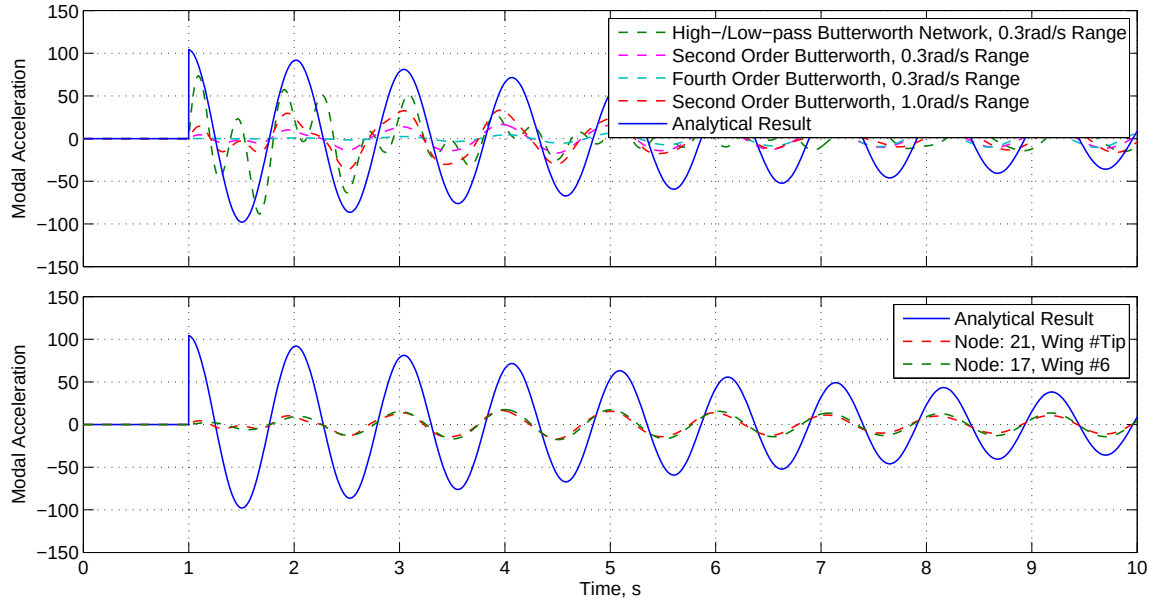

Figure 6.37: Wing accelerometer and filtered response to unit load

The location of the wing accelerometers used to measure the vertical wing bending acceleration must be specified. It is convenient here then to select an accelerometer location such that the ratio of the first wing bending mode acceleration to the total measured acceleration is greatest. This is achieved by consideration of the structural mode shapes for the wing [Figure 6.36]. It can be seen that locating the accelerometers at the wing tip would provide the largest amplitude vertical acceleration for the first wing bending mode (Mode 2, where the asymmetric first wing bending mode is Mode 1). However, this is also an anti-node point for many of the other modes, and so the total measured acceleration would include the acceleration components of these modes. A more ideal position would be at 60% of the wing span, which is a node point for many of the higher frequency modes. The result of locating the accelerometer at the wing tip (Node 21) and 60% of the wing span (Node 17) is shown in Figure 6.37. Figure 6.37 / 2 shows the measured acceleration for an accelerometer located at these two locations, filtered using the second-order Butterworth filter, for a unit step load. It can be seen that the initial response of the accelerometer located at the wing tip includes higher frequencies modes. As these higher frequency modes have higher damping ratios and their response is quickly damped out, the signals from both accelerometers match more closely. The 60% wing span accelerometer location was selected for use in the AMC law.

The selection of the appropriate feedback gains was achieved using a root-locus plot, shown in Figure 6.38 for the linearised flexible structural model at 180 m s^{-1} and 12,000 ft. It can be seen that the influence of wing accelerometer feedback to symmetric aileron has a stabilising influence on the first wing bending mode, increasing damping from 0.0765 to 0.117 for a gain of 0.0302. However, for the same gain feedback is destabilising for the

second wing bending mode, reducing damping from 0.173 to 0.133. The influence on the rigid-body modes is minimal, increasing SPPO damping by 0.004 to 0.639 for the same gain, and having no measurable influence on the phugoid mode.

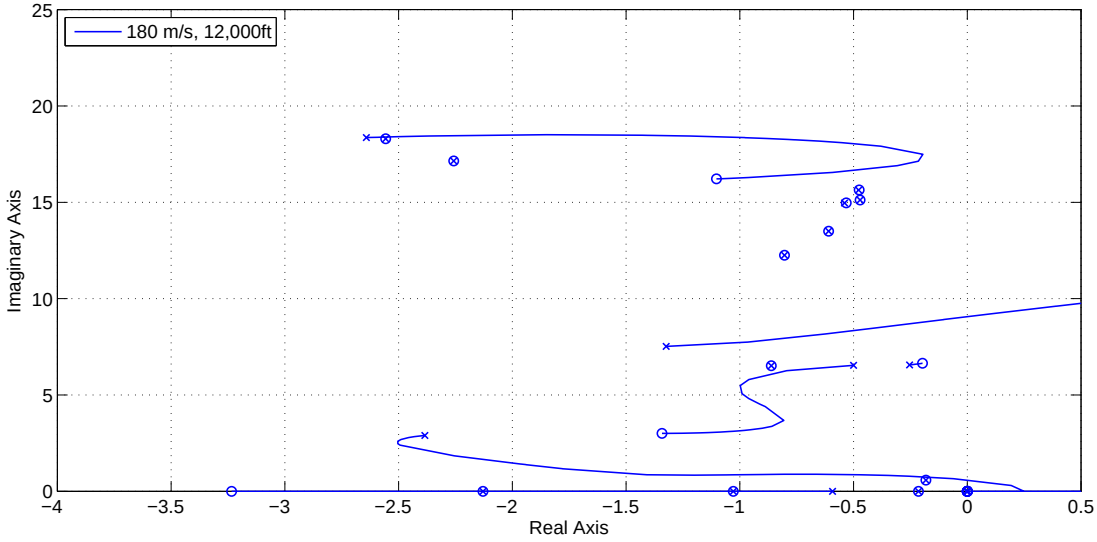

Figure 6.38: Root-locus plot for AMC wing accelerometer feedback at 12,000 ft

With the inclusion of unsteady aerodynamics, the open-loop damping of the second wing bending mode is reduced, from 0.165 to 0.123. The first wing bending mode is less affected, with damping only reduced from 0.0464 to 0.0421. Given this, a gain, K_a, was selected in order to provide a relatively high damping ratio, greater than 0.10, for both first and second wing bending modes [Table 6.22].

	Flight Point		
Gain	4000 ft	8000 ft	12000 ft
K_a	0.03021	0.03238	0.03481

Table 6.22: Closed-loop system AMC controller gains at 180 m s^{-1}

	4000 ft		8000 ft		12000 ft	
Mode	Frequency, rad s^{-1}	Damping	Frequency, rad s^{-1}	Damping	Frequency, rad s^{-1}	Damping
SPPO	3.838	0.6071	3.650	0.6030	3.428	0.6098
Phugoid	0.002398	0.7801	0.003180	0.7352	0.003276	0.7701
Dutch Roll	0.6392	0.2191	0.6151	0.2342	0.6239	0.2468
Roll	$\tau = 0.3751$s		$\tau = 0.3789$s		$\tau = 0.3843$s	
Spiral	$\tau = 6.925$s		$\tau = 5.794$s		$\tau = 4.625$s	
Flexible Mode 1	6.475	0.1080	6.458	0.1080	6.441	0.1080
Flexible Mode 2	6.754	0.1243	6.729	0.1172	6.704	0.1108
Flexible Mode 3	8.029	0.1251	7.935	0.1114	7.850	0.1008
Flexible Mode 4	12.31	0.05232	12.27	0.05049	12.22	0.04917
Flexible Mode 5	13.57	0.04158	13.56	0.04037	13.55	0.03887
Flexible Mode 6	14.97	0.03423	14.97	0.03332	14.96	0.03324
Flexible Mode 7	15.13	0.03089	15.13	0.03108	15.12	0.03103
Flexible Mode 8	15.64	0.03023	15.64	0.03023	15.64	0.03023
Flexible Mode 9	17.92	0.06701	17.63	0.06041	17.36	0.05297
Flexible Mode 10	18.87	0.07471	18.49	0.06810	18.14	0.06430
Flexible Mode 11	18.94	0.05321	18.57	0.04811	18.24	0.04251
Flexible Mode 12	20.65	0.06872	19.94	0.06814	19.30	0.06504

Table 6.23: Closed-loop AMC aeroplane longitudinal, lateral-directional and flexible dynamics at 180 m s^{-1}

This page is intentionally left blank.

CHAPTER 7

Handling Qualities Assessment

In this chapter, the influence on unsteady aerodynamics and structural flexibility, including airframe component stiffness, on the longitudinal and lateral-directional handling qualities of the flexible aircraft is assessed using existing handling qualities criteria and specifications. The impact of LAF systems, including Manoeuvre Load Alleviation (MLA), Gust Load Alleviation (GLA) and Active Mode Control (AMC), on the closed-loop aeroplane handling and flying qualities is also reviewed.

7.1 Structure and Aerodynamics

In order to investigate the influence of structural dynamics and unsteady aerodynamics on the lateral handling qualities of the aeroplane, a number model variants were developed and analysed, and the results compared. A single degree of freedom reduced-order model was developed to investigate the roll response of the aircraft to asymmetric aileron input in both the frequency- and time-domain. The four model variants considered are:

- **Model A: Rigid Aeroplane**
  The model dynamics are defined by the standard rigid-body equations of motion. Structural flexibility, either elastic or quasi-rigid, is not considered. Unsteady aerodynamics are not considered.
- **Model C: Aeroelastic Aeroplane, including Elastic Structural Flexibility and Unsteady Aerodynamics**
  The standard rigid-body equations of motion, applying the mean-axis system approximations, describe the aeroplane rigid body dynamics. The structure is assumed to deform elastically, the dynamic response including damping and inertial effects. Unsteady aerodynamics are included, and the build-up of aerodynamic forces described by the indicial aerodynamic model.
- **Model D: Aeroelastic Aeroplane, including Unsteady Aerodynamics**
  The model dynamics are defined by the standard rigid-body equations of motion.

Structural flexibility, either elastic or quasi-rigid, is not considered. Unsteady aerodynamics are included, and the build-up of aerodynamic forces described by the indicial aerodynamic model.

- **Model E: Aeroelastic Aeroplane, including Quasi-static Structural Flexibility and Unsteady Aerodynamics**
  The standard rigid-body equations of motion, applying the mean-axis system approximations, describe the aeroplane rigid body dynamics. The structure is assumed to deform quasi-statically, and reach its steady-state deflection under loading instantaneously. Unsteady aerodynamics are included, and the build-up of aerodynamic forces described by the indicial aerodynamic model.

Assuming the aileron deflection is small, the lateral response of the aircraft to the control input can be seen to involve almost pure rolling motion, with little or no coupling in side-slip and yaw [Cook, 1997]. The reduced-order model for the roll response due to aileron with fixed rudder, representing the roll subsidence mode, can then be expressed by:

$$\dot{p} = \frac{L}{I_{xx}} \tag{7.1.1}$$

where $\dot{p}$ is the roll acceleration, and I_{xx} is the moment of inertia about the x-axis. In agreement with the use of the mean-axis system, the rolling moment L is defined about the instantaneous centre of gravity. Each of the models was trimmed in steady, level flight at 165 m s^{-1} and 7,000 ft. The heavy mass configuration, with a total mass of 252,210 kg, defined in Appendix B is used here.

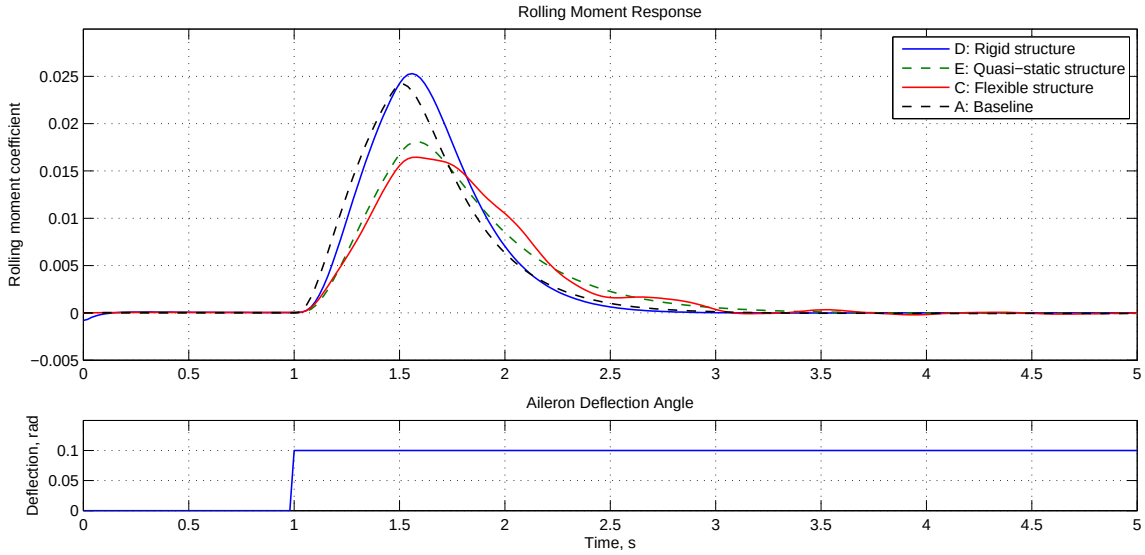

Figure 7.1: Rolling moment coefficient response of reduced-order aircraft model to aileron step input

Analysis of the aircraft response to aileron was first compared in the time-domain. Figure 7.1 shows the rolling moment response of the aeroplane to an asymmetric aileron step

input. It can be seen that both the quasi-static and elastic structural models, Models E and C respectively, predict the static aeroelastic reduction in control surface effectiveness; this is evident in the reduction in the peak rolling moment. The full aeroelastic Model C in addition also predicts the dynamic aeroelastic effects, namely the effect of the time-dependent oscillatory structural motion on the build-up and peak rolling moment. All three aeroelastic variants exhibit a delay in the build-up of rolling moment compared to the baseline rigid Model A as a result of a combination of structural dynamics and unsteady aerodynamics.

The resultant time histories for aircraft roll rate, p, and bank angle, ϕ, are shown in Figure 7.2. The short delay in the build-up of rolling moment for the unsteady aerodynamic Model D variant manifests itself as a lag in the roll response of the aeroplane. A much larger lag in the roll response of the quasi-static structural Model E variant is also visible when compared to the classical rigid aeroplane Model A response. The roll mode time constant, T_R, is an important measure of the aircraft's handling qualities. It is calculated here from the time taken for the roll-rate response to aileron step input to reach 63.2% of the steady-state value. The time constant T_R is increased from 0.6822 seconds for the baseline, rigid aeroplane Model A to 0.9068 seconds for the full aeroelastic Model C, while the time constant of the quasi-static Model E matches closely that of the fully flexible model at 0.8641 seconds. The time constant for each of the four model variants is given in Table 7.1.

The lateral-directional handling qualities of an aircraft are a function of the roll damping, which is expressed in terms of the roll-mode time constant. Increases in the roll mode time constant are known to make the aircraft response to pilot control "sluggish" [Cook, 1997]. MIL-STD-1797A [1990] stipulates a maximum Level 1 roll-mode time constant of 1.4 seconds for all flight phase categories for Class III aircraft. While all model variants here are within this limit, there is a significant increase in the time constant from the classical rigid aircraft model, and it can be expected that for some flight conditions this would result in degraded handling qualities.

Model Variant	Time constant, s
A: Baseline	0.6822
D: Rigid structure	0.7213
E: Quasi-static structure	0.8641
C: Flexible structure	0.9068

Table 7.1: Roll mode time constant for aeroelastic and baseline model variants

The frequency response of the non-linear model was estimated from a Fourier analysis of the time history of the response of aeroplane bank angle to asymmetric aileron deflection. A sinusoidal, or "chirp", signal with linearly increasing frequency (0.1–10 rad s^{-1}) and constant amplitude was used as the aileron input signal. Analysis of the frequency response for aileron to roll attitude [Figure 7.3] shows that at low frequencies the quasi-static Model E matches the fully flexible Model C closely, with both models predicting the reduction in gain output associated with static aeroelastic control effectiveness. At higher frequencies however, the quasi-static Model E does not predict the interaction of structural modes with the rigid-body response at 8 and 18 rad s^{-1} and its effect on the gain and phase characteristics of the rigid-body aircraft. The bandwidth, ω_{BW}, of the

aircraft is the highest frequency at which some tracking task can be performed without threatening its stability. It is defined as the lower of two values, the phase and gain bandwidths. The roll-off in phase for a high-order aircraft above the bandwidth frequency can be approximated by the linear roll-off in phase given by a time delay. The phase delay here is again calculated using the equation [Hoh et al., 1982]:

$$\tau_p = \frac{-\left(\phi_{2\omega_{180}} + 180\right)}{(57.3 \times 2\omega_{180})} \tag{7.1.2}$$

The bandwidth of the classical rigid aircraft Model A is reduced from 2.089 to 1.612 rad s^{-1} for the full aeroelastic Model C [Table 7.2]. The phase delay for the classical rigid Model A aircraft is also increased, from 0.1921 seconds to 0.2974 seconds for the full aeroelastic model. There has been relatively little research into equivalent system models for the lateral and directional aircraft response, and MIL-STD-1797A [1990] only specifies minimum requirements for bandwidth for longitudinal pitch response. MIL-STD-1797A [1990] does however specify a maximum value for the roll-attitude phase delay, though these limits are taken directly from the longitudinal pitch requirements. Increases in the phase delay of the aircraft and a reduction in the bandwidth are known to degrade the aircraft handling qualities and increase susceptibility to Pilot Induced Oscillations (PIOs) [Hoh et al., 1982]. If we apply the maximum allowed phase delay requirements specified in MIL-STD-1797A [1990] for longitudinal, and therefore lateral-directional, control, and the results should therefore be treated with caution, we could expect that the handling qualities would be reduced from Level 2 to Level 3 by the inclusion of structural dynamics and unsteady aerodynamics [Figure 7.4].

Model Variant	Bandwidth, rad s^{-1}	Phase delay, s
A: Baseline	2.089	0.1921
D: Rigid structure	2.004	0.2340
E: Quasi-static structure	1.653	0.2548
C: Flexible structure	1.612	0.2974

Table 7.2: Bandwidth and phase delay for aeroelastic and baseline model variants

7.2 Airframe Stiffness

The mode shapes of an aeroplane are often a complex coupled function of many different airframe components, e.g. wing and engine. The aircraft designer is likely to define the required strength and stiffness of a structural component. The relationship between stiffness and frequency is easily defined for a simple component. It is not so clear however how a change in the stiffness of a single component, e.g. the fuselage, might influence both the natural frequencies and mode shapes of the complete aeroplane. Instead of scaling the natural frequencies of all or some of the modes arbitrarily, the mode shape set here is calculated for a modified stiffness model of the aeroplane. This is not entirely representative of an actual modification of the airframe stiffness, which would likely be achieved only together with a change in airframe mass. However, it provides a more useful

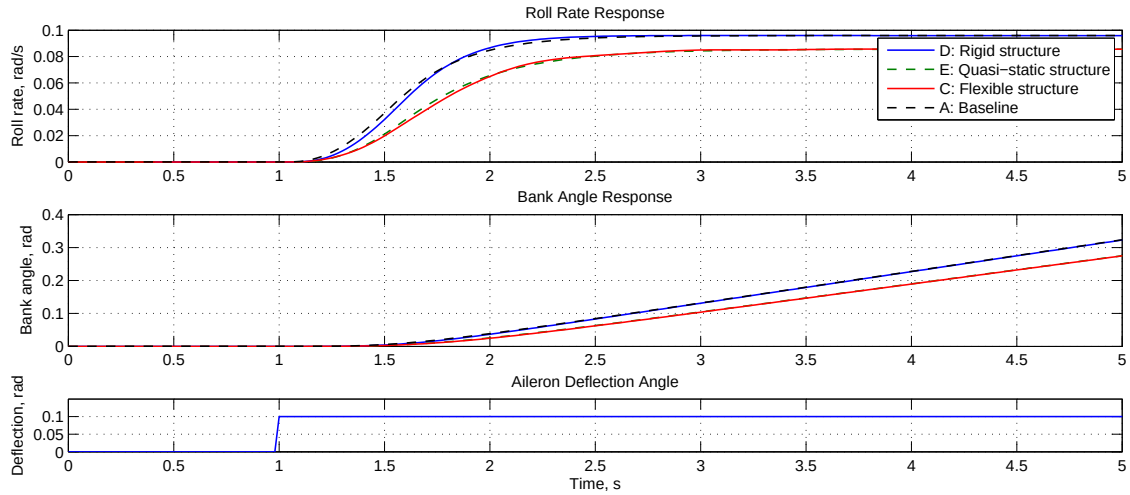

Figure 7.2: Roll response of reduced-order aircraft model to aileron step input

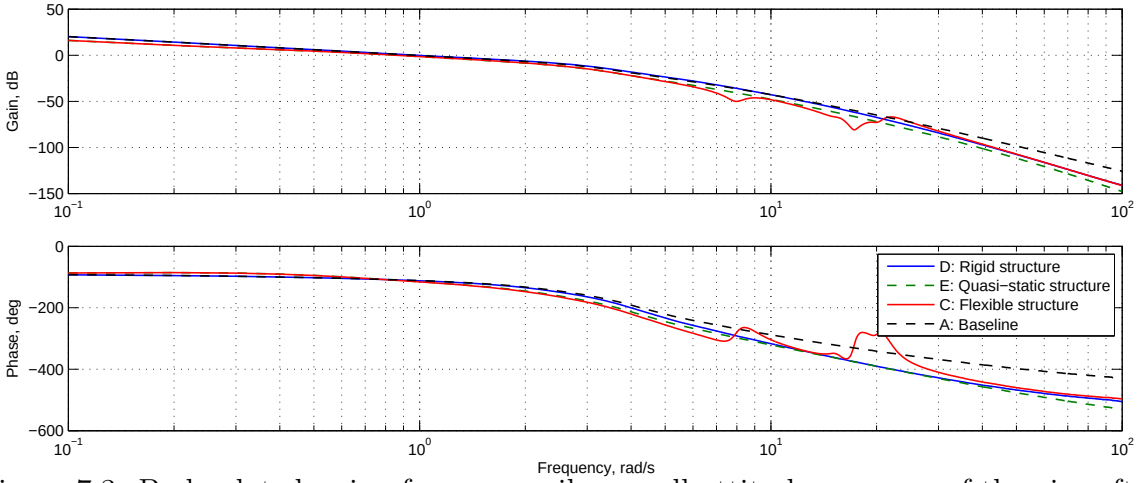

Figure 7.3: Bode plot showing frequency aileron-roll attitude response of the aircraft for four model variants

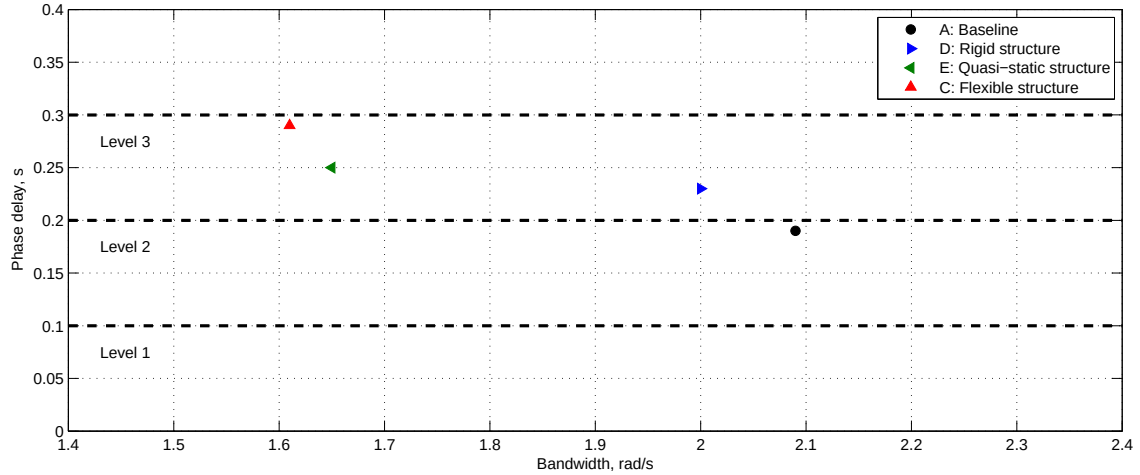

Figure 7.4: Bandwidth and phase delay for aeroelastic and baseline model variants

insight into the influence of the stiffness of a component without a global modification of the mode shape natural frequencies.

7.2.1 Fuselage and Tailplane Stiffness

It has been shown previously that the natural frequency of the fuselage bending mode is an important factor in determining the longitudinal handling qualities for certain aircraft types [Waszak and Schmidt, 1985a]. Given in Equation 7.2.1 is the elevator to pitch-rate transfer function extracted from the linearised flexible structure aeroplane model at 180 m s^{-1} and 8,000 ft. Alternatively, we can express the same function in symbolic form [Equation 7.2.2]. We can see that many of the poles and zeros, with the exception of those highlighted, cancel nearly exactly or completely, and therefore have little effect on the overall response. This includes the roll, spiral, and dutch-roll modes. We would expect these modes to have little influence on the longitudinal dynamics of a conventional aeroplane configuration whose longitudinal and lateral-directional dynamics are largely decoupled.

$$\frac{q}{\eta} = \frac{\begin{array}{c}-\mathbf{50.71}s(\mathbf{s}-\mathbf{243.0})\,(s+3.361)\,(\mathbf{s}+\mathbf{0.5251})\,(s+0.07309)\\ (\mathbf{s}+\mathbf{0.009072})\,(s^2+0.3148s+0.6321)\,(s^2+1.814s+51.79)\\ (s^2+0.4177s+51.62)\,(s^2+2.863s+70.29)\,(s^2+1.365s+186.2)\\ (s^2+0.9913s+221.8)\,(s^2+0.7036s+261.2)\,(\mathbf{s^2}+\mathbf{1.027s}+\mathbf{283.4})\\ (s^2+1.018s+304.3)\,(s^2+6.888s+363.3)\,(\mathbf{s^2}+\mathbf{1.654s}+\mathbf{346.7})\\ (s^2+6.652s+473.1)\,(\mathbf{s^2}+\mathbf{7.046s}+\mathbf{413.5})\end{array}}{\begin{array}{c}(\mathbf{s}+\mathbf{26.95})\,(\mathbf{s}+\mathbf{75.92})\,(s+3.361)\,(s+0.07322)\\ (\mathbf{s^2}+\mathbf{0.001433s}+\mathbf{0.004873})\,(s^2+0.3150s+0.6317)\\ (\mathbf{s^2}+\mathbf{1.692s}+\mathbf{5.768})\,(s^2+1.814s+51.79)\,(s^2+0.5029s+52.09)\\ (s^2+2.877s+70.23)\,(s^2+1.365s+186.2)\,(s^2+0.9908s+221.7)\\ (s^2+0.6803s+263.3)\,(\mathbf{s^2}+\mathbf{0.9905s}+\mathbf{297.7})\,(s^2+1.018s+304.3)\\ (s^2+6.888s+363.3)\,(\mathbf{s^2}+\mathbf{7.207s}+\mathbf{407.4})\\ (s^2+6.650s+473.1)\,(\mathbf{s^2}+\mathbf{7.023s}+\mathbf{485.4})\end{array}} \qquad (7.2.1)$$

The longitudinal response of the aircraft to elevator is dominated by the complex short period and phugoid modes, given by the subscripts s and p respectively. In addition, we can see the real poles and zeros of the elevator actuator, given by the subscript a, also influence the overall response. We can see that many of the structural modes, including the first wing bending mode, have little effect on the response, with the poles and zeroes almost completely cancelling each other. However three structural modes in particular, their complex poles and zeros not cancelling completely, can be seen to have a significant effect on the longitudinal response of the aeroplane. These three modes, given in Figure 7.6, correspond to wind-off Modes 6, 9, and 12, and are symmetric fuselage and tail bending modes. The wind-off natural frequencies of these modes are 16.05, 16.85, and 18.39 rad s^{-1} respectively.

$$\frac{q}{\eta} = \frac{\begin{array}{c}-\boldsymbol{K_{q/\eta}} s(\boldsymbol{s+1/T_{a_1}})\,(s+1/T_r)\,(\boldsymbol{s+1/T_{\theta_2}})\,(s+1/T_s) \\ (\boldsymbol{s+1/T_{\theta_1}})\,(s^2+2\zeta_d\omega_d s+\omega_d^2)\,\left(s^2+2\zeta_{f_1}\omega_{f_1}s+\omega_{f_1}^2\right) \\ \left(s^2+2\zeta_{f_2}\omega_{f_2}s+\omega_{f_2}^2\right)\left(s^2+2\zeta_{f_3}\omega_{f_3}s+\omega_{f_3}^2\right)\left(s^2+2\zeta_{f_4}\omega_{f_4}s+\omega_{f_4}^2\right) \\ \left(s^2+2\zeta_{f_5}\omega_{f_5}s+\omega_{f_5}^2\right)\left(s^2+2\zeta_{f_6}\omega_{f_6}s+\omega_{f_6}^2\right)\left(\boldsymbol{s^2+2\zeta_{f_7}\omega_{f_7}s+\omega_{f_7}^2}\right) \\ \left(s^2+2\zeta_{f_8}\omega_{f_8}s+\omega_{f_8}^2\right)\left(s^2+2\zeta_{f_9}\omega_{f_9}s+\omega_{f_9}^2\right)\left(\boldsymbol{s^2+2\zeta_{f_{10}}\omega_{f_{10}}s+\omega_{f_{10}}^2}\right) \\ \left(s^2+2\zeta_{f_{11}}\omega_{f_{11}}s+\omega_{f_{11}}^2\right)\left(\boldsymbol{s^2+2\zeta_{f_{12}}\omega_{f_{12}}s+\omega_{f_{12}}^2}\right)\end{array}}{\begin{array}{c}(\boldsymbol{s+1/T_{a_2}})\,(\boldsymbol{s+1/T_{a_3}})\,(s+1/T_r)\,(s+1/T_s)\left(\boldsymbol{s^2+2\zeta_p\omega_p s+\omega_p^2}\right) \\ (s^2+2\zeta_d\omega_d s+\omega_d^2)\left(\boldsymbol{s^2+2\zeta_s\omega_s s+\omega_s^2}\right)\left(s^2+2\zeta_{f_1}\omega_{f_1}s+\omega_{f_1}^2\right) \\ \left(s^2+2\zeta_{f_2}\omega_{f_2}s+\omega_{f_2}^2\right)\left(s^2+2\zeta_{f_3}\omega_{f_3}s+\omega_{f_3}^2\right)\left(s^2+2\zeta_{f_4}\omega_{f_4}s+\omega_{f_4}^2\right) \\ \left(s^2+2\zeta_{f_5}\omega_{f_5}s+\omega_{f_5}^2\right)\left(s^2+2\zeta_{f_6}\omega_{f_6}s+\omega_{f_6}^2\right)\left(\boldsymbol{s^2+2\zeta_{f_7}\omega_{f_7}s+\omega_{f_7}^2}\right) \\ \left(s^2+2\zeta_{f_8}\omega_{f_8}s+\omega_{f_8}^2\right)\left(s^2+2\zeta_{f_9}\omega_{f_9}s+\omega_{f_9}^2\right)\left(\boldsymbol{s^2+2\zeta_{f_{10}}\omega_{f_{10}}s+\omega_{f_{10}}^2}\right) \\ \left(s^2+2\zeta_{f_{11}}\omega_{f_{11}}s+\omega_{f_{11}}^2\right)\left(\boldsymbol{s^2+2\zeta_{f_{12}}\omega_{f_{12}}s+\omega_{f_{12}}^2}\right)\end{array}} \tag{7.2.2}$$

The step response of a reduced-order model [Equation 7.2.3], including only those poles and zeroes highlighted in Equation 7.2.1, is compared to the full-order response in Figure 7.5. The response of the reduced- and full-order models matches closely, and confirms the assumption that it is the highlighted modes which dominate the response and that the other modes in the full-order model have little effect on the response of the system.

$$\frac{q}{\eta_r} = \frac{\begin{array}{c}-50.71s\,(s-243.0)\,(s+0.5251)\,(s+0.009072) \\ (s^2+1.027s+283.4)\,(s^2+1.654s+346.7)\,(s^2+7.046s+413.5)\end{array}}{\begin{array}{c}(s+26.95)\,(s+75.92)\,(s^2+0.001433s+0.004873)\,(s^2+1.692s+5.768) \\ (s^2+0.9905s+297.7)\,(s^2+7.207s+407.4)\,(s^2+7.023s+485.4)\end{array}} \tag{7.2.3}$$

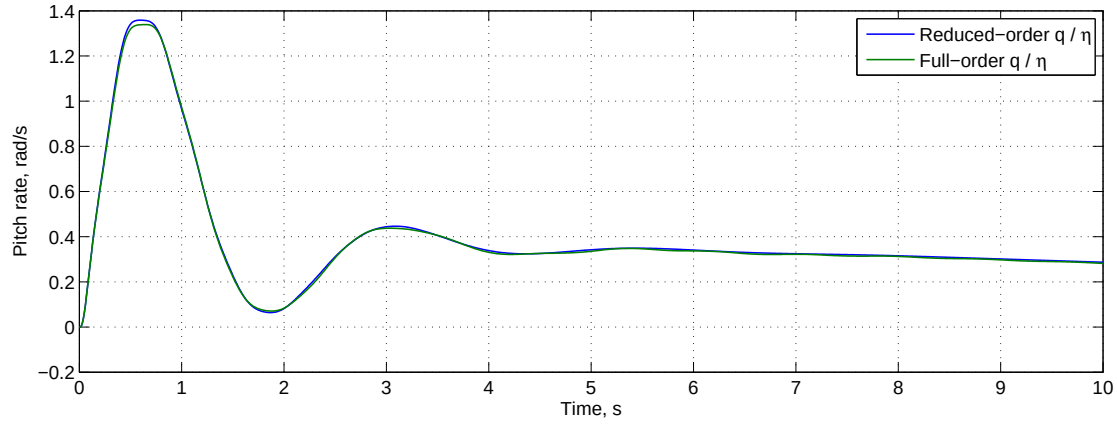

Figure 7.5: Step-response of pitch rate to elevator for reduced-order and full-order baseline aeroplane model at 180 m s^{-1} and 8,000 ft

The three dominant modes shown in Figure 7.6 are symmetric fuselage and tail bending modes. It is known that the natural frequency of the fuselage bending mode has a

significant influence on the longitudinal dynamics of an aeroplane. In this case then, what significance does fuselage flexibility and tailplane flexibility have on the effect of these three modes on the longitudinal dynamics of the aeroplane. Let us first consider what effect fuselage stiffness has on these structural modes, and in turn how that influences the dynamic characteristics of the aeroplane. In order to answer to that question, four fuselage stiffness variants, plus the baseline stiffness case, were compared. The bending and torsional stiffness of the fuselage was scaled for each of the four model variants by +/-15% and +/-30% respectively.

The model was trimmed in steady, level flight at 180 m s^{-1} and 8,000 ft and linearised. A medium mass case, with a total mass of 220,032 kg is considered here [Appendix B]. The open-loop characteristics of the full aeroelastic models, including unsteady aerodynamic effects, are given in Table 7.6. The wind-off natural frequencies for the five model variants are given in Table 7.3.

We can see that the wind-off natural frequency of Mode 5, an asymmetric fuselage tail bending mode, is affected by the change in fuselage stiffness. The natural frequency of the mode, as would be expected, is reduced with increasing flexibility, and increased with increasing stiffness. However, it is Modes 6 and 9 which are of interest in the longitudinal dynamics of the aeroplane. We can see that Mode 6 is also affected by the change in fuselage stiffness, and the wind-off frequency is reduced by 9.13% for the -30% stiffness variant, and increased by 1.74% for the +30% variant. A similar trend is evident for Mode 9, with the wind-off frequency reduced by 2.01% for the -30% stiffness variant, and increased by 3.54% for the +30% variant. Figure 7.7 shows that with increasing fuselage stiffness, the modeshape is also modified. The vertical modal displacement of the fuselage and tailplane in Mode 6 is reduced. In Mode 9, the reduction in normalised fuselage and wing modal displacement results in an increase in the normalised vertical displacement of the tail. While the natural frequencies of two of the critical longitudinal modes (Modes 6 and 9), as well the asymmetric fuselage bending mode (Mode 5), are modified by fuselage stiffness, the influence of these modes on the stability and dynamic characteristics of the aeroplane is relatively small. We can see from Table 7.6 that the open-loop characteristics of the aeroplane are only slightly modified by the fuselage stiffness. With increasing fuselage stiffness, we can see that the short-period mode is increased in frequency, from 2.283 to 2.383 rad s^{-1} for the +30% and -30% variants respectively, while damping is decreased 0.329 to 0.322. The other rigid-body modes are not affected by changes in fuselage stiffness. It is unlikely that this small change in the rigid-body stability and dynamic characteristics of the aeroplane would have any significant influence on the handling qualities of the aeroplane. The natural frequency of the fuselage for this aircraft is also much higher than for more slender fuselaged aircraft, and the possibility of pilot biodynamic feedthrough is therefore not considered here.

Let us then consider what effect tailplane stiffness has on these structural modes, and hence what influence that has on the overall handling qualities of the aeroplane. Again, four stiffness variants, plus the baseline stiffness case, were compared. The bending and torsional stiffness of the tailplane was scaled for each of the four model variants by +/-15% and +/-30% respectively. The wind-off natural frequencies of the structure are given in Table 7.4. We can see that the natural frequencies of Mode 6, a coupled tail and fuselage bending mode, are reduced with the decrease in tailplane stiffness. Modes 11 and 12 are symmetric and asymmetric tailplane bending; Mode 12, the symmetric mode, being critical to the longitudinal dynamics of the aeroplane. The natural frequency of these

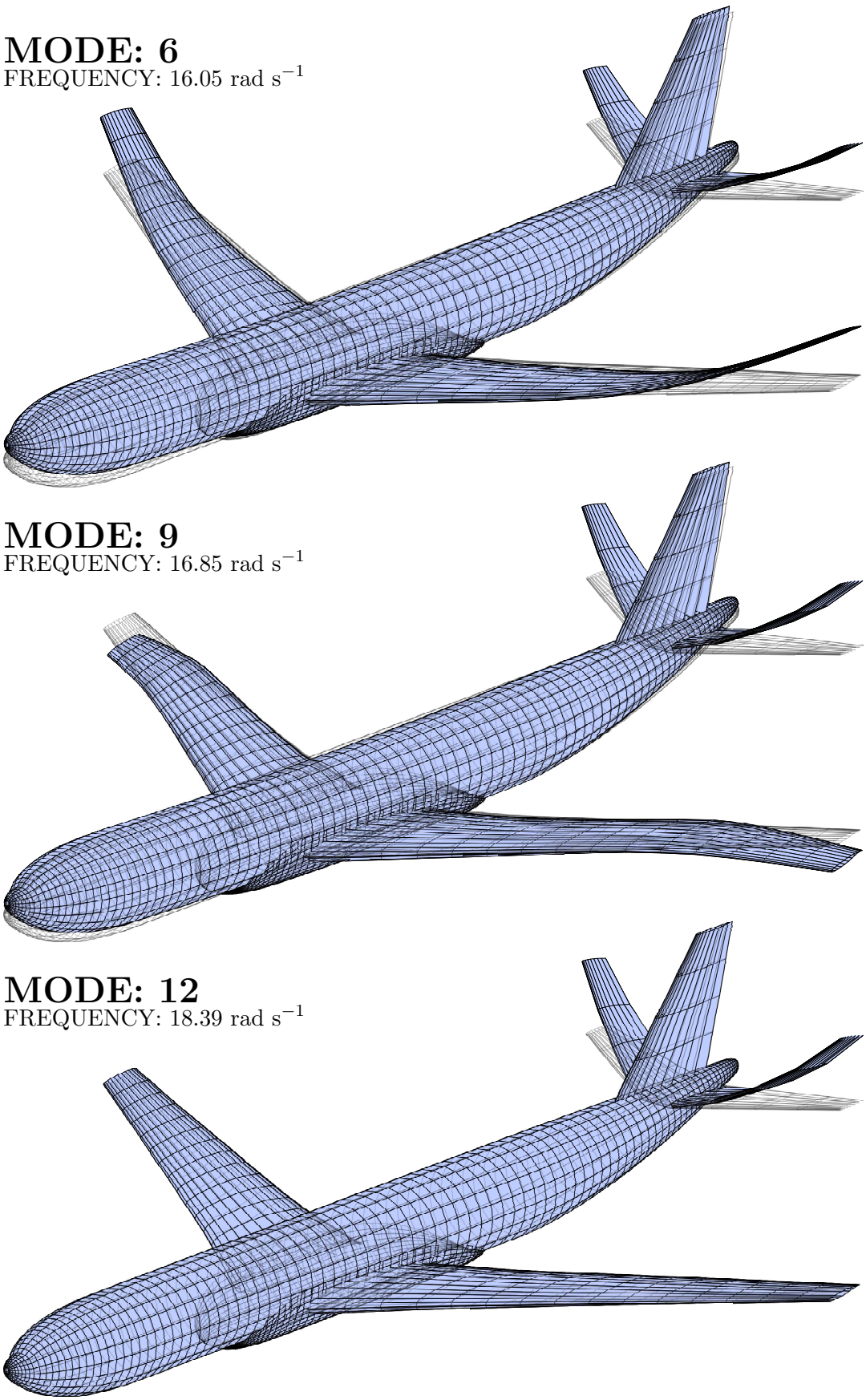

Figure 7.6: Airframe structure normal modes 6, 9, and 12 for baseline, medium mass case

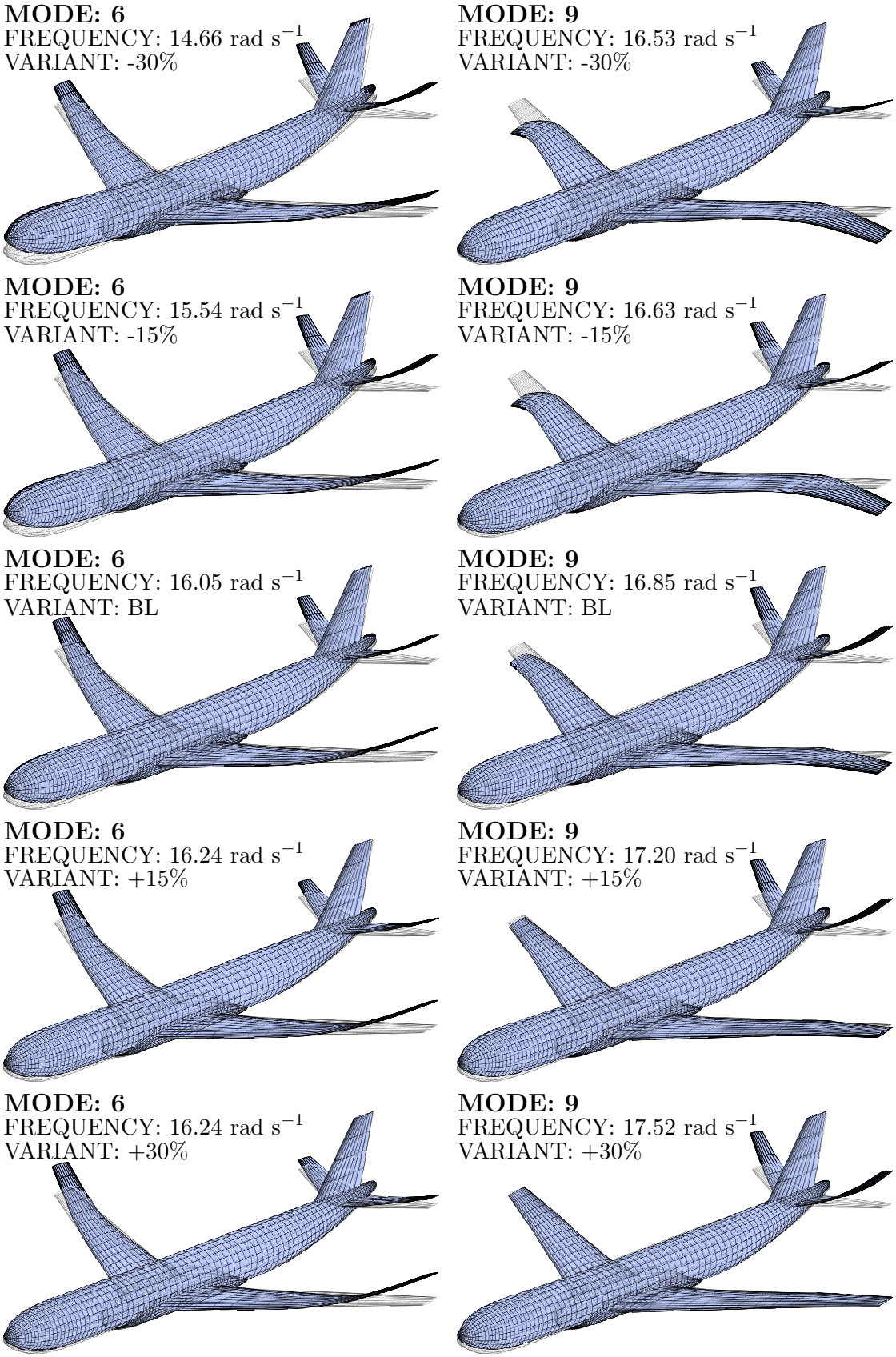

Figure 7.7: Airframe structure normal modes 6 and 9 for five fuselage stiffness variants

	Model Variant				
Mode	-30%	-15%	BL	+15%	+30%
Flexible Mode 1	6.891	6.891	6.891	6.891	6.891
Flexible Mode 2	6.891	6.891	6.891	6.891	6.891
Flexible Mode 3	7.435	7.485	7.518	7.541	7.559
Flexible Mode 4	12.08	12.61	12.83	12.92	12.97
Flexible Mode 5	**13.58**	**14.06**	**14.68**	**15.29**	**15.81**
Flexible Mode 6	**14.66**	**15.54**	**16.05**	**16.24**	**16.24**
Flexible Mode 7	16.24	16.24	16.24	16.24	16.24
Flexible Mode 8	16.24	16.24	16.24	16.24	16.31
Flexible Mode 9	**16.53**	**16.63**	**16.85**	**17.20**	**17.52**
Flexible Mode 10	16.84	17.05	17.20	17.32	17.44
Flexible Mode 11	18.39	18.39	18.39	18.39	18.39
Flexible Mode 12	18.39	18.39	18.39	18.39	18.39

Table 7.3: Airframe structural mode wind-off natural frequencies for five fuselage stiffness variants

two modes are reduced by 16.33% for the -30% stiffness case, and increased by 14.01% for the +30% stiffness case. This is close to the value that would be expected, given the equation $\omega = \sqrt{K/M}$. It can be seen in Table 7.7 that changes in the tailplane stiffness has a significant influence on the rigid-body stability characteristics of the aeroplane. The natural frequency and damping of the dominant short-period mode are both influenced considerably by tailplane stiffness. The short-period natural frequency is reduced by 9.69% for the -30% tailplane stiffness case, while damping is reduced by 0.31%. For the +30% stiffness case, the short-period frequency is increased by 6.06%, while damping is increased by 1.85%. The other rigid-body modes, including the phugoid mode, are not affected to any degree by changes in tailplane stiffness. The natural frequency of a number of higher structural modes is however reduced by the decrease in tailplane stiffness, increasing the likelihood of interaction between these modes and the rigid-body aeroplane modes. Let us then assess what influence tailplane stiffness has on the handling qualities of the aeroplane.

The selection of dominant modes from the High-order System (HOS), as described previously, is unsuitable for handling qualities analysis; it does not provide an accurate or satisfactory prediction of the handling qualities of an aircraft, neglecting the influence of higher order modes on the low order dynamics [Cook, 1997]. In order to estimate the handling qualities of an high-order aeroplane, and apply the wealth of existing established, and essentially low-order, criteria to this problem, an approach known as Low-order Equivalent System (LOES) modelling has been developed [Hodgkinson et al., 1976]. While the original purpose of equivalent system modelling was to estimate the characteristics of highly augmented aircraft, it seems ideally suited to aeroelastic aircraft analysis although caution should be exercised in the interpretation of the results [Crother et al., 1973]. The LOES model describes a linearised, reduced-order transfer function model of the pitch-rate and normal acceleration response to elevator:

	Model Variant				
Mode	-30%	-15%	BL	+15%	+30%
Flexible Mode 1	6.891	6.891	6.891	6.891	6.891
Flexible Mode 2	6.891	6.891	6.891	6.891	6.891
Flexible Mode 3	7.514	7.516	7.518	7.519	7.520
Flexible Mode 4	12.67	12.78	12.83	12.85	12.87
Flexible Mode 5	14.63	14.67	14.68	14.69	14.69
Flexible Mode 6	**14.88**	**15.72**	**16.05**	**16.14**	**16.18**
Flexible Mode 7	16.24	16.24	16.24	16.24	16.24
Flexible Mode 8	16.24	16.24	16.24	16.24	16.24
Flexible Mode 9	16.38	16.52	16.85	17.19	17.43
Flexible Mode 10	15.20	16.31	17.20	17.67	17.86
Flexible Mode 11	**15.39**	**16.96**	**18.39**	**19.72**	**20.97**
Flexible Mode 12	**15.39**	**16.96**	**18.39**	**19.72**	**20.97**

Table 7.4: Airframe structural mode wind-off natural frequencies for five tailplane stiffness variants

$$\frac{q}{\eta} = \frac{K_q s \left(1 + 1/T_{\theta_1}\right)\left(1 + 1/T_{\theta_2}\right) e^{-\tau_e s}}{\left(s^2 + 2\zeta_p\omega_p + \omega_p^2\right)\left(s^2 + 2\zeta_s\omega_s + \omega_s^2\right)} \tag{7.2.4}$$

$$\frac{n_z}{\eta} = \frac{K_n s \left(1 + 1/T_{n_1}\right) e^{-\tau_n s}}{\left(s^2 + 2\zeta_p\omega_p + \omega_p^2\right)\left(s^2 + 2\zeta_s\omega_s + \omega_s^2\right)} \tag{7.2.5}$$

The phase delay term, $e^{-\tau s}$, is intended to approximate the total phase lag due to the additional dynamics of the HOS system. The roll-off in phase for a high-order aircraft above the bandwidth frequency has been found to very well approximated by the linear roll-off in phase given by a time delay τ. It is typical that the short-period and phugoid modes are sufficiently separated, usually by a factor of 10, and as such it is possible to further reduce the LOES model, given here for the elevator to pitch-rate transfer function by:

$$\frac{q_p}{\eta} = \frac{s\left(1 + 1/T_{\theta_1}\right)}{\left(s^2 + 2\zeta_p\omega_p + \omega_p^2\right)} \qquad \frac{q_s}{\eta} = \frac{K_q\left(1 + 1/T_{\theta_2}\right) e^{-\tau_e s}}{\left(s^2 + 2\zeta_s\omega_s + \omega_s^2\right)} \tag{7.2.6, 7.2.7}$$

The parameters in Equations 7.2.4 and 7.2.5 are obtained by matching the gain and phase frequency response of the LOES model to the response of the high-order system. The high-order frequency response may be obtained from the linearised, high-order model, parameter estimation techniques, or Fourier analysis of flight time histories. Here, the high-order model response is given by the linearised aeroelastic model. The frequency response of the LOES model is matched to the HOS model between two frequencies, typically 0.1 and 10 rad s^{-1}. The mismatch between the LOES and HOS models is given by the cost function:

$$M = \frac{20}{n}\sum\left(G_{HOS} - G_{LOES}\right)^2 + K\sum\left(\phi_{HOS} - \phi_{LOES}\right)^2 \tag{7.2.8}$$

where the weighting factor K of 0.02 is applied such that the gain and phase mismatch is given equal significance [MIL-STD-1797A, 1990]. Envelopes of maximum unnoticeable dynamics are defined in the relevant military specification [MIL-STD-1797A, 1990], though a cost function of 200 has been found to be unnoticeable to pilots [Hodgkinson and Johnston, 1979]. One important issue is whether to hold the variable T_{θ_2} fixed, or allow it vary freely. The variable T_{θ_2} has particular physical significance in aircraft attitude control, and is an invariant function of the aerodynamic characteristics of the aeroplane. If T_{θ_2} is allowed to vary freely, it may take a very large or small value; one which is different from its fixed, aerodynamic value. This may result incorrect handling qualities predictions. In order to ensure the correct relationship between flight path and attitude, and thereby yield the fixed value for T_{θ_2}, the pitch-rate and normal accelerations transfer functions should be matched simultaneously [Equations 7.2.4 and 7.2.5].

	Variant				
Coefficient	−30%	−15%	Base	+15%	+30%
ζ_p	+0.02129	+0.01238	+0.006214	+0.003452	+0.002497
ω_p	+0.06365	+0.06324	+0.06426	+0.06529	+0.06559
ζ_s	+0.2941	+0.2962	+0.2993	+0.3030	+0.3063
ω_s	+2.139	+2.263	+2.363	+2.438	+2.503
$1/T_{\theta_1}$	+0.0000	+0.0000	+0.0000	+0.0000	+0.0000
$1/T_{\theta_2}$	+0.5981	+0.5862	+0.5782	+0.5723	+0.5695
$1/T_{n_1}$	+0.004437	+0.002436	+0.001237	+0.0000	+0.0000
K_q	+2.988	+3.329	+3.627	+3.877	+4.077
K_n	+38.28	+41.99	+45.22	+47.89	+50.02
τ_e	+0.08243	+0.08448	+0.08547	+0.08527	+0.08612
τ_n	+0.1402	+0.1421	+0.1423	+0.1432	+0.1433
M	+6.070	+4.527	+3.779	+3.374	+3.145

Table 7.5: Low-order equivalent system coefficients for five tailplane stiffness variants at 180 m s^{-1} and 8,000 ft

The approach used here differs in several respects to Crother et al. [1973], who found that LOES modelling was inadequate in the prediction of the handling qualities of the B-1B Lancer bomber. Firstly, the complete phugoid and short-period LOES model is matched here with the HOS model, and not only the short-period model. Secondly, the elevator to pitch-rate and elevator to normal acceleration transfer functions are matched simultaneously, and not only the pitch-rate transfer function. Crother et al. [1973] found that better results were obtained by allowing T_{θ_2} to vary freely, and this approach is taken here. T_{θ_2} was found to take a value similar to the equivalent dominant zero in the high-order system [Tables 7.8 and 7.5]. This was considered more than acceptable, and a fixed T_{θ_2} approach is not considered here. The LOES parameters for each of the five model variants are given in Table 7.5. Figures 7.12 and 7.13 show the elevator to pitch-rate phase and gain frequency response for the LOES and HOS models for two of the model variants (-30% and +30% stiffness respectively). It can be seen that the LOES

matches very closely the HOS system response for both variants, and this is reflected in the low mismatch cost [Table 7.5]. The pitch-rate step response of the LOES and HOS models, again for the same two stiffness variants, is shown in Figures 7.8 and 7.9. It can be seen that for both stiffness variants, the LOES model matches closely the response of HOS, particularly so for the +30% stiffness variant, and this is reflected in the lower mismatch cost compared to the -30% variant.

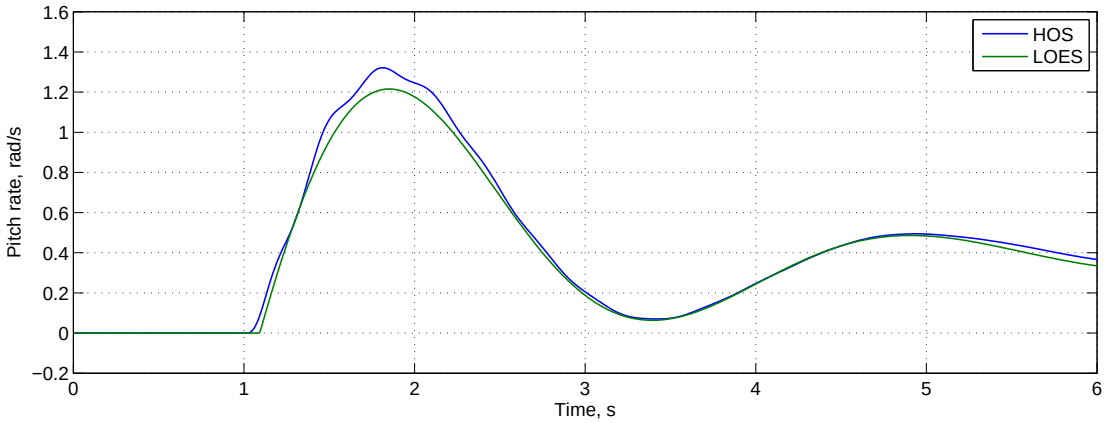

Figure 7.8: Pitch rate step response to elevator for high and low-order equivalent aeroplane models for −30% tailplane stiffness

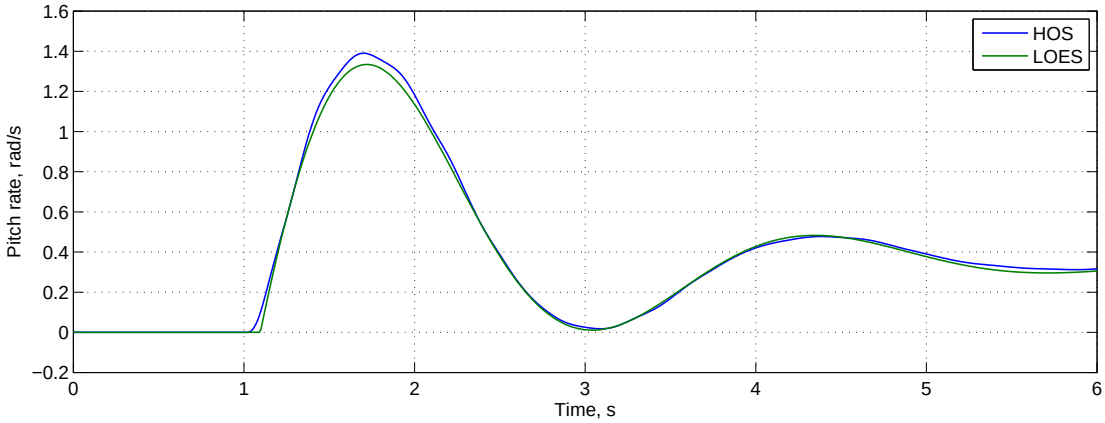

Figure 7.9: Pitch rate step response to elevator for high and low-order equivalent aeroplane models for +30% tailplane stiffness

	-30%		-15%		Base		+15%		+30%	
Mode	Frequency, rad s^{-1}	Damping	Frequency, rad s^{-1}	Damping	Frequency, rad s^{-1}	Damping	Frequency, rad s^{-1}	Damping	Frequency, rad s^{-1}	Damping
SPPO	2.383	0.3222	2.391	0.3194	2.342	0.3230	2.309	0.3264	2.283	0.3298
Phugoid	0.06745	0.01123	0.06754	0.01112	0.06754	0.01165	0.06842	0.01167	0.06872	0.01134
Dutch Roll	0.8101	0.09958	0.8092	0.09843	0.8082	0.09875	0.8070	0.09754	0.8061	0.09754
Roll	$\tau = 0.2961$s		$\tau = 0.2972$s		$\tau = 0.2984$s		$\tau = 0.2984$s		$\tau = 0.2991$s	
Spiral	$\tau = 14.05$s		$\tau = 13.98$s		$\tau = 13.93$s		$\tau = 13.89$s		$\tau = 13.86$s	
Flexible Mode 1	7.189	0.03128	7.206	0.03087	7.218	0.03198	7.226	0.03279	7.232	0.03256
Flexible Mode 2	7.349	0.1152	7.348	0.1158	7.347	0.1151	7.347	0.1142	7.346	0.1141
Flexible Mode 3	8.464	0.1324	8.483	0.1324	8.496	0.1324	8.505	0.1321	8.512	0.1329
Flexible Mode 4	**12.28**	**0.02527**	**13.10**	**0.03165**	**13.57**	**0.03938**	**13.78**	**0.04412**	**13.88**	**0.04654**
Flexible Mode 5	**14.35**	**0.04341**	**14.54**	**0.03741**	**14.91**	**0.02907**	**15.40**	**0.02306**	**15.88**	**0.02138**
Flexible Mode 6	**15.30**	**0.02737**	**16.02**	**0.02310**	**16.22**	**0.02038**	**16.27**	**0.02022**	**16.29**	**0.02012**
Flexible Mode 7	**16.46**	**0.02143**	**16.71**	**0.02323**	**17.19**	**0.02349**	**17.44**	**0.02712**	**17.52**	**0.02847**
Flexible Mode 8	17.16	0.02612	17.29	0.02748	17.37	0.02734	17.59	0.02175	17.86	0.02032
Flexible Mode 9	19.39	0.06234	19.41	0.06094	19.44	0.06017	19.46	0.06038	19.47	0.05918
Flexible Mode 10	19.89	0.04565	19.89	0.04587	19.90	0.04597	19.91	0.04610	19.91	0.04571
Flexible Mode 11	21.12	0.05612	21.30	0.05965	21.38	0.06748	21.38	0.06622	21.38	0.06576
Flexible Mode 12	21.31	0.06858	21.36	0.06734	21.52	0.06212	21.74	0.06435	21.93	0.06537

Table 7.6: Open-loop aeroplane longitudinal, lateral-directional and flexible dynamics at 180 m s^{-1} and 8,000 ft for five fuselage stiffness variants

	-30%		-15%		Base		+15%		+30%	
Mode	Frequency, rad s^{-1}	Damping	Frequency, rad s^{-1}	Damping	Frequency, rad s^{-1}	Damping	Frequency, rad s^{-1}	Damping	Frequency, rad s^{-1}	Damping
SPPO	**2.115**	**0.322**	**2.241**	**0.321**	**2.342**	**0.323**	**2.419**	**0.326**	**2.484**	**0.329**
Phugoid	0.06636	0.01432	0.06647	0.01312	0.06754	0.01157	0.06833	0.01134	0.06923	0.01215
Dutch Roll	0.8082	0.09749	0.8081	0.09745	0.8081	0.09834	0.8072	0.09842	0.8071	0.09954
Roll	$\tau = 0.2911$s		$\tau = 0.2932$s		$\tau = 0.2981$s		$\tau = 0.3021$s		$\tau = 0.3039$s	
Spiral	$\tau = 13.86$s		$\tau = 13.90$s		$\tau = 13.93$s		$\tau = 13.96$s		$\tau = 13.99$s	
Flexible Mode 1	7.215	0.03147	7.217	0.03104	7.218	0.03112	7.218	0.03222	7.218	0.03212
Flexible Mode 2	7.357	0.1171	7.355	0.11634	7.347	0.1159	7.336	0.1136	7.331	0.1131
Flexible Mode 3	8.503	0.1323	8.499	0.1324	8.496	0.1328	8.495	0.1332	8.494	0.1334
Flexible Mode 4	13.43	0.03845	13.54	0.03945	13.57	0.03912	13.58	0.04034	13.58	0.0464
Flexible Mode 5	14.92	0.02805	14.91	0.02987	14.91	0.02983	14.92	0.02912	14.9	0.02913
Flexible Mode 6	**15.12**	**0.02133**	**16.09**	**0.02144**	**16.22**	**0.02012**	**16.24**	**0.02012**	**16.24**	**0.02001**
Flexible Mode 7	**15.32**	**0.02123**	**16.50**	**0.02123**	**17.19**	**0.02332**	**17.53**	**0.03454**	**17.52**	**0.03624**
Flexible Mode 8	**16.30**	**0.02012**	**16.55**	**0.02164**	**17.37**	**0.02793**	**17.67**	**0.02517**	**17.96**	**0.02728**
Flexible Mode 9	18.99	0.06934	19.15	0.06734	19.44	0.06121	19.89	0.04637	19.88	0.04732
Flexible Mode 10	**19.75**	**0.07647**	**19.90**	**0.04613**	**19.90**	**0.04623**	**19.92**	**0.05345**	**20.11**	**0.05137**
Flexible Mode 11	**19.86**	**0.04668**	**20.66**	**0.07413**	**21.38**	**0.06712**	**21.94**	**0.05665**	**22.81**	**0.04904**
Flexible Mode 12	**20.00**	**0.07074**	**20.76**	**0.06743**	**21.52**	**0.06245**	**22.36**	**0.05793**	**23.27**	**0.05323**

Table 7.7: Open-loop aeroplane longitudinal, lateral-directional and flexible dynamics at 180 m s^{-1} and 8,000 ft for five tailplane stiffness variants

The flight point considered here for a civil transport aircraft, at at 180 m s^{-1} and 8,000 ft, might be typical of a Category B flight phase [MIL-STD-1797A, 1990]. This flight phase would typically involve gradual manoeuvres without precision tracking, including climb, cruise, loiter, and descent. There exist a number of handling qualities criteria to enable the prediction of the handling characteristics of the aircraft model. One of the earliest, and simplest, criteria is the thumbprint criteria [Chalk, 1958]. This defines minimum combinations of short-period damping and frequency for satisfactory, acceptable, and poor handling qualities as a series of circular and semi-circular boundaries not unlike the appearance of a fingerprint. The low-order equivalent frequency and damping for each of the five model variants is shown in Figure 7.10 against the thumbprint criteria requirements. It can be seen that a reduction in short-period damping and frequency is known to degrade handling qualities. The baseline model lies in the poor region, and it was this low short-period damping and frequency which was addressed in the design of the Flight Control System in Section 6.2 in order to improve the handling qualities of the aircraft. With a reduction in tailplane stiffness of 30%, it can be seen that the damping and frequency of the short-period mode are reduced, and in this case it is likely to result in degraded poor, or even unacceptable, handling qualities. The opposite can be seen for an increase in tailplane stiffness, with the short-period damping and frequency increased, suggesting improved handling qualities and, with a further increase in stiffness, acceptable handling qualities.

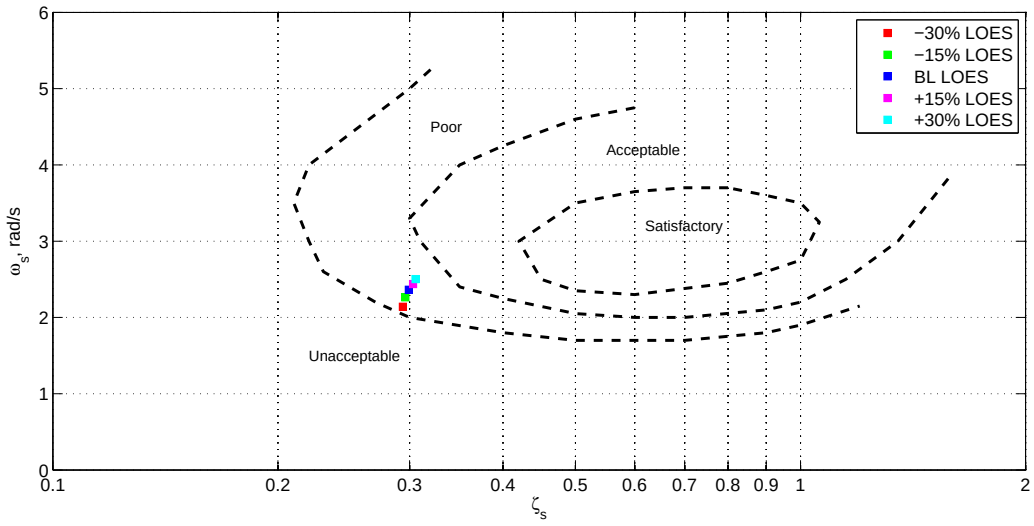

Figure 7.10: Aeroplane ω_s and ζ_s model characteristics against thumbprint requirements [Chalk, 1958]

However, achieving the desired short-period mode damping and frequency characteristics does not guarantee good handling qualities, especially for a non-classical augmented or high-order aircraft. Another criteria is the Control Anticipation Parameter [Birhrle, 1966]. Birhrle [1966] notes that when the pilot initiates a manoeuvre, he senses the initial pitch acceleration in order to anticipate the final response of the aircraft. Birhrle [1966] defines a measure of this anticipatory characteristic of the aircraft called the Control Anticipation Parameter (CAP). The CAP is defined as the amount of instantaneous pitching acceleration per unit of steady-state normal acceleration, and is given by the expression:

$$CAP = \frac{\omega_s^2}{n/\alpha} \tag{7.2.9}$$

where the parameter n/α, the sensitivity of normal-acceleration to pitch control, is given by:

$$n/\alpha = \frac{V}{g} 1/T_{\theta_2} \tag{7.2.10}$$

MIL-STD-1797A [1990] provides minimum acceptable requirements for short-period frequency, ω_s, and normal-acceleration sensitivity, n/α; implicitly defining acceptable values for the CAP parameter for each flying quality level. The short-period frequency, normal-acceleration sensitivity, and CAP parameter for each of the LOES model variants models are given in Table 7.9. These are plotted against the Category B requirement defined by MIL-STD-1797A [1990] in Figure 7.14. The HOS values are also given for comparison. It can be seen that all variants meet the requirements for Level 1 flying qualities. However, as it has been noted, as tailplane stiffness is reduced, there is a decrease in the short-period frequency. This effect has also been shown to be more significant at higher airspeeds. While there is considerable margin between the minimum CAP value of 0.09 and the -30% stiffness variant value of 0.415 for a Category B flight phase, this margin is dramatically reduced for Category A flight. The minimum CAP requirement for Level 1 Category A flight is increased to 0.28, and so any further reduction in tailplane stiffness might possibly result in degraded, Level 2 handling qualities.

	Variant				
Coefficient	−30%	−15%	Base	+15%	+30%
ζ_p	0.01002	0.01041	0.01123	0.01142	0.0168
ω_p	0.0659	0.06612	0.06701	0.06799	0.06913
ζ_s	0.3221	0.3212	0.3230	0.3256	0.3291
ω_s	2.115	2.241	2.342	2.419	2.484
$1/T_{\theta_2}$	0.5501	0.5492	0.5479	0.5477	0.5458

Table 7.8: High-order system coefficients for five tailplane stiffness variants at 180 m s^{-1} and 8,000 ft

The CAP assumes that angular pitch-acceleration is used by the pilot to anticipate the steady-state normal acceleration response of the aeroplane, and that normal acceleration is an important factor affecting the aircraft's handling qualities. However, pitch attitude response itself is also an important factor in describing the handling qualities of an aircraft. The relationship between pitch attitude and flight path angle is defined by a time lag with time constant T_{θ_2}. If T_{θ_2} is too large with respect to the short-period frequency, changes in path and attitude can occur almost simultaneously, and the pilot can find it difficult to separate the response, resulting in abrupt heave responses to elevator. However, a too small value of T_{θ_2} could result in a large pitch-rate overshoot. The pitch-rate overshoot response is also influenced by the short-period damping, ζ_s. A desirable pitch-attitude characteristic would be be a pure integral-type response, often

described as K/s-like pitch-attitude response. MIL-STD-1797A [1990] therefore defines, in combination with short-period damping, the minimum required value for $\omega_s T_{\theta_2}$. The values of $\omega_s T_{\theta_2}$ and ζ_s for each of the five stiffness variant models are given in Table 7.9, and are displayed in Figure 7.15 with Category B requirements. It can be seen that the reduction in damping and natural frequency due to the decrease in tailplane stiffness would result in degraded handling qualities. The short-period damping for the -15% and -30% stiffness cases is reduced below the threshold defined by MIL-STD-1797A [1990] for Level 1 handling qualities. There is also a trend for the reduction in seperation between the pitch-attitude and flight path angle response, given by the term $\omega_s T_{\theta_2}$. While the separation is adequate at this flight point for Level 1 handling qualities, it might be expected that at a different flight point, such as at lower airspeeds where the natural frequency of the short-period mode is reduced, that this might not be the case.

		Variant				
Order	Parameter	-30%	-15%	Base	$+15\%$	$+30\%$
Low	CAP	0.4152	0.4738	0.5259	0.5661	0.5990
	n/α	11.03	10.81	10.62	10.51	10.47
	$\omega_s T_{\theta_2}$	3.562	3.845	4.086	4.259	4.389
	ζ_s	0.294	0.296	0.299	0.303	0.306
High	CAP	0.4431	0.4977	0.5452	0.5831	0.6163
	n/α	10.10	10.08	10.06	10.04	10.02
	$\omega_s T_{\theta_2}$	3.845	4.082	4.274	4.422	4.549
	ζ_s	0.3223	0.3210	0.3234	0.3257	0.3292

Table 7.9: High and low-order equivalent control anticipation and short-period criteria parameters for five tailplane stiffness variants at 180 m s^{-1} and 8,000 ft

Hoh et al. [1982] identified that an important measure of the handling qualities, and particularly the susceptibility to Pilot-Induced Oscillations (PIOs), of an aircraft when operated in a closed-loop compensatory tracking task is the stability margin. The bandwidth, ω_{BW}, of the aircraft is the highest frequency at which some tracking task can be performed without threatening its stability. It is defined as the lower of two values, the phase and gain bandwidths. The phase bandwidth, $\omega_{BW_{phase}}$, is defined as the frequency at which the phase margin is 45°, and corresponds to the point where the phase first passes through 135°. The gain bandwidth, $\omega_{BW_{gain}}$, is the frequency at which the gain margin is 6 dB. These two bandwidths define the pilot's ability to add a time delay or to double his gain without causing an instability. Hoh et al. [1982] states that the Bandwidth Criterion is especially applicable to highly augmented aircraft, whose dynamics cannot be described by the classical second-order response and for which a low-order equivalent system model may have a large mismatch error. This phase delay, τ_p, in this case can be estimated from the frequency response, and an approximate expression is given by:

$$\tau_p = \frac{-\left(\phi_{2_{\omega_{180}}} + 180\right)}{(57.3 \times 2\omega_{180})} \tag{7.2.11}$$

Care should be taken in the calculation of the phase lag, $\phi_{2_{\omega_{180}}}$, at twice the neutral stability frequency, $2\omega_{180}$, as it can be seen at this frequency the gain and phase response

includes the effects of structural dynamics [Figure 7.11]. The bandwidth and phase delay, calculated from the high-order system response, are shown in Table 7.10 and Figure 7.16. The phase delay, τ_e, estimated using the LOES model, is reproduced here for comparison, and shows a close correlation with the values estimated using Equation 7.2.11. While no bandwidth requirements are yet stipulated for Category B flight by MIL-STD-1797A [1990], it can be seen that there is a large reduction in the bandwidth of the aeroplane with the decrease in tailplane stiffness, from 2.812 rad s^{-1} at +30% stiffness to 2.399 rad s^{-1} at -30% stiffness. The bandwidth of the aeroplane is limited for all variants by the gain bandwidth, $\omega_{BW_{gain}}$. Hoh et al. [1982] showed that a reduction in bandwidth is likely to lead to a reduction in handling qualities, and an increased susceptibility to PIOs.

	Variant				
Parameter	−30%	−15%	Base	+15%	+30%
$\omega_{BW_{gain}}$	2.399	2.538	2.651	2.738	2.812
$\omega_{BW_{phase}}$	2.953	3.075	3.177	3.257	3.324
τ_p	0.06418	0.06914	0.07127	0.07248	0.07241
τ_e	0.08221	0.08453	0.08519	0.08573	0.08604

Table 7.10: Bandwidth criterion parameters for five tailplane stiffness variants at 180 m s^{-1} and 8,000 ft

The phase delay, $e^{-\tau_e s}$, in the pitch-attitude response to elevator transfer function is an important parameter in aircraft handling qualities. MIL-STD-1797A [1990] defines maximum allowable requirements for this time delay. These are applicable to all flight phase categories and aircraft classes, and are shown in Figure 7.16. Exceeding these requirements may result in an increased susceptibility to PIOs. The phase delay, calculated both using the equation provided by the Bandwidth Criterion, τ_e, and estimated from the LOES model, τ_p, are given in Table 7.10. While there is a small increase in the estimated phase delay with increasing tailplane stiffness, this increase is small, and the results show that overall there is no large change in the value of phase delay for each of the model variants, and all variants meet the requirements for Level 1 handling qualities.

While the short-period mode dominates the short-term longitudinal response of the aeroplane, it is also important to remember that the long-term response of the aeroplane is governed by the phugoid mode. MIL-STD-1797A [1990] does not specify a minimum or maximum phugoid mode natural frequency, though it is generally assumed that the short-period and phugoid modes should be well separated, with the ratio ω_p/ω_s less than 0.1. This is the case with all of the variants considered here. MIL-STD-1797A [1990] does stipulate minimum damping requirements however: 0.04 for Level 1 flight, and 0.0 for Level 2 flight. All of the variants considered here then would fall into the Level 2 flight category. The damping of the phugoid mode is reduced with increasing tailplane flexibility, for example by 10% to 0.010 for the -30% tailplane stiffness case when compared to the baseline variant. It was shown in Section 6.1 that at high airspeeds the normally oscillatory phugoid mode was transformed into an unstable, non-oscillatory mode for the flexible aircraft model. In that case, the handling qualities would likely be degraded to Level 3, an unstable mode with time constant greater than 55 seconds [MIL-STD-1797A, 1990].

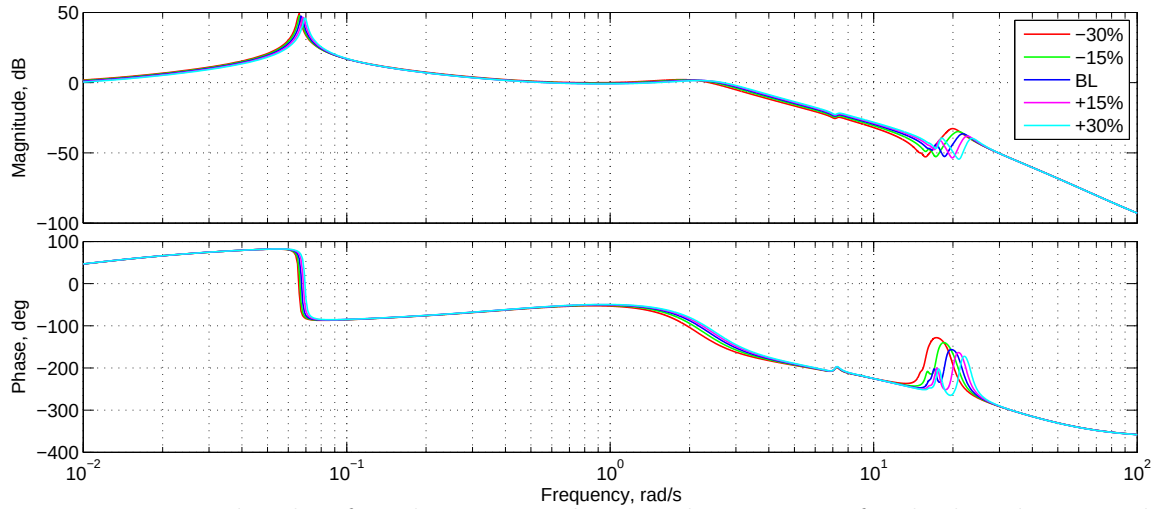

Figure 7.11: Bode plot for elevator–pitch-attitude response for high-order aeroplane model for five tailplane stiffness variants

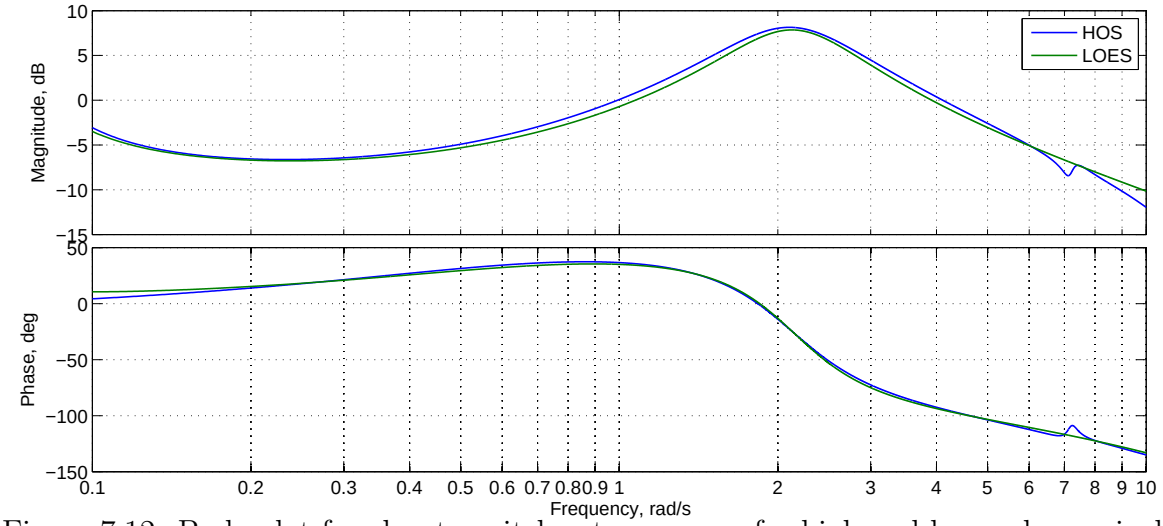

Figure 7.12: Bode plot for elevator-pitch rate response for high and low-order equivalent aeroplane models for −30% tailplane stiffness

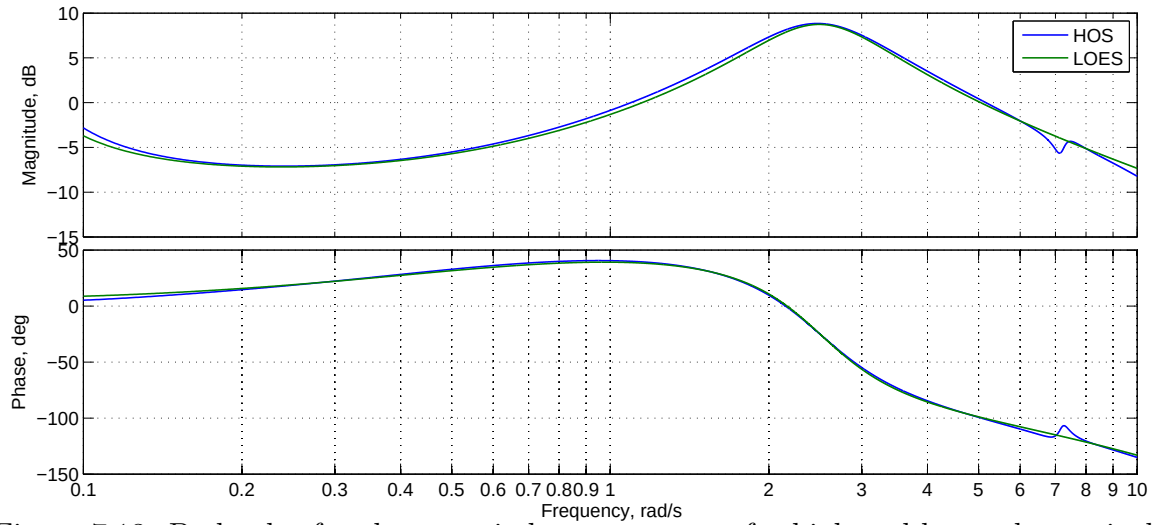

Figure 7.13: Bode plot for elevator-pitch rate response for high and low-order equivalent aeroplane models for +30% tailplane stiffness

In order to address some of the general trends identified in the analysis of a Category B flight point at 180 m s^{-1} and 8,000 ft, a second flight point was analysed. This second flight point, at 120 m s^{-1} and 1,500 ft, is representative of a Category C flight phase. This flight phase includes gradual manoeuvres requiring accurate flight-path control, for example take-off, approach and landing [MIL-STD-1797A, 1990]. Extracting the low-order equivalent model for each of the variants from the high-order system model [Table 7.11], and applying the handling qualities criteria defined above, the results are shown in Figures 7.17 through 7.19. It was identified in Section 6.1 that the influence of structural flexibility on the short-period natural frequency, ω_s, was more significant at higher airspeeds. This can be seen in the reduced ω_s frequency range for the model variants at this second, lower airspeed flight point. The short-period natural frequency, for example, is increased by 3.00% for the +30% stiffness case at 120 m s^{-1} compared with an increase of 5.92% at 180 m s^{-1}. However, that is not to say that the influence on handling qualities is also reduced, and it can be seen that in particular the short-period damping and pitch-attitude bandwidth have an important, and detrimental, effect on the predicted handling qualities of the aeroplane.

	Variant				
Coefficient	−30%	−15%	Base	+15%	+30%
ζ_p	0.02830	0.02887	0.02918	0.03024	0.03041
ω_p	0.1052	0.1054	0.1055	0.1060	0.1062
ζ_s	0.3452	0.3501	0.3553	0.3586	0.3621
ω_s	1.829	1.888	1.933	1.967	1.991
$1/T_{\theta_1}$	0.005180	0.006791	0.008022	0.009118	0.009235
$1/T_{\theta_2}$	0.4994	0.4902	0.4838	0.4807	0.4781
$1/T_{n_1}$	0.004322	0.004487	0.004491	0.004501	0.004523
K_q	1.964	2.113	2.232	2.326	2.398
K_n	15.42	16.42	17.21	17.82	18.27
τ_e	0.09720	0.09812	0.09897	0.09917	0.09924
τ_n	0.1541	0.1541	0.1543	0.1548	0.1549
M	11.36	10.02	9.307	8.853	8.539

Table 7.11: Low-order equivalent system coefficients for five tailplane stiffness variants at 120 m s^{-1} and 1,500 ft

The short-period frequency, ω_s, and normal-acceleration sensitivity, n/α, characteristics of each of the model variants comfortably meet the requirements for Level 1 handling qualities [Figure 7.17]. However, again, it must be noted that there is an overall trend in the reduction of the natural frequency of the short-period mode with increasing tailplane flexibility. Figure 7.18 shows the pitch response characteristics of the aeroplane against the requirements for Category C flight. It can be seen that with increasing structural flexibility, there is both a reduction in short-period damping and the separation of the pitch-attitude and flight-path response, described by ω_s and T_{θ_2} respectively. There is a comfortable margin between the measured value of $\omega_s T_{\theta_2}$ and the requirements for Level 1 Category C flight for this flight point, however the trend in the reduction in this value, both at this and the first flight point, is towards a degradation in the handling qualities of the aircraft as described by the requirements defined by MIL-STD-1797A [1990]. It can

also be seen that at this flight point there is a reduction in the short-period damping with the decrease in tailplane stiffness, and the -30% variant is again predicted to have Level 2 handling qualities compared to Level 1 handling qualities for the baseline stiffness case. Figure 7.19 shows the bandwidth and phase-delay characteristics of the high-order system model [Table 7.12]. At this flight point, a small increase in phase delay is predicted with the reduction in tailplane stiffness. This is in contrast to the results found for the first flight point considered. It has been noted that the incursion of higher-order, in this case structural, dynamics into the bandwidth frequency range can make the estimation of the phase delay difficult [Hoh et al., 1982], and these contrasting results can be explained by a peak in the phase response due to inclusion of the first wing bending mode at 7.2 rad s^{-1}. The bandwidth of the aeroplane can also be seen to be reduced with the decrease in tailplane stiffness, from 2.283 rad s^{-1} for the +30% stiffness case to 2.085 rad s^{-1} for the -30% case. Given the requirements provided by MIL-STD-1797A [1990] then we might therefore expect the handling qualities to be reduced, from Level 1 for the +30% stiffness case to Level 2 for all other cases.

	Variant				
Parameter	−30%	−15%	Base	+15%	+30%
$\omega_{BW_{gain}}$	2.663	2.730	2.785	2.827	2.859
$\omega_{BW_{phase}}$	2.085	2.155	2.211	2.252	2.283
τ_p	0.08524	0.08202	0.08073	0.08008	0.07967

Table 7.12: Bandwidth criterion parameters for five tailplane stiffness variants at 120 m s^{-1} and 1,500 ft

It can therefore be seen, and for both flight points considered, that the stiffness of the tailplane has a significant influence on the rigid-body dynamics of the aeroplane, and in turn its handling qualities. With increasing tailplane flexibility, there is a reduction in the damping and natural frequency of the short-period mode, a reduction in the separation of the pitch-attitude and flight-path response, and a reduction in the gain and phase bandwidth of the aeroplane. All of these factors are known to degrade the handling qualities of the aeroplane. When the model characteristics are compared against existing specifications [MIL-STD-1797A, 1990], then it is found that the handling qualities may be degraded from Level 1 to Level 2 by an increase in tailplane flexibility of 30%.

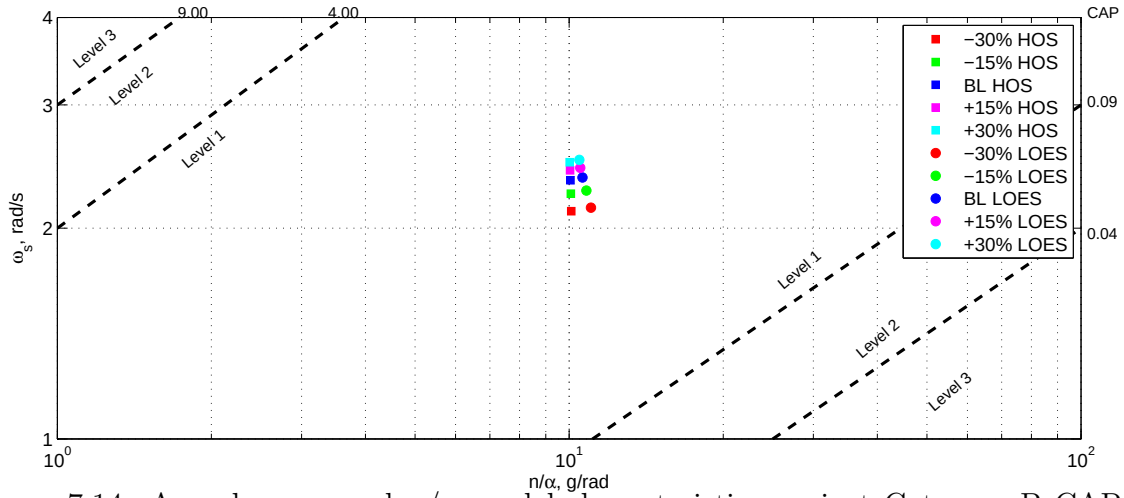

Figure 7.14: Aeroplane ω_s and n/α model characteristics against Category B CAP requirements [MIL-STD-1797A, 1990]

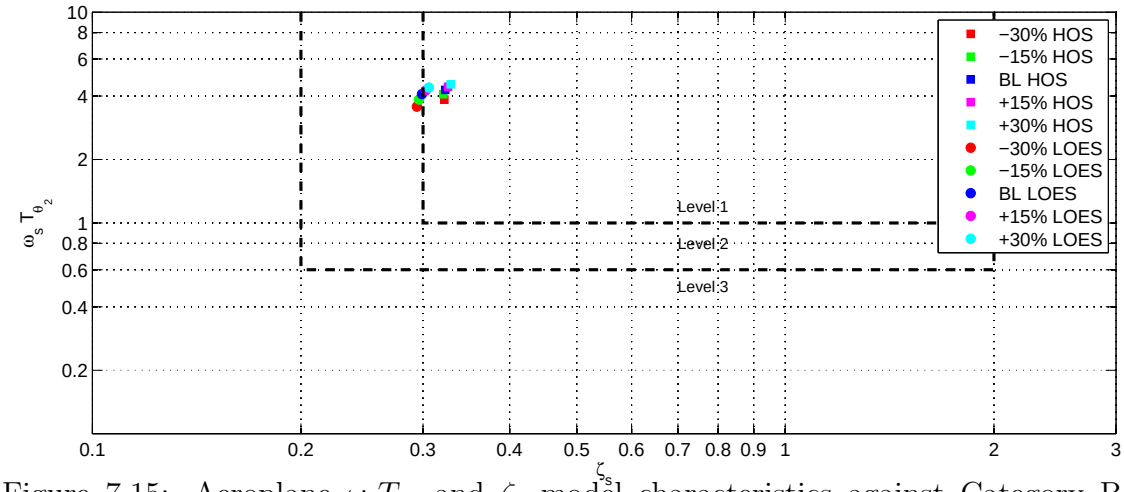

Figure 7.15: Aeroplane $\omega_s T_{\theta_2}$ and ζ_s model characteristics against Category B pitch response requirements [MIL-STD-1797A, 1990]

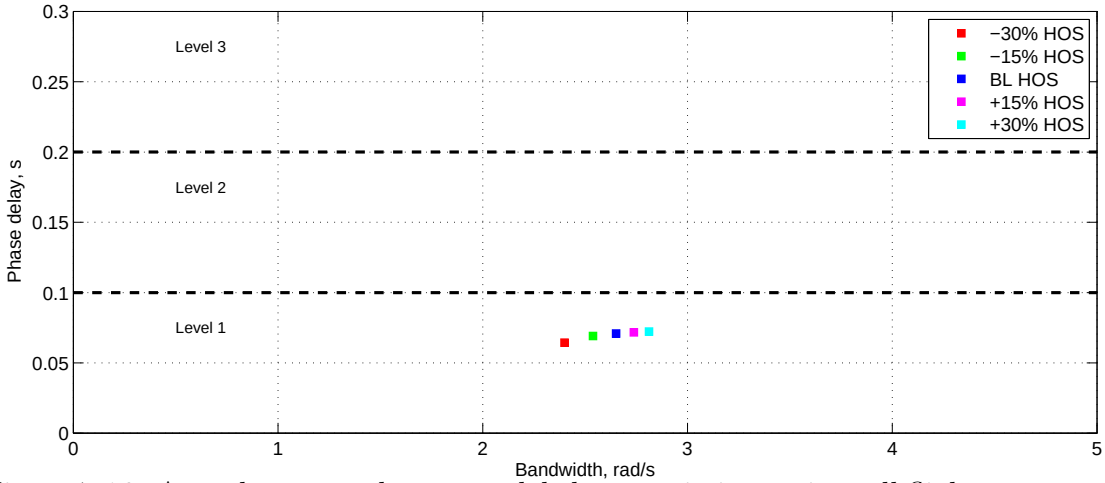

Figure 7.16: Aeroplane τ_e and ω_{BW} model characteristics against all flight category phase delay requirements [MIL-STD-1797A, 1990]

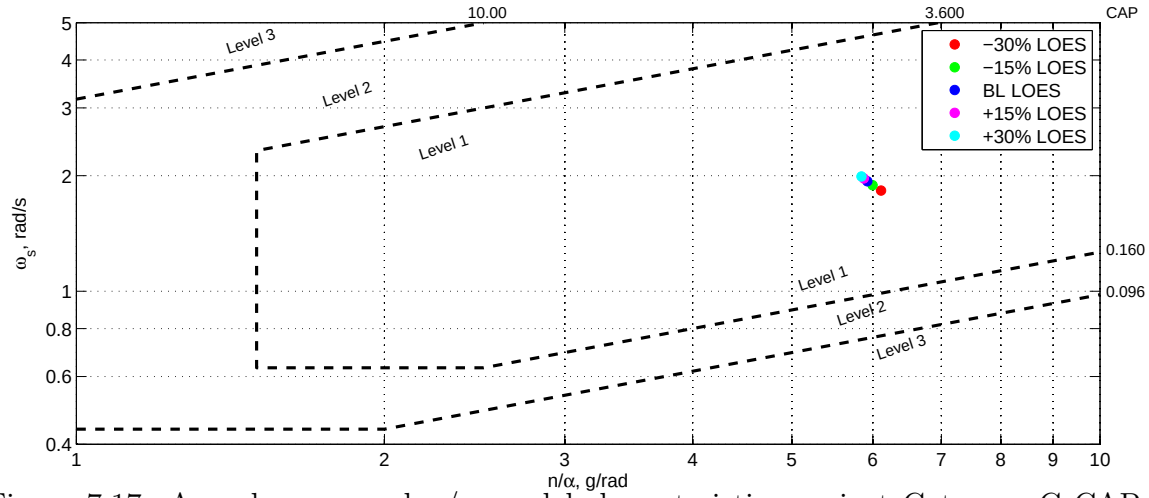

Figure 7.17: Aeroplane ω_s and n/α model characteristics against Category C CAP requirements [MIL-STD-1797A, 1990]

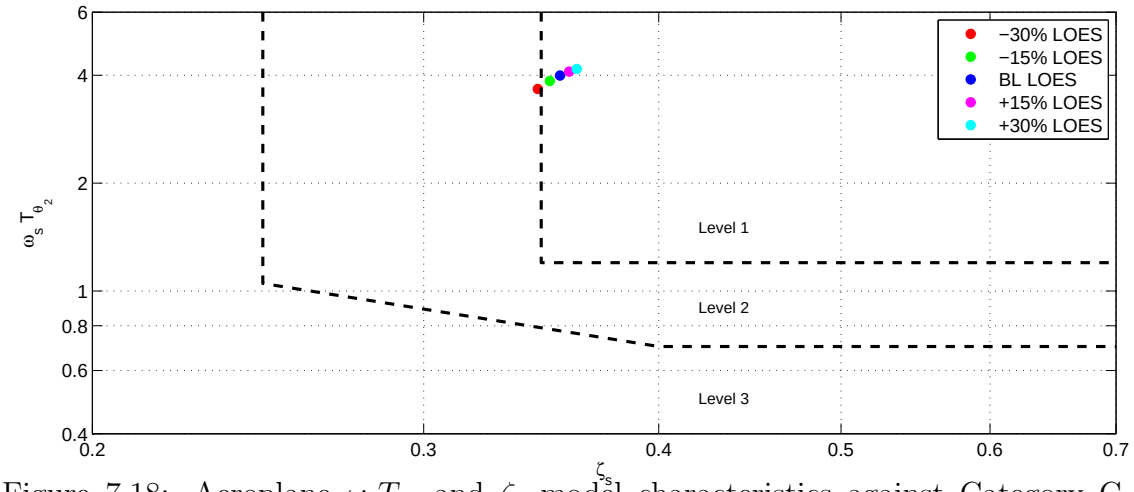

Figure 7.18: Aeroplane $\omega_s T_{\theta_2}$ and ζ_s model characteristics against Category C pitch response requirements [MIL-STD-1797A, 1990]

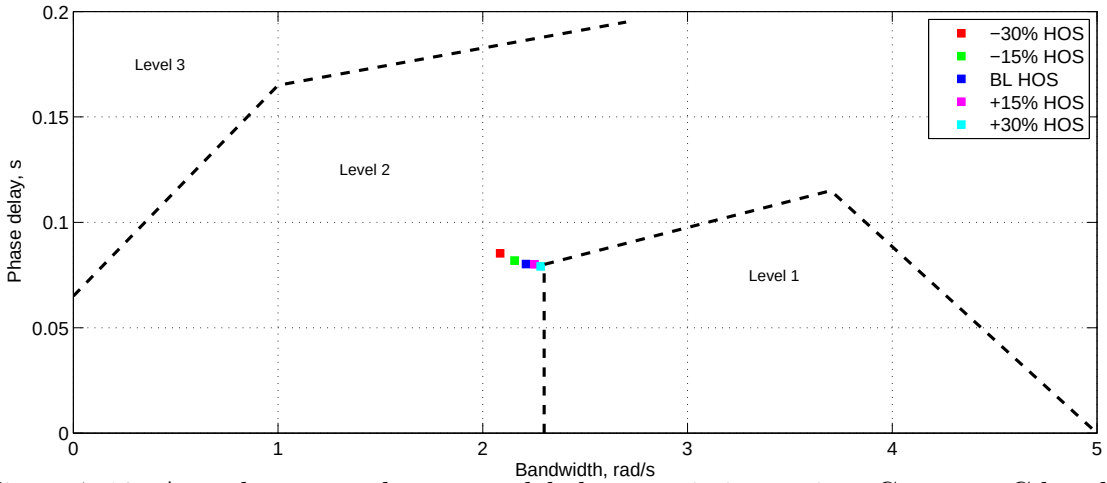

Figure 7.19: Aeroplane τ_e and ω_{BW} model characteristics against Category C bandwidth requirements [MIL-STD-1797A, 1990]

7.2.2 Wing Stiffness

It was shown in Section 7.1 that structural dynamics and unsteady aerodynamics have a significant influence on the lateral-directional characteristics of an aeroplane. In Figure 7.3 of Section 7.1, showing the frequency response of the reduced-order aeroplane roll model to asymmetric aileron deflection, it can be seen that the gain and phase characteristics in the frequency range 6–12 rad s^{-1} are dominated by the response of the structural modes. The first peak visible in Figure 7.3 in this frequency range corresponds to the first and second wing bending modes, and the second peak to an asymmetric wing and fuselage bending mode. It may be concluded then that the stiffness of the wing has an important role in determining the characteristics of these structural modes, and thus the rigid-body handling qualities, of the aeroplane.

In order to further investigate the influence of these modes on the roll characteristics of the aeroplane, four structural models, each varying the bending and torsional stiffness of the wing by +/-15% and +/-30% respectively, and the baseline stiffness model were compared. Again, the model was trimmed in steady, level flight at 180 m s^{-1} at 8,000 ft and linearised. A medium mass case, with a total mass of 220,032 kg is considered here. The open-loop characteristics of the full six degree of freedom aeroelastic model, including unsteady aerodynamic effects, are given in Table 7.15. The wind-off natural frequencies for the five model variants are given in Table 7.13, and the complete mode shapes are shown in Appendix B.

	Model Variant				
Mode	-30%	-15%	BL	+15%	+30%
Flexible Mode 1	5.765	6.353	6.891	7.389	7.857
Flexible Mode 2	5.765	6.353	6.891	7.389	7.857
Flexible Mode 3	6.336	6.957	7.518	8.030	8.503
Flexible Mode 4	10.91	11.95	12.83	13.53	14.03
Flexible Mode 5	13.62	14.20	14.68	15.16	15.68
Flexible Mode 6	13.69	15.02	16.05	16.45	16.59
Flexible Mode 7	13.59	14.98	16.24	17.42	18.52
Flexible Mode 8	13.59	14.98	16.24	17.42	18.52
Flexible Mode 9	16.24	16.50	16.85	17.70	18.71
Flexible Mode 10	15.14	16.43	17.20	17.49	17.65
Flexible Mode 11	18.39	18.39	18.39	18.39	18.39
Flexible Mode 12	18.39	18.39	18.39	18.39	18.39

Table 7.13: Airframe structural mode wind-off natural frequencies for five wing stiffness variants

Nearly all of the twelve modes considered, with the exception of the symmetric and asymmetric tailplane bending modes (Modes 11 and 12), are influenced to some degree by the change in wing stiffness [Table 7.13]. The natural frequency of the first symmetric and asymmetric wing bending modes (Modes 1 and 2) is increased by 14.02% for the +30% stiffness case, and reduced by 16.34% for the -30% stiffness case. Again, this is close to the value that would be expected, given the equation $\omega = \sqrt{K/M}$. This trend in increasing frequency with an increase in wing stiffness is visible in many of the other

wing and fuselage coupled modes, though the actual change in frequency is complicated by the coupling between the fuselage and wing. For example, the natural frequency of the tenth mode is reduced by 11.99% for the -30% stiffness case, but only increased by 2.65% for the +30% case as the frequency is limited by the minimum natural frequency of the fuselage. Let us then consider the coupled aeroelastic model, and the influence of the structural modes on the rigid-body aeroplane characteristics [Table 7.15]. It can be seen that the longitudinal characteristics of the aeroplane are largely unaffected by wing stiffness, with just 0.08 rad s^{-1} separating the natural frequency of the short-period mode for the -30% and +30% stiffness variants. A similar result can be seen for the phugoid mode. The stiffness of the wing does also not appear to influence the dutch-roll mode. The dutch-roll natural frequency is increased by just 0.014 rad s^{-1} from the -30% stiffness case to the +30% stiffness case, with a reduction in damping of 0.004 over the same stiffness range. The roll and spiral modes however are siginificantly affected by the change in wing stiffness. The roll mode time constant is increased by 0.031 seconds and reduced by 0.029 seconds for the -30% and +30% stiffness cases; a change of +6.0% and -5.7% respectively. The spiral mode time constant is conversely reduced by 1.704 seconds and increased by 1.512 seconds for the -30% and +30% stiffness cases; a change of +12.2% and -10.9% respectively.

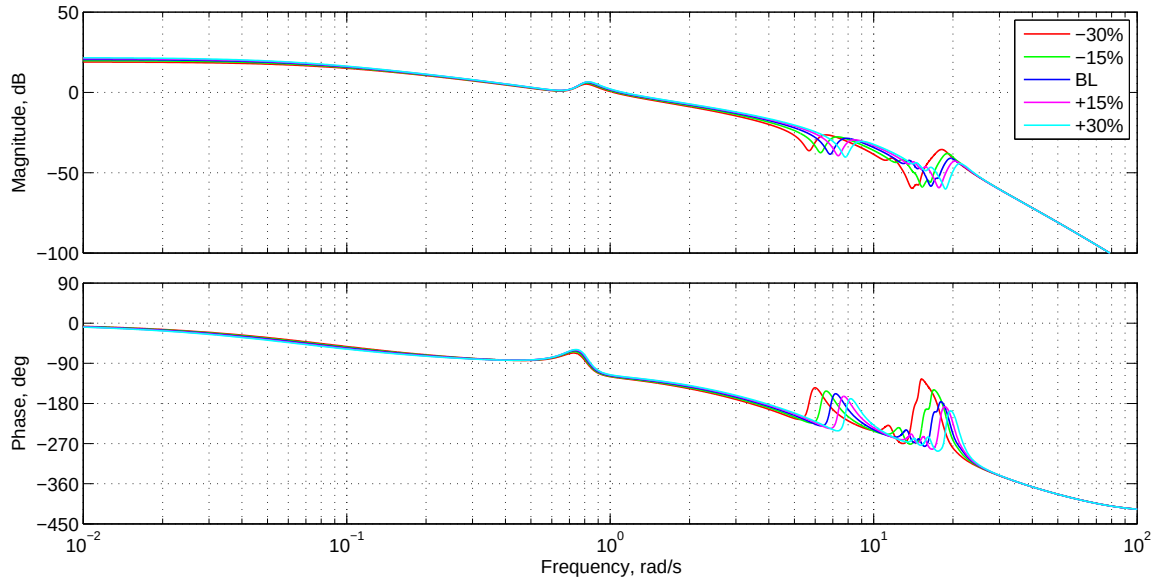

Figure 7.20: Bode plot showing aileron-roll attitude frequency response of the aircraft for five wing stiffness variants at 180 m s^{-1} and 8,000 ft

It can also be seen that the frequency response of the aeroplane roll attitude to asymmetric aileron deflection is modified by the stiffness of the wing [Figure 7.20]. Confirming the results of Section 6.2, which identified significant yaw and roll coupling in response to aileron, the phase and gain curves show a peak in roll attitude response at 0.8 rad s^{-1}, the natural frequency of the dutch-roll mode. With the reduction in the wind-off natural frequency of the first wing bending mode, the first structural mode peak at 5–7 rad s^{-1} is seen to shift left with decreasing wing stiffness.

MIL-STD-1797A [1990] defines a maximum Level 1 roll-mode time constant of 1.4 seconds for all flight phase categories. It can be seen therefore that all variants meet this criteria [Table 7.15]. However, there is a notable increase in the time constant, by 12.4% between

the -30% and +30% stiffness variants. The roll mode time constant is a linear function of velocity, as given by the approximate expression [Cook, 1997]:

$$T_R \cong -\frac{I_{xx}}{\overset{\circ}{L}_p} \tag{7.2.12}$$

where

$$\overset{\circ}{L}_p \cong -\rho V_0 \int_0^s \left(a_y + C_{D_y}\right) c_y y^2 dy \tag{7.2.13}$$

and it might therefore be expected that at lower airspeeds the roll mode time constant would be reduced such that the handling qualities would be degraded as a result of increased wing flexibility. It was shown in Section 7.1 that the bandwidth and phase delay of the aeroplane also have a significant influence on its handling qualities. Table 7.14 shows the bandwidth and phase delay, calculated again using Equation 7.1.2, for each of the five variants. The results are plotted in Figure 7.14. It can be seen that the roll attitude bandwidth of the aeroplane is reduced with increasing structural flexibility, from 1.788 rad s^{-1} for the +30% stiffness case to 1.533 rad s^{-1} for the -30% stiffness case. This is limited for all cases by the phase bandwidth. The phase delay is also increased with the reduction in wing stiffness, from 0.345 seconds for +30% stiffness case to 0.383 seconds for the -30% stiffness case. While MIL-STD-1797A [1990] does not specify any requirements for bandwidth for lateral-directional flight, and applies the longitudinal pitch requirements for phase delay, this trend is known to result in degraded handling qualities and an increased succeptibility to PIOs.

	Variant				
Parameter	−30%	−15%	Base	+15%	+30%
$\omega_{BW_{gain}}$	2.297	2.355	2.418	2.470	2.511
$\omega_{BW_{phase}}$	1.533	1.603	1.679	1.742	1.788
τ_p	0.3827	0.3739	0.3630	0.3536	0.3452

Table 7.14: Bandwidth criterion parameters for five wing stiffness variants at 180 m s^{-1} and 8,000 ft

Returning to the spiral mode, MIL-STD-1797A [1990] specifies the minimum time to double amplitude for each flying quality level. It is however more convenient here to express this criteria in terms of the spiral mode time constant, T_S [Cook, 1997]. The minimum Level 1 spiral mode time constant is given as 17.3 seconds for flight phase Categories A and C, and a minimum of 28.9 seconds for Category B. This is justified because for Categories A and C, the pilot is in active, continuous control of the aircraft, and the long-term attitude characteristics of the aeroplane are of less importance than in Category B flight. It can be seen then that all five structural variants would fail to meet the requirements for Level 1 Category A and C flight [Table 7.15]. The substantial reduction in the spiral mode time constant due to wing flexibility is the likely cause of this. The time constant is reduced from 15.438 seconds for the +30% wing stiffness case

to 12.222 seconds for the -30% stiffness case. It might be expected then that this trend would be further exacerbated and result in continued degraded handling qualities with any further reduction in wing stiffness.

It has been found that the dutch-roll mode is largely unaffected by changes in the wing stiffness [Table 7.15]. It is however worth noting the predicted handling qualities with reference to the relevant military specifications for each of the model variants. MIL-STD-1797A [1990] specifies minimum damping, ζ_d, minimum natural frequency, ω_d, and a minimum value for the product $\zeta_d\omega_d$ for each flight phase. All of the model variants fall into the Level 2 handling qualities category for all flight phases. The natural frequency of the dutch-roll mode is sufficient for Level 1 handling qualities for all flight phases, i.e. greater than 0.4, and the damping coefficient is sufficiently greater than 0.08 for Level 1 handling qualities in flight phase Categories B and C. However, the product of these two parameters, $\zeta_d\omega_d$, only meets the criteria for Level 2 handling qualities, having a value greater than 0.05. The required minimum values for dutch-roll damping and natural frequency are not independent, and larger values for dutch-roll damping are necessary at lower natural frequencies, hence the requirement stipulated by MIL-STD-1797A [1990] for $\zeta_d\omega_d$.

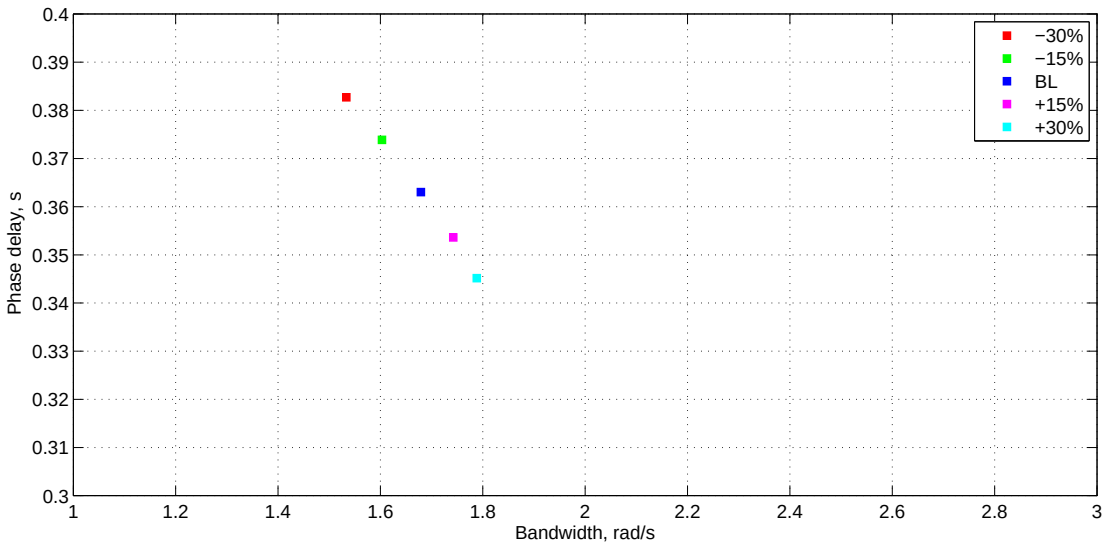

Figure 7.21: Bandwidth and phase delay for five wing stiffness variants at 180 m s^{-1} and 8,000 ft

It can be seen that the wing stiffness is likely to have a considerable effect on the lateral-directional handling qualities of the aeroplane. A significant reduction in the spiral mode time constant due to wing flexibility has been shown to lead to a considerable degradation in the handling qualities of the aeroplane. An increase in the roll mode time constant as a result of a reduction in wing stiffness has also been shown to lead to reduced handling qualities.

	-30%		-15%		Base		+15%		+30%	
Mode	Frequency, rad s^{-1}	Damping	Frequency, rad s^{-1}	Damping	Frequency, rad s^{-1}	Damping	Frequency, rad s^{-1}	Damping	Frequency, rad s^{-1}	Damping
SPPO	2.289	0.3283	2.343	0.3210	2.342	0.3235	2.355	0.3243	2.369	0.3246
Phugoid	0.06832	0.01321	0.06821	0.01218	0.06781	0.01110	0.06745	0.01045	0.06693	0.009756
Dutch Roll	0.8003	0.1010	0.8043	0.09972	0.8087	0.09864	0.8112	0.09743	0.8145	0.09732
Roll	τ **= 0.5443**s		τ **= 0.5318**s		τ **= 0.5134**s		τ **= 0.5015**s		τ **= 0.4843**s	
Spiral	τ **= 12.22**s		τ **= 13.10**s		τ **= 13.93**s		τ **= 14.71**s		τ **= 15.44**s	
Flexible Mode 1	6.070	0.03345	6.670	0.03264	7.218	0.03174	7.723	0.03121	8.194	0.03065
Flexible Mode 2	6.176	0.1153	6.784	0.1143	7.347	0.1152	7.863	0.1146	8.343	0.1121
Flexible Mode 3	7.260	0.1294	7.912	0.1316	8.496	0.1324	9.030	0.1327	9.524	0.1329
Flexible Mode 4	11.72	0.04884	12.77	0.04564	13.57	0.03932	14.09	0.03210	14.40	0.02854
Flexible Mode 5	13.62	0.02132	14.29	0.02375	14.91	0.02946	15.61	0.03590	16.33	0.03941
Flexible Mode 6	13.64	0.02010	15.01	0.02039	16.22	0.02047	16.99	0.02310	17.16	0.02421
Flexible Mode 7	14.87	0.03666	16.25	0.03543	17.19	0.02373	17.65	0.02193	18.00	0.021941
Flexible Mode 8	16.83	0.01821	17.05	0.02357	17.37	0.02784	17.81	0.02223	18.61	0.02001
Flexible Mode 9	17.86	0.05946	18.92	0.05084	19.44	0.06031	20.09	0.06121	20.86	0.05883
Flexible Mode 10	18.10	0.06688	18.98	0.05963	19.90	0.04632	20.80	0.04411	21.60	0.04883
Flexible Mode 11	20.49	0.05012	20.74	0.05613	21.38	0.06742	21.59	0.06273	21.70	0.05722
Flexible Mode 12	21.31	0.05943	21.45	0.06134	21.52	0.06254	21.67	0.07161	21.79	0.07223

Table 7.15: Open-loop aeroplane longitudinal, lateral-directional and flexible dynamics at 180 m s^{-1} and 8,000 ft for five wing stiffness variants

7.3 Load Alleviation

7.3.1 Manoeuvre Load Alleviation

In Section 6.2, a Manoeuvre Load Alleviation (MLA) system was developed around the Control and Stability Augmented (CSAS) closed-loop aircraft. The system was designed to have minimal influence on the rigid- and flexible-body modes. This was achieved by using a filtered elevator feedback to approximately cancel the pitching moment of the symmetric aileron deployment used to reduce the wing loading. It was shown that the open- and closed-loop MLA models had similar stability characteristics, and that the influence on the rigid-body modes of the MLA system was small. However, as was shown in Section 7.2.1, it is not necessarily sufficient to assume that the flying and handling qualities of an aircraft are satisfactory by only considering the rigid-body modes. This is especially important for a high-order aircraft model, such as the model considered here which includes additional structural and control modes. Let us then assess the handling qualities of the closed-loop aircraft using a number of suitable existing criteria and specifications. A total of three flight points shall be considered: 4,000, 8,000 and 12,000 ft at 180 m s^{-1}. In this study, only the inner-loop pitch-rate feedback CSAS control law is implemented, and any discontinuities in the MLA function are removed in order to simplify the analysis.

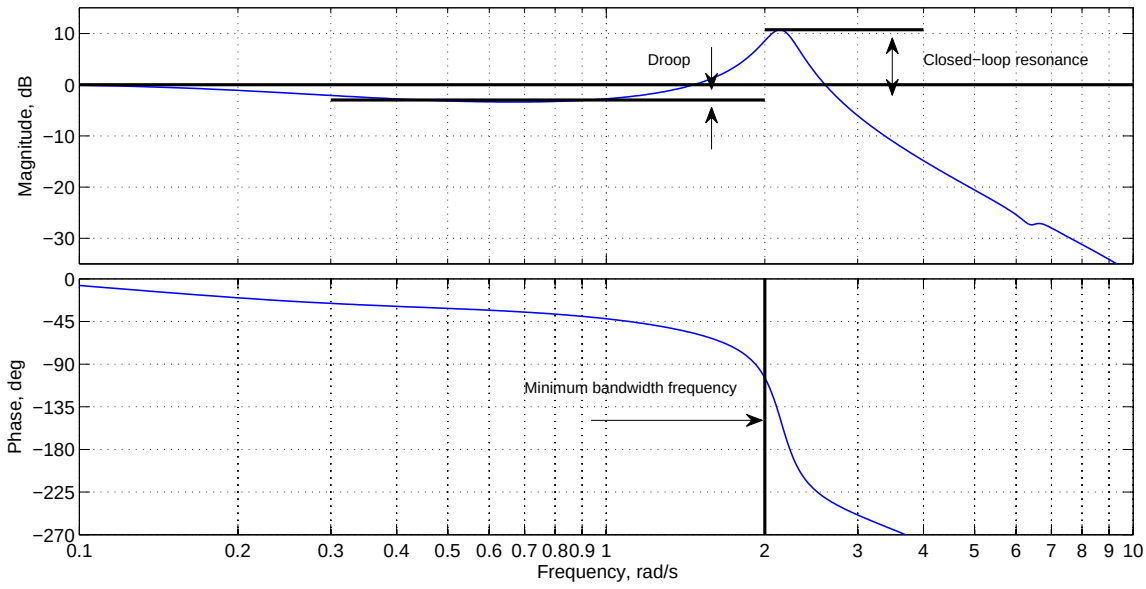

Figure 7.22: Bode plot for elevator-pitch attitude response showing Neal-Smith Criterion parameters

The Neal-Smith criterion [Neal and Smith, 1971] assumes that a pilot will automatically compensate for the aircraft to improve its handling qualities such that he is able to complete a given task. The criterion assumes that the pilot acts to control pitch-attitude, and forms a closed-loop system with the aircraft. The gain and phase that the pilot must provide then determines the handling qualities rating of the aircraft. For certain tasks, such as a compensatory tracking task [Stevens and Lewis, 1992], the pilot may be modelled as a transfer function plus a random signal used to account for differences in experimental

and theoretical pilot models referred to as the remnant. The transfer function form assumes that the human pilot adjusts the lead, lag, and gain of the aircraft, plus a pure time delay which represents the pilot's neuromuscular delays. It may be expressed as:

$$Y(s) = K_p e^{-ds} \frac{\tau_l s + 1}{\tau_i s + 1} \tag{7.3.1}$$

The pilot is assumed to automatically optimise the lead time constant, τ_l, lag time constant, τ_i, and gain, K_p for a given control task. The time delay, d, is assumed to vary between different pilots, and values between 0.2 and 0.4 seconds have been recorded. It is taken here to have an average fixed value of 0.3s.

The pitch-attitude observed by the pilot is the sum of the rigid-body pitch-attitude of the aeroplane and the flexible pitch-attitude of the fuselage at the cockpit [Figure 7.23]. This is given by the following equation:

$$\theta_{rf} = \theta_r + \theta_f \tag{7.3.2}$$

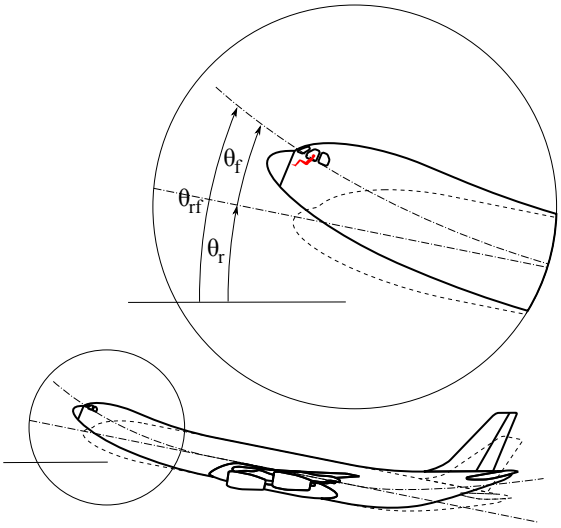

Figure 7.23: Pitch-attitude observed by the pilot at cockpit

The Neal-Smith criterion assumes that the pilot adjusts the phase and gain characteristics to minimise the low-frequency droop and closed-loop resonance [Figure 7.22] of the aircraft [Neal and Smith, 1971]. Droop is described as the maximum drop in gain below 0 dB at frequencies lower than the bandwidth frequency, where the phase first reaches -90°, while the closed-loop resonance is the gain magnitude of any resonant peak. The original criterion defines a fixed minimum bandwidth frequency of 3.5 rad s^{-1} [Neal and Smith, 1971]. MIL-STD-1797A [1990] extends this definition to other flight phase categories, with the requirement for Category B and C flight equal to 1.5 rad s^{-1}, or 2.5 rad s^{-1} for the landing phase. An average minimum bandwidth of 2.0 rad s^{-1} was assumed here. The criterion specifies a maximum low-frequency droop of -3 dB.

The closed-loop pilot-aeroplane system assumes a unity negative feedback. As such, it is convenient to express the closed-loop criterion droop and phase requirements on Nichols chart [Figure 7.24]. Once the phase and gain characteristics of the pilot model

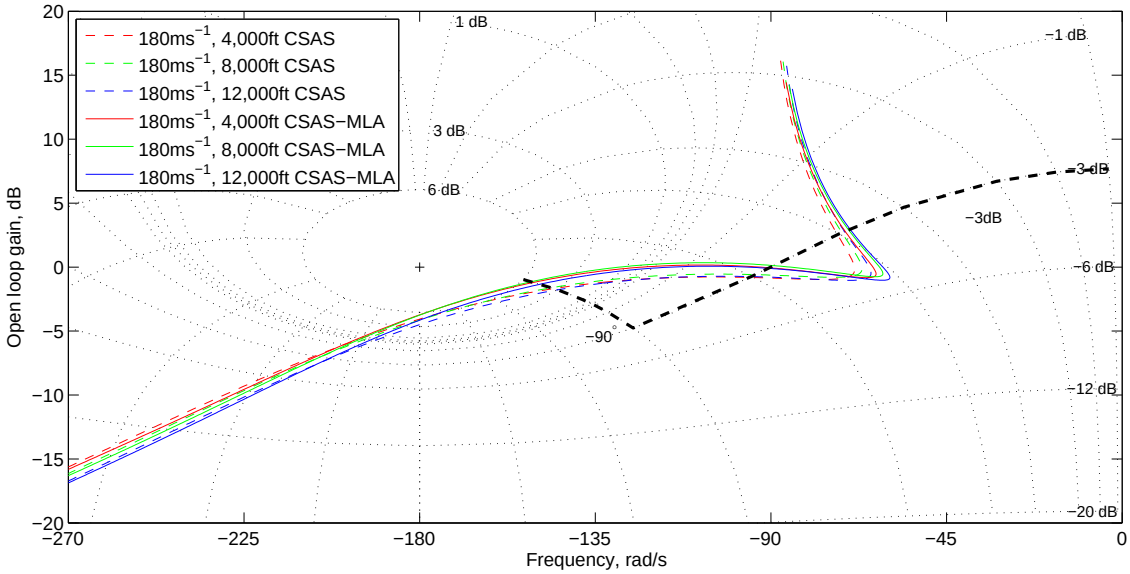

Figure 7.24: Nichols chart for elevator-pitch attitude response for open-loop CSAS and CSAS-MLA aeroplane models

are adjusted, the criterion defines the handling qualities of the aircraft as a function of the maximum pilot phase compensation and the closed loop resonance [Figure 7.28].

The open-loop aeroplane pitch-attitude frequency response to elevator demand is shown in Figure 7.25 for each of the three flight points considered. Alternatively, the pitch-attitude phase and gain response can be plotted on a Nichols chart [Figure 7.24]. The pilot-aeroplane closed-loop Neal-Smith criterion requirements for low-frequency droop and closed-loop phase lag are shown in bold. The pilot model variables τ_l, τ_i, and K_p were selected for each of the flight points and models in order to bring the pilot-aeroplane open-loop phase and gain characteristics into alignment with the criterion requirements [Table 7.16, Figure 7.26]

	CSAS			CSAS-MLA		
Coefficient	4,000ft	8,000ft	12,000ft	4,000ft	8,000ft	12,000ft
ϕ_p	-18.20	-17.60	-17.90	-23.40	-22.80	-23.20
τ_l	0.3626	0.3663	0.3641	0.3284	0.3325	0.3301
τ_i	0.6913	0.6835	0.6878	0.7615	0.7532	0.7585
K_p	1.365	1.396	1.488	1.462	1.496	1.603
Z_r	8.210	9.610	10.68	11.46	13.48	14.81

Table 7.16: Pilot phase compensation and resonant peak amplitude for CSAS and CSAS-MLA pilot-aeroplane models

The closed-loop pitch-attitude frequency response of the pilot-aeroplane model is shown in Figure 7.27. It can be seen that there is a considerable increase in the closed-loop resonant peak amplitude for the CSAS-MLA aeroplane. For example, at 8,000 ft this increase is equal to 3.87 dB. A larger value of pilot phase compensation was also necessary for CSAS-MLA aeroplane to achieve the requirement for -90° phase lag at the bandwidth frequency

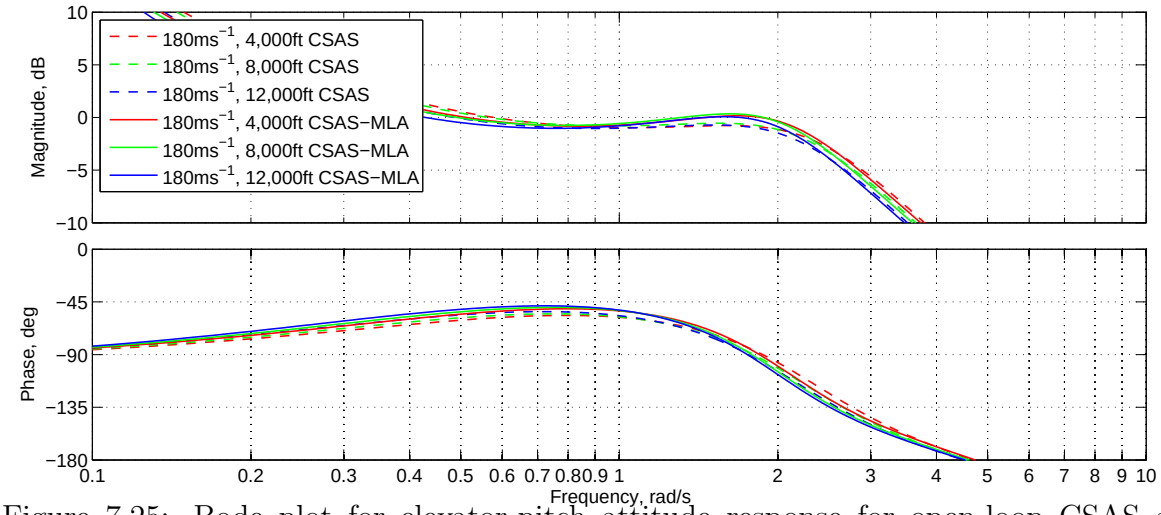

Figure 7.25: Bode plot for elevator-pitch attitude response for open-loop CSAS and CSAS-MLA aeroplane models

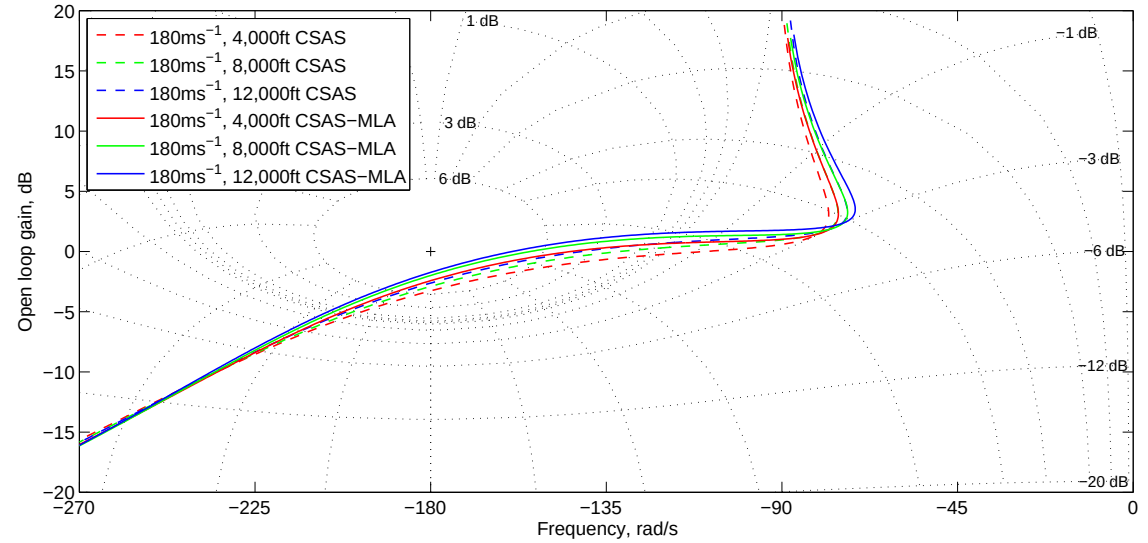

Figure 7.26: Nichols chart for elevator-pitch attitude response for open-loop CSAS and CSAS-MLA pilot-aeroplane models

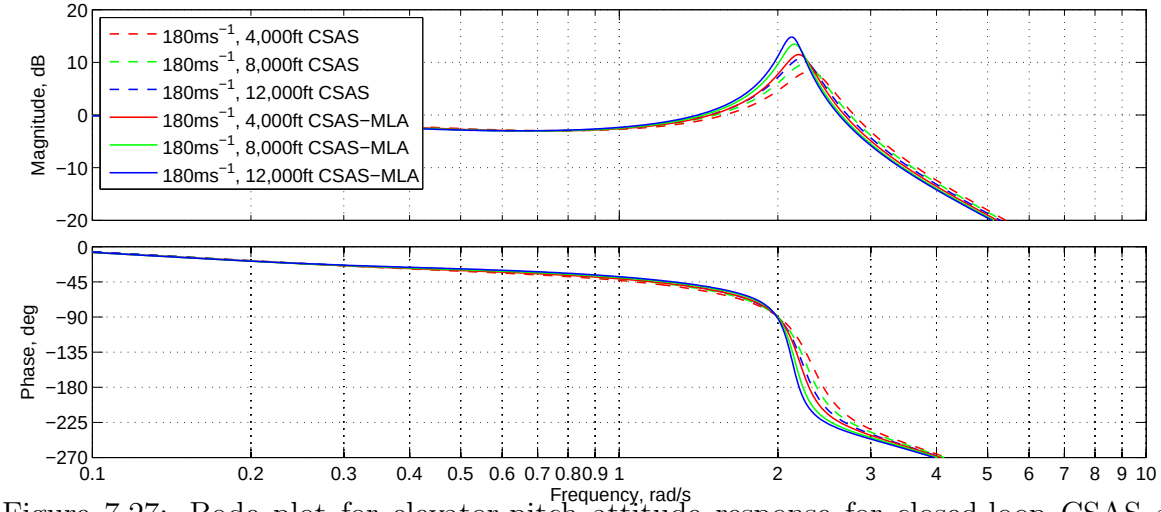

Figure 7.27: Bode plot for elevator-pitch attitude response for closed-loop CSAS and CSAS-MLA pilot-aeroplane models

[Table 7.16]. At 8,000 ft, it was necessary to increase the pilot phase compensation from -17.6° for the CSAS model to -22.8° for the CSAS-MLA model. It can also be seen in Figure 7.27 that there is a significant increase in the rate of phase lag roll-off for the MLA system. At -135° phase lag, the frequency for the CSAS model at 8,000 ft is 2.22 rad s^{-1}, compared to 2.13 rad s^{-1} for the CSAS-MLA model.

Figure 7.28 shows the closed-loop peak resonance amplitude, Z_r, against the maximum pilot phase compensation, ϕ_p. Overlaid are the handling qualities requirements specified by the Neal-Smith criterion [Neal and Smith, 1971]. We can see that the aeroplane model including only the CSAS control law meets the requirements for Level 2 flying qualities at all flight points, though there is a general trend towards increasing resonance amplitude with increasing altitude. However, for the CSAS-MLA system, we can see that the increase in the required pilot compensation, as well as the significant increase in the closed-loop resonance, results in a prediction of considerably degraded handling qualities. All flight points for the CSAS-MLA model are predicted by the Neal-Smith criterion to lie outside the boundaries for Level 3 flight.

In Section 7.2.1, an alternative criteria, the Bandwidth criterion [Hoh et al., 1982], was used to predict the handling qualities of the open-loop aeroplane. Using the same methodology, we can calculate the phase bandwidth, $\omega_{BW_{phase}}$, gain bandwidth, $\omega_{BW_{gain}}$, and phase delay, $e^{-\tau_e s}$ [Table 7.17]. The bandwidth, ω_{BW}, is again defined as the lower of the phase and gain bandwidths.

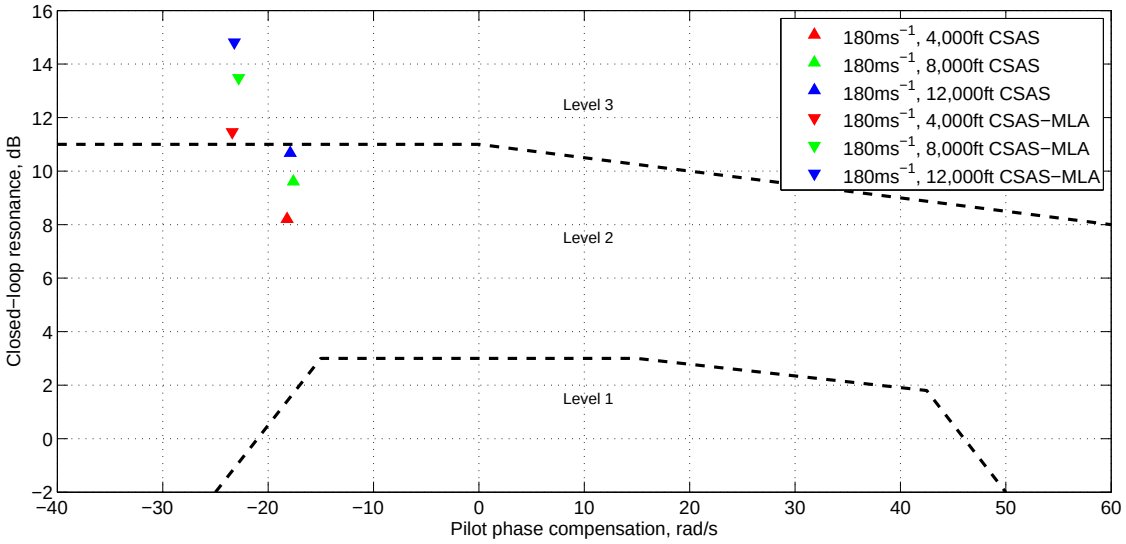

Figure 7.28: CSAS and CSAS-MLA aeroplane closed-loop resonance and pilot phase compensation against Neal-Smith requirements [Neal and Smith, 1971]

Figure 7.29 plots the bandwidth and phase delay against the Bandwidth criterion requirements for Category C flight [MIL-STD-1797A, 1990]. It can be seen that the closed-loop CSAS model exhibits improved handling qualities when compared to the open-loop results of Section 7.2.1, with the aeroplane at all altitudes considered meeting the requirements for Level 1 flying qualities. If we compare the results for the closed-loop CSAS-MLA aeroplane, we can see that there is a reduction in the bandwidth of the aeroplane for all the flight points considered. For example, at 8,000 ft the bandwidth is reduced by 0.113

rad s^{-1} from 2.768 to 2.665 rad s^{-1}. The phase delay for all the flight points and for both the CSAS and CSAS-MLA models remains constant at an average value of 0.0715.

	CSAS			CSAS-MLA		
Coefficient	4,000ft	8,000ft	12,000ft	4,000ft	8,000ft	12,000ft
$\omega_{BW_{gain}}$	3.478	3.382	3.326	3.473	3.382	3.328
$\omega_{BW_{phase}}$	2.768	2.655	2.596	2.665	2.557	2.5100
τ_e	0.07083	0.07145	0.07227	0.0724	0.07102	0.07164

Table 7.17: Bandwidth criterion parameters for CSAS and CSAS-MLA aeroplane models

A Low-order Equivalent System (LOES) modelling technique was presented in Section 7.2.1 in order to to estimate the characteristics of higher-order aircraft and apply existing handling qualities criteria to the problem. The LOES parameters for the CSAS and CSAS-MLA models [Table 7.18] were again obtained by simultaneously matching the pitch-rate and normal acceleration frequency response of the LOES model to the response of the high-order system [Figure 7.25]. The frequency response of the high-order system was matched between 0.1 and 10 rad s^{-1}, and the variable T_{θ_2} was allowed to vary freely in the optimisation.

The LOES model suggests that the short-period damping, ζ_s, is reduced by an average of 4.55% for the CSAS-MLA model when compared to the CSAS model [Table 7.18]. This would correlate with the open-loop frequency response [Figure 7.25] which showed an higher gain at the short-period frequency for the CSAS-MLA model. It can also be seen that the value of $1/T_{\theta_2}$ is reduced for the CSAS-MLA model. Given the difficulty in selecting a fixed or free value for this parameter, this result should be treated with caution. However, it useful to note that for an aircraft with known problems, any deficiency manifests itself whether the value of $1/T_{\theta_2}$ is fixed or free, for example as an increased time delay. In most cases then, it has been found either method predicts similar handling qualities, though the suggested cause can differ greatly [MIL-STD-1797A, 1990]. Finally, the value for the LOES time delay, τ_e, matches closely the result predicted by the Bandwidth criterion [Table 7.17]

Section 7.2.1 presented two further handling qualities criteria, the Control Anticipation Parameter (CAP) and the pitch-attitude response criteria. The results for the LOES CSAS and CSAS-MLA models are shown in Figures 7.30 and 7.31 respectively against the relevant Category C criteria [MIL-STD-1797A, 1990]. Figure 7.30 shows a reduction in the normal-acceleration sensitivity, n/α, for the CSAS-MLA model, though the CAP parameter is largely unchanged by altitude or control law and has an average value of 0.267. The handling qualities for both CSAS and CSAS-MLA models is predicted to be Level 1 at all altitudes. Figure 7.31 shows the reduction in short-period mode damping identified for the LOES model in Table 7.18 together with the increase in the value of T_{θ_2} for the CSAS-MLA model. The criteria predicts that both aeroplane control laws yield Level 1 handling qualities, though if the trend in the reduction in short-period damping were continue then it is likely the CSAS-MLA model would show degraded handling qualities.

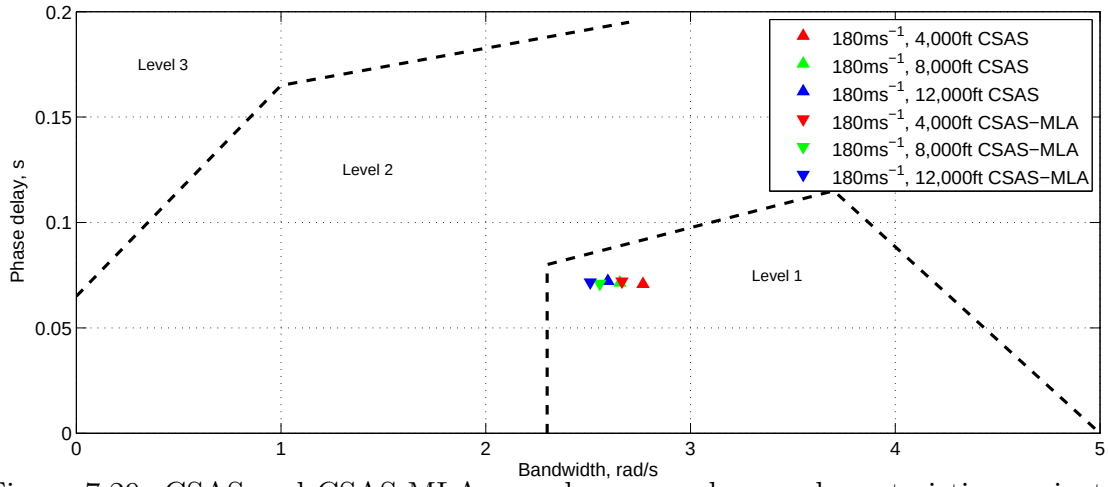

Figure 7.29: CSAS and CSAS-MLA aeroplane τ_e and ω_{BW} characteristics against Category C bandwidth requirements [MIL-STD-1797A, 1990]

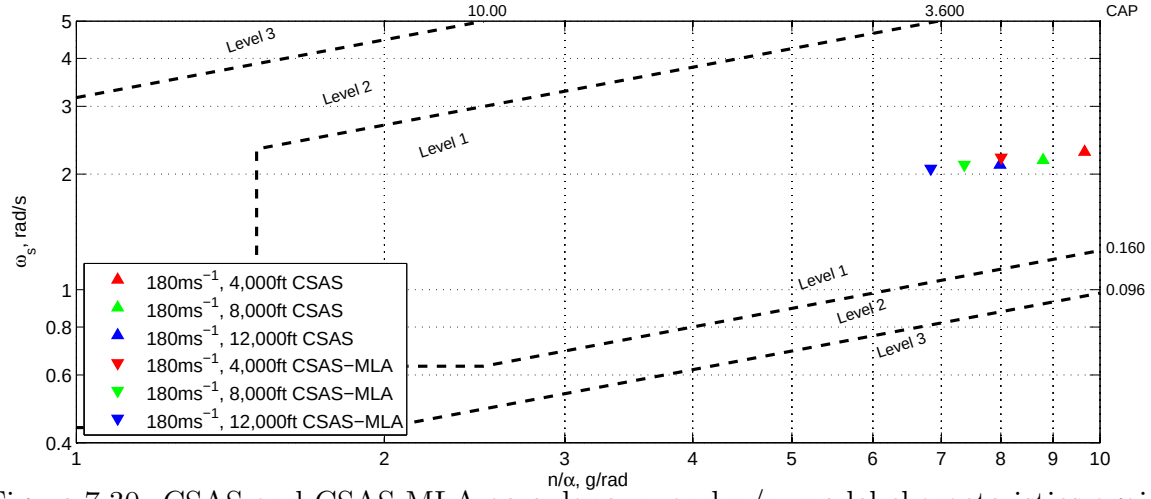

Figure 7.30: CSAS and CSAS-MLA aeroplane ω_s and n/α model characteristics against Category C CAP requirements [MIL-STD-1797A, 1990]

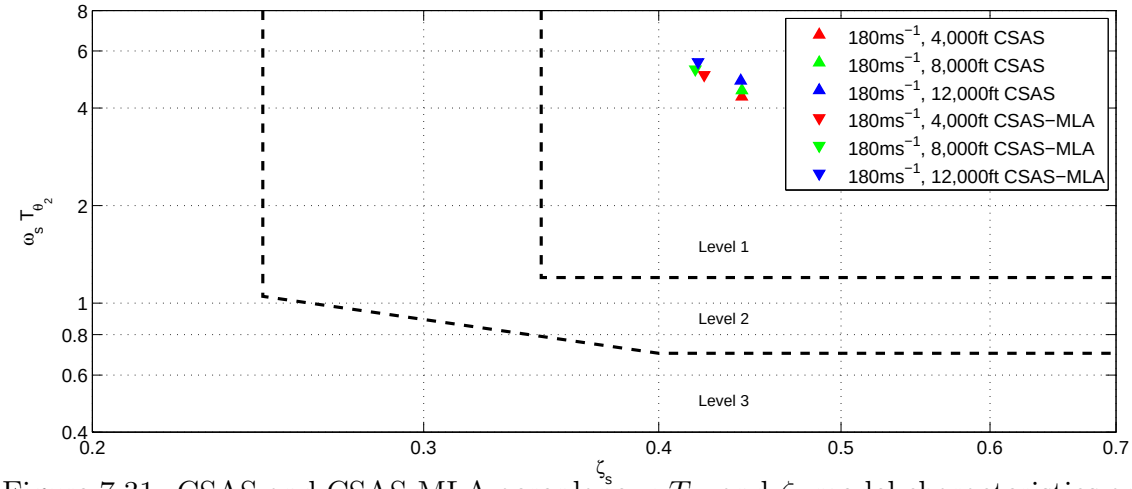

Figure 7.31: CSAS and CSAS-MLA aeroplane $\omega_s T_{\theta_2}$ and ζ_s model characteristics against Category C pitch response requirements [MIL-STD-1797A, 1990]

	CSAS			CSAS-MLA		
Coefficient	4,000ft	8,000ft	12,000ft	4,000ft	8,000ft	12,000ft
ζ_p	0.0000	0.0000	0.0000	0.04932	0.04018	0.02734
ω_p	0.06845	0.06974	0.07121	0.05832	0.06043	0.06367
ζ_s	0.4435	0.4435	0.4423	0.4232	0.4181	0.4200
ω_s	2.283	2.174	2.113	2.209	2.115	2.067
$1/T_{\theta_1}$	0.003321	0.003213	0.003001	0.01241	0.01184	0.009123
$1/T_{\theta_2}$	0.5263	0.4798	0.4355	0.4363	0.4022	0.3720
$1/T_{n_1}$	0.0043	0.0051	0.0056	0.0000	0.0000	0.0000
K_q	3.475	3.237	3.006	3.434	3.195	2.971
K_n	36.47	31.40	26.79	34.25	29.57	25.42
τ_e	0.08432	0.08650	0.08845	0.08231	0.08372	0.08554
τ_n	0.3072	0.3085	0.3092	0.2804	0.2813	0.2845
M	7.815	7.392	7.159	8.316	7.796	7.475

Table 7.18: Low-order equivalent system coefficients for CSAS and CSAS-MLA aeroplane models

In summary, each of the different criteria predict slightly different handling qualities. However, there is a general trend towards Level 1/2 handling qualities for the closed-loop CSAS model. The different criteria do agree though that the influence of the Manoeuvre Load Alleviation (MLA) function is to reduce the handling qualities of the aeroplane. The Neal-Smith criterion suggests a significant increase in the necessary required pilot compensation. This is likely a result of reduced bandwidth of the aeroplane, as defined by the Bandwidth criterion, and the reduction in the short-period damping.

7.3.2 Gust Load Alleviation

In Section 6.2, a Gust Load Alleviation (GLA) control function was developed in order to manage and alleviate the transient loads due to gusts. In order to reduce the interaction of the GLA system with the rigid-body dynamics, the commanded normal acceleration was subtracted from the measured acceleration. This should ideally prevent the GLA system activating as a result of commanded manoeuvres. A sixth-order approximation of the normal acceleration response to pilot command was used to approximate the response of the aeroplane. The GLA function also included a number of discontinuities, including a minimum activation threshold of 0.1 g, rate limiting, limited control authority, and a short hold function. The purpose of the hold function is to minimise the transient response of the system to gusts.

In order to model the effect of these discontinuities, the time history of the response of the complete aircraft to pilot command, including discontinuities, was calculated. A sinusoidal signal with linearly increasing frequency and constant amplitude, otherwise known as a chirp signal, was used as the command input. A input signal frequency of 0.1–10 rad s^{-1} was input over a time period of 1,000 seconds. The response of the aeroplane pitch-rate was recorded at a sample rate of 500 Hz [Figure 7.32]. The choice of pitch-rate as the system response output was chosen in order to measure the largest magnitude

response of the aeroplane. The response of the aeroplane including the standard Control and Stability Augment System (CSAS) and GLA control law was analysed at two flight points: 8,000 and 12,000 ft at 180 m s^{-1}.

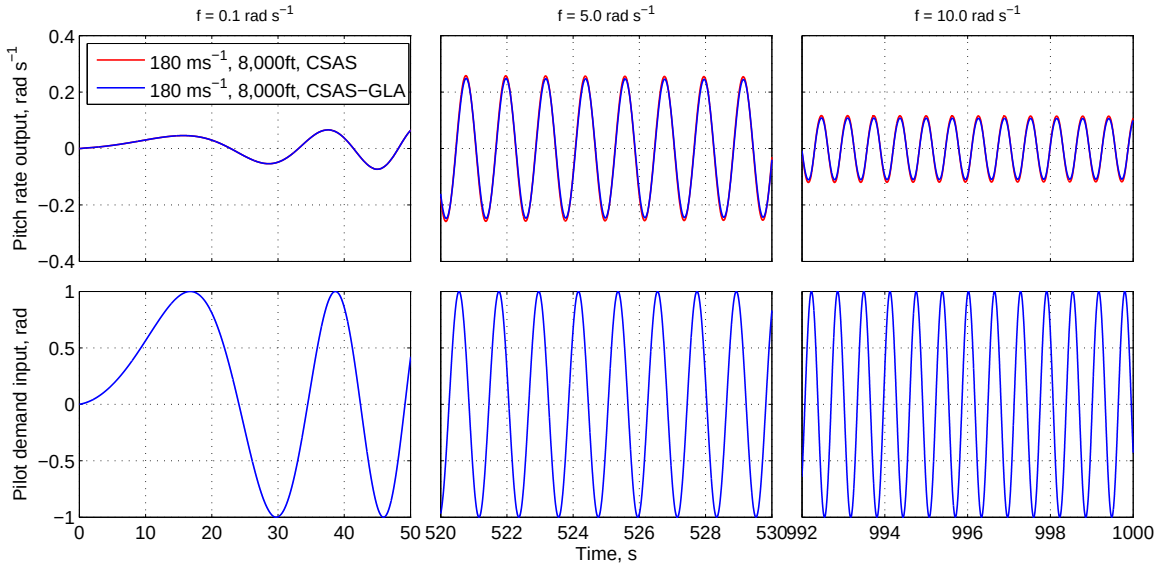

Figure 7.32: Pitch-rate response of aeroplane to chirp signal pilot command

The pitch-rate response of the complete model in the frequency domain was estimated from a Fourier analysis of the time history. The pitch-attitude frequency response was then calculated by adding the influence of an integrator to the pitch-rate response (An integrator reduces the gain by -20 dB $decade^{-1}$, and introduces -90° of phase lag). The frequency response of the aeroplane pitch -rate and -attitude is shown in Figures 7.33 and 7.34 respectively.

Figure 7.34 shows the pitch-attitude frequency response of the aeroplane at 8,000 ft and 180 m s^{-1}. It can be seen that at low frequencies the pitch-attitude frequency response of the CSAS-GLA aeroplane to pilot command matches very closely or almost exactly the response of the aeroplane including the CSAS control law alone. However above 1 rad s^{-1}, the response of two aeroplane control law models differ, with the gain of the CSAS-GLA aeroplane model reduced and the phase lag increased.

	CSAS		CSAS-GLA	
Coefficient	8,000ft	12,000ft	8,000ft	12,000ft
ϕ_p	-13.35	-17.40	-13.00	-17.10
τ_l	0.3957	0.3678	0.3986	0.3695
τ_i	0.6334	0.6813	0.6292	0.6770
K_p	7.852	7.763	7.943	7.852
Z_r	0.5000	-0.7500	0.8750	-0.5000

Table 7.19: Pilot phase compensation and resonant peak amplitude for CSAS and CSAS-GLA pilot-aeroplane models

Using the Neal-Smith criterion described in Section 7.3.1, the pilot-aeroplane closed-loop

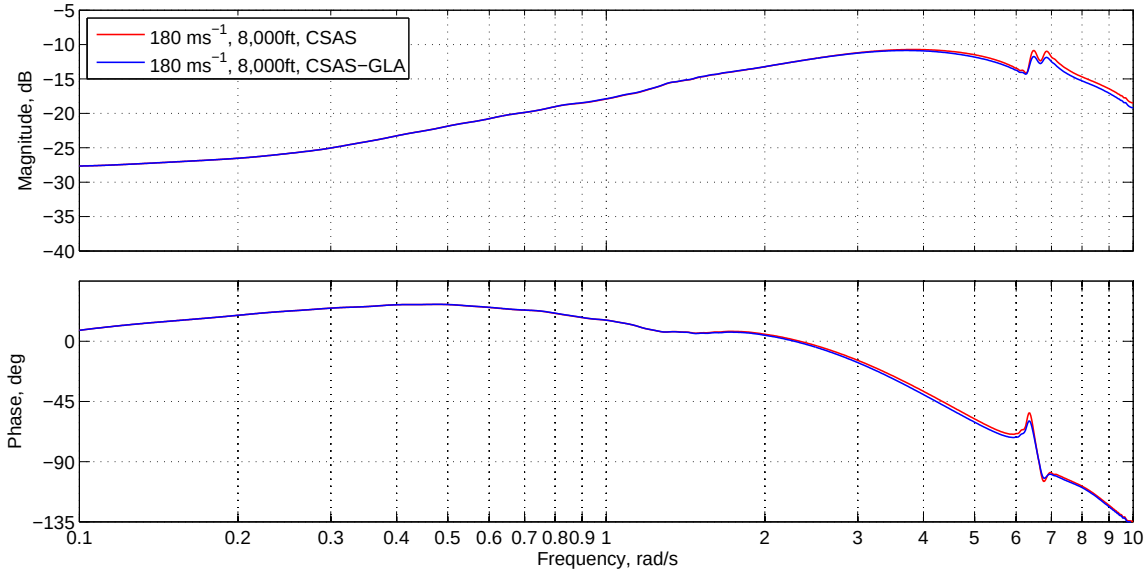

Figure 7.33: Bode plot for pilot–pitch-rate response at 8,000 ft and 180 m s^{-1}

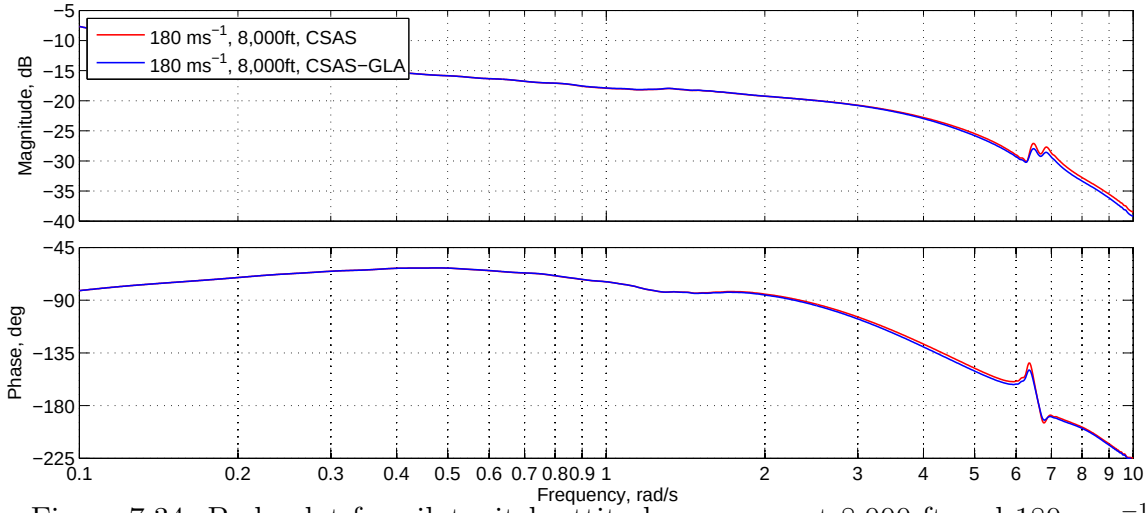

Figure 7.34: Bode plot for pilot–pitch-attitude response at 8,000 ft and 180 m s^{-1}

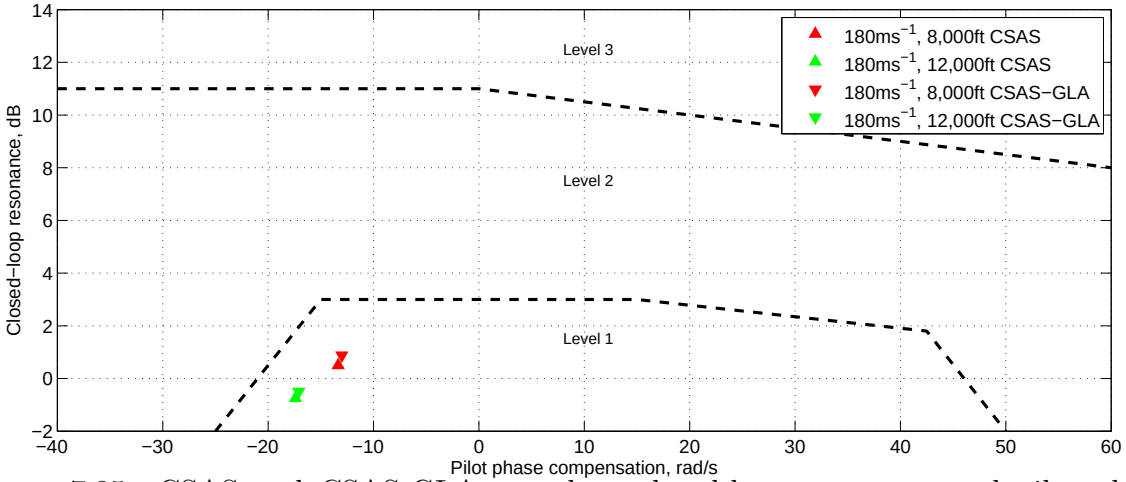

Figure 7.35: CSAS and CSAS-GLA aeroplane closed-loop resonance and pilot phase compensation against Neal-Smith requirements [Neal and Smith, 1971]

handling qualities can be estimated from the pitch-attitude frequency response. The pilot model phase and gain compensation required to bring the pitch-attitude response of the aeroplane into agreement with the Neal-Smith pilot criteria for the CSAS and CSAS-GLA aeroplane models is given in Table 7.19 and Figure 7.35. It is shown in Table 7.19 that in order to meet the Neal-Smith requirements, it is necessary for the pilot to introduce a phase lag of -13.5° at 8,000 ft and 180 m s^{-1} for the CSAS aeroplane model alone. As a result of the increase in phase lag due to the GLA system, the necessary pilot phase lag is reduced to -13.0° for the CSAS-GLA aeroplane model. The closed-loop resonance of the CSAS-GLA model is also increased, from 0.500 to 0.875 dB at 8,000 ft and from -0.750 to -0.500 dB at 12,000 ft. However, both aeroplane control law models meet the requirements for Level 1 handling qualities at the two altitudes considered.

In addition to the Neal-Smith criterion, the Bandwidth criterion was also used to assess the handling qualities of the aeroplane. The Bandwidth criterion does not assume a fixed bandwidth frequency, instead assuming a fixed phase and gain margin. The increase in phase lag as a result of the GLA control law is reflected perhaps more accurately by the Bandwidth criterion as a reduction in the bandwidth of the aeroplane [Table 7.20]. The reduction in the phase bandwidth of the aeroplane at 12,000 ft, for example, is 0.359 rad s^{-1}. The phase delay introduced as a result of the CSAS control law means the handling qualities of both the CSAS and CSAS-GLA models only meet the criteria for Level 2 handling qualities [MIL-STD-1797A, 1990].

	CSAS		CSAS-GLA	
Coefficient	8,000ft	12,000ft	8,000ft	12,000ft
$\omega_{BW_{gain}}$	4.322	5.392	4.302	4.962
$\omega_{BW_{phase}}$	4.341	5.367	4.223	5.008
τ_e	0.1420	0.1661	0.1453	0.1704

Table 7.20: Bandwidth criterion parameters for CSAS and CSAS-GLA aeroplane models

In order to understand the interaction of the GLA function with the rigid-body motion of the aeroplane, the response of the normal acceleration approximation transfer function [Equation 6.2.2] to pilot command was compared to the actual response of the aeroplane model. The time history of the two accelerations at 8,000 ft for 0.1, 1.0 and 10 rad s^{-1} is shown in Figure 7.36. The frequency response of the approximate and measured acceleration signals was calculated again from a Fourier analysis of the time history [Figure 7.37].

At low frequencies it can be seen that the approximate model predicts the phase and gain characteristics of the plane sufficiently well to cancel the normal acceleration response to pilot demand. The activation of the GLA system as a result of pilot command is therefore prevented. However at higher frequencies the approximate model provides a poor match for the measured response of the complete aeroplane model. The resulting difference between the two signals is sufficiently high to cross the threshold for activation of the GLA system at +0.1 g. The GLA function is then activated erroneously by the pilot-commanded normal acceleration. As a consequence the pitching moment generated by the deployment of symmetric aileron and elevator by the GLA function modifies the rigid-body motion of the aeroplane. The approximation of the normal acceleration

response of the aeroplane was calculated in Section 6.2 from the linearised aeroplane at 8,000 ft only. This approximation hence provides a much worse estimate of the response of the aeroplane at 12,000 ft for which it was not designed. This is reflected in the larger reduction in the bandwidth at this altitude compared to the result at 8,000 ft [Table 7.20].

It can be seen then that careful consideration must be given to the approximation of the linearised normal acceleration response of the aeroplane. The sixth-order approximation given by Equation 6.2.2 is adequate at low frequencies, and the difference between the two signals is sufficiently small that it does not exceed the activation threshold. However at higher frequencies the difference between the two signals is sufficient to cross the activation threshold. This leads to unwanted deployment of the GLA system during commanded manoeuvres. The erroneous deployment of aileron and elevator by the GLA function introduces additional phase lag in the pitch-attitude response of the aeroplane. The normal acceleration response of the aeroplane will also change with flight condition. The challenge of generating a good approximation for the response of the aeroplane across the flight envelope to pilot command is hence made more difficult.

Where the approximation of the normal acceleration response aeroplane is poor, it is likely then that the GLA function will be activated mistakenly during manoeuvring flight of the aeroplane. As a consequence of this, the bandwidth of the aeroplane is shown to be reduced, and this is likely to lead to degraded handling qualities and an increased susceptibility to PIOs.

7.3.3 Active Mode Control

In Section 6.2, an Active Mode Control (AMC) law was developed to improve damping of the first structural symmetric wing bending mode. This was achieved using wing acceleration feedback to control symmetric aileron deflection. It was found in Section 7.1 that wing stiffness had little effect on the longitudinal rigid-body modes, however the effect of increased damping was not considered. A number of different existing handling qualities criteria are used here to assess the impact of a wing AMC control law on the handling qualities of the aeroplane. Again, three flight points are considered: 4,000, 8,000 and 12,000 ft at 180 m s^{-1}.

Using the Neal-Smith criterion described in Section 7.3.1, the pilot-aeroplane closed-loop handling qualities can be estimated. Figure 7.38 shows the elevator to pitch-attitude frequency response of the closed-loop pilot-aeroplane system. The closed-loop response for the CSAS and CSAS-AMC aeroplane models overlay almost exactly and show nearly identical characteristics. As such, the required pilot phase and gain compensation in the Neal-Smith pilot model for the CSAS and CSAS-AMC aeroplane models is also nearly identical [Table 7.21].

Figure 7.28 shows the closed-loop peak resonance amplitude, Z_r, against the maximum pilot phase compensation, ϕ_p for each of the three flight points and the CSAS and CSAS-AMC aircraft models. Again overlaid are the handling qualities requirements specified by the Neal-Smith criterion [Neal and Smith, 1971]. It can be seen that the Neal-Smith criteria estimates similar handling qualities for both aeroplane control laws, predicting Level 2 handling qualities for both models. Table 7.21 shows that in fact there is a small

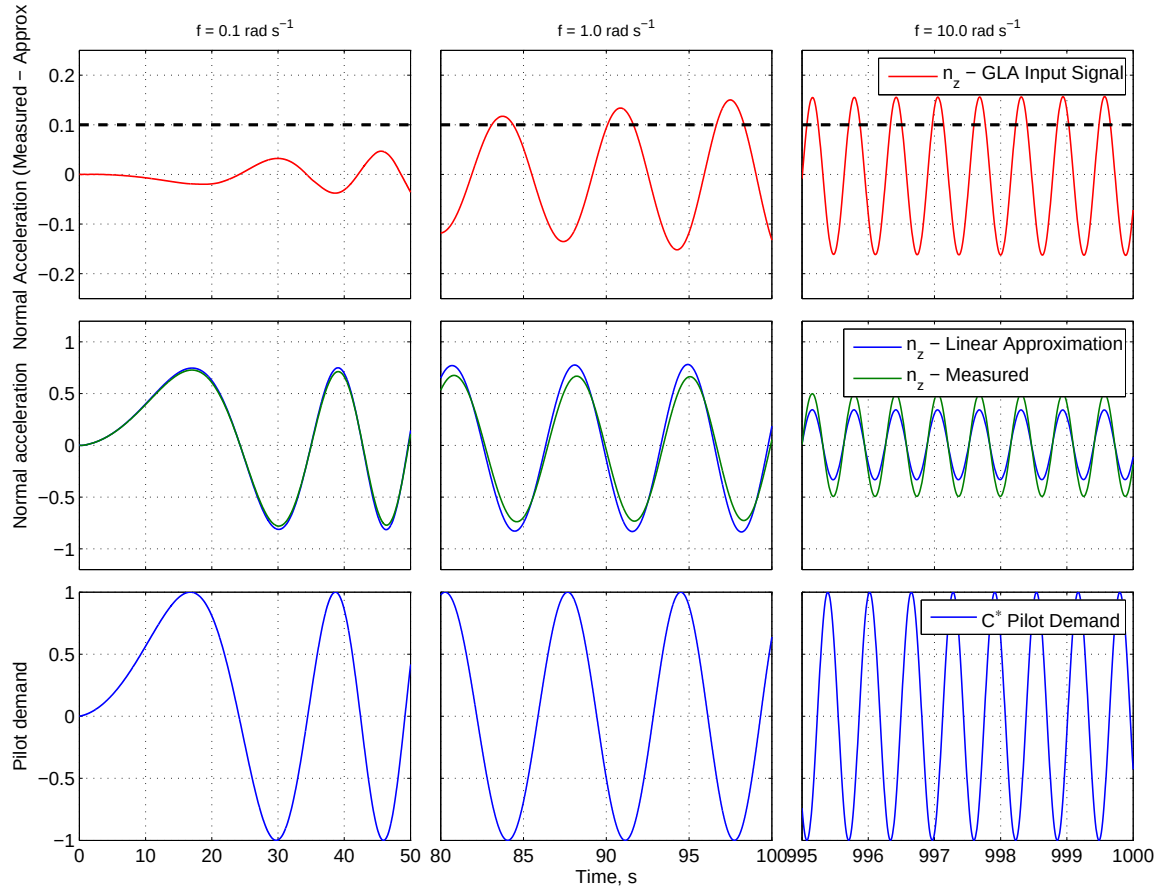

Figure 7.36: Time history of measured/approximated normal acceleration response for 0.1, 1.0 and 10 rad s^{-1} at 8,000 ft and 180 m s^{-1}

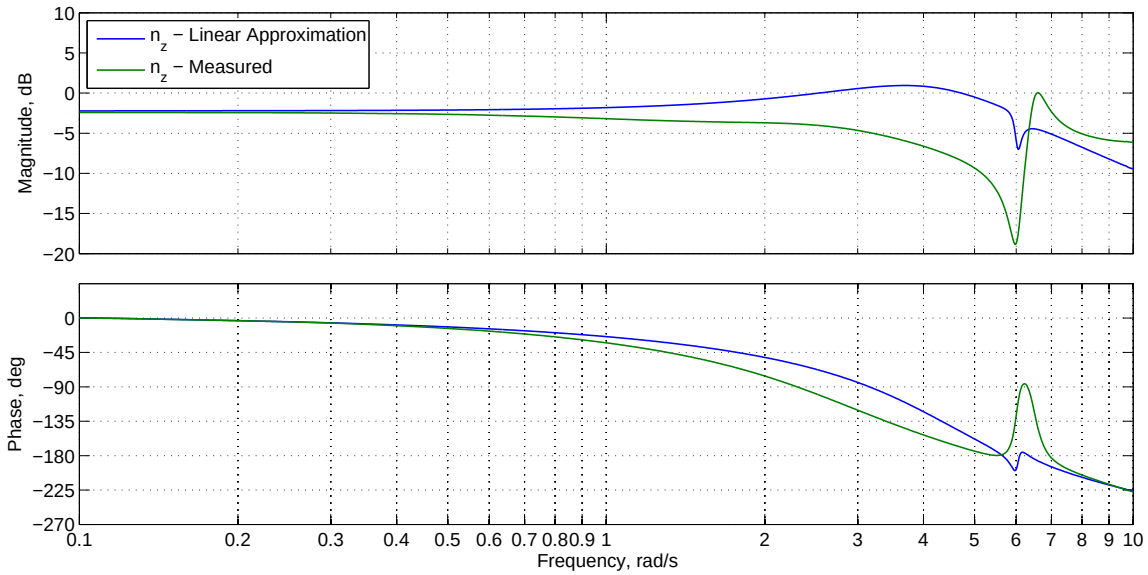

Figure 7.37: Bode plot for pilot–measured/approximated normal acceleration response at 8,000 ft and 180 m s^{-1}

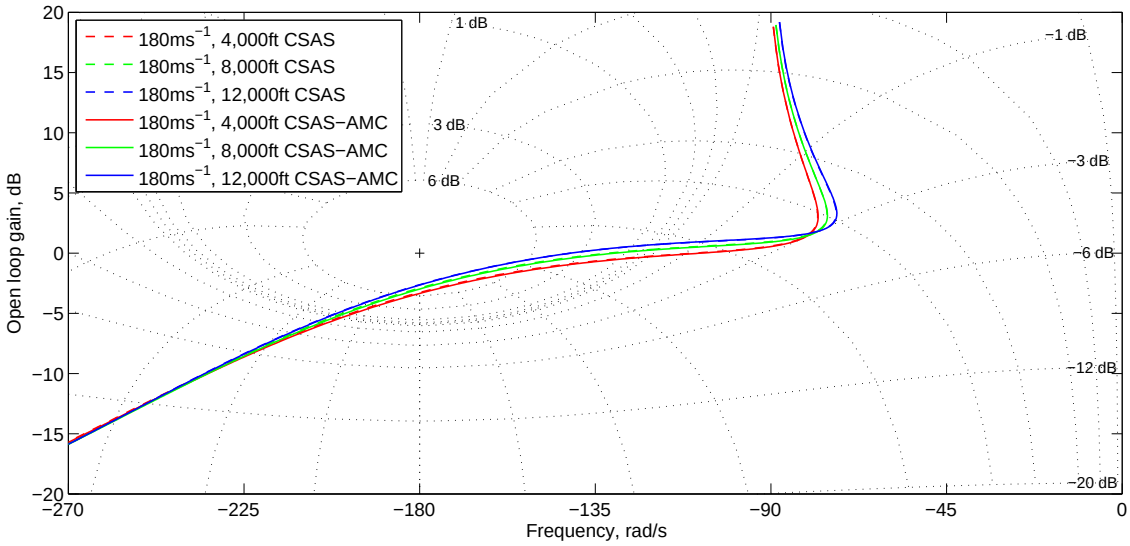

Figure 7.38: Nichols chart for elevator-pitch attitude response for open-loop CSAS and CSAS-AMC pilot-aeroplane models

reduction in the necessary pilot compensation for the CSAS-AMC model. For example, at 8,000 ft the required phase compensation is reduced from -17.6° to -17.3°. There is also a reduction in the peak closed-loop resonance, Z_r. At 8,000 ft, for example, the resonance is reduced from 9.610 to 9.360. These results suggest that the AMC control law is successful in reducing the interaction of the flexible- and rigid-body modes, tending to handling qualities more similar to the rigid aircraft. However, as it was found in Section 7.1, wing flexibility has little influence on the longitudinal dynamics of the aeroplane. As a result, any improvement in wing damping only has a limited improvement on the longitudinal handling qualities of the aeroplane.

	CSAS			CSAS-AMC		
Coefficient	4,000ft	8,000ft	12,000ft	4,000ft	8,000ft	12,000ft
ϕ_p	-18.20	-17.60	-17.90	-17.90	-17.30	-17.50
τ_l	0.3623	0.3666	0.3643	0.3642	0.3685	0.3673
τ_i	0.6916	0.6833	0.6875	0.6874	0.6790	0.6821
K_p	1.365	1.396	1.488	1.349	1.380	1.479
Z_r	8.210	9.610	10.680	7.940	9.360	10.610

Table 7.21: Pilot phase compensation and resonant peak amplitude for CSAS and CSAS-AMC pilot-aeroplane models

A similar result can be seen when the Bandwidth criterion is used to assess the impact of the AMC law on the longitudinal handling qualities of the aeroplane. Following the methodology outlined in Section 7.2.1, the phase delay and bandwidth were calculated for the CSAS and CSAS-AMC models at each of the three flight points [Table 7.22, Figure 7.40]. It can be seen from Table 7.22 that the gain and phase bandwidth are almost unaffected by the addition of the AMC law, as is the phase delay. When compared to the Category C requirements [MIL-STD-1797A, 1990], the criteria predicts Level 1 handling

qualities for all three flight points [Figure 7.40].

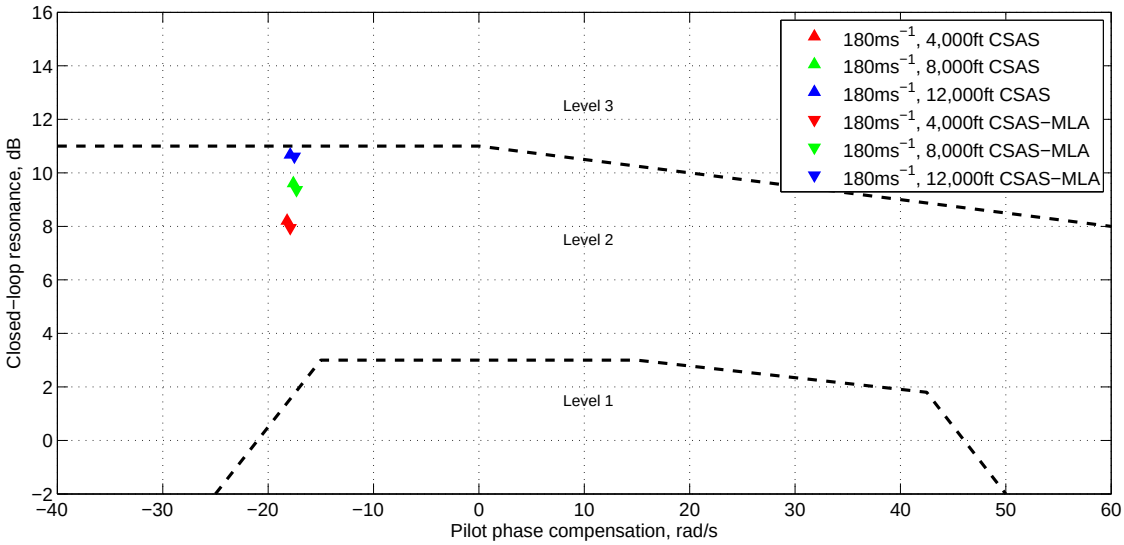

Figure 7.39: CSAS and CSAS-AMC aeroplane closed-loop resonance and pilot phase compensation against Neal-Smith requirements [Neal and Smith, 1971]

The Low-order Equivalent System (LOES) technique was again used to estimate the characteristic parameters of the higher-order CSAS and CSAS-AMC aeroplane models [Table 7.23]. The results show the two control laws provide very similar aeroplane characteristics, and there is little difference between the CSAS and CSAS-AMC LOES models. In order to assess the handling qualities of the LOES model, the Control Anticipation Parameter (CAP) and the pitch-attitude response criteria have been employed.

	CSAS			CSAS-AMC		
Coefficient	4,000ft	8,000ft	12,000ft	4,000ft	8,000ft	12,000ft
$\omega_{BW_{gain}}$	3.478	3.382	3.326	3.47	3.374	3.327
$\omega_{BW_{phase}}$	2.768	2.655	2.596	2.766	2.653	2.593
τ_e	0.07083	0.07145	0.07223	0.07102	0.07150	0.07252

Table 7.22: Bandwidth criterion parameters for CSAS and CSAS-AMC aeroplane models

Figure 7.41 shows the LOES short-period frequency, ω_s and normal-acceleration sensitivity, n/α, against the Category C requirement defined by MIL-STD-1797A [1990]. Again, the CSAS and CSAS-AMC aeroplane models suggests almost identical handling qualities, with both models comfortably yielding Level 1 handling qualities at all altitudes. The pitch-attitude variables $\omega_s T_{\theta_2}$ and ζ_s are shown in Figure 7.42 against the Category C requirements [MIL-STD-1797A, 1990]. The LOES model predicts are a very small increase in the short-period mode damping, ζ_s, of 0.5% for the CSAS-AMC model at all altitudes, and this is shown in Figure 7.42. However, this difference is small and both models again exhibit Level 1 handling qualities for all flight points.

In summary then, the findings here would suggest that symmetric wing bending damping augmentation achieved using Active Mode Control (AMC) does not improve the longi-

	CSAS			CSAS-MLA		
Coefficient	4,000ft	8,000ft	12,000ft	4,000ft	8,000ft	12,000ft
ζ_p	0.0000	0.0000	0.0000	0.0000	0.0000	0.0000
ω_p	0.06842	0.06925	0.07101	0.06854	0.06954	0.07108
ζ_s	0.4432	0.4430	0.4428	0.4454	0.4453	0.4452
ω_s	2.283	2.174	2.113	2.278	2.170	2.109
$1/T_{\theta_1}$	0.003210	0.003341	0.003476	0.002873	0.003211	0.003321
$1/T_{\theta_2}$	0.5267	0.4794	0.4351	0.5277	0.4793	0.4350
$1/T_{n_1}$	0.004640	0.005012	0.005230	0.004431	0.004750	0.005183
K_q	3.475	3.237	3.006	3.477	3.240	3.009
K_n	36.47	31.40	26.79	36.46	31.38	26.77
τ_e	0.08432	0.08645	0.08870	0.08443	0.08656	0.08891
τ_n	0.3073	0.3084	0.3092	0.3086	0.3085	0.3090
M	7.815	7.392	7.159	8.686	8.159	7.826

Table 7.23: Low-order equivalent system coefficients for CSAS and CSAS-AMC aeroplane models

tudinal handling qualities of the aeroplane to any great degree. This would agree with the findings of Section 7.1 that suggested that wing flexibility had little influence on the longitudinal rigid-body dynamics of the aeroplane. The results using the Neal-Smith criteria suggest a small decrease in the necessary pilot compensation and closed-loop resonance for the AMC law. The AMC law developed in Section 6.2 was designed to increase the first symmetric wing bending mode damping to 10%. It is feasible then that with a further increase in damping, by control augmentation or structural design, that this would improve handling qualities, though any effect would be limited due to low influence of the wing flexibility on the longitudinal rigid-body dynamics. In Section 7.1, it was found that wing flexibility significantly influenced the lateral-directional handling qualities of the aeroplane. It should not be assumed therefore AMC will not influence the lateral-directional handling qualities of the aeroplane.

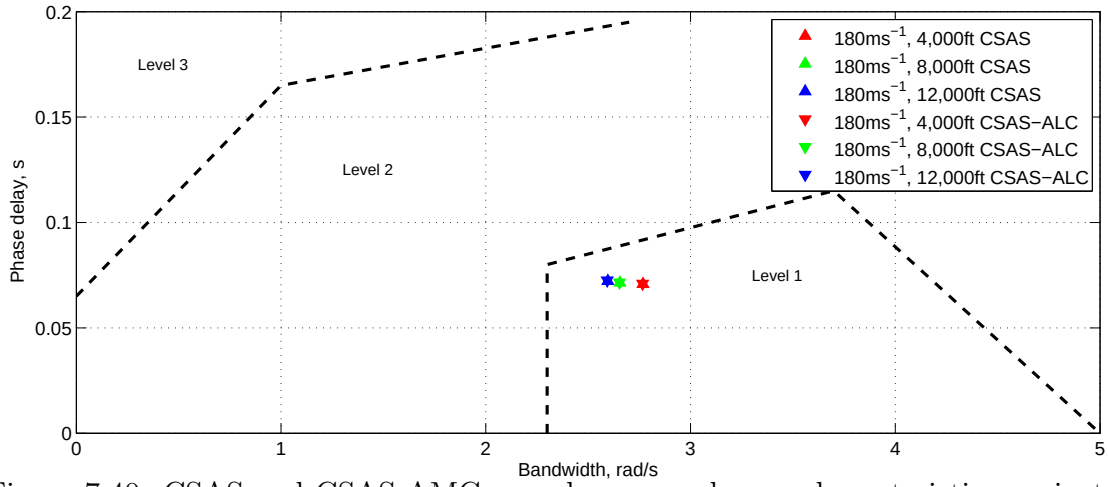

Figure 7.40: CSAS and CSAS-AMC aeroplane τ_e and ω_{BW} characteristics against Category C bandwidth requirements [MIL-STD-1797A, 1990]

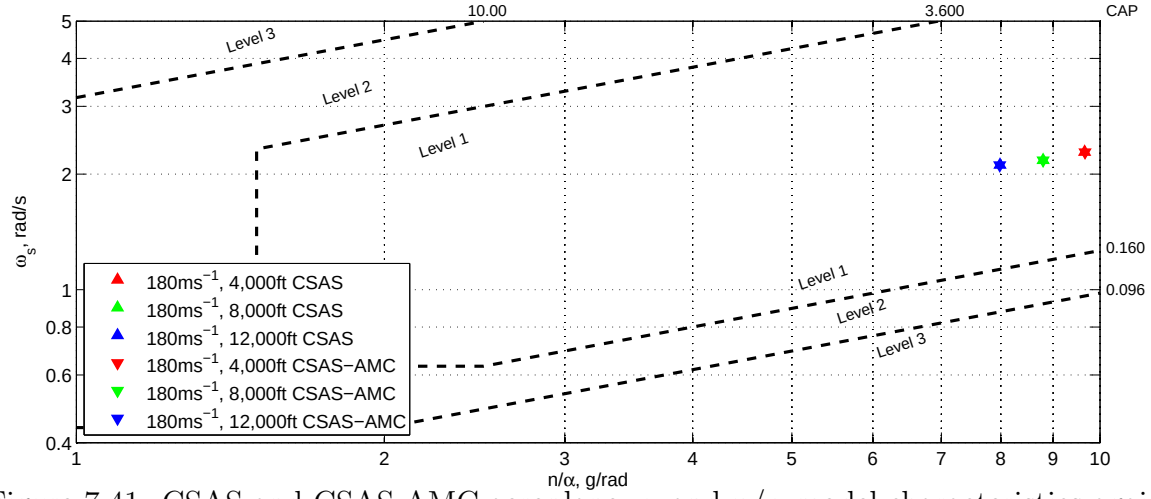

Figure 7.41: CSAS and CSAS-AMC aeroplane ω_s and n/α model characteristics against Category C CAP requirements [MIL-STD-1797A, 1990]

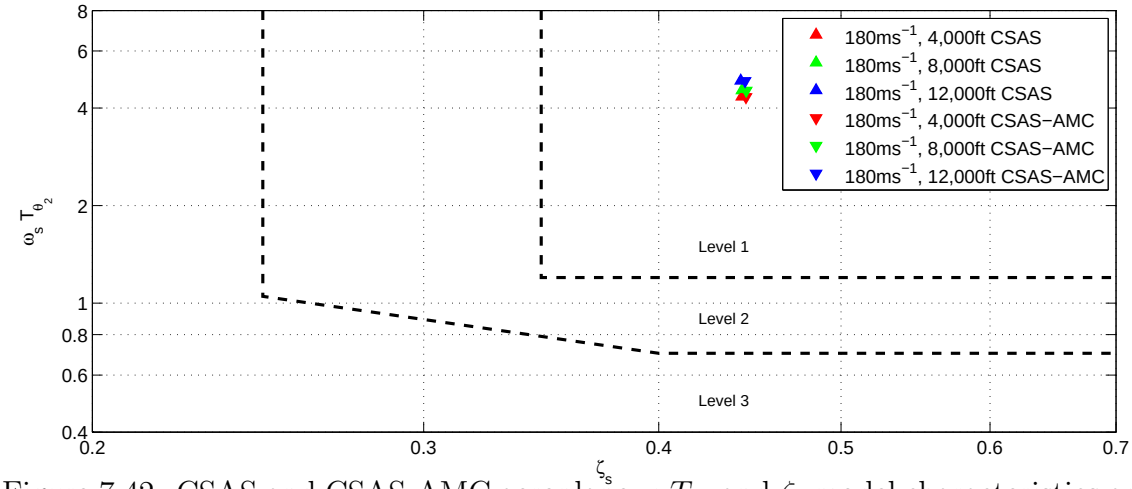

Figure 7.42: CSAS and CSAS-AMC aeroplane $\omega_s T_{\theta_2}$ and ζ_s model characteristics against Category C pitch response requirements [MIL-STD-1797A, 1990]

This page is intentionally left blank.

CHAPTER 8

Conclusions and Recommendations

8.1 Concluding Remarks

This thesis presents a numerical simulation of a flexible aeroplane, capturing the effects of structural dynamics and unsteady aerodynamics. The simulation provides a method for real-time pilot-in-the-loop simulation, handling qualities and flight loads analysis, and control law development. This is implemented in the MATLAB/Simulink environment.

The open-loop stability and dynamics of the aeroplane are considerably altered by the inclusion of structural flexibility and unsteady aerodynamic effects. Aeroelastic effects were found to influence the longitudinal and lateral-directional stability of the aeroplane as a function of altitude and airspeed. In particular:

- The influence of structural flexibility on the rigid-body dynamics of the aeroplane is a function of airspeed and altitude.
- The open-loop longitudinal and lateral-directional dynamics of the aeroplane are significantly modified by the inclusion of both unsteady aerodynamics and structural dynamics.

Mitchell et al. [2003] reiterated the importance of aeroelastic effects for the modern transport aircraft. The results presented here confirm the considerable influence unsteady aerodynamics and structural flexibility have on the stability and dynamics of this aircraft type. These results agree well with previous studies into the open-loop dynamic characteristics of other flexible aircraft. The reduction in the rigid-body short-period mode and the destabilising effect on the phugoid mode for example was also identified by Yen [1977] and Waszak and Schmidt [1985a,b] for the flexible Rockwell B-1B bomber.

The relative influence of airframe component stiffness on aeroplane handling qualities has been assessed by modifying the component stiffness properties of the airframe. This differs from previous studies, for example Raney et al. [2001], which have generally applied a scaling factor to the flexible modal natural frequencies. A number of existing flying

specifications and handling qualities criteria [Ashkenas et al., 1983b] were used to assess the aircraft handling qualities:

- The longitudinal handling qualities of the modern civil transport aeroplane are significantly altered by tailplane stiffness, likely resulting in the handling qualities of the aeroplane being degraded. The identified increase in the pitch-attitude phase delay is in agreement with previous studies [Ashkenas et al., 1983b].
- The natural frequency of the fuselage vertical bending mode for the AX-1 transport aircraft is relatively high compared to the aeroplane rigid-body modes and in comparison with other more slender-fuselaged aircraft types studied previously [Yen, 1977; Schmidt and Raney, 2001]. The impact of fuselage flexibility on the rigid-body modes for the AX-1 aircraft type is small.
- The lateral-directional handling qualities of the aeroplane are degraded by the inclusion of unsteady aerodynamics and structural dynamics.
- The stiffness of the wing influences the lateral-directional handling qualities of the aeroplane, and could lead to degraded handling qualities and an increased susceptibility to Pilot Induced Oscillations.

Previous studies have considered the open-loop [Waszak and Schmidt, 1985a,b] or CSAS closed-loop aeroplane handling qualities [Tuzcu, 2007]. The study of flexible aircraft handling qualities has been extended here to include the separate effects of LAF systems, such as manoeuvre, gust, and active mode control:

- Manoeuvre Load Alleviation significantly increases the required pilot compensation in a pitch tracking task, likely due to a reduction in the short-period damping and pitch-attitude bandwidth. This is predicted to result in a degradation in handling qualities.
- Gust Load Alleviation notably increased the pitch-attitude phase lag and reduced the gain response to pilot command. This was a result of the poor match for the normal acceleration approximation used to cancel the commanded response of the aeroplane.
- Improved symmetric wing damping achieved through Active Mode Control reduces the necessary pilot compensation, however the influence on the handling qualities of the aeroplane is found to be small.

These results confirm the significant impact that aeroservoelasticity can have on the closed-loop aircraft handling qualities [Kubica, 1998; Tuzcu and Meirovitch, 2005].

8.2 Recommendations for Further Work

The findings presented here pose some interesting questions and topics for further research. These are conveniently grouped into the following categories: numerical simulation, handling qualities, and flight control.

The aerodynamic model presented here combines a two-dimensional indicial state-space model with a three-dimensional modified strip theory. The resulting model, while an order of magnitude lower than any other unsteady aerodynamic model, still includes in the order of 1,000 states. This presents a computational challenge in achieving real-time simulation. The modular design of the simulation allows the easy substitution of this aerodynamic model, and an interesting improvement might thus be a reduced-order unsteady aerodynamic model. This might be based on a low-order truncation of the aerodynamic model by analysis of the Hankel Singular Values of the system, or a low-order approximation of the complete three-dimensional aerodynamic system produced through system identification.

It is assumed here that it is possible to inertially decouple the equations of motion for the rigid- and flexible-bodies. This was achieved through the use of the mean-axes system, and enables the use of the standard rigid-body equations of motion. This is a convenient approximation, however previous studies have found inertial coupling to be significant in some cases. A topic of further research would be to derive the equations of motion including inertial coupling, and compare the results with those presented here.

The analysis of the handling qualities of the aeroplane presented here used a wide range of different criteria and flying specifications, many of which are best suited to low-order classical aircraft. This problem was addressed by generating a Low-Order Equivalent System model of the aeroplane, and applying the criteria to this model. The application of higher-order criteria, such as the Bandwidth criterion, is also complicated by the inclusion in the frequency response of additional modes due to structural dynamics. It has been shown here that the handling qualities of the aeroplane can be characterised as a function of the airframe stiffness and natural frequency. An interesting development would therefore be a handling qualities criteria based on these results.

Ideally the bandwidth of the aircraft should be greater than that of the pilot. However, this is not feasible for an aircraft such as the one considered here. Existing criteria do not consider higher-order structural modes within the bandwidth of the pilot but outside the bandwidth of the aeroplane except to estimate their effect on the overall phase lag. An example mode in this case is the wing bending mode at 6.0 rad s^{-1}. The use of command-path filtering would likely be used to limit the excitation of this mode, but this would also result in the introduction of phase lag in the aeroplane response. During some flight event, it is quite possible that the pilot might excite such a mode, either directly or indirectly through bio-dynamic feedthrough. The resulting handling qualities, and the possible occurrence of structurally-coupled Pilot Induced Oscillations, are an interesting topic for further research.

The use of primary flight control surfaces for load alleviation presents some interesting challenges not addressed here. The load alleviation control laws presented here are representative of those employed on modern large transport aircraft, however recent interest has focused on the development of integrated load alleviation and control and stability augmentation control systems. As the primary flight control surfaces are required for control of the rigid-body aircraft motion, the maximum authority of the load alleviation system must be limited. An integrated control law offers the opportunity for novel load and flight control strategies, for example differential and asymmetric control surface deflections or higher load alleviation authorities. This is likely to present an interesting interaction between the load alleviation system and handling qualities of the aeroplane.

This page is intentionally left blank.

References

N. Abramov, M. Goman, and A. Khrabrov. Aircraft dynamics at high incidence flight with account of unsteady aerodynamic effects. In *AIAA Atmospheric Flight Mechanics Conference and Exhibit*, Providence, Rhode Island, 16-19 Aug. 2004. AIAA Paper 2004-5274.

N. Abramov, M. Goman, M. Demenkov, and A. Khrabrov. Lateral-directional aircraft dynamics at high incidence flight with account of unsteady aerodynamic effects. In *AIAA Atmospheric Flight Mechanics Conference and Exhibit*, San Francisco, California, 15-18 Aug. 2005. AIAA Paper 2005-6331.

M. Abramowitz and I.A. Stegun, editors. *Handbook of Mathematical Functions with Formulas, Graphs, and Mathematical Tables*. National Bureau of Standards, tenth edition, 1972.

A. Al-Shehabi and B. Newman. Optimal blending filter parameters and sensor placement for flight control. In *AIAA Guidance, Navigation, and Control Conference and Exhibit*, Monterey, California, 5-8 Aug. 2002. AIAA Paper 2002-4750.

E. Albano and W.P. Rodden. A doublet lattice method for calculating lift distributions on oscillating surfaces in subsonic flows. *AIAA Journal*, 7(2):279–285, Feb. 1969. doi: 10.2514/3.5086.

Anon. Standard atmosphere - tables and data for altitudes to 65,800 feet. Technical Report NASA-TR-1235, National Aeronautics and Space Administration, 1955.

Anon. Selected advanced aerodynamics and active controls technology concepts development on a derivative B-747 aircraft. Technical Report NASA-CR-3295, National Aeronautics and Space Administration, 1980.

Anon. *Military standard - Flying qualities of piloted aircraft.* MIL-STD-1797A. Department of Defense Military Specifications and Standards, 1990.

Anon. *Federal Aviation Regulations - Part 25, Subpart B - Flight.* Federal Aviation Administration, United States Department of Transportation, 1994.

I.L. Ashkenas, R.H. Hoh, and G.L. Teper. Analysis of shuttle orbiter approach and landing. *Journal of Guidance, Control, and Dynamics*, 6(6):448–455, Nov.-Dec. 1983a.

I.L. Ashkenas, R.E. Magdaleno, and D.T. McRuer. Flight control and analysis methods for studying flying and ride qualities of flexible transport aircraft. Technical Report NASA-CR-172201, National Aeronautics and Space Administration, 1983b.

M.L. Baker, P.J. Goggin, and B.A. Winther. Aeroservoelastic modeling, analysis and design techniques for transport aircraft. In *RTO MP-36, Structural Aspects of Flexible Aircraft Control*, Ottawa, Canada, 18-20 Oct. 1999. NATO Research and Technology Organisation, May 2000.

H.A. Baluch, P. Lisandrin, R. Slingerland, and M. J. L. van Tooren. Effects of flexibility on aircraft dynamic loads and structural optimization. In *45th AIAA Aerospace Sciences Meeting and Exhibit*, Reno, Nevada, 8-11 Jan. 2007. AIAA Paper 2007-768.

J.G. Barmby, H.J. Cunningham, and L.E. Garrick. Study of effects of sweep on the flutter of cantilever wings. Technical Report NACA-TR-1014, National Advisory Committee for Aeronautics, 1951.

D.T. Berry, B.G. Powers, K.J. Szalai, and R.J. Wilson. In-flight evaluation of control system pure time delays. *Journal of Aircraft*, 19(4):318–323, Apr. 1982.

P. J. Berry. Program BEMMODES: Beam element model MODES. Technical Report HAD.R.GEN.AE.0872, British Aerospace, 1989.

W. Birhrle. A handling qualities theory for precise flight path control. Technical Report AFFDL-TR-65-198, Air Force Flight Dynamics Laboratory, 1966.

R. L. Bisplinghoff, H. Ashley, and R. L. Halfman. *Aeroelasticity*. Addison-Wesley Pub. Co, 1955.

M. Blair. A compilation of the mathematics leading to the doublet lattice method. Technical Report WL-TR-92-3028, Wright-Patterson Air Force Base, Air Force Wright Laboratory, 1994.

G. Brewer. The collapse of monoplane wings. *Flight*, 5(2):33, 11 Jan. 1913.

G.H. Bryan. *Stability in Aviation*. Macmillan, first edition, 1911.

P.M. Burris and M.A Bender. Aircraft load alleviation and mode stabilisation (lams), B-52 system analysis, synthesis, and design. Technical Report AFFDL-TR-68-161, Air Force Flight Dynamics Laboratory, 1969.

C.S. Buttrill, T.A. Zeiler, and P.D. Arbuckle. Nonlinear simulation of a flexible aircraft in maneuvering flight. In *AIAA Flight Simulation Technologies Conference*, Monterey, California, 17-19 Aug. 1987. AIAA Paper 87-2501.

C.E.S. Cesnik and E.L. Brown. Modeling of high aspect ratio active flexible wings for roll control. In *43rd AIAA/ASME/ASCE/AHS/ASC Structures, Structural Dynamics, and Materials Conference*, Denver, Colorado, 22-25 Apr. 2002. AIAA Paper 2002-1719.

C.R. Chalk. Additional flight evaluations of various longitudinal handling qualities in a variable-stability jet fighter. Technical Report WADC-TR-57-719, Wright-Patterson Air Force Base, Wright Air Development Center, 1958.

D. Chatrenet. Flight simulation and digital flight controls. In *17th Congress of the International Council of the Aeronautical Sciences*, Stockholm, Sweden, 9-14 Sept. 1990.

B. Churchill. High speed civil transport Reference H Cycle 3 simulation data base. Technical Report NAS1-20220 Task Assignment No. 36, National Aeronautics and Space Administration, 1996.

A.R. Collar. The first fifty years of aeroelasticity. *Aerospace*, 5(2):12–20, Feb. 1978.

M. V. Cook. *Flight Dynamics Principles*. Butterworth Heinemann, second edition, 1997.

M. V. Cook. Flying qualities and flight control, lecture course notes. *Department of Aerospace Sciences, School of Engineering, Cranfield University*, 2007.

R.D. Cook, D.S. Malkus, and M.E. Plesha. *Concepts and Applications of Finite Element Analysis*. John Wiley & Sons, third edition, 1989.

G.E. Cooper and R.P. Harper, Jr. The use of pilot rating in the evaluation of aircraft handling qualities. Technical Report NASA-TN-D-5153, National Aeronautics and Space Administration, 1969.

W.L. Cowley and H. Glauert. The effect of the lag of the downwash on the longitudinal stability of an aeroplane and on the rotary derivative. Technical Report ARC R.&M. 718, Aeronautical Research Council, 1921.

C.A. Crother, B. Gabelman, and D. Langton. Structural mode effects on flying qualities in turbulence. Technical Report AFFDL-TR-73-88, Air Force Flight Dynamics Laboratory, 1973.

J.R. Dawdy, G.M. Domfield, and B.A. Phillips. High speed civil transport Reference H Cycle 1 simulation data base. Technical Report NAS1-19360 Task Assignment No. 49, National Aeronautics and Space Administration, 1994.

J. DeYoung and C.W. Harper. Theoretical symmetric span loading at subsonic speeds for wings having arbitrary plan form. Technical Report NACA-TR-921, National Advisory Committee for Aeronautics, 1948.

F.W. Diederich. Calculation of the aerodynamic loading of swept and unswept flexible wings of arbitrary stiffness. Technical Report NACA-TR-1000, National Advisory Committee for Aeronautics, 1950.

T.E. Disney and D.C. Eckholdt. Historical review of C-5 lift distribution control systems. Technical report, National Aeronautics and Space Administration, 1976.

R.C. Dorf and R.H. Bishop. *Modern Control Systems*. Prentice-Hall, Inc., ninth edition, 2001.

Q. Douchet. Emirates Airbus A380, Charles de Gaulle, Paris, France. Wikimedia Commons, 2010. Source: http://commons.wikimedia.org/wiki/File:A380_Emirates_A6-EDC.jpg.

E.H. Dowell. A simple method for converting frequency-domain aerodynamics to the time domain. Technical Report NASA-TM-81844, National Aeronautics and Space Administration, 1980.

J. A. Drischler. Approximate indicial lift functions for several wings of finite span in incompressible flow as obtained from oscillatory lift coefficients. Technical Report NACA-TN-3639, National Advisory Committee for Aeronautics, 1956.

A.R. Dusto, G.W. Brune, G.M. Dornfeld, J.E. Mercer, S.C. Pilet, P.E. Rubbert, R.C. Schwanz, P. Smutny, E.N. Tinoco, and J.A. Weber. A method for predicting the stability characteristics of an elastic airplane, volume 1 - FLEXSTAB theoretical description. Technical Report NASA-CR-114712, National Aeronautics and Space Administration, 1974.

J. W. Edwards. Unsteady aerodynamic modeling for arbitrary motions. *AIAA Journal*, 17(4):365–374, 1979.

ESDU 00027. *Aerofoil profile drag for Mach numbers below the drag-rise condition.* ESDU International, 2000. With Amendment A, January 2006.

ESDU 07002. *Wing viscous drag coefficient in shock-free attached flow.* ESDU International, 2008.

ESDU 07003. *Modelling of wing viscous drag coefficient in shock-free attached flow.* ESDU International, 2008.

ESDU 70011. *Lift-curve slope and aerodynamic centre position of wings in inviscid subsonic flow.* ESDU International, 1996. With Amendments A to I, August 1996.

ESDU 72024. *Aerodynamic characteristics of aerofoils in compressible inviscid airflow at subcritical Mach numbers (Method for estimating aerodynamic characteristics of airfoils in compressible inviscid flow based on thickness and camber line parameters).* ESDU International, 1972. With Amendments A to D, January 1999.

ESDU 76003. *Geometrical properties of cranked and straight tapered wing planforms.* ESDU International, 1976. With Amendment A, October 1981.

ESDU 77012. *Aerodynamic centre of wing-fuselage-nacelle combinations: effect of wing-pylon mounted nacelles.* ESDU International, 1977.

ESDU 77028. *Geometrical characteristics of typical bodies.* ESDU International, 1990. With Amendments A to F, July 1990.

ESDU 78019. *Profile drag of axisymmetric bodies at zero incidence for subcritical Mach numbers.* ESDU International, 1998. With Amendments A and B, July 1998.

ESDU 81032. *Estimation of rolling moment derivative due to sideslip for complete aircraft at subsonic speeds.* ESDU International, 1981. With Amendments A to D, October 2000.

ESDU 82011. *Estimation of Sideforce and Yawing Moment Derivatives due to Sideslip for Complete Aircraft at Subsonic Speeds.* ESDU International, 1982. With Amendments A and B, October 2000.

ESDU 84002. *Estimation of sideforce, yawing moment and rolling moment derivatives due to rate of yaw for complete aircraft at subsonic speeds.* ESDU International, 1984.

ESDU 85010. *Estimation of sideforce, yawing moment and rolling moment derivatives due to rate of roll for complete aircraft at subsonic speeds.* ESDU International, 1985.

ESDU 86021. *Introduction to aerodynamic derivatives, equations of motion and stability.* ESDU International, 2003. With Amendments A to C, July 2003.

ESDU 87024. *Low-speed drag coefficient increment at constant lift due to full-span plain flaps or controls.* ESDU International, 1987. With Amendments A to D, August 2006.

ESDU 87033. *Normal force and pitching moment of conical boat-tails.* ESDU International, 1992. With Amendments A and C, July 1992.

ESDU 89008. *Normal-force-curve and pitching-moment-curve slopes of forebody-cylinder combinations at zero angle of attack for Mach numbers up to 5.* ESDU International, 1990. With Amendments A and C, December 1990.

ESDU 89014. *Normal force, pitching moment and side force of forebody-cylinder combinations for angles of attack up to 90 degrees and Mach numbers up to 5.* ESDU International, 2004. With Amendments A to D, September 2004.

ESDU 91007. *Lift-curve slope of wing-body combinations.* ESDU International, 1995. With Amendments A and D, December 1995.

ESDU 92024. *Aerodynamic centre of wing-body combinations.* ESDU International, 1992. With Amendments A and B, December 1995.

ESDU 94009. *Symmetric Steady Manaeuvre Loads on Rigid Aircraft of Classical Configuration at Subsonic Speeds.* ESDU International, 1994.

ESDU 95009. *Effect of wing height on lift and aerodynamic centre for a slender wing-body combination.* ESDU International, 1995.

ESDU 97020. *Slope of Aerofoil Lift Curve for Subsonic Two-dimensional Flow.* ESDU International, 1997.

B. Etkin. *Dynamics of Flight - Stability and Control.* John Wiley & Sons, Inc., first edition, 1959.

C. Favre. *Fly-by-wire for commercial aircraft: the Airbus experience*, pages 211–229. Advances in Aircraft Flight Control. Taylor & Francis, first edition, 1996.

G.E. Franklin, J.D. Powell, and A. Emami-Naeini. *Feedback Control of Dynamic Systems.* Prentice-Hall, Inc., fourth edition, 2002.

R.A. Frazer and W.J. Duncan. The flutter of aeroplane wings. Technical Report ARC R.&M. 1155, Aeronautical Research Council, 1928a.

R.A. Frazer and W.J. Duncan. Wing flutter as influenced by the mobility of the fuselage. Technical Report ARC R.&M. 1207, Aeronautical Research Council, 1928b.

Y. Fung. *An Introduction to the Theory of Aeroelasticity.* Dover Publications, 1969.

I. E. Garrick. On some reciprocal relations in the theory of nonstationary flows. Technical Report NACA-TR-629, National Advisory Committee for Aeronautics, 1938.

J.C. Gibson. *Development of a methodology for excellence in handling qualities design for fly by wire aircraft.* Delft University Press, first edition, 1999.

M. Goman and A. Khrabrov. State-space representation of aerodynamic characteristics of an aircraft at high angles of attack. *Journal of Aircraft*, 31(5):1109–1115, Sept.-Oct. 1994. doi: 10.2514/3.46618.

D. I. Greenwell. A review of unsteady aerodynamic modelling for flight dynamics of manoeuvrable aircraft. In *AIAA Atmospheric Flight Mechanics Conference and Exhibit*, Providence, Rhode Island, 16-19 Aug. 2004. AIAA Paper 2004-5276.

G.Romeo, G.Frulla, E.Cestino, P.Marzocca, and I. Tuzcu. Non-linear aeroelastic modeling and experiments of flexible wings. In *47th AIAA/ASME/ASCE/AHS/ASC Structures, Structural Dynamics, and Materials Conference*, Newport, Rhode Island, 1-4 May 2006. AIAA Paper 2006-2186.

G. J. Hancock. *An Introduction to the Flight Dynamics of Rigid Aeroplanes*. Ellis Horwood, 1995.

W.J. Hargrove. The C-5A active lift distribution control system. Technical report, National Aeronautics and Space Administration, 1976.

N. Hariharan and J. G. Leishman. Unsteady aerodynamics of a flapped airfoil in subsonic flow by indicial concepts. *Journal of Aircraft*, 33(5):855–868, Sept.-Oct. 1996. doi: 10.2514/3.47028.

R.P. Harper, Jr. and G.E. Cooper. Handling qualities and pilot evaluation. *Journal of Guidance, Control, and Dynamics*, 9(5):515–529, 1986. doi: 10.2514/3.20142.

C. Harris. NASA supercritical airfoils: A matrix of family-related airfoils. Technical Report NASA-TP-2969, National Aeronautics and Space Administration, 1990.

W.S. Hemp. Note on the dynamics of a slightly deformable body. Technical Report 5, Cranfield College of Aeronautics, 1947.

J. Hodgkinson and K.A. Johnston. Initial results of an inflight simulation of augmented dynamics in fighter approach and landing. In *Guidance and Control Conference*, Boulder, Colorado, 6-8 Aug. 1979. AIAA Paper 79-1783.

J. Hodgkinson, W.J. Manna, La, and J.L. Heyde. Handling qualities of aircraft with stability and control augmentation systems - a fundamental approach. *Aeronautical Journal*, 80(782):75–81, Feb. 1976.

J. Hofstee, T. Kier, C. Cerulli, and G. Looye. A variable, fully flexible dynamic response tool for special investigations. In *International Forum on Aeroelasticity and Structural Dynamics*, Amsterdam, Netherlands, 4-6 Jun. 2003.

R. H. Hoh, D. G. Mitchell, and J. Hodgkinson. Bandwidth: A criterion for highly augmented airplanes. In *AGARD Conference Proceedings No.333, Criteria for Handling Qualities of Military Aircraft, Flight Mechanics Panel Symposium*, Apr. 1982.

W.C. Hurty and M.F. Rubinstein. *Dynamics of Structures*. Prentice-Hall, Inc., 1964.

E.B. Jackson, D.L. Raney, D.E. Hahne, and S.D. Derry. Reference H piloted assessment (LaRC.1) pilot briefing guide. Technical Report NASA-TM-209533, National Aeronautics and Space Administration, 1999.

P. Jackson. *Jane's All the World's Aircraft*. Jane's Information Group, 2006.

R.T. Jones. The unsteady lift of a wing of finite aspect ratio. Technical Report NACA-TR-681, National Advisory Committee for Aeronautics, 1940.

R.T. Jones and L.F. Fehlner. Transient effects of the wing wake on the horizontal tail. Technical Report NACA-TN-771, National Advisory Committee for Aeronautics, 1940.

W. P. Jones. Aerodynamic forces on wings in non-uniform motion. Technical Report ARC R.&M. 2117, Aeronautical Research Council, 1945.

S.M. Joshi and A.G. Kelkar. On longitudinal control of high speed aircraft in the presence of aeroelastic modes. Technical Report NASA-TM-110254, National Aeronautics and Space Administration, 1996.

T. M. Kier. Comparison of unsteady aerodynamic modelling methodologies with respect to flight loads analysis. In *AIAA Atmospheric Flight Mechanics Conference and Exhibit*, San Francisco, California, 15-18 Aug. 2005. AIAA Paper 2005-6026.

V. Klein. Modeling of longitudinal unsteady aerodynamics of a wing-tail combination. Technical Report NASA/CR-1999-209547, National Aeronautics and Space Administration, 1999.

F. Kubica. New flight control laws for large capacity aircraft experimentation on airbus a340. In *21st Congress of the International Council of the Aeronautical Sciences*, Melbourne, Australia, 13-18 Sept. 1998. A98-31462.

F. Kubica and C. Le Garrec. Method and device for reducing the virbratory motions of the fuselage of an aircraft, 10 Aug. 2004. U.S. Patent 6,772,979.

F. Kubica and T. Livet. Design of flight control system for an aeroelastic aircraft. In *3rd IEEE Conference on Control Applications*, volume 1, pages 335–340, 24-26 Aug. 1994a. doi: 10.1109/CCA.1994.381445.

F. Kubica and T. Livet. Flight control law synthesis for a flexible aircraft. In *AIAA Guidance, Navigation and Control Conference*, volume 2, pages 775–783, Scottsdale, Arizona, 1-3 Aug. 1994b.

H. G. Kussner. Zusammenfassender bericht uber den instationaren auftrieb von flugeln. *Luftfahrtforschung*, 13(12):410–424, 1936.

H. Lamb. *Higher Mechanics*. Cambridge University Press, first edition, 1920.

F.W. Lanchester. Torsional vibration of the tail of an airplane. Technical Report ARC R.&M. 276 Part I, Aeronautical Research Council, 1916.

D.H. Lee, D.H. Baldelli, N.J. Lindsley, and M.J. Brenner. Static aeroelastic and open-loop aeroservoelastic analyses for the F/A-18 aaw aircraft. In *48th AIAA/ASME/ASCE/AHS/ASC Structures, Structural Dynamics, and Materials Conference*, Honolulu, Hawaii, 23-26 Apr. 2007. AIAA Paper 2007-2135.

J. G. Leishman. Indicial lift approximations for two-dimensional subsonic flow as obtained from oscillatory measurements. *Journal of Aircraft*, 30(3):340–351, May-Jun. 1993. doi: 10.2514/3.46340.

J. G. Leishman. Unsteady lift of a flapped airfoil by indicial concepts. *Journal of Aircraft*, 31(2):288–297, Mar.-Apr. 1994. doi: 10.2514/3.46486.

J. G. Leishman. Subsonic unsteady aerodynamics caused by gusts using the indicial method. *Journal of Aircraft*, 33(5):869–879, Sept.-Oct. 1996. doi: 10.2514/3.47029.

J.G. Leishman. Two-dimensional model for airfoil unsteady drag below stall. *Journal of Aircraft*, 25(7):665–666, Jul. 1988. doi: 10.2514/3.45639.

J.G. Leishman and K.Q. Nguyen. State-space representation of unsteady airfoil behaviour. *AIAA Journal*, 28(5):836–844, May 1990. doi: 10.2514/3.25127.

L. Librescu, Z. Qin, S. Na, and G. Yoon. Aeroelastic response and active control of aircraft wings modeled as thin-walled beams. In *47th AIAA/ASME/ASCE/AHS/ASC Structures, Structural Dynamics, and Materials Conference*, Newport, Rhode Island, 1-4 May 2006. AIAA Paper 2006-1939.

T. Livet, P. Fabre, F. Kubica, and J.F. Magni. Robust flight control design with respect to delays and control efficiencies. In *13th IFAC Symposium on Automatic Control in Aerospace*, pages 273–278, Palo Alto, California, 12-16 Sept. 1994a.

T. Livet, P. Fabre, F. Kubica, and J.F. Magni. Robust flight control design for a highly flexible aircraft by pole migration. In *13th IFAC Symposium on Automatic Control in Aerospace*, pages 425–430, Palo Alto, California, 12-16 Sept. 1994b.

H. Lomax, M. A. Heaslet, F. B. Fuller, and L. Sluder. Two-and three-dimensional unsteady lift problems in high-speed flight. Technical Report NACA-TR-1077, National Advisory Committee for Aeronautics, 1952.

E. Marmet. Air India Boeing 707, EuroAirport Basel-Mulhouse-Freiburg, Basel, Switzerland. Wikimedia Commons, 1976. Source: http://commons.wikimedia.org/wiki/File:Boeing_707_Air_India_Basle_-_1976.jpg.

P. Marzocca, G. Chiocchia, and L. Librescu. Unsteady aerodynamics in various flight speed regimes for flutter /dynamic response analyses. In *18th AIAA Applied Aerodynamics Conference*, volume 1, page 14, 2000.

MathWorks Inc. *MATLAB 7.8.0 (2009a)*. Natick, Massachusetts, 2009.

B. Mazelsky. Numerical determination of indicial lift of a two-dimensional sinking airfoil at subsonic mach numbers from oscillatory lift coefficients with calculations for mach number 0.7. Technical Report NACA-TN-2562, National Advisory Committee for Aeronautics, 1951.

B. Mazelsky. On the noncirculatory flow about a two-dimensional airfoil at subsonic speeds. *Journal of the Aeronautical Sciences*, 19(12):848–849, Dec. 1952.

B. Mazelsky and J. A. Drischler. Numerical determination of indicial lift and moment functions for a two-dimensional sinking and pitching airfoil at mach numbers 0.5 and 0.6. Technical Report NACA-TN-2739, National Advisory Committee for Aeronautics, 1952.

C.A. McCarty, J.B. Feather, J.R. Dykman, M.A. Page, and J. Hodgkinson. Design and analysis issues of integrated control systems for high-speed civil transports. Technical Report NASA-CR-186022, National Aeronautics and Space Administration, 1992.

D. McLean. *Automatic Flight Control Systems*. Prentice-Hall, Inc., first edition, 1990.

D. McRuer, I. Ashkenas, and D. Graham. *Aircraft Dynamics and Automatic Control*. Princeton University Press, first edition, 1973.

D.T. McRuer. Pilot-induced oscillations and human dynamic behaviour. Technical Report NASA-CR-4683, National Aeronautics and Space Administration, 1995.

L. Meirovitch and I. Tuzcu. Integrated approach to flight dynamics and aeroservoelasticity of whole flexible aircraft - Part I: System modelling. In *AIAA Guidance, Navigation, and Control Conference*, Monterey, California, 5-8 Aug. 2002a. AIAA Paper 2002-4747.

L. Meirovitch and I. Tuzcu. Integrated approach to flight dynamics and aeroservoelasticity of whole flexible aircraft - Part II: Control design. In *AIAA Guidance, Navigation, and Control Conference*, Monterey, California, 5-8 Aug. 2002b. AIAA Paper 2002-5055.

L. Meirovitch and I. Tuzcu. Integrated approach to the dynamics and control of maneuvering flexible aircraft. Technical Report NASA-CR-211748, National Aeronautics and Space Administration, 2003a.

L. Meirovitch and I. Tuzcu. Time simulations of the response of maneuvering flexible aircraft. In *44th AIAA/ASME/ASCE/AHS Structures, Structural Dynamics, and Materials Conference*, Norfolk, Virginia, 7-10 Apr. 2003b. AIAA Paper 2003-1403.

R. D. Milne. Dynamics of the deformable aeroplane. Technical Report ARC R.&M. 3345, Aeronautical Research Council, 1962.

D.G. Mitchell, D.B. Doman, D.L. Key, D.H. Klyde, D.B. Leggett, D.J. Moorhouse, D.H. Mason, D.L. Raney, D.R. Riley, and D.K. Schmidt. The evolution, revolution, and challenges of handling qualities. Technical Report AFRL-VA-WP-TP-2003-328, Wright-Patterson Air Force Base, Air Force Research Laboratory, 2003.

S. Na, I. Jeong, L. Librescu, and P. Marzocca. Aeroelastic response and active control of an airfoil in subsonic compressible flow. In *46th AIAA/ASME/ASCE/AHS/ASC Structures, Structural Dynamics, and Materials Conference*, Austin, Texas, 18-21 Apr 2005. AIAA Paper 2005-1992.

NASA Dryden Flight Research Centre Photo Collection. USAF NAA XB-70, 1965. NASA Photo: ECN-792. Source: http://www.dfrc.nasa.gov/gallery/photo/XB-70/HTML/ECN-792.html.

NASA Dryden Flight Research Centre Photo Collection. USAF Lockheed YF-12, 1972. NASA Photo: EC72-3150. Source: http://www.dfrc.nasa.gov/gallery/photo/YF-12/HTML/EC72-3150.html.

NASA Dryden Flight Research Centre Photo Collection. Orbital Sciences Lockheed L-1011, Meadows Field Runway, Bakersfield, California, 1997. NASA Photo: EC97-44077-3. Source: http://www.dfrc.nasa.gov/gallery/Photo/L-1011/HTML/EC97-44077-3.html.

NASA Dryden Flight Research Centre Photo Collection. USAF Boeing B-52, Dryden Flight Research Center, Edwards, California, 2001. NASA Photo: EC01-0126-07. Source: http://www.dfrc.nasa.gov/Gallery/Photo/X-43A/HTML/EC01-0126-07.html.

T.P. Neal and R.E. Smith. A flying qualities criterion for the design of flight flight-control systems. *Journal of Aircraft*, 8(10):803–809, Oct. 1971.

B. Newman and C. Buttrill. Conventional flight control for an aeroelastic relaxed static stability high-speed transport. In *AIAA Guidance, Navigation and Control Conference*, pages 717–726, Baltimore, MD, 7-10 Aug. 1995. AIAA Paper 95-3250.

N. Nguyen. Integrated flight dynamic modeling of flexible aircraft with inertial force-propulsion-aeroelastic coupling. In *46th AIAA Aerospace Sciences Meeting and Exhibit*, Reno, Nevada, 7-10 Jan. 2008. AIAA Paper 2008-194.

W.J. Norton. Aeroelastic pilot-in-the-loop oscillations. In *AGARD-AR-335, Flight Vehicle Integration Panel Workshop on Pilot Induced Oscillations*, pages 10–1–10–14. Advisory Group for Aerospace Research and Development, 1995.

W.J. Norton. Balancing modelling & simulation with flight test in military aircraft development. In *AGARD-CP-593, Advances in Flight Testing*, pages 13–1–13–25. Advisory Group for Aerospace Research and Development, 1996.

J.J. Olsen. Unified flight mechanics and aeroelasticity for accelerating, maneuvering, flexible aircraft. In *RTO MP-36, Structural Aspects of Flexible Aircraft Control*, Ottawa, Canada, 18-20 Oct. 1999. NATO Research and Technology Organisation, May 2000.

M.J. Patil and D. H. Hodges. Nonlinear aeroelasticity and flight dynamics of aircraft in subsonic flow. In *21st Congress of International Council of the Aeronautical Sciences*, Melbourne, Australia, 13-18 Sept. 1998.

M.J. Patil, D.H. Hodges, and C.E.S. Cesnik. Nonlinear aeroelasticity and flight dynamics of high-altitude long-endurance aircraft. In *40th AIAA Structures, Structural Dynamics and Materials Conference*, St. Louis, Missouri, 12-15 Apr. 1999. AIAA Paper 99-1470.

D.A. Peters, S. Karunamoorthy, and W. Cao. Finite state induced flow models, Part I: Two-dimensional thin airfoil. *Journal of Aircraft*, 32(2):313–322, Mar.-Apr. 1995. doi: 10.2514/3.46718.

A. Pingstone. RAF de Havilland DH.106 Comet Mk 2C, Filton, Bristol, UK. Wikimedia Commons, 1964. Source: http://commons.wikimedia.org/wiki/File:DeHavilland_Comet.jpg.

A. Pingstone. Turkish Airlines A340, Heathrow, London, UK. Wikimedia Commons, 2009. Source: http://commons.wikimedia.org/wiki/File:Turkish_a340-300_tc-jih_arp.jpg.

Z. Qin, P. Marzocca, and L. Librescu. Aeroelastic instability and response of advanced aircraft wings at subsonic flight speeds. *Aerospace Science and Technology*, 6(3):195–208, 2002. doi: 10.1016/S1270-9638(02)01158-6.

D. L. Raney, E. B. Jackson, and C. S. Buttrill. Simulation study of impact of aeroelastic characteristics on flying qualities of a high speed civil transport. Technical Report NASA-TP-211943, National Aeronautics and Space Administration, 2002.

D.L. Raney, E.B. Jackson, C.S. Buttrill, and W.M. Adams. The impact of structural vibration on flying qualities of a supersonic transport. In *AIAA Atmospheric Flight Mechanics Conference and Exhibit*, Montreal, Canada, 6-9 Aug. 2001. AIAA Paper 2001-4006.

C. Reschke. Flight loads analysis with inertially coupled equations of motion. In *AIAA Atmospheric Flight Mechanics Conference and Exhibit*, San Francisco, California, 15-18 Aug. 2005. AIAA Paper 2005-6026.

J.A. Samareh and K.G. Bhatia. A unified approach to modeling multidisciplinary interactions. In *8th AIAA/USAF/NASA/ISSMO Symposium on Multidisciplinary Analysis and Optimization*, Long Beach, California, 6-8 Sept. 2000. AIAA Paper 2000-4704.

D. K. Schmidt. Modal analysis of flexible aircraft dynamics with handling qualities implications. *Journal of Guidance, Control, and Dynamics*, 8(2):194–200, Mar.-Apr. 1985. doi: 10.2514/3.19959.

D. K. Schmidt and D. L. Raney. Modeling and simulation of flexible flight vehicles. *Journal of Guidance, Control, and Dynamics*, 24(3):539–546, May-Jun. 2001. doi: 10.2514/2.4744.

C. M. Shearer and C. E. S. Cesnik. Nonlinear flight dynamics of very flexible aircraft. In *AIAA Atmospheric Flight Mechanics Conference and Exhibit*, San Francisco, California, 15-18 Aug. 2005. AIAA Paper 2005-5805.

N. Siepenkotter and W. Alles. Stability analysis of the nonlinear dynamics of flexible aircraft. *Aerospace Science and Technology*, 9(2):135–141, 2005. doi: 10.1016/j.ast.2004.10.005.

J. Sitaraman and J.D. Baeder. Computational-fluid-dynamics-based enhanced indicial aerodynamic models. *Journal of Aircraft*, 41(4):798–810, Jul.-Aug. 2004.

R.B. Skoog and H.H. Brown. A method for the determination of the spanwise load distribution of a flexible swept wing at subsonic speeds. Technical Report NACA-TN-2222, National Advisory Committee for Aeronautics, 1951.

J.W. Smith and D.T. Berry. Analysis of longitudinal pilot-induced oscillation tendencies of yf-12 aircraft. Technical Report NASA-TN-D-7900, National Aeronautics and Space Administration, 1975.

R.A. Sotack, R.S. Chowdhry, and C.S. Buttrill. High speed civil transport aircraft simulation: Reference-H Cycle 1. Technical Report NASA-TM-209530, National Aeronautics and Space Administration, 1999.

R.F. Stengel. *Flight Dynamics*. Princeton University Press, first edition, 2004.

A.T. Stephens, G.M. Dornfield, J.F. Kuta, J.K. Lanier, K.H. Milligan, and B.A. Phillips. High speed civil transport Reference H Cycle 2A simulation data base. Technical Report NAS1-20220 Task Assignment No. 7, National Aeronautics and Space Administration, 1995a.

A.T. Stephens, G.M. Dornfield, J.K. Lanier, K.H. Milligan, J.M. Parker, and B.A. Phillips. High speed civil transport Reference H Cycle 2B simulation data base. Technical Report NAS1-20220 Task Assignment No. 7, National Aeronautics and Space Administration, 1995b.

B.L. Stevens and F.L. Lewis. *Aircraft Control and Simulation*. John Wiley & Sons, Inc, first edition, 1992.

J. Stringer. *Hydraulic Systems Analysis: An Introduction*. Macmillan, first edition, 1976.

W. Su and C.E. S. Cesnik. Dynamic response of highly flexible flying wings. In *47th AIAA/ASME/ASCE/AHS/ASC Structures, Structural Dynamics, and Materials Conference*, Newport, Rhode Island, 1-4 May 2006. AIAA Paper 2006-1636.

T. Theodorsen. General theory of aerodynamic instability and the mechanism of flutter. Technical Report NACA-TR-496, National Advisory Committee for Aeronautics, 1935.

T. Theodorsen. General theory of aerodynamic instability and the mechanism of flutter. Technical Report NACA-TR-496, National Advisory Committee for Aeronautics, 1949.

T. Theodorsen and I. E. Garrick. Nonstationary flow about a wing-aileron-tab combination including aerodynamic balance. Technical Report NACA-TR-736, National Advisory Committee for Aeronautics, 1942.

C. Tillier. Giant Plane Comparison. Wikimedia Commons, 2006. Source: http://commons.wikimedia.org/wiki/File:Giant_planes_comparison.svg.

M. Tobak. On the use of the indicial function concept in the analysis of unsteady motions of wings and wing-tail combinations. Technical Report NACA-TR-1188, National Advisory Committee for Aeronautics, 1954.

H.N. Tobie, E.M. Elliot, and L.G. Malcom. A new longitudinal handling qualities criterion. In *National Aerospace Electronics Conference*, pages 93–99, May 1966.

I. Tuzcu. *Dynamics and Control of Flexible Aircraft*. PhD thesis, Virginia Polytechnic Institute and State University, 2001.

I. Tuzcu. On the stability of flexible aircraft. *Aerospace Science and Technology*, 12(5): 376–384, 2007. doi: 10.1016/j.ast.2007.09.003.

I. Tuzcu and L. Meirovitch. Effects of flexibility on the stability of flying aircraft. *Journal of Dynamic Systems, Measurement, and Control*, 127(1):41–49, Mar. 2005. doi: 10.1115/1.1870040.

I. Tuzcu, P. Marzocca, E. Cestino, G. Romeo, and G. Frulla. Stability, control, and simulation of high-altitude-long-endurance uavs. In *47th AIAA/ASME/ASCE/AHS/ASC Structures, Structural Dynamics, and Materials Conference*, Newport, Rhode Island, 1-4 May 2006. AIAA Paper 2006-1641.

R.W. Valenca. USAF NAA B-1 Lancer, Indian Springs Air Force Auxiliary Field, Nevada, 2004. VIRIN: 041008-F-RG506-005. Source: http://www. defenseimagery.mil/imagery.html#guid=44e9b054181df27c0363e20078e15767f96125f5.

R. Vepa. Finite state modeling of aeroelastic systems. Technical Report NASA-CR-2779, National Aeronautics and Space Administration, 1977.

H. Wagner. Uber die entstehung des dynamischen auftriebs von tragflun. *Zeitschrift fur Angewandte Mathematic and Mechanic*, 5(1):17–35, 1925.

Z. Wang, P. C. Chen, D. D. Liu, D. T. Mook, and M. J. Patil. Time domain nonlinear aeroelastic analysis for HALE wings. In *47th AIAA/ASME/ASCE/AHS/ASC Structures, Structural Dynamics, and Materials Conference*, Newport, Rhode Island, 1-4 May 2006. AIAA Paper 2006-1640.

G.N. Ward and U.L. Ly. Stability augmentation design of a large subsonic transport. In *AIAA Guidance, Navigation and Control Conference*, volume 1, pages 429–439, Scottsdale, Arizona, 1-3 Aug. 1994.

M. R. Waszak and D. K. Schmidt. Analysis of flexible aircraft longitudinal dynamics and handling qualities - Volume I: analysis methods. Technical Report NASA-CR-177943-VOL-1, National Aeronautics and Space Administration, 1985a.

M. R. Waszak and D. K. Schmidt. Analysis of flexible aircraft longitudinal dynamics and handling qualities - Volume II: data. Technical Report NASA-CR-177943-VOL-2, National Aeronautics and Space Administration, 1985b.

M. R. Waszak and D. K. Schmidt. Flight dynamics of aeroelastic vehicles. *Journal of Aircraft*, 25(6):563–571, June 1988.

M. R. Waszak, J. B. Davidson, and D. K. Schmidt. A simulation study of the flight dynamics of elastic aircraft - Volume I: experiment, results and analysis. Technical Report NASA-CR-4102-VOL-1, National Aeronautics and Space Administration, 1987a.

M. R. Waszak, J. B. Davidson, and D. K. Schmidt. A simulation study of the flight dynamics of elastic aircraft - Volume II: data. Technical Report NASA-CR-4102-VOL-2, National Aeronautics and Space Administration, 1987b.

M. R. Waszak, C. S. Buttrill, and D. K. Schmidt. Modeling and model simplification of aeroelastic vehicles: An overview. Technical Report NASA-TM-107691, National Aeronautics and Space Administration, 1992.

J. Weissinger. The lift distribution of swept-back wings. Technical Report NACA-TN-1120, National Advisory Committee for Aeronautics, 1947.

J.R. Wright and J.E. Cooper. *Introduction to Aircraft Aeroelasticity and Loads*. American Institute of Aeronautics and Astronautics, first edition, 2007.

W. Wright. Some aeronautical experiments. In *Proceedings of Western Society of Engineers*, Chicago, Illinois, Sept. 1901.

W. Wright and O. Wright. Distant view of the Wright airplane just after landing, taken from the starting point, with wing-rest in center of picture and launching rail at right (abr.). Prints and Photographs Division, Library of Congress, Washington D.C., Dec. 1903. Reproduction Number: LC-W861-38 (LOT 11512).

J.H. Wykes, L.U. Nardi, and A.S. Mori. XB-70 structural mode control system design and performance analysis. Technical Report NASA-CR-1557, National Aeronautics and Space Administration, 1970.

E. C. Yates. Calculation of flutter characteristics for finite-span swept or unswept wings at subsonic and supersonic speeds by a modified strip analysis. Technical Report NACA-RM-L57L10, National Advisory Committee for Aeronautics, 1958.

W. Yen. *Effects of Dynamic Aeroelasticity on Handling Qualities and Pilot Rating*. PhD thesis, Purdue University, 1977.

APPENDIX A

Aerodynamic Data

This chapter describes the calculation of the aerodynamic coefficients and data for the Aeroplane AX-1 from empirical estimates based on the geometry of the aeroplane.

A.1 Wing-Body Combination

The lift of the wing is modified by the addition of the fuselage. The lift produced by the inboard section of the wing, the "carry-over lift", is reduced, while the lift produced by the outboard exposed section of the wing is increased slightly [ESDU 94009, 1994]. The ratio of the wing lift to the wing-body lift may be estimated using slender-body theory [ESDU 91007, 1995].

ESDU 91007 [1995] provides a method for the calculation of the lift-curve slope of the wing in the presence of the fuselage, assumed to be a body of axi-symmetric revolution. The total lift of the wing-body combination is calculated as the sum of the lift produced by the body, L_B, the wing in the presence of the body, $L_{W(B)}$, and the body in the presence of the wing, $L_{B(W)}$.

Dimension	Notation	Wing	Tail
Maximum body radius, m	r	2.793	1.507
Gross semi-span, m	s	29.00	9.702
Root chord, m	c_r	10.55	5.345
Tip chord, m	c_t	2.480	2.019
Area, m^2	S	341.6	60.35
Wing height angle, rad	ϕ_1	1.095	-
Quarter-chord sweep angle, deg	$\Lambda_{\frac{1}{4}}$	30.00	30.00

Table A.1: Wing-body geometry for Aeroplane AX-1

The lift of the wing in the presence of the body is given by:

$$(L_W)_{W(B)} = K_{W(B)}\,(L_W) \tag{A.1.1}$$

The ratio of the wing lift in the presence of the body to the net wing lift, $K_{W(B)}$, is given by the following equation:

$$K_{W(B)} = \frac{\frac{2}{\pi}\left\{\left(1+\frac{r^4}{s^4}\right)\left[\frac{1}{2}\tan^{-1}\frac{1}{2}\left(\frac{s}{r}-\frac{r}{s}\right)+\frac{\pi}{4}\right]-\frac{r^2}{s^2}\left[\left(\frac{s}{r}-\frac{r}{s}\right)+2\tan^{-1}\frac{r}{s}\right]\right\}}{\left(1-\frac{r}{s}\right)^2} \tag{A.1.2}$$

The lift of the body in the presence of the wing is then given by:

$$(L_W)_{B(W)} = K_{B(W)}\,(L_W) \tag{A.1.3}$$

And for subsonic speeds, the ratio of the body lift in the presence of the wing to the net wing lift, $K_{B(W)}$, is given by the following equation:

$$K_{B(W)} = \frac{\left(1-\frac{r^2}{s^2}\right)^2-\frac{2}{\pi}\left\{\left(1+\frac{r^4}{s^4}\right)\left[\frac{1}{2}\tan^{-1}\frac{1}{2}\left(\frac{s}{r}-\frac{r}{s}\right)+\frac{\pi}{4}\right]-\frac{r^2}{s^2}\left[\left(\frac{s}{r}-\frac{r}{s}\right)+2\tan^{-1}\frac{r}{s}\right]\right\}}{\left(1-\frac{r}{s}\right)^2} \tag{A.1.4}$$

For the geometric data given in Table A.1, see Figure A.2, the ratios $K_{W(B)}$ and $K_{B(W)}$ can be calculated. The results are given in Table A.2.

Ratio	Wing	Tail
$K_{W(B)}$	1.074	1.123
$K_{B(W)}$	0.1281	0.2120
F_{WBO}	0.9753	-
$\frac{(x'_{ac})}{c_r}$	0.4643	0.4210

Table A.2: Wing-body lift-curve slope ratios

ESDU 91007 [1995] estimates the lift-curve slope of a wing-body combination for a wing mounted at mid-height. However, the wing of the Aeroplane AX-1 is mounted off-centre, below the centre-line of the fuselage. ESDU 95009 [1995] provides a method for calculating the effect of mounting the wing off-centre on the lift of the wing-body combination.

The effect of mounting the wing off-centre is expressed as the ratio, F_{WBO}, of the lift of the actual wing-body combination to that of a wing-body combination where the wing is remounted at the centre-line of the fuselage [ESDU 95009, 1995]. The lift of the off-centre wing-body combination is then given by:

$$(L)_{WBO} = F_{WBO}\left((L_W)_{W(B)} + (L_W)_{B(W)}\right) \tag{A.1.5}$$

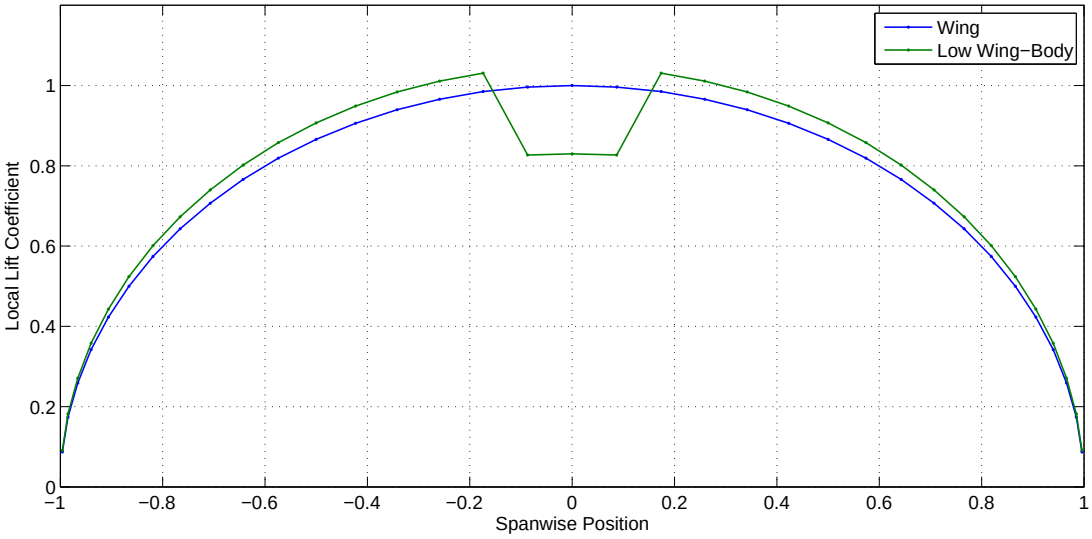

Figure A.1: Wing-body lift distribution for theoretical elliptic wing distribution

The ratio F_{WBO} is plotted in Figure 2 of as a function of ϕ_1 and ψ_1', the angle defining the wing height at the wing tip and the ratio of the maximum body radius to the reference wing semi-span respectively (Figure A.3). F_{WBO} is only plotted for values of ϕ_1/π between 0 and 0.5, i.e. values for the wing above the centre-line, as the effect is symmetrical. The ratio ψ_1' is given by:

$$\psi_1' = \frac{r}{s_1'} \tag{A.1.6}$$

where r is the radius of the body and s' is the semi-span of the reference wing, given by the following equation. The resulting ratio is given for the wing in Table A.2.

$$s_1' = s + r\,(1 - \sin\phi_1) \tag{A.1.7}$$

The result is a prediction of the lift distribution for a wing and fuselage combination, for which the lift of the wing and body are scaled using the calculated factors. For a theoretical elliptic wing lift distribution, the resulting lift distribution for the wing-body combination is shown in Figure A.1.

The aerodynamic centre of the carry-over lift on the fuselage due to the presence of the wing may also be estimated [ESDU 92024, 1992]. At subsonic speeds, the location of the aerodynamic centre is given by:

$$\frac{(x_{ac}')}{c_r} = \frac{1}{4} + \frac{1+\lambda}{4} F A \tan\Lambda_{\frac{1}{4}} \tag{A.1.8}$$

where $\Lambda_{\frac{1}{4}}$ is the sweep of the wing quarter-chord line, A is the net wing aspect ratio, and F is given by:

$$F = \frac{1}{1-\frac{s}{r}} + \left[\frac{\left(1-2\frac{r}{s}\right)^{1/2} \cosh^{-1}\left(\frac{s}{r}-1\right) + \frac{r}{s}\left(1+\frac{\pi}{2}\right) - 1}{\frac{\frac{r}{s}\left(1-\frac{r}{s}\right)}{\left(1-2\frac{r}{s}\right)^{1/2}} \cosh^{-1}\left(\frac{s}{r}-1\right) + \frac{s}{r} + \frac{r}{s} - \frac{\pi}{2}\left(1-\frac{r}{s}\right) - 2} \right] \tag{A.1.9}$$

The net wing aspect ratio, A, is given by:

$$A = \frac{4\,(s-r)^2}{S} \tag{A.1.10}$$

The aerodynamic centre of the carry-over lift on the fuselage for the wing and tail of the Aeroplane AX-1 is calculated in Table A.2.

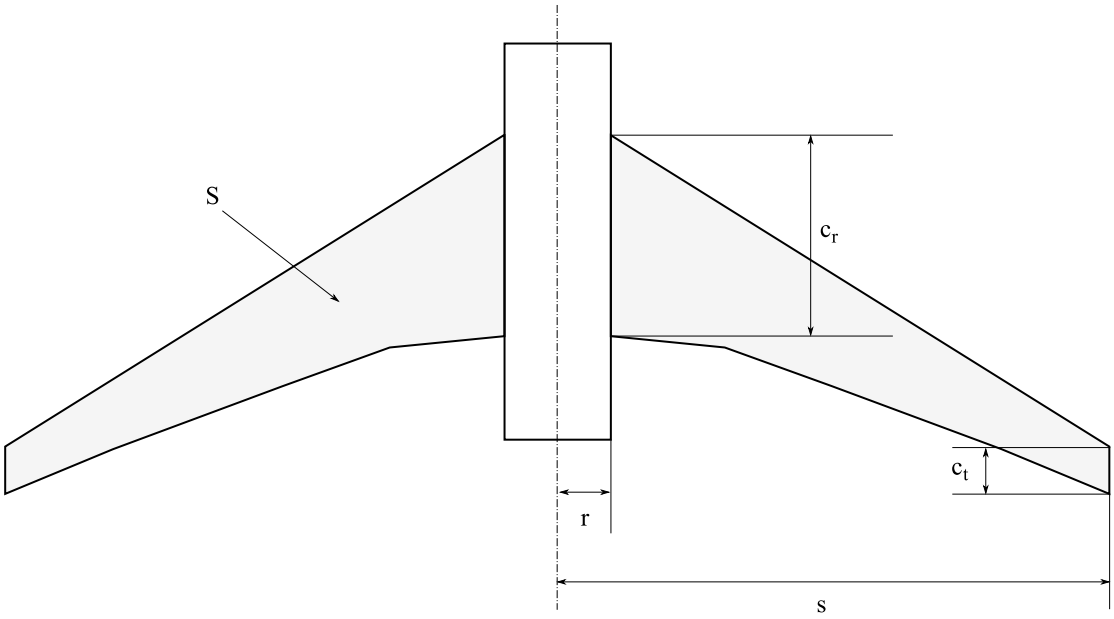

Figure A.2: Wing-body lift-curve slope geometrical parameters

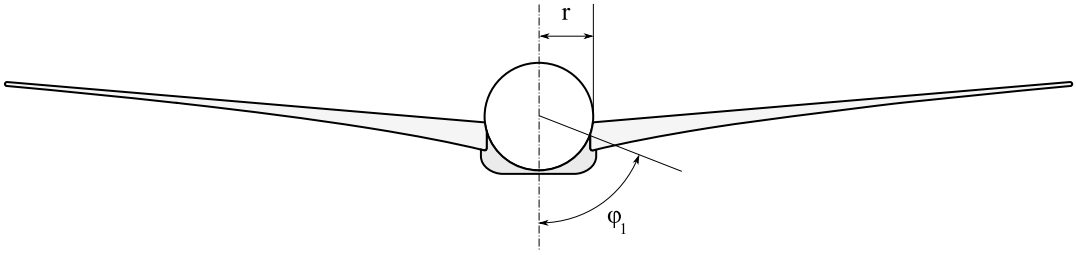

Figure A.3: Off-centre wing geometrical parameters

A.2 Fuselage

A.2.1 Forebody Lift

The aerodynamic force and pitching moment of the fuselage forebody may also be estimated [ESDU 89008, 1990; ESDU 89014, 2004]. ESDU 89008 [1990] provides a method for the calculation of the normal force and pitching moment curve slopes of a fuselage, or forebody-cylinder combination, at zero angle of attack. The normal force curve slope of a forebody-cylinder combination is given as:

$$C_{N\alpha} = kGC_{N\alpha l} + \Delta C_{N\alpha\delta^*} + \Delta C_{N\alpha F} \tag{A.2.1}$$

The major contribution to the normal force is due to the inviscid flow over the forebody, $C_{N\alpha l}$, which produces a loading distribution over the forebody, extending onto the cylindrical section of the fuselage. The scaling factor k is used to scale this value where the length of the cylindrical fuselage is too short to contain all of this carry-over loading. The remaining contributions to the normal force are due to the development of a viscous boundary layer. $\Delta C_{N\alpha\delta^*}$ is caused by the modified flow due to the displacement thickness of the boundary layer, while $\Delta C_{N\alpha F}$ is due to the frictional force acting on the body. The method presented in ESDU 89008 [1990] assumes that the boundary layer is fully turbulent. The scaling factor G is used to scale results for forebody shapes other than tangent-ogive.

Dimension	Notation	Value
Forebody length, m	l_f	9.534
Aftbody length, m	l_a	20.43
Midbody length, m	l_m	39.44
Cylinder Length, m	l_c	54.16
Body Length, m	L	63.69
Maximum body diameter, m	D	5.640
Body base diameter, m	D_b	0.6721

Table A.3: Fuselage geometry for Aeroplane AX-1

The pitching moment curve slope of a forebody-cylinder combination is given by:

$$(C_m)_{0\alpha} = GkC_{N\alpha l}\left\{\left[\frac{(C_m)_{0\alpha}}{C_{N\alpha}}\right]_{i,t} + \Delta\left[\frac{(C_m)_{0\alpha}}{C_{N\alpha}}\right]_i\right\} + \Delta\,(C_m)_{0\alpha\delta^*} + \Delta\,(C_m)_{0\alpha F} \tag{A.2.2}$$

The centre of pressure for a tangent-ogive forebody as the angle of attack tends to zero, $\left[\frac{(C_m)_{0\alpha}}{C_{N\alpha}}\right]_{i,t}$, is extended to other forebody shapes the amount $\Delta\left[\frac{(C_m)_{0\alpha}}{C_{N\alpha}}\right]_i$, the difference between the centre of pressure for the forebody in question and a tangent-ogive forebody of the same fineness ratio. It is given by:

$$\Delta \left[\frac{(C_m)_{0\alpha}}{C_{N\alpha}} \right]_i = (C_{Vf} - 0.54) \frac{l_f}{D} \tag{A.2.3}$$

where C_{Vf}, the volume coefficient of the forebody, is calculated using ESDU 77028 [1990], and the forebody-cylinder geometrical properties, l_f and D are shown in Figure A.4, and are defined for the Aeroplane AX-1 in Table A.3.

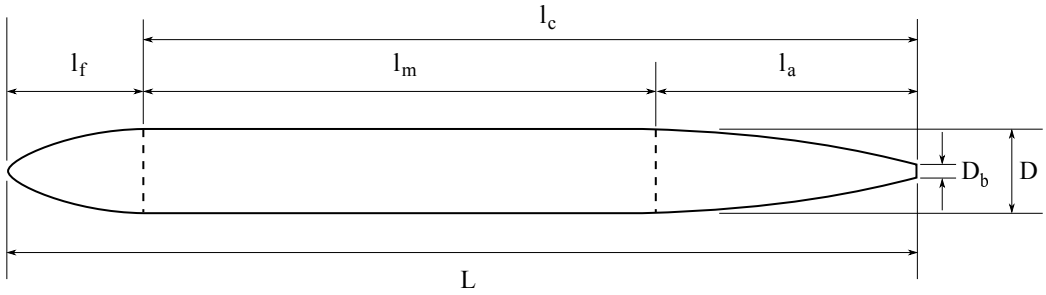

Figure A.4: Fuselage geometrical parameters

Using Figures 1 through 8 of ESDU 89008 [1990], and the geometrical properties defined Table A.3, the normal force and pitching moment curve slope components of the forebody-cylinder fuselage of the Aeroplane AX-1 can be calculated as a function of Mach number and Reynolds number. The total normal force and pitching moment slopes are then given by Equations A.2.2 and A.2.1. This was calculated for a range of Reynolds number from 1.00×10^7 to $\times10^9$, and for Mach numbers 0.0 to 1.0. The results are tabulated in Tables A.4 and A.5, and plotted in Figures A.5 and A.6.

ESDU 89014 [2004] further provides a method to calculate the normal force and pitching moment coefficient, or centre of pressure, of the fuselage forebody-cylinder at angles of attack up to 90°. The normal force coefficient is given by:

$$C_N = C_{N\alpha} \sin\alpha \cos\alpha + \frac{4}{\pi} \frac{L}{D} C_{PL} C_{Nc} \tag{A.2.4}$$

where $C_{N\alpha}$ is the normal force slope at zero angle of attack calculated using ESDU 89008 [1990]. The second term represents cross-flow effects, which result as the flow breaks away from the body on the leeward side, causing symmetric vortex formation. The geometric coefficient C_{PL} is calculated in ESDU 77028 [1990], while the cross flow normal force coefficient, C_{Nc}, is given in Figure 1 of ESDU 89014 [2004] as a function of Mach number and angle of attack.

The centre of pressure is given aft of the nose by:

$$x_{cp} = -\frac{(C_m)_0}{C_N} D \tag{A.2.5}$$

where D is the maximum diameter of the fuselage, and the pitching moment coefficient, $(C_m)_0$, is given by:

$$(C_m)_0 = (C_m)_{0\alpha} \sin\alpha \cos\alpha - \frac{2}{\pi} \left(\frac{L}{D} \right)^2 C_{PL} C_{CL} C_{Nc} \tag{A.2.6}$$

The second term again represents the result of cross-flow effects on the pitching moment. The geometric coefficient C_{CL} is again given in ESDU 77028 [1990]. The normal force coefficient and centre of pressure for the Aeroplane AX-1 fuselage was calculated for the given Mach number and Reynolds number range, over an angle of attack range of +/-15°.

Tables A.6 and A.7 provide the calculated variation of the calculated normal force coefficient and centre of pressure with angle of attack and Mach number for a Reynolds number of 1.00×10^8 respectively. This data is plotted in Figures A.7 and A.8.

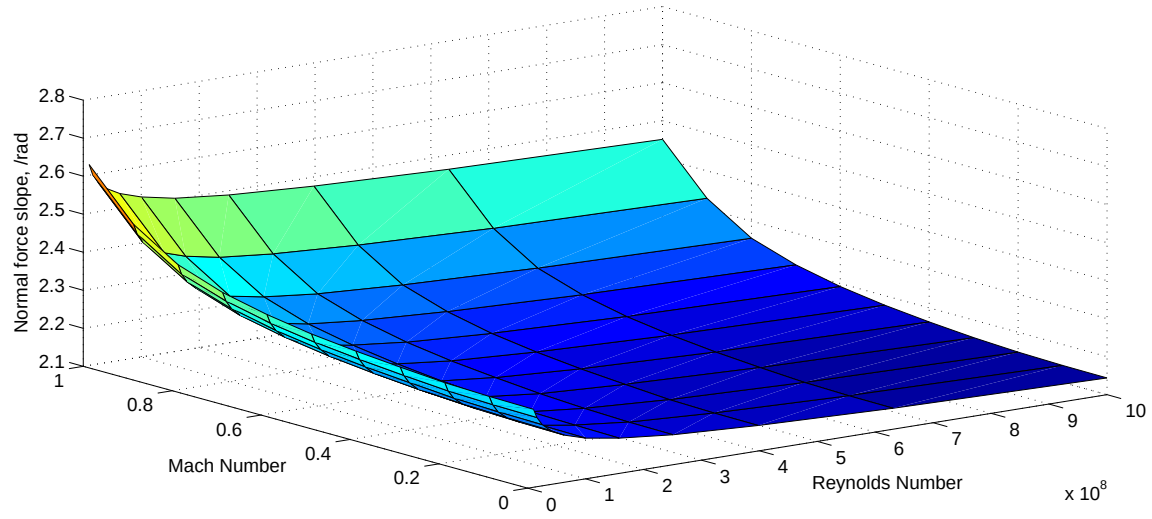

Figure A.5: Variation of fuselage forebody-cylinder zero angle of attack normal force with Reynolds number and Mach number

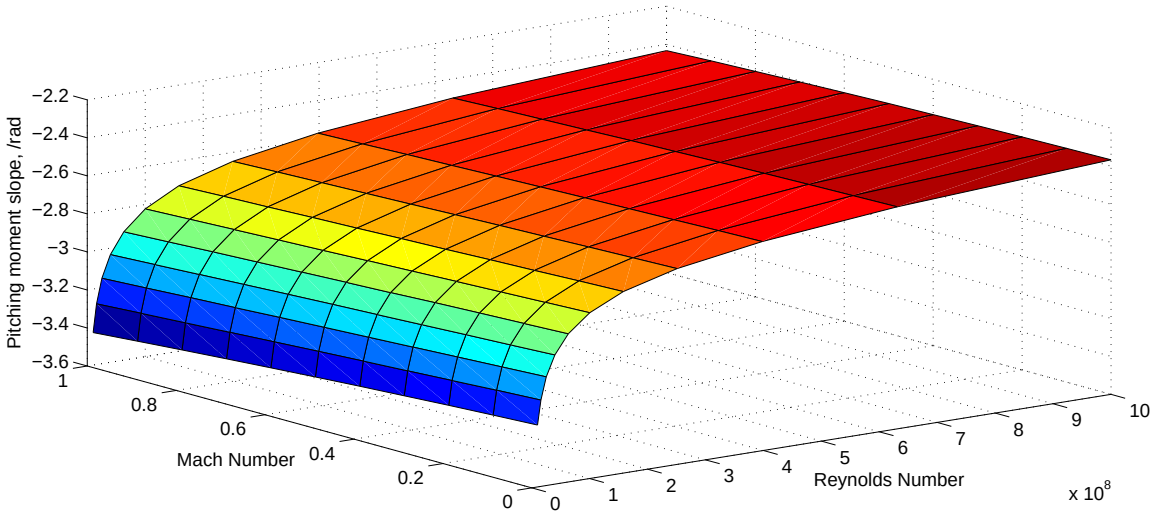

Figure A.6: Variation of fuselage forebody-cylinder zero angle of attack pitching moment with Reynolds number and Mach number

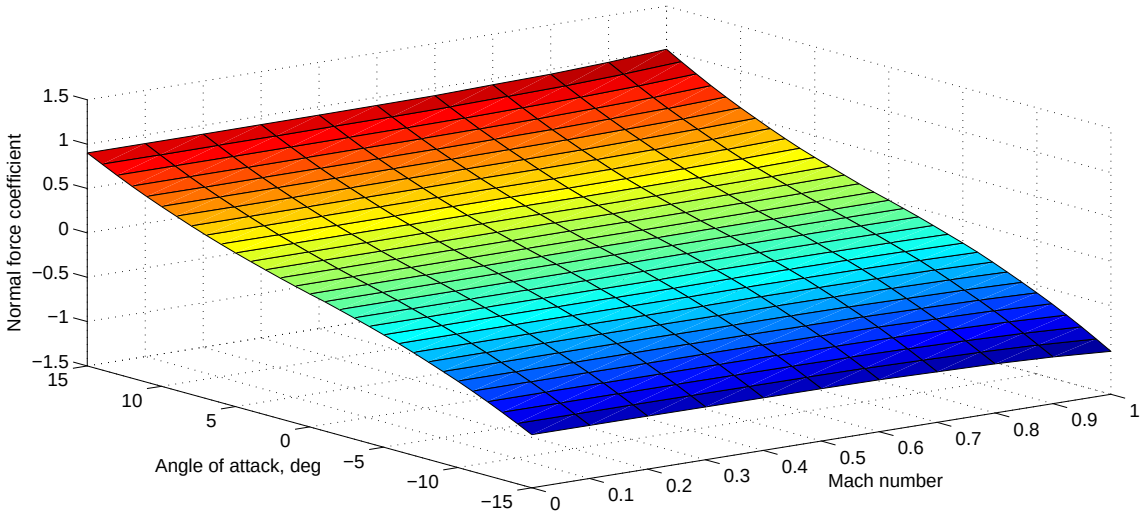

Figure A.7: Variation of fuselage forebody-cylinder normal force coefficient with Mach number and incidence at Re = 1.00×10^8

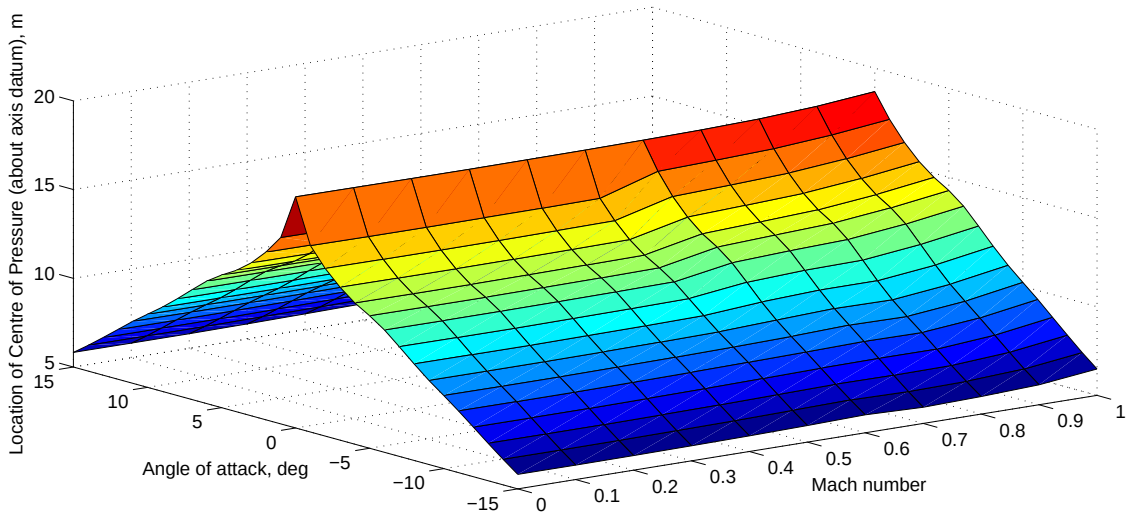

Figure A.8: Variation of fuselage forebody-cylinder centre of pressure with Mach number and incidence at Re = 1.00×10^8

	Reynolds Number										
Mach	1.0×10^7	1.6×10^7	2.5×10^7	4.0×10^7	6.3×10^7	1.0×10^8	1.6×10^8	2.5×10^8	4.0×10^8	6.3×10^8	1.0×10^9
0.1	+2.307	+2.284	+2.263	+2.244	+2.226	+2.209	+2.195	+2.180	+2.168	+2.156	+2.145
0.2	+2.311	+2.288	+2.267	+2.248	+2.230	+2.212	+2.198	+2.184	+2.171	+2.159	+2.148
0.3	+2.320	+2.297	+2.276	+2.255	+2.237	+2.220	+2.206	+2.191	+2.179	+2.166	+2.154
0.4	+2.330	+2.307	+2.286	+2.265	+2.247	+2.229	+2.215	+2.201	+2.188	+2.175	+2.163
0.5	+2.343	+2.320	+2.299	+2.278	+2.260	+2.242	+2.228	+2.213	+2.200	+2.187	+2.175
0.6	+2.362	+2.338	+2.317	+2.296	+2.278	+2.260	+2.245	+2.230	+2.217	+2.204	+2.192
0.7	+2.388	+2.364	+2.342	+2.321	+2.303	+2.285	+2.269	+2.255	+2.242	+2.229	+2.217
0.8	+2.429	+2.403	+2.381	+2.361	+2.342	+2.324	+2.308	+2.293	+2.280	+2.267	+2.255
0.9	+2.503	+2.477	+2.454	+2.434	+2.415	+2.397	+2.380	+2.366	+2.353	+2.340	+2.328
1.0	+2.628	+2.601	+2.578	+2.558	+2.539	+2.521	+2.503	+2.489	+2.476	+2.463	+2.451

Table A.4: Variation of fuselage forebody-cylinder zero angle of attack normal force with Reynolds number and Mach number

	Reynolds Number										
Mach	1.0×10^7	1.6×10^7	2.5×10^7	4.0×10^7	6.3×10^7	1.0×10^8	1.6×10^8	2.5×10^8	4.0×10^8	6.3×10^8	1.0×10^9
0.1	−3.286	−3.158	−3.040	−2.931	−2.830	−2.737	−2.653	−2.577	−2.506	−2.437	−2.370
0.2	−3.299	−3.171	−3.052	−2.942	−2.839	−2.746	−2.662	−2.584	−2.513	−2.442	−2.374
0.3	−3.313	−3.184	−3.064	−2.953	−2.849	−2.755	−2.670	−2.592	−2.519	−2.448	−2.379
0.4	−3.327	−3.197	−3.076	−2.964	−2.860	−2.765	−2.679	−2.599	−2.526	−2.454	−2.385
0.5	−3.342	−3.210	−3.088	−2.975	−2.870	−2.774	−2.687	−2.607	−2.533	−2.461	−2.391
0.6	−3.358	−3.224	−3.100	−2.986	−2.881	−2.784	−2.696	−2.615	−2.540	−2.468	−2.398
0.7	−3.375	−3.238	−3.113	−2.998	−2.891	−2.793	−2.704	−2.623	−2.548	−2.476	−2.406
0.8	−3.392	−3.252	−3.125	−3.010	−2.902	−2.803	−2.713	−2.631	−2.555	−2.484	−2.414
0.9	−3.410	−3.266	−3.138	−3.022	−2.914	−2.813	−2.721	−2.639	−2.563	−2.492	−2.423
1.0	−3.429	−3.281	−3.151	−3.034	−2.925	−2.823	−2.730	−2.647	−2.571	−2.501	−2.433

Table A.5: Variation of fuselage forebody-cylinder zero angle of attack pitching moment with Reynolds number and Mach number

	Mach number										
Incidence	0.0	0.1	0.2	0.3	0.4	0.5	0.6	0.7	0.8	0.9	1.0
-15.0	-0.9008	-0.9012	-0.9021	-0.9040	-0.9064	-0.9095	-0.9140	-0.9306	-0.9454	-0.9740	-1.015
-14.0	-0.8192	-0.8196	-0.8204	-0.8222	-0.8245	-0.8274	-0.8321	-0.8454	-0.8601	-0.8846	-0.9210
-13.0	-0.7403	-0.7406	-0.7414	-0.7431	-0.7452	-0.7480	-0.7527	-0.7629	-0.7774	-0.7981	-0.8300
-12.0	-0.6647	-0.6650	-0.6657	-0.6673	-0.6692	-0.6718	-0.6763	-0.6840	-0.6979	-0.7154	-0.7431
-11.0	-0.5931	-0.5934	-0.5941	-0.5955	-0.5973	-0.5997	-0.6037	-0.6093	-0.6224	-0.6370	-0.6611
-10.0	-0.5263	-0.5265	-0.5272	-0.5285	-0.5301	-0.5323	-0.5353	-0.5396	-0.5514	-0.5639	-0.5851
-9.0	-0.4626	-0.4629	-0.4634	-0.4646	-0.4661	-0.4680	-0.4696	-0.4730	-0.4831	-0.4939	-0.5127
-8.0	-0.4006	-0.4008	-0.4013	-0.4024	-0.4037	-0.4054	-0.4050	-0.4078	-0.4159	-0.4253	-0.4421
-7.0	-0.3411	-0.3413	-0.3417	-0.3426	-0.3438	-0.3453	-0.3430	-0.3454	-0.3516	-0.3597	-0.3745
-6.0	-0.2848	-0.2850	-0.2854	-0.2862	-0.2872	-0.2885	-0.2850	-0.2869	-0.2915	-0.2984	-0.3112
-5.0	-0.2327	-0.2328	-0.2331	-0.2338	-0.2346	-0.2357	-0.2322	-0.2338	-0.2372	-0.2430	-0.2538
-4.0	-0.1830	-0.1831	-0.1834	-0.1839	-0.1846	-0.1854	-0.1825	-0.1838	-0.1865	-0.1912	-0.1998
-3.0	-0.1341	-0.1342	-0.1344	-0.1348	-0.1353	-0.1360	-0.1335	-0.1346	-0.1366	-0.1401	-0.1466
-2.0	-0.08683	-0.08689	-0.08701	-0.08728	-0.08761	-0.08805	-0.08624	-0.08698	-0.08829	-0.09071	-0.09503
-1.0	-0.04186	-0.04189	-0.04196	-0.04209	-0.04226	-0.04248	-0.04143	-0.04183	-0.04249	-0.04373	-0.04589
0.0	0.000	0.000	0.000	0.000	0.000	0.000	0.000	0.000	0.000	0.000	0.000
+1.0	+0.04186	+0.04189	+0.04196	+0.04209	+0.04226	+0.04248	+0.04143	+0.04183	+0.04249	+0.04373	+0.04589
+2.0	+0.08683	+0.08689	+0.08701	+0.08728	+0.08761	+0.08805	+0.08624	+0.08698	+0.08829	+0.09071	+0.09503
+3.0	+0.1341	+0.1342	+0.1344	+0.1348	+0.1353	+0.1360	+0.1335	+0.1346	+0.1366	+0.1401	+0.1466
+4.0	+0.1830	+0.1831	+0.1834	+0.1839	+0.1846	+0.1854	+0.1825	+0.1838	+0.1865	+0.1912	+0.1998
+5.0	+0.2327	+0.2328	+0.2331	+0.2338	+0.2346	+0.2357	+0.2322	+0.2338	+0.2372	+0.2430	+0.2538
+6.0	+0.2848	+0.2850	+0.2854	+0.2862	+0.2872	+0.2885	+0.2850	+0.2869	+0.2915	+0.2984	+0.3112
+7.0	+0.3411	+0.3413	+0.3417	+0.3426	+0.3438	+0.3453	+0.3430	+0.3454	+0.3516	+0.3597	+0.3745
+8.0	+0.4006	+0.4008	+0.4013	+0.4024	+0.4037	+0.4054	+0.4050	+0.4078	+0.4159	+0.4253	+0.4421
+9.0	+0.4626	+0.4629	+0.4634	+0.4646	+0.4661	+0.4680	+0.4696	+0.4730	+0.4831	+0.4939	+0.5127
+10.0	+0.5263	+0.5265	+0.5272	+0.5285	+0.5301	+0.5323	+0.5353	+0.5396	+0.5514	+0.5639	+0.5851

Table A.6: Variation of fuselage forebody-cylinder normal force coefficient with Mach number and incidence at Re = 1.00×10^8

	Mach number										
Incidence	0.0	0.1	0.2	0.3	0.4	0.5	0.6	0.7	0.8	0.9	1.0
+11.0	+0.5931	+0.5934	+0.5941	+0.5955	+0.5973	+0.5997	+0.6037	+0.6093	+0.6224	+0.6370	+0.6611
+12.0	+0.6647	+0.6650	+0.6657	+0.6673	+0.6692	+0.6718	+0.6763	+0.6840	+0.6979	+0.7154	+0.7431
+13.0	+0.7403	+0.7406	+0.7414	+0.7431	+0.7452	+0.7480	+0.7527	+0.7629	+0.7774	+0.7981	+0.8300
+14.0	+0.8192	+0.8196	+0.8204	+0.8222	+0.8245	+0.8274	+0.8321	+0.8454	+0.8601	+0.8846	+0.9210
+15.0	+0.9008	+0.9012	+0.9021	+0.9040	+0.9064	+0.9095	+0.9140	+0.9306	+0.9454	+0.9740	+1.015

Table A.6: Variation of fuselage forebody-cylinder normal force coefficient with Mach number and incidence at Re = 1.00×10^8 (continued)

	Mach number										
Incidence	0.0	0.1	0.2	0.3	0.4	0.5	0.6	0.7	0.8	0.9	1.0
-15.0	+5.823	+5.818	+5.823	+5.849	+5.885	+5.936	+6.015	+5.913	+5.990	+6.127	+6.491
-14.0	+6.449	+6.443	+6.447	+6.473	+6.508	+6.559	+6.627	+6.564	+6.615	+6.789	+7.189
-13.0	+7.112	+7.106	+7.110	+7.135	+7.170	+7.220	+7.276	+7.258	+7.280	+7.496	+7.936
-12.0	+7.799	+7.792	+7.796	+7.820	+7.854	+7.903	+7.952	+7.981	+7.975	+8.234	+8.715
-11.0	+8.483	+8.476	+8.478	+8.501	+8.535	+8.583	+8.635	+8.709	+8.678	+8.978	+9.495
-10.0	+9.119	+9.111	+9.113	+9.135	+9.167	+9.214	+9.288	+9.395	+9.354	+9.683	+10.22
-9.0	+9.748	+9.739	+9.740	+9.762	+9.793	+9.838	+9.972	+10.10	+10.07	+10.41	+10.96
-8.0	+10.45	+10.44	+10.44	+10.46	+10.49	+10.53	+10.77	+10.91	+10.91	+11.27	+11.80
-7.0	+11.18	+11.17	+11.17	+11.19	+11.22	+11.26	+11.65	+11.80	+11.85	+12.20	+12.71
-6.0	+11.90	+11.89	+11.89	+11.91	+11.93	+11.97	+12.52	+12.67	+12.78	+13.12	+13.60
-5.0	+12.47	+12.46	+12.46	+12.47	+12.50	+12.54	+13.17	+13.32	+13.47	+13.81	+14.26
-4.0	+12.96	+12.95	+12.95	+12.96	+12.99	+13.02	+13.70	+13.84	+13.99	+14.32	+14.76

Table A.7: Variation of fuselage forebody-cylinder centre of pressure with Mach number and incidence at Re = 1.00×10^8

	Mach number										
Incidence	0.0	0.1	0.2	0.3	0.4	0.5	0.6	0.7	0.8	0.9	1.0
-3.0	+13.62	+13.60	+13.60	+13.61	+13.64	+13.67	+14.41	+14.54	+14.70	+15.01	+15.43
-2.0	+14.45	+14.44	+14.43	+14.45	+14.47	+14.50	+15.34	+15.46	+15.60	+15.89	+16.28
-1.0	+15.50	+15.49	+15.48	+15.49	+15.51	+15.53	+16.54	+16.63	+16.75	+16.99	+17.35
0.0	+18.03	+18.01	+18.00	+18.00	+18.01	+18.02	+18.05	+18.10	+18.20	+18.38	+18.68
+1.0	+15.50	+15.49	+15.48	+15.49	+15.51	+15.53	+16.54	+16.63	+16.75	+16.99	+17.35
+2.0	+14.45	+14.44	+14.43	+14.45	+14.47	+14.50	+15.34	+15.46	+15.60	+15.89	+16.28
+3.0	+13.62	+13.60	+13.60	+13.61	+13.64	+13.67	+14.41	+14.54	+14.70	+15.01	+15.43
+4.0	+12.96	+12.95	+12.95	+12.96	+12.99	+13.02	+13.70	+13.84	+13.99	+14.32	+14.76
+5.0	+12.47	+12.46	+12.46	+12.47	+12.50	+12.54	+13.17	+13.32	+13.47	+13.81	+14.26
+6.0	+11.90	+11.89	+11.89	+11.91	+11.93	+11.97	+12.52	+12.67	+12.78	+13.12	+13.60
+7.0	+11.18	+11.17	+11.17	+11.19	+11.22	+11.26	+11.65	+11.80	+11.85	+12.20	+12.71
+8.0	+10.45	+10.44	+10.44	+10.46	+10.49	+10.53	+10.77	+10.91	+10.91	+11.27	+11.80
+9.0	+9.748	+9.739	+9.740	+9.762	+9.793	+9.838	+9.972	+10.10	+10.07	+10.41	+10.96
+10.0	+9.119	+9.111	+9.113	+9.135	+9.167	+9.214	+9.288	+9.395	+9.354	+9.683	+10.22
+11.0	+8.483	+8.476	+8.478	+8.501	+8.535	+8.583	+8.635	+8.709	+8.678	+8.978	+9.495
+12.0	+7.799	+7.792	+7.796	+7.820	+7.854	+7.903	+7.952	+7.981	+7.975	+8.234	+8.715
+13.0	+7.112	+7.106	+7.110	+7.135	+7.170	+7.220	+7.276	+7.258	+7.280	+7.496	+7.936
+14.0	+6.449	+6.443	+6.447	+6.473	+6.508	+6.559	+6.627	+6.564	+6.615	+6.789	+7.189
+15.0	+5.823	+5.818	+5.823	+5.849	+5.885	+5.936	+6.015	+5.913	+5.990	+6.127	+6.491

Table A.7: Variation of fuselage forebody-cylinder centre of pressure with Mach number and incidence at Re = 1.00×10^8 (continued)

A.2.2 Aftbody Lift

ESDU 87033 [1992] provides a method for calculating the normal force and pitching moment due to the shape of the fuselage aftbody. It is assumed again that the fuselage can be approximated by an axi-symmetric body of revolution, and the influence of the aftbody conical boat-tailing is calculated from empirical estimates. The change in normal force due to the aftbody is given by:

$$\Delta C_N = \Delta C_{N\alpha} \sin\alpha \cos\alpha \left(1 - \sin^{0.6}\alpha\right) + \Delta C_{Dc} \sin^2\alpha \tag{A.2.7}$$

in which the first term, $\Delta C_{N\alpha}$, the inviscid contribution, is calculated using slender-body theory. The second term, ΔC_{Dc}, is the viscous cross-flow contribution. The inviscid contribution is given in Figure 1 of ESDU 87033 [1992], while the viscous drag term is given in Figure 2; both are given as a function of Mach number.

The centre of pressure for the change in normal force due to the aftbody is approximated by:

$$x'_{cp} = 0.5 l_a \tag{A.2.8}$$

where l_a is the length of the aftbody boat-tail. The geometrical parameters required by ESDU 87033 [1992], i.e. l_a, the length of the boat-tail; D, the maximum body diameter; and D_b, the body base diameter; are given for the Aeroplane AX-1 in Table A.3. The normal force coefficient due to the aftbody for the Aeroplane AX-1 fuselage was calculated for the given Mach number and angle of attack range, and is shown in Figure A.9 and Table A.8.

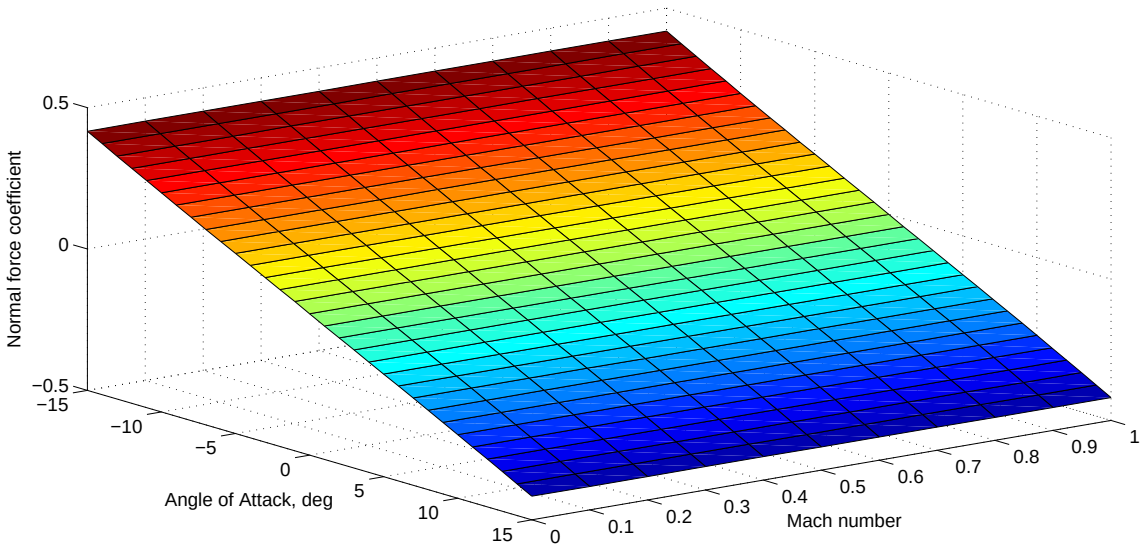

Figure A.9: Variation of fuselage aftbody normal force coefficient with Mach number and angle of attack

	Mach number										
Incidence	0.0	0.1	0.2	0.3	0.4	0.5	0.6	0.7	0.8	0.9	1.0
-15.0	+0.4164	+0.4166	+0.4168	+0.4171	+0.4173	+0.4176	+0.4179	+0.4182	+0.4185	+0.4189	+0.4193
-14.0	+0.3877	+0.3878	+0.3880	+0.3882	+0.3884	+0.3886	+0.3889	+0.3891	+0.3894	+0.3897	+0.3900
-13.0	+0.3591	+0.3593	+0.3594	+0.3595	+0.3597	+0.3599	+0.3601	+0.3603	+0.3605	+0.3607	+0.3609
-12.0	+0.3307	+0.3308	+0.3310	+0.3311	+0.3312	+0.3313	+0.3315	+0.3316	+0.3318	+0.3319	+0.3321
-11.0	+0.3025	+0.3026	+0.3027	+0.3028	+0.3029	+0.3030	+0.3031	+0.3032	+0.3033	+0.3035	+0.3036
-10.0	+0.2745	+0.2746	+0.2746	+0.2747	+0.2748	+0.2749	+0.2749	+0.2750	+0.2751	+0.2752	+0.2753
-9.0	+0.2467	+0.2467	+0.2468	+0.2468	+0.2469	+0.2469	+0.2470	+0.2470	+0.2471	+0.2471	+0.2472
-8.0	+0.2190	+0.2190	+0.2190	+0.2191	+0.2191	+0.2191	+0.2192	+0.2192	+0.2193	+0.2193	+0.2193
-7.0	+0.1914	+0.1915	+0.1915	+0.1915	+0.1915	+0.1915	+0.1916	+0.1916	+0.1916	+0.1916	+0.1917
-6.0	+0.1640	+0.1640	+0.1641	+0.1641	+0.1641	+0.1641	+0.1641	+0.1641	+0.1641	+0.1642	+0.1642
-5.0	+0.1367	+0.1368	+0.1368	+0.1368	+0.1368	+0.1368	+0.1368	+0.1368	+0.1368	+0.1368	+0.1368
-4.0	+0.1096	+0.1096	+0.1096	+0.1096	+0.1096	+0.1096	+0.1096	+0.1096	+0.1096	+0.1096	+0.1096
-3.0	+0.08241	+0.08242	+0.08242	+0.08242	+0.08242	+0.08242	+0.08242	+0.08243	+0.08243	+0.08243	+0.08243
-2.0	+0.05525	+0.05525	+0.05525	+0.05525	+0.05525	+0.05525	+0.05525	+0.05525	+0.05525	+0.05525	+0.05525
-1.0	+0.02791	+0.02791	+0.02791	+0.02791	+0.02791	+0.02791	+0.02791	+0.02791	+0.02791	+0.02791	+0.02791
0.0	0.000	0.000	0.000	0.000	0.000	0.000	0.000	0.000	0.000	0.000	0.000
+1.0	-0.02791	-0.02791	-0.02791	-0.02791	-0.02791	-0.02791	-0.02791	-0.02791	-0.02791	-0.02791	-0.02791
+2.0	-0.05525	-0.05525	-0.05525	-0.05525	-0.05525	-0.05525	-0.05525	-0.05525	-0.05525	-0.05525	-0.05525
+3.0	-0.08241	-0.08242	-0.08242	-0.08242	-0.08242	-0.08242	-0.08242	-0.08243	-0.08243	-0.08243	-0.08243
+4.0	-0.1096	-0.1096	-0.1096	-0.1096	-0.1096	-0.1096	-0.1096	-0.1096	-0.1096	-0.1096	-0.1096
+5.0	-0.1367	-0.1368	-0.1368	-0.1368	-0.1368	-0.1368	-0.1368	-0.1368	-0.1368	-0.1368	-0.1368
+6.0	-0.1640	-0.1640	-0.1641	-0.1641	-0.1641	-0.1641	-0.1641	-0.1641	-0.1641	-0.1642	-0.1642
+7.0	-0.1914	-0.1915	-0.1915	-0.1915	-0.1915	-0.1915	-0.1916	-0.1916	-0.1916	-0.1916	-0.1917
+8.0	-0.2190	-0.2190	-0.2190	-0.2191	-0.2191	-0.2191	-0.2192	-0.2192	-0.2193	-0.2193	-0.2193
+9.0	-0.2467	-0.2467	-0.2468	-0.2468	-0.2469	-0.2469	-0.2470	-0.2470	-0.2471	-0.2471	-0.2472

Table A.8: Variation of fuselage aftbody normal force coefficient with Mach number and angle of attack

	Mach number										
Incidence	0.0	0.1	0.2	0.3	0.4	0.5	0.6	0.7	0.8	0.9	1.0
+10.0	-0.2745	-0.2746	-0.2746	-0.2747	-0.2748	-0.2749	-0.2749	-0.2750	-0.2751	-0.2752	-0.2753
+11.0	-0.3025	-0.3026	-0.3027	-0.3028	-0.3029	-0.3030	-0.3031	-0.3032	-0.3033	-0.3035	-0.3036
+12.0	-0.3307	-0.3308	-0.3310	-0.3311	-0.3312	-0.3313	-0.3315	-0.3316	-0.3318	-0.3319	-0.3321
+13.0	-0.3591	-0.3593	-0.3594	-0.3595	-0.3597	-0.3599	-0.3601	-0.3603	-0.3605	-0.3607	-0.3609
+14.0	-0.3877	-0.3878	-0.3880	-0.3882	-0.3884	-0.3886	-0.3889	-0.3891	-0.3894	-0.3897	-0.3900
+15.0	-0.4164	-0.4166	-0.4168	-0.4171	-0.4173	-0.4176	-0.4179	-0.4182	-0.4185	-0.4189	-0.4193

Table A.8: Variation of fuselage aftbody normal force coefficient with Mach number and angle of attack (continued)

A.2.3 Profile Drag

ESDU 78019 provides a method for the calculation of the profile drag of the fuselage. The fuselage is again modelled as an axi-symmetric body of revolution, and the profile drag coefficient is given normalised with respect to the skin friction coefficient of a flat plate with the same boundary layer transition location. The profile drag coefficient is given as a function of Mach number and Reynolds number. The coefficient for the body is given by:

$$C_D = \left\{ \frac{C_V^{2/3}}{2\left(2\pi L/D\right)^{1/3} C_S} \right\} C_D^* \tag{A.2.9}$$

where C_D^* is the body profile drag coefficient based on $(volume)^{2/3}$. The geometric coefficients C_V and C_S are given by the following equations respectively, and can be calculated using ESDU 77028:

$$C_V = \frac{4V}{\pi D^2 L} \tag{A.2.10}$$

$$C_S = \frac{S}{\pi D L} \tag{A.2.11}$$

The profile drag coefficient, C_D^*, normalised with respect to $(volume)^{2/3}$, is given by:

$$C_D^* = \lambda^* C_F \tag{A.2.12}$$

where C_F is equivalent mean skin friction coefficient of a flat plate with the same boundary layer transition location, Mach number and Reynolds number. The normalised drag parameter, λ^*, is given by:

$$\lambda^* = K_{tr} K_M \lambda_G^* \tag{A.2.13}$$

in which λ_G^* is the value of λ^* at the datum boundary layer and flow conditions defined in ESDU 78019 [1998]. The correction factors K_M and K_{tr}, for Mach number and boundary layer transition location respectively, are designed to correct for the value of λ_G^* for values of Mach number and Reynolds number different to the datum condition. The datum value λ_G^* is given by the approximate expression:

$$\lambda_G^* = C_{DG}^*/C_{F0} \tag{A.2.14}$$

$$\approx 3.764\left[(D/L)^{-1/3} + 1.75\,(D/L)^{7/6} + 3.48\,(D/L)^{8/3}\right] \tag{A.2.15}$$

The correction factor K_{tr} was found not to depend on the forebody bluffness parameter, b, assuming that transition at x_{tr}, the boundary layer transition location, occurred before the forebody suction peak. For forebodies with moderate nose radius and smooth variation in curvature then, the factor K_{tr} is given by:

$$K_{tr} = 1 + 0.36\frac{x_{tr}}{L} - 3.3\left(\frac{x_{tr}}{L}\right)^3 \tag{A.2.16}$$

The Mach correction factor, K_M, was found to be a function of body diameter-length ratio, D/L, and the forebody bluffness parameter, b. It is given by:

$$K_M = 1 + F_M F_b \left(\frac{D}{L}\right)^2 \tag{A.2.17}$$

where the coefficients F_M and F_b are given for $0.03 \leq b \leq 0.15$ by:

$$F_M = 1.50M^2\left(1 + 1.50M^4\right) \tag{A.2.18}$$
$$F_b = 0.0924b^{-1} + 0.725b + 12.2b^2 \tag{A.2.19}$$

in which the forebody bluffness parameter, b, is given by:

$$b = \left(\frac{l_f}{L}\right)(1 - C_{Vf}) \tag{A.2.20}$$

The geometric parameter C_{Vf}, the volume coefficient of the forebody, is calculated again using ESDU 77028 [1990]. The flat plate mean skin friction coefficient, C_F, in Equation A.2.12 is given by:

$$C_F = (C_F/C_{F0})\, C_{F0} \tag{A.2.21}$$

in which:

$$C_{F0} = \frac{0.455}{\left\{F_{M1}\left[\log_{10}\left(F_{M2}R_L\right)\right]^B\right\}} \tag{A.2.22}$$

while the ratio (C_F/C_{F0}) is used to account for the effect of changes in the boundary layer transition location. The coefficients F_{M1}, F_{M2}, and B meanwhile are given by:

$$F_{M1} = 0.175M^2/\left[\tan^{-1}\left(0.4219M\right)\right]^2 \tag{A.2.23}$$
$$F_{M2} = \left[1 + 0.178M^2\right]^{-0.702}/F_{M1} \tag{A.2.24}$$
$$B = 2.62105 - 0.0042167\log_{10}\left(F_{M2}R_L\right) \tag{A.2.25}$$

where R_L is the Reynolds number based on body length. The ratio (C_F/C_{F0}) is expressed as a combination of the turbulent and laminar parts of the boundary layer, as is given for transition locations $0 \leq x_{tr}/L < 0.01$ by:

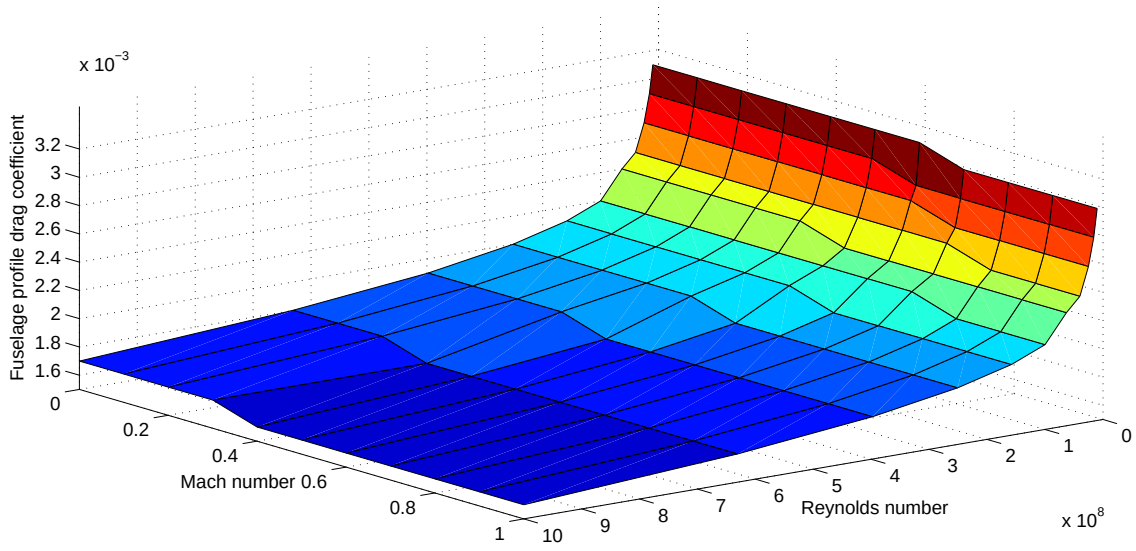

Figure A.10: Variation of fuselage profile drag at zero angle of attack with Mach number and Reynolds number

$$(C_F/C_{F0}) = 1 - 100\,(x_{tr}/L)\,[1 - (C_F/C_{F0})_{0.01}] \tag{A.2.26}$$

where $(C_F/C_{F0})_{0.01}$ is the value of C_F/C_{F0} for $x_{tr}/L = 0.01$. The ratio (C_F/C_{F0}) for the boundary layer transition location $x_{tr}/L = 0.01$ is given by:

$$(C_F/C_{F0}) = [1 - x_{tr}/L + F_1\,(x_{tr}/L)^g]^h - F_2 \tag{A.2.27}$$

where:

$$F_1 = 41.1463 R_L^{-0.377849} \tag{A.2.28}$$
$$F_2 = 1.1669\,(\log_{10} R_L)^{-3.0336} - 0.001487 \tag{A.2.29}$$
$$g = 0.71916 - 0.0164 \log_{10} R_L \tag{A.2.30}$$
$$h = 0.66584 + 0.2307 \log_{10} R_L \tag{A.2.31}$$

The required geometrical parameters for the Aeroplane AX-1 are given in Table A.3. The profile drag coefficient for the Aeroplane AX-1 fuselage was calculated for the given Mach number and Reynolds number range, and is shown in Table A.9 and Figure A.10.

	Reynolds Number			
Mach	1.0×10^7	1.6×10^7	2.5×10^7	4.0×10^7
0.1	$+3.129 \times 10^{-3}$	$+2.914 \times 10^{-3}$	$+2.719 \times 10^{-3}$	$+2.541 \times 10^{-3}$
0.2	$+3.123 \times 10^{-3}$	$+2.908 \times 10^{-3}$	$+2.713 \times 10^{-3}$	$+2.536 \times 10^{-3}$
0.3	$+3.112 \times 10^{-3}$	$+2.898 \times 10^{-3}$	$+2.703 \times 10^{-3}$	$+2.527 \times 10^{-3}$
0.4	$+3.098 \times 10^{-3}$	$+2.884 \times 10^{-3}$	$+2.691 \times 10^{-3}$	$+2.515 \times 10^{-3}$
0.5	$+3.080 \times 10^{-3}$	$+2.867 \times 10^{-3}$	$+2.675 \times 10^{-3}$	$+2.500 \times 10^{-3}$
0.6	$+3.060 \times 10^{-3}$	$+2.848 \times 10^{-3}$	$+2.657 \times 10^{-3}$	$+2.483 \times 10^{-3}$
0.7	$+3.039 \times 10^{-3}$	$+2.828 \times 10^{-3}$	$+2.638 \times 10^{-3}$	$+2.465 \times 10^{-3}$
0.8	$+3.019 \times 10^{-3}$	$+2.809 \times 10^{-3}$	$+2.619 \times 10^{-3}$	$+2.447 \times 10^{-3}$
0.9	$+3.003 \times 10^{-3}$	$+2.793 \times 10^{-3}$	$+2.604 \times 10^{-3}$	$+2.433 \times 10^{-3}$
1.0	$+2.994 \times 10^{-3}$	$+2.785 \times 10^{-3}$	$+2.596 \times 10^{-3}$	$+2.425 \times 10^{-3}$

	Reynolds Number			
Mach	6.3×10^7	1.0×10^8	1.6×10^8	2.5×10^8
0.1	$+2.380 \times 10^{-3}$	$+2.233 \times 10^{-3}$	$+2.099 \times 10^{-3}$	$+1.975 \times 10^{-3}$
0.2	$+2.375 \times 10^{-3}$	$+2.228 \times 10^{-3}$	$+2.094 \times 10^{-3}$	$+1.971 \times 10^{-3}$
0.3	$+2.367 \times 10^{-3}$	$+2.220 \times 10^{-3}$	$+2.086 \times 10^{-3}$	$+1.964 \times 10^{-3}$
0.4	$+2.355 \times 10^{-3}$	$+2.209 \times 10^{-3}$	$+2.076 \times 10^{-3}$	$+1.954 \times 10^{-3}$
0.5	$+2.341 \times 10^{-3}$	$+2.196 \times 10^{-3}$	$+2.063 \times 10^{-3}$	$+1.942 \times 10^{-3}$
0.6	$+2.325 \times 10^{-3}$	$+2.180 \times 10^{-3}$	$+2.048 \times 10^{-3}$	$+1.927 \times 10^{-3}$
0.7	$+2.307 \times 10^{-3}$	$+2.164 \times 10^{-3}$	$+2.033 \times 10^{-3}$	$+1.913 \times 10^{-3}$
0.8	$+2.291 \times 10^{-3}$	$+2.148 \times 10^{-3}$	$+2.018 \times 10^{-3}$	$+1.898 \times 10^{-3}$
0.9	$+2.277 \times 10^{-3}$	$+2.135 \times 10^{-3}$	$+2.005 \times 10^{-3}$	$+1.886 \times 10^{-3}$
1.0	$+2.269 \times 10^{-3}$	$+2.127 \times 10^{-3}$	$+1.997 \times 10^{-3}$	$+1.878 \times 10^{-3}$

	Reynolds Number		
Mach	4.0×10^8	6.3×10^8	1.0×10^9
0.1	$+1.862 \times 10^{-3}$	$+1.758 \times 10^{-3}$	$+1.662 \times 10^{-3}$
0.2	$+1.858 \times 10^{-3}$	$+1.754 \times 10^{-3}$	$+1.658 \times 10^{-3}$
0.3	$+1.851 \times 10^{-3}$	$+1.747 \times 10^{-3}$	$+1.652 \times 10^{-3}$
0.4	$+1.842 \times 10^{-3}$	$+1.738 \times 10^{-3}$	$+1.643 \times 10^{-3}$
0.5	$+1.830 \times 10^{-3}$	$+1.727 \times 10^{-3}$	$+1.632 \times 10^{-3}$
0.6	$+1.816 \times 10^{-3}$	$+1.714 \times 10^{-3}$	$+1.620 \times 10^{-3}$
0.7	$+1.802 \times 10^{-3}$	$+1.701 \times 10^{-3}$	$+1.607 \times 10^{-3}$
0.8	$+1.788 \times 10^{-3}$	$+1.688 \times 10^{-3}$	$+1.595 \times 10^{-3}$
0.9	$+1.777 \times 10^{-3}$	$+1.676 \times 10^{-3}$	$+1.584 \times 10^{-3}$
1.0	$+1.770 \times 10^{-3}$	$+1.669 \times 10^{-3}$	$+1.577 \times 10^{-3}$

Table A.9: Variation of fuselage profile drag at zero angle of attack with Mach number and Reynolds number

A.3 Wing and Aerofoil

A.3.1 Profile Drag

ESDU 00027 [2000] provides a method for the calculation of the profile drag coefficient for cambered aerofoils with attached flow at low lift coefficients. The predicted value is given as a function of Mach number and Reynolds number for a given boundary-layer transition position. The aerofoil profile drag coefficient is given by:

$$C_{\mathfrak{D}_0} = k_c k_M \left(C_{\mathfrak{D}_0}\right)_{th} \tag{A.3.1}$$

where $\left(C_{\mathfrak{D}_0}\right)_{th}$ is the profile drag coefficient given for the basic thickness distribution. This is given by the following equation:

$$\left(C_{\mathfrak{D}_0}\right)_{th} = k_1 + k_2 \frac{t_m}{c} + k_3 \frac{t_{0.75}}{t_m} + k_4 \left(\frac{t_m}{c}\right)\left(\frac{t_{0.75}}{t_m}\right) \tag{A.3.2}$$

where the parametric factors k_1, k_2, k_3, and k_4 are given respectively by:

$$k_1 = \left(+4.0 + 0.84\left(8.5 - \log_{10} Re_c\right)^2 - 3.40\frac{x_{tr}}{c} - 0.25\frac{x_{tr}}{c}\left(8.5 - \log_{10} Re_c\right)^2\right) \times 10^{-3} \tag{A.3.3}$$

$$k_2 = \left(+8.46 + 1.15\left(8.5 - \log_{10} Re_c\right)^2 - 27.40\frac{x_{tr}}{c} - 3.97\frac{x_{tr}}{c}\left(8.5 - \log_{10} Re_c\right)^2\right) \times 10^{-3} \tag{A.3.4}$$

$$k_3 = \left(-0.29 - 0.12\left(8.5 - \log_{10} Re_c\right)^2 + 0.31\frac{x_{tr}}{c} - 0.12\frac{x_{tr}}{c}\left(8.5 - \log_{10} Re_c\right)^2\right) \times 10^{-3} \tag{A.3.5}$$

$$k_4 = \left(+6.97 - 3.10\left(8.5 - \log_{10} Re_c\right)^2 + 16.60\frac{x_{tr}}{c} + 2.10\frac{x_{tr}}{c}\left(8.5 - \log_{10} Re_c\right)^2\right) \times 10^{-3} \tag{A.3.6}$$

The correction factors k_c and k_M are introduced in Equation A.3.1 to take account of compressibility and aerofoil rear camber. The value for these factors is given by Figures 5, 6 and 7 of ESDU 00027 [2000].

The span-wise variation of thickness-to-chord ratio for the Aeroplane AX-1 wing is given in Table A.14, and the aerofoil is assumed to be the NASA SC(2)-06 series section defined in Harris [1990]. The profile drag coefficient for the Aeroplane AX-1 wing as a function of Reynolds number is given in Figure A.11 and Table A.10 at $M = 0.3125$. The profile drag coefficient for the AX-1 tailplane, which is assumed to have a symmetrical NASA SC(2)-00 aerofoil series section and fixed thickness-to-chord ratio of 0.08. is given as a function of Reynolds number and Mach number in Table A.11.

	Reynolds number					
η	5.000×10^5	1.000×10^6	2.000×10^6	4.000×10^6	8.000×10^6	1.600×10^7
0.0000	$+1.092 \times 10^{-2}$	$+9.467 \times 10^{-3}$	$+8.290 \times 10^{-3}$	$+7.322 \times 10^{-3}$	$+6.530 \times 10^{-3}$	$+5.852 \times 10^{-3}$
0.1742	$+1.080 \times 10^{-2}$	$+9.354 \times 10^{-3}$	$+8.182 \times 10^{-3}$	$+7.225 \times 10^{-3}$	$+6.440 \times 10^{-3}$	$+5.762 \times 10^{-3}$
0.3423	$+1.073 \times 10^{-2}$	$+9.286 \times 10^{-3}$	$+8.119 \times 10^{-3}$	$+7.162 \times 10^{-3}$	$+6.382 \times 10^{-3}$	$+5.708 \times 10^{-3}$
0.5000	$+1.070 \times 10^{-2}$	$+9.258 \times 10^{-3}$	$+8.093 \times 10^{-3}$	$+7.136 \times 10^{-3}$	$+6.358 \times 10^{-3}$	$+5.685 \times 10^{-3}$
0.6432	$+1.069 \times 10^{-2}$	$+9.250 \times 10^{-3}$	$+8.085 \times 10^{-3}$	$+7.128 \times 10^{-3}$	$+6.351 \times 10^{-3}$	$+5.679 \times 10^{-3}$
0.7664	$+1.070 \times 10^{-2}$	$+9.258 \times 10^{-3}$	$+8.093 \times 10^{-3}$	$+7.136 \times 10^{-3}$	$+6.358 \times 10^{-3}$	$+5.685 \times 10^{-3}$
0.8663	$+1.072 \times 10^{-2}$	$+9.270 \times 10^{-3}$	$+8.104 \times 10^{-3}$	$+7.147 \times 10^{-3}$	$+6.369 \times 10^{-3}$	$+5.695 \times 10^{-3}$
0.9401	$+1.073 \times 10^{-2}$	$+9.284 \times 10^{-3}$	$+8.117 \times 10^{-3}$	$+7.160 \times 10^{-3}$	$+6.380 \times 10^{-3}$	$+5.706 \times 10^{-3}$
0.9852	$+1.074 \times 10^{-2}$	$+9.293 \times 10^{-3}$	$+8.125 \times 10^{-3}$	$+7.168 \times 10^{-3}$	$+6.388 \times 10^{-3}$	$+5.713 \times 10^{-3}$

	Reynolds number				
η	3.200×10^7	6.400×10^7	1.280×10^8	2.560×10^8	5.000×10^8
0.0000	$+5.273 \times 10^{-3}$	$+4.774 \times 10^{-3}$	$+4.334 \times 10^{-3}$	$+3.954 \times 10^{-3}$	$+3.618 \times 10^{-3}$
0.1742	$+5.188 \times 10^{-3}$	$+4.698 \times 10^{-3}$	$+4.265 \times 10^{-3}$	$+3.892 \times 10^{-3}$	$+3.560 \times 10^{-3}$
0.3423	$+5.138 \times 10^{-3}$	$+4.648 \times 10^{-3}$	$+4.218 \times 10^{-3}$	$+3.847 \times 10^{-3}$	$+3.524 \times 10^{-3}$
0.5000	$+5.117 \times 10^{-3}$	$+4.627 \times 10^{-3}$	$+4.198 \times 10^{-3}$	$+3.828 \times 10^{-3}$	$+3.509 \times 10^{-3}$
0.6432	$+5.111 \times 10^{-3}$	$+4.621 \times 10^{-3}$	$+4.192 \times 10^{-3}$	$+3.822 \times 10^{-3}$	$+3.505 \times 10^{-3}$
0.7664	$+5.117 \times 10^{-3}$	$+4.627 \times 10^{-3}$	$+4.198 \times 10^{-3}$	$+3.828 \times 10^{-3}$	$+3.509 \times 10^{-3}$
0.8663	$+5.126 \times 10^{-3}$	$+4.636 \times 10^{-3}$	$+4.207 \times 10^{-3}$	$+3.836 \times 10^{-3}$	$+3.516 \times 10^{-3}$
0.9401	$+5.136 \times 10^{-3}$	$+4.646 \times 10^{-3}$	$+4.216 \times 10^{-3}$	$+3.845 \times 10^{-3}$	$+3.523 \times 10^{-3}$
0.9852	$+5.143 \times 10^{-3}$	$+4.653 \times 10^{-3}$	$+4.222 \times 10^{-3}$	$+3.851 \times 10^{-3}$	$+3.528 \times 10^{-3}$

Table A.10: Variation of wing span-wise station profile drag coefficient with Reynolds number at $M = 0.3125$

	Reynolds number					
Mach	5.000×10^5	2.000×10^6	8.000×10^6	3.200×10^7	1.280×10^8	5.000×10^8
0.050	1.093×10^{-2}	1.088×10^{-2}	1.076×10^{-2}	1.058×10^{-2}	1.033×10^{-2}	9.972×10^{-3}
0.125	9.439×10^{-3}	9.391×10^{-3}	9.291×10^{-3}	9.135×10^{-3}	8.914×10^{-3}	8.603×10^{-3}
0.200	8.231×10^{-3}	8.189×10^{-3}	8.101×10^{-3}	7.966×10^{-3}	7.774×10^{-3}	7.503×10^{-3}
0.275	7.243×10^{-3}	7.209×10^{-3}	7.129×10^{-3}	7.008×10^{-3}	6.840×10^{-3}	6.602×10^{-3}
0.350	6.439×10^{-3}	6.406×10^{-3}	6.337×10^{-3}	6.230×10^{-3}	6.080×10^{-3}	5.872×10^{-3}
0.425	5.748×10^{-3}	5.721×10^{-3}	5.659×10^{-3}	5.560×10^{-3}	5.429×10^{-3}	5.247×10^{-3}
0.500	5.162×10^{-3}	5.140×10^{-3}	5.081×10^{-3}	4.997×10^{-3}	4.879×10^{-3}	4.716×10^{-3}
0.575	4.662×10^{-3}	4.640×10^{-3}	4.588×10^{-3}	4.510×10^{-3}	4.404×10^{-3}	4.255×10^{-3}
0.650	4.221×10^{-3}	4.201×10^{-3}	4.158×10^{-3}	4.090×10^{-3}	3.991×10^{-3}	3.865×10^{-3}
0.725	3.840×10^{-3}	3.828×10^{-3}	3.786×10^{-3}	3.719×10^{-3}	3.637×10^{-3}	3.517×10^{-3}
0.800	3.511×10^{-3}	3.492×10^{-3}	3.457×10^{-3}	3.399×10^{-3}	3.319×10^{-3}	3.214×10^{-3}

Table A.11: Variation of tailplane profile drag coefficient with Reynolds number and Mach number

A.3.2 Viscous Drag

ESDU 07002 [2008] and ESDU 07003 [2008] provide a method for the calculation of the lift-dependent viscous drag coefficient for the wing as a function of the spanwise position. The lift-dependent viscous drag factor, K_v, is given by:

$$K_v = \frac{k_{v\eta}}{a_{1w}} \left(1 - \left(\frac{a_0}{a_{0T}} \right)_\eta \right) \tag{A.3.7}$$

where a_{1w} is the lift-curve slope of the wing in viscous flow, calculated using ESDU 70011 [1996]; a_0 is the viscous lift-curve slope of the aerofoil section at the span-wise position η, calculated using ESDU 97020 [1997]; and a_{0T} is the inviscid lift-curve slope of the aerofoil section at η, calculated using ESDU 72024 [1972]. The factor $k_{v\eta}$ is assumed to have the value of 1.15 [ESDU 07003, 2008].

The lift-dependent viscous drag factor, K_v, was calculated for the Aeroplane AX-1 wing for the range of Reynolds numbers 5.00×10^5 to 5.00×10^8, and the results are shown in Figure A.12.

Similarly, this method can be applied to the calculation of the local span-wise lift dependent viscous drag coefficient of the aircraft tailplane. The lift-dependent viscous drag factor, K_v, was calculated for Aeroplane AX-1 tailplane for the same range of Reynolds numbers, i.e. 5.00×10^5 to 5.00×10^8, and the results are shown in Figure A.13.

A.3.3 Wing Viscous Lift-curve Slope

ESDU 70011 [1996] provides a method for the calculation of the viscous lift-curve slope of the wing, a_{1w}. The variation of lift-curve slope with aspect ratio, A, half-chord sweep angle, $\Lambda_{1/2}$, and taper ratio, λ is calculated using lifting-surface theory, and presented in carpet form in Figures 1a through 2g of ESDU 70011 [1996]. ESDU 70011 [1996] is applicable to wings with straight-tapered planforms. The wing of the Aeroplane AX-1 has a number of cranks, however an equivalent straight-tapered planform wing can be generated using ESDU 76003 [1976] for use with ESDU 70011 [1996]. The geometrical properties of an equivalent A340-300 wing are presented in Table A.12.

Dimension	Notation	Wing (Equivalent)	Tail
Half-chord sweep angle, deg	$\Lambda_{1/2}$	25.16	26.19
Taper ratio	λ	0.2892	0.3780
Aspect Ratio	AR	9.302	5.270

Table A.12: Tailplane geometry for Aeroplane AX-1

Using the Aeroplane AX-1 wing geometry listed in Table A.12, the viscous lift-curve slope of an equivalent straight wing was found to be 4.580 /rad. ESDU 70011 [1996] can similarly be applied to the calculation of the viscous lift-curve slope of the tailplane, a_{1t}. Using the Aeroplane AX-1 tailplane geometry listed in Table A.12, the viscous lift-curve slope was found to be 3.903 /rad.

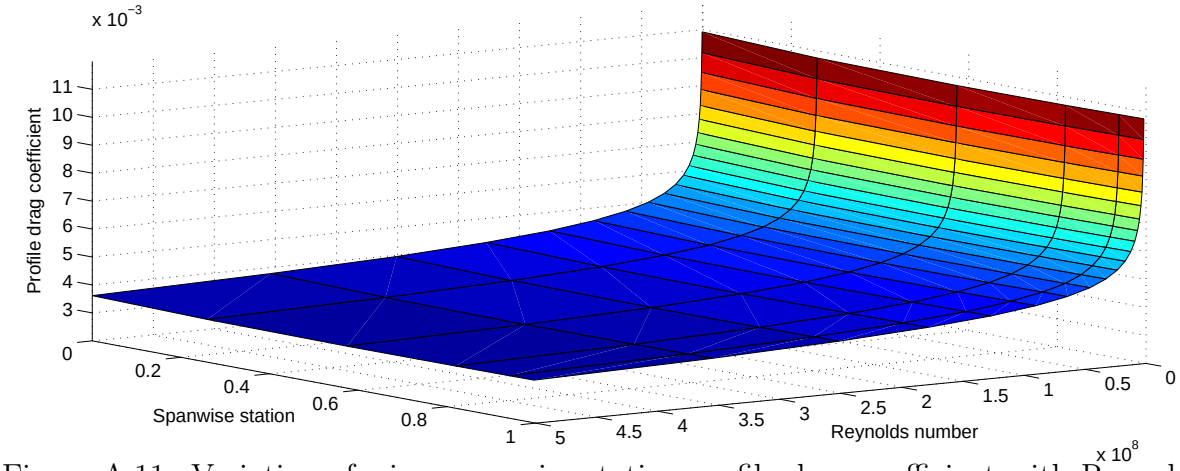

Figure A.11: Variation of wing span-wise station profile drag coefficient with Reynolds number at $M = 0.3125$

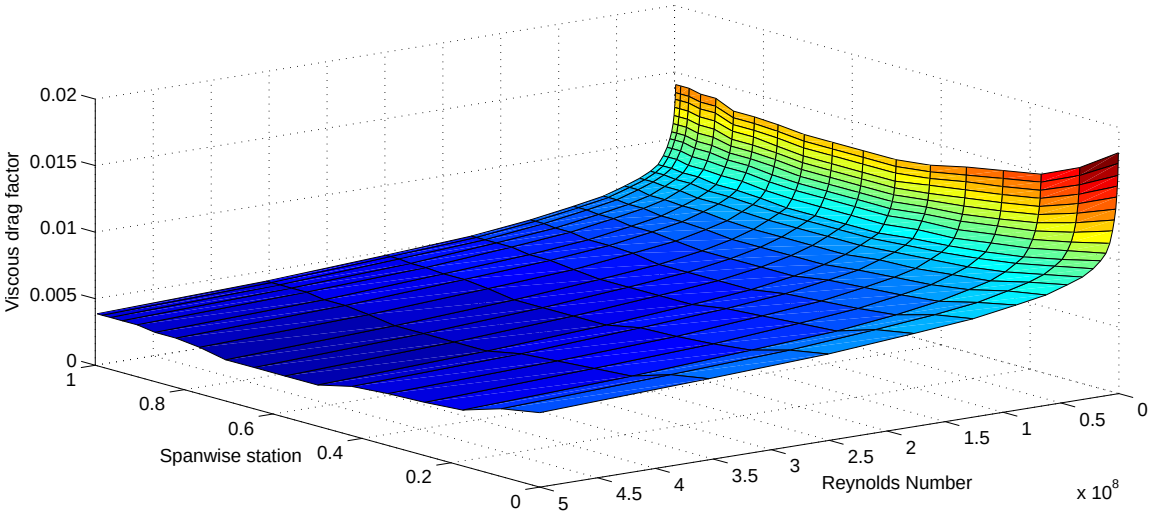

Figure A.12: Variation of wing span-wise station viscous drag factor with Reynolds number

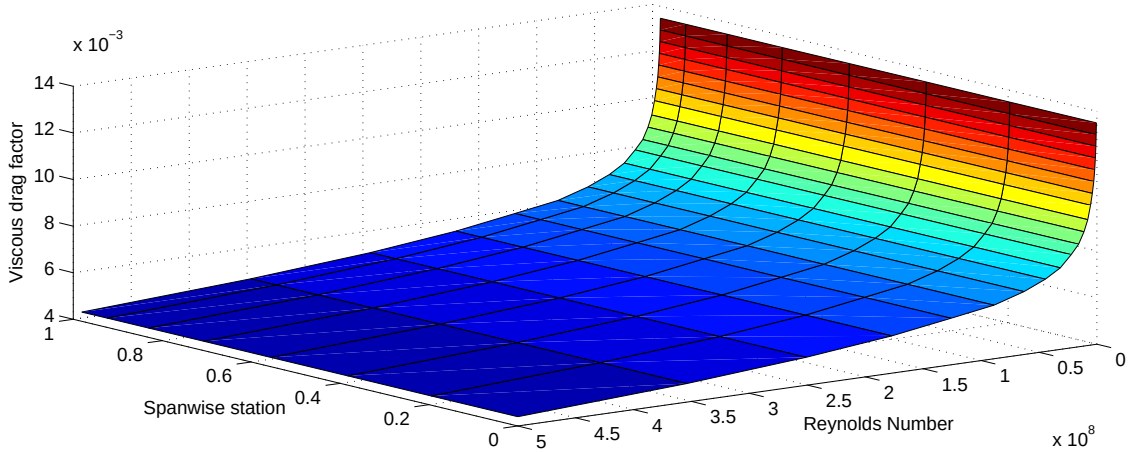

Figure A.13: Variation of tailplane span-wise station viscous drag factor with Reynolds number

A.3.4 Equivalent Wing Planform

ESDU 76003 [1976] provides a method to approximate a cranked, swept wing-body combination as an equivalent straight-tapered wing. With reference to Figure A.14, the root chord is calculated such that the exposed area of the wing planform for the equivalent and true wings is equal. The root chord, c_r, is then given by:

$$c_r = \frac{S_e}{s - s_0} - c_t \tag{A.3.8}$$

in which S_e is the exposed planform area of the true wing. Assuming that the true wing can be approximated by a series of trapezoidal areas defined by the wing cranks, the total exposed area of the wing may be calculated from the sum of each trapezoidal area. The total area is then given for m cranks by:

$$S_e = \sum_{i=0}^{m} (c_i + c_{i+1})(s_{i+1} - s_i) \tag{A.3.9}$$

The location of the root-chord leading-edge of the equivalent wing is located such that the area enclosed by the leading-edge of the equivalent wing and true wing is equal inboard and outboard of intersection of the equivalent and true wing leading-edges. The location of the root-chord leading-edge, given as the distance from the nose, l_n, is given by:

$$l_n = x_b + \sum_{i=0}^{m} (\tan\Lambda_{0,i} - \tan\Lambda_{0,i+1}) \frac{(s_{i+1} - s_0)(s - s_{i+1})}{(s - s_0)} \tag{A.3.10}$$

The centre-line chord of the equivalent wing is given by:

$$c_0 = \frac{sc_r - s_0 c_t}{s - s_0} \tag{A.3.11}$$

The taper ratio of the equivalent wing can then be given by:

$$\lambda = \frac{c_t}{c_0} \tag{A.3.12}$$

The aspect ratio and wing area of the equivalent wing are given by:

$$A = \frac{2s}{\bar{c}} \tag{A.3.13}$$

$$S = 2s\bar{c} \tag{A.3.14}$$

where the standard mean chord, $\bar{c}$, is given by:

$$\bar{c} = c_0 \frac{1 + \lambda}{2} \tag{A.3.15}$$

The sweep angle of the leading-edge and half-chord are given by the following respectively:

$$\Lambda_0 = \tan^{-1}\left(\frac{l_t - l_n}{s - s_0}\right) \tag{A.3.16}$$

$$\Lambda_{1/2} = \tan^{-1}\left[\tan\Lambda_0 - \frac{2}{A}\left(\frac{1-\lambda}{1+\lambda}\right)\right] \tag{A.3.17}$$

Given the geometrical data for the Aeroplane AX-1 wing presented in Table A.13, an equivalent wing planform may be estimated. The relevant geometrical parameters required for the prediction of the viscous lift-curve slope of this equivalent wing, ESDU 70011 [1996], are given in Table A.12.

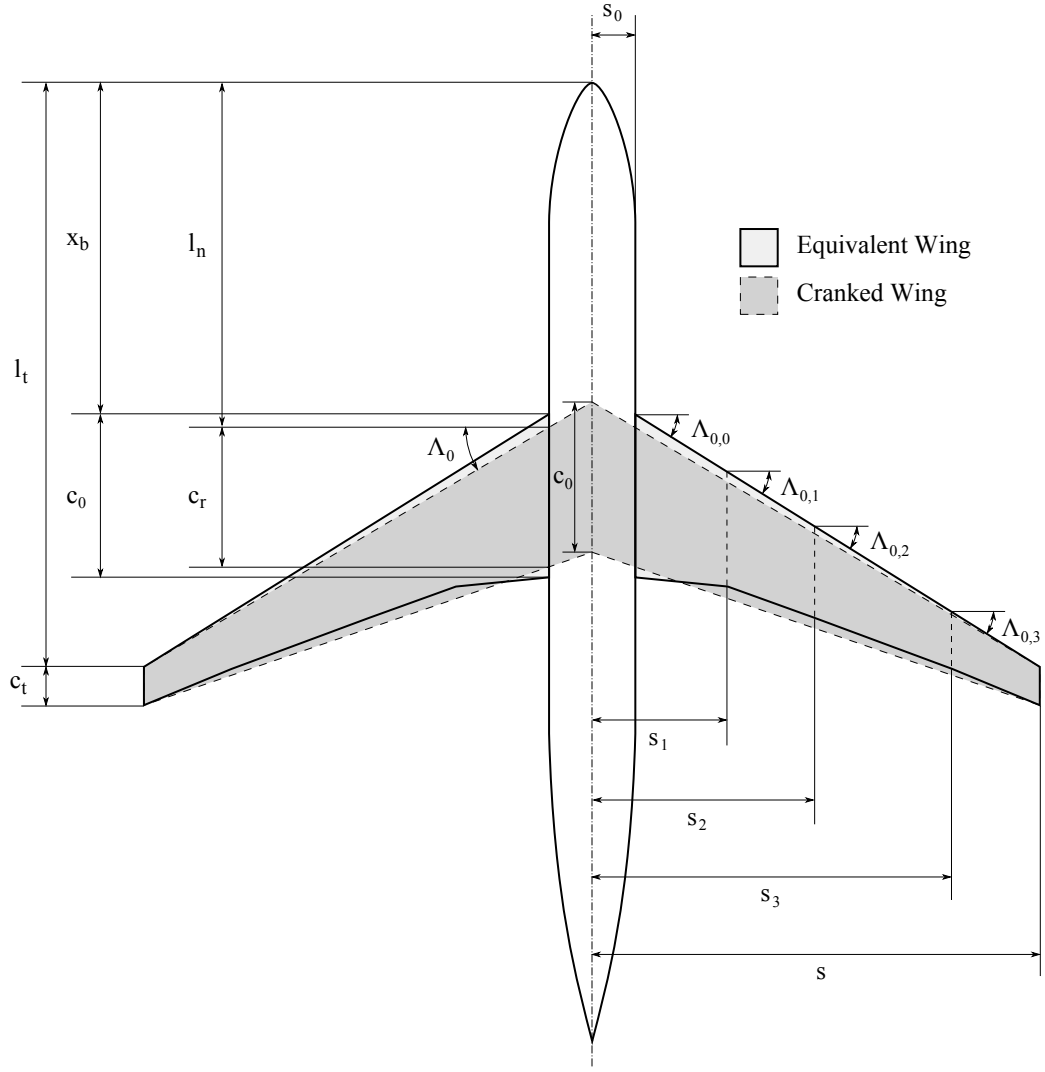

Figure A.14: Equivalent cranked-wing geometrical parameters

Dimension	Notation	Value
Location of wing tip leading-edge, m	l_t	39.15
Location of wing root leading-edge, m	x_b	22.80
Wing semi-span, m	s	29.00
Tip chord, m	c_t	2.480
Fuselage radius, m	s_0	2.793
Spanwise distance to..., m		
...Crank 1	s_1	8.399
...Crank 2	s_2	14.42
...Crank 3	s_3	23.34
Leading-edge sweep at..., deg		
...Root	$\Lambda_{0,0}$	31.96
...Crank 1	$\Lambda_{0,1}$	31.96
...Crank 2	$\Lambda_{0,2}$	31.96
...Crank 3	$\Lambda_{0,3}$	31.96

Table A.13: Wing-body geometry for Aeroplane AX-1

A.3.5 Inviscid Aerofoil Lift-curve Slope

In order to calculate the viscous drag coefficient of each wing section [ESDU 07002, 2008], it is necessary to calculate the inviscid lift-curve slope of the aerofoil, a_{0T}. ESDU 72024 [1972] provides a method for the calculation of the lift-curve slope of an aerofoil in inviscid, compressible flow as a function only of the thickness distribution and camber line of the aerofoil.

The necessary required geometrical parameters of the aerofoil are the thickness to chord ratio, t/c; trailing-edge angle, τ; normalised maximum positive camber, $h+/c$; and the normalised aerofoil thickness at 5% of chord, $2z_{t2}/t$. These are shown in Figure A.15. The trailing edge angle, τ is given by:

$$\tau = 2\tan^{-1}\left(\frac{dz_t}{dx}\right)_{x=c} \tag{A.3.18}$$

where $(dz_t/dx)_{x=c}$ is the thickness gradient at the trailing-edge.

The inviscid lift-curve slope of the aerofoil section is then given by:

$$a_{0T} = 0.10967\left(1 + F_1\frac{t}{c}\right) \tag{A.3.19}$$

where F_1 is given as a function of the geometrical parameters shown in Figure A.15 in Figure 1 of ESDU 72024 [1972].

Assuming the given thickness-to-chord ratio, see Table A.14, for a NASA SC(2)-06 aerofoil series section defined in Harris [1990], the inviscid lift-curve slope for the Aeroplane AX-1 wing is given in Table A.14.

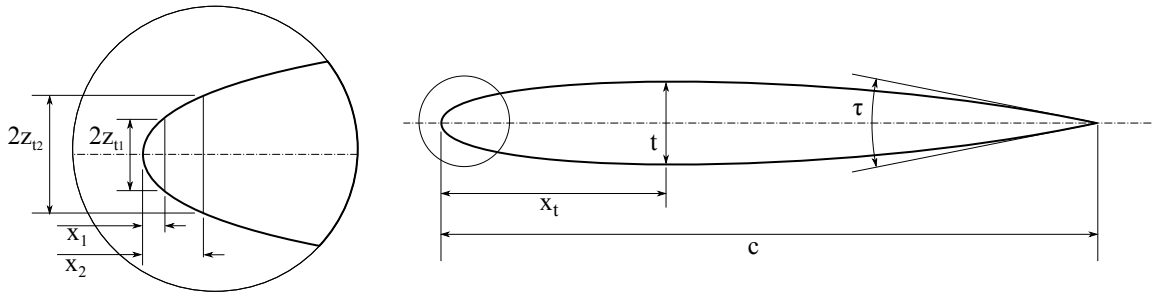

Figure A.15: Inviscid aerofoil lift-curve slope geometry

ESDU 72024 [1972] can similarly be used to estimate the inviscid lift-curve slope of the tailplane aerofoil section. The tailplane is assumed to have a symmetrical NASA SC(2)-00 aerofoil series section [Harris, 1990], with a fixed thickness-to-chord ratio of 0.08. Given this information, the inviscid lift-curve slope of the tailplane aerofoil section was calculated to be 6.679 /rad.

Spanwise Position	t/c	a_{0T}, /rad
0.0000	0.1400	6.997
0.2591	0.1103	6.839
0.5745	0.1000	6.784
0.8193	0.1031	6.802
0.9401	0.1072	6.822
0.9962	0.1093	6.831

Table A.14: Spanwise variation of wing inviscid aerofoil lift-curve slope

A.3.6 Viscous Aerofoil Lift-curve Slope

ESDU 97020 [1997] provides a method for the calculation of the viscous lift-curve slope of an aerofoil section.

The circulation, and thereby lift, of an aerofoil in inviscid flow is determined only by the geometrical properties of the aerofoil and its incidence. In viscous flow however, a boundary-layer develops on the surface of the aerofoil, reducing the circulation and therefore lift of the aerofoil. ESDU 97020 [1997] provides a method for the estimation of this reduction in circulation due to the boundary layer by estimating the boundary-layer profile at the trailing-edge of the aerofoil. Using the inviscid lift-curve slope of an aerofoil, estimated using ESDU 72024 [1972], ESDU 97020 [1997] estimates this viscous lift-curve slope reduction factor a_0/a_{0T} as a function of Reynolds number, Mach number, boundary-layer transition location, and two geometrical parameters, τ_a and τ_{au}.

The first geometrical parameter, the trailing-edge parameter τ_a, is suitable for symmetric aerofoils, and is given by:

$$\tau_a = 2tan^{-1}\left(\frac{t_{0.9} - t_{0.99}}{0.18c}\right) \tag{A.3.20}$$

where $t_{0.9}$ and $t_{0.99}$ is the thickness of the aerofoil at 90% and 99% of chord, c, respectively.

The second geometrical parameter, τ_{au}, required for cambered aerofoils, is defined by:

$$\tau_{au} = tan^{-1}\left(\frac{z_{u0.9} - z_{u0.99}}{0.09c}\right) \tag{A.3.21}$$

where $z_{u0.9}$ and $z_{u0.99}$ is the aerofoil thickness ordinate of the upper surface at 90% and 99% of chord, c, respectively.

The viscous lift-curve slope reduction factor is given for a cambered aerofoil by:

$$[a_0/a_{0T}]_{camb} = [a_0/a_{0T}]_{sym} + \Delta\,[a_0/a_{0T}] \tag{A.3.22}$$

where the viscous lift-curve slope reduction factor for the symmetric aerofoil, $[a_0/a_{0T}]_{sym}$ can be found from Figures 1 through 6 of ESDU 97020 [1997]. The cambered aerofoil correction factor, $\Delta\,[a_0/a_{0T}]$, can be found from Figures 7 through 9 of ESDU 97020 [1997].

Once again assuming the thickness-to-chord ratio given in Table A.14, and a NASA SC(2)-06 aerofoil series section defined in Harris [1990], the viscous lift-curve slope for the Aeroplane AX-1 wing as a function of Reynolds number is given in Figure A.16. Again, given that the tailplane is assumed to have a symmetrical NASA SC(2)-00 aerofoil series section [Harris, 1990] with thickness-to-chord ratio of 0.08, the viscous lift-curve slope for the Aeroplane AX-1 tailplane as a function of Reynolds number is given in Figure A.17.

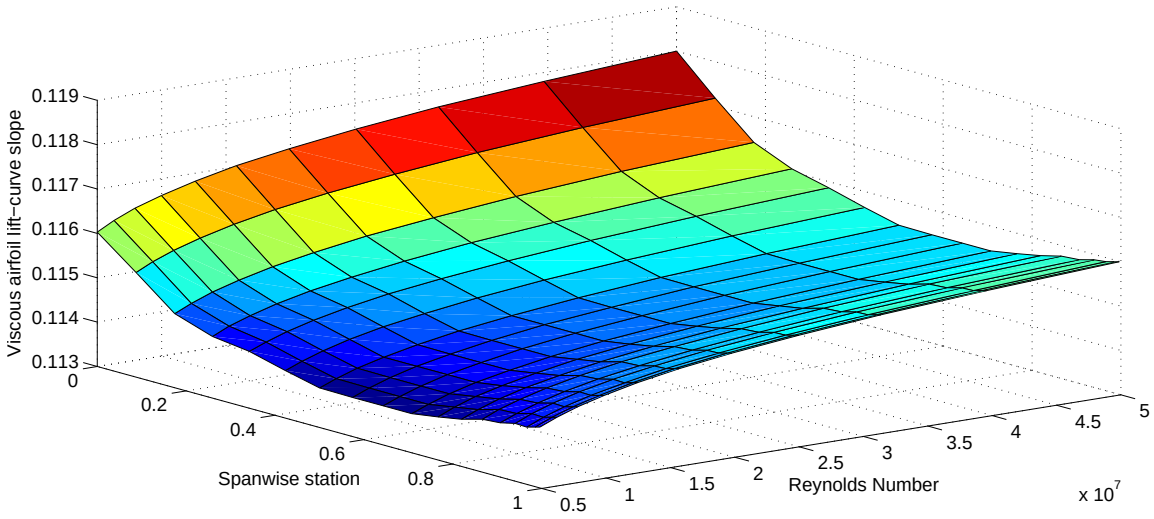

Figure A.16: Spanwise variation of wing viscous aerofoil lift-curve slope

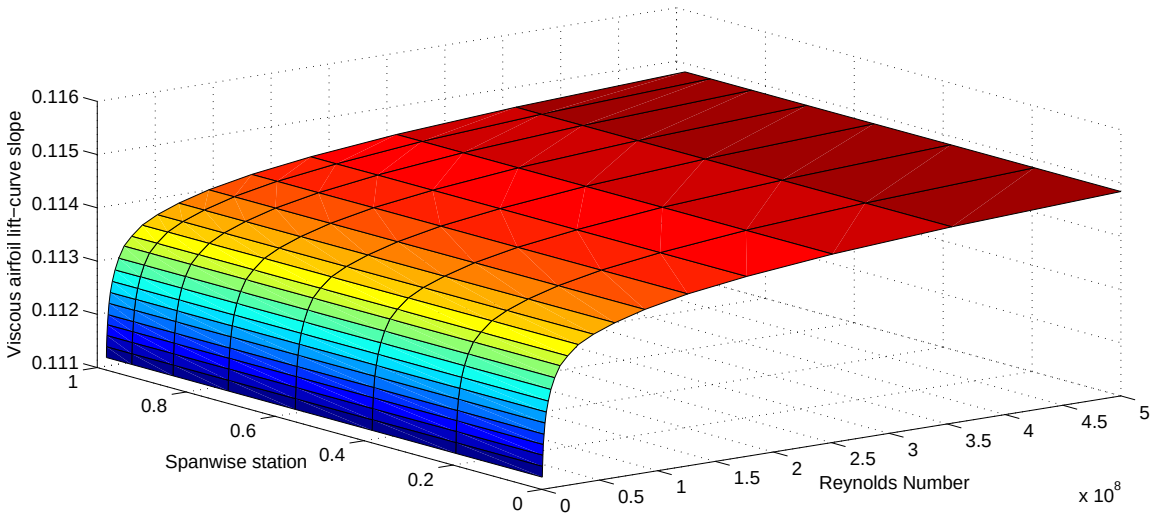

Figure A.17: Spanwise variation of tailplane viscous aerofoil lift-curve slope

	Reynolds number					
η	5.0×10^5	1.0×10^6	2.0×10^6	4.0×10^6	7.9×10^6	1.6×10^7
0.0000	$+1.813 \times 10^{-2}$	$+1.645 \times 10^{-2}$	$+1.476 \times 10^{-2}$	$+1.308 \times 10^{-2}$	$+1.142 \times 10^{-2}$	$+1.017 \times 10^{-2}$
0.1742	$+1.486 \times 10^{-2}$	$+1.368 \times 10^{-2}$	$+1.250 \times 10^{-2}$	$+1.130 \times 10^{-2}$	$+1.012 \times 10^{-2}$	$+0.891 \times 10^{-2}$
0.3423	$+1.394 \times 10^{-2}$	$+1.276 \times 10^{-2}$	$+1.160 \times 10^{-2}$	$+1.045 \times 10^{-2}$	$+0.929 \times 10^{-2}$	$+0.819 \times 10^{-2}$
0.5000	$+1.298 \times 10^{-2}$	$+1.195 \times 10^{-2}$	$+1.095 \times 10^{-2}$	$+0.992 \times 10^{-2}$	$+0.891 \times 10^{-2}$	$+0.771 \times 10^{-2}$
0.6432	$+1.298 \times 10^{-2}$	$+1.195 \times 10^{-2}$	$+1.095 \times 10^{-2}$	$+0.992 \times 10^{-2}$	$+0.891 \times 10^{-2}$	$+0.771 \times 10^{-2}$
0.7664	$+1.318 \times 10^{-2}$	$+1.215 \times 10^{-2}$	$+1.110 \times 10^{-2}$	$+1.007 \times 10^{-2}$	$+0.904 \times 10^{-2}$	$+0.786 \times 10^{-2}$
0.8663	$+1.331 \times 10^{-2}$	$+1.228 \times 10^{-2}$	$+1.122 \times 10^{-2}$	$+1.019 \times 10^{-2}$	$+0.916 \times 10^{-2}$	$+0.798 \times 10^{-2}$
0.9401	$+1.394 \times 10^{-2}$	$+1.276 \times 10^{-2}$	$+1.160 \times 10^{-2}$	$+1.045 \times 10^{-2}$	$+0.929 \times 10^{-2}$	$+0.819 \times 10^{-2}$
0.9852	$+1.414 \times 10^{-2}$	$+1.296 \times 10^{-2}$	$+1.180 \times 10^{-2}$	$+1.065 \times 10^{-2}$	$+0.949 \times 10^{-2}$	$+0.834 \times 10^{-2}$

	Reynolds number				
η	3.2×10^7	6.3×10^7	1.3×10^8	2.5×10^8	5.0×10^8
0.0000	$+0.921 \times 10^{-2}$	$+0.831 \times 10^{-2}$	$+0.741 \times 10^{-2}$	$+0.653 \times 10^{-2}$	$+0.562 \times 10^{-2}$
0.1742	$+0.798 \times 10^{-2}$	$+0.706 \times 10^{-2}$	$+0.610 \times 10^{-2}$	$+0.517 \times 10^{-2}$	$+0.424 \times 10^{-2}$
0.3423	$+0.736 \times 10^{-2}$	$+0.650 \times 10^{-2}$	$+0.562 \times 10^{-2}$	$+0.475 \times 10^{-2}$	$+0.387 \times 10^{-2}$
0.5000	$+0.696 \times 10^{-2}$	$+0.600 \times 10^{-2}$	$+0.505 \times 10^{-2}$	$+0.409 \times 10^{-2}$	$+0.314 \times 10^{-2}$
0.6432	$+0.696 \times 10^{-2}$	$+0.600 \times 10^{-2}$	$+0.505 \times 10^{-2}$	$+0.409 \times 10^{-2}$	$+0.314 \times 10^{-2}$
0.7664	$+0.708 \times 10^{-2}$	$+0.618 \times 10^{-2}$	$+0.527 \times 10^{-2}$	$+0.439 \times 10^{-2}$	$+0.349 \times 10^{-2}$
0.8663	$+0.718 \times 10^{-2}$	$+0.630 \times 10^{-2}$	$+0.545 \times 10^{-2}$	$+0.457 \times 10^{-2}$	$+0.372 \times 10^{-2}$
0.9401	$+0.736 \times 10^{-2}$	$+0.650 \times 10^{-2}$	$+0.562 \times 10^{-2}$	$+0.475 \times 10^{-2}$	$+0.387 \times 10^{-2}$
0.9852	$+0.751 \times 10^{-2}$	$+0.660 \times 10^{-2}$	$+0.570 \times 10^{-2}$	$+0.480 \times 10^{-2}$	$+0.389 \times 10^{-2}$

Table A.15: Variation of wing span-wise station viscous drag factor with Reynolds number

	Reynolds number					
η	5.0×10^5	1.0×10^6	2.0×10^6	4.0×10^6	7.9×10^6	1.6×10^7
0.0000	$+1.353 \times 10^{-2}$	$+1.249 \times 10^{-2}$	$+1.149 \times 10^{-2}$	$+1.046 \times 10^{-2}$	$+0.943 \times 10^{-2}$	$+0.837 \times 10^{-2}$
0.1949	$+1.353 \times 10^{-2}$	$+1.249 \times 10^{-2}$	$+1.149 \times 10^{-2}$	$+1.046 \times 10^{-2}$	$+0.943 \times 10^{-2}$	$+0.837 \times 10^{-2}$
0.3832	$+1.353 \times 10^{-2}$	$+1.249 \times 10^{-2}$	$+1.149 \times 10^{-2}$	$+1.046 \times 10^{-2}$	$+0.943 \times 10^{-2}$	$+0.837 \times 10^{-2}$
0.5558	$+1.353 \times 10^{-2}$	$+1.249 \times 10^{-2}$	$+1.149 \times 10^{-2}$	$+1.046 \times 10^{-2}$	$+0.943 \times 10^{-2}$	$+0.837 \times 10^{-2}$
0.7071	$+1.353 \times 10^{-2}$	$+1.249 \times 10^{-2}$	$+1.149 \times 10^{-2}$	$+1.046 \times 10^{-2}$	$+0.943 \times 10^{-2}$	$+0.837 \times 10^{-2}$
0.8310	$+1.353 \times 10^{-2}$	$+1.249 \times 10^{-2}$	$+1.149 \times 10^{-2}$	$+1.046 \times 10^{-2}$	$+0.943 \times 10^{-2}$	$+0.837 \times 10^{-2}$
0.9244	$+1.353 \times 10^{-2}$	$+1.249 \times 10^{-2}$	$+1.149 \times 10^{-2}$	$+1.046 \times 10^{-2}$	$+0.943 \times 10^{-2}$	$+0.837 \times 10^{-2}$
0.9811	$+1.353 \times 10^{-2}$	$+1.249 \times 10^{-2}$	$+1.149 \times 10^{-2}$	$+1.046 \times 10^{-2}$	$+0.943 \times 10^{-2}$	$+0.837 \times 10^{-2}$

	Reynolds number				
η	3.2×10^7	6.3×10^7	1.3×10^8	2.5×10^8	5.0×10^8
0.0000	$+0.751 \times 10^{-2}$	$+0.675 \times 10^{-2}$	$+0.595 \times 10^{-2}$	$+0.516 \times 10^{-2}$	$+0.439 \times 10^{-2}$
0.1949	$+0.751 \times 10^{-2}$	$+0.675 \times 10^{-2}$	$+0.595 \times 10^{-2}$	$+0.516 \times 10^{-2}$	$+0.439 \times 10^{-2}$
0.3832	$+0.751 \times 10^{-2}$	$+0.675 \times 10^{-2}$	$+0.595 \times 10^{-2}$	$+0.516 \times 10^{-2}$	$+0.439 \times 10^{-2}$
0.5558	$+0.751 \times 10^{-2}$	$+0.675 \times 10^{-2}$	$+0.595 \times 10^{-2}$	$+0.516 \times 10^{-2}$	$+0.439 \times 10^{-2}$
0.7071	$+0.751 \times 10^{-2}$	$+0.675 \times 10^{-2}$	$+0.595 \times 10^{-2}$	$+0.516 \times 10^{-2}$	$+0.439 \times 10^{-2}$
0.8310	$+0.751 \times 10^{-2}$	$+0.675 \times 10^{-2}$	$+0.595 \times 10^{-2}$	$+0.516 \times 10^{-2}$	$+0.439 \times 10^{-2}$
0.9244	$+0.751 \times 10^{-2}$	$+0.675 \times 10^{-2}$	$+0.595 \times 10^{-2}$	$+0.516 \times 10^{-2}$	$+0.439 \times 10^{-2}$
0.9811	$+0.751 \times 10^{-2}$	$+0.675 \times 10^{-2}$	$+0.595 \times 10^{-2}$	$+0.516 \times 10^{-2}$	$+0.439 \times 10^{-2}$

Table A.16: Variation of tail span-wise station viscous drag factor with Reynolds number

	Reynolds number										
η	5.0×10^5	1.0×10^6	2.0×10^6	4.0×10^6	7.9×10^6	1.6×10^7	3.2×10^7	6.3×10^7	1.3×10^8	2.5×10^8	5.0×10^8
0.0000	+0.1133	+0.1141	+0.1149	+0.1158	+0.1166	+0.1172	+0.1176	+0.1181	+0.1185	+0.1190	+0.1194
0.1742	+0.1128	+0.1134	+0.1139	+0.1145	+0.1151	+0.1156	+0.1161	+0.1165	+0.1170	+0.1174	+0.1179
0.3423	+0.1124	+0.1130	+0.1135	+0.1141	+0.1146	+0.1152	+0.1156	+0.1160	+0.1164	+0.1168	+0.1172
0.5000	+0.1123	+0.1128	+0.1133	+0.1137	+0.1142	+0.1148	+0.1151	+0.1156	+0.1160	+0.1165	+0.1169
0.6432	+0.1123	+0.1128	+0.1132	+0.1137	+0.1142	+0.1148	+0.1151	+0.1156	+0.1160	+0.1165	+0.1169
0.7664	+0.1123	+0.1128	+0.1133	+0.1138	+0.1143	+0.1149	+0.1152	+0.1157	+0.1161	+0.1165	+0.1169
0.8663	+0.1126	+0.1130	+0.1135	+0.1140	+0.1145	+0.1151	+0.1155	+0.1159	+0.1163	+0.1167	+0.1171
0.9401	+0.1125	+0.1130	+0.1136	+0.1141	+0.1147	+0.1152	+0.1156	+0.1160	+0.1164	+0.1168	+0.1172
0.9852	+0.1125	+0.1131	+0.1136	+0.1142	+0.1147	+0.1152	+0.1156	+0.1161	+0.1165	+0.1169	+0.1174

Table A.17: Spanwise variation of wing viscous aerofoil lift-curve slope

	Reynolds number										
η	5.0×10^5	1.0×10^6	2.0×10^6	4.0×10^6	7.9×10^6	1.6×10^7	3.2×10^7	6.3×10^7	1.3×10^8	2.5×10^8	5.0×10^8
0.0000	+0.1112	+0.1116	+0.1120	+0.1124	+0.1128	+0.1133	+0.1136	+0.1139	+0.1142	+0.1145	+0.1148
0.1949	+0.1112	+0.1116	+0.1120	+0.1124	+0.1128	+0.1133	+0.1136	+0.1139	+0.1142	+0.1145	+0.1148
0.3832	+0.1112	+0.1116	+0.1120	+0.1124	+0.1128	+0.1133	+0.1136	+0.1139	+0.1142	+0.1145	+0.1148
0.5558	+0.1112	+0.1116	+0.1120	+0.1124	+0.1128	+0.1133	+0.1136	+0.1139	+0.1142	+0.1145	+0.1148
0.7071	+0.1112	+0.1116	+0.1120	+0.1124	+0.1128	+0.1133	+0.1136	+0.1139	+0.1142	+0.1145	+0.1148
0.8310	+0.1112	+0.1116	+0.1120	+0.1124	+0.1128	+0.1133	+0.1136	+0.1139	+0.1142	+0.1145	+0.1148
0.9244	+0.1112	+0.1116	+0.1120	+0.1124	+0.1128	+0.1133	+0.1136	+0.1139	+0.1142	+0.1145	+0.1148
0.9811	+0.1112	+0.1116	+0.1120	+0.1124	+0.1128	+0.1133	+0.1136	+0.1139	+0.1142	+0.1145	+0.1148

Table A.18: Spanwise variation of tail viscous aerofoil lift-curve slope

A.3.7 Drag Coefficient due to Control Deflection

ESDU 87024 [1987] provides a method for the estimation of the increase in drag coefficient due to the deflection of trailing-edge flaps. This is suitable for the estimation of the drag increment due to the deflection of trailing-edge control surfaces, such as aileron, rudder and elevator. The drag increment is estimated from empirical data [ESDU 87024, 1987], and assumes that within the linear regime that the drag increment due to flap deflection is independent of lift.

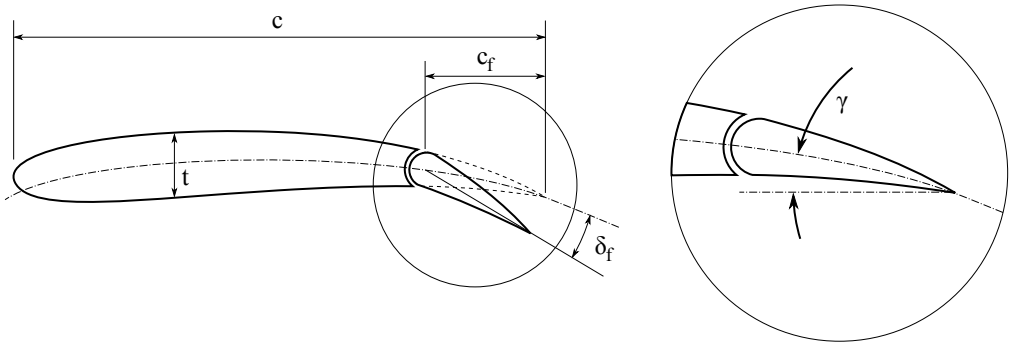

Figure A.18: Trailing-edge flap geometry

With reference to Figure A.18, ESDU 87024 [1987] gives the drag coefficient increment to be a function of the flap deflection angle, δ_f, the trailing-edge camber angle, γ, and the flap chord to aerofoil chord ratio, c_f/c. For positive flap deflections, the drag coefficient increment is given by:

$$\Delta C_{Du} = F\left(\delta_f, \gamma; c_f/c\right) - F\left(0, \gamma; c_f/c\right) \tag{A.3.23}$$

where the flap drag function F is given by:

$$F\left(\delta_f, \gamma; c_f/c\right) = c_f/c \sin^2\left(\delta_f + \gamma\right) \cos\left(\delta_f + \gamma\right) \tag{A.3.24}$$

The effect of camber is to produce an asymmetric variation of drag coefficient increment with flap deflection [ESDU 87024, 1987]. As such, for negative flap deflection angles, the drag coefficient is given by:

$$\Delta C_{Du} = k\left(\gamma\right) F\left(\delta_f, \gamma; c_f/c\right) - F\left(0, \gamma; c_f/c\right) \tag{A.3.25}$$

where $k\left(\gamma\right)$, an empirical factor to account for the biased negative flap deflection drag predictions for cambered aerofoils, is given by:

$$k\left(\gamma\right) = 1.0 - 0.005\gamma^2 \tag{A.3.26}$$

It is assumed that the A340-300 wing aerofoil section thickness-to-chord ratio is given in Table A.14, and that the aerofoil profile is given by the NASA SC(2)-06 aerofoil series section defined in Harris [1990]. The tailplane aerofoil section is again assumed to have

a thickness-to-chord ratio of 0.08, and the aerofoil profile is defined by the symmetrical NASA SC(2)-00 aerofoil series section [Harris, 1990]. A flap chord to aerofoil chord ratio, c_f/c, of 0.2 was further assumed. Given this, the variation of the increase in drag coefficient due to the deflection of a trailing-edge flap for the A340-300 wing and tailplane is shown in Figure A.19.

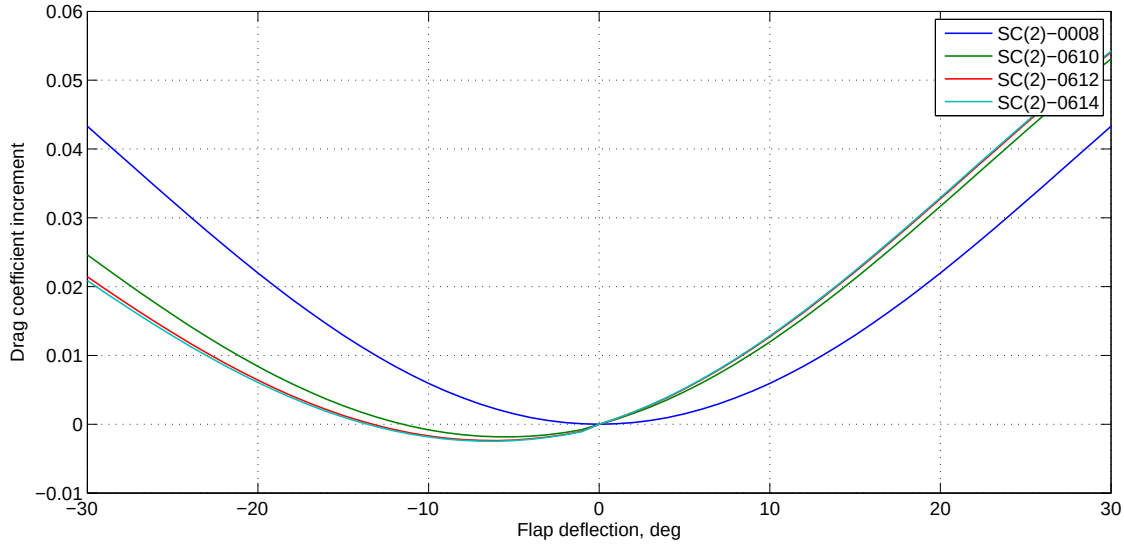

Figure A.19: Variation of drag coefficient increment due to flap deflection with flap deflection angle

A.4 Nacelle

ESDU 77012 provides a method by which the aerodynamic centre of a wing-fuselage-nacelle combination may be estimated. The nacelle is essentially modelled as an annular aerofoil with a correction made for the upwash due to the wing [Figure A.20]. The effect of the nacelle on the aerodynamic centre is then estimated. A similar methodology is outlined here to derive the effect of the upwash on the nacelle alone, and thus calculate the lift-curve slope of the nacelle. It is assumed here that the lift distribution on the wing is elliptical, and as such the downwash is assumed to be constant across the span. The lift is assumed to act at the nacelle lip [ESDU 77012].

The induced velocity by a vortex line of strength Γ is given by:

$$w_z = w \cos\theta \tag{A.4.1}$$

where $\theta = \cos^{-1}\frac{r'}{R}$ and $w = \frac{\Gamma}{2\pi R}$. Substituting for θ and w:

$$w_z = \frac{r'}{2\pi R^2} \tag{A.4.2}$$

	Thickness/chord ratio			
Incidence	8%	10%	12%	14%
−30	$+4.330 \times 10^{-2}$	$+2.462 \times 10^{-2}$	$+2.142 \times 10^{-2}$	$+2.087 \times 10^{-2}$
−28	$+3.892 \times 10^{-2}$	$+2.104 \times 10^{-2}$	$+1.806 \times 10^{-2}$	$+1.755 \times 10^{-2}$
−26	$+3.454 \times 10^{-2}$	$+1.758 \times 10^{-2}$	$+1.484 \times 10^{-2}$	$+1.437 \times 10^{-2}$
−24	$+3.023 \times 10^{-2}$	$+1.429 \times 10^{-2}$	$+1.180 \times 10^{-2}$	$+1.137 \times 10^{-2}$
−22	$+2.602 \times 10^{-2}$	$+1.122 \times 10^{-2}$	$+8.975 \times 10^{-3}$	$+8.594 \times 10^{-3}$
−20	$+2.198 \times 10^{-2}$	$+8.404 \times 10^{-3}$	$+6.403 \times 10^{-3}$	$+6.065 \times 10^{-3}$
−18	$+1.816 \times 10^{-2}$	$+5.873 \times 10^{-3}$	$+4.114 \times 10^{-3}$	$+3.819 \times 10^{-3}$
−16	$+1.461 \times 10^{-2}$	$+3.661 \times 10^{-3}$	$+2.138 \times 10^{-3}$	$+1.882 \times 10^{-3}$
−14	$+1.136 \times 10^{-2}$	$+1.793 \times 10^{-3}$	$+4.969 \times 10^{-4}$	$+2.800 \times 10^{-4}$
−12	$+8.457 \times 10^{-3}$	$+2.944 \times 10^{-4}$	-7.879×10^{-4}	-9.689×10^{-4}
−10	$+5.939 \times 10^{-3}$	-8.182×10^{-4}	-1.701×10^{-3}	-1.849×10^{-3}
−8	$+3.836 \times 10^{-3}$	-1.531×10^{-3}	-2.232×10^{-3}	-2.350×10^{-3}
−6	$+2.173 \times 10^{-3}$	-1.835×10^{-3}	-2.373×10^{-3}	-2.465×10^{-3}
−4	$+9.708 \times 10^{-4}$	-1.726×10^{-3}	-2.123×10^{-3}	-2.194×10^{-3}
−2	$+2.434 \times 10^{-4}$	-1.206×10^{-3}	-1.486×10^{-3}	-1.538×10^{-3}
0	$+0.000 \times 10^{+0}$	$+0.000 \times 10^{+0}$	$+0.000 \times 10^{+0}$	$+0.000 \times 10^{+0}$
+2	$+2.434 \times 10^{-4}$	$+1.555 \times 10^{-3}$	$+1.725 \times 10^{-3}$	$+1.754 \times 10^{-3}$
+4	$+9.708 \times 10^{-4}$	$+3.556 \times 10^{-3}$	$+3.887 \times 10^{-3}$	$+3.943 \times 10^{-3}$
+6	$+2.173 \times 10^{-3}$	$+5.978 \times 10^{-3}$	$+6.460 \times 10^{-3}$	$+6.540 \times 10^{-3}$
+8	$+3.836 \times 10^{-3}$	$+8.791 \times 10^{-3}$	$+9.411 \times 10^{-3}$	$+9.515 \times 10^{-3}$
+10	$+5.939 \times 10^{-3}$	$+1.196 \times 10^{-2}$	$+1.271 \times 10^{-2}$	$+1.283 \times 10^{-2}$
+12	$+8.457 \times 10^{-3}$	$+1.545 \times 10^{-2}$	$+1.630 \times 10^{-2}$	$+1.644 \times 10^{-2}$
+14	$+1.136 \times 10^{-2}$	$+1.921 \times 10^{-2}$	$+2.016 \times 10^{-2}$	$+2.031 \times 10^{-2}$
+16	$+1.461 \times 10^{-2}$	$+2.320 \times 10^{-2}$	$+2.422 \times 10^{-2}$	$+2.439 \times 10^{-2}$
+18	$+1.816 \times 10^{-2}$	$+2.737 \times 10^{-2}$	$+2.844 \times 10^{-2}$	$+2.862 \times 10^{-2}$
+20	$+2.198 \times 10^{-2}$	$+3.167 \times 10^{-2}$	$+3.277 \times 10^{-2}$	$+3.295 \times 10^{-2}$
+22	$+2.602 \times 10^{-2}$	$+3.604 \times 10^{-2}$	$+3.715 \times 10^{-2}$	$+3.734 \times 10^{-2}$
+24	$+3.023 \times 10^{-2}$	$+4.042 \times 10^{-2}$	$+4.153 \times 10^{-2}$	$+4.171 \times 10^{-2}$
+26	$+3.454 \times 10^{-2}$	$+4.477 \times 10^{-2}$	$+4.584 \times 10^{-2}$	$+4.602 \times 10^{-2}$
+28	$+3.892 \times 10^{-2}$	$+4.901 \times 10^{-2}$	$+5.004 \times 10^{-2}$	$+5.021 \times 10^{-2}$
+30	$+4.330 \times 10^{-2}$	$+5.311 \times 10^{-2}$	$+5.407 \times 10^{-2}$	$+5.422 \times 10^{-2}$

Table A.19: Variation of drag coefficient increment due to flap deflection with flap deflection angle

Dimension	Notation	Inboard	Outboard
Quarter-chord to nacelle lip (horiz), m	r'	6.238	5.546
Quarter-chord to nacelle inlet (vert.), m	z_n	2.018	1.862
Quarter-chord to nacelle inlet (diag.), m	R	6.556	5.850
Nacelle width, m	w	1.749	1.749
Nacelle length, m	l	5.533	5.533

Table A.20: Nacelle geometry for Aeroplane AX-1

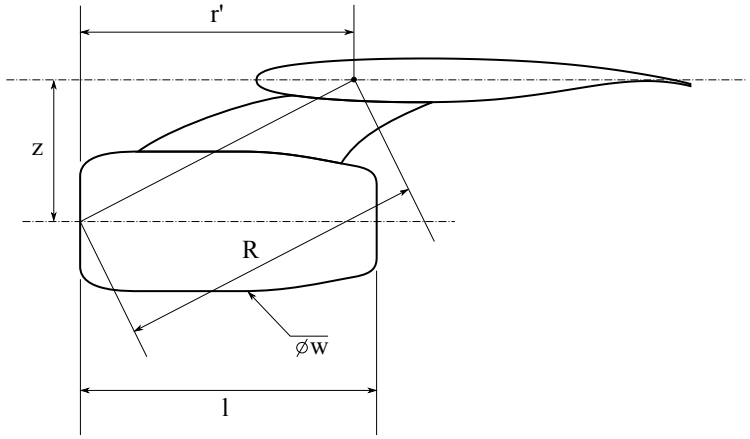

Figure A.20: Nacelle dimensions and geometry

Given that the lift coefficient of the wing, $(a_1)_w$, is given by $(a_1)_w = \frac{L}{\frac{1}{2}\rho V^2 c}$, the circulation, Γ, can be defined as:

$$\Gamma = \frac{L}{\rho V} \tag{A.4.3}$$

$$= \frac{(a_1)_w V c}{2} \tag{A.4.4}$$

The lift curve slope of the wing, $(a_1)_w$, can be estimated using ESDU 70011, with the equivalent straight-tapered wing again approximated using ESDU 76003.

Substituting into Equation A.4.2:

$$w_z = \frac{r' (a_1)_w V c}{4\pi R^2} \tag{A.4.5}$$

For small angles of attack, where $\tan\alpha = \alpha$:

$$\alpha_i = \frac{w}{V} \tag{A.4.6}$$

$$= \left(\frac{r' (a_1)_w V c}{4\pi R^2} \right) / V \tag{A.4.7}$$

$$= \frac{r' (a_1)_w c}{4\pi R^2} \tag{A.4.8}$$

Hence:

$$\frac{d\alpha_i}{d\alpha} = \frac{r' (a_1)_w c}{4\pi R^2} \tag{A.4.9}$$

The lift of the nacelle alone is therefore given by:

$$C_{L_n} = a_n \left(\alpha + \frac{d\alpha_i}{d\alpha} \alpha \right) \tag{A.4.10}$$

$$= a_n \left(1 + \frac{d\alpha_i}{d\alpha} \right) \alpha \tag{A.4.11}$$

The lift curve slope of the nacelle, a_n, is given in Figure 1 of ESDU 77012 as a function of the ratio of the width to the length of the nacelle, w/l. The lift-curve slope of the nacelle, $(a_n)_w$, in the influence of the upwash of the wing is then given by:

$$(a_n)_w = a_n \left(1 + \frac{r' (a_1)_w c}{4\pi R^2} \right) \tag{A.4.12}$$

Using the Aeroplane AX-1 nacelle geometry given in Table A.20, the lift-curve slope of the inboard and outboard nacelles was calculated. The lift-curve slope of the nacelle, a_n, and the nacelle in the upwash of the wing, $(a_n)_w$, for both inboard and outboard engines is given in Table A.21.

Lift-curve Slope	Inboard	Outboard
a_n	0.9251	0.9251
$(a_n)_w$	1.281	1.322

Table A.21: Nacelle lift-curve slopes

APPENDIX B

Structural Data

This chapter presents the mass and stiffness data for the structural model of the Aeroplane AX-1. The mass and structural stiffness data for the airframe alone are published here in normalised format for reference. The mass and distribution of the fuel, cargo and passengers are given in full detail in Sections B.2.2 through B.2.4.

B.1 Stiffness Model

The structural stiffness of the airframe is given separately for the fuselage, wing, tail and fin. The bending and torsional stiffness of each of the airframe components is given about the elastic axis shown in Figure B.5. The aircraft is assumed to be symmetric about the x-axis centreline. The normalised stiffness is given for fuselage, wing, tail, and fin in Figures B.1, B.2, B.3, and B.4 respectively.

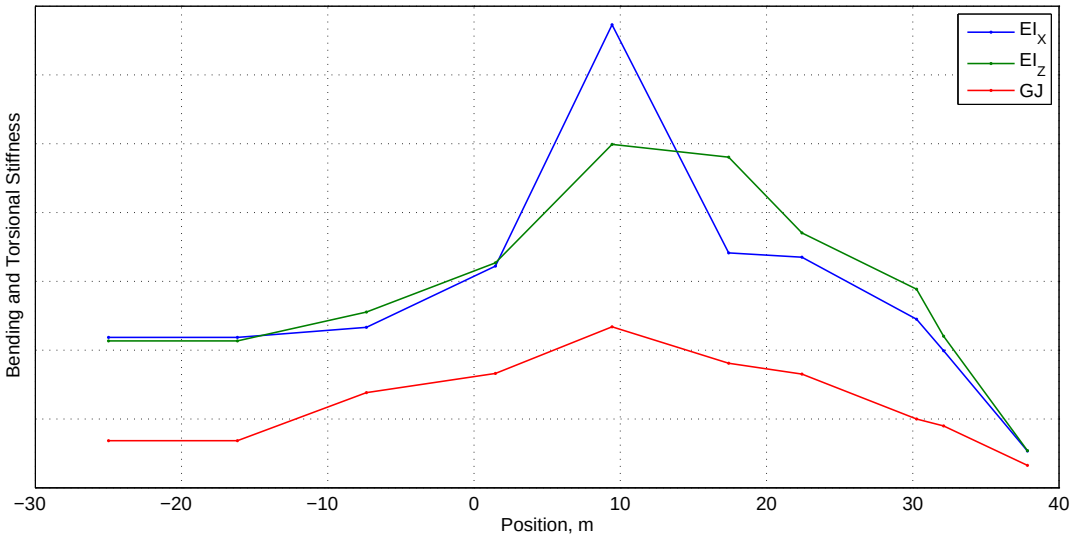

Figure B.1: Normalised bending and torsional stiffness of the fuselage

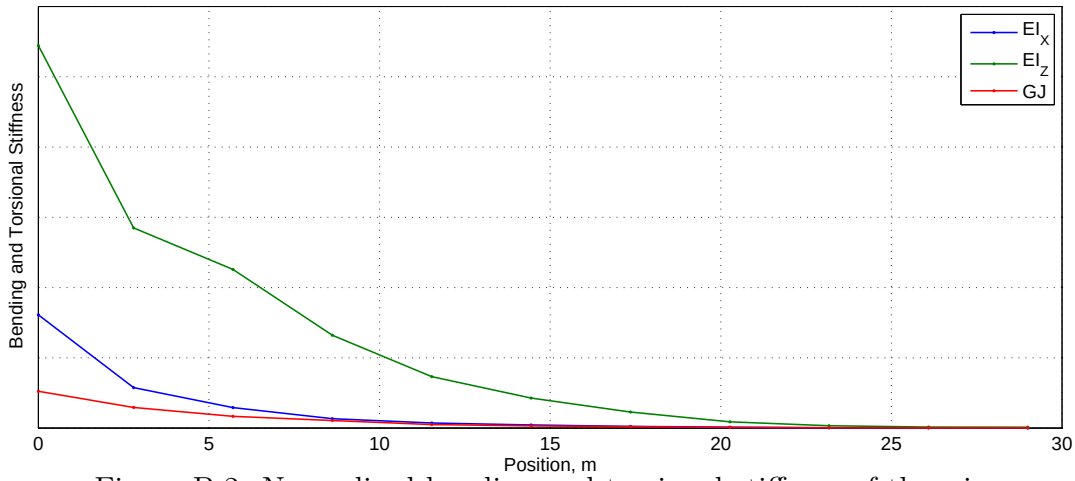

Figure B.2: Normalised bending and torsional stiffness of the wing

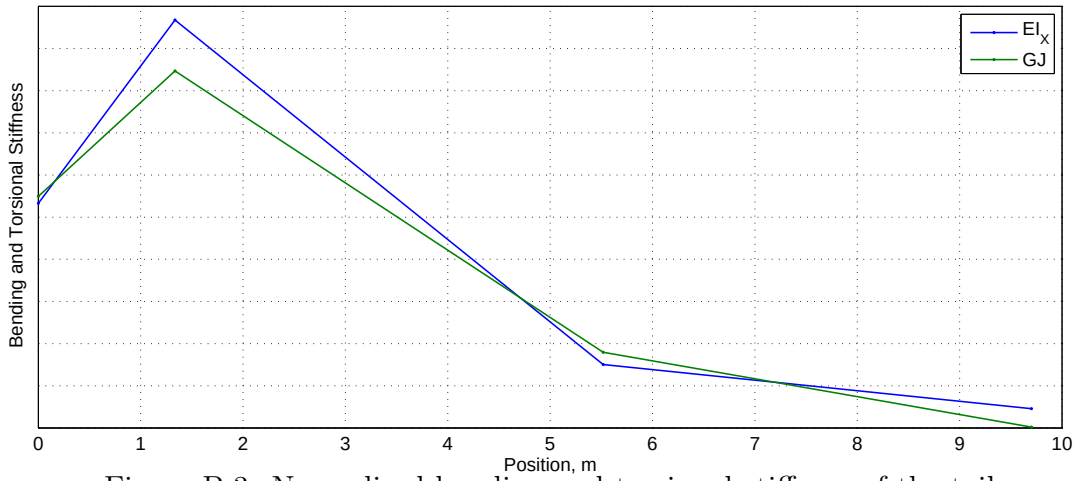

Figure B.3: Normalised bending and torsional stiffness of the tail

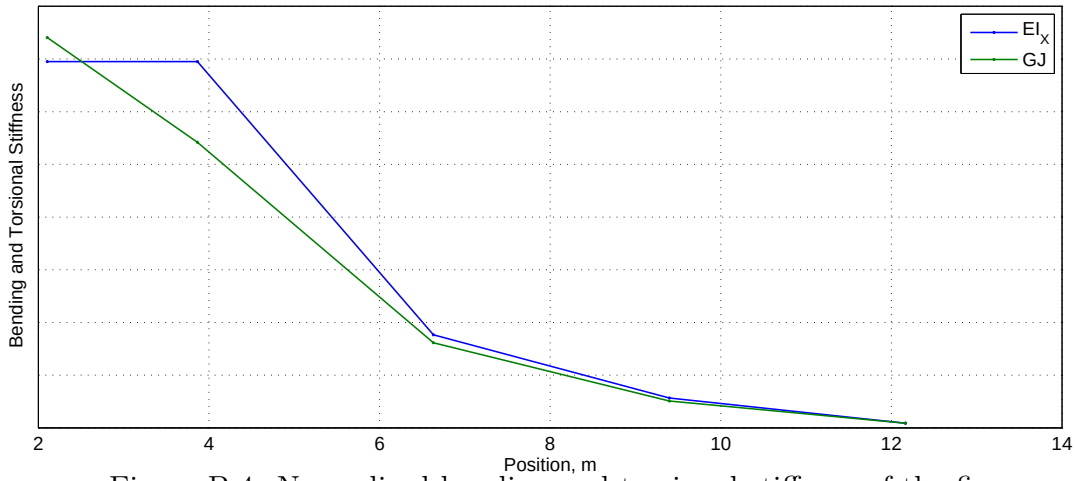

Figure B.4: Normalised bending and torsional stiffness of the fin

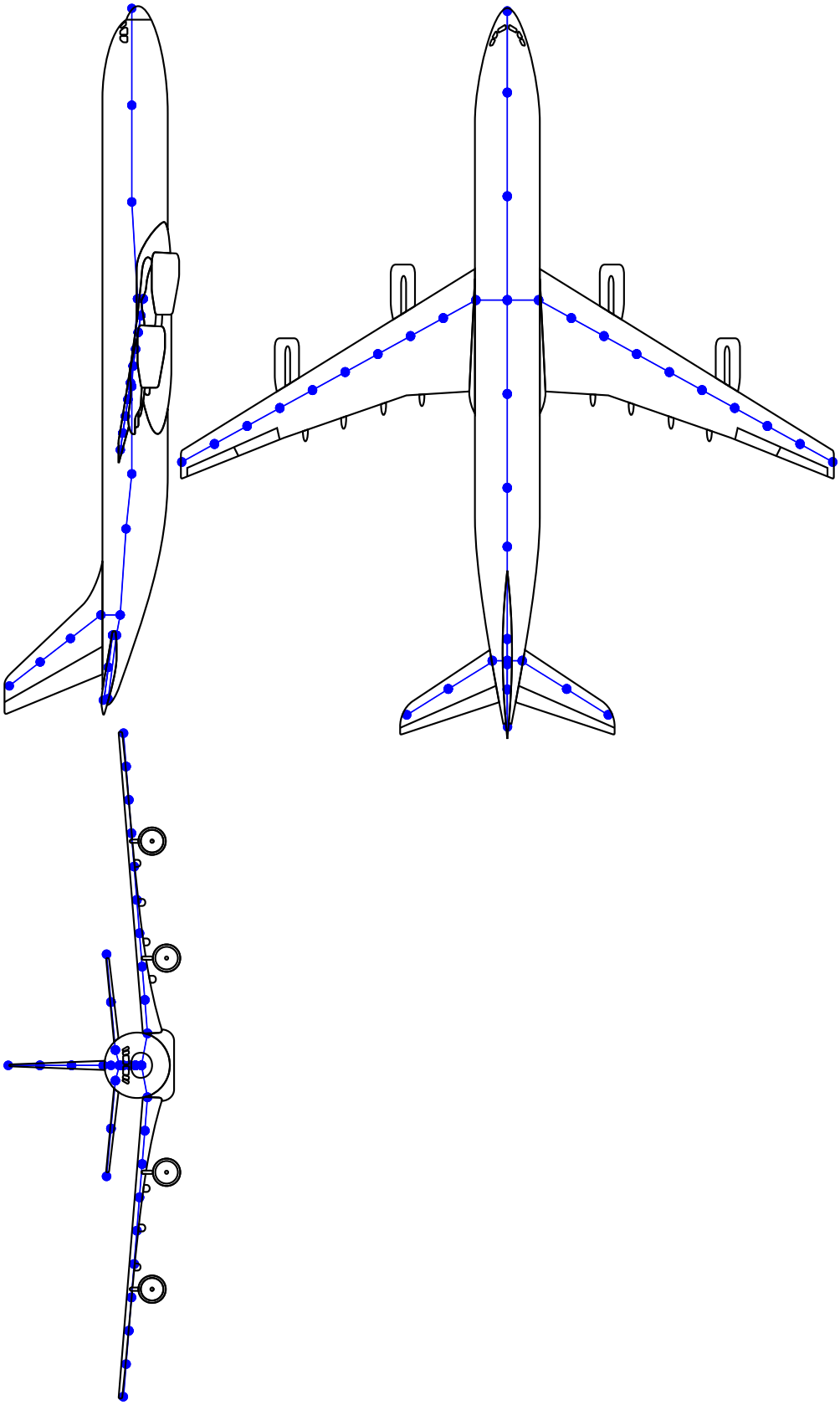

Figure B.5: Location of structural elastic axis and nodes

B.2 Mass Model

B.2.1 Airframe

The Operational Weight Empty (OWE) mass of the Aeroplane AX-1 is 131,218 kg. The mass distribution of the OWE airframe mass is shown in Figure B.6.

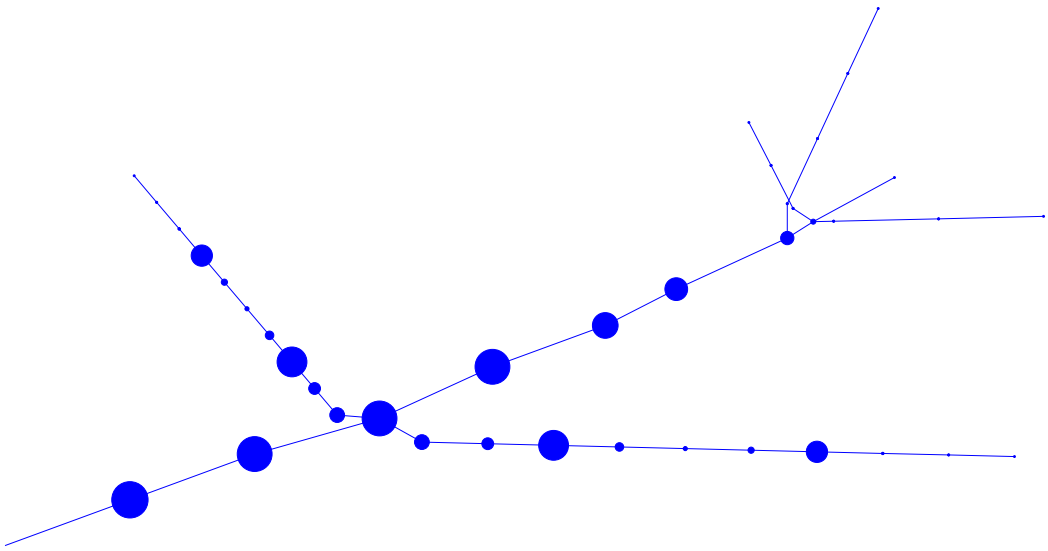

Figure B.6: Aeroplane AX-1 Operational Weight Empty airframe mass distribution

B.2.2 Passengers

The Aeroplane AX-1 cabin is modelled in a two-class passenger configuration. First-class passengers are assumed to sit six abreast, while tourist-class is arranged in an eight-abreast layout [Figure B.7].

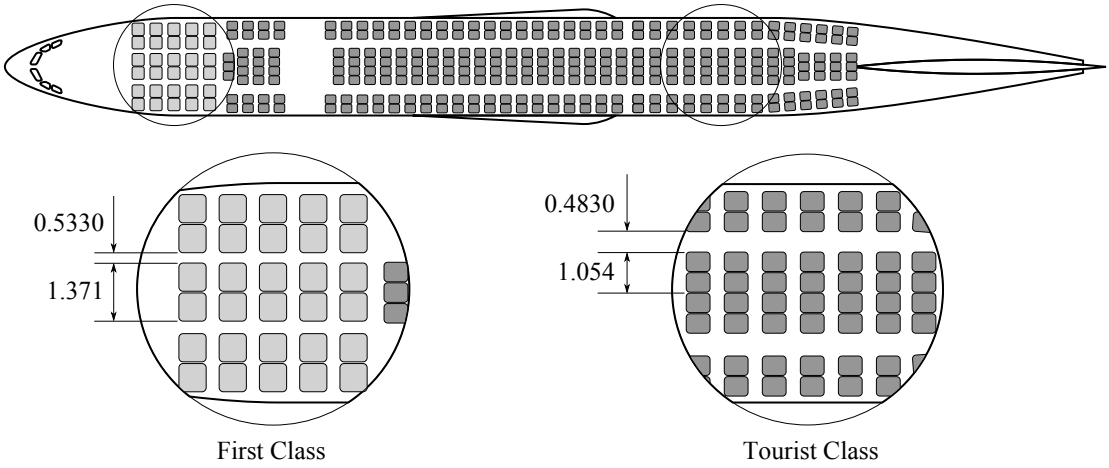

Figure B.7: Aeroplane AX-1 passenger configuration

Each passenger is assumed to weigh 85 kg, including carry-on luggage. The maximum number of first- and tourist-class passengers is 36 and 280 respectively. The total mass

for any passenger configuration is calculated as a percentage of the total number of passengers, with the passengers placed, or randomly positioned, within the cabin area. Table B.1 gives a summary of the total mass and inertia properties for each seating row for a full configuration. This is shown in Figure B.12.

B.2.3 Cargo

The Aeroplane AX-1 is capable of carrying a total of 32 LD-3 [Figure B.9] cargo containers; 18 in the forward cargo compartment and 14 in the rear compartment. This is in addition to the bulk cargo compartment located at the rear of the fuselage. Figure B.8 shows the position and dimensions of the forward, rear and bulk cargo compartments. The total mass of the containered cargo is calculated as a percentage of the certified maximum gross mass for each LD-3 container of 1,588 kg. The total mass of the bulk cargo compartment is given as a percentage of its total mass, calculated using its volume, 19.7 m^3, and the estimated density of the bulk cargo, 378.1 kg m^{-3}. The mass distribution within each container and the bulk cargo hold is assumed to be uniform.

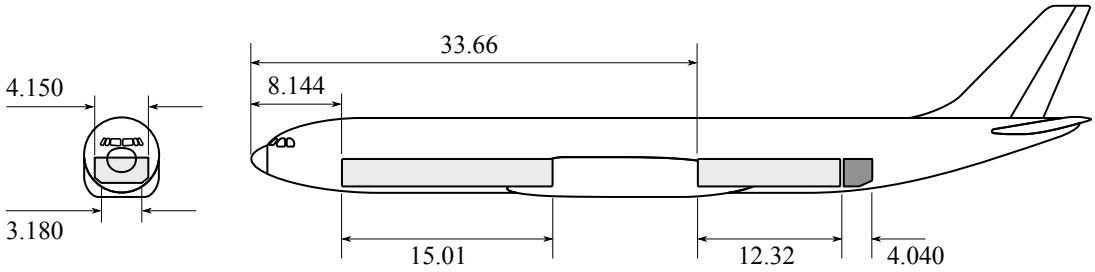

Figure B.8: Aeroplane AX-1 cargo hold geometry

Table B.2 shows the total gross mass, centre of gravity and inertia properties about the axis datum for the containered and bulk cargo. The container numbering ID is shown in Figure B.10. Each unit mass is discretised longitudinally into a number of mass "strips", and the mass and inertia properties of the rigid and flexible aircraft calculated. This is shown in Figure B.13.

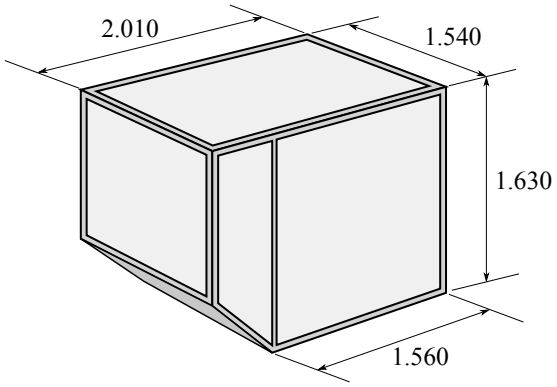

Description	Value
Classification	LD-3
IATA description	AKE contoured container
Tare mass	190 kg
Gross mass	1,588 kg
Volume	4.2 m^3

Figure B.9: Aeroplane AX-1 LD-3 container specification and dimensions

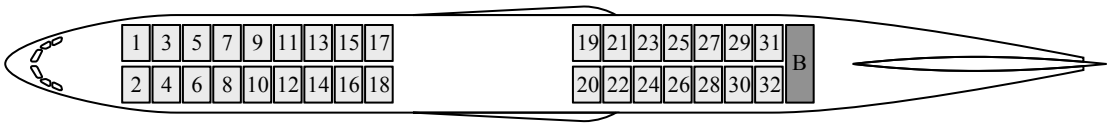

Figure B.10: Aeroplane AX-1 cargo container layout

B.2.4 Fuel

The Aeroplane AX-1 has six fuel tanks: two outer-wing tanks, two inner-wing tanks, one centre tank, and one tail trim tank [Figure B.11]. The maximum mass of the fuel contained within these tanks is 2,845kg, 33,285kg, 32,550kg and 4,800kg respectively. Each tank is discretised into a number of spanwise "strips", for which the centre of mass assumed to act at the centre of this strip. The mass distribution for the fuel is assumed to be symmetric. Table B.3 provides the total mass and inertia properties for the starboard wing only for a full fuel configuration. The complete mass distribution is shown in Figure B.14.

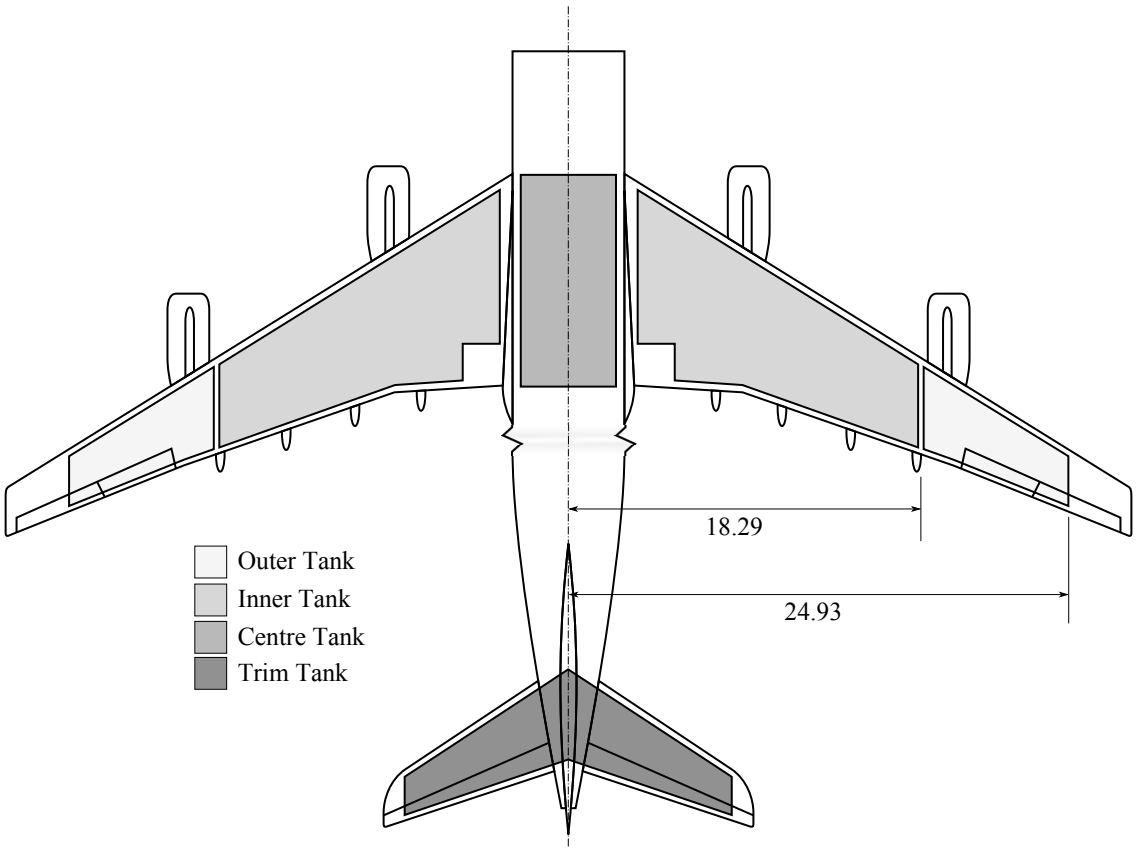

Figure B.11: Aeroplane AX-1 fuel tank configuration

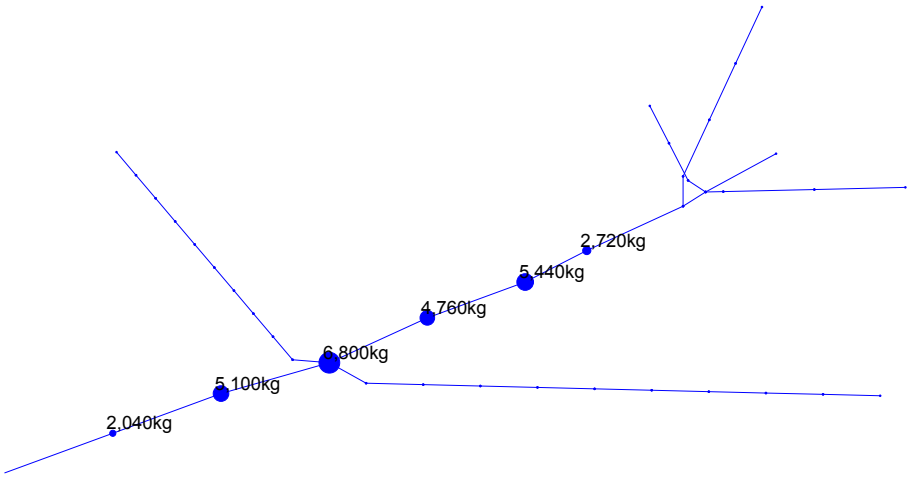

Figure B.12: Aeroplane AX-1 passenger mass distribution

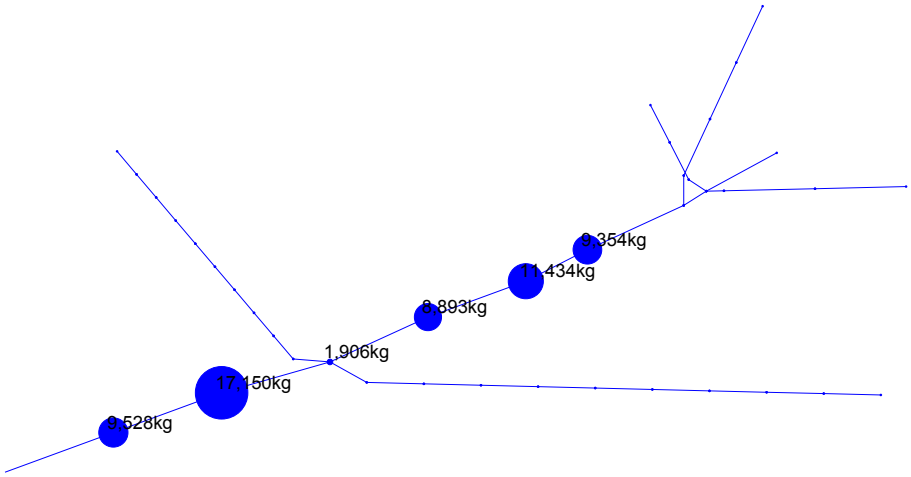

Figure B.13: Aeroplane AX-1 cargo mass distribution

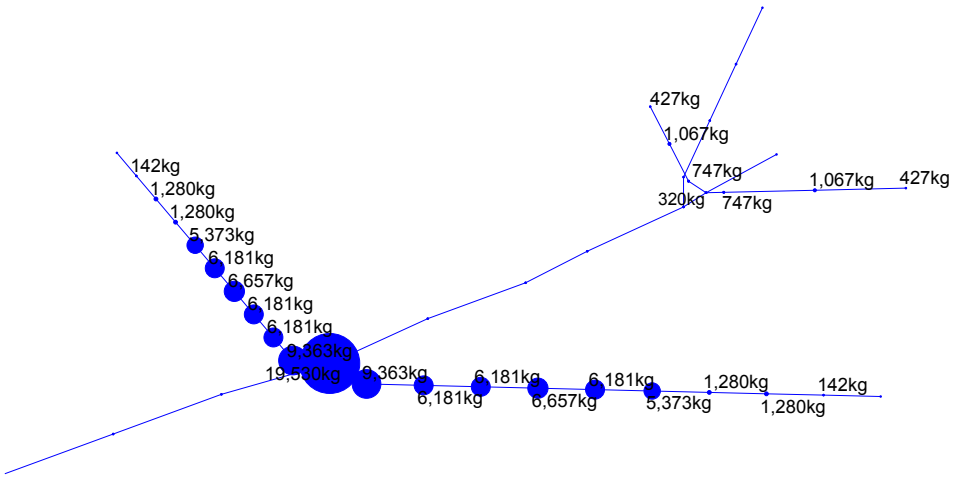

Figure B.14: Aeroplane AX-1 fuel mass distribution

B.2.5 Data

			Centre of Gravity			Moments of Inertia					
Row	Class	Mass, kg	x, m	y, m	z, m	I_{XX}, kg m^2	I_{YY}, kg m^2	I_{ZZ}, kg m^2	I_{XY}, kg m^2	I_{XZ}, kg m^2	I_{YZ}, kg m^2
1	F	510.0	+16.54	0.000	−1.268	$+2.113 \times 10^3$	$+1.403 \times 10^5$	$+1.408 \times 10^5$	0.000×10^3	$+1.070 \times 10^4$	0.000×10^3
2	F	510.0	+15.33	0.000	−1.268	$+2.113 \times 10^3$	$+1.207 \times 10^5$	$+1.211 \times 10^5$	0.000×10^3	$+0.991 \times 10^4$	0.000×10^3
3	F	510.0	+14.12	0.000	−1.268	$+2.113 \times 10^3$	$+1.025 \times 10^5$	$+1.030 \times 10^5$	0.000×10^3	$+0.913 \times 10^4$	0.000×10^3
4	F	510.0	+12.91	0.000	−1.268	$+2.113 \times 10^3$	$+0.858 \times 10^5$	$+0.863 \times 10^5$	0.000×10^3	$+0.835 \times 10^4$	0.000×10^3
5	F	510.0	+11.70	0.000	−1.268	$+2.113 \times 10^3$	$+0.706 \times 10^5$	$+0.711 \times 10^5$	0.000×10^3	$+0.757 \times 10^4$	0.000×10^3
6	F	510.0	+10.49	0.000	−1.268	$+2.113 \times 10^3$	$+0.569 \times 10^5$	$+0.574 \times 10^5$	0.000×10^3	$+0.678 \times 10^4$	0.000×10^3
14	Y	680.0	+7.192	0.000	−1.268	$+2.680 \times 10^3$	$+0.363 \times 10^5$	$+0.368 \times 10^5$	0.000×10^3	$+0.620 \times 10^4$	0.000×10^3
15	Y	680.0	+6.329	0.000	−1.268	$+2.680 \times 10^3$	$+0.283 \times 10^5$	$+0.288 \times 10^5$	0.000×10^3	$+0.546 \times 10^4$	0.000×10^3
16	Y	680.0	+5.516	0.000	−1.268	$+2.680 \times 10^3$	$+0.218 \times 10^5$	$+0.223 \times 10^5$	0.000×10^3	$+0.476 \times 10^4$	0.000×10^3
17	Y	680.0	+4.703	0.000	−1.268	$+2.680 \times 10^3$	$+0.161 \times 10^5$	$+0.166 \times 10^5$	0.000×10^3	$+0.406 \times 10^4$	0.000×10^3
18	Y	680.0	+3.890	0.000	−1.268	$+2.680 \times 10^3$	$+0.114 \times 10^5$	$+0.119 \times 10^5$	0.000×10^3	$+0.335 \times 10^4$	0.000×10^3
19	Y	680.0	+3.077	0.000	−1.268	$+2.680 \times 10^3$	$+0.075 \times 10^5$	$+0.080 \times 10^5$	0.000×10^3	$+0.265 \times 10^4$	0.000×10^3
20	Y	680.0	+2.264	0.000	−1.268	$+2.680 \times 10^3$	$+0.046 \times 10^5$	$+0.051 \times 10^5$	0.000×10^3	$+0.195 \times 10^4$	0.000×10^3
21	Y	680.0	+1.451	0.000	−1.268	$+2.680 \times 10^3$	$+0.025 \times 10^5$	$+0.030 \times 10^5$	0.000×10^3	$+0.125 \times 10^4$	0.000×10^3
22	Y	680.0	+0.638	0.000	−1.268	$+2.680 \times 10^3$	$+0.014 \times 10^5$	$+0.019 \times 10^5$	0.000×10^3	$+0.055 \times 10^4$	0.000×10^3
23	Y	680.0	−0.175	0.000	−1.268	$+2.680 \times 10^3$	$+0.011 \times 10^5$	$+0.016 \times 10^5$	0.000×10^3	-0.015×10^4	0.000×10^3
24	Y	680.0	−0.988	0.000	−1.268	$+2.680 \times 10^3$	$+0.018 \times 10^5$	$+0.023 \times 10^5$	0.000×10^3	-0.085×10^4	0.000×10^3
25	Y	680.0	−1.801	0.000	−1.268	$+2.680 \times 10^3$	$+0.033 \times 10^5$	$+0.038 \times 10^5$	0.000×10^3	-0.155×10^4	0.000×10^3
26	Y	680.0	−2.614	0.000	−1.268	$+2.680 \times 10^3$	$+0.057 \times 10^5$	$+0.062 \times 10^5$	0.000×10^3	-0.225×10^4	0.000×10^3
27	Y	680.0	−3.427	0.000	−1.268	$+2.680 \times 10^3$	$+0.091 \times 10^5$	$+0.096 \times 10^5$	0.000×10^3	-0.296×10^4	0.000×10^3
28	Y	680.0	−4.240	0.000	−1.268	$+2.680 \times 10^3$	$+0.133 \times 10^5$	$+0.138 \times 10^5$	0.000×10^3	-0.366×10^4	0.000×10^3
29	Y	680.0	−5.053	0.000	−1.268	$+2.680 \times 10^3$	$+0.185 \times 10^5$	$+0.189 \times 10^5$	0.000×10^3	-0.436×10^4	0.000×10^3
30	Y	680.0	−5.866	0.000	−1.268	$+2.680 \times 10^3$	$+0.245 \times 10^5$	$+0.250 \times 10^5$	0.000×10^3	-0.506×10^4	0.000×10^3
31	Y	680.0	−6.628	0.000	−1.268	$+2.680 \times 10^3$	$+0.310 \times 10^5$	$+0.315 \times 10^5$	0.000×10^3	-0.572×10^4	0.000×10^3

Table B.1: Aeroplane AX-1 passenger mass and inertial properties

			Centre of Gravity			Moments of Inertia					
Row	Class	Mass, kg	x, m	y, m	z, m	I_{XX}, kg m^2	I_{YY}, kg m^2	I_{ZZ}, kg m^2	I_{XY}, kg m^2	I_{XZ}, kg m^2	I_{YZ}, kg m^2
32	Y	680.0	−9.473	0.000	−1.268	$+2.680 \times 10^3$	$+0.621 \times 10^5$	$+0.626 \times 10^5$	0.000×10^3	-0.817×10^4	0.000×10^3
33	Y	680.0	−10.28	0.000	−1.268	$+2.680 \times 10^3$	$+0.730 \times 10^5$	$+0.735 \times 10^5$	0.000×10^3	-0.887×10^4	0.000×10^3
34	Y	680.0	−11.09	0.000	−1.268	$+2.680 \times 10^3$	$+0.847 \times 10^5$	$+0.852 \times 10^5$	0.000×10^3	-0.956×10^4	0.000×10^3
35	Y	680.0	−11.90	0.000	−1.268	$+2.680 \times 10^3$	$+0.973 \times 10^5$	$+0.978 \times 10^5$	0.000×10^3	-1.026×10^4	0.000×10^3
36	Y	680.0	−12.71	0.000	−1.268	$+2.680 \times 10^3$	$+1.109 \times 10^5$	$+1.113 \times 10^5$	0.000×10^3	-1.096×10^4	0.000×10^3
37	Y	680.0	−13.51	0.000	−1.268	$+2.680 \times 10^3$	$+1.253 \times 10^5$	$+1.258 \times 10^5$	0.000×10^3	-1.165×10^4	0.000×10^3
38	Y	680.0	−14.32	0.000	−1.268	$+2.680 \times 10^3$	$+1.405 \times 10^5$	$+1.410 \times 10^5$	0.000×10^3	-1.235×10^4	0.000×10^3
39	Y	680.0	−15.13	0.000	−1.268	$+2.680 \times 10^3$	$+1.567 \times 10^5$	$+1.572 \times 10^5$	0.000×10^3	-1.305×10^4	0.000×10^3
40	Y	680.0	−15.94	0.000	−1.268	$+2.680 \times 10^3$	$+1.738 \times 10^5$	$+1.743 \times 10^5$	0.000×10^3	-1.374×10^4	0.000×10^3
41	Y	680.0	−16.74	0.000	−1.268	$+2.680 \times 10^3$	$+1.917 \times 10^5$	$+1.922 \times 10^5$	0.000×10^3	-1.444×10^4	0.000×10^3
42	Y	680.0	−17.55	0.000	−1.268	$+2.680 \times 10^3$	$+2.106 \times 10^5$	$+2.111 \times 10^5$	0.000×10^3	-1.514×10^4	0.000×10^3
43	Y	680.0	−18.36	0.000	−1.268	$+2.680 \times 10^3$	$+2.303 \times 10^5$	$+2.308 \times 10^5$	0.000×10^3	-1.583×10^4	0.000×10^3
44	Y	680.0	−19.17	0.000	−1.268	$+2.680 \times 10^3$	$+2.509 \times 10^5$	$+2.514 \times 10^5$	0.000×10^3	-1.653×10^4	0.000×10^3
45	Y	680.0	−19.98	0.000	−1.268	$+2.680 \times 10^3$	$+2.724 \times 10^5$	$+2.729 \times 10^5$	0.000×10^3	-1.723×10^4	0.000×10^3
46	Y	680.0	−20.78	0.000	−1.268	$+2.680 \times 10^3$	$+2.948 \times 10^5$	$+2.953 \times 10^5$	0.000×10^3	-1.792×10^4	0.000×10^3
47	Y	680.0	−21.59	0.000	−1.268	$+2.680 \times 10^3$	$+3.181 \times 10^5$	$+3.186 \times 10^5$	0.000×10^3	-1.862×10^4	0.000×10^3
48	Y	680.0	−22.40	0.000	−1.268	$+2.680 \times 10^3$	$+3.423 \times 10^5$	$+3.428 \times 10^5$	0.000×10^3	-1.932×10^4	0.000×10^3

Table B.1: Aeroplane AX-1 passenger mass and inertial properties (continued)

		Centre of Gravity			Moments of Inertia					
ID	Mass, kg	x, m	y, m	z, m	I_{XX}, kg m^2	I_{YY}, kg m^2	I_{ZZ}, kg m^2	I_{XY}, kg m^2	I_{XZ}, kg m^2	I_{YZ}, kg m^2
1	1588	+14.35	+1.397	+0.3350	$+3.275 \times 10^3$	$+3.272 \times 10^5$	$+3.301 \times 10^5$	-3.182×10^4	-7.634×10^3	-0.7430×10^3
2	1588	+14.35	−1.397	+0.3350	$+3.275 \times 10^3$	$+3.272 \times 10^5$	$+3.301 \times 10^5$	$+3.182 \times 10^4$	-7.634×10^3	-0.7430×10^3
3	1588	+12.68	+1.397	+0.3350	$+3.275 \times 10^3$	$+2.555 \times 10^5$	$+2.584 \times 10^5$	-2.812×10^4	-6.746×10^3	-0.7430×10^3
4	1588	+12.68	−1.397	+0.3350	$+3.275 \times 10^3$	$+2.555 \times 10^5$	$+2.584 \times 10^5$	$+2.812 \times 10^4$	-6.746×10^3	-0.7430×10^3
5	1588	+11.01	+1.397	+0.3350	$+3.275 \times 10^3$	$+1.927 \times 10^5$	$+1.956 \times 10^5$	-2.442×10^4	-5.857×10^3	-0.7430×10^3
6	1588	+11.01	−1.397	+0.3350	$+3.275 \times 10^3$	$+1.927 \times 10^5$	$+1.956 \times 10^5$	$+2.442 \times 10^4$	-5.857×10^3	-0.7430×10^3
7	1588	+9.341	+1.397	+0.3350	$+3.275 \times 10^3$	$+1.387 \times 10^5$	$+1.417 \times 10^5$	-2.072×10^4	-4.969×10^3	-0.7430×10^3
8	1588	+9.341	−1.397	+0.3350	$+3.275 \times 10^3$	$+1.387 \times 10^5$	$+1.417 \times 10^5$	$+2.072 \times 10^4$	-4.969×10^3	-0.7430×10^3
9	1588	+7.672	+1.397	+0.3350	$+3.275 \times 10^3$	$+9.364 \times 10^4$	$+9.656 \times 10^4$	-1.701×10^4	-4.081×10^3	-0.7430×10^3
10	1588	+7.672	−1.397	+0.3350	$+3.275 \times 10^3$	$+9.364 \times 10^4$	$+9.656 \times 10^4$	$+1.701 \times 10^4$	-4.081×10^3	-0.7430×10^3
11	1588	+6.002	+1.397	+0.3350	$+3.275 \times 10^3$	$+5.739 \times 10^4$	$+6.031 \times 10^4$	-1.331×10^4	-3.193×10^3	-0.7430×10^3
12	1588	+6.002	−1.397	+0.3350	$+3.275 \times 10^3$	$+5.739 \times 10^4$	$+6.031 \times 10^4$	$+1.331 \times 10^4$	-3.193×10^3	-0.7430×10^3
13	1588	+4.333	+1.397	+0.3350	$+3.275 \times 10^3$	$+2.999 \times 10^4$	$+3.291 \times 10^4$	-9.608×10^3	-2.305×10^3	-0.7430×10^3
14	1588	+4.333	−1.397	+0.3350	$+3.275 \times 10^3$	$+2.999 \times 10^4$	$+3.291 \times 10^4$	$+9.608 \times 10^3$	-2.305×10^3	-0.7430×10^3
15	1588	+2.663	+1.397	+0.3350	$+3.275 \times 10^3$	$+1.144 \times 10^4$	$+1.436 \times 10^4$	-5.906×10^3	-1.417×10^3	-0.7430×10^3
16	1588	+2.663	−1.397	+0.3350	$+3.275 \times 10^3$	$+1.144 \times 10^4$	$+1.436 \times 10^4$	$+5.906 \times 10^3$	-1.417×10^3	-0.7430×10^3
17	1588	+0.993	+1.397	+0.3350	$+3.275 \times 10^3$	$+1.746 \times 10^3$	$+4.664 \times 10^3$	-2.203×10^3	-0.529×10^3	-0.7430×10^3
18	1588	+0.993	−1.397	+0.3350	$+3.275 \times 10^3$	$+1.746 \times 10^3$	$+4.664 \times 10^3$	$+2.203 \times 10^3$	-0.529×10^3	-0.7430×10^3
19	1588	−11.31	+1.397	+0.3350	$+3.275 \times 10^3$	$+2.031 \times 10^5$	$+2.060 \times 10^5$	$+2.507 \times 10^4$	$+6.014 \times 10^3$	-0.7430×10^3
20	1588	−11.31	−1.397	+0.3350	$+3.275 \times 10^3$	$+2.031 \times 10^5$	$+2.060 \times 10^5$	-2.507×10^4	$+6.014 \times 10^3$	-0.7430×10^3
21	1588	−13.07	+1.397	+0.3350	$+3.275 \times 10^3$	$+2.713 \times 10^5$	$+2.742 \times 10^5$	$+2.898 \times 10^4$	$+6.951 \times 10^3$	-0.7430×10^3

Table B.2: Aeroplane AX-1 bulk and container cargo mass and inertial properties

		Centre of Gravity			Moments of Inertia					
ID	Mass, kg	x, m	y, m	z, m	I_{XX}, kg m^2	I_{YY}, kg m^2	I_{ZZ}, kg m^2	I_{XY}, kg m^2	I_{XZ}, kg m^2	I_{YZ}, kg m^2
22	1588	−13.07	−1.397	+0.3350	$+3.275 \times 10^3$	$+2.713 \times 10^5$	$+2.742 \times 10^5$	-2.898×10^4	$+6.951 \times 10^3$	$+0.7430 \times 10^3$
23	1588	−14.83	+1.397	+0.3350	$+3.275 \times 10^3$	$+3.494 \times 10^5$	$+3.523 \times 10^5$	$+3.289 \times 10^4$	$+7.889 \times 10^3$	$+0.7430 \times 10^3$
24	1588	−14.83	−1.397	+0.3350	$+3.275 \times 10^3$	$+3.494 \times 10^5$	$+3.523 \times 10^5$	-3.289×10^4	$+7.889 \times 10^3$	$+0.7430 \times 10^3$
25	1588	−16.59	+1.397	+0.3350	$+3.275 \times 10^3$	$+4.373 \times 10^5$	$+4.402 \times 10^5$	$+3.679 \times 10^4$	$+8.826 \times 10^3$	$+0.7430 \times 10^3$
26	1588	−16.59	−1.397	+0.3350	$+3.275 \times 10^3$	$+4.373 \times 10^5$	$+4.402 \times 10^5$	-3.679×10^4	$+8.826 \times 10^3$	$+0.7430 \times 10^3$
27	1588	−18.35	+1.397	+0.3350	$+3.275 \times 10^3$	$+5.351 \times 10^5$	$+5.380 \times 10^5$	$+4.070 \times 10^4$	$+9.764 \times 10^3$	$+0.7430 \times 10^3$
28	1588	−18.35	−1.397	+0.3350	$+3.275 \times 10^3$	$+5.351 \times 10^5$	$+5.380 \times 10^5$	-4.070×10^4	$+9.764 \times 10^3$	$+0.7430 \times 10^3$
29	1588	−20.12	+1.397	+0.3350	$+3.275 \times 10^3$	$+6.428 \times 10^5$	$+6.457 \times 10^5$	$+4.461 \times 10^4$	$+1.070 \times 10^4$	$+0.7430 \times 10^3$
30	1588	−20.12	−1.397	+0.3350	$+3.275 \times 10^3$	$+6.428 \times 10^5$	$+6.457 \times 10^5$	-4.461×10^4	$+1.070 \times 10^4$	$+0.7430 \times 10^3$
31	1588	−21.88	+1.397	+0.3350	$+3.275 \times 10^3$	$+7.603 \times 10^5$	$+7.632 \times 10^5$	$+4.852 \times 10^4$	$+1.164 \times 10^4$	$+0.7430 \times 10^3$
32	1588	−21.88	−1.397	+0.3350	$+3.275 \times 10^3$	$+7.603 \times 10^5$	$+7.632 \times 10^5$	-4.852×10^4	$+1.164 \times 10^4$	$+0.7430 \times 10^3$
B	7448	−22.96	0.000	+0.3350	$+0.836 \times 10^3$	$+39.264 \times 10^5$	$+39.255 \times 10^5$	0.000×10^3	$+5.728 \times 10^4$	0.000×10^3

Table B.2: Aeroplane AX-1 bulk and container cargo mass and inertial properties (continued)

			Centre of Gravity			Moments of Inertia					
Tank	Strip	Mass, kg	x, m	y, m	z, m	I_{XX}, kg m^2	I_{YY}, kg m^2	I_{ZZ}, kg m^2	I_{XY}, kg m^2	I_{XZ}, kg m^2	I_{YZ}, kg m^2
O	1	142.3	−9.274	−18.28	−1.241	$+4.779 \times 10^4$	$+1.245 \times 10^4$	$+5.981 \times 10^4$	-2.412×10^4	-0.164×10^4	-0.323×10^4
O	2	142.3	−9.636	−18.95	−1.294	$+5.133 \times 10^4$	$+1.345 \times 10^4$	$+6.430 \times 10^4$	-2.598×10^4	-0.177×10^4	-0.349×10^4
O	3	142.3	−9.817	−19.28	−1.321	$+5.314 \times 10^4$	$+1.396 \times 10^4$	$+6.660 \times 10^4$	-2.693×10^4	-0.184×10^4	-0.362×10^4
O	4	142.3	−9.998	−19.61	−1.348	$+5.499 \times 10^4$	$+1.448 \times 10^4$	$+6.895 \times 10^4$	-2.790×10^4	-0.192×10^4	-0.376×10^4
O	5	142.3	−10.17	−19.94	−1.374	$+5.687 \times 10^4$	$+1.501 \times 10^4$	$+7.134 \times 10^4$	-2.888×10^4	-0.199×10^4	-0.390×10^4
O	6	142.3	−10.36	−20.27	−1.401	$+5.878 \times 10^4$	$+1.555 \times 10^4$	$+7.377 \times 10^4$	-2.988×10^4	-0.206×10^4	-0.404×10^4
O	7	142.3	−10.54	−20.61	−1.427	$+6.072 \times 10^4$	$+1.610 \times 10^4$	$+7.623 \times 10^4$	-3.090×10^4	-0.214×10^4	-0.418×10^4
O	8	142.3	−10.72	−20.94	−1.454	$+6.269 \times 10^4$	$+1.665 \times 10^4$	$+7.874 \times 10^4$	-3.194×10^4	-0.222×10^4	-0.433×10^4
O	9	142.3	−10.90	−21.27	−1.481	$+6.470 \times 10^4$	$+1.722 \times 10^4$	$+8.129 \times 10^4$	-3.300×10^4	-0.230×10^4	-0.448×10^4
O	10	142.3	−11.08	−21.60	−1.507	$+6.673 \times 10^4$	$+1.780 \times 10^4$	$+8.389 \times 10^4$	-3.407×10^4	-0.238×10^4	-0.463×10^4
O	11	142.3	−11.26	−21.93	−1.534	$+6.880 \times 10^4$	$+1.839 \times 10^4$	$+8.652 \times 10^4$	-3.516×10^4	-0.246×10^4	-0.479×10^4
O	12	142.3	−11.44	−22.27	−1.560	$+7.090 \times 10^4$	$+1.898 \times 10^4$	$+8.919 \times 10^4$	-3.626×10^4	-0.254×10^4	-0.494×10^4
O	13	142.3	−11.62	−22.60	−1.587	$+7.303 \times 10^4$	$+1.959 \times 10^4$	$+9.190 \times 10^4$	-3.738×10^4	-0.262×10^4	-0.510×10^4
O	14	142.3	−11.80	−22.93	−1.613	$+7.519 \times 10^4$	$+2.020 \times 10^4$	$+9.466 \times 10^4$	-3.852×10^4	-0.271×10^4	-0.526×10^4
O	15	142.3	−11.98	−23.26	−1.640	$+7.739 \times 10^4$	$+2.083 \times 10^4$	$+9.745 \times 10^4$	-3.968×10^4	-0.280×10^4	-0.543×10^4
O	16	142.3	−12.17	−23.59	−1.667	$+7.961 \times 10^4$	$+2.146 \times 10^4$	$+10.029 \times 10^4$	-4.085×10^4	-0.289×10^4	-0.559×10^4
O	17	142.3	−12.35	−23.93	−1.693	$+8.187 \times 10^4$	$+2.211 \times 10^4$	$+10.316 \times 10^4$	-4.204×10^4	-0.297×10^4	-0.576×10^4
O	18	142.3	−12.53	−24.26	−1.720	$+8.416 \times 10^4$	$+2.276 \times 10^4$	$+10.608 \times 10^4$	-4.325×10^4	-0.307×10^4	-0.594×10^4
O	19	142.3	−12.71	−24.59	−1.746	$+8.648 \times 10^4$	$+2.342 \times 10^4$	$+10.903 \times 10^4$	-4.448×10^4	-0.316×10^4	-0.611×10^4
O	20	142.3	−12.89	−24.92	−1.773	$+8.883 \times 10^4$	$+2.410 \times 10^4$	$+11.203 \times 10^4$	-4.572×10^4	-0.325×10^4	-0.629×10^4
I	1	475.5	−1.596	−2.793	0.000	$+0.371 \times 10^4$	$+0.121 \times 10^4$	$+0.492 \times 10^4$	-0.212×10^4	0.000×10^4	0.000×10^4
I	2	475.5	−1.816	−3.236	−0.035	$+0.498 \times 10^4$	$+0.157 \times 10^4$	$+0.655 \times 10^4$	-0.279×10^4	-0.003×10^4	-0.005×10^4
I	3	475.5	−1.925	−3.457	−0.053	$+0.568 \times 10^4$	$+0.176 \times 10^4$	$+0.745 \times 10^4$	-0.316×10^4	-0.005×10^4	-0.009×10^4
I	4	475.5	−2.035	−3.678	−0.071	$+0.644 \times 10^4$	$+0.197 \times 10^4$	$+0.840 \times 10^4$	-0.356×10^4	-0.007×10^4	-0.012×10^4
I	5	475.5	−2.145	−3.900	−0.089	$+0.724 \times 10^4$	$+0.219 \times 10^4$	$+0.942 \times 10^4$	-0.398×10^4	-0.009×10^4	-0.016×10^4

Table B.3: Aeroplane AX-1 fuel mass and inertial properties

			Centre of Gravity			Moments of Inertia					
Tank	Strip	Mass, kg	x, m	y, m	z, m	I_{XX}, kg m^2	I_{YY}, kg m^2	I_{ZZ}, kg m^2	I_{XY}, kg m^2	I_{XZ}, kg m^2	I_{YZ}, kg m^2
I	6	475.5	-2.254	-4.121	-0.106	$+0.808 \times 10^4$	$+0.242 \times 10^4$	$+1.049 \times 10^4$	-0.442×10^4	-0.011×10^4	-0.021×10^4
I	7	475.5	-2.364	-4.342	-0.124	$+0.897 \times 10^4$	$+0.266 \times 10^4$	$+1.162 \times 10^4$	-0.488×10^4	-0.014×10^4	-0.026×10^4
I	8	475.5	-2.474	-4.564	-0.142	$+0.991 \times 10^4$	$+0.292 \times 10^4$	$+1.281 \times 10^4$	-0.537×10^4	-0.017×10^4	-0.031×10^4
I	9	475.5	-2.583	-4.785	-0.160	$+1.090 \times 10^4$	$+0.319 \times 10^4$	$+1.406 \times 10^4$	-0.588×10^4	-0.020×10^4	-0.036×10^4
I	10	475.5	-2.693	-5.006	-0.177	$+1.193 \times 10^4$	$+0.346 \times 10^4$	$+1.537 \times 10^4$	-0.641×10^4	-0.023×10^4	-0.042×10^4
I	11	475.5	-2.803	-5.228	-0.195	$+1.301 \times 10^4$	$+0.375 \times 10^4$	$+1.673 \times 10^4$	-0.697×10^4	-0.026×10^4	-0.048×10^4
I	12	475.5	-2.913	-5.449	-0.213	$+1.414 \times 10^4$	$+0.406 \times 10^4$	$+1.815 \times 10^4$	-0.755×10^4	-0.029×10^4	-0.055×10^4
I	13	475.5	-3.022	-5.670	-0.231	$+1.531 \times 10^4$	$+0.437 \times 10^4$	$+1.963 \times 10^4$	-0.815×10^4	-0.033×10^4	-0.062×10^4
I	14	475.5	-3.132	-5.892	-0.248	$+1.654 \times 10^4$	$+0.469 \times 10^4$	$+2.117 \times 10^4$	-0.877×10^4	-0.037×10^4	-0.070×10^4
I	15	475.5	-3.242	-6.113	-0.266	$+1.780 \times 10^4$	$+0.503 \times 10^4$	$+2.277 \times 10^4$	-0.942×10^4	-0.041×10^4	-0.077×10^4
I	16	475.5	-3.351	-6.334	-0.284	$+1.912 \times 10^4$	$+0.538 \times 10^4$	$+2.442 \times 10^4$	-1.009×10^4	-0.045×10^4	-0.085×10^4
I	17	475.5	-3.461	-6.556	-0.301	$+2.048 \times 10^4$	$+0.574 \times 10^4$	$+2.613 \times 10^4$	-1.079×10^4	-0.050×10^4	-0.094×10^4
I	18	475.5	-3.571	-6.777	-0.319	$+2.189 \times 10^4$	$+0.611 \times 10^4$	$+2.790 \times 10^4$	-1.151×10^4	-0.054×10^4	-0.103×10^4
I	19	475.5	-3.680	-6.999	-0.337	$+2.334 \times 10^4$	$+0.649 \times 10^4$	$+2.973 \times 10^4$	-1.225×10^4	-0.059×10^4	-0.112×10^4
I	20	475.5	-3.790	-7.220	-0.355	$+2.485 \times 10^4$	$+0.689 \times 10^4$	$+3.162 \times 10^4$	-1.301×10^4	-0.064×10^4	-0.122×10^4
I	21	475.5	-3.900	-7.441	-0.372	$+2.639 \times 10^4$	$+0.730 \times 10^4$	$+3.356 \times 10^4$	-1.380×10^4	-0.069×10^4	-0.132×10^4
I	22	475.5	-4.009	-7.663	-0.390	$+2.799 \times 10^4$	$+0.772 \times 10^4$	$+3.556 \times 10^4$	-1.461×10^4	-0.074×10^4	-0.142×10^4
I	23	475.5	-4.119	-7.884	-0.408	$+2.963 \times 10^4$	$+0.815 \times 10^4$	$+3.762 \times 10^4$	-1.544×10^4	-0.080×10^4	-0.153×10^4
I	24	475.5	-4.229	-8.105	-0.426	$+3.132 \times 10^4$	$+0.859 \times 10^4$	$+3.974 \times 10^4$	-1.630×10^4	-0.086×10^4	-0.164×10^4
I	25	475.5	-4.338	-8.327	-0.443	$+3.306 \times 10^4$	$+0.904 \times 10^4$	$+4.192 \times 10^4$	-1.718×10^4	-0.091×10^4	-0.176×10^4
I	26	475.5	-4.448	-8.548	-0.461	$+3.484 \times 10^4$	$+0.951 \times 10^4$	$+4.415 \times 10^4$	-1.808×10^4	-0.098×10^4	-0.187×10^4
I	27	475.5	-4.558	-8.769	-0.479	$+3.667 \times 10^4$	$+0.999 \times 10^4$	$+4.644 \times 10^4$	-1.900×10^4	-0.104×10^4	-0.200×10^4
I	28	475.5	-4.667	-8.991	-0.496	$+3.855 \times 10^4$	$+1.048 \times 10^4$	$+4.879 \times 10^4$	-1.995×10^4	-0.110×10^4	-0.212×10^4
I	29	475.5	-4.777	-9.212	-0.514	$+4.048 \times 10^4$	$+1.098 \times 10^4$	$+5.120 \times 10^4$	-2.093×10^4	-0.117×10^4	-0.225×10^4
I	30	475.5	-4.887	-9.433	-0.532	$+4.245 \times 10^4$	$+1.149 \times 10^4$	$+5.367 \times 10^4$	-2.192×10^4	-0.124×10^4	-0.239×10^4

Table B.3: Aeroplane AX-1 fuel mass and inertial properties (continued)

			Centre of Gravity			Moments of Inertia					
Tank	Strip	Mass, kg	x, m	y, m	z, m	I_{XX}, kg m^2	I_{YY}, kg m^2	I_{ZZ}, kg m^2	I_{XY}, kg m^2	I_{XZ}, kg m^2	I_{YZ}, kg m^2
I	31	475.5	−4.996	−9.655	−0.550	$+4.447 \times 10^4$	$+1.201 \times 10^4$	$+5.619 \times 10^4$	-2.294×10^4	-0.131×10^4	-0.252×10^4
I	32	475.5	−5.106	−9.876	−0.567	$+4.653 \times 10^4$	$+1.255 \times 10^4$	$+5.878 \times 10^4$	-2.398×10^4	-0.138×10^4	-0.266×10^4
I	33	475.5	−5.216	−10.09	−0.585	$+4.864 \times 10^4$	$+1.310 \times 10^4$	$+6.142 \times 10^4$	-2.504×10^4	-0.145×10^4	-0.281×10^4
I	34	475.5	−5.326	−10.31	−0.603	$+5.080 \times 10^4$	$+1.366 \times 10^4$	$+6.411 \times 10^4$	-2.613×10^4	-0.153×10^4	-0.296×10^4
I	35	475.5	−5.435	−10.54	−0.621	$+5.301 \times 10^4$	$+1.423 \times 10^4$	$+6.687 \times 10^4$	-2.724×10^4	-0.160×10^4	-0.311×10^4
I	36	475.5	−5.545	−10.76	−0.638	$+5.526 \times 10^4$	$+1.481 \times 10^4$	$+6.969 \times 10^4$	-2.837×10^4	-0.168×10^4	-0.327×10^4
I	37	475.5	−5.655	−10.98	−0.656	$+5.756 \times 10^4$	$+1.541 \times 10^4$	$+7.256 \times 10^4$	-2.953×10^4	-0.176×10^4	-0.343×10^4
I	38	475.5	−5.764	−11.20	−0.674	$+5.991 \times 10^4$	$+1.602 \times 10^4$	$+7.549 \times 10^4$	-3.071×10^4	-0.185×10^4	-0.359×10^4
I	39	475.5	−5.874	−11.42	−0.692	$+6.230 \times 10^4$	$+1.663 \times 10^4$	$+7.848 \times 10^4$	-3.191×10^4	-0.193×10^4	-0.376×10^4
I	40	475.5	−5.984	−11.64	−0.709	$+6.474 \times 10^4$	$+1.726 \times 10^4$	$+8.152 \times 10^4$	-3.314×10^4	-0.202×10^4	-0.393×10^4
I	41	475.5	−6.093	−11.86	−0.727	$+6.723 \times 10^4$	$+1.791 \times 10^4$	$+8.463 \times 10^4$	-3.439×10^4	-0.211×10^4	-0.410×10^4
I	42	475.5	−6.203	−12.08	−0.745	$+6.976 \times 10^4$	$+1.856 \times 10^4$	$+8.779 \times 10^4$	-3.566×10^4	-0.220×10^4	-0.428×10^4
I	43	475.5	−6.313	−12.31	−0.762	$+7.234 \times 10^4$	$+1.923 \times 10^4$	$+9.101 \times 10^4$	-3.695×10^4	-0.229×10^4	-0.446×10^4
I	44	475.5	−6.422	−12.53	−0.780	$+7.497 \times 10^4$	$+1.990 \times 10^4$	$+9.429 \times 10^4$	-3.827×10^4	-0.238×10^4	-0.465×10^4
I	45	475.5	−6.532	−12.75	−0.798	$+7.764 \times 10^4$	$+2.059 \times 10^4$	$+9.763 \times 10^4$	-3.961×10^4	-0.248×10^4	-0.484×10^4
I	46	475.5	−6.642	−12.97	−0.816	$+8.036 \times 10^4$	$+2.129 \times 10^4$	$+10.102 \times 10^4$	-4.098×10^4	-0.258×10^4	-0.503×10^4
I	47	475.5	−6.751	−13.19	−0.833	$+8.313 \times 10^4$	$+2.200 \times 10^4$	$+10.448 \times 10^4$	-4.236×10^4	-0.268×10^4	-0.523×10^4
I	48	475.5	−6.861	−13.41	−0.851	$+8.595 \times 10^4$	$+2.273 \times 10^4$	$+10.799 \times 10^4$	-4.377×10^4	-0.278×10^4	-0.543×10^4
I	49	475.5	−6.971	−13.63	−0.869	$+8.881 \times 10^4$	$+2.346 \times 10^4$	$+11.156 \times 10^4$	-4.521×10^4	-0.288×10^4	-0.563×10^4
I	50	475.5	−7.080	−13.86	−0.887	$+9.172 \times 10^4$	$+2.421 \times 10^4$	$+11.518 \times 10^4$	-4.666×10^4	-0.298×10^4	-0.584×10^4
I	51	475.5	−7.190	−14.08	−0.904	$+9.467 \times 10^4$	$+2.497 \times 10^4$	$+11.887 \times 10^4$	-4.814×10^4	-0.309×10^4	-0.605×10^4
I	52	475.5	−7.300	−14.30	−0.922	$+9.768 \times 10^4$	$+2.574 \times 10^4$	$+12.261 \times 10^4$	-4.965×10^4	-0.320×10^4	-0.627×10^4
I	53	475.5	−7.410	−14.52	−0.940	$+10.073 \times 10^4$	$+2.653 \times 10^4$	$+12.641 \times 10^4$	-5.117×10^4	-0.331×10^4	-0.649×10^4
I	54	475.5	−7.519	−14.74	−0.957	$+10.382 \times 10^4$	$+2.732 \times 10^4$	$+13.027 \times 10^4$	-5.272×10^4	-0.342×10^4	-0.671×10^4
I	55	475.5	−7.629	−14.96	−0.975	$+10.697 \times 10^4$	$+2.813 \times 10^4$	$+13.419 \times 10^4$	-5.429×10^4	-0.354×10^4	-0.694×10^4

Table B.3: Aeroplane AX-1 fuel mass and inertial properties (continued)

			Centre of Gravity			Moments of Inertia					
Tank	Strip	Mass, kg	x, m	y, m	z, m	I_{XX}, kg m^2	I_{YY}, kg m^2	I_{ZZ}, kg m^2	I_{XY}, kg m^2	I_{XZ}, kg m^2	I_{YZ}, kg m^2
I	56	475.5	−7.739	−15.18	−0.993	$+11.016 \times 10^4$	$+2.894 \times 10^4$	$+13.816 \times 10^4$	-5.589×10^4	-0.365×10^4	-0.717×10^4
I	57	475.5	−7.848	−15.41	−1.011	$+11.339 \times 10^4$	$+2.977 \times 10^4$	$+14.220 \times 10^4$	-5.751×10^4	-0.377×10^4	-0.741×10^4
I	58	475.5	−7.958	−15.63	−1.028	$+11.668 \times 10^4$	$+3.062 \times 10^4$	$+14.629 \times 10^4$	-5.915×10^4	-0.389×10^4	-0.764×10^4
I	59	475.5	−8.068	−15.85	−1.046	$+12.001 \times 10^4$	$+3.147 \times 10^4$	$+15.044 \times 10^4$	-6.081×10^4	-0.401×10^4	-0.789×10^4
I	60	475.5	−8.177	−16.07	−1.064	$+12.339 \times 10^4$	$+3.233 \times 10^4$	$+15.465 \times 10^4$	-6.250×10^4	-0.414×10^4	-0.813×10^4
I	61	475.5	−8.287	−16.29	−1.082	$+12.681 \times 10^4$	$+3.321 \times 10^4$	$+15.891 \times 10^4$	-6.421×10^4	-0.426×10^4	-0.838×10^4
I	62	475.5	−8.397	−16.51	−1.099	$+13.028 \times 10^4$	$+3.410 \times 10^4$	$+16.323 \times 10^4$	-6.594×10^4	-0.439×10^4	-0.863×10^4
I	63	475.5	−8.506	−16.73	−1.117	$+13.380 \times 10^4$	$+3.500 \times 10^4$	$+16.762 \times 10^4$	-6.770×10^4	-0.452×10^4	-0.889×10^4
I	64	475.5	−8.616	−16.95	−1.135	$+13.737 \times 10^4$	$+3.591 \times 10^4$	$+17.206 \times 10^4$	-6.948×10^4	-0.465×10^4	-0.915×10^4
I	65	475.5	−8.726	−17.18	−1.153	$+14.098 \times 10^4$	$+3.684 \times 10^4$	$+17.655 \times 10^4$	-7.128×10^4	-0.478×10^4	-0.942×10^4
I	66	475.5	−8.835	−17.40	−1.170	$+14.464 \times 10^4$	$+3.777 \times 10^4$	$+18.111 \times 10^4$	-7.311×10^4	-0.492×10^4	-0.968×10^4
I	67	475.5	−8.945	−17.62	−1.188	$+14.835 \times 10^4$	$+3.872 \times 10^4$	$+18.572 \times 10^4$	-7.496×10^4	-0.505×10^4	-0.995×10^4
I	68	475.5	−9.055	−17.84	−1.206	$+15.210 \times 10^4$	$+3.968 \times 10^4$	$+19.039 \times 10^4$	-7.683×10^4	-0.519×10^4	-1.023×10^4
I	69	475.5	−9.164	−18.06	−1.223	$+15.590 \times 10^4$	$+4.065 \times 10^4$	$+19.512 \times 10^4$	-7.872×10^4	-0.533×10^4	-1.051×10^4
I	70	475.5	−9.274	−18.28	−1.241	$+15.975 \times 10^4$	$+4.163 \times 10^4$	$+19.991 \times 10^4$	-8.064×10^4	-0.547×10^4	-1.079×10^4
C	1	2170	−1.596	2.793	0.000	$+1.693 \times 10^4$	$+0.553 \times 10^4$	$+2.246 \times 10^4$	$+0.968 \times 10^4$	0.000×10^4	0.000×10^4
C	2	2170	−1.596	2.048	0.000	$+0.910 \times 10^4$	$+0.553 \times 10^4$	$+1.463 \times 10^4$	$+0.710 \times 10^4$	0.000×10^4	0.000×10^4
C	3	2170	−1.596	1.676	0.000	$+0.609 \times 10^4$	$+0.553 \times 10^4$	$+1.162 \times 10^4$	$+0.581 \times 10^4$	0.000×10^4	0.000×10^4
C	4	2170	−1.596	1.303	0.000	$+0.369 \times 10^4$	$+0.553 \times 10^4$	$+0.922 \times 10^4$	$+0.452 \times 10^4$	0.000×10^4	0.000×10^4
C	5	2170	−1.596	0.931	0.000	$+0.188 \times 10^4$	$+0.553 \times 10^4$	$+0.741 \times 10^4$	$+0.323 \times 10^4$	0.000×10^4	0.000×10^4
C	6	2170	−1.596	0.559	0.000	$+0.068 \times 10^4$	$+0.553 \times 10^4$	$+0.621 \times 10^4$	$+0.194 \times 10^4$	0.000×10^4	0.000×10^4
C	7	2170	−1.596	0.186	0.000	$+0.008 \times 10^4$	$+0.553 \times 10^4$	$+0.561 \times 10^4$	$+0.065 \times 10^4$	0.000×10^4	0.000×10^4
C	8	2170	−1.596	0.000	0.000	$+0.000 \times 10^4$	$+0.553 \times 10^4$	$+0.553 \times 10^4$	0.000×10^4	0.000×10^4	0.000×10^4
T	1	106.7	−38.05	−9.702	−4.049	$+1.179 \times 10^4$	$+15.618 \times 10^4$	$+16.447 \times 10^4$	-3.938×10^4	-1.644×10^4	-0.419×10^4
T	2	106.7	−37.57	−8.858	−3.973	$+1.005 \times 10^4$	$+15.226 \times 10^4$	$+15.895 \times 10^4$	-3.550×10^4	-1.592×10^4	-0.375×10^4

Table B.3: Aeroplane AX-1 fuel mass and inertial properties (continued)

			Centre of Gravity			Moments of Inertia					
Tank	Strip	Mass, kg	x, m	y, m	z, m	I_{XX}, kg m^2	I_{YY}, kg m^2	I_{ZZ}, kg m^2	I_{XY}, kg m^2	I_{XZ}, kg m^2	I_{YZ}, kg m^2
T	3	106.7	−37.33	−8.437	−3.935	$+0.924 \times 10^4$	$+15.032 \times 10^4$	$+15.626 \times 10^4$	-3.360×10^4	-1.567×10^4	-0.354×10^4
T	4	106.7	−37.09	−8.015	−3.897	$+0.847 \times 10^4$	$+14.839 \times 10^4$	$+15.363 \times 10^4$	-3.171×10^4	-1.542×10^4	-0.333×10^4
T	5	106.7	−36.85	−7.593	−3.859	$+0.774 \times 10^4$	$+14.648 \times 10^4$	$+15.104 \times 10^4$	-2.985×10^4	-1.517×10^4	-0.313×10^4
T	6	106.7	−36.61	−7.171	−3.821	$+0.704 \times 10^4$	$+14.458 \times 10^4$	$+14.850 \times 10^4$	-2.801×10^4	-1.493×10^4	-0.292×10^4
T	7	106.7	−36.37	−6.749	−3.783	$+0.639 \times 10^4$	$+14.269 \times 10^4$	$+14.602 \times 10^4$	-2.619×10^4	-1.468×10^4	-0.272×10^4
T	8	106.7	−36.13	−6.327	−3.745	$+0.577 \times 10^4$	$+14.081 \times 10^4$	$+14.358 \times 10^4$	-2.439×10^4	-1.444×10^4	-0.253×10^4
T	9	106.7	−35.90	−5.906	−3.707	$+0.519 \times 10^4$	$+13.894 \times 10^4$	$+14.120 \times 10^4$	-2.261×10^4	-1.420×10^4	-0.234×10^4
T	10	106.7	−35.66	−5.484	−3.669	$+0.464 \times 10^4$	$+13.709 \times 10^4$	$+13.886 \times 10^4$	-2.086×10^4	-1.396×10^4	-0.215×10^4
T	11	106.7	−35.42	−5.062	−3.631	$+0.414 \times 10^4$	$+13.525 \times 10^4$	$+13.657 \times 10^4$	-1.913×10^4	-1.372×10^4	-0.196×10^4
T	12	106.7	−35.18	−4.640	−3.593	$+0.367 \times 10^4$	$+13.342 \times 10^4$	$+13.434 \times 10^4$	-1.741×10^4	-1.349×10^4	-0.178×10^4
T	13	106.7	−34.94	−4.218	−3.555	$+0.325 \times 10^4$	$+13.160 \times 10^4$	$+13.215 \times 10^4$	-1.572×10^4	-1.325×10^4	-0.160×10^4
T	14	106.7	−34.70	−3.796	−3.517	$+0.286 \times 10^4$	$+12.980 \times 10^4$	$+13.002 \times 10^4$	-1.405×10^4	-1.302×10^4	-0.142×10^4
T	15	106.7	−34.46	−3.375	−3.479	$+0.251 \times 10^4$	$+12.801 \times 10^4$	$+12.793 \times 10^4$	-1.241×10^4	-1.279×10^4	-0.125×10^4
T	16	106.7	−34.22	−2.953	−3.441	$+0.219 \times 10^4$	$+12.623 \times 10^4$	$+12.590 \times 10^4$	-1.078×10^4	-1.256×10^4	-0.108×10^4
T	17	106.7	−33.98	−2.531	−3.403	$+0.192 \times 10^4$	$+12.447 \times 10^4$	$+12.391 \times 10^4$	-0.918×10^4	-1.234×10^4	-0.092×10^4
T	18	106.7	−33.75	−2.109	−3.365	$+0.168 \times 10^4$	$+12.271 \times 10^4$	$+12.198 \times 10^4$	-0.759×10^4	-1.211×10^4	-0.076×10^4
T	19	106.7	−33.51	−1.687	−3.327	$+0.148 \times 10^4$	$+12.097 \times 10^4$	$+12.009 \times 10^4$	-0.603×10^4	-1.189×10^4	-0.060×10^4
T	20	106.7	−33.27	−1.265	−3.289	$+0.132 \times 10^4$	$+11.924 \times 10^4$	$+11.826 \times 10^4$	-0.449×10^4	-1.167×10^4	-0.044×10^4
T	21	106.7	−33.03	−0.844	−3.251	$+0.120 \times 10^4$	$+11.753 \times 10^4$	$+11.648 \times 10^4$	-0.297×10^4	-1.146×10^4	-0.029×10^4
T	22	106.7	−32.79	−0.422	−3.213	$+0.112 \times 10^4$	$+11.582 \times 10^4$	$+11.474 \times 10^4$	-0.148×10^4	-1.124×10^4	-0.014×10^4
T	23	106.7	−32.55	0.000	−3.175	$+0.108 \times 10^4$	$+11.413 \times 10^4$	$+11.306 \times 10^4$	0.000×10^4	-1.103×10^4	0.000×10^4

Table B.3: Aeroplane AX-1 fuel mass and inertial properties (continued)

B.3 Mode Shapes

B.3.1 Mass Case: OWE

MODE: 1
FREQUENCY: 7.958 rad s^{-1}

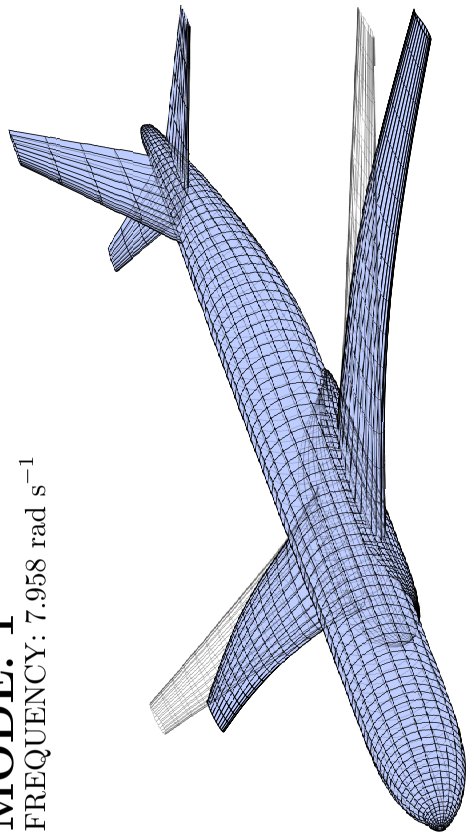

MODE: 2
FREQUENCY: 7.958 rad s^{-1}

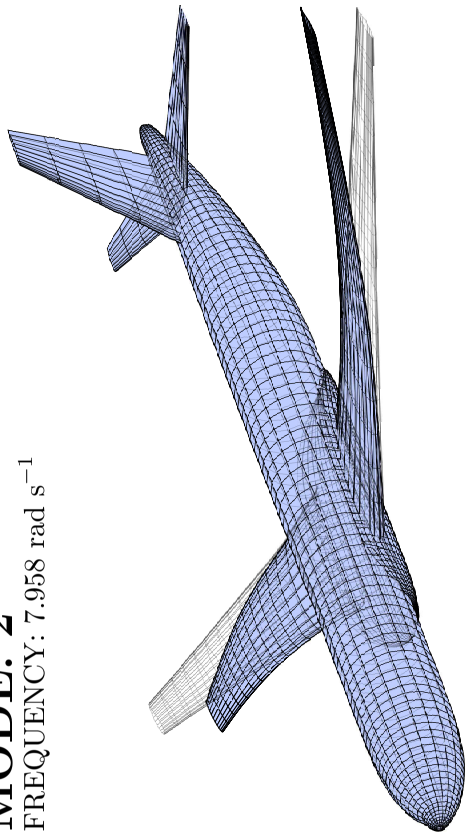

MODE: 5
FREQUENCY: 16.817 rad s^{-1}

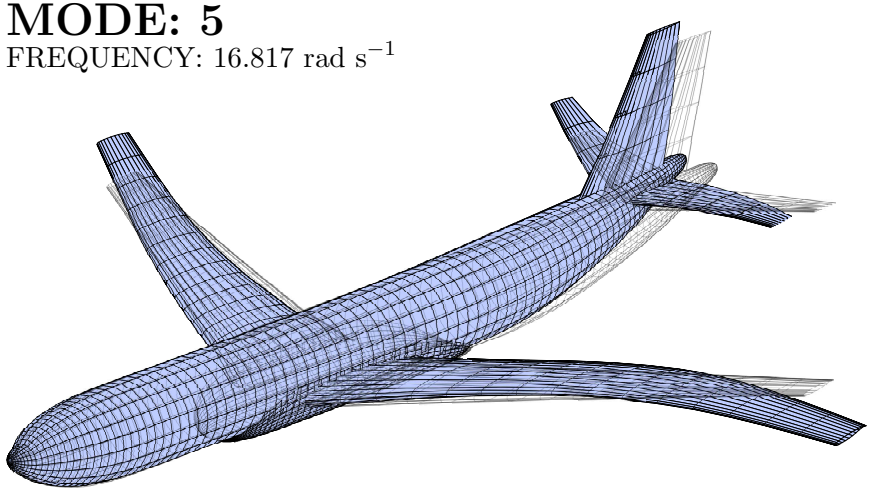

MODE: 3
FREQUENCY: 8.698 rad s^{-1}

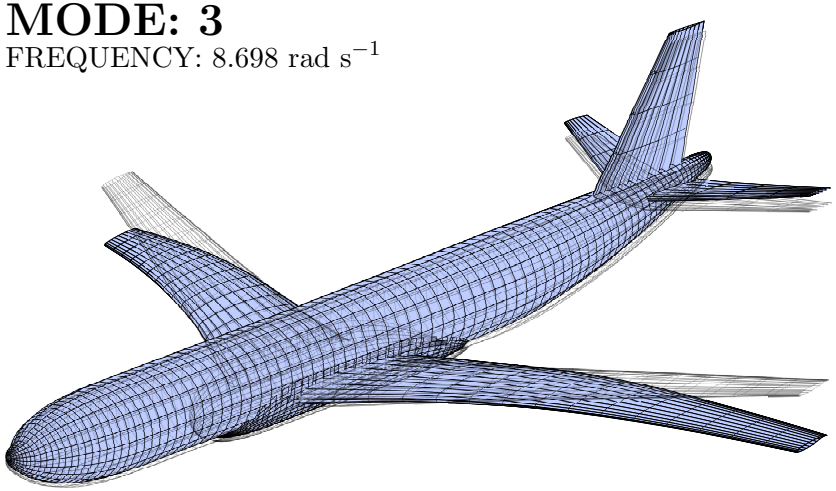

MODE: 6
FREQUENCY: 16.817 rad s^{-1}

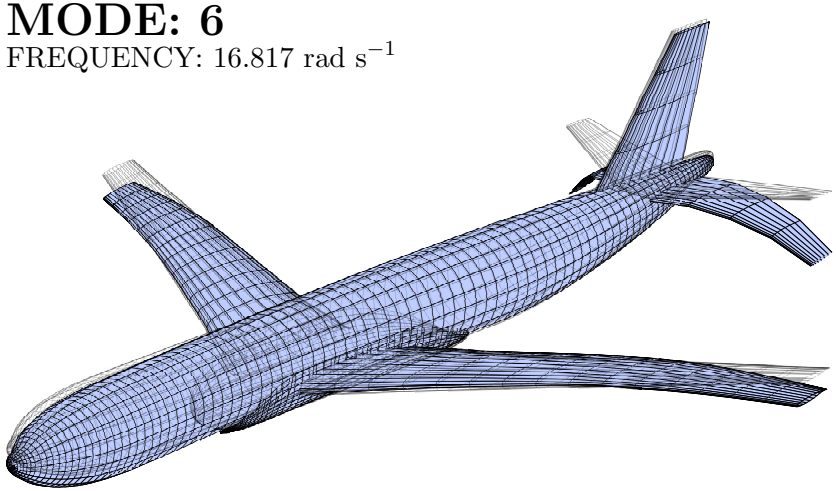

MODE: 4
FREQUENCY: 14.891 rad s^{-1}

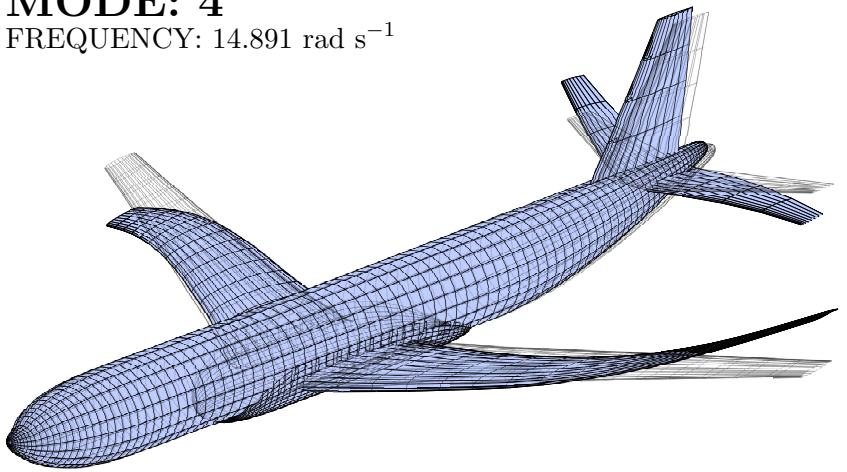

MODE: 9
FREQUENCY: 20.439 rad s^{-1}

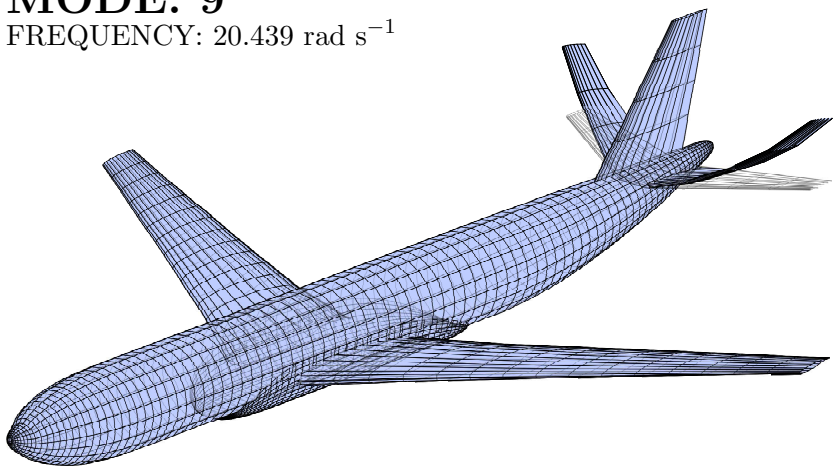

MODE: 7
FREQUENCY: 16.924 rad s^{-1}

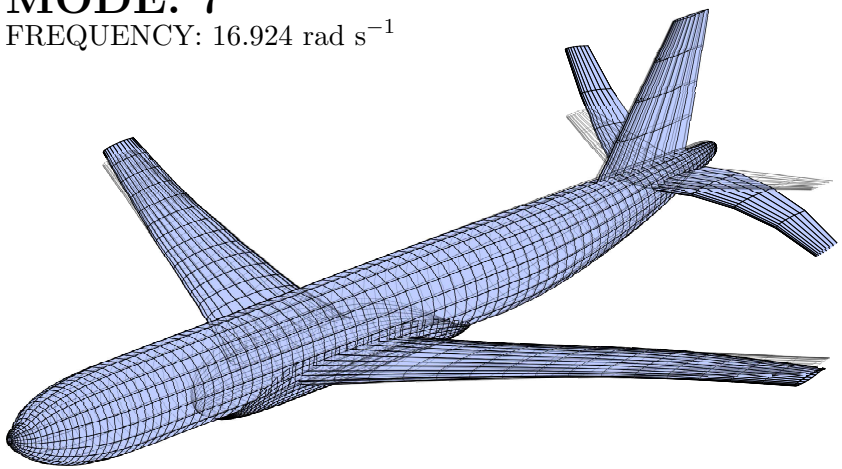

MODE: 10
FREQUENCY: 21.434 rad s^{-1}

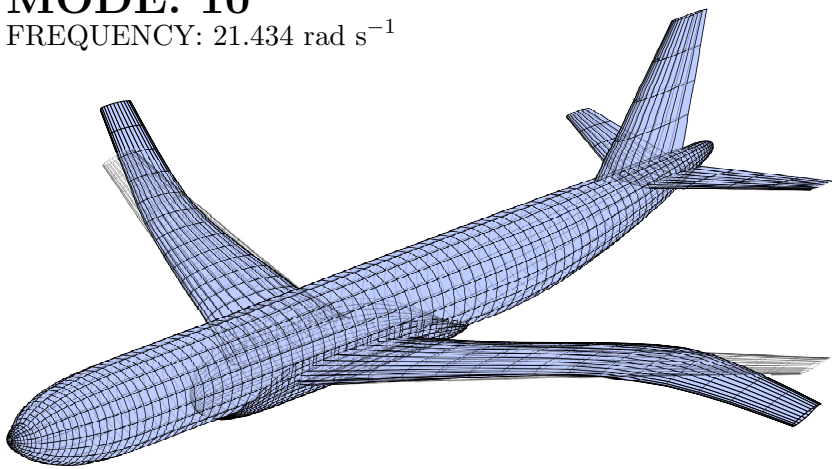

MODE: 8
FREQUENCY: 17.254 rad s^{-1}

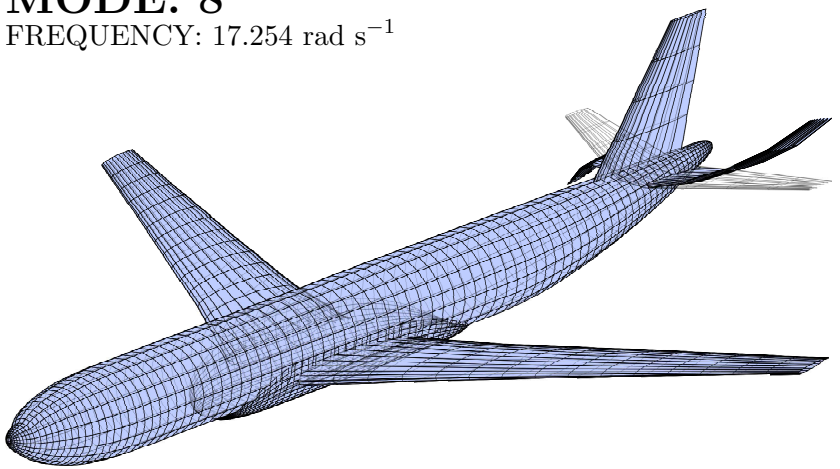

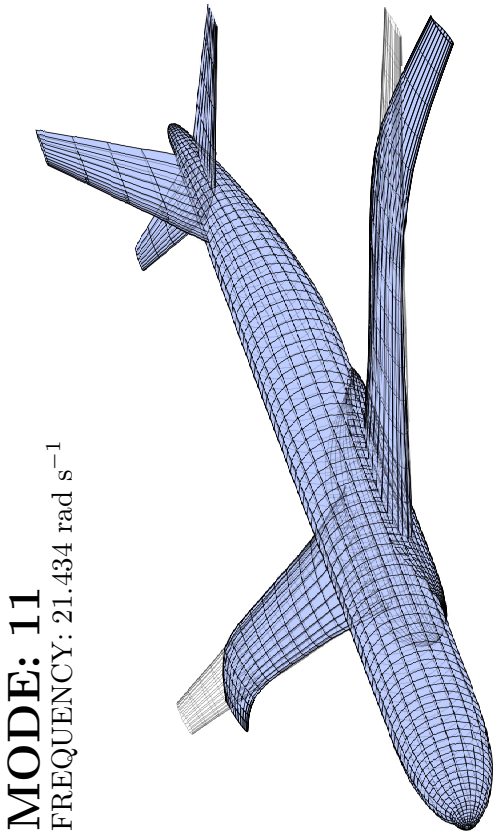

MODE: 11
FREQUENCY: 21.434 rad s^{-1}

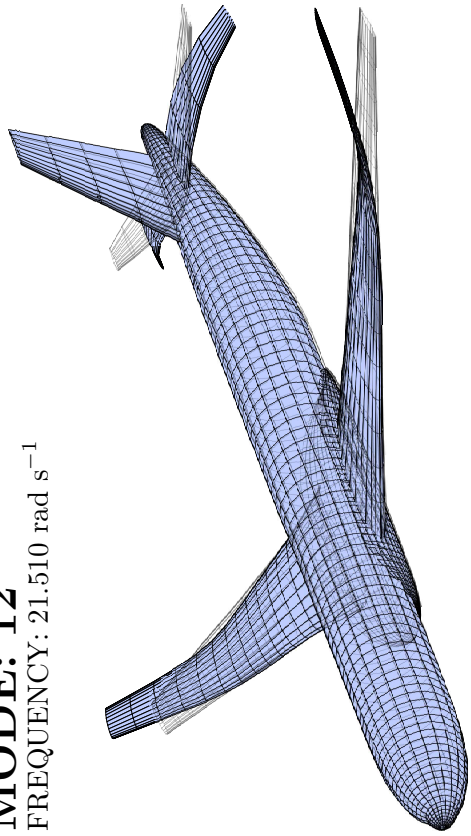

MODE: 12
FREQUENCY: 21.510 rad s^{-1}

B.3.2 Mass Case: Light

MODE: 1
FREQUENCY: 7.296 rad s^{-1}

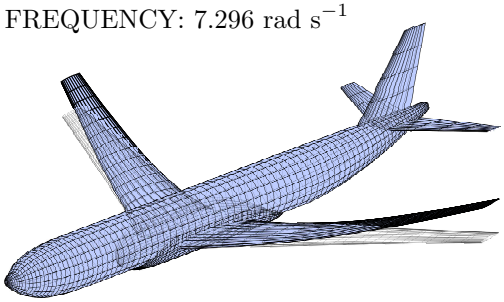

MODE: 2
FREQUENCY: 7.296 rad s^{-1}

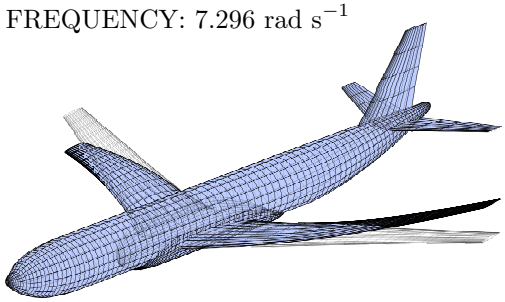

MODE: 3
FREQUENCY: 8.024 rad s^{-1}

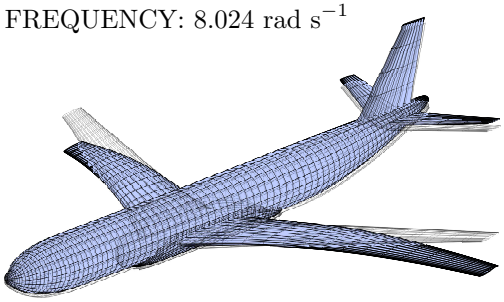

MODE: 4
FREQUENCY: 13.685 rad s^{-1}

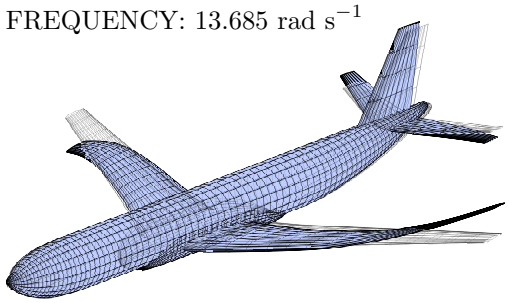

MODE: 5
FREQUENCY: 15.807 rad s^{-1}

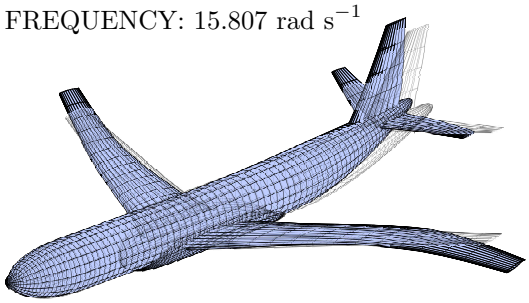

MODE: 6
FREQUENCY: 16.451 rad s^{-1}

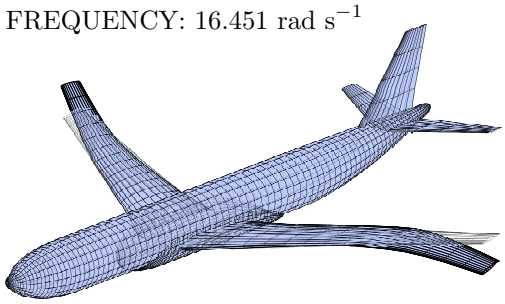

MODE: 7
FREQUENCY: 16.451 rad s^{-1}

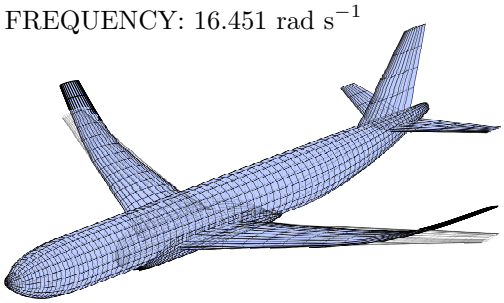

MODE: 8
FREQUENCY: 16.530 rad s^{-1}

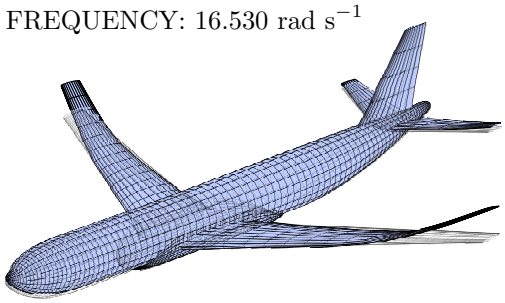

MODE: 9
FREQUENCY: 18.717 rad s^{-1}

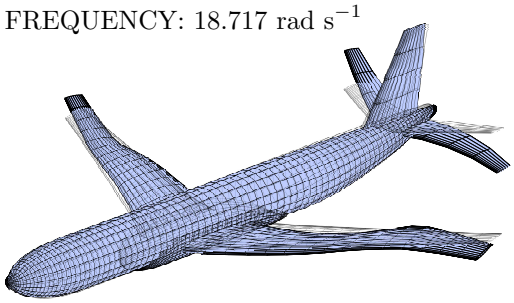

MODE: 10
FREQUENCY: 19.138 rad s^{-1}

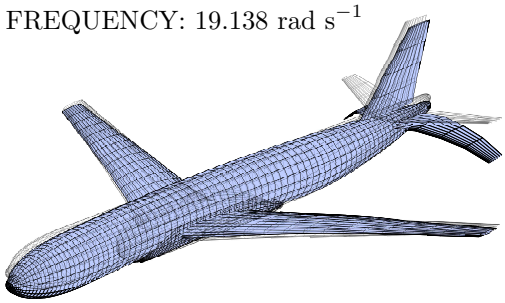

MODE: 11
FREQUENCY: 19.515 rad s^{-1}

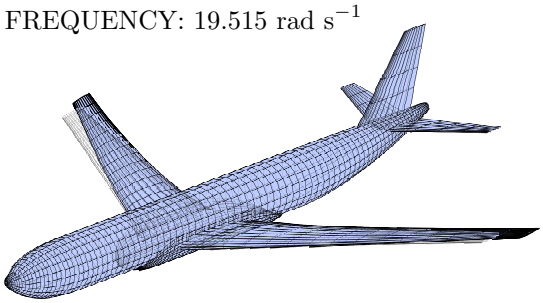

MODE: 12
FREQUENCY: 19.515 rad s^{-1}

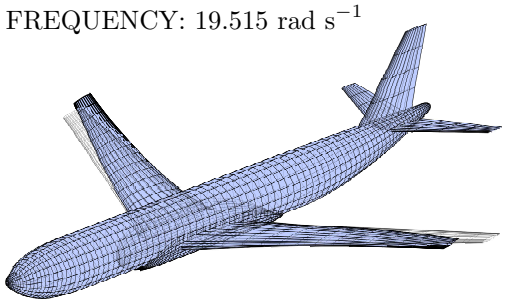

B.3.3 Mass Case: Heavy

MODE: 1
FREQUENCY: 6.135 rad s^{-1}

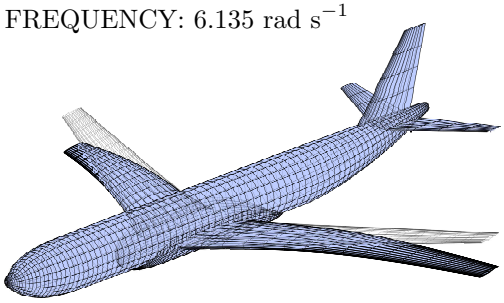

MODE: 2
FREQUENCY: 6.135 rad s^{-1}

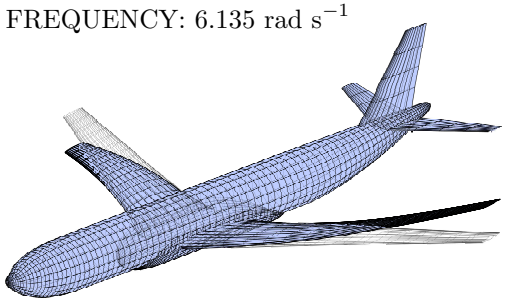

MODE: 3
FREQUENCY: 6.803 rad s^{-1}

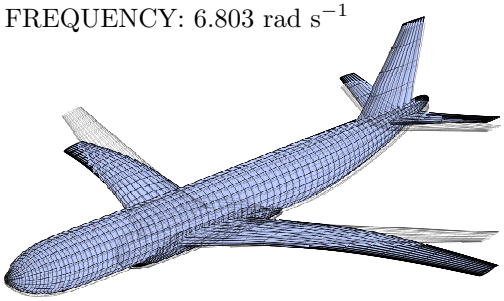

MODE: 4
FREQUENCY: 11.457 rad s^{-1}

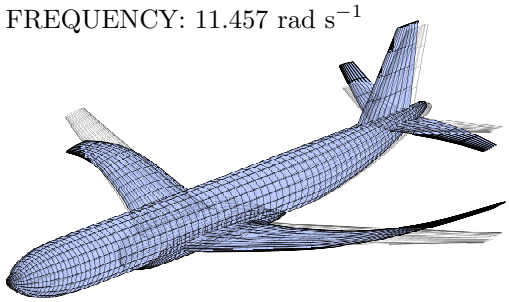

MODE: 5
FREQUENCY: 13.344 rad s^{-1}

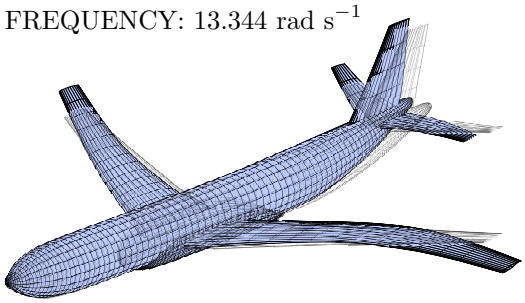

MODE: 6
FREQUENCY: 14.513 rad s^{-1}

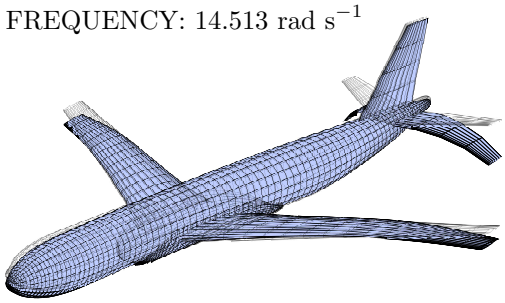

MODE: 7
FREQUENCY: 14.865 rad s^{-1}

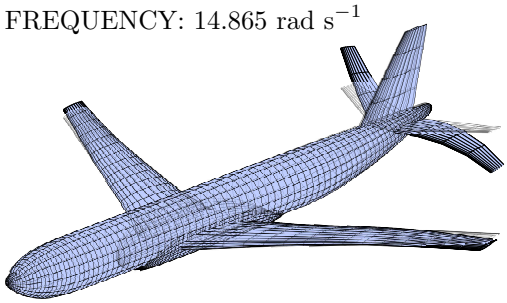

MODE: 8
FREQUENCY: 15.453 rad s^{-1}

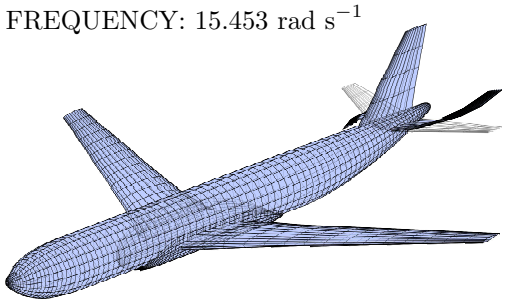

MODE: 9
FREQUENCY: 15.453 rad s^{-1}

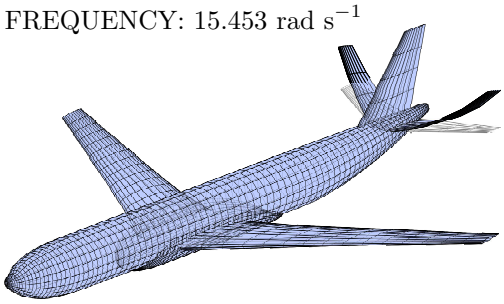

MODE: 10
FREQUENCY: 15.463 rad s^{-1}

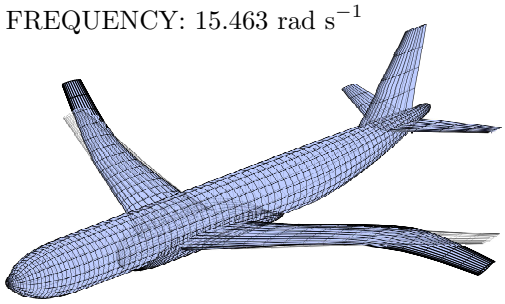

MODE: 11
FREQUENCY: 15.463 rad s^{-1}

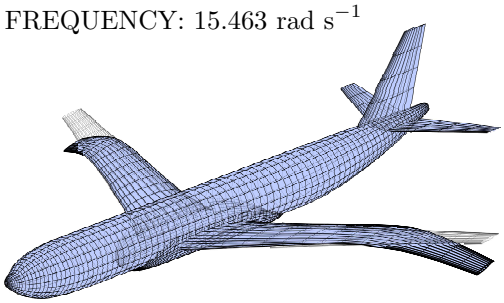

MODE: 12
FREQUENCY: 15.838 rad s^{-1}

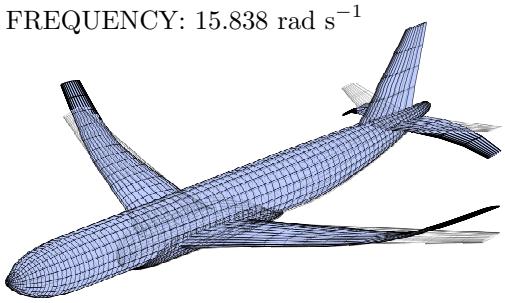

This page is intentionally left blank.

APPENDIX C

MATLAB/Simulink Model

This chapter presents a brief description of the MATLAB/Simulink implementation of the flexible aeroplane model described in Chapter 3.

C.1 Introduction

An implementation of the aeroelastic flexible aircraft model defined in Chapter 3 has been developed in MATLAB/Simulink [Figure C.1]. The aircraft model itself is implemented in Simulink, incorporating a number of user-defined functions, as well as existing blocks from the standard Simulink and Aerospace Blockset libraries. Initialisation and post-processing MATLAB scripts and functions are included for trim and linearisation of the model. The generic, modular structure of the Simulink model easily allows the definition of all input parameters. However, a numerical example representative of a large aeroplane, the Aeroplane AX-1 [Section 5.1], is provided. The requisite aerodynamic, structural, and geometric aircraft data is defined in Appendices A, B, and D.

This appendix includes a description of the provided MATLAB initialisation and post-processing scripts and functions (including a definition of the required inputs and outputs); a description of the required workspace variables and their correct format; a brief introduction to the provided Simulink models and libraries; and an overview of the Simulink model subsystems. Additional documentation is provided within the MATLAB/Simulink model.

C.2 MATLAB Functions

Script: `data_aircraft`
Inputs: –
Outputs: –
Description: Defines all aerodynamic, structural, and aircraft properties of the Simulink model to be used in the initialisation and trim of the model

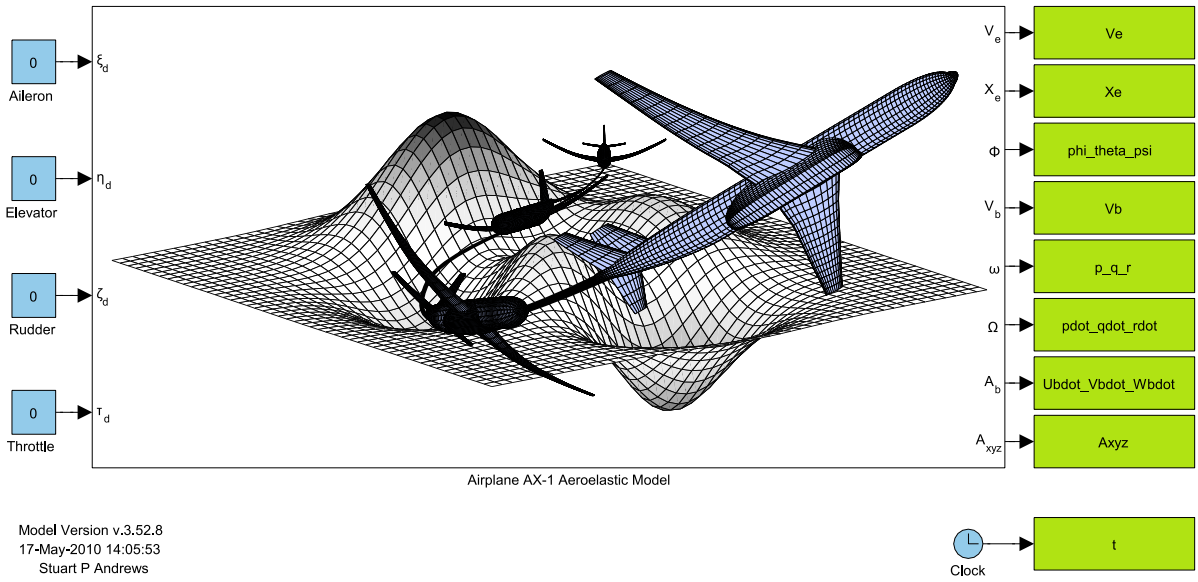

Figure C.1: MATLAB/Simulink Aeroelastic Aircraft Model

Script: `data_lookup_tables`
Inputs: –
Outputs: –
Description: Define lookup tables used for simulating aerodynamics of fuselage and wing

Script: `data_unsteady_aero`
Inputs: –
Outputs: –
Description: Define state-space unsteady aerodynamic coefficients

Script: `data_unsteady_aero`
Inputs: –
Outputs: –
Description: Define state-space unsteady aerodynamic coefficients

Script: `initialise`
Inputs: –
Outputs: –
Description: Initialise aircraft model variables for simulation

Function: `initialise_aero_ss_model`
Inputs: `A1 A2 A3 A4 b1 b2 b3 b4 b5 b6 k1 k2 a_s chord_aero eta_xi F1 F4 F8 F10 F11 Beta m_aero U_e Mach x_e`
Outputs: `A_ua B_ua C_ua D_ua D_sa`
Description: Calculate unsteady aerodynamic state-space model

Function: `initialise_aero_stations`

Inputs: `semispan lambda chord_root chord_tip eta_crank thickchord_crank gamma_crank alpha_twist_crank U_e m_aero Mach nu x_ac x_zero x_root`
Outputs: `thickchord_aero alpha_twist_aero eta_aero chord_aero gamma_aero liftcurve_aero xyz_ac_aero xyz_ce_aero xyz_te_aero`
Description: Initialise aerodynamic data for the wing at each spanwise station for given flight condition

Function: `initialise_aero_striptheory`
Inputs: `Beta liftcurve_aero chord_aero semispan lambda`
Outputs: `A_striptheory B_striptheory`
Description: Calculate aerodynamic influence matrix using modified strip theory

Function: `initialise_aero_tail`
Inputs: `m_aero_tail chord_aero_tail U_e Mach nu`
Outputs: `liftcurve_aero_tail thickchord_aero_tail`
Description: Initialise tail aerodynamic properties from local aerodynamic coefficient data for fixed spanwise thickness/chord ratio

Function: `initialise_flight_condition`
Inputs: `U_e h`
Outputs: `Mach Beta rho a_s nu`
Description: Calculate atmospheric flight conditions at altitude, `h`, and velocity, `U_e`

Script: `initialise_model_aircraft`
Inputs: –
Outputs: –
Description: Initialise model parameters at desired flight point

Script: `initialise_states`
Inputs: –
Outputs: –
Description: Define state-space state trim initial values and constraints

Function: `initialise_struct`
Inputs: `modes_struct struct_mode_damp`
Outputs: `nmm_mass nmm_freq nmm_damp mode_shape mode_shape_trnsp mass_vctr`
Description: Initialise structural model, calculate mode shapes and natural frequencies, truncate, and generate modal damping matrices

Function: `initialise_struct_beam3d_eigensolve`
Inputs: `K M`
Outputs: `mode_shape natural_freq`
Description: Calculate eigenvectors and values from mass and stiffness matrices

Function: `initialise_struct_beam3d_identify`
Inputs: `mode`
Outputs: `mode_shape natural_freq M`
Description: Identify natural frequencies and mode shapes of structure from .in file

Function: `initialise_struct_beam3d_opmass`
Inputs: –
Outputs: `struct_opmass`
Description: Calculate total mass of airframe, including fuel, payload, and airframe mass

Function: `initialise_struct_beam3d_read`
Inputs: –
Outputs: `K M`
Description: Read full aircraft model .out file

Function: `initialise_struct_beam3d_selection`
Inputs: –
Outputs: `modes`
Description: Graphical user selection of structural modes [Figure C.2]

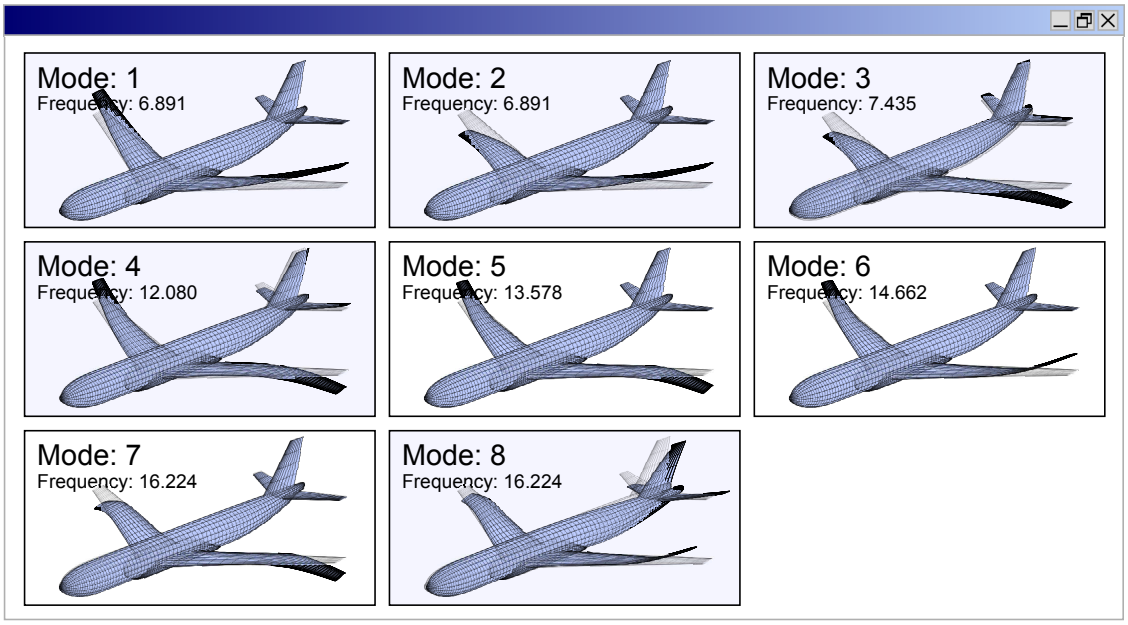

Figure C.2: Aeroelastic Aircraft Model – Structural mode selection GUI

Function: `initialise_struct_beam3d_sort`
Inputs: `mode_shape natural_freq`
Outputs: `mode_shape natural_freq`
Description: Sort mode shapes in ascending order of natural frequency

Function: `initialise_struct_beam3d_unified`
Inputs: –
Outputs: `mode_shape natural_freq mass_matrix`
Description: Write .out, read .in files, and calculate natural frequencies and mode shapes

Function: `initialise_struct_beam3d_write`
Inputs: `mode EI_RB GJ_RB`
Outputs: –
Description: Write full aircraft model .in file

Function: `initialise_struct_mass_matrix`
Inputs: –
Outputs: `mass_matrix`
Description: Generate structural mass matrix

Function: `initialise_tail`
Inputs: `m_aero_tail eta_aero eta_aero_tail semispan semispan_tail xyz_te_aero xyz_ce_aero xyz_le_aero_tail U_e`
Outputs: `ss_coeff_tail fir_coeff_tail fir_vortex_coeff_tail fir_sample_tail fir_gain`
Description: Initialise tailplane downwash steady and unsteady aerodynamic state-space models

Function: `initialise_wing_control`
Inputs: `x_e`
Outputs: `F1 F4 F8 F10 F11`
Description: Define aerodynamic surface, i.e. wing, tail and fin, control surface geometric properties

Function: `initialise_wing_control_stations`
Inputs: `eta_xi_inboard eta_xi_outboard m_aero`
Outputs: `eta_xi`
Description: Define spanwise aerodynamic stations that include a control surface

Function: `initialise_wing_equivalent`
Inputs: `n_crank chord_root chord_crank y_crank semispan y_fuselage chord_tip x_tip lambda_crank`
Outputs: `chord_root chord_tip x_root lambda wingarea`
Description: Calculate equivalent swept wing from swept, cranked wing

Script: `trim_model_aircraft`
Inputs: –
Outputs: –
Description: Trim reduced-order model, and analytically calculate unknown states in full-order aircraft model

Function: `trim_states`
Inputs: `U V W p q r xi_port xi_stbd eta zeta mode_eta mode_shape eta_struct eta_struct_tail eta_struct_fin eta_aero eta_aero_tail eta_aero_fin fir_gain_tail D_sa lambda lambda_tail lambda_fin semispan semispan_tail semispan_fin alpha_twist_aero alpha_twist_aero_tail gamma_aero gamma_aero_tail fir_vortex_coeff_tail h A_st xyz_struct xyz_cog xyz_ea_aero xyz_ea_aero_tail xyz_ea_aero_fin A_ua B_ua A_ua_tail B_ua_tail A_ua_fin B_ua_fin chord_aero thickchord_aero C_LDM_col C_LDM_row C_LDM_tri C_L_alphazero ss_coeff_tail`
Outputs: `x_wing x_tail x_fin x_dwnsh`
Description: Calculate unknown trimmed states for unsteady aerodynamics, downwash and engine from trimmed structural states

C.3 Simulink Models

Model: `model_aircraft`
Description: The primary MATLAB/Simulink model, it includes the complete flexible aeroelastic aircraft model defined in the library `model_structure_library`), the standard six degree-of-freedom rigid-body equations of motion, as well as actuator dynamics. All final signals are output to the MATLAB workspace. Includes real-time beam element aircraft animation [Figure C.3].

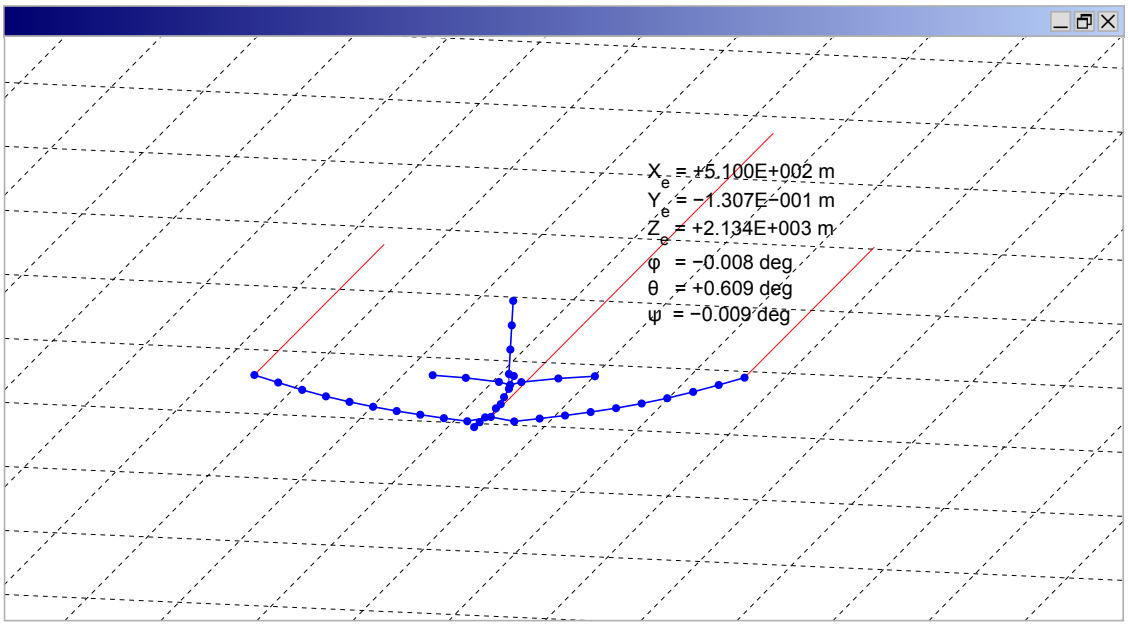

Figure C.3: Aeroelastic Aircraft Model – Beam element aircraft animation

Model: `model_aircraft_trim`

Description: A reduced-order version of the primary model, `model_aircraft`, this version removes unsteady aerodynamic dynamic states and engine dynamics. This reduced-order aeroelastic aircraft model is defined in the library `model_structure_trim_library`. The standard six degree-of-freedom rigid-body equations of motion are included. This version of the model is designed to enable a steady-state trim solution to be found easily, and initial state values and constraints are defined in the workspace `state_` variables. The function `trim_states` is provided to estimate the steady-state state values for the full-order model.

Library: `model_structure_library`
Description: A MATLAB/Simulink library defining the complete aeroelastic aircraft model excluding rigid-body dynamics. This library is used in the primary model, `model_aircraft`.

Library: `model_structure_trim_library`
Description: A MATLAB/Simulink library defining the reduced-order aeroelastic aircraft model excluding rigid-body dynamics. All unsteady aerodynamic and engine dynamic states have been removed. This library is used in the trim model, `model_aircraft_trim`.

C.4 Simulink Subsystem Blocks

This section describes in brief the subsystems contained within the MATLAB/Simulink model libraries. The block diagrams [Figures C.1 through C.10] are colour-coded according to the following key:

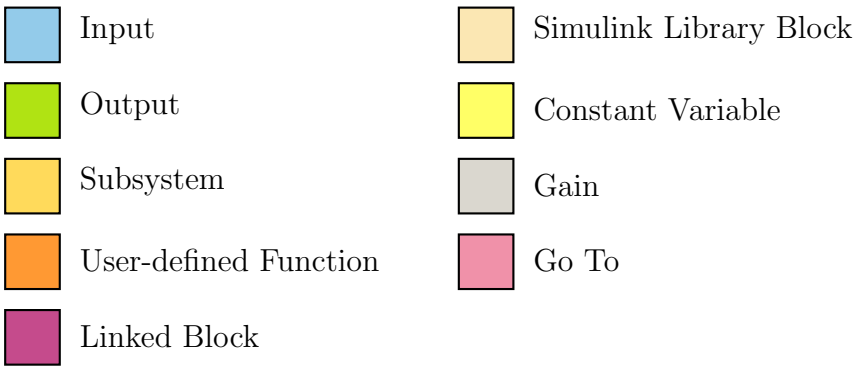

Subsystem: Aeroelastic Aircraft Model
Location: `model_aircraft`
Figure: C.1
Description: The top level model structure includes the basic aeroelastic aircraft model. Inputs are the standard rigid-aircraft control surface deflections, i.e. elevator, aileron, rudder and throttle. Outputs are the standard rigid-body aircraft states, i.e. attitude, position, acceleration and linear and angular velocity.

Subsystem: Aeroelastic Aircraft Model – Model Aircraft
Location: `model_aircraft\aircraft_model`
Figure: C.4
Description: The model aircraft subsystem separates the model aircraft from the control surface inputs, which here include actuator dynamics, saturation and rate limits, as well as trimmed flight initial values.

Subsystem: Aeroelastic Aircraft Model – Equations of Motion
Location: `model_aircraft\aircraft_model\equations_motion`
Figure: C.5
Description: The equations of motion are defined in this subsystem separately for the aeroelastic, flexible-body and rigid-body modes. The standard, fixed mass six degree-of-freedom equations of motion are taken from the MATLAB/Simulink Aerospace Blockset.

Subsystem: Aeroelastic Aircraft Model – Aeroelastic Model
Location: `model_aircraft\aircraft_model\equations_motion\...`
`aeroelastic_model`
Figure: C.6
Description: The aeroelastic model couples the unsteady aerodynamic model of the aircraft, which is a function of the rigid-body motion, with the structural dynamics of the airframe.

Subsystem: Aeroelastic Aircraft Model – Aerodynamic Model
Location: `model_aircraft\aircraft_model\equations_motion\...`
`aeroelastic_model\aerodynamic_model`
Figure: C.7
Description: The aerodynamic model separates the calculation of the individual component aerodynamic forces and moments, in addition to the thrust produced by the engines. The calculation of the wing and tail aerodynamic forces are coupled through the unsteady tailplane downwash function.

Subsystem: Aeroelastic Aircraft Model – Lifting Surface Model
Location: `model_aircraft\aircraft_model\equations_motion\...`
`aeroelastic_model\aerodynamic_model\lifting_surface`
Figure: C.8
Description: The aerodynamic surface subsystem calculates the aerodynamic forces generated by the primary aircraft lifting surfaces, i.e. the wing, tailplane and fin. The local nodal angle of attack is calculated for each spanwise station as a function of the rigid-body motion, structural deformation, and local gust velocity.

Subsystem: Aeroelastic Aircraft Model – Unsteady Strip Theory Model
Location: `model_aircraft\aircraft_model\equations_motion\...`
`aeroelastic_model\aerodynamic_model\lifting_surface\...`
`unsteady_strip_theory`

Figure: C.9
Description: The aerodynamic forces and moments for each primary aircraft lifting surface are calculated from the local nodal angle of attack. The unsteady aerodynamic response for each spanwise section is calculated using the indicial aerodynamic model, and the local lift and drag coefficient transformed back into body-axis. The local aerodynamic forces and moments are then calculated at the structural nodes, and the total aerodynamic forces calculated for the three-dimensional surface using the modified strip theory. The total forces and moments for the rigid-body aircraft and at each structural node are then output.

Subsystem: Aeroelastic Aircraft Model – Structural Equations of Motion
Location: `model_aircraft\aircraft_model\equations_motion\...`
`aeroelastic_model\structural_model\equations_motion`
Figure: C.10
Description: The structural equations of motion are defined using the normal mode method. The generalised force and mass are calculated, and the product integrated to return the generalised acceleration, velocity, and displacement of the structure. The absolute displacement of the structure is calculated from the modal amplitudes by multiplication of the mode shapes, and the absolute displacements are output.

C.5 Requirements

The following MathWorks product licence minimum requirements are as follows:

MATLAB	Version 7.8	(R2009a)
Simulink	Version 7.3	(R2009a)
Aerospace Blockset	Version 3.3	(R2009a)
Control System Toolbox	Version 8.3	(R2009a)
Signal Processing Toolbox	Version 6.11	(R2009a)

C.6 Block Diagrams

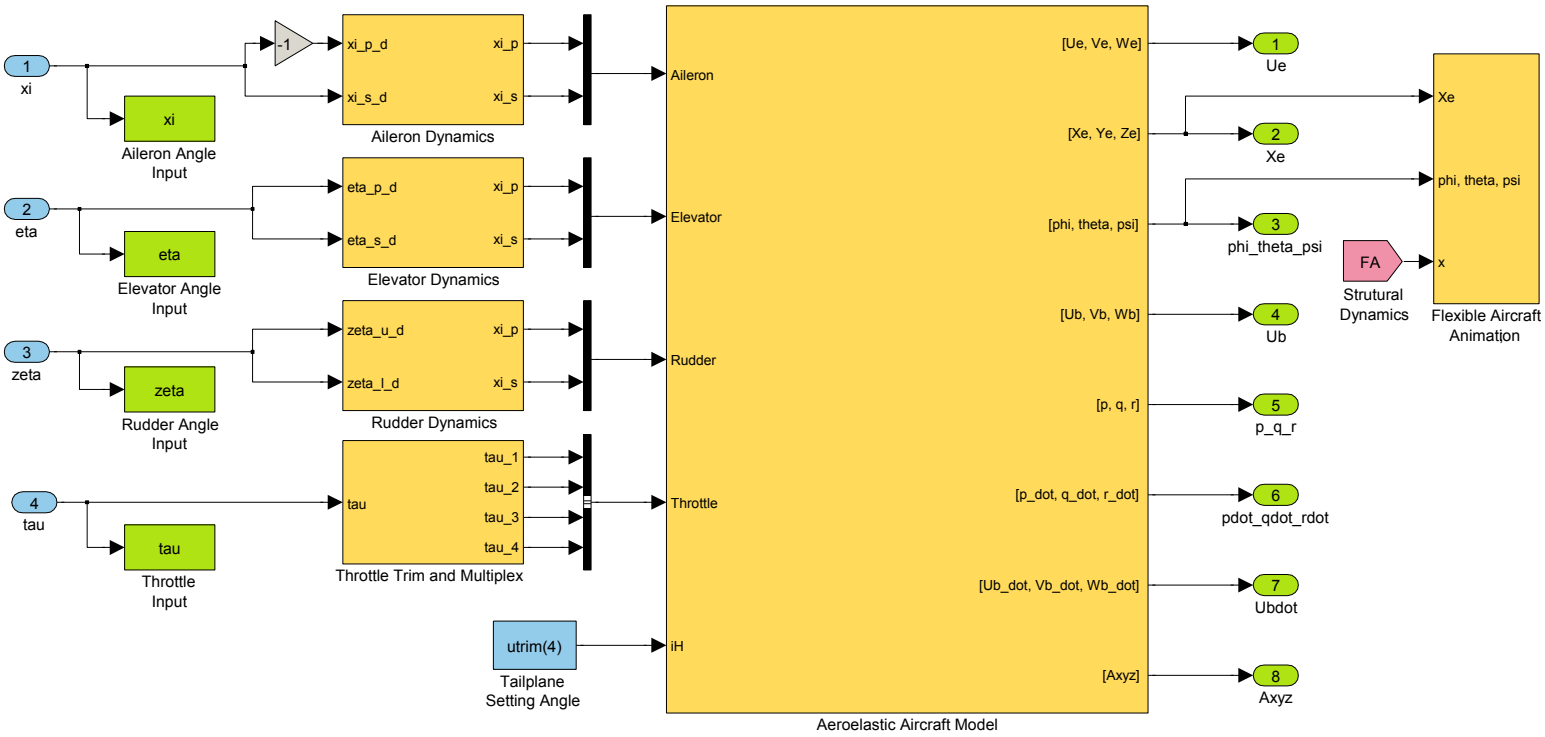

Figure C.4: Aeroelastic Aircraft Model – Model Aircraft

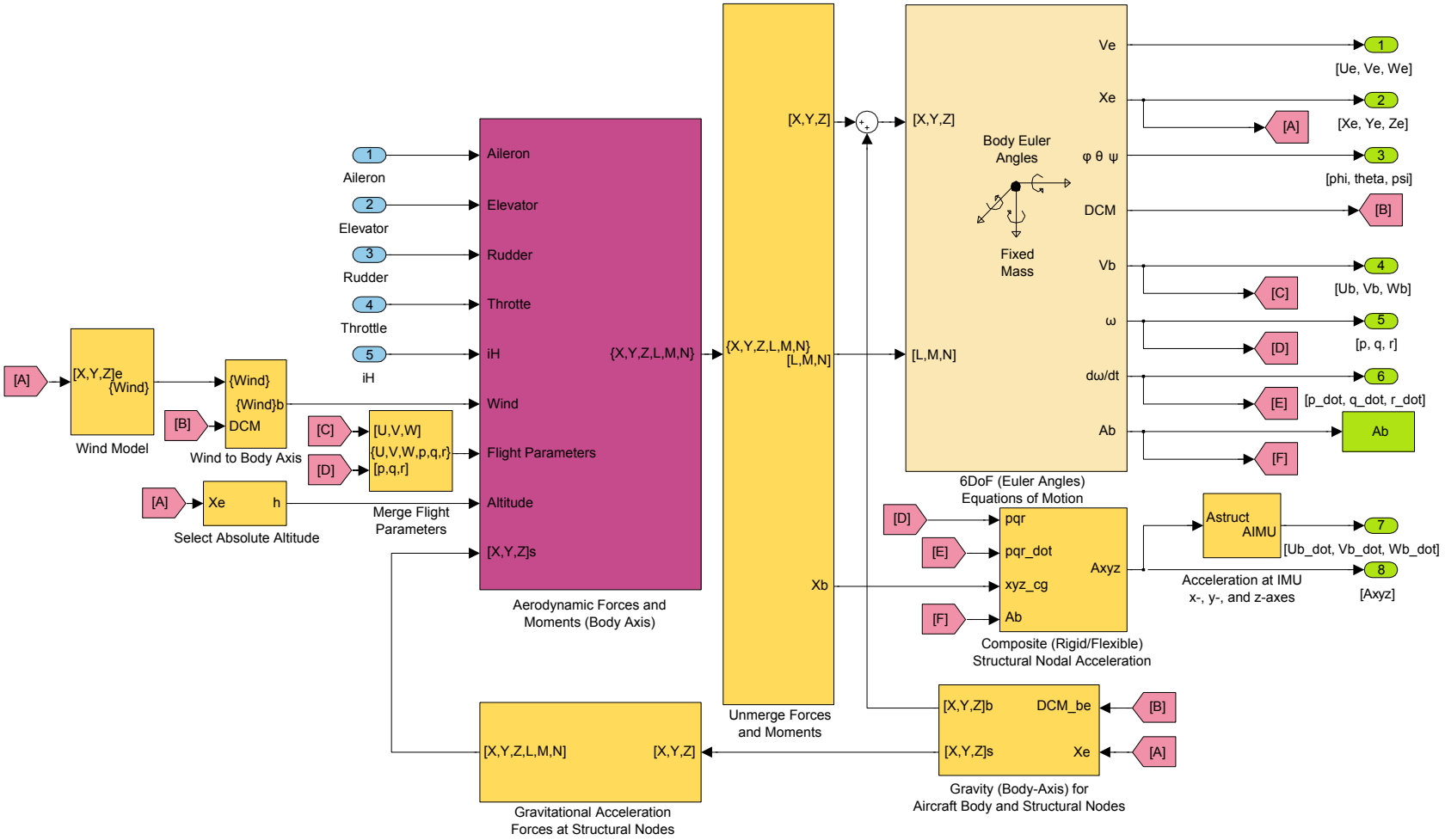

Figure C.5: Aeroelastic Aircraft Model – Equations of Motion

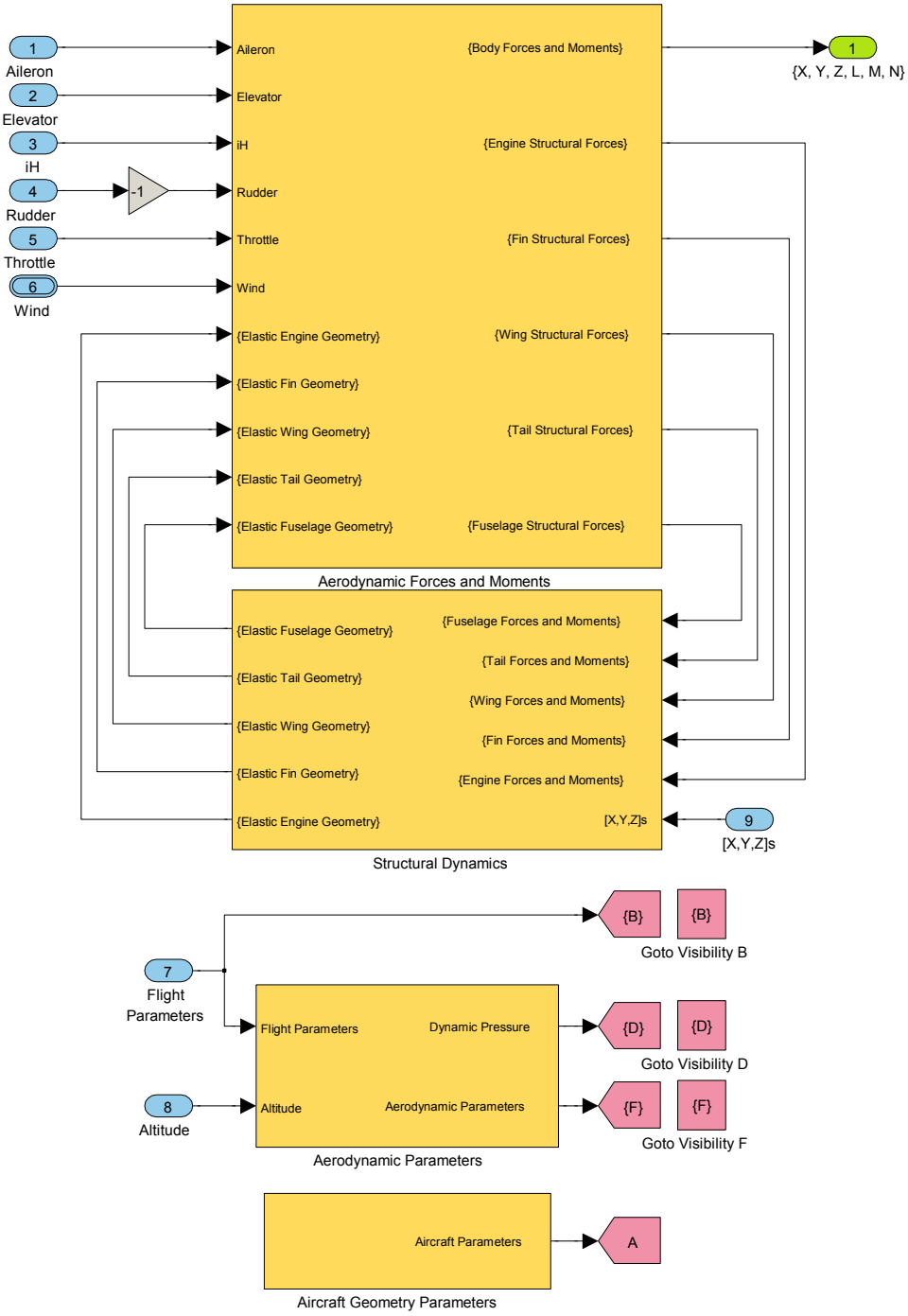

Figure C.6: Aeroelastic Aircraft Model – Aeroelastic Model

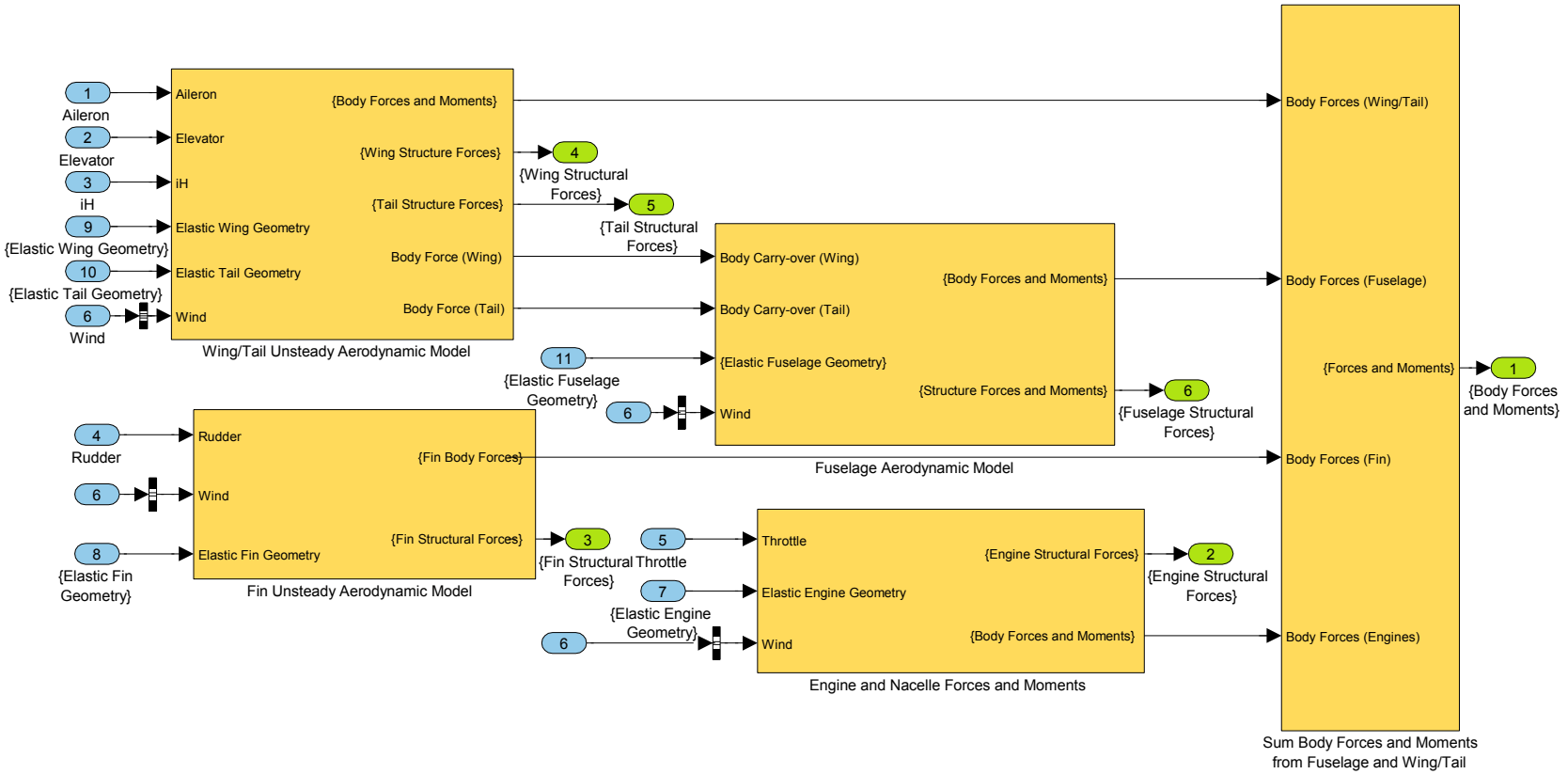

Figure C.7: Aeroelastic Aircraft Model – Aerodynamic Model

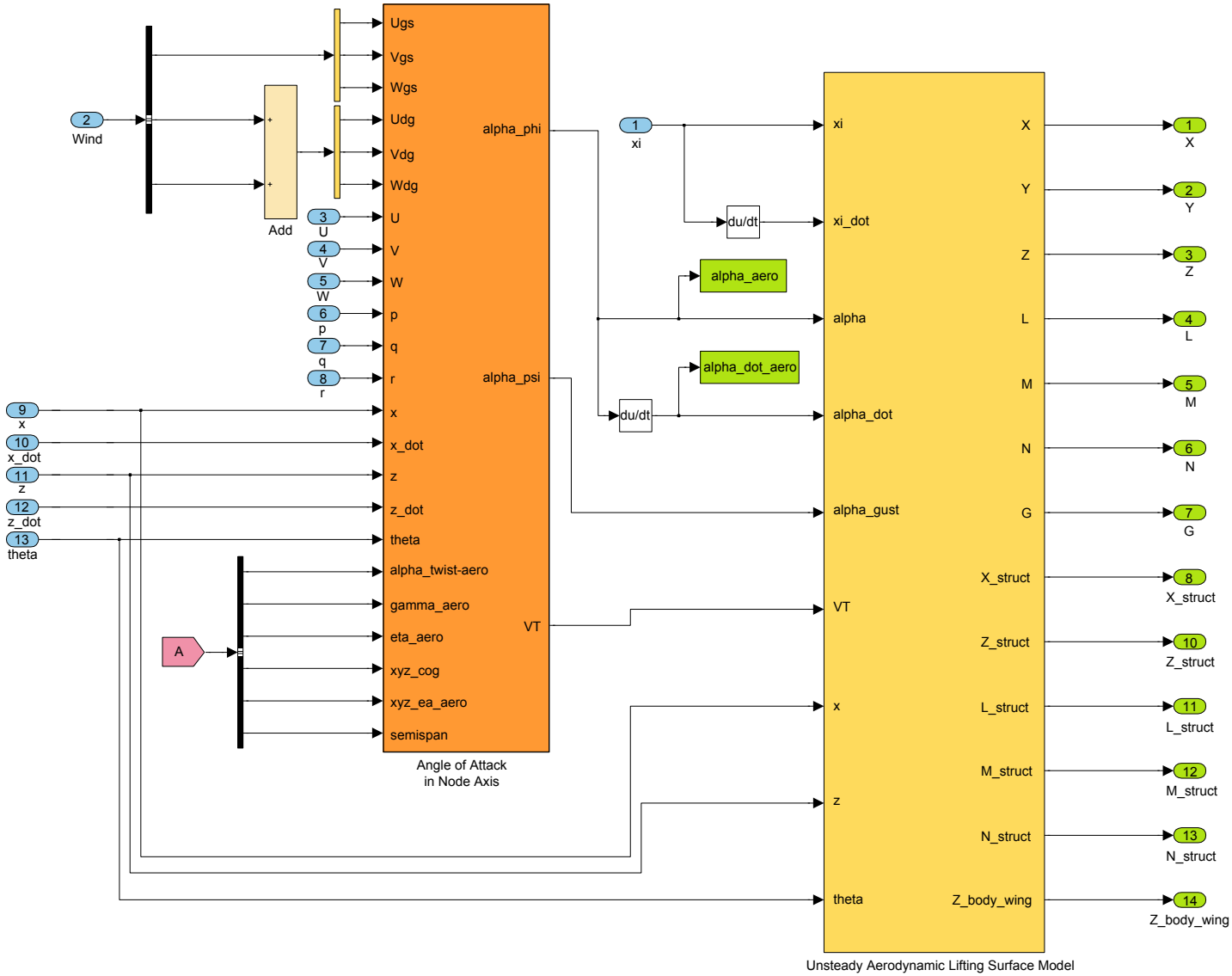

Figure C.8: Aeroelastic Aircraft Model – Lifting Surface Model

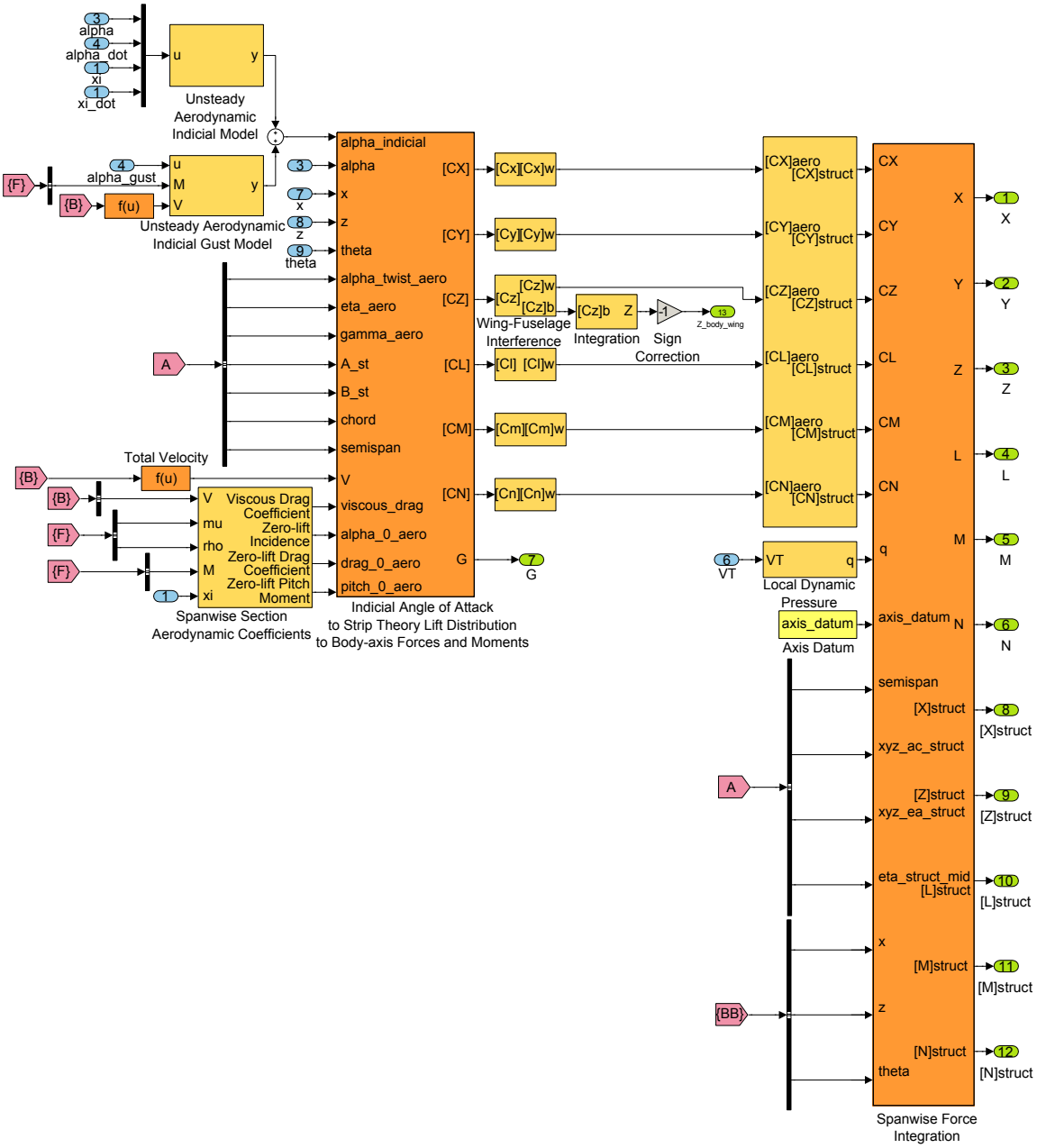

Figure C.9: Aeroelastic Aircraft Model – Unsteady Strip Theory Model

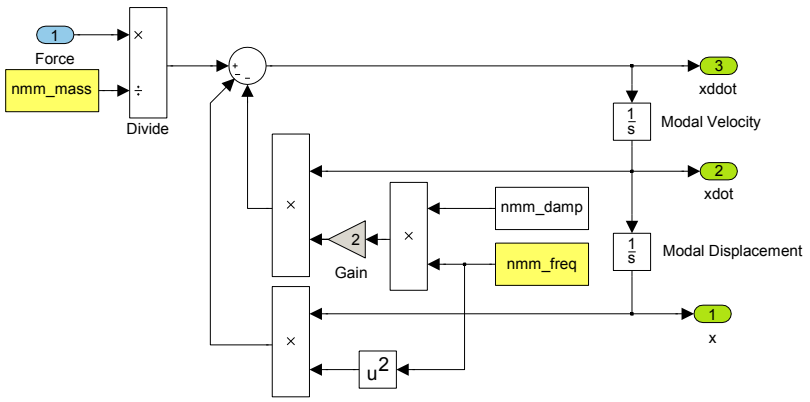

Figure C.10: Aeroelastic Aircraft Model – Structural Equations of Motion

This page is intentionally left blank.

APPENDIX D

Aircraft Geometry

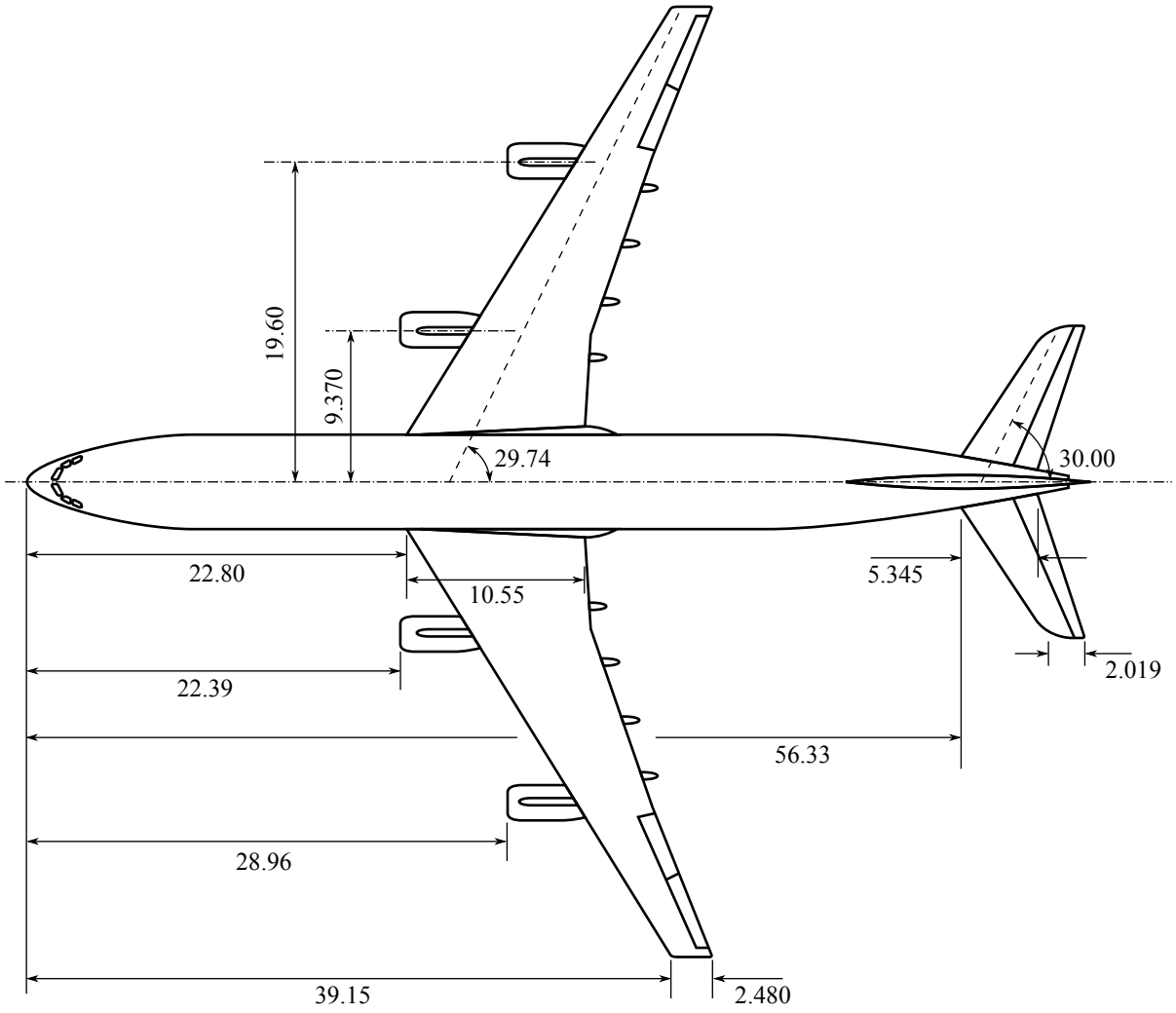

Figure D.1: Aeroplane AX-1 geometry - plan view

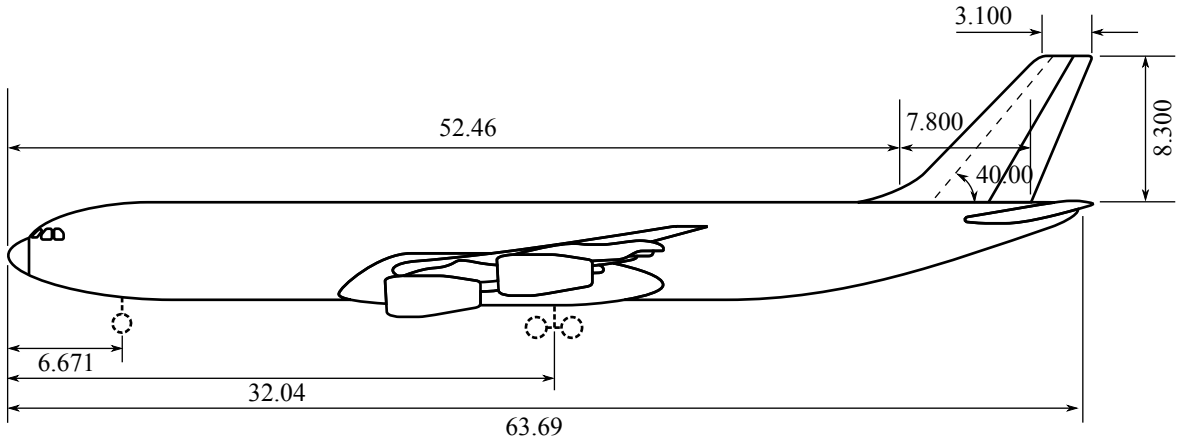

Figure D.2: Aeroplane AX-1 geometry - side view

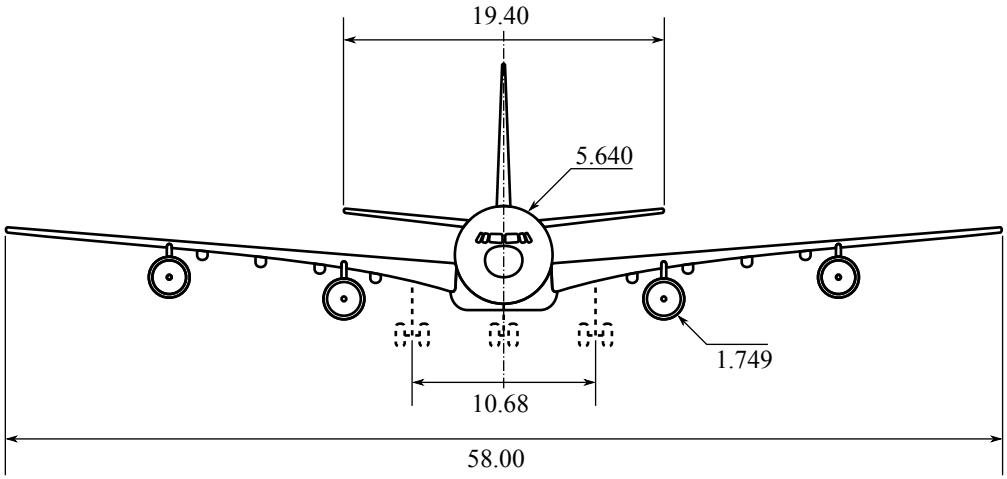

Figure D.3: Aeroplane AX-1 geometry - end view